Laser Powder Bed Fusion of Cemented Tungsten Carbide Cutting Tools

by
Devon Hagedorn-Hansen

Dissertation presented for the degree of
Doctor of Philosophy in the
Faculty of Engineering at
Stellenbosch University

Supervisor: Prof Natasha Sacks
Co-supervisor: Prof Oliver Damm
Co-supervisor: Prof Stephen Matope

April 2022

Declaration

By submitting this dissertation electronically, I declare that the entirety of the work contained therein is my own, original work, that I am the sole author thereof (save to the extent explicitly otherwise stated), that reproduction and publication thereof by Stellenbosch University will not infringe any third party rights and that I have not previously in its entirety or in part submitted it for obtaining any qualification.

Date:

……April 2022……..

Abstract

Cemented carbides are extremely hard, wear resistant materials, and one of the most widely used tool materials in numerous manufacturing industries. Metal cutting tools are commonly manufactured from cemented carbides using standard powder metallurgy processes such as the press and sinter process. The tooling market is highly competitive and the companies with the best research and development departments have the competitive advantage when it comes to cutting edge technology. However, historically, the development process for a new cutting tool or production technology is a lengthy and costly venture.

The use of laser powder bed fusion (L-PBF) for research, development, and small-batch production of cemented tungsten carbide cutting tools has not been extensively reported, and commercialisation does not seem apparent as yet. While the usage of L-PBF to produce cutting tools may be beneficial to advancing cutting tool technology, the process has many inherent drawbacks that affect part quality. However, there are many changes to the current L-PBF process that can be investigated to improve the final quality of L-PBF-produced tools before post-processing. The successful application of L-PBF technology could help develop and manufacture cutting tools at an improved rate.

The aim of this study was to determine and manage the influences of certain factors encountered during L-PBF of tungsten carbide cobalt (WC-Co) and their effects on specific cutting tool properties and cutting performance to produce L-PBF cutting tools that could be comparable to a conventionally produced tool. To accomplish this, three powders were analysed and investigated for their use in the L-PBF process. Then, characterisation of an existing cutting tool was performed to be used as a quality benchmark for L-PBF cutting tools. After a reasonable understanding of powders and conventional cutting tools was obtained, single track scans were performed on a tool steel base plate to understand adhesion and the feasibility of using a conventional base plate.

The next stage of the study involved understanding the effects of different laser parameters and scanning strategies on the track morphology, density, hardness, and cobalt content of L-PBF-produced WC-12wt%Co samples. Various parameter optimisation methods and strategies were tested and L-PBF-produced cutting tools were utilised in preliminary cutting tests to determine their cutting ability and to deduce which factors had the greatest effects on cutting contact time. The L-PBF scanning strategy was observed to be the most significant factor for successful cutting operations. A diagonal raster strategy with an 80-degree alternating rotation produced the best cutting inserts for the specific insert geometry and grade.

Verification WC-12wt%Co inserts were produced with L-PBF for final cutting tests. These inserts were comparable to conventionally produced tungsten carbide inserts with respect to cutting performance indicators such as contact time and workpiece surface roughness. On average, after roughly 16M30S contact time, the L-PBF cutting tools exhibited 0.7 mm maximum flank wear versus 0.4 mm for similar conventional inserts. These results suggest that L-PBF could, one day, be a viable solution for research, developments, and small-batch production of WC-Co cutting tools.

Opsomming

Sinterkarbiede is uiters hard, slytasiebestand en een van die gereedskapsmateriale wat die algemeenste in talle vervaardigingsbedrywe gebruik word. Metaalsnygereedskap word gewoonlik met behulp van standaard poeiermetallurgieprosesse, soos die pers- en sinterproses, uit sinterkarbiede vervaardig. Die werktuigmark is baie mededingend en ondernemings met die beste navorsingen-ontwikkelingsdepartemente, het die mededingende voordeel as dit by die nuutste tegnologie kom. Histories is die ontwikkelingsproses vir ’n nuwe snybeitel of produksietegnologie egter ’n lang en duur proses.

Die gebruik van laser- poeierbedsamesmelting (L-PBF) vir navorsing, ontwikkeling en kleinskaalproduksie van gesementeerde-wolframkarbiedsnygereedskap is nog nie wyd gerapporteer of gekommersialiseer nie. Hoewel die gebruik van L-PBF voordelig vir die bevordering van snygereedskaptegnologie kan wees, het die proses baie inherente nadele wat die gehalte van die onderdele beïnvloed. Daar is egter baie veranderinge aan die huidige L-PBF-proses wat ondersoek kan word om die finale gehalte van L-PBF-vervaardigde gereedskap voor ná-vervaardiging te verbeter. Die suksesvolle toepassing van L-PBF-tegnologie kan help om snygereedskap vinniger te ontwikkel en te vervaardig.

Die doel van hierdie studie was om die invloed van sekere faktore tydens die L-PBF van wolframkarbied-kobalt (WC-Co), en die uitwerking daarvan op spesifieke snygereedskapseienskappe en -snyprestasie te bepaal en te bestuur, om uiteindelik L-PBF-snygereedskap te vervaardig wat met ’n konvensioneel vervaardigde werktuig vergelykbaar is. Om dit te bewerkstellig, is drie poeiers vir gebruik in die L-PBF-proses ontleed en ondersoek. Vervolgens is karakterisering van ’n bestaande snybeitel uitgevoer om as ’n gehaltenorm vir L-PBF-snygereedskap te dien. Nadat ’n redelike begrip van poeiers en konvensionele snygereedskap verkry is, is enkelbaanskanderings op ’n basisplaat van gereedskapstaal uitgevoer om die aanklewing en dus die haalbaarheid van die gebruik van ’n konvensionele staalbasisplaat te ondersoek.

Die volgende fase van die werk het die bestudering van die effekte van verskillende laserparameters en skanderingstrategieë op die baanmorfologie, digtheid, hardheid en kobaltinhoud van L-PBF-geproduseerde WC-12wt%Co-monsters behels. Verskeie parameter-optimaliseringsmetodes en -strategieë is getoets en L-PBF-vervaardigde snygereedskap is in voorlopige snytoetse gebruik om hulle snyvermoë te bepaal en af te lei watter faktore die grootste effek op die snykontaktyd het. Waarneming het aangedui dat die L-PBF-skanderingstrategie die belangrikste faktor vir suksesvolle

snywerk is. ’n Diagonale rasterstrategie met ’n wisselrotasie van 80 grade het die beste snyinvoegstukke opgelewer vir die spesifieke invoegstukgeometrie en -graad wat bestudeer is.

Verdere WC-12wt%Co-snyinvoegstukke is ter bevestiging vir finale snytoetse met behulp van L-PBF vervaardig. Hierdie invoegstukke was met betrekking tot snyprestasie, soos kontaktyd en oppervlakruheid van die werkstuk, met konvensioneel vervaardigde wolframkarbied-invoegstukke vergelykbaar. Na ongeveer 16M30S se kontaktyd vertoon die L-PBF-snybeitel ’n gemiddelde flankslytasie van 0.7 mm teenoor 0.4 mm vir soortgelyke konvensionele invoegstukke. Hierdie resultate dui daarop dat L-PBF in die toekoms wel ’n lewensvatbare oplossing vir die navorsing, ontwikkeling en kleinskaalproduksie van WC-Co-snygereedskap kan wees.

Acknowledgements

I would like to acknowledge the financial support received from the *DSI-NRF Centre of Excellence in Strong Materials (CoE-SM)*. Opinions expressed and conclusions arrived at, are those of the author and are not necessarily to be attributed to the *CoE-SM*. I, furthermore, would like to express my profound sense of gratitude to the following people who contributed in various ways to make this work possible.

My original supervisor *Professor Dimiter Marinov Dimitrov*. Thank you for everything you have done for me and for believing in me. My supervisors, *Professor Natasha Sacks, Professor Oliver Damm* and *Professor Stephen Matope*, thank you for your guidance and invaluable assistance during my write-up.

A special thanks goes to *Anel de Beer, Martin Bezuidenhout, Emad Uheida, Philip Hugo, Xola Madyibi, Ferdi Zietsman,* and *Graham Hamerse* for helping and assisting me throughout the years. Even if it was just for sound boarding or constructive debate, I truly appreciate you giving me the time of day and hearing me out.

The *Industrial Engineering Department* and *Mechanical and Mechatronic Engineering Department* for supporting me with the right equipment and environment to complete my PhD. I would like to acknowledge the support received from the *Central Analytical Facility (CAF)* and the *Barbour Laboratory* at *Stellenbosch University*. I would also like to thank *Leigh Loots* and *Alicia Botes* for their assistance and training on the various equipment used in their facilities. To *Mitsubishi Materials Corporation*, Japan, for their continued support and contributions to the study.

I would like to thank my amazing wife, *Niquelle*, for putting up with me and for all of the sacrifices she made during the writing process. Without her, I would not be the man I am today. I am truly blessed to have such a loving wife. Thanks for keeping the kids out of my office during 'lockdown' as that task alone was probably more challenging than the writing of this thesis. My parents, *Johny* and *Yolande* for their unconditional love, affirmation and never-ending support and encouragement to achieve in life whatever I set my mind to.

My Heavenly Father for granting me the time to complete my PhD when everything was against me. For always looking out for me in the sense that the bigger plan is for my best interest, even if I can't always see it.

In Loving Memory of

Professor Dimiter Marinov Dimitrov

Table of Contents

List of Figures

List of Tables

Nomenclature

Acronyms and Abbreviations

AES	Auger Electron Spectroscopy
AM	Additive Manufacturing
AMTS	Advanced Manufacturing Technology Strategy
ANOVA	Analysis of Variance
ASTM	American Society for Testing and Materials
BCC	Body-Centred Cubic
BD	Building Direction
CAD	Computer Aided Design
CAE	Computer Aided Engineering
CAF	Central Analytical Facilities
CBN	Cubic Boron Nitride
CLS	Concept Laser Slice
CNC	Computer Numerical Control
CNMA	ISO Insert Designation
CRPM	Centre for Rapid Prototyping and Manufacturing
CSC	Centre for Statistical Consultation
CT	Computerised Tomography
CTE	Coefficient of Thermal Expansion
CUT	Central University of Technology
CVD	Chemical Vapour Deposition
DED	Directed Energy Deposition
DMLS	Direct Metal Laser Sintering
DoE	Design of Experiments
EBM	Electron Beam Melting
EDM	Electrical Discharge Machine
EDS	Energy Dispersive Spectroscopy
FCC	Face-Centred Cubic
FDM	Fused Deposition Modeling
FEA	Finite Element Analysis
FEM	Finite Element Method
FFF	Fused Filament Fabrication
FIB	Focused Ion Beam
GE	General Electric
HCP	Hexagonal Close Packed
HIP	Hot Isostatic Pressing
HPD	Hatch Pattern Design
HR	Rockwell Hardness
HRSA	Heat resistant super alloys
HSS	High-Speed Steel
HV	Vickers Hardness
HVOF	High Velocity Oxygen Fuel

LENS	Laser Engineered Net Shaping
LOM	Laminated Object Manufacturing
L-PBF	Laser Powder Bed Fusion
LPS	Liquid Phase Sintering
MAM	Metal Additive Manufacturing
MJM	Multi-Jet Modeling
MMC	Metal Matrix Composite
OFAT	One-Factor-at-a-Time
OM	Optical Microscopy
PBF	Powder Bed Fusion
PCBN	Polycrystalline Cubic Boron Nitride
PCD	Polycrystalline Diamond
PDS	Product Design Specification
PIM	Powder Injection Moulding
PM	Powder Metallurgy
ppm	Parts per million
PSD	Particle Size Distribution
PXRD	Powder X-ray Diffraction
R&D	Research and Development
ROI	Return on Investment
SED	Specific Energy Density
SEM	Scanning Electron Microscope
SHS	Selective Heat Sintering
SLA	Stereolithography
SLM	Selective Laser Melting
SLS	Selective Laser Sintering
SM	Subtractive manufacturing
SSS	Solid State Sintering
STC-LAM	Stellenbosch Technology Centre – Laboratory for Advanced Manufacturing
STL	Stereolithography or Standard Triangulation Language
T3DP	Thermoplastic 3D Printing
TEM	Transmission Electron Microscope
TGM	Temperature Gradient Mechanism
TRS	Transverse Rupture Strength
UAM	Ultrasonic Additive Manufacturing
UV	Ultraviolet
VED	Volumetric Energy Density
WC	Tungsten Carbide
WEDM	Wire Electrical Discharge Machine
XPS	X-ray Photoelectron Spectroscopy
XRD	X-ray Diffraction
2D	Two-dimensional
3D	Three-dimensional
3DP	Three-Dimensional Printing

List of Symbols

Symbol	Description	Units
a_p	Depth of cut	mm
α	Coefficient of thermal expansion	$\mu m/m \cdot K$
A	Area	m^2 or mm^2
γ	Surface tension of liquid	N/m
C	Specific heat capacity	$J/kg \cdot K$
C	Taylor machining constant	
$\frac{\partial T}{\partial x}$ or $\frac{\partial T}{\partial y}$	Temperature gradient in the direction of heat flow	K/m
ρ	Density	kg/m^3
d	Powder particle diameter	m
d_{50}	Average powder particle diameter	µm
D	Thermal diffusivity	m^2/s
E	Young's Modulus	N/m^2
E_l	Linear energy density	J/mm
E_d	Specific energy density	J/mm^2
VED	Volumetric energy density	J/mm^3
ε_0	Permittivity	F/m
ε	Emissivity	-
f	Feed	mm/rev
F	Powder cohesive force	N
F_{ec}	Electrostatic Coulomb forces	N
h	Hatch spacing	mm
h	Convection heat transfer coefficient	$W/m^2 \cdot °C$
ΔH	Latent heat of fusion	J/kg
H	Volumetric Enthalpy	J/kg
h_p	Height of L-PBF part	mm
h_b	Height of base plate	mm
h_s	Enthalpy at melting	kJ/kg
I	Laser intensity	W/m^2
k	Thermal conductivity	$W/m \cdot K$
λ	Thermal conductivity	$W/m \cdot K$
λ	Laser wavelength	nm
K	Bulk modulus	N/m^2
l	Vector length	mm
n	Taylor exponent	
n_s	Laser absorptivity of bulk material	
n	Spindle speed	RPM
P	Power of the laser	W
Q_L	Input laser energy	W

Q_{CD}	Conduction losses	W
Q_{CD}	Convection losses	W
Q_R	Radiation losses	W
q_1	Point charge of particles	C
q_x	Heat transfer rate	W
$\dot{q}$	Energy generated per unit volume	W/m^3
q_c	Heat loss from the surface to the atmosphere	W
q_e	Energy density of the fibre laser	J/m^3
q_g	Internal heat generation (Used by [107])	W
Φ	Internal heat generation (Used by [130])	W
ω	Equivalent radius of the laser beam	mm
r	Distance between powder particles	m
R	Gas constant	kg m²/(s² kg-mole K)
σ	Proportionality constant called the Stefan-Boltzmann constant $5.669 \times 10^{-8}\ W/m^2 \cdot K^4$	$W/m^2 \cdot K^4$
s	Distance between particles	m
s_{th}	Thermal stress	Nm^{-2}
θ	Liquid-solid contact angle	°
τ	Delay period	s
ΔT	Temperature gradient	K
t	Time	s
t	Thickness of L-PBF layer	mm
T	Temperature	K
T	Taylor tool life	min
T_s	Sintering temperature	K
T_ω	Temperature of the surface	K
T_∞	Temperature of the fluid	K
T_0	Initial or ambient temperature	K
T^{inf}	Temperature of the environment	K
U	Heat source due to volumetric absorption of the laser radiation	W
V	Volume fraction	m³
v	Scanning speed of the laser	mm/s
V_C	Cutting speed	m/min
z	Distance from the laser focal point	m

Chapter 1

Introduction

Hardmetals or cemented carbides are one of the most widely used tool materials in numerous manufacturing and heavy industries such as automotive and aerospace manufacturing, oil and gas drilling, mining, and even construction [1], [2]. Metal cutting tools are commonly manufactured from cemented tungsten carbide using standard powder metallurgy (PM) processes, as tungsten carbide (WC) is a hard and wear resistant material. However, in order to meet the ever improving requirements of industry, there are currently a number of researchers and research projects focused on producing cemented tungsten carbide cutting tools with additive manufacturing (AM) technologies [3]–[5].

1.1. Background

Powder metallurgy is the primary solid-state synthesis technique used for production of cemented tungsten carbide parts [6]. The parts are referred to as green parts after the pressing/compaction stage and sintered parts, once they have completed the sintering stage. Depending on the geometry, green parts are conventionally produced by either uniaxial pressing, extrusion processes, or powder injection moulding (PIM). Cemented carbide parts with internal cooling channels and complex geometries are currently only possible with a high level of green machining and finishing, if at all possible. The dies and punches essential to form the desired part geometry, can be costly and time consuming to manufacture and thus require a large initial investment. Over 50% of the manufacturing costs for a cutting insert are spent on the geometric shaping through pressing, grinding, and edge honing processes [7]. The moulds are manufactured to a narrow tolerance to allow clearance between the die and the punches without powder interference in the gap. The press and sinter process is best suited for medium to high production quantities of cutting inserts in order to generate an adequate return on investment (ROI) from the initial die and punch manufacturing costs [8]. Thus, the use of conventional PM processes to produce complex geometry parts in small batches may not be financially viable for specific cases. Therefore, to cost effectively manufacture tungsten carbide tools with internal cooling channels, complex geometries, or in small-lots, engineers and scientists are exploring possibilities to produce tools with additive manufacturing to meet the requirements of industry [8]–[12].

ASTM F2792-12a defined additive manufacturing as “the process of joining materials to make objects from 3D model data, usually layer upon layer, as opposed to subtractive manufacturing methodologies” [13]. A number of research efforts have been aimed at the application of various

additive manufacturing technologies to produce tungsten carbide parts or tools [14]. These technologies can be distinguished by the requirement for post sintering. The technologies that require post sintering are 3D gel-printing [15], [16], Thermoplastic 3D Printing (T3DP) [17], [18], Slurry-based Three Dimensional Printing (3DP) [19], and Binder Jetting [20]. With all of these processes, the tungsten carbide raw materials are mixed with organic binders for shape forming. The shape is then fashioned in a layer-wise manner to form the green parts. The green parts then require a sintering process to remove the organic materials and to obtain the final desired geometry. The AM technologies that do not conventionally require post-sintering processes are Laser Engineered Net Shaping (LENS) [11], [21], Electron Beam Melting (EBM) [22], [23], and Laser Powder Bed Fusion [24]–[26]. The powders used in these processes do not contain organic binders and are generally consolidated by the laser or electron beam, one layer at a time until the final part is formed. The L-PBF process has by far received the most attention in comparison to other technologies with respect to tungsten carbide additive manufacturing [27]. However, due to tungsten's intrinsic properties (such as high melting point, good thermal conductivity, high ductile-to-brittle transition temperature, and high surface tension), the L-PBF of tungsten carbides is a challenging task, mainly resulting in cracked and/or porous parts [28]. But even with these negative issues, there have been some positive publications of work on L-PBF of crack free and high-density parts [29], [30].

Laser powder bed fusion is suggested as a possible alternative to the press and sinter process for research and development (R&D) and special tool production. L-PBF has been selected because of its superior process flexibility and its ability to produce highly complex geometries with relative ease [31]–[33]. Currently, there is limited knowledge on some of the influencing factors associated with L-PBF of tungsten carbide cutting tools. There are also a number of issues associated with and inherent to the L-PBF process, especially when being applied to a metal matrix composite (MMC) like cemented tungsten carbides. Some of the defects observed in WC-based parts produced with L-PBF are pores, cracks, delamination of layers, warping or curling, and changes in local material properties [34]. Numerous studies exist covering the use of tungsten carbide based powder composites in the L-PBF process, to manufacture parts for cutting or high wear applications [4], [25], [35]–[37]. However, there are a limited number of publications [3], [29], [30] that could be found from main stream sources, which link the L-PBF process parameters used, to the cutting or wear performance of the L-PBF produced samples. Despite the progress and benefits presented by L-PBF, these issues remain a significant challenge that limit the wider uptake of the process for commercial applications.

1.2. Problem Statement

There are numerous interactions between factors, such as laser parameters and scanning strategies, which influence integrity and quality of tungsten carbide cobalt cutting tools produced using L-PBF. A lack of understanding of these interactions, inhibits the effective use of the L-PBF process for R&D of new cutting tools and commercial manufacturing of small-batch special tooling. Scarce availability of information and publications on cutting tests performed with L-PBF cutting tools, further limits the understanding of these factors and their effects on cutting performance.

1.3. Research Aim and Objectives

The main aim of this research was to study and manage the influences of certain factors encountered during L-PBF of WC-Co and their effects on specific cutting tool properties and cutting performance in order to produce a cutting tool with L-PBF that could be comparable to a conventionally produced tool.

In line with the main aim of this research, the specific objectives of this study were to:

1. Research and understand the history, materials, manufacturing processes, and properties required for conventional cutting tools, ss well as the L-PBF process and the drawbacks and limitations of manufacturing tungsten carbide cutting tools using L-PBF.
2. Experimentally determine and model the effects of specific influencing factors that occur during L-PBF production of WC-Co cutting tools with a focus on the effects of the laser parameters and scanning strategies on specific cutting tool properties.
3. Investigate how the various parameters, scanning strategies, and part properties affect the cutting ability of L-PBF WC-12wt%Co cutting tools.
4. Experimentally compare the cutting performance of optimised L-PBF produced cutting tools to commercially available cutting tools of a similar grade for a specific application and material.

1.4. Research Methodology

To achieve the different research objectives, the research was separated into various stages and experiments. An overview of the research methodology followed can be observed in Figure 1.1. Each aspect of the research methodology is colour coded and can be linked to the various chapters highlighted in Figure 1.2. The research initially focused on a comprehensive literature study to aid in understanding metal cutting tools and the various qualities they possess. The attention was then shifted to the L-PBF process and its utilisation to produce WC based components. Process parameters and scanning strategies were identified as critical to improving the quality of WC-Co components with L-PBF. Three studies were conducted to gain a deeper insight into the powders available, cutting tool qualities, and various strategies that could be used to improve the results and feasibility of the

study. To understand the effects of different process parameters on the properties of L-PBF produced tungsten carbide tools, several experiments were designed and conducted. All the results were derived through physical experimentation and not simulation. A combination of qualitative and quantitative analyses was employed to evaluate the responses of various factors. To link some of the factors and properties of samples produced with L-PBF to the cutting ability, preliminary and verification cutting tests were performed.

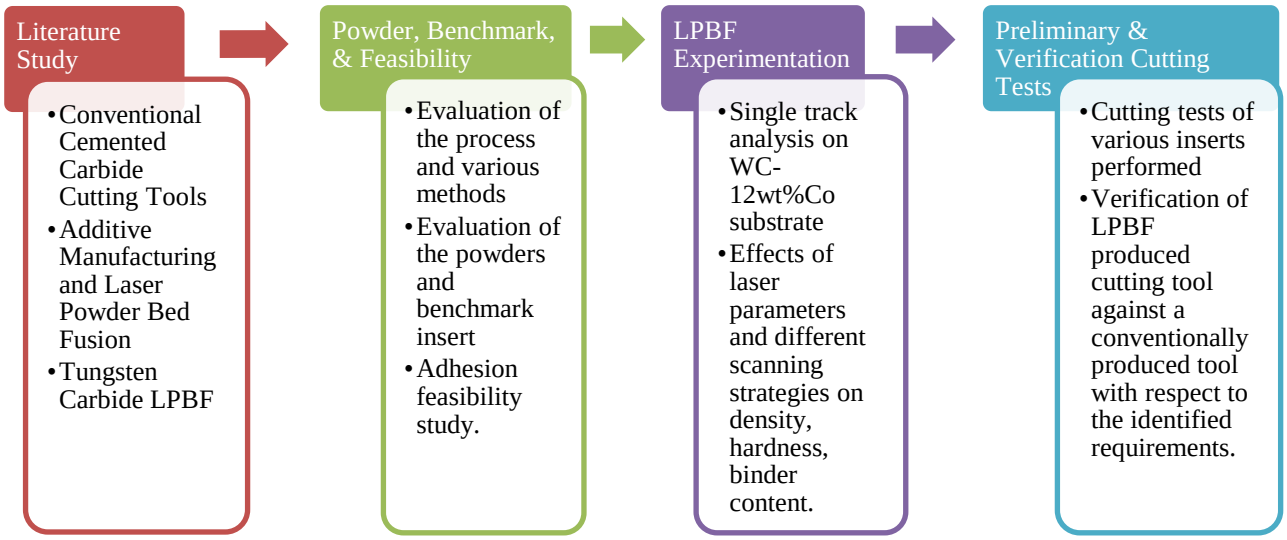

Figure 1.1: Summary representation of the phases of research methodology

1.5. Scope and Limitations

In order to accomplish the objectives of this study efficiently, a well-defined scope was crucial. An understanding of the machinery and measurement instruments that were available for use in this study was fundamental to developing the scope and defining the limitations. The experimental and research outputs are generally limited by the capabilities of the research instruments and machinery, as well as the operators knowledge of them. To complete the research, several machines and apparatus were used. These machines and apparatus can be reviewed in greater detail in Appendix A alongside their specifications and setup processes. The scope was developed and refined over the course of the study as specific knowledge was obtained and certain changes occurred. The general scope and limitations in this study are listed below.

- Through the powder study in Section 6.1 where three different powders were analysed, the powder selected for all of the proceeding L-PBF optimisation studies was the WC-12wt%Co, agglomerated and sintered grade from Praxair Technology Inc. (Connecticut, USA).
- There are two cutting tool types used in metal cutting operations namely, integral tools and solid tools. In this study the focus was on the inserts of specific integral tools.
- For parameter and process optimisation, the power limitations for the L-PBF process were set to 200 W due to the restrictions of the readily accessible L-PBF machine.

- Although heating of the powder during the L-PBF process was reported to be beneficial for WC-Co parts [3], [4], a L-PBF machine without preheating capabilities was used considering there were none readily available in the geographical location of this study.
- An infinitely variable speed lathe is preferred per the ISO 3685:1993 Standard for the cutting tests. However, in this study, a conventional geared lathe with set spindle speeds was used due to the availability of the machines.
- To reduce the costs of the L-PBF process, the goal was to only utilise the commercially available recoater blades, base plates, and software to achieve the objectives of the study.
- Since the costs of parts increase proportionally with the number of processes applied to them, the intention of this study was to also keep the pre and post processing operations to a minimum throughout.
- Post heat treatment operations can have significant effects on the final properties of the L-PBF WC-Co parts as highlighted by Agyapong [38]. Thus, to limit the number of factors, no post heat treatment operations were performed on any of the WC-12wt%Co parts produced with L-PBF.

1.6. Scientific Contribution of the Research

The original contributions of this research in the field of L-PBF of WC-Co cutting tools are summarised in the three areas that follow:

- Several laser parameters were tested throughout the study to gain a better understanding of the various influencing factors and their effects on the L-PBF produced WC-12wt%Co cutting tools. The influence of different parameter sets for laser power, scan speed, hatch spacing, and scanning strategy were evaluated for the density, hardness, and cobalt content responses. It was found that evaporation of the cobalt binder cannot be attributed to the laser power and scan speed alone and other factors such as scanning strategy, maximum vector length, and scan rotation between layers should be considered.

- Several scanning strategies were developed and utilised throughout this study. The effects of different maximum vector lengths, hatch spacings, and scanning strategies on the density, hardness, and cobalt content were also performed and found to have significant effects on a parts density and hardness.

- The various parameters, tool properties, and scanning strategies were linked to the cutting ability for L-PBF WC-12wt%Co produced tools. A L-PBF tool was manufactured and tested against conventional inserts in the cutting of cast iron. This was different to the works of other researchers since a different grade and workpiece material was used. The cutting tests were successful even without any preheating or thermal post processing being applied to the L-PBF cutting tools.

1.7. Dissertation Outline

The dissertation is logically separated into 9 chapters excluding the appendices (Figure 1.2). This chapter (Chapter 1) introduces the area of interest for this research, the background, problem statement, and the research aim and objectives. An overview of the research methodology, scope and limitations, as well as the scientific contribution of the research were also discussed. To provide the reader with a better understanding of the development of cutting tools, manufacturing processes, and the different requirements, Chapter 2 discussed the history, materials, manufacturing processes, and properties required for conventional cutting tools. Chapter 3 introduces laser powder bed fusion and how it is classed under the different additive manufacturing technologies. Emphasis is placed on the L-PBF process parameters, and the different phenomena present during the process. Chapter 4 specifically reviews the studies where the L-PBF process was applied to tungsten carbide-based materials. The gaps in literature were also analysed and discussed in this chapter.

The problem solving and experimental methodologies are presented in Chapter 5, for the proceeding experimental chapters. The analyses of the different powders available and the benchmarking of the conventionally produced cutting tool were performed alongside a single-track feasibility study. These studies formed Chapter 6. Chapter 7 includes all the process and parameter optimisation studies that were performed. Each of the studies in Chapter 7 were derived from various perspectives in order to obtain different solutions to the problem. The resulting optimised samples produced throughout the different studies were utilised in preliminary cutting tests, which were reported in Chapter 8. The verification of optimised L-PBF inserts and testing against conventionally produced ones were also included in this chapter. The research conclusions, contribution to the practice and field of study, as well as future work are summarised in Chapter 9.

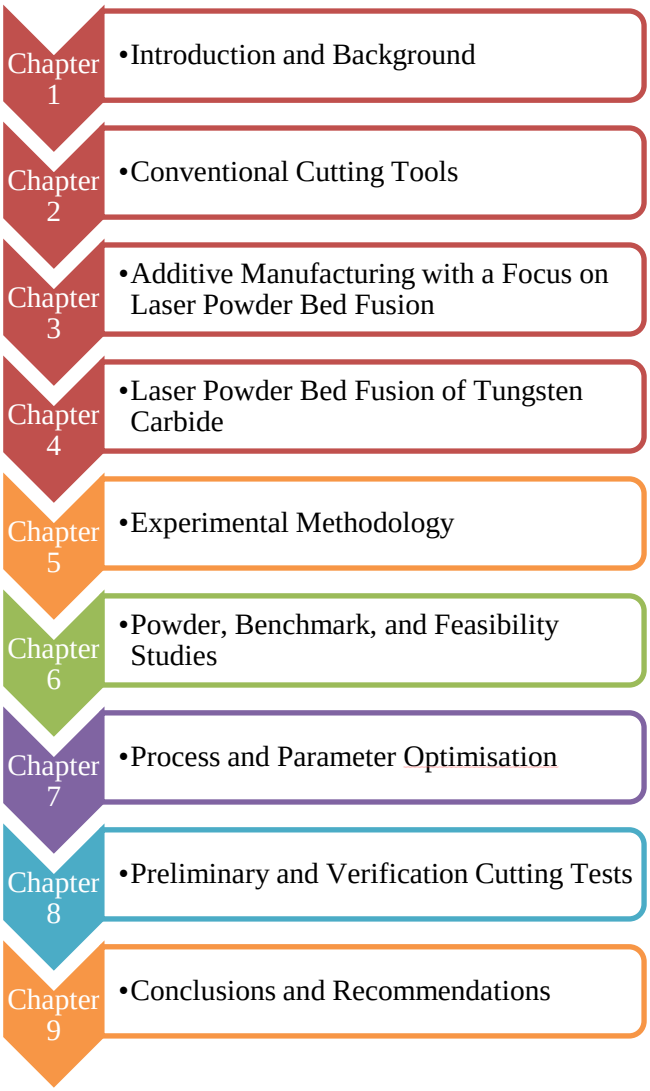

Figure 1.2: Outline of the different sections in this dissertation

1.8. Summary of Chapter 1

Chapter 1 presented the introduction to the study and some background to the problem. A problem statement was formalised along with the main and specific research objectives. An overview of the research methodology was displayed and some of the specific research aspects were discussed briefly. The scope and limitations, and scientific contributions of the study were brought forward, before the final outline of the dissertation was revealed and briefly discussed.

Chapter 2
Conventional Cutting Tools

This chapter discusses cutting tools and cutting tool materials. Firstly, the history of the cutting tool is discussed to understand the timeline for development of various cutting tool materials and subsequently how the cutting tool has improved throughout the years. This should also assist the reader with understanding the lengthy time factors for research and development of new tools and materials. Then tool materials, with a focus on cemented carbides, are discussed, to gain an understanding of the various materials available and their characteristics and properties. This is then followed by the cutting tool development and manufacturing processes. The reader should take note of the iterative and lengthy process for the development of new cutting tools, as well as the process chain for manufacturing a cutting tool. One should note how each process in the manufacturing chain has an influence on the next, as well as on the final quality of the tool. The chapter ends with the discussion of cutting tool characteristics as well as the wear and failure modes of cutting tools. These sections are fundamentally important in order to understand what specifications for a cutting tool manufactured with a different process, like L-PBF, should be considered and what are the failure modes and factors acting on the degradation of the current cutting tools.

2.1. The History of the Cutting Tool

Cutting tools are used for a number of tasks in our everyday lives. Regularly used cutting tools can be found in the form of knives or razor blades. More industrialised cutting tools can be found in mines, woodworking shops, or metal-working shops. In the context of metal cutting, a cutting tool can be defined as any tool that is used to remove metal from the workpiece body by shear deformation [39]. To achieve successful material removal from the workpiece, the cutting tool must be mechanically harder than the material to be machined. Cutting tools first became popular during the industrial revolution in the nineteenth century.

One of the earliest reported advances in cutting tool history is one made by British metallurgist, Robert Forester Mushet in 1868. He discovered that adding tungsten to steel can improve the hardness and subsequently the tool life [40]. Mushet steel was considered to be one of the first tool steels which later led to the discovery of high-speed steels (HSS). In 1898, an American engineer by the name of Frederick Winslow Taylor succeeded in developing a high speed steel that maintained its hardness under high temperature conditions [41]. This led to the dramatic improvement in the machining of iron. Taylor also studied cutting tools and their performance and developed the Taylor equation for tool life. The simple equation was derived as [41]:

$$V_C T^n = C \qquad (2\text{-}1)$$

Where V_C is the cutting speed, T is the tool life, n is the Taylor exponent, and C is a constant. Both C and n depend on feed, depth of cut, work material, tooling material, and the tool life criterion used.

The ever-increasing need for cutting tool materials that were capable of enduring higher cutting speeds and high temperatures led to the development of cemented carbide. Cemented carbide was developed in the 1920's by German scientists named Dr Karl Schroter and Dr Heinrich Baumhauer of Osram Lamp Works. Cemented carbide transformed the cutting tool industry by achieving steel cutting speeds of almost four times faster than the cutting speeds of HSS. In 1926, a German company named Friedrich Krupp AG (now ThyssenKrupp AG) successfully marketed and sold cemented carbide products under the name "WIe DIAmant" or WIDIA (like diamond) [42], [43]. In 1928, American company General Electric (GE), marketed cemented carbide products under the name Carboloy [41]. At the same time, Japanese company, Sumitomo Electric Industries Ltd. succeeded in the test production of a cemented carbide wire drawing die [44]. Japanese companies such as Toshiba and Mitsubishi Materials also established their own research and development facilities in order to develop cemented carbide cutting tools. Tungsten carbide, titanium carbide (TiC), tantalum carbide (TaC), and niobium carbide (NbC and Nb2C) were the most popular hard carbides that were and are currently used in the tooling industry [39]. The additions of these carbides have been studied and performed over the years since tungsten carbide was first used in tooling. The timeline of the development of cemented tungsten carbides and the technologies related to processing them from 1920 to 1997 can be observed in Figure 2.1.

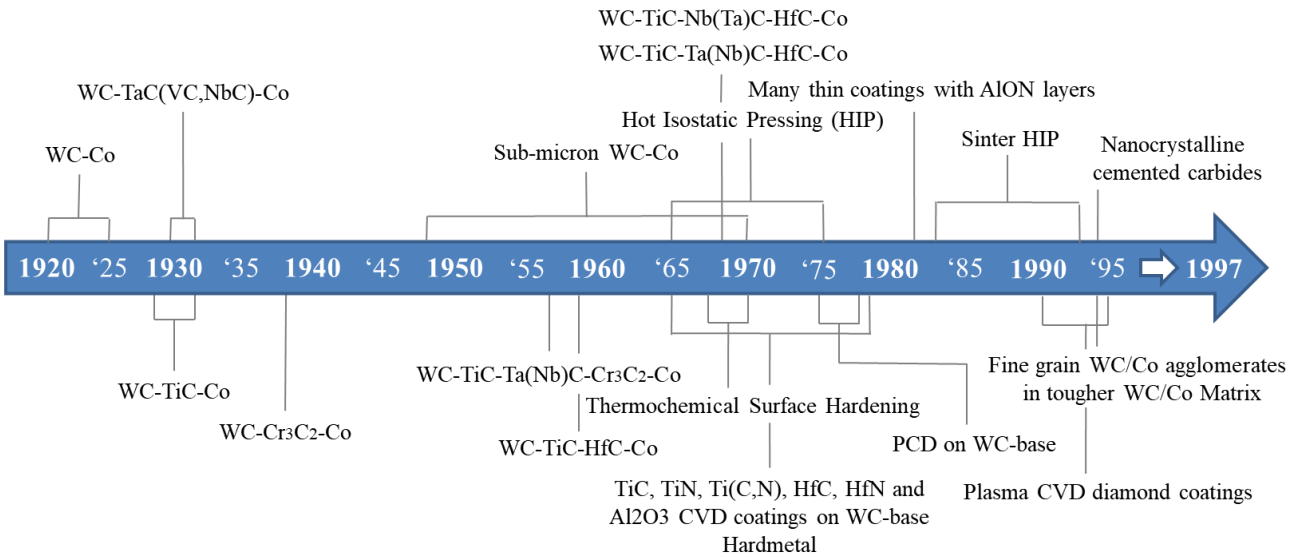

Figure 2.1: Timeline of the Development of Cemented Tungsten Carbide adapted from [42]

Ceramic tooling was introduced in the middle of the 20th century. Ceramic tools contain aluminium oxide (Al2O3), silicon nitride (Si3N4), and sialon grains, which are sintered under high temperatures

(1700 ºC) and pressure (25 MPa). Unlike the majority of cutting tools, ceramic cutting tools do not rapidly decrease in hardness at elevated temperatures. Ceramic tools are capable of retaining their hardness under these conditions. Ceramic tools however, do lack in toughness and as a result, do not handle any types of shock or impact during machining [45].

In 1930, a hard material which consisted of carbides other than just tungsten was developed. Cermets were not widely used due to their inferior toughness compared to cemented carbide. A cermet is a composite material made up with a combination of ceramic and metallic materials (ceramic + metal). After years of research and development, cermets were developed for cutting tool applications owing to their extremely low reactivity with steel. Cermets are commonly used as a finishing tool material [44].

Around the 1950's, polycrystalline diamond (PCD), cubic boron nitride (CBN), and polycrystalline cubic boron nitride (PCBN) were introduced to the industrial market. These materials exhibit extremely high hardness, second only to diamonds. PCD, CBN and PCBN tools possess great wear resistance but lack toughness. They also react with iron, which makes them unsuitable for machining of steels [39].

Throughout the history of cutting tools there has been an ever-increasing need for cutting tool materials that are capable of enduring higher cutting speeds and high temperatures. The leading company in the cutting tool industry, Sandvik, spent roughly 3,532 million SEK on research and development in 2016. This corresponded to roughly 4% of the Sandvik Group's revenues for the year. Sandvik Coromant reported that they spend more money on R&D than any other company in the metal cutting industry [46], [47]. Kennametal, Sandvik Coromant's biggest competitor, claims that $39.4 million dollars US was spent on R&D activities in 2016 [48]. Kennametal stated that they continually strengthen their competitive position by developing new and innovative metalworking products and services [48]. A definitive relation between R&D expenditure and competitiveness is apparent, as the leaders in the cutting tool industry spend substantial amounts on research and development so as to retain their market share.

As new technologies and materials are developed, higher quality cutting tools can be produced, thus resulting in a drastic increase in cutting speed capability [41]. In the timeline in Figure 2.1 some of these technologies are highlighted, including the introduction of hot isostatic pressing (HIP) and plasma chemical vapour deposition (CVD) coatings. Technological processes such as HIP and CVD being applied in the tool manufacturing industry brought about a harder, denser, and superior cutting tool. Research on selective laser sintering of tungsten carbide powders started in 1992 by Zong et al. [26]. There have been a number of projects and publications since then [49]–[52], which are discussed

in Chapter 4, but no commercialisation potential at this point is apparent. Perhaps in time and with more research being funded in this avenue, L-PBF will become the new HIP technology for tungsten carbide tools.

2.2. Materials for Cutting Tool Manufacturing

A quality of a good cutting tool material is the ability to simultaneously withstand large mechanical loads and high temperatures. Temperatures in the chip and tool interface can reach in excess of 700 °C, thus making it important for the substrate material to be physically and chemically stable at these elevated temperatures [53]. The material hardness must also be maintained during the exposure to these high temperatures. Other requirements of a cutting tool material are that the tool should sustain a low wear ratio for both abrasion and adhesion wear mechanisms. Subsequently, the toughness of the material should also be high enough to avoid fracture during interrupted or intermittent cutting operations. The most commonly used materials for manufacturing of cutting tools are high speed steels, cemented carbides, ceramics, and extra-hard materials i.e. polycrystalline cubic boron nitrides and polycrystalline diamonds [39], [53]. For the purpose of this study, only cemented carbides are discussed in further detail.

2.2.1. Cemented carbide

Cemented carbide (also known as sintered carbide or hardmetal) is known for its outstanding wear resistance properties and hardness. Cemented carbide tools are usually made with a mixture of tungsten carbide micrograins mixed with a binder. Tantalum, titanium, niobium, or vanadium carbides can also be added in small proportions. Tungsten carbide tools are conventionally manufactured using high pressure and temperature. Tungsten carbide on its own is a brittle material and a binder such as cobalt, nickel, or even iron is required to fuse the carbide micrograins during the sintering process [53]. Tungsten carbides are sorted by different grades according to what application they can be used in, as well as their underlying constituents. There are two main factors that define a carbide grade:

1. The ratio of tungsten carbide and the binder. The binder content usually ranges from 6 to 15%. Cobalt is the most common binder but can be substituted for nickel, chromium, molybdenum, iron, or a combination of these elements. Cobalt has a particularly high melting point of 1493 °C and a solid solution with WC with a eutectic at 1275 °C is formed, thus reducing any porosity.
2. The grain size, as there are many different powder particle distributions. Carbide powders that have WC particles with a size of 1 µm or more are classified as micrograin grades. Carbide powders with WC particles smaller than 1 µm are referred to as submicron grades. The smaller

the grain is, the harder the hardmetal will be. Hardness increases with the reduction in binder content and tungsten carbide grain sizes and vice versa.

The wide range of applications linked to the tungsten carbide's grain size and cobalt content can be observed in Figure 2.2. For metal cutting it should be noted that the common range for grain size and cobalt content is 0.4 – 2.5 µm and 6 – 17 % respectively. These ranges correspond to a Vickers hardness range of roughly 1200 – 2000 HV (88.3 – 94 HRA) [54].

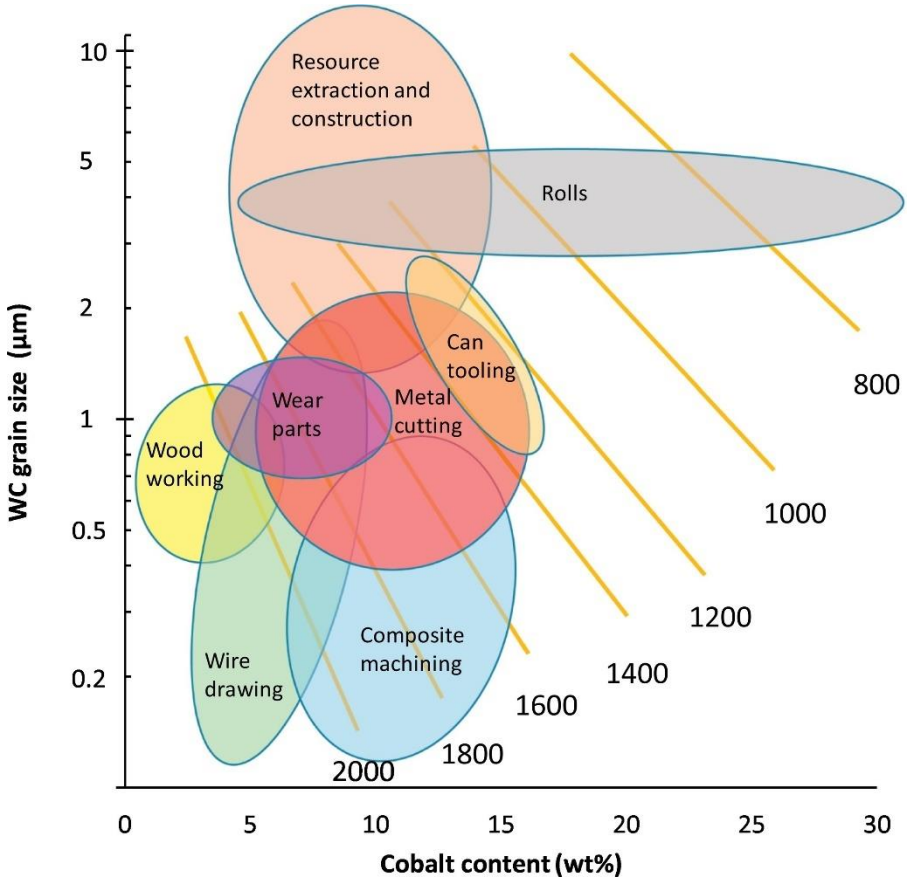

Figure 2.2: Combinations of WC grain size and cobalt content in cemented carbides, showing a wide range of applications. The lines indicate values of microhardness (Vickers) (Reproduced from [54])

The performance and mechanical characteristics of carbide cutting tools are greatly reliant on the type of carbide that is used to produce them, as well as the percentage content of the different elements. For example, increasing the tungsten content results in an increase in wear resistance, however the tool toughness will be negatively affected. A higher cobalt content can improve the toughness of the tool but reduce the hardness and subsequently the wear resistance [39]. The following sections discuss the standards for grade classification as well as the different microstructures and material properties of cemented tungsten carbides.

2.2.1.1. Cemented carbide material grades

There are many different tungsten carbide grades for cutting tools. There are also many different standards/classifications for these grades. Both ISO and ANSI have a grade classification method.

The ISO 513:2012 [55] standard classifies cemented carbides into six groups, namely: P, M, K, H, N, and S following a numerical scale for each of these groups. The ANSI scale makes use of C-x where the x is a numerical scale, and these are then grouped according to their application. The manufacturers of tungsten carbide tools also have their own classification method or designation to their grades. Many attempt to align their classification with those in ISO and ANSI. However, their grades are often grouped into more than one classification. As a consequence, many tools that have the same classification may vary in performance [53]. The ISO group recommendations are [55]:

- P, for low- and medium-carbon steels, and light alloyed steels;
- M, composed of sintered carbides, suitable for stainless steels machining;
- K, for cast irons and alloyed steels, and harder than the P and M series;
- H, for tempered and hardened steels;
- N, for aluminium alloys;
- S, for heat-resistant alloys and titanium alloys.

The two-digit numbers proceeding these letters from 01 to 40 (or 50 in group P) defines the hardness and toughness of the grade. The higher number corresponds to the tougher grades and the lower numbers to the harder grades. The Mitsubishi Materials Corporation cutting tool grades with their ISO comparison are displayed in Figure 2.3.The most versatile grade from Mitsubishi Materials Corporation is the UTi20T grade. It has a low thermal conductivity and a relatively high toughness. This grade has been chosen for further study as it is the most versatile and commonly used grade by Mitsubishi Materials Corporation.

	Work Material	Recommended Grade	Recommended Cutting Speed (m/min)	ISO	Application Range
P	Steel	UTi20T	100 (60 – 130)	P10	
				P20	UTi20T
				P30	
M	Stainless Steel	UTi20T	100 (60 – 130)	M10	
				M20	UTi20T
				M30	
K	Cast Iron	HTi05T	120 (80 – 150)	K01	HTi05T
				K10	HTi10
		HTi10	100 (50 – 150)	K20	UTi20T
		UTi20T	100 (50 – 150)	K30	
N	Non-Ferrous Metal	HTi10	600 (400 – 800)	N01	
				N10	HTi10
				N20	
				N30	
S	Heat-resistant Alloy Ti Alloy	MT9005 RT9005	70 (50 – 100)	S01	MT9005 RT9005
		MT9015 RT9010	60 (40 – 80)	S10	MT9015 RT9010
				S20	TF15
		TF15	50 (40 – 70)	S30	

Figure 2.3: Mitsubishi Materials tungsten carbide ISO grades comparison and characteristics reproduced from [56]

2.2.1.2. Cemented carbide material properties

The mechanical properties of tungsten carbide are strongly dependent on the grade of the material and the microstructure. The material properties of each of the constituents that make up a typical tungsten carbide tool can be observed in Table 2.1. It is important to note that the range for hardness and other properties is quite substantial. This is due to the wide variety of possible microstructures and their effects they have on the material properties. This is also due to the crystal structures and forms that they may be in [54].

Table 2.1: Mechanical and physical properties of the elemental constituents of cemented tungsten carbides

Properties	Units	Compound			
		W	C	WC	Co
Density	**[g/cm³]**	19.3	1.61 - 2.49	15.25 - 15.88	8.8
Hardness	**[HRA]**	66	-	70 - 100	< 20
Melting Point	**[°C]**	3370	3800	3250 - 3460	1493
Boiling Point	**[°C]**	5900	-	-	2927
Tensile Strength	**[MPa]**	980	4.8 - 76	370 - 530	225
Youngs Modulus	**[GPa]**	400	4.1 - 27.6	600 - 686	211
Poisson's Ratio	**-**	0.28	0.17 - 0.23	0.2 - 0.22	0.32
Thermal Expansion Co-efficient	**[µm/m°C]**	4.4	0.6 - 5.2	4.5 - 7.1	12.5
Thermal Conductivity	**[W/m.K]**	163.3	8.7 - 114	28 - 88	69.21
Source	**-**	[57]	[58]	[59]	[60]

Table 2.2 shows the properties of different tungsten carbide grades varying the cobalt content from 6% to 15% and the grain size from ultra-fine to coarse, which is in the range for cutting tools observed in Figure 2.2. The hardness ranges from 90.0 HRA to 92.0 HRA with the varying grades.

Table 2.2: Properties of different tungsten carbide grades that are commercially available

Manufacturer Designation	WC-6wt%Co	WC-10wt%Co	WC-12wt%Co	WC-15wt%Co
ISO	K10	K40	K30	K35
WC [%wt]	94%	90%	88%	85%
Co [%wt]	6%	10%	12%	15%
TiC [%wt]	0%	0%	0%	0%
TaC [%wt]	0%	0%	0%	0%
NiC [%wt]	0%	0%	0%	0%
Rockwell Hardness A [HRA]	92.0	90.0	91.8	91.2
Density [g/cm³]	14.9	14.5	14.2	13.94
Grain Size	Fine	Coarse	Ultra Fine	Ultra Fine
TRS [GPa]	2.2	2.4	3.8	4.1
Source	[61]	[62]	[62]	[62]

It should be noted that many of the suppliers do not share all the information on the compositions and properties of the tools. García et al. [54] explains how many authors report of several different measures related to cemented carbide microstructures such as carbide contiguity, WC grain size, volume fraction of binder, and binder mean free path. However, García et al. [54] goes on to argue that only WC grain size and cobalt content is required for full description of the microstructure, as the other variables are inter-related. So, by adjusting the WC grain size and the cobalt content, the mechanical properties such as bulk/edgeline toughness, hardness, and thermal conductivity can be

optimised. This relationship is displayed in Figure 2.4. Thus, this could justify why many cemented carbide suppliers only supply the cobalt content and grain size to customers.

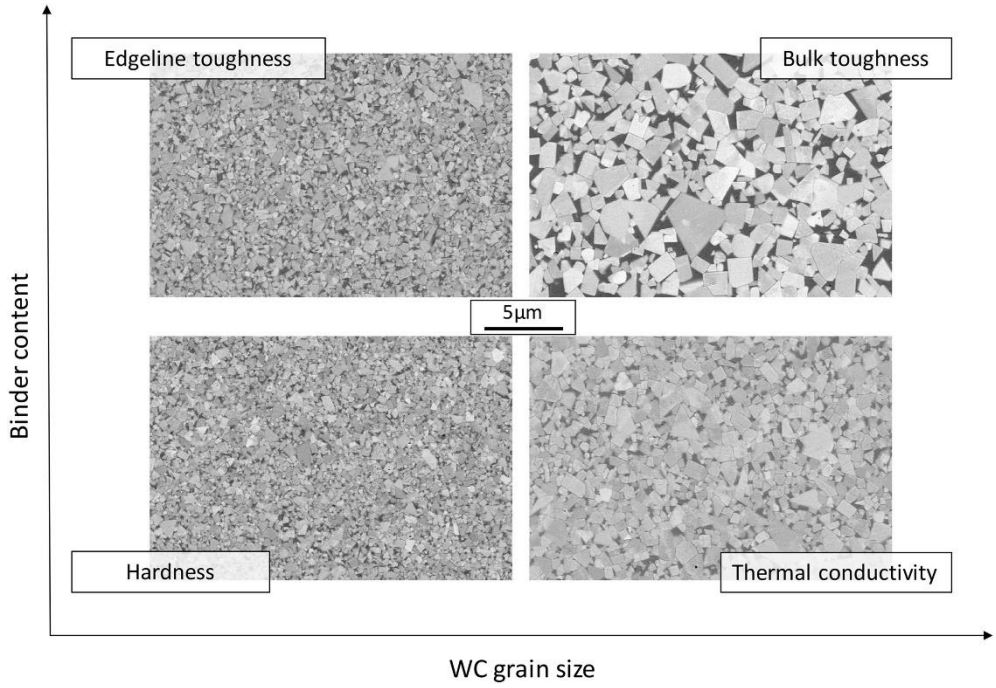

Figure 2.4: Correlation between binder content and WC grain size with main properties of cemented carbides reproduced from [54]

2.2.1.3. Cemented carbide microstructures

For the design of cemented tungsten carbide microstructures, all production steps must be taken into consideration and are crucial for the quality of the final product [54]. By inspecting the microstructure, one can often determine whether the WC-Co tool will be suitable for the final application or not. Many mechanical properties are reliant on the final microstructure of the tool. The transverse rupture strength of a WC-Co composite is determined by intrinsic mechanical properties such as hardness and fracture toughness, which are dependent on the microstructure and the compositions [63]. Figure 2.5 shows the different tungsten carbide microstructures with varying WC grain sizes. The grain size varies from submicron (< 0.5 µm) to micron (> 5.0 µm). The grain size is dependent on several things, namely, the starting powder sizes, the chemical composition of the powder (presence of grain-growth inhibitors), and the energy input of the manufacturing processes into the final part. Controlling grain growth during sintering remains a critical technological challenge [64]. A number of authors [64]–[67] found the grain size to increase in a matter of seconds during the sintering phase. Wang et al. [66] also speculated that there is a critical temperature that exists and above which, the grain growth accelerates dramatically as a function of temperature.

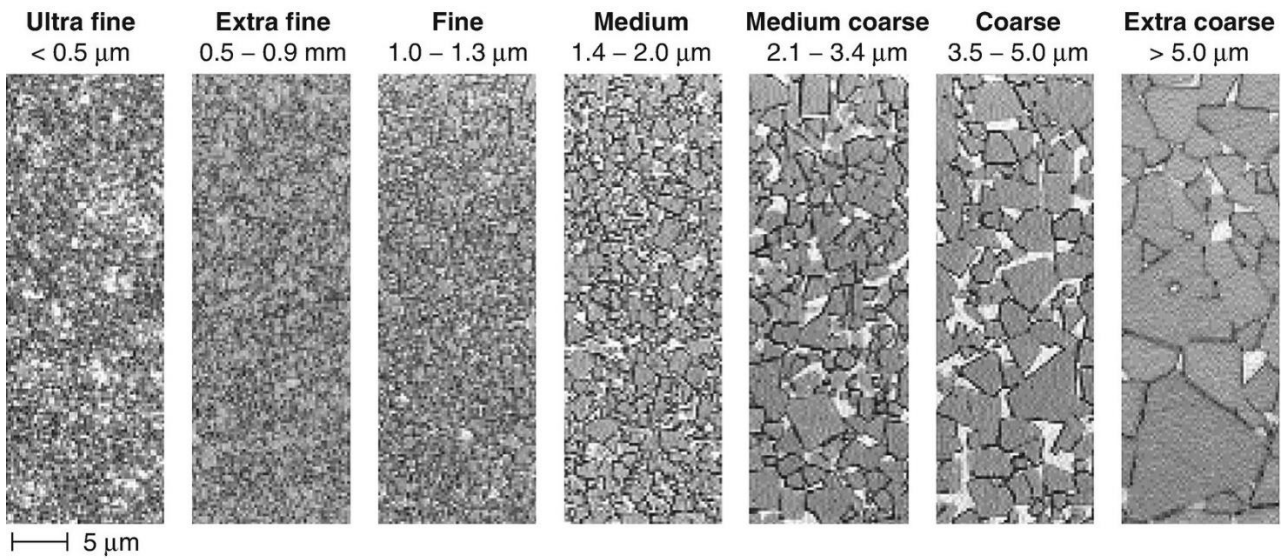

Figure 2.5: WC-Co microstructures for different grain sizes reproduced from [68]

Generally, in the processing of WC-Co, grain growth is a problem and requires the addition of a grain growth inhibitor to the starting powder composition. Achieving a large grain size is generally not a problem with cemented carbide sintering, however, it becomes a challenge when a submicron grain is desired [64]. Fast sintering techniques such as spark plasma sintering (SPS) are characterised by shorter densification time at lower temperatures have been found to have a high potential to make nano-crystalline WC-Co. It should be noted that shape change and faceting of surface WC grains occurred at low temperatures (1000 °C), even with a very fast heating rate of 1400 °C/min [69]. With L-PBF, the heating of the WC powder can occur even more rapidly than with SPS, which makes the process somewhat unique for this application. However, it must be noted that unlike SPS the presence of high pressures (30 – 100 MPa) does not occur during L-PBF, barring any radiation pressure applied by the laser over the spot size diameter (roughly 500 Pa) [70]. The different microstructures of WC can be observed in Figure 2.6. From left to right one can observe how the microstructure varies with changes in the starting powders, and processes.

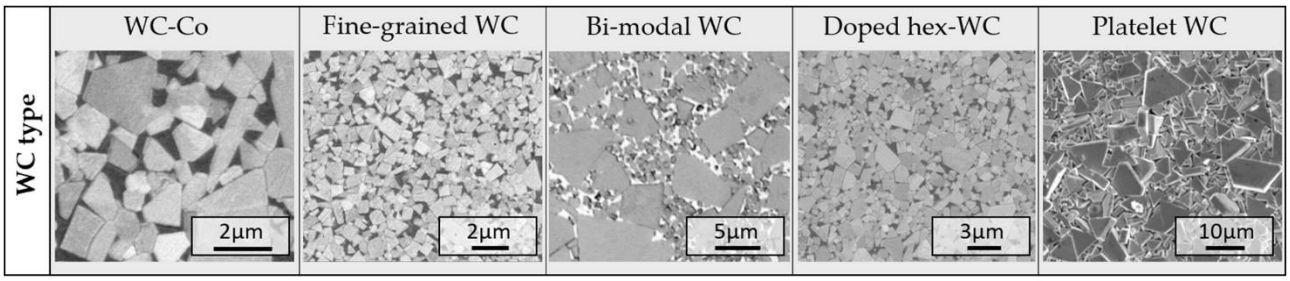

Figure 2.6: Map of real WC microstructures covered in the work by [54]

The difference between the medium (micron grade) and fine (submicron grade) grained microstructures can be observed in the two far left images in Figure 2.6. The grain sizes depend heavily on the process energy into the WC part. The larger grain size will possess a higher toughness, but the submicron grain size will possess a higher hardness. A bi-modal structure is reported to

increase both hardness and the fracture toughness. Bimodality is characterised by two clearly separate peaks in the tungsten carbide grain size. In the middle image in Figure 2.6, one could note the large WC grains mixed with the smaller grains around them. Bimodality occurs through the powder milling process as it tends to broaden the grain size distribution [54]. Doped hexagonal-WC is an alternative technique, which aims to dope the WC grains while maintaining their hexagonal structure. When Ta is used to pre-alloy WC powder, the Ta was found to have a softening effect on the material, which may point to the fact that doping with Ta could improve the ductility. The far-right image shows a platelet WC structure. It is suggested that WC crystallites resembling a platelet structure may have an improved toughness [54]. The carbide crystal shape develops during the first few minutes of the liquid phase sintering stage and is influenced by two processes, namely, carbide crystal growth and shape relaxation [71]. Growth rate anisotropy of WC particles can also lead to platelet shape formation. Each of these microstructures depicted in Figure 2.6 would possess different advantages and disadvantages. Some of these microstructures are produced intentionally but some are the biproduct of the procedure used to process the WC-Co powder. Sintering or melting through L-PBF could present different microstructures, or a combination of the ones depicted in Figure 2.6.

2.2.1.4. Thermal properties of cemented tungsten carbide

Thermal expansion and thermal conductivity are two common thermal properties. Thermal expansion is the tendency of matter to change in volume in a response to temperature changes. Thermal conductivity is the ability of the material to conduct heat [1]. During cutting operations, the tool's cutting edge gets extremely hot while the rest of the tool stays relatively cool. This creates a temperature gradient in the tool which leads to disproportional thermal expansion, resulting in thermal stress build-up in the tool material. Thermal stress can be estimated by the following equation:

$$\boldsymbol{s_{th} = E \times \alpha \times \Delta T} \qquad \textbf{(2-2)}$$

Where s_{th} is the thermal stress, E is Young's modulus, α is the coefficient of thermal expansion (CTE), and ΔT is the temperature gradient [1]. When thermal cycling is experienced during the cutting operation, for instance during interrupted cutting with coolant, thermal fatigue can transpire. Thermal fatigue in carbide tools leads to the formation of microcracks on the surface of the tool, which results in crack initiation sites and the cracks propagate to result in complete tool failure. Thermal properties like thermal conductivity and thermal expansion can be controlled in carbide tools with the grain size and metal binder content. Wang et al. [1] found that the CTE of WC-Co is largely dependent on the cobalt content with a directly proportional relationship. The effects of the grain size on the CTE are not significant and should be ignored. Conversely, Wang et al. [1] also noted that the thermal conductivity of WC-Co is significantly affected by both the WC grain size and cobalt content. It was found that the lower cobalt content and coarser WC grain size led to higher thermal conductivity in

WC-Co tools. With respect to processing WC-Co with L-PBF, a higher thermal conductivity is preferred in order to remove the high heats rapidly from the process. If heat is removed too quickly, thermal cracking could occur during the manufacturing process, however, if heat is removed too slowly, the melt pools will become instable. Thermal conductivity of the powdered material plays a large role in the quality of the final parts [72], [73].

2.3. Cutting Tool Development and Manufacturing Process

There are many different types of cutting operations in the metal cutting industry such as milling, turning, boring, etc. There are two cutting tool types used for these operations namely, integral tools and solid tools. Integral tools comprise of two sections, the cutting edge (insert) and the cutter body (tool holder). Solid tools generally comprise of a solid body cutter with the cutting edge. Both tools have very similar development and manufacturing processes, to a point, when manufactured from tungsten carbide. However, solid tools are easier to redesign and manufacture single components, since the flutes are machined on a tungsten carbide cylindrical rod with a 5-axis grinding machine. Thus, there are no expensive dies or punches needed to change a design, only reprogramming of the 5-axis grinder. There are, however, limitations to this process as well as for the introduction of through spindle cooling channels. For the purpose of this study, only integral tools are discussed further. The following sections describe the iterative cutting tool research and development process as well as the extensive manufacturing process for integral tools.

2.3.1. Research and development process for cutting tools

The development process of a new cutting tool shape is a costly and time-consuming endeavour where designs go through several iterations before ever being considered for production. A new product starts as an idea in the researcher's or engineer's mind. The idea is then designed and then realised using a computer aided design (CAD) program. The design is further refined and then digitally tested through finite element analysis (FEA) and computer aided engineering (CAE). Once digitally refined, a prototype is produced and put through extensive testing and analyses. Repeated refinements, analyses, and testing are performed until the desired results are achieved. In order to produce the prototypes, the conventional press and sinter dies and punches are required. With every new design iteration, a new die or punch set needs to be produced until the prototype is completely refined. Only once the extensive development and testing is completed, the newly refined prototype can move to the development for manufacturing phase [74]. The FEA approach for tool development is not widespread due to the fact that FEA optimised tools cannot be efficiently manufactured using conventional methods [30]. The process followed for the research and development of new cutting

tools is displayed in Figure 2.7 as observed at a conventional cutting tool manufacturer's production facility.

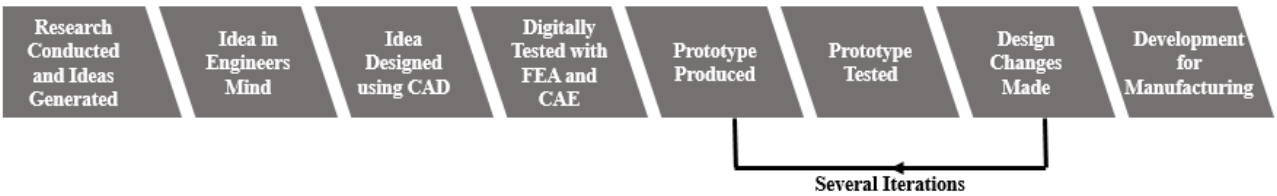

Figure 2.7: Research and development process for the development of a new cutting tool for production

The following must be taken into consideration for each new design:

- Grade of powder
- Micro geometry: cutting edge preparation
- Macro geometry: rake face topography
- Chip breaker geometry
- Coating

By applying the proper combination of micro and macro geometries in conjunction with the proper substrate and coating, the chip control, tool life, workpiece finish, and accuracy can be greatly improved. Correct control of the chip, dissipation or deflection of heat via restricted contact topographies, and reduced cutting forces resulting from positive rake surfaces can lead to improved performance of todays modern moulded cutting insert geometries [75]. Producing special, small batch inserts through L-PBF could remove some of the design constraints currently experienced in the industry. The manufacturing of these unique designs could be improved and be more cost effective in comparison to other currently available processes.

2.3.2. Manufacturing process

From the separate elements to the final insert, the manufacturing process for integral tools has several stages. Some phases have more than one method to them. However, all the manufacturing processes are linked, meaning any change to any of the steps in the process chain, will influence the subsequent process and the quality of the final product. A generic manufacturing sequence from standalone element to final part is summarised from Pappafava [76] in Figure 2.8.

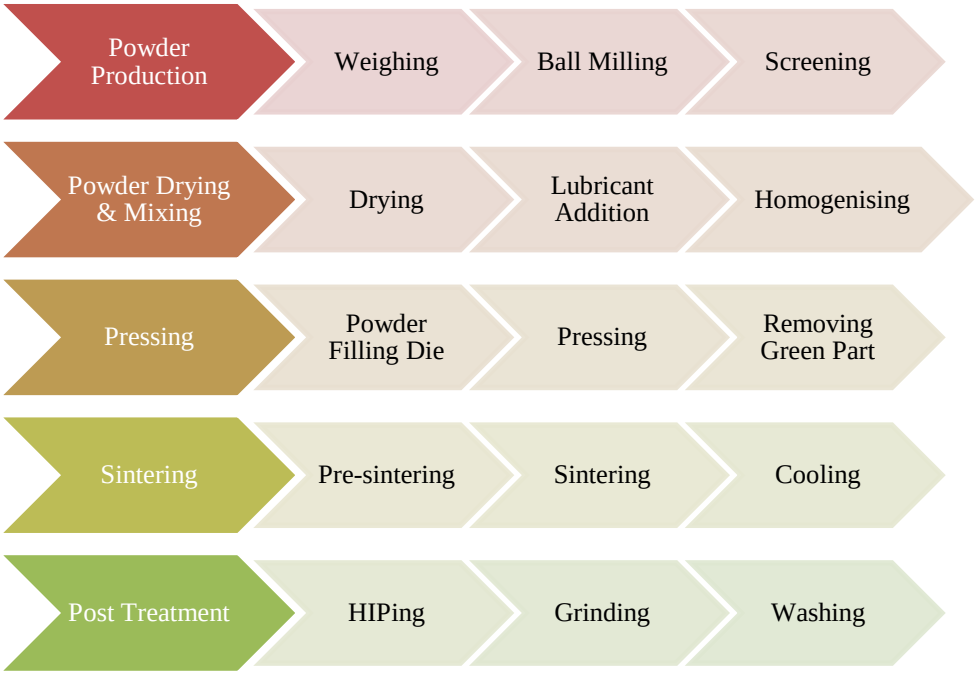

Figure 2.8: Generic cemented carbide tool manufacturing process chain summarised and created from [76]

The processes highlighted in Figure 2.8 are briefly described in the following section. It should be noted that there are other processes that can be substituted in the presented production process chain, as several other older and newer technologies can be used to manufacture cutting tools. The start of the production process begins with material or powder preparation. This begins with the calculation of the weights of each material to be used in order to satisfy the final part's design specifications such as mechanical and metallurgical properties. Finite calculations are required so as to not produce carbon excess or carbon deficient carbide lots. Finer powders are more susceptible to oxygen absorption and thus, care must be taken with the addition of carbon. Depending on the sintering process, the oxygen will bond with the carbon and thus remove it from the final product, causing an inferior microstructure. Martins et al. [77] highlights how the addition of other elements, other than the binder and the tungsten, is not uncommon. Adding elements such as titanium, tantalum, niobium, chromium, molybdenum or vanadium is performed to alter the grain growth activity during sintering [54]. The addition or substitution of other binders other than cobalt is also not uncommon practice. For instance, the addition of nickel as a binder assists with the corrosion resistance of the hardmetal [77].

Once all the constituents are weighed, they are then mixed or bonded together through various processes. Ball milling is a popular process used for the crushing and mixing of the powders. It is commonly performed with balls that are made from tungsten carbide in order to reduce contamination from another material. Ball milling is always performed in an organic solvent such as acetone, heptane, alcohols, etc. to keep the balls clean and clear of build-up [76].

After the ball milling process, a screening process is undergone through various sized screens or sieves to remove contaminants, ball chips, unmilled, and foreign particles. This can be done with dry or wet powder; however, the latter is preferred. After the screening is performed the powder then moves over to drying where the powder is spray dried while mixed under a vacuum or inert atmosphere. This is performed to form agglomerate particles that are mixtures of all constituent powders. The next step involves the addition of lubricants and organic binders to the powder followed by homogenising or blending. The binder is added to give the green part strength after the pressing phase. This allows for the green part to be handled without it breaking up. The lubricants are added to allow the powder to flow through the manufacturing process and not stick to the mould or machinery. An example of powder that has not been treated through the lubrication and binding process can be observed on the left in Figure 2.9 versus the final powder that is used in the pressing process on the right. Some manufacturers, such as Sandvik Coromant, add the organic binder before the spray drying process and after which the screening process will take place.

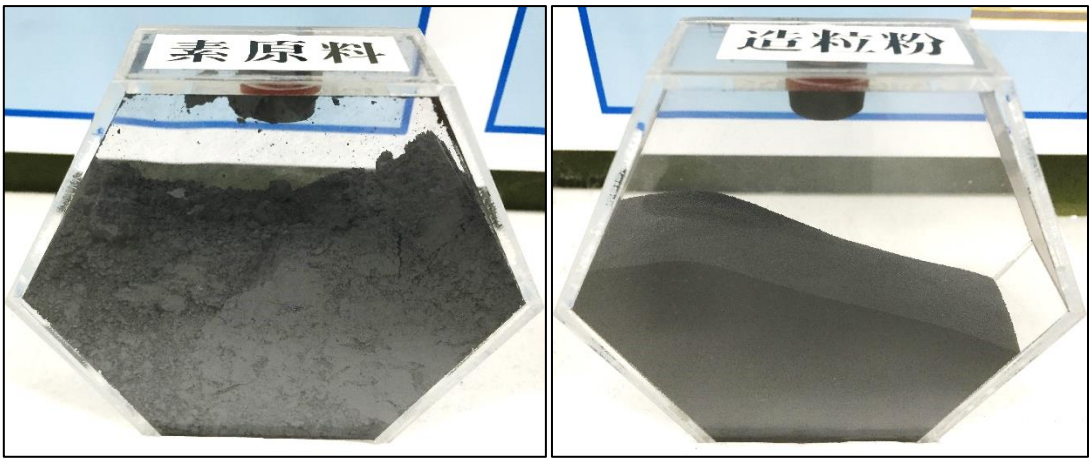

Figure 2.9: Mitsubishi Tungsten Carbide Powder: (Left) Raw untreated powder (Right) Processed granulated powder (picture taken at the Mitsubishi Materials Tsukuba Plant)

Once the powder has been treated to a practicable state, the pressing process can be performed. Compaction can be performed in two different ways, cold compaction, or hot compaction. Automatic cold compaction or pressing is performed in a closed die set. The die set is filled in a strategic fashion by using flowable powdered granules. Once the die is filled to the desired level, the punches are pressed closed to a set point or pressure. Cemented carbides are pressed with a pressure ranging from 140 MPa to 400 MPa. Once the mould opens, a green part (compacted powders) is removed from the mould set and the whole process is repeated. The pressed parts are usually identical in weight and size due to the accuracy of the mould, powder filling process, and the press.

The green part from the pressing process is loaded onto heat resistant inert discs or trays and loaded into a sintering furnace or sinter-HIP furnace. In terms of adjusting the microstructure and mechanical properties of cemented carbides, the sintering step is one of the most important processes [54]. The

parts often undergo sintering under a vacuum or inert atmosphere to avoid oxidation. The sintering process can be described in four main steps [78]. The initial step (dewaxing) is where shrinkage takes place due to the reduction of oxides and degassing of the binder and impurities. The second step (pre-sintering) involves solid-state sintering as the temperature increases. The binder phase starts to fuse to the tungsten carbide grains, allowing dissolution and transport of material to take place by solid state diffusion and bulk transport. The part porosity starts to decrease as the temperature increases and the particles begin to rearrange. Material (such as W) dissolved in the binder metal, starts to re-precipitate on undissolved WC grains. In the third step (sintering) of the sintering process the melting temperature of the binder is reached (roughly 1300 °C – 1600 °C [79]) and liquid phase sintering begins (at the eutectic point). According to Fang et al. [64] and González-Oliver et al. [80] the Ostwald Ripening process leads to complete densification and coarsening of the tungsten carbide grains. This happens through the WC grains dissolving in the binder phase until saturation. The smaller grains dissolve first and then the larger grains grow at the expense of the smaller ones. In the fourth step (cooling down) the binder phase solidifies and the grains coarsen further due to some re-precipitation [54]. Each of these processes take about 3.5 hours long including the heating and cooling time. Some manufacturers make use of a rotary furnace for the sintering process, as the parts can just be rotated through the different stages whilst still in the furnace environment.

Prolonged exposure to high temperatures during the sintering process may lead to undesirable effects such as initiating and sustaining grain growth or increasing hardness through tempering [81]. These effects can often be mitigated through the addition of beneficial elements in the powder weighing process. Another approach is through the precise control of the sintering process in terms of temperature and duration. For tungsten carbides there are three dominant influences on the hardness and toughness relationship in the final parts, namely: 1) binder content, 2) the addition of grain growth inhibitors, and 3) sintering conditions [81].

Once the sintering process is completed, the parts can be subjected to several post treatment operations. Hot isostatic pressing, otherwise known as HIPing, is a secondary consolidation process whereby parts are subjected to high temperatures and pressures in order to reduce the porosity. The tungsten carbide parts are heated to just below the normal sintering temperature and then an inert atmospheric pressure of about 1000 bar is applied to the part. Effectively, this process brings the binder phase to near plastic conditions and the atmospheric pressure exerted in all directions on the part then forces or moves the carbides and binder to fill any voids in the part [76].

The final processes that may not be applicable to some inserts are the grinding and washing processes. If dimensional accuracy is of high concern, honing and lapping will need to be performed on the

insert. Honing is a low-velocity abrading process, used for size and geometry control. Very little heat and pressure are used in this process, which assists with not damaging the inserts. Lapping is a final abrasive finishing operation that produces very high dimensional accuracy, removes any imperfections, and refines the surface finish. After grinding is performed, the inserts are washed in order to remove any residue left from the grinding process [79].

The sintering process is one of the most important steps in the production of cemented carbide parts, in terms of adjusting the microstructure and mechanical properties [54]. Thus, even though this step will be replaced with the L-PBF process, it may still be important to consider a post process operation of heat treatment (sintering) or HIPing. One should take the time to appreciate the complexity of the sintering process and how it has developed over the years.

2.4. Cutting Tool Characteristics

Although there are many different types of materials for cutting tools that are now being used in industry, there are certain fundamental characteristics of a cutting tool that have to exist for it to be classed as a decent tool. These characteristics are hardness, density, toughness, and wear resistance. A desired cutting tool is one which demonstrates a balanced combination of these characteristics.

2.4.1. Hardness

Hardness is one of the most important properties of a cemented carbide. Hardness is a measure of the strength of intermolecular bonds in maintaining their original shape without any permanent deformation. In the context of cutting tools, hardness is defined as the ability to penetrate or deform softer materials (workpiece) [39], [82]. The Hall-Petch relation determines that the hardness of tungsten cemented carbides increases with decreasing grain size [43]. Hardness is determined through indenting a sample with a diamond penetrator as per ASTM standard B-294 or ISO 3738-1:1982. Tungsten carbide hardness values are usually given in terms of Rockwell ‘A’ or Vickers hardness. The conversion tables for Vickers to Rockwell A and for Rockwell A to Rockwell C can be observed in Appendix A under the Hardness Testing Section.

2.4.2. Density

Density is a very important characteristic, as the presence of pores leads to premature failure of cutting tools. Density of tungsten carbide tools with sealed surfaces is determined by an Archimedes test according to the ASTM B311 standard. However, if there is a surface connected porosity, such as with L-PBF parts, the ASTM B962-15 standard should be used. Since cemented carbide is a composite material containing a number of different elements, the density varies with the composition

of these elements [43]. For the L-PBF process the density can also vary depending on the homogeneity of the starting powder as well as the stability of the production process [83].

2.4.3. Toughness

Toughness can be defined as the ability of a cutting tool to absorb strain energy before fracture. A cutting tool that is capable of absorbing the energy imposed by cyclic forces and vibrations without showing signs of fracture would be considered to have a high toughness [39], [82]. For application and metallurgical engineers, transverse rupture strength (TRS) is often viewed as the measure of toughness for cemented carbides. However, fracture toughness is also a very important measure used for tooling design.

2.4.3.1. Transverse rupture strength

TRS is the mechanical or intrinsic strength of the cemented carbide part. TRS is very sensitive to the porosity levels in the part. If the porosity levels are high, then the TRS values will be poor and inconsistent. TRS can be used as an indicator of the quality and consistency of the sintered WC-Co manufacturing process. Intrinsic strength of WC-Co parts is a function of grain size, cobalt content, carbon balance, and other microstructure and chemical composition factors [63]. As grain size and cobalt content increase, so does the mechanical strength of the part. The test method for determining the TRS is ASTM standard B-406 or ISO 3327. Tool designers also have to consider the size effect when using design strength values, as TRS decreases when the size of the part increases [43].

2.4.3.2. Impact strength/fracture toughness

Since cemented carbide has a high modulus of elasticity (two to three times higher than steel), it is not suitable for all impact applications. TRS is often mistakenly used as a measure of the cemented carbide's impact resistance when, in fact, fracture toughness is a more suited indicator of the materials ability to withstand mechanical impact or shock [43]. Fracture toughness is dependent on the grain size and binder content of the WC-Co composite [43]. However, fracture toughness is inversely proportional to the grain size [84]. This is the opposite of the directly proportional relation that both hardness and TRS share with the grain size.

2.4.4. Wear resistance

Wear can be defined as the erosion of particles by means of another moving surface. Wear resistance therefore, is the ability of a cutting tool material to retain its integrity against erosion [39], [82]. Hardness and fracture toughness are the two most important mechanical properties of WC-Co cemented carbides due to the dependence of other factors such as wear and impact resistance [84]. Tool wear is crucial to the economics of machining, as it affects the integrity and net shape of the

generated surfaces (workpiece). One of the dominating trends is to coat the cemented carbide substrate with a material that possesses high mechano-chemical properties. However, in practice it has been noted that some coatings exhibit failure very early on in the machining process, thus exposing the carbide substrate material to the harsh operating environment [85]. It has also been observed that the substrate may deform without any noticeable wear of the coating [86]. Therefore, it is very important to have a substrate with the correct wear resistance and mechanical properties in order to prolong the tool life during a machining process. There are many different factors that affect the tool life during a machining process, and this is discussed further in the following section.

2.5. Modes of Wear and Failure of Carbide Cutting Tools

Tool wear can be defined as the change of shape of the tool from the original shape, during cutting, resulting from the gradual loss of tool material or deformation [87]. There are many different types of wear and wear factors that a cutting tool can be exposed to during operation. In this section, the different types of wear as well as the factors that influence tool deterioration are highlighted and discussed.

2.5.1. Types of wear and failure

There are various kinds of wear that can occur during a metal cutting process. This is also dependent on the tool design as well as the cutting method and process conditions that are being used. In metal cutting, one or more of the following modes will be in effect [86]:

- Abrasive wear
- Adhesive wear
- Diffusion wear
- Delamination
- Erosive wear
- Fretting wear
- Surface fatigue
- Thermal wear

Although there are many different types of tests to determine wear destructively and non-destructively, many tests for coated and uncoated cutting tools are conducted on machine tools. Testing on the machine tool allows for the tool to experience almost identical conditions to those experienced in the machining process. Tools will be subjected to many wear parameters, including abrasion, adhesion, impact and shock, and hot corrosion [86]. There are various modes of tool failure such as gradual wear, fracture, and thermal failure. These modes are discussed in the following sections.

2.5.1.1. Tool wear types

Gradual wear is the preferred mode of tool failure as this usually occurs during cutting and is indicative of the tool life. Gradual wear can be observed in the diagram in Figure 2.10. Gradual wear occurs through two areas on the cutting tool, namely [88]:

- Crater wear which occurs on the top rake face, which is perpendicular to the direction of cutting.
- Flank wear which occurs on the side of the tool (flank), which is generally parallel to the direction of cutting.

Other forms of wear include:

- Notch wear, which occurs on the flank and rake of the tool, generally at the depth of cut level. It is caused by adhesion and a deformation hardened workpiece surface.
- Built-up edge, which occurs when the workpiece material adheres to and builds up on the surface of the tool.
- Chipping, which happens when the tool is heavily shocked, during interrupted cutting or cutting with long overhangs and higher vibrations.
- Thermal cracking, which is caused by abrupt changes in temperature at the cutting edge. This is common when interrupted cutting is being performed with a cutting fluid.
- Plastic deformation of the cutting edge, which arises when there are high temperatures and high cutting forces present on the tool. The cutting edge will deform and bulge out when this occurs.

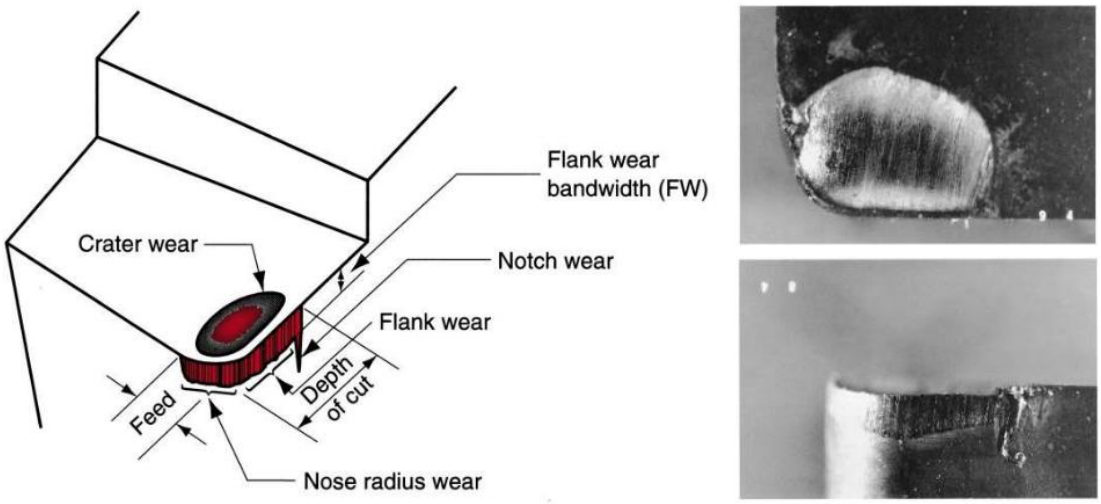

Figure 2.10: (Left) Diagram of worn cutting tool showing types of wear, (Right) Crater wear (Top), and Flank wear (Bottom) adapted from [89], [90]

2.5.1.2. Tool failure types

According to the ISO 3685:1993 standard, there are three listed failure types, namely, premature failure, preliminary failure, and catastrophic failure. Premature failure is abnormally quick, unreliable, and unpredictable. This type of failure is often caused by hard spots on the workpiece material or operator error. Preliminary failure is observed prior to catastrophic failure and often will

be witnessed through rapid deterioration of the workpiece surface finish. Catastrophic failure occurs when the tool fails before the expected tool life is reached [87]. There are two types of catastrophic failure namely, fracture failure and temperature failure. Fracture failure is when the cutting force becomes too excessive, which leads to brittle fracture of the cutting tool. Temperature failure occurs when the cutting temperature is too high for the tool material and the tool subsequently fails faster due to one of the primary wear mechanisms.

2.5.1.3. Wear identification on inserts

To understand the advantages and limitations of each material, it is important to have some knowledge of the different wear mechanisms which a cutting tool can be subjected to. Table 2.3 shows how the different wear mechanisms look on a cutting insert edge to identify them early on during cutting operations. The table highlights the possible causes of the wear and suggests possible remedial action.

Table 2.3: Wear on insert cutting edges adapted from [79], [91], [92]

Tool Wear/Failure Mode		Causes	Remedial Action
Flank Wear		- Tool grade is too soft. - v_c is too high. - Flank angle is too small. - f_z is extremely low.	- Tool grade with high wear resistance. - Lower v_c - Increase flank angle. - Increase f_z
Crater Wear		- Tool grade is too soft. - v_c is too high. - $f_z$is too high.	- Tool grade with high wear resistance. - Lower v_c - Lower f_z
Notch Wear		- Hard surfaces such as uncut surface or machining hardened layer. - Friction caused by jagged chips (vibrations)	- Tool grade with high wear resistance. - Increase rake angle to improve sharpness. - Increase a_e and f_z
Built-Up Edge (BUE)		- v_c is low - Poor sharpness	- Increase v_c - Increase rake angle - Tool grade with low affinity.
Plastic Deformation		- Tool grade is too soft. - v_c is too high. - f_z and a_e are too high.	- Harder tool grade - Tool grade with high thermal conductivity. - Lower v_c - Decrease a_e and f_z
Thermal Cracks		- Expansion or shrinkage due to cutting temp. - Tool grade is too hard. - Interrupted cutting	- Dry cutting. - For wet cutting flood workpiece. - Tool grade with high toughness. - Change cutting strategy
Edge Chipping / Fracturing		- Tool grade is too hard. - f_z and a_e are too high. - Lack of cutting edge strength. - Lack of shank or holder rigidity.	-Tool grade with high toughness. - Decrease a_e and f_z - Increase honing. - Use large shank size.

2.5.2. Tool life

In order to determine the tool life of an insert or cutting tool there is a specific relation that was derived by Frederick Winslow Taylor. Taylor's tool life equation described in Section 2.1 gives a relation between tool life and cutting speed. From the equation, one can derive tool wear as a function of cutting time for flank wear, as depicted in Figure 2.11. For end milling cutters, the tool-life testing procedure to follow is the ISO 8688-2 standard. For single point turning tools, the tool-life testing procedure that is followed is the ISO 3685 standard.

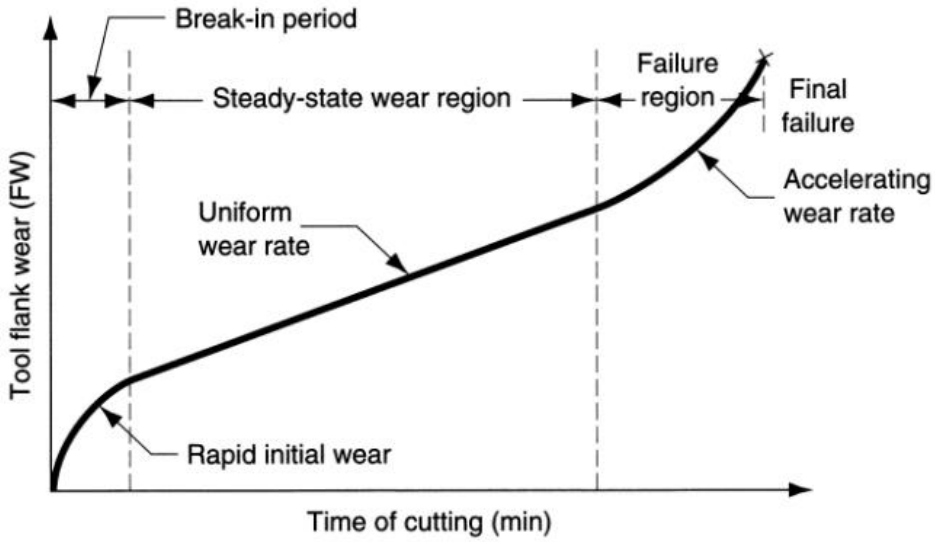

Figure 2.11: Tool flank wear as a function of cutting time reproduced from [89]

One could note that the tool flank wear goes through three different stages. The flank initially wears down rapidly until it reaches the steady-state wear region. After some cutting time, the gradual wear will become too great and cause the tool to fail. The tool is often classed as failed when various signs and symptoms are apparent. The factors influencing tool life as well as the signs and symptoms of a deteriorated tool are discussed in the next section.

2.5.3. Tool deterioration

Certain tools could be ideal for one application and inferior with regards to tool life for another, even if the wear mechanisms present are exactly the same. Thus, there are several factors that influence tool deterioration during the cutting process, both wear and non-wear related. These factors were identified and are summarised in Figure 2.12.

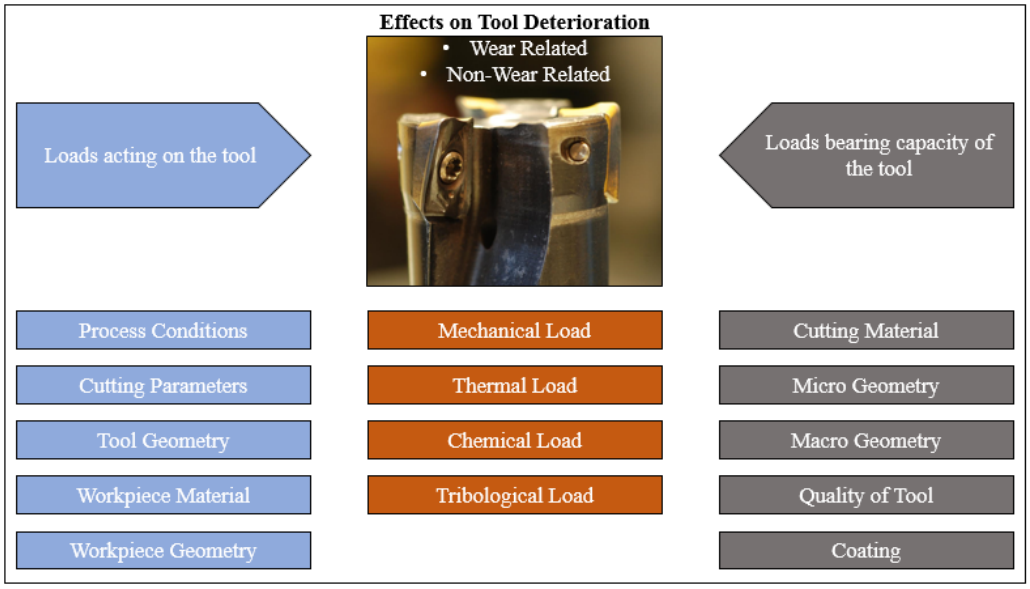

Figure 2.12: Various factors effecting tool deterioration during the cutting process adapted from [93]

There are several other issues, other than wear, that can influence the tool life. For instance, utilising the same tool type for different cutting processes on a part, may result in different results. This is due to one of the loads acting on the tool being different because the workpiece geometry is different. So just changing the cutting strategy or the way the cutting tool engages with the workpiece, could either have dire consequences or be beneficial to the tool life. For the purpose of this study, most of these factors highlighted in Figure 2.12 will be kept constant or controlled in order to analyse and compare the conventionally produced tool to the L-PBF produced tool.

2.5.3.1. Signs and symptoms of tool deterioration

Besides visually inspecting the tool, there are a number of ways to identify whether a cutting tool is worn to near the failure region. The signs and symptoms of tool deterioration are [88]:

- Visible signs on the insert
- Increased machine load
- Part size inaccuracy
- Work-piece finish diminishing
- Burr generation
- Work-piece temperature changes
- Increased vibrations
- Difference in sound
- Chatter marks
- Colour of chip changes/oxidation
- Chip control difficulties/changes

For the purpose of this study, it is in the interest to try and monitor or measure as many of these signs as possible. Besides the visual signs on the insert, the available equipment will allow for the measurement of part size inaccuracy, work piece finish, and the chip control changes.

2.6. Summary of Chapter 2

This chapter discussed tungsten carbide cutting tools in depth. The history of the material and cutting tools were first discussed. The material properties, microstructures, R&D, and manufacturing methods were all broadly deliberated. Next, the cutting tool characteristics and various wear mechanisms were mentioned. The chapter helps to generate an understanding of the complexity of cutting tools. From the manufacturing processes of the inserts to the use and testing of them. There are a number of factors throughout that have an effect on the cutting tool properties, as well as the performance of the cutting tool. By measuring, monitoring, controlling, or keeping factors constant, one could confidently produce and test different inserts.

Chapter 3

Additive Manufacturing with a Focus on Laser Powder Bed Fusion

The ASTM F42 Committee created the term Additive Manufacturing as the standard term for a model or part that has been initially generated using three-dimensional model data and fabricated layer upon layer without extensive process planning [94]. There are many different types of additive manufacturing technologies. For the purpose of this study, this chapter broadly covers the different types of technologies being used to produce WC parts, before focusing on laser powder bed fusion. There are many terms for technologies classified under L-PBF. These terms are discussed briefly to assist with the understanding of all the different synonyms used for the L-PBF process. The L-PBF process chain is summarised and discussed along with the various influencing factors on the L-PBF process. Factors and the science behind the L-PBF technology are identified and discussed in detail.

3.1. Additive Manufacturing Technologies

Additive manufacturing has evolved over the years and has assisted designers and manufacturers to create and develop physical models at a fraction of the time and costs, in comparison to conventional methods. AM is an essential part of the product development stage and the prototyping aspect of AM allows products to be assessed in terms of the form, fit, and functionality before the final investment in the tooling is made [95]. Prototyping also plays a large role in the marketing stage, as potential consumers can interact with the design and modify it before any significant costs are incurred. In the past, before the introduction of computer numerical control (CNC) and AM technologies into industry, new concept models and prototypes had to be manufactured using standard subtractive machining operations with two-dimensional (2D) engineering drawings. Skilled artisans were needed in order to manufacture these prototypes and the processes were excessively time consuming and costly [96]. AM is a simpler process to produce 3D objects where less skill is required, compared to other manufacturing processes. With other manufacturing processes, a detailed analysis of the object geometry is required to determine the different features that can be fabricated and the different machines and tools needed to do so [94]. An extensive process chain needs to be developed in order to produce just one part. With AM the process chain can be considerably shorter and less complex than other traditional manufacturing methods. There are several systems that are used to classify and categorise AM technologies. The one proposed by the ASTM F42 Committee [13] classifies AM technologies into seven areas. These seven areas and how they link can be observed in Figure 3.1.

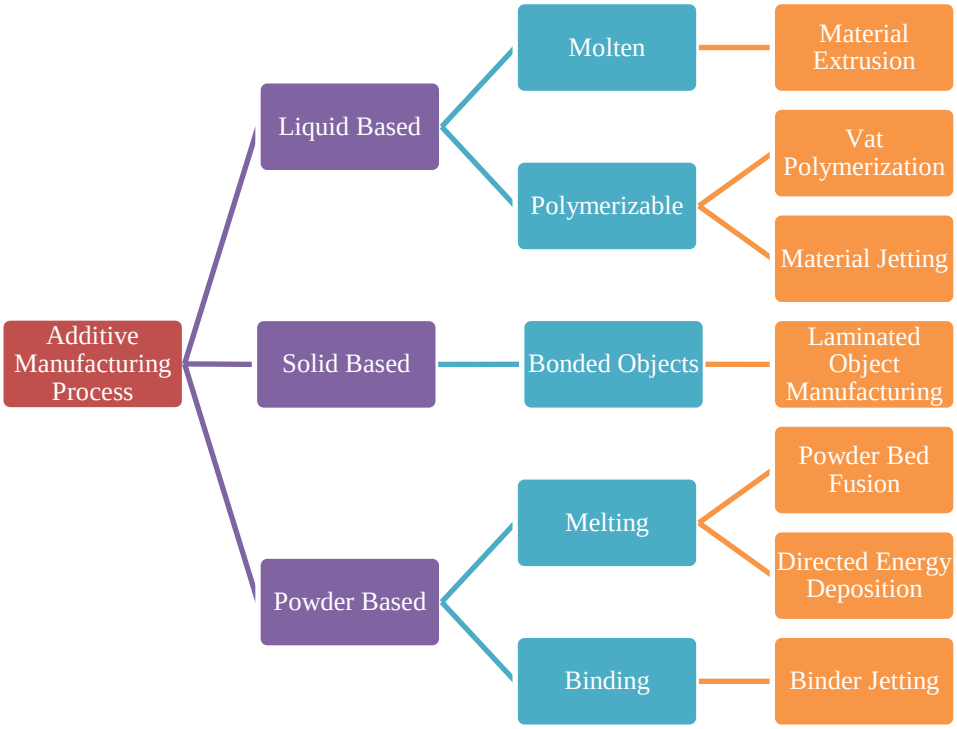

Figure 3.1: ASTM F42 Classification of AM Processes adapted from [13]

Considering there are many different systems used to class AM technologies [13], [97]–[100] in order to keep to a standard, the ASTM classifications was used for this study. Some of the different AM technologies as well as available commercial machines, have been classed into the categories described by the ASTM F42 Committee in Table 3.1 below. All of these technologies have been selected due to the fact that researchers are currently producing tungsten carbide samples with them [101].

Table 3.1: Different types of AM technologies, which are classed into the categories described by the ASTM F42 Committee [94], [102]

Name	Acronym	Area of Classification	Material	Commercial Machine
3D Printing	3DP	Binder Jetting	Specialised Powder and Binder Materials	Innovent+ - ExOne
Fused Deposition Modelling	FDM	Material Extrusion	Thermoplastics, Metals	Stratasys -F270
Selective Laser Melting	SLM	Powder Bed Fusion	Metal Powders	SLM 280
Electron Beam Melting	EBM	Powder Bed Fusion	Titanium Alloys	Spectra L - ARCAM

To gain a better understanding of the differences in the AM technologies. The different types of AM technologies, which have been used to manufacture tungsten carbide parts, are briefly described in the following sections.

3.1.1. Binder Jetting processes

The binder jetting process makes use of two different materials. The powder-based material is usually bonded with a liquid binder material. The binder acts as an adhesive and solidifies the powder in a layer wise manner. Once a slice is completed, the build platform is lowered by one layer and a new layer of powder is rolled over the platform. This process is repeated until the part is complete [94]. An AM technology that falls under this category is called 3D Printing (3DP), which is the copyright of ExOne. With binder jetting of WC-Co, the powder would need to have the correct particle size distribution and flowability. The correct binder would need to be used to bond each layer together to form the green part. Post processing, such as de-binding and sintering, is always required for binder jetting in order to solidify metallic components. Shrinkage should also be considered when designing the parts as they will decrease in size due to the post processing operations.

3.1.2. Material extrusion

Fused deposition modelling, also referred to as fused filament fabrication (FFF), is a material extrusion process whereby a solid filament is extruded through a heated nozzle in a layer wise fashion. The filament is heated to above its melting temperature where it starts to transition to a liquid. It is then extruded through the nozzle onto a base plate in the shape of the two-dimensional slice. As it is extruded out of the nozzle, it is conventionally cooled either naturally or with a fan. With tungsten carbide, the filament is carefully prepared with WC-Co powder and a binder. The filament is used to form a green part which also requires post process de-binding and sintering [17].

3.1.3. Powder Bed Fusion processes

Powder bed fusion (PBF) processes utilise an energy source, such as a laser beam or an electron beam, to melt/sinter and fuse stagnant powder layers together on a powder bed. Selective Laser Sintering (SLS), Direct Metal Laser Sintering (DMLS), Electron Beam Melting, Selective Heat Sintering (SHS), and Selective Laser Melting (SLM) all fall under the powder bed fusion process category. Some of these terminologies refer to the same technology and are discussed in more detail in the following sections.

The fundamental difference between SLM (SLS, DMLS) and EBM is the energy source used to melt the powdered material. Studies show that the energy source used to melt the powder plays a role in other aspects such as the material and mechanical properties [103]. With SLS, SLM, and DMLS, a laser beam is used to fuse or melt the powder bed layers together and are classed as laser powder bed fusion technologies. In the case of EBM an electron beam is used to melt the fine powder layer to create a 3-dimensional (3D) object once all the layers are melted and fused together. Due to the scope of the study only the L-PBF technology is reviewed in further detail.

3.2. Laser Powder Bed Fusion

Laser powder bed fusion is a process whereby fine powder is sintered or melted, layer by layer, by means of a laser energy source, in order to create a 3D object. L-PBF is an umbrella term for all the similar technologies. SLM is almost identical to the DMLS or LaserCUSING processes and the names only vary due to patent and trademark constraints [104]. The different terms used for the L-PBF technology are quite broad and the main terms used in industry and academia are summarised in Table 3.2. The umbrella term, laser powder bed fusion is preferred throughout this study, as it incorporates all the different trademark technologies regardless of whether full melting occurs or not.

Table 3.2: Laser powder bed fusion technology terms courtesy of Alexander Liu

Term	Abbreviation	Users	Comments
Direct Metal Laser Melting	DMLM	GE Additive	GE Additive uses the term to describe the Metal AM technology more and more often.
Direct Metal Laser Sintering	DMLS	EOS GmbH Optima 3D	While the term sintering is used, complete melting and fusion of powder particles occur during the process.
Selective Laser Melting	SLM	SLM Solutions Group AG Realizer GmbH Shining 3D Farsoon Technologies E-Plus-3D Bright Laser Technology	By far one of the most commonly used terms to describe Laser PBF in the metal research and general 3D Printing community.
Laser Metal Fusion	LMF	Sisma SpA TRUMPF Group	
Direct Metal Printing	DMP	3D Systems, Inc	
LaserCUSING	-	Concept Laser GmbH	A combination of [C]oncept and Laser F[using] giving rise to LaserCUSING.

3.2.1. Process description

The L-PBF process is usually performed in a sealed, pressure-controlled chamber, which is filled with an inert gas such as nitrogen or argon. This is done to prevent oxidation and degradation of the powdered material during the laser sintering/melting process [105]. The L-PBF system consists of several key components, specifically, a laser, a scanner, a powder chamber, a build chamber, and a recoater. The most influential parameters in L-PBF are the laser parameters, namely: power, scan speed, spot size, and hatch spacing [72], [106]–[109]. A graphical representation of the Concept Laser M2 Cusing (Lichtenfels, Germany) system can be observed in Figure 3.2.

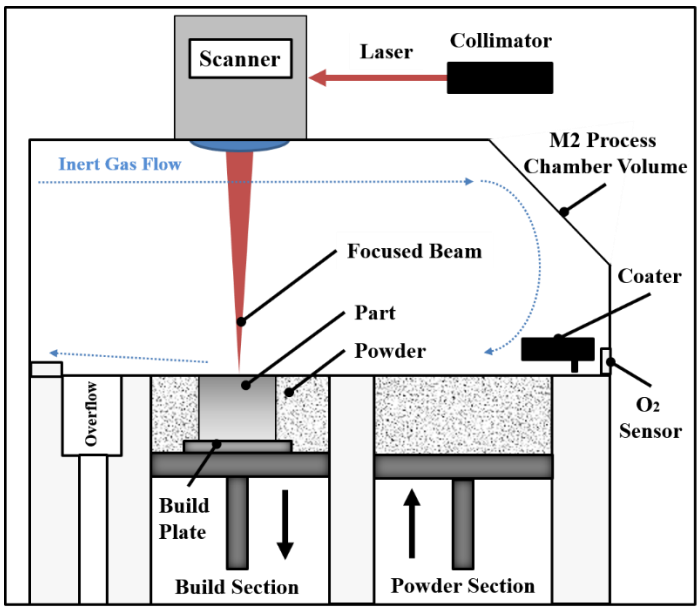

Figure 3.2: Graphical representation of Concept Laser M2 Cusing system, which shows the layout of the key L-PBF components

The L-PBF process can be described as a layer metal additive manufacturing (MAM) process. From Figure 3.2, the part is built in a layer-wise fashion in the build section of the machine. The build plate, which is secured to the machine's build chamber piston, is incrementally dropped by a predefined value (layer thickness) and the powder section is incrementally raised by a predefined value (powder delivering height). The powder delivering height is usually the layer thickness multiplied by a factor of roughly 1.3 (dose step). The recoater, which is equipped with either a hard or soft coating blade, then coats the powder from the powder section to the build section on the left at a user defined speed. After the recoater moves back to its starting position on the right, the laser then scans and melts the powder layer according to the slice file vectors [32].

3.2.2. The L-PBF process chain

The summarised process chain for the Concept Laser M2 Cusing machine is depicted in Figure A.2 in Appendix A. The process chains differ from machine to machine and manufacturer to manufacturer. The process chain has been divided into four sections namely software, machine setup, LaserCUSING machine, and post processing. These sections, along with an additional section on powder preparation, are discussed in more detail in the proceeding sections.

3.2.2.1. Powder preparation

Powder preparation and conformity testing is a crucial aspect of the L-PBF process chain. If the powder is received from a supplier, the powder properties should be checked against the certificate of conformity. The particle size distribution, chemical composition, flow properties, and apparent density should be checked according to the applicable standards. If the powder has been used in the L-PBF process, care must be taken to ensure the powder particle distribution is maintained through

sieving and mixing with new batches. The powder should also remain dry and free of oxidation during preparation and storage.

3.2.2.2. Software

The initial step for most AM technologies is to design the component that is to be manufactured in CAD or to scan a physical object with a 3D scanner. The CAD file is then converted to Stereolithography or Standard Triangulation Language (STL) file format. Most AM technologies can utilise any 3-dimensional solid model data if it is converted into the STL file format before being loaded onto the machine's slicing software. This is, however, dependent on the STL quality and whether it requires repair done by a software. The 3D mesh model then needs to be prepared on Materialise Magics 3D software (Leuven, Belgium) and sliced with the Concept Laser Slicer module. The part orientation and supports can be changed/added in the Magics software. Once finalised, the Concept Laser Slicer module is opened in Magics. Here the Concept Laser specific parameters such as, island size, island orientation, island shift, and contour dimensions can be chosen. Once the model is sliced and converted to a Concept Laser Slice (CLS) file, it can be imported directly onto the M2 Cusing machine's software. The user can then set up the required process parameters for the part.

There are many different parameters that the user can define on the M2 Cusing machine. Some parameters have been optimised by Concept Laser and some could still undergo parameter optimisation to derive better results. It is recommended that many of the parameters should not be changed as it could have a detrimental effect on the final part quality [72], [106]. The editable parameters for the M2 Cusing system can be observed in Appendix A.

3.2.2.3. Machine setup

The first step in the machine setup requires the base plates surface be sandblasted with a specific media. This is performed to increase the surface roughness of the plate so that the laser wavelength (1.070 µm) is less than the surface roughness R_a value. This will limit the reflection of the laser during the L-PBF process. This is also performed to improve adhesion between the plate and the AM part. The base plate also undergoes demagnetisation and cleaning with acetone and ethanol before it is ready to be placed in the machine. Once cleaned, the plate is dried and then mechanically fastened to the machine with four M8 screws. The height of the base plate is then zeroed with reference to the recoater blade, and the glove box chamber is then flooded with an inert gas in order to safely add the powder into the machine. The recoater blade type is very important as it could have a significant effect on the end part quality. The sieved (45 µm mesh size) and dried powder is then added to the powder chamber section through an additional mechanical sieve (100 µm mesh size). Any trapped

air bubbles are worked out with a steel scraper. The first and most important layer is then coated onto the base plate and visually inspected for an even coat.

3.2.2.4. LaserCUSING machine

Since the M2 Cusing machine has two sections (a handling station, and a process station), the technology module needs to be moved from the handling station to the process station. The process chamber then needs to be flooded by the correct inert gas, depending on whether the material being processed is reactive or not. The oxygen content on the M2 Cusing machine is kept to roughly 0.1% or 1000 parts per million (ppm). The laser exposes and melts the first layer of powder onto the base plate. This step is crucial and is often repeated about two times. One should take care to not overexpose the base plate, as the laser would be heat treating the base plate after each pass. This could negatively affect the microstructure of the base plate, making it brittle. Once this initial preparation is completed the build process can be initiated. After the process has concluded, the technology unit is moved back to the handling station so that the part and base plate can be removed from the machine.

3.2.2.5. Post processing

The final step for most additive manufactured parts is a post processing operation. For metals, this is a crucial step, as the L-PBF process involves a lot of rapid heating and cooling, which results in residual stress build-up. The part should often undergo a heat treatment operation. Once the part is stress relieved and/or heat treated, the part can be removed from the base plate either with wire electrical discharge machining (WEDM) or a bandsaw. If the part has any support structures, then these should also be removed. If the part is to be used in a quality strict industry such as the aerospace industry, then the part will have to undergo HIPing to reduce or remove any inherent porosity or damage in components such as cracks or fatigue [110]. Finally, if the part requires high tolerance dimensions or a smooth surface finish, then a surface treatment or machining operation could be done. Machining is often a challenge, as clamping of the part in the correct orientation could be an issue requiring specialised clamps and fixtures or adding lugs and fixturing points to the initial design.

3.2.3. Challenges with the L-PBF technology and process

Although the L-PBF process is an innovative manufacturing method, the technology has faced and still faces many challenges and drawbacks [111]. Some of these challenges are:

- Efficiency in terms of time and cost [112]
- Dimensional inaccuracies [97], [113]–[115]
- Poor surface finish [113], [114], [116]
- Porosity [117]–[122]
- Geometric deviation [113], [123]–[125]

- High residual stress [31], [119], [126]–[130]
- Crack formation [105], [119], [122], [131]
- Delamination of layers and delamination from build plate [105], [130]–[132]

Some of these drawbacks will be applicable for the production of tungsten carbide cutting tools. However, through constant improvement and development of the technologies, and the improvement of research in the field, some of these drawbacks have been mitigated and others could be controlled or nullified in due course.

3.3. Important Parameters in Laser Powder Bed Fusion

Even though L-PBF technology has a number of drawbacks, researchers are continuously finding ways to improve the quality of parts for different materials [130], [133]–[135]. However, due to the vast number of parameters that have an effect on the L-PBF process, reliable and repeatable metal printing is still not well understood [136]. The Ishikawa diagram in Figure 3.3 shows the characteristics of influences with regards to the part cost, time, and quality for the L-PBF process [137].

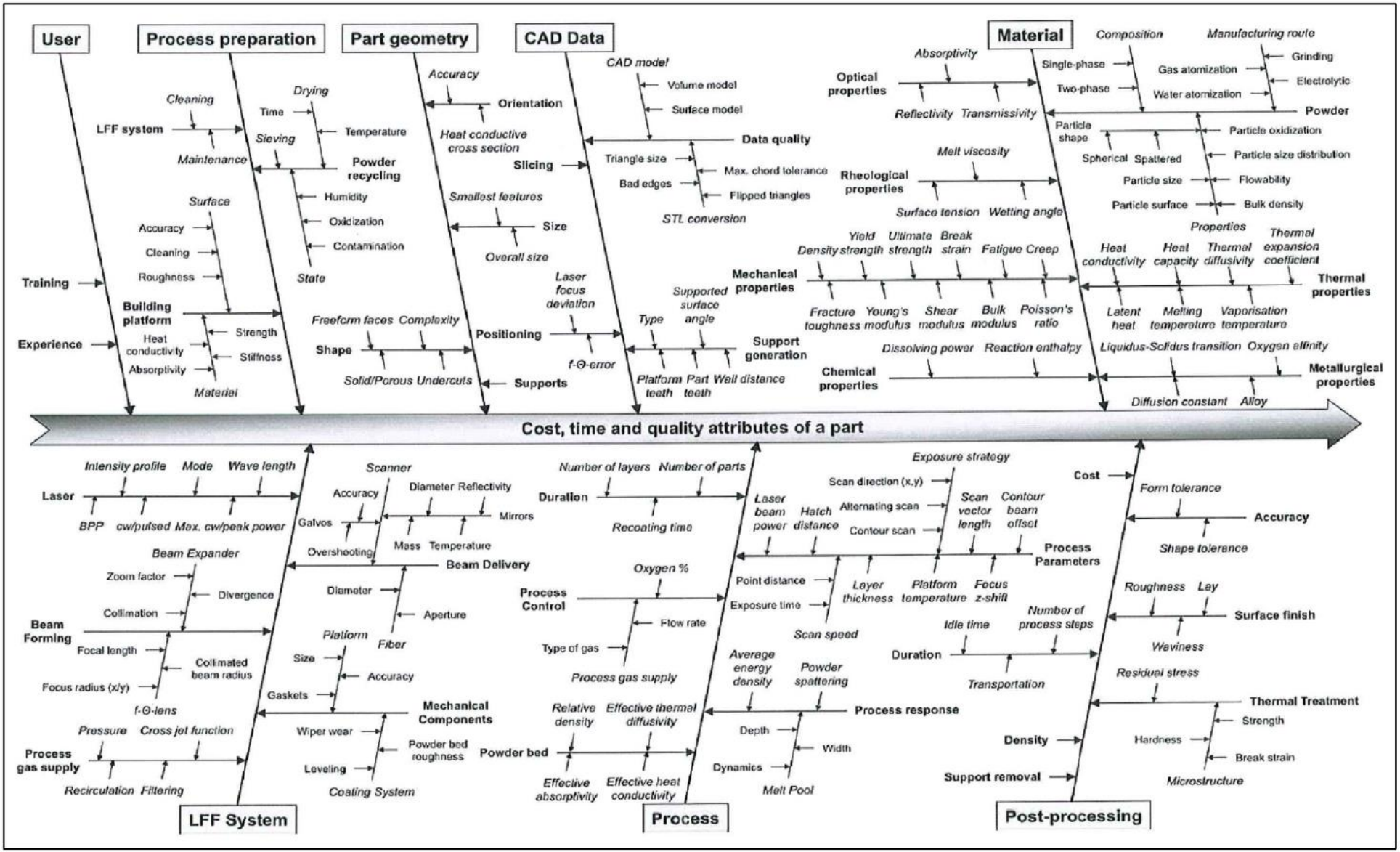

Figure 3.3: Ishikawa Diagram of characteristic influences on part cost, time, and quality for L-PBF process reproduced from [137]

From the Ishikawa diagram in Figure 3.3 it can be noted that there are 207 factors that can influence the part cost, time, and quality. Some of these factors have a higher impact than others. Some of these factors can be changed or managed by the user, but some of them are just inherent of the technology and will only improve once the technology matures and the knowledge gap is closed. A few of the major and minor categories from the Ishikawa diagram are discussed further in the succeeding sections. A focus is put on the Material, LFF System, and Process sections.

3.3.1. Material/powder properties

One of the fundamental aspects of the laser powder bed fusion process, is the starting powder material. The state and characteristics of the powder could have a large impact on the build process and final part quality [138]. Without knowing the powder properties, an inaccurate correlation could be derived between the L-PBF process parameters and the final part properties [139]. Sutton et al. [138] summarised how morphological properties of powder influence the density of the powder bed after recoating, sintering kinetics between particles, and the surface roughness and density of the final parts. Figure 3.4 shows the classification of powder properties that should be monitored to yield improved part quality.

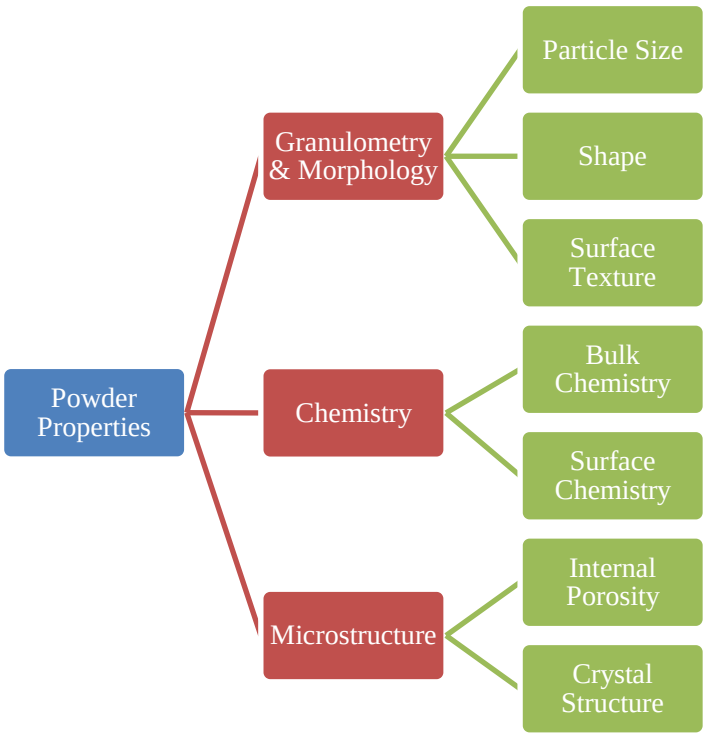

Figure 3.4: Classification of Powder Properties adapted from [138]

The seven final categories classified in Figure 3.4 present valuable information on the powder performance characteristics, which in turn effects the final part properties. These seven categories are discussed in further detail under the three subsequent classification headings.

3.3.1.1. Particle granulometry and morphology

Powders produced from different techniques, such as gas or water atomisation, will vary in terms of their size and shapes. Highly dense, spherical, and smooth particles are often desired for L-PBF processing. The particle granulometry or particle size distribution (PSD) is commonly used to quantify the sizes in terms of volume composition. The PSD is a very important parameter that often fluctuates during the L-PBF process, and during powder storage and recycling, which causes variations in the feedstock behaviour [139]. It is thus, crucial to have the correct sieving and analyses procedures in place to ensure the particle distribution is suitable and consistent for the L-PBF process and parameters. The particle size distribution can be analysed through various techniques such as, sieve analysis, microscopy, and laser light diffraction. Care should be taken, depending on the analysis technique performed, as each has their benefits and limitations which have been highlighted by Sutton et al. [138]. A typical PSD follows a normal distribution as per Figure 3.5. For L-PBF, it is generally required that the average particle size (D_{50}) is less than the selected layer thickness.

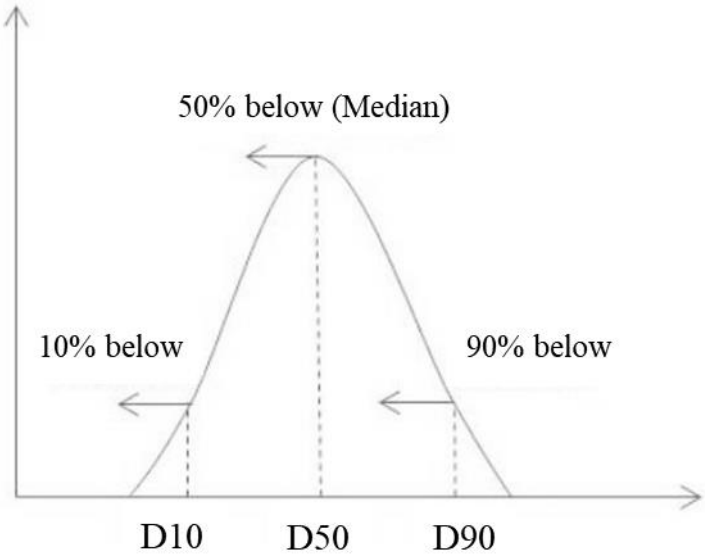

Figure 3.5: Normal PSD indicating the D10, D50, and D90 adapted from [140]

Liu et al. [141] observed that widening the PSD (1 – 60 µm) led to a higher part density and a lower surface roughness. While narrowing the PSD (15 – 60 µm) led to a higher ultimate tensile strength and hardness. Decreasing the minimum powder particle size has been shown to have its advantages with regards to increased particle packing [142], [143] and reduced surface roughness [141], however, one of the disadvantages of this is that fine powders tend to agglomerate due to different natural forces [144]. Thus, the correct particle size distribution should be selected keeping in mind the finished part's final application.

Powder shape is one of the most important aspects for L-PBF processes, due to the packing density and flowability of powder and the effects of the particle shape on this flowability [139]. Granulated spherical powders, agglomerated from fine powder particles, is often used in L-PBF. However, in the

case of Maeda and Childs [8] porosity inside the WC-Co granules was apparent, which had a negative effect on the final part porosity. Thus, it is important to inspect the starting powder for shape, size, and internal porosity. The powder morphology analysis commonly involves visual assessments through techniques such as X-Ray Computed Tomography (CT) scans, scanning electron microscopy (SEM), and optical microscopy (OM). There are a number of different shapes that can be classified according to ASTM B243. Some shapes used to describe powder particles are acicular, flaky, dendritic, irregular, round, or spherical.

The particle shape and roughness are generally reviewed in combination, as the shape will change if the roughness changes. As mentioned previously a smooth spherical surface is desired for L-PBF. It is known that the particle shape and surface roughness influences the final part properties, but the exact effects of these powder characteristics are not yet well understood [138]. Meier et al. [145] concluded that the cohesion of powder particles to each other and the substrate, is of high importance for a high layer quality. Potential surface contamination and variations in the surface roughness of the solidified layer and particles could lead to variations in the adhesion of particles by a factor of four due to the short-range nature of van der Waals interactions. However, particles and solidified substrates with a higher surface roughness, would also have higher friction forces and normal forces due to the friction coefficient and the higher piles of powder particles in the rough surface [145].

3.3.1.2. Chemical composition

Powder chemistry refers to the elemental composition of the powder and can be divided into surface chemistry and bulk chemistry. In surface chemistry, surface oxides on powder particles have been linked to increased porosity formation in L-PBF parts, by increasing balling during the process [146]. Bulk chemistry is important to ensure the chemistry and microstructure of the final parts is as per the original requirements. There are many different techniques available to quantify the surface and bulk chemistry [147]. Sutton et al. [144] summarised these techniques and lists their limitations. For surface chemistry two characterisation methods are suitable, namely, x-ray photoelectron spectroscopy (XPS), and Auger electron spectroscopy (AES). For bulk chemistry, one could utilise any of the following, depending on the elements being quantified: Energy dispersive X-ray spectroscopy (EDS or EDX), infrared spectroscopy, or inductively coupled plasma optical emission spectroscopy (ICP-OES).

A number of researchers [148]–[152] have shown that the chemical composition of the powder may sufficiently influence the L-PBF process and the effects of process parameters. Two research papers found that the crack sensitivity of Hastelloy X and IN738LC, depends greatly on the quantity of minor elements such as Mn and Si [149], [150]. Kempen et al. [151] found that a higher Si content in L-

PBF processing of AlSi10Mg has a positive impact due to the increase of laser absorptivity. Averyanova et al. [152] showed that minor variations in the chemical composition of 17-4 PH Stainless Steel did not have significant effects on the densification behaviour. However, the microstructure and subsequently, mechanical properties, were severely influenced.

Thus, when selecting the WC-Co powder for L-PBF of cutting tools, the correct chemical composition is of high importance. Cobalt has been the binder of choice for tungsten carbides since 1926 and even today, cobalt is used in more than 90% of WC tools [153]. So, a cobalt based powder is better suited for this study, due to availability. The required percentage of cobalt is imperative, too much cobalt and the cutting tools will be soft, too little cobalt and the cutting tools will be brittle. However, there is a fine balance due to evaporation and sintering conditions when exposing the powder with a laser. The phase diagram in Figure 3.6 demonstrates how sensitive the material is to temperature and how crucial it is to have the correct chemical composition from the start to remain in the liquid + WC range to avoid phase change of the WC to the brittle W_2C structure.

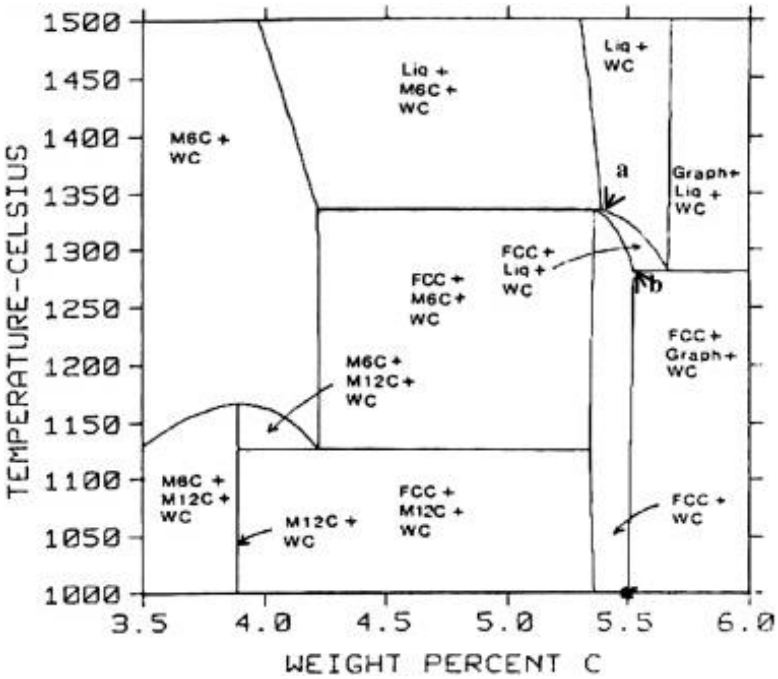

Figure 3.6: Vertical section of the W–C–Co phase diagram calculated at 10 wt.% Co. The solid symbol on the composition axis indicates the stoichiometric composition (5.5 wt.% C) reproduced from [153]

During the L-PBF process, the thermodynamic and kinetic characteristics of the material is very important. Gåård et al. [154] confirmed that the stress in composite materials, like WC-Co, develops as a result of internal constraints caused by differing coefficients of thermal expansion of various phases. The Turner model shows how the average CTE of a multi-phase material can be calculated with equation 3-1:

$$\alpha_t = \frac{\sum_{i-1}^{n} \alpha_i V_i K_i}{\sum_{i-1}^{n} V_i K_i} \quad \textbf{(3-1)}$$

where α_i is the CTE, V is the volume fraction, and K is the bulk modulus. For a composite like WC-Co, using a larger amount of cobalt leads to a higher average CTE, which results in thermal microcracks between the reinforcement and the matrix [155]. Table 3.3 displays the CTE for the different chemical components of WC-Co. The CO_2 laser absorptance for WC is also given.

Table 3.3: Material Properties of various components in the powder system [155]

Material	CTE ($\times 10^{-6}\ K^{-1}$)	Absorptance to CO_2 Laser
WC	6.0	0.48
W	4.5	*
Co	12.5	*

*No data available

3.3.1.3. Microstructure

The powder microstructure corresponds to the phases present in the powder and consequently effect the final parts characteristics with L-PBF. Particle porosity influences the formation of certain crystallographic phases, thus the two are often studied together. In L-PBF, porosity in the final parts is often attributed to the process parameters. However, porosity in parts can also arise as a result of voids within powder particles [156]. Therefore, it is imperative to identify if internal porosity is present in the powder particles so that a strategy for pore removal can be employed either during or after the L-PBF process. Since WC-Co is a metal matrix composite and the powders are generally agglomerated and sintered, there is a high chance of voids being present in the particles. The WC-17wt%Co particles from Fries et al. [3] are depicted in Figure 3.7, with the internal voids clearly visible in the cross-section of a particle.

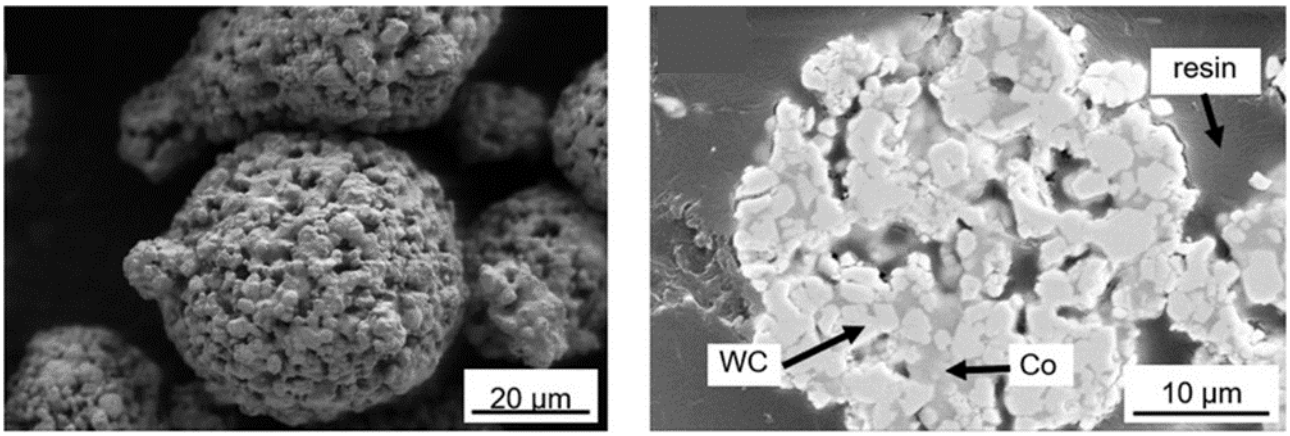

Figure 3.7: Agglomerated and sintered WC-17wt%Co powder (Left) powder morphology; (Right) cross-section of a powder agglomerate with internal porosity adapted from [3]

With the presence of internal porosity in WC-Co particles, the apparent density will be lower and thus other forces acting on the particle will also vary. This could have a negative effect on the final

part properties as the particles are more susceptible to being forced out of the laser path by forces acting against the particle.

The crystal structure of the powder is just as important as the chemical composition. The chemical composition of two powders could be exactly the same, but the crystal structure could differ immensely and thus one could be inferior to the other [157]. Slotwinski and Garboczi [157] noted that the powder manufacturing process also has a significant impact on the established particle microstructure. Just through gas atomising a powder under argon versus nitrogen, the final particle microstructure could vary drastically [138].

There are a number of methods utilised to study the crystal structure of L-PBF powder particles for characterisation of material properties [138]. These methods are metallography, X-ray diffraction (XRD), focused ion beam (FIB), and transmission electron microscopy (TEM). For WC-Co powders, there are a number of phases which can possess different crystal structures. In all W_2C modifications, tungsten atoms form a hcp metallic sublattice, in which one-half of octahedral interstitials are occupied by carbon atoms. Depending on the distribution of carbon atoms, the lower carbide W_2C can be disordered at a high temperature or ordered at a low temperature. The presence of different types of carbon atoms distribution causes the possibility of the formation of several structural modifications of W_2C [158]. The structures for W, C, Co, WC, and CoC should also be observed to determine the different crystal structures present. Many of these phases can change through the L-PBF process.

3.3.1.4. Cohesive forces of metal powders

The tendency of powders to stick together due to interparticle attractive forces is referred to as cohesion. At a macroscopic level, contact and friction forces are the dominant particle interactions. Cohesive forces should always be considered for particles less than 100 µm in diameter [159]. These forces are largely capillary, electrostatic, and van der Waals forces.

The capillary effect is when there is partial saturation of granular media. Both liquids and gasses fill the voids between the particles. Saturation of the material occurs in a natural environment due to humidity in the air and can only be avoided in a vacuum environment. The humidity causes a film to encase individual powder particles where a liquid bridge forms across two adjacent particles. The surface tension of the liquid creates an attractive force between the two particles [160]. This force can be expressed as [160]:

$$F = \pi d \gamma \cos\theta \quad \textbf{(3-2)}$$

where γ is the surface tension of the liquid, d is the particle diameter, and θ is the liquid-solid contact angle [161]. Drying of powder before utilising it in the L-PBF process is thus a crucial step to avoid quality issues caused by conglomerated powder layers and water vapour on the particles due to humidity. Since moisture can affect the flowability of the powder, all powders should be kept in a dry environment or dried before use in the L-PBF process. Different studies utilise different drying techniques. Liu et al. [141] heated their powder in a sample oven at 80 °C until the relative humidity was less than 0.01% (measured by A&D MS-70 moisture analyser) before being put inside the processing chamber. Wen et al. [162] dried their powder at 200 °C for 5 hours to reduce the humidity of the powder. Baitimerov et al. [148] heated their powder batches for 60 minutes at 100 °C to remove the possible moisture layer on the powder particles. There are currently no standards on drying of powders. This may be due to the fact that many assume powders are kept in controlled environments and under inert atmospheres. However, many machines do not allow the users to remove the powder without exposing it to air in the room. So, to ensure there are no inclusions of hydrogen and oxygen in the microstructures of finished parts, the powder should be dried before adding it to the machine.

Electrostatic forces include electrostatic potential difference, image force, and Coulomb force which are caused by the differences in charge potential between particles and is defined by:

$$F_{ec} = \frac{1}{4\pi\varepsilon_0} \frac{q_1 q_2}{r^2} \quad \textbf{(3-3)}$$

where ε_0 is the permittivity of the medium, q_1 and q_2 are the point charges of the particles, and r is the distance between particles [163].

Van der Waals forces can arise from induced particle dipoles, which is based on a difference of potential. Small particles agglomerate more easily due to van der Waals forces, which reduces powder flowability, causing poor quality powder layers [164]. The difference of potential is given by:

$$w(r) = -\frac{C}{r^6} \quad \textbf{(3-4)}$$

where C is an interaction parameter and r is the distance between particles. This interaction of potential was characterised by H. C. Hamaker where the following equation can be used:

$$F_{vdw} = \frac{A}{6s^2} R^* \quad \textbf{(3-5)}$$

where A is the Hamaker constant, $R^* = \frac{R_1 R_2}{R_1 + R_2}$ is the reduced radius and s is the distance between particles [165]. Walton [163] suggests that adhesion of charged particles may be dominated by image-charge forces rather than van der Waals forces.

3.3.2. Laser fused fabrication system

The laser system relies on a number of parameters to melt/sinter the metal powder acceptably. Most of the laser parameters are reliant on each other. Power, scan speed, beam diameter, mode, and scan spacing are the laser parameters that can be specified by the machine user on certain systems. The laser mode, however, is dependent on the type of laser installed. Most fibre lasers can alternate between a continuous wave or pulsed laser system. The laser energy is crucial for the L-PBF process and successful builds. The laser energy can be varied and applied in a number of different ways.

3.3.2.1. Laser scanning system

The laser beam is directed and focused by means of the galvanometric scanning system and a lens. The galvanometric laser scanning system can be observed in Figure 3.8. The galvanometric scanning system consists of two mirrors driven by limited-rotation motors which use the reflection angles to position the laser in the x-y plane of the build plate. The first mirror (X-Scanner) controls the laser beam along the x coordinates and the second mirror (Y-Scanner) controls the laser beam along the y coordinates [166]. The scanner mirrors are usually fabricated out of beryllium, due to its low material density (1.85 g/cm^3) and high specific stiffness of 160 x 10^6 m^2/s^2 compared to other mirror materials such as silicon carbide, fused silica, and silicon [167].

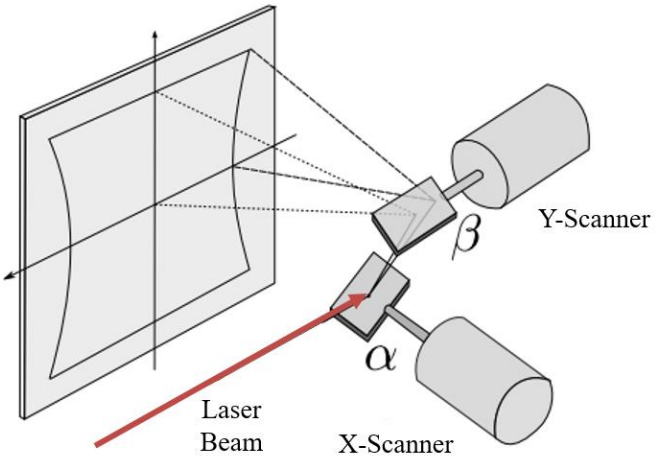

Figure 3.8: A galvanometric scanning system, which is directed onto a two-dimensional plane that represents the L-PBF powder bed reproduced from [166]

The accuracy of the machine and the final part is reliant on the accuracy of the galvanometric scanning system. Since the scanning system can reach high speeds (up to 7 m/s on conventional machines), the moment of inertia and weight of the mirrors could have an adverse effect on the accuracy. The long-term drift and thermal drift of the motors could also play a role in the final parts accuracy [167]. The speed at which the system moves could also affect the final accuracy since the system would have to have a 'look ahead' function in order to pre-empt and accommodate a rapid change in movement and move the laser beam according to the proceeding vectors. However, any deceleration or acceleration of the laser would affect the laser power density experienced by the powder bed. An example to

explain this phenomenon would be when two vectors are perpendicular to each other. The scanner does not simply scan the first vector in the x-direction, stop, and then scan the next vector in the y-direction. The scanner tends to circular interpolate between the two vectors and the resultant scanned track tends to follow a radius connecting the two vectors instead of a sharp right angle where the two vectors meet. This issue can be observed Figure 3.9.

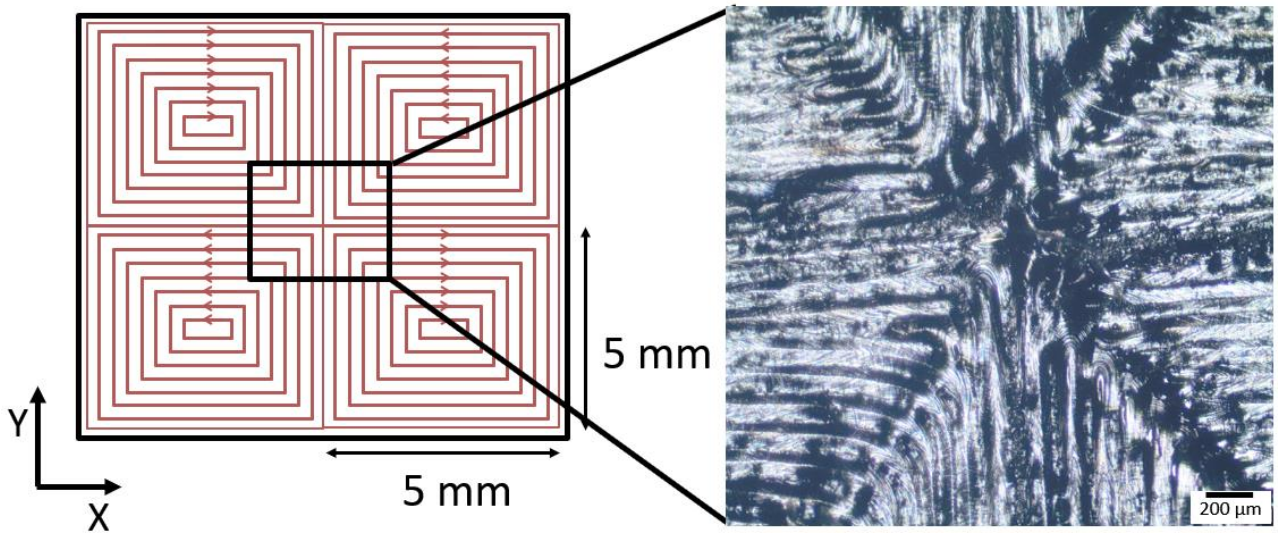

Figure 3.9: Visual depiction of circular interpolation of laser tracks adapted from [168]

In order to mitigate these issues with the scanning system Luo et al. [167] has proposed a combination of two solutions. The one method is to modulate the laser power as the function of the scanning speed during the acceleration or deceleration periods. The other method is to maintain the constant scanning speed while accurately coordinating the laser on and off operation throughout the job. The combination of these two strategies was found to deliver uniform laser density on the material and improve the overall throughput of a typical L-PBF part [167]. The laser on and off operation is referred to as 'Skywriting' and has been included on newer L-PBF systems. However, this feature is not included on the machines used in this study and should be noted as a possible cause for concern.

3.3.2.2. Laser focus shift

The laser has many different characteristics that can be controlled. For instance, a shift in the laser focus, inadvertently has an effect on the laser energy density, which has been shown to have an effect on the final part porosity [169]. The laser energy density is directly related to the divergence of the Gaussian distribution of the laser beam. The Gaussian distribution compared to the beam diameter can be observed in Figure 3.10. The laser intensity is at its highest in the centre of the focal point, and the intensity decreases according to the Gaussian distribution at the outer diameter of the focal point.

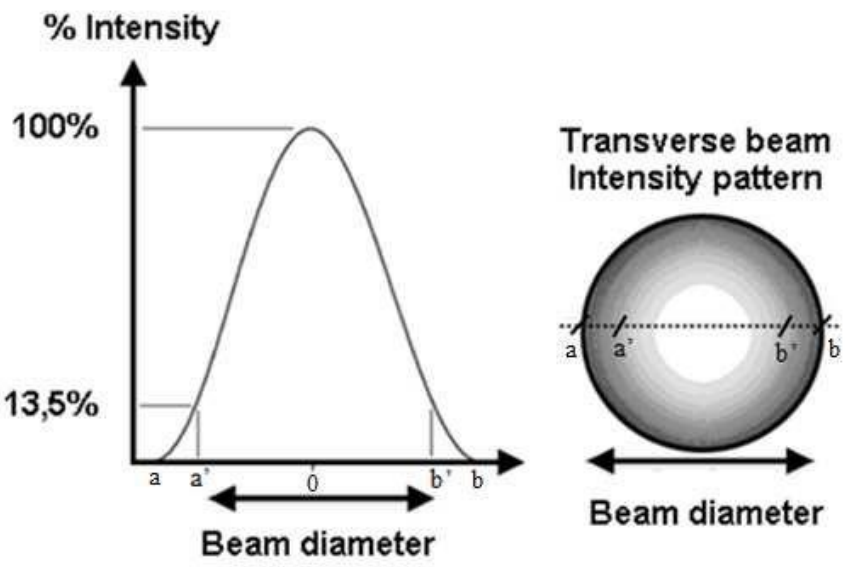

Figure 3.10: Cross beam intensity pattern and beam diameter reproduced from [170], [171]

The following divergence equations can be used to calculate the change in spot size with relative movement of the part towards or away from the laser. Power density or laser intensity at the build plate surface can be described by the equation [169]:

$$\boldsymbol{PD = I = \frac{P}{\pi\omega^2}} \qquad \textbf{(3-6)}$$

where P is the laser output power [W] and ω is the laser spot size radius, which is described by the function:

$$\boldsymbol{\omega(z) = \omega_0\sqrt{1 + \left(\frac{z}{Z_r}\right)^2}} \qquad \textbf{(3-7)}$$

where ω_0 is the minimum laser spot size, corresponding to the laser focal point, Z_r is the Rayleigh length, and z is the distance from the laser focal point. This can be calculated using the equation:

$$\boldsymbol{Z_r = \frac{\pi\omega_0^2}{\lambda}} \qquad \textbf{(3-8)}$$

where λ is the laser wavelength. The Rayleigh length is the distance from the laser focal point, where the laser spot area is doubled, halving the power density. The Concept Laser M2 Cusing machine uses an Ytterbium continuous fibre laser with nominal wavelength $\lambda = 1070$ nm. The Rayleigh distance is calculated to be 1.835 mm. Using this information, the laser spot size radius variation and power density diminution was plotted by Bean et al. [169] with respect to the build plate focus shift in the Concept Laser M2 Cusing machine and can be observed in Figure 3.11.

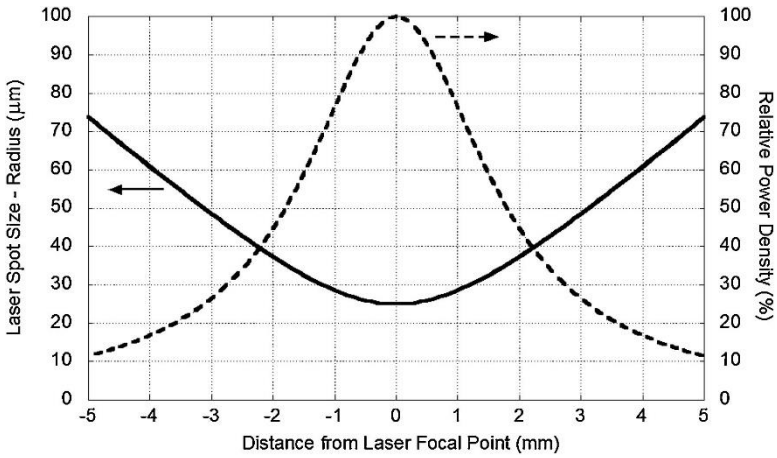

Figure 3.11: Variation in laser spot diameter and power density, calculated with respect to build focus shift reproduced from [169]

Due to the design of the M2 Cusing machine's process chamber and gas flow, the rate of convection into the inert gas is varied when altering the laser's focal point. This is because the build plate and subsequently, the part, drops into or is raised out of the build section when adjusting the focal point. This phenomenon can be observed in Figure 3.12 where the build plate has been dropped by a z height of -5 mm.

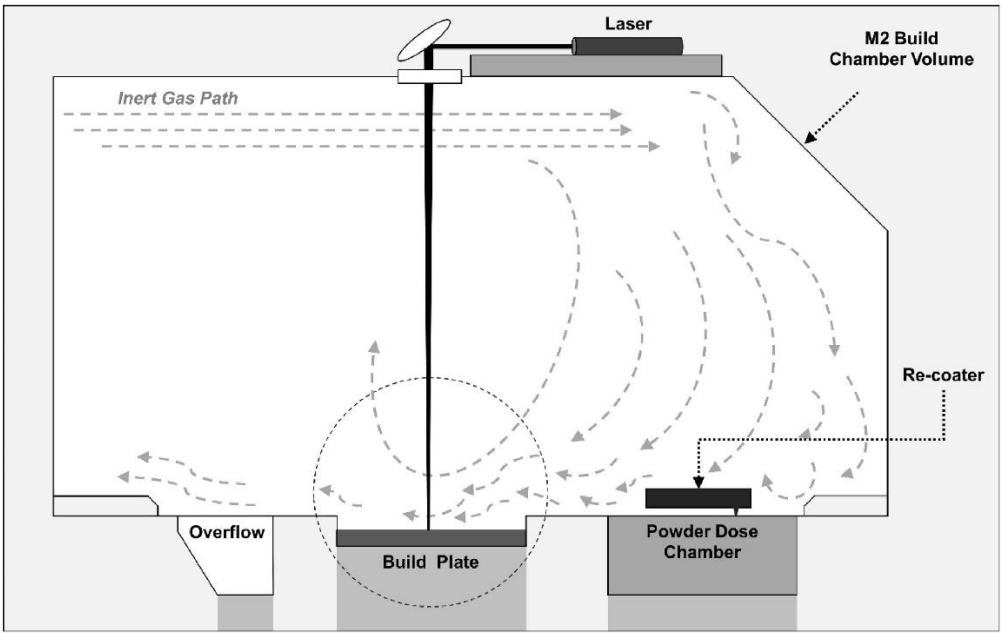

Figure 3.12: Internal Chamber of Concept Laser M2 Cusing machine with gas flow and laser focus shift reproduced from [169]

It can be noted, that depending on the height of the powder bed/build plate, as well as the location of the part on the build plate, the effective gas flow over the part will vary. This could affect the subsequent cooling rate experienced by the part. Thus, this additional factor should be mitigated as it could present an effect on the final part quality.

3.3.2.3. Recoater

The recoater or coater blade is responsible for coating the fine layer of powder from the powder feedstock side over the build platform. The physical interaction of the recoater and the powder has been shown as a shear force and a normal force as depicted in Figure 3.13 [172]. Optimising powder bed parameters such as powder PSD and recoating method used may lead to improved results in surface quality, part density, mechanical properties, and microstructure [139].

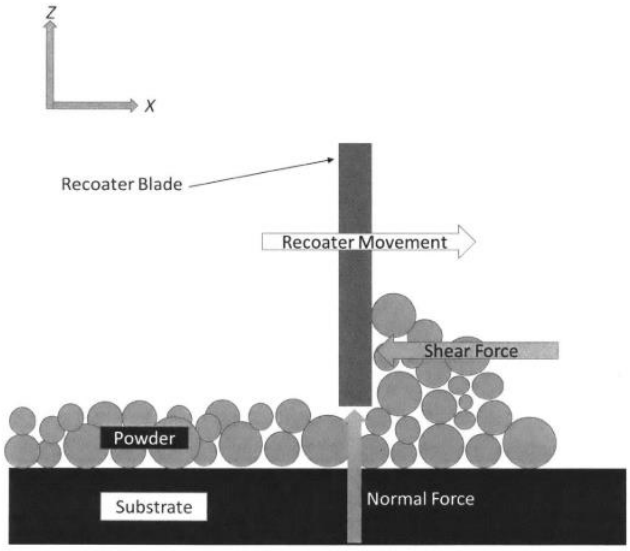

Figure 3.13: Recoater blade forces adapted from [161]

The forces experienced by the powder bed during coating are reliant on the blade shape, blade type, and speed of the recoater. There are a number of different recoater blade types used in industry. There are hard and soft variations such as high-speed steel, ceramic, carbon fibre, rubber, and silicon. With rigid type blades, a consistent layer thickness is ensured, and any splatter generated during the building process is often wiped off the part by hard recoater blades. This assists with any issues caused by lack of fusion later on in the build. The rigid steel blades tend to be more sensitive to poor process parameters, as they collide with any sections protruding from the powder bed, resulting in a stopped build. The rigid blade also compacts the powder as it coats a layer, resulting in a higher density powder bed. In certain industries, there has been some reservation against the soft type recoater blades, as they wear during the build process this could lead to contamination of the powder bed with the blade material. With soft blades, any wear during the build will be present on each subsequent coated layer. This in turn affects the final part quality as the deformations due to successive poor quality layers will be visible [173]. A disadvantage of the rigid type blades is the friction forces transmitted into the part during the coating operation. The friction forces acting on the part from the rigid recoater blade could cause unnecessary vibrations in the powder bed, which could lead to poor quality layers. Thus, the recoater material type and recoater speed are fundamental parameters in ensuring good part quality during a build.

3.3.2.4. Process gas supply

The atmosphere under which metal is processed can affect the chemistry, processability, and heat transfer. Inert gas or vacuum systems are typically used, and each has unique concerns. Metal powders tend to collect moisture and oxidise when exposed to air [156]. At elevated temperatures, the oxidation can be accelerated. L-PBF processes commonly use inert gases such as Nitrogen or Argon to fill the process chamber and flow over the build surface. The flow rates of the inert gas, type of flow, and the pathway of the flow are important in reducing porosity with some materials [174]. Small build features also may lead to heat concentration points which can cause localised oxidation [175].

Murr et al. [176] determined that building 17-4 PH parts under an argon or nitrogen atmosphere produces different microstructures in the final parts depending on the gas that is used. This was attributed to the large difference in thermal conductivity of the different gases. Nitrogen has a thermal conductivity 40% greater than that of Argon. Theoretically, use of Nitrogen as the inert gas in the process chamber will cool the parts faster than Argon.

Ladewig et al. [177] investigated the influence of shielding gas flow on the removal of process by-products in the L-PBF process. Several phenomena during the L-PBF process were studied and more specifically three issues were highlighted, namely:

- Inadequate removal of process by-products can cause scattering and therefore increase the width of single scan vectors,
- By-products can absorb incident laser energy when present in the laser path, which can lead to instable melting,
- Redepositing of process by-products in the laser path causes process irregularities.

Based on their findings, Ladewig et al. [177] recommended some general solutions to remedy gas flow issues. These remedies are, homogeneous gas flow directed over the entire build surface, high gas flow velocity to remove any by-products and avoid redeposition, directed gas flow should be close to the building surface to avoid interaction with the laser, and upwards flow separations and turbulences should be reduced to a minimum. Unfortunately, with the standard Concept Laser M2 Cusing machine, there is little control over the gas flow homogeneity and turbulences, so these factors need to be considered going forward. However, the Concept Laser machine does consider the second point and the laser scans the part in the opposite direction of gas flow, thus avoiding laser energy absorption.

3.3.3. L-PBF process

The L-PBF process is influenced by more than 130 different parameters, with a combination of interference and control variables [137], [178]. Around 10% of these parameters can be identified as critical for part quality [137]. Many of these variables have a mutual interdependence on each other, thus further research and experimentation is required in order to fully understand these relationships and their effects on the final quality [179]. A common method for determining the correct process parameters, to ensure the final parts meet the required standards, is to scan and melt single tracks of powder onto a metallic substrate. This practice is suggested by Yadroitsev et al. [178], [180], [181] and Li et al. [182]. There are two laser melting parameters that have a substantial effect on the scan track quality specifically: laser power, and scan speed. Scan track formation is fundamentally important since the quality of the final part relies heavily on the quality of the individual scan tracks. Yadroitsev et al. [180] suggests a number of steps to take to find the optimal L-PBF parameters for a certain material. The first step is simulation, where the user would simulate the laser radiation and its interaction with the material. In this, the user would vary the laser power, spot diameter, and scan speed accordingly to determine the effects on the temperature fields. The next step requires single track runs on the L-PBF system that will be used to manufacture the final part. The single tracks are run with varying laser power densities and scanning speeds derived from the simulation step for different powder layer thicknesses. The tracks are then microscopically analysed with a top view and a cross sectional view. The tracks are required to have stability without the balling effect and irregularities. They also require a penetration depth into the substrate of 30-50% of the whole melted height to provide a strong metallurgical bond [180]. An example of an acceptable single track can be observed in Figure 3.14.

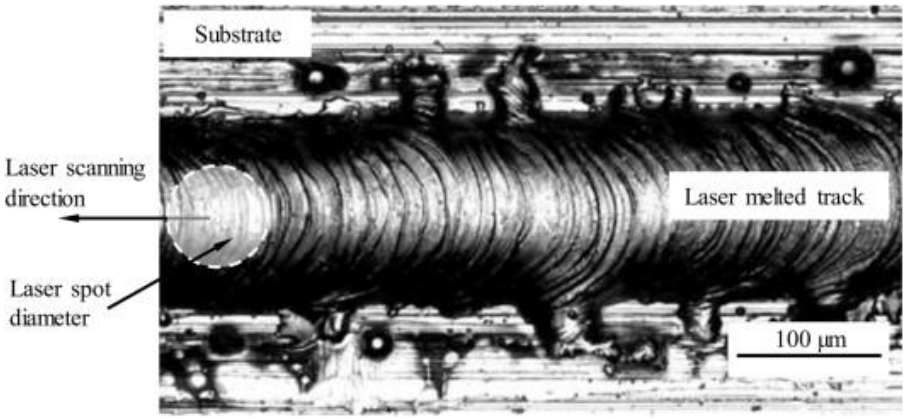

Figure 3.14: Single track from AISI 420 powder on the substrate (top view): laser power P = 50 W; laser spot diameter 70 µm; scanning speed V = 0.10 m/s; powder layer thickness h = 50 µm reproduced from [180]

Once the single-track parameters are finalised, a scanning pattern and scanning strategy are selected. With the scanning pattern selected and the track width observed from the single-track runs, the hatch spacing can be chosen. It is important to consider the width of the tracks, the shape of the tracks, the

height of the tracks, the denudation zones, and the estimation of shrinkage. Once suitable parameters and strategies have been chosen, single layer fabrication can be performed. The melted layer should also be microscopically analysed with a top view and a cross-sectional view. The track height, penetration depth, thickness of the layer, and valley depth should all be observed and measured. After the single layer analysis is concluded and appropriate parameters are derived, the fabrication of the 3D L-PBF object can commence. To quantify whether the parameter optimisation was successful, porosity measurements of the final part should be conducted. If the porosity value is adequate, then the process parameter optimisation was a success. If the porosity measurements are not suitable, then the single layer parameters should be re-evaluated and the single layer runs should be repeated using different parameter sets [107], [180].

Another commonly used method for parameter optimisation is the cuboid fabrication method [51], [111], [164], [183]–[185]. This method makes use of a cuboid test specimen of specific dimensions (roughly 10 x 10 x 10 mm^3). Process parameters are then chosen to be varied and run using a design of experiments (DoE) method, constrained by their specified range. The DoE outputs several experimental runs with varying parameters that are required in order to have a significant statistical power. The experimental runs are then performed on the L-PBF machine and the cuboid samples are analysed for porosity, hardness, etc. The samples with the best results are then used as the baseline parameters for a second iteration of experimental runs with fine-tuned parameter sets.

3.3.3.1. Layer thickness

The layer thickness is defined as the minimum distance the heat source must travel through the powder to reach the previous layer. In commercial systems layer thickness is configured with the build platform displacement distance [161]. The layer thickness is often limited by the powder particle size distribution and the laser's ability to penetrate through the layer. It is recommended that the layer thickness not be smaller than the average powder particle size [144]. The layer thickness is a very important parameter because it also dictates the final part accuracy. If the layer thickness after melting is smaller than the chosen dimension, then the error in size will be multiplied through all of the layers making the final part smaller than what it should be. The same goes for melt pools that build up and protrude from the chosen layer thickness. These issues also multiply over the number of layers and also interfere with the machines recoater blade during the building process.

3.3.3.2. Exposure/scanning strategies

A scanning strategy can be defined as any scan pattern or exposure method that is used to influence a dependent variable during the L-PBF process. This includes, but is not limited to, different vector, segment, or layer scanning methods [186]. There are many different vector, segment, and layer scan

strategies. Each is used for different features and each has their own advantages and disadvantages. Many are machine/manufacturer dependent, and many are being developed and combined to improve the L-PBF process. A working summary of scanning strategies has been initialised and is depicted in Figure 3.15.

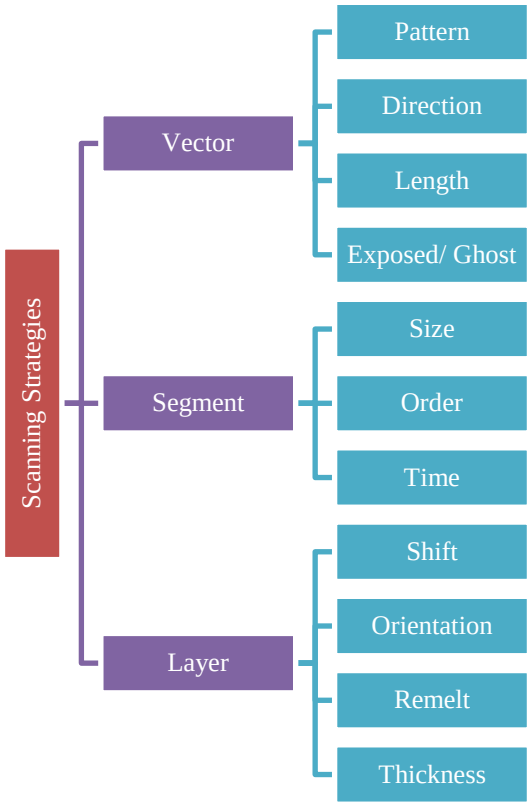

Figure 3.15: Breakdown of a scanning strategy and the sections encompassed

From Figure 3.15 one can combine a number of the vector, segment, or layers strategies and employ them in the L-PBF process to improve the quality of a part. However, care must be taken, as too many changes to the strategies can also diminish the quality of a part for a given set of process parameters. Thus, the strategies should be well understood and used in conjunction with the process parameters. Scan strategies affect the material properties of the final part. The orientation of the material's grains is highly dependent on the scan strategy that is used. The scanning strategy can be used to control the grain orientation as well as the microstructural texture [72]. Due to the fact that there is no standard terminology for strategies, some strategies may be known by different terms. Most authors also tend to explain or label the strategy by using their own analogies. The different scan strategies along with the different terms and diagrams are listed in the following sections.

Vector strategies

Vector scan strategies incorporate several features that can be varied. The pattern in which the vectors are laid out to cover the exposure area is fundamental. However, the pattern only covers the area to be exposed but does not specify how the laser should travel through the pattern to expose the area.

Thus, the direction and length of the vectors in the exposure pattern are also important. Often referred to as 'ghost' vectors (or 'Skywriting'), these are the vectors followed by the scanning system for repositioning while the laser is off. Since the galvanometric scanning system is always moving, the laser and shutter shut-off/on time and strategies surrounding this are also fundamental for certain quality aspects of a part.

The M2 Cusing machine has a limited amount of scan patterns that can be chosen using the machine software. The software package that came with the M2 Cusing machine only allows contour scans as well as the scan patterns displayed in Figure 3.16. These patterns are the hatch vectors that will be used to expose the powder. Scan patterns 1 and 2 are the same but just are oriented through different axes. The same goes for patterns 3 and 4. Pattern 5 is the combination of patterns 3 and 4 and the laser would scan 3 and 4 consecutively on top of each other. Scan pattern 6 is also a combination of patterns 3 and 4 but the part is divided into islands as displayed in the figure.

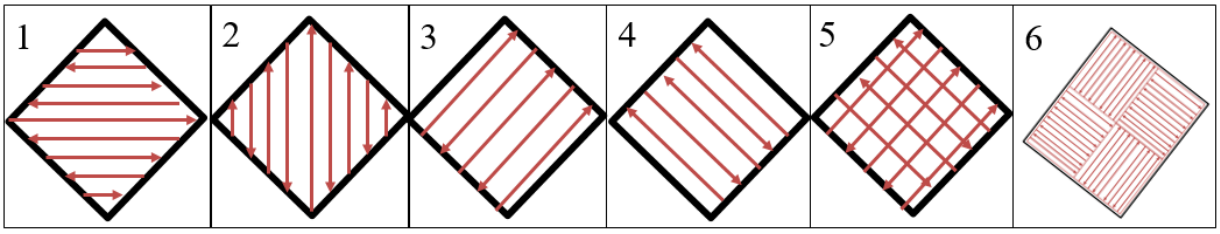

Figure 3.16: M2 Cusing scan pattern options reproduced from [168]

Although there are a number of ways in which a layer can be exposed by the laser, there are three vector strategies used, which can be applied in many different ways to suit the needs of the user. These strategies are the unidirectional, bidirectional, and contour strategies [187]. The unidirectional scan ensures the laser direction does not change between each scan track. The bidirectional (or also commonly referred to as the raster strategy) strategy alternates the vector direction after each scan [188]. The contour scan is an exposure scan that is usually performed around the perimeter of the desired CAD sliced section [188]. The contour scan can also be used to derive the helix scan depending on the part geometry and scanning strategy used. The unidirectional and bidirectional scans are displayed in Figure 3.17. Note the different directions of the scan vectors.

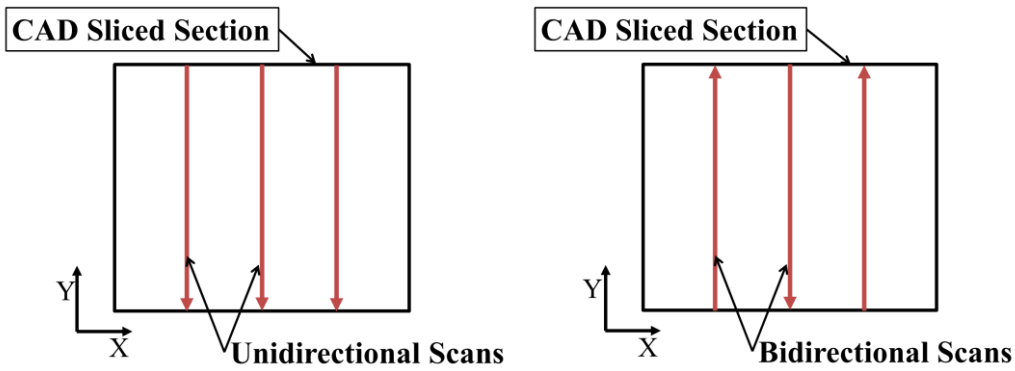

Figure 3.17: (Left) Unidirectional scan strategy and (Right) Bidirectional (raster) scan strategy adapted from [188]

The contour scan is used to create a distinct melt pool around the boarder of the CAD slice. The helix scan can be made up of many contour scans. Both scans can be observed in Figure 3.18.

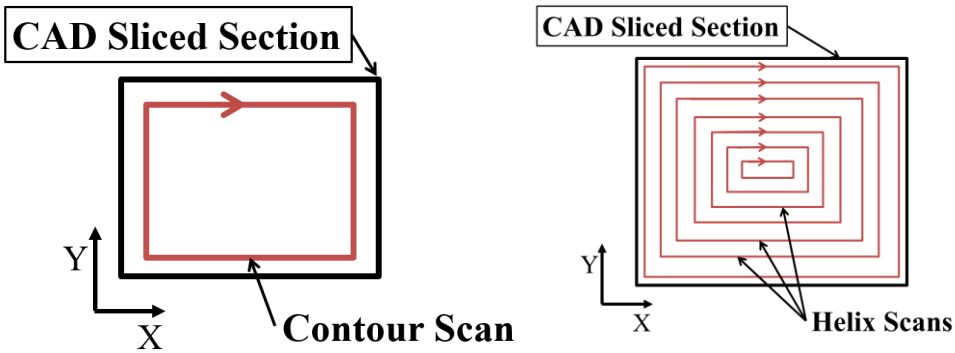

Figure 3.18: (Left) Contour scan strategy adapted from [188] **and (Right) Helix scan strategy adapted from** [168]

Segment scan strategies

Segment scan strategies are derived from conventional welding techniques, where long welds are often divided into smaller weld lines to avoid warping of the parts being welded. Segmenting can be done in various ways. The cross-sectional slice of a part can be divided into islands, stripes, or even specific shapes for a specific geometric feature. To further this, segments can also be exposed in a strategic or random order, in a specific or random time interval.

The "island" scanning strategy is a patented strategy that was developed by Concept Laser GmbH. In order to decrease the residual stresses in the part, caused by steep thermal gradients, the island strategy reduces the area to be scanned into smaller square sections (roughly 5 *mm* x 5 *mm*). The islands are also scanned in a random order with shorter scan tracks, which means localised heating of large sections does not take place [189], [190]. Other commercial machine manufacturers use a similar strategy called 'striping' where the part is subdivided into long stripes instead of square islands. The island strategy can be observed in Figure 3.19. Note that for the default strategy, each island is made up of bidirectional scan vectors.

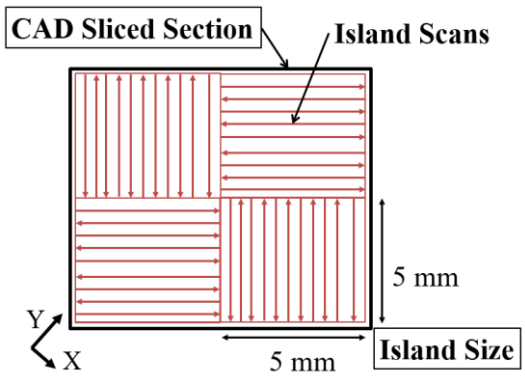

Figure 3.19: Island scan strategy adapted from [189]

Layer scan strategies

Layer scanning strategies are the strategies employed in a layer wise fashion. This includes the shift and orientation of the scan pattern between layers, exposure of the layer (remelt or not), and the thickness of the layers throughout the build and whether they vary or not. Layer scanning strategies are extremely important to ensure adequate properties and layer adhesion throughout the height of the build.

The inter-layer stagger strategy (also known as the knitting strategy or refill strategy) is used to repair defects in the previously scanned layers by scanning the next layer at an offset, so that the laser is exposed at the scan track overlapping zone [191], [192]. Often powder situated in the overlapping zone is not completely melted. The refill scanning strategy corrects this flaw by melting all of the powder situated in the overlapping zone, which results in stronger bonds between layers. The inter-layer stagger scan strategy is depicted in Figure 3.20. The offset can be applied in either the x or y directions or even both. The offset should be chosen strategically to ensure there is no repeat or pattern observable through the layers.

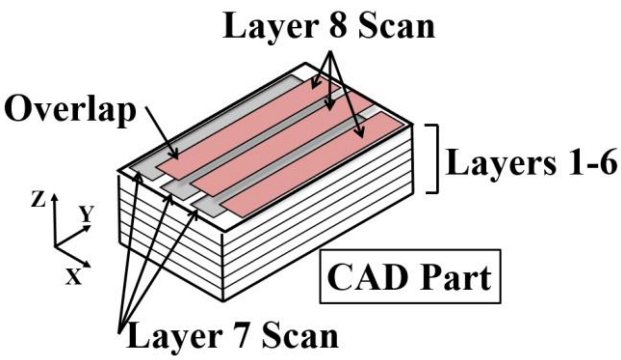

Figure 3.20: Inter-Layer stagger scan strategy adapted from [192]

The orthogonal scan strategy (cross-hatching strategy) is when successive layers are scanned orthogonally to each other [191]. This strategy is used to reduce the stress build up along the scans, by changing the direction of the scan after each layer in a 90 degree fashion [193]. Figure 3.21 displays four different layers. Layers 1 and 3 are scanned in the y-direction and layers 2 and 4 are

scanned in the x-direction. The layer rotation can be varied through a number of angles throughout the build depending on the system used and should not just be limited to 90 degrees. EOS GmbH (Krailling, Germany) makes use of a 47 degree or 67-degree rotation of scan pattern after each layer.

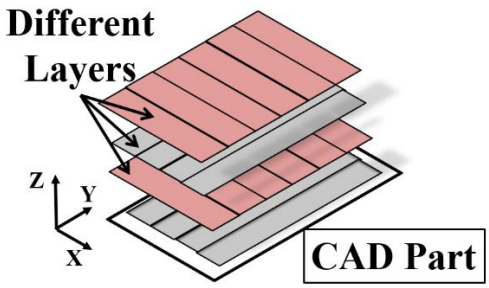

Figure 3.21: Orthogonal scan strategy adapted from [192]

The effects of scanning strategies

Simchi [194] discussed how the scanning strategy can influence the sintering rate by showing the effect of scanning vector length on the fractional density. It was noted that the sintered density slightly decreased as the vector length increased. This observation can be explained by the delay period (τ) between successive irradiation defined by:

$$\boldsymbol{\tau} = \frac{\boldsymbol{l}}{\boldsymbol{v}} \qquad \textbf{(3-9)}$$

where l is the vector length [mm] and v is the scan speed [mm/s]. As the vector length increases, the delay period between successive irradiation leads to the decrease in energy stored on the surface. Consequently of this, the density is decreased as a result [194].

Hooper [195] found there is a significant difference in the cooling rate of a hatch vector at the turns of the vectors vs the first hatch line. He found that the cooling rate at the turns was 1.5 K/µs vs 40 K/µs at the first scan track. This significant difference shows the importance of the scanning pattern and scanning strategy and the effects on the cooling rates and subsequently the residual stresses.

Robinson et al. [196] tested a number of scanning strategies to determine their effects on residual stress in the parts. They concluded that the stress levels in different parts of the same geometry varies depending on the scanning strategy used to realise the specific part. They also found that the residual stress in L-PBF components manufactured with unidirectional vectors is primarily orientated in the scanning direction. They went on to state that a stress of approximately half the magnitude in the direction normal to the scan vectors exists, which needs to be considered when selecting a scanning strategy.

Wang et al. [197] concluded that with L-PBF of pure molybdenum, in the denser samples, cracks could be distinguished into longitudinal and transverse ones. Growth direction of the longitudinal cracks was parallel to molten tracks, while that of transverse cracks was perpendicular to the surface

ripple of the molten pool. Layer-wise scanning rotation was found to be beneficial for reducing cracks [197].

Jhabvala et al. [198] found that the scanning strategy used can aid in homogenous heating of the slice until the material reaches its melting point. They showed several types of scanning strategies and suggested certain ones for certain materials with respect to their thermal conductivity properties. The spiral (or helix) scanning strategy was suggested for high conductive powders but is part geometry dependent.

Scanning strategies are fundamental to the L-PBF process as they influence many of the part properties. The scanning strategy could contribute to the success or failure of a part, especially when it comes to materials with a high thermal conductivity. Utilising the wrong part geometry coupled with the incorrect scanning strategy could result in the part deforming and failing during the L-PBF process.

3.4. Physics, Thermodynamics, and Fluid Dynamics of Laser Powder Bed Fusion

Sintering or melting of the powders takes place when the powder bed is irradiated by the moving laser beam up to the temperature at which the binder or metal melts. Wang et al. [12] summarised the thermal process in laser sintering into four main stages namely:

1. Energy input and absorption
2. Heating of the powder bed
3. Binder melting and sintering
4. Cooling of the sintered layer

In stage 1 the light energy of the laser source is converted into thermal energy that causes heating of the powder bed. In stage 2 the heating of the powder bed occurs along with all the associated losses defined by the laws of thermodynamics. In stage 3 various binding mechanisms occur depending on the laser energy as well as the powdered material properties. In stage 4, rapid cooling and solidification of the melt pool and layer occur. The first three stages are discussed in further detail in the sections to follow.

3.4.1. Energy input and absorption

Wang et al. [12] describes the absorption of energy of the powder bed irradiated by a laser beam with the “total energy incoupling”. This is defined as the ratio between the absorbed energy and the total input energy:

$$\boldsymbol{Total\ energy\ incoupling} = \frac{\boldsymbol{Absorbed\ energy}}{\boldsymbol{Input\ energy}}\ \boldsymbol{x\ 100}(\%) \qquad \textbf{(3-10)}$$

According to Wang et al. [12], the total energy incoupling into the powder bed should be distinguished from the material absorption coefficient. The total energy incoupling is often studied experimentally but there are a number of methods to do so with a high diversity in the results.

3.4.1.1. Energy density and normalised enthalpy

The energy density is often used as a metric to compare process parameters for laser powder bed fusion [199]. There are a number of different types of energy equations used in literature [169], [194], [200] in an attempt to quantify the relationship between the laser parameters and the properties of final parts. With respect to the energy density, there are three different equations used, namely: linear, specific, and volumetric. The linear energy density equation can be observed below [201]:

$$\boldsymbol{E_l = \frac{P}{v}} \qquad \textbf{(3-11)}$$

where E_l is the linear energy density [J/mm], P is laser power [W], and v is scanning speed [mm/s]. In order to distinguish between the different laser parameters and the layer thickness, the specific energy density equation is utilised:

$$\boldsymbol{E_d = \frac{P}{vd}} \qquad \textbf{(3-12)}$$

where E_d is the specific energy density [J/mm^2], and d is the layer thickness [mm]. However, a more suitable estimate of the absorbed laser energy in the powder bed is the volumetric energy density. The volumetric energy density can be utilised to estimate the absorbed energy within the powder melt pool [194], [202], [203]:

$$\boldsymbol{VED = \frac{P}{vdh}} \qquad \textbf{(3-13)}$$

where VED is the volumetric energy density [J/mm^3], and h is the hatch spacing of the laser pattern [mm]. One main issue with the approach to defining the volumetric energy density with hatch spacing, as done by Guo et al. [204], is that the effects of the beam diameter are not accounted for. Thus, other authors [199] have expressed the VED as:

$$\boldsymbol{VED = \frac{P}{vd\sigma}} \qquad \textbf{(3-14)}$$

where σ is the laser beam diameter [mm]. This expression is better suited in some cases since the hatch spacing has no relationship to the laser beam diameter and can be easily varied by the user without affecting the track width. Oliveira et al. [205] articulated that the VED makes it difficult to compare investigations conducted with different powder and machine types and thus introduced a dimensionless parameter into the VED:

$$\boldsymbol{\beta} = \frac{\boldsymbol{d_{50}}}{\boldsymbol{\sigma}} \qquad \textbf{(3-15)}$$

where d_{50} is the average powder particle diameter [µm], and σ is the laser beam diameter [µm]. It should be noted that the VED equation is only valid for a specific process window region with stable melt pool behaviour. Where neither balling, nor keyholing are dominant in the process.

It should be observed that there are a number of different VED equations that can be found in literature. Koutiri et al. [206] used the following VED equation:

$$\boldsymbol{VED} = \frac{\boldsymbol{P}}{\boldsymbol{vA}} \qquad \textbf{(3-16)}$$

where A is the laser spot area [m^2]. Other approaches to the VED include that suggested by Simchi [194]. Simchi displayed how the VED can be utilised to calculate the apparent sintering temperature with the following equation:

$$\boldsymbol{T_s} = \boldsymbol{T_O} + \frac{\boldsymbol{1}}{\boldsymbol{C}}\left[\left(\frac{\boldsymbol{\pi\eta}}{\boldsymbol{4\rho}}\right)\left(\frac{\boldsymbol{P}}{\boldsymbol{vdh}}\right) - \boldsymbol{\Delta H}\right] \qquad \textbf{(3-17)}$$

where T_s is the sintering temperature [K], T_O is the initial temperature [K], C is the specific heat capacity [J/kg K], η is the coupling efficiency, ρ is the fractional density, and ΔH is the latent heat of fusion [J/kg]. Often, authors utilise the VED as a design parameter in order to generate experimental runs, which cover a number of parameters such as scan speed, laser power, etc. Scipioni Bertoli et al. [199] explains how caution should be exercised when utilising the VED as a design parameter for L-PBF due to the narrow band of applicability and the inability to capture the multifaceted physics behind the melt pool. VED is a thermodynamic quantity and cannot capture the complex melt pool physics such as Marangoni flow, hydrodynamic instabilities and recoil pressure that drive heat and mass transport [199].

The issue with equation (3-17) proposed by Simchi [194] is that once calculated the solution does not present a temperature in Kelvin but requires that the dimensionless fractional density be allocated the units for density in order for the equation to be solved. When the energy density is set too high, a condition known as “keyhole mode” is present whereby the melt pool penetrates and re-melts preceding layers. Due to the high energy input, certain metals in alloyed materials can reach their boiling point which leads to evaporation of that alloy. This also leads to inward Marangoni flow in the melt pool, which results in trapping of gas bubbles in the melt pool subsequently increasing part porosity [199]. Normalised enthalpy is another function used to compare parameters and determine the desired process window and melting mode. Normalised enthalpy is defined as [199]:

$$\frac{\Delta H}{h_S} = \frac{AP}{\pi h_S \sqrt{Dv\sigma^3}} \quad \textbf{(3-18)}$$

where A is the laser absorptivity, D is the material's thermal diffusivity, h_S is the enthalpy at melting, and σ is the half-width of Gaussian beam. King et al. [200] shows that the calibration of the normalised enthalpy is:

$$\frac{\Delta H}{h_S} = \frac{AP}{h_S \sqrt{\pi Dv\sigma^3}} \quad \textbf{(3-19)}$$

The enthalpy at melting can be written as:

$$h_S = \kappa T_m / D \quad \textbf{(3-20)}$$

where κ is the thermal conductivity, T_m is the melting temperature, and D is the thermal diffusivity.

3.4.1.2. Laser absorptivity

The thermal interaction between the laser beam and the powder feedstock is greatly affected by the powder granulometry, the packing density, and local particle arrangement among other things. Thus, the laser absorption varies with the number and size of the particles exposed by the irradiated beam area. Reflectivity of the powder bed increases with decreasing particle size, which causes less absorption of laser power [138]. Higher thermal absorptivity is achieved when the powder packing density increases, involving greater surface reflections within a closely packed group of particles [139].

Laser absorptivity of the powder, n, is an important parameter for L-PBF and is defined as the fraction of incident laser power absorbed by the material [207]. Bramson [208] relates laser absorptivity of the bulk material with the wavelength of the incident laser and the electrical resistivity of the material. However, the following equation that was proposed, does not account for surface effects as metal powders display higher laser absorptivity values than the wrought material because of the multiple reflections and surface changes between powder particles:

$$n_s = 0.365\sqrt{\frac{\mu}{\lambda}} - 0.0667\left(\frac{\mu}{\lambda}\right) + 0.006\sqrt{\left(\frac{\mu}{\lambda}\right)^3} \quad \textbf{(3-21)}$$

where n_s is the laser absorptivity of bulk material, λ is the wavelength of the incident laser [m], and μ is the electrical resistivity of the material [Ω m]. The surface effects and the scattering due to individual powder particle reflectivity was studied by Zhang et al. [209] and is depicted in Figure 3.22.

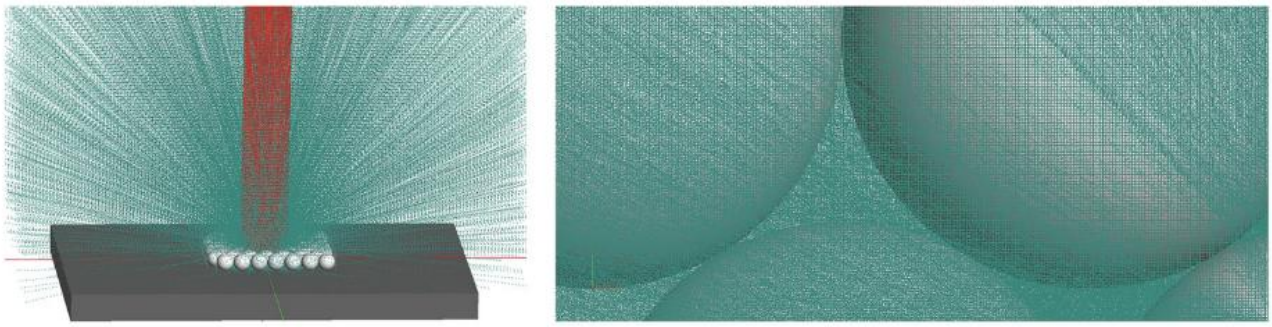

Figure 3.22: (Left) The laser beam is perpendicular to the powder layers and is scattered to the external environment (the red ray is incident light and the green ray is reflected light); (Right) multiple scattering occurs from spherical surfaces reproduced from [209]

Zhang et al. [209] found that the actual irradiation area decreases with increasing particle size, which limits the absorbed irradiance obtained in the powder array/bed. This indicated a negative correlation between powder particle size and laser absorptivity. Although it should be noted that the simulations performed by Zhang et al. utilised powder particles of the same size and attempted to pack them as closely as possible on a single plane.

3.4.1.3. Radiation pressure

Electromagnetic waves and thus laser radiation are carriers of energy and momentum. The laser radiation and its impact on irradiated matter is commonly described in terms of laser intensity as a continuous field quantity, nevertheless it can also be described as a flux of photons. Mahrle and Beyer [70] derived the radiation pressure distribution in the case of a Gaussian intensity distribution as:

$$\boldsymbol{P_{Rad(z,r)}} = \frac{\boldsymbol{I_{L,CW}\,(z,r)}}{\boldsymbol{c}} = \frac{\boldsymbol{1}}{\boldsymbol{c}} \cdot \frac{\boldsymbol{2 \cdot P_{L,CW}}}{\boldsymbol{\pi \cdot (r_B(z))^2}} \cdot \boldsymbol{exp}\left(-\frac{\boldsymbol{2 \cdot r^2}}{\boldsymbol{(r_B(z))^2}}\right) \qquad \textbf{(3.22)}$$

where c is the vacuum speed of light $c = 3 \times 10^8$ ms^{-1}, P is laser power, z is the coordinate in propagation direction of the beam, r is the coordinate in radial direction, and $r_B(z)$ is the actual beam radius. The calculated radiation pressures for various laser powers and beam radii can be observed in Figure 3.23. For a Concept Laser M2 machine with a beam radius of 25 µm and a max laser power of 200 W, the radiation pressure is roughly 679 Pa (at 200 W at the centre of the beam) and 169 Pa (at 50 W at the centre of the beam).

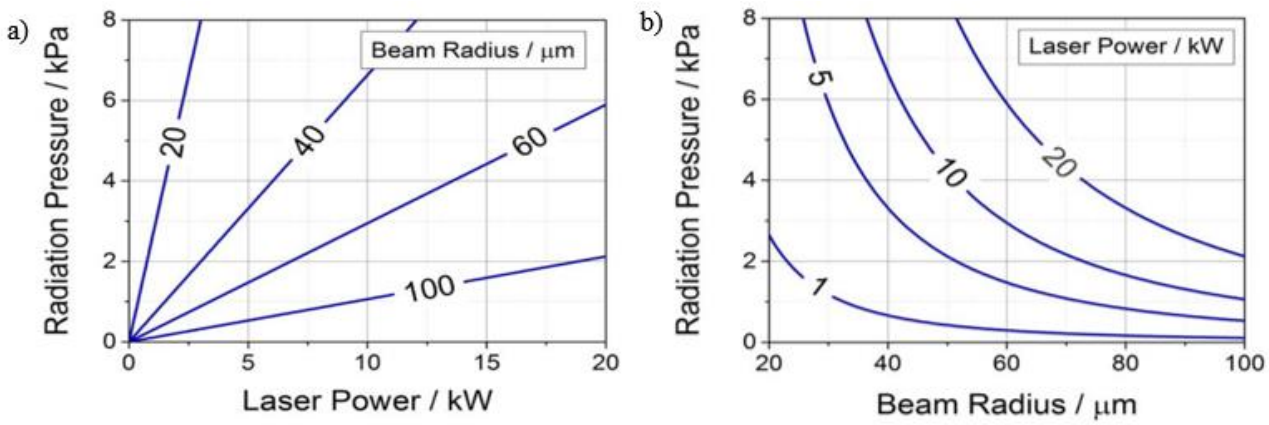

Figure 3.23: (a) Calculated values of radiation pressure as a function of laser power in the working area of high-power laser material processing. (b) Calculated values of radiation pressure as a function of beam radius in the working area of high-power laser material processing reproduced from [70]

When sintering particles that have segments that should not melt (WC), the application of the correct radiation pressure is extremely important. If the radiation pressure is too high the particles will be forced away from the melt pool. If the power, and subsequent pressure, is too low the particles may not melt or fuse to the plate as the laser intensity would be too small.

3.4.2. Heating of the powder bed/heat transfer

Localised sintering or melting occurs once the laser beam comes into contact with the surface of the powder bed. Most of the energy is absorbed by the powder particles during this process. A single solid scan track is formed by consolidation of the melted powder once the Gaussian laser heat source moves over the melt region. There are three main heat transfer mechanisms that occur during the L-PBF process. These mechanisms are heat radiation from the laser beam to the powder bed, heat conduction between the powder particles and the previous layers, and heat convection between the inert ambient atmosphere and consolidated layer. These heat transfer mechanisms make the thermal behaviour during the L-PBF process complex [210]. Figure 3.24 displays the physical model of the thermal behaviour during the L-PBF process.

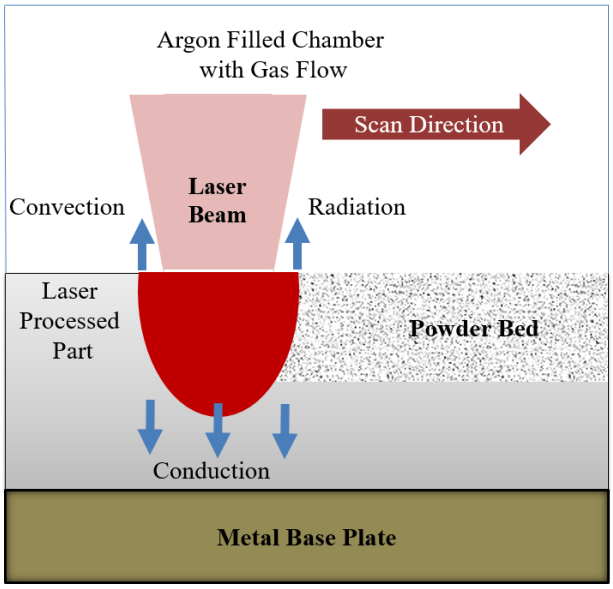

Figure 3.24: Schematic of the L-PBF physical model adapted from [210]

Research shows that there are many different methods employed to calculate the heat transfer mechanisms [124], [210]–[217]. The L-PBF system first needs to be defined, as well as all the modes of energy transfer in the system. Using the first law of thermodynamics, the general energy balance equation in the closed L-PBF system can be written as

$$\boldsymbol{Q_L = Q_{CD} + Q_{CV} + Q_R} \qquad \textbf{(3.23)}$$

where Q_L is the input laser energy, Q_{CD} is the conduction losses, Q_{CV} is the convection losses, and Q_R is the radiation losses [210], [215]. Heat conduction losses can be described by Fourier's law, which satisfies the second principle of thermodynamics. This equation is [218]

$$\boldsymbol{q_x = -kA\frac{\partial T}{\partial x}} \qquad \textbf{(3.24)}$$

where q_x is the heat transfer rate, k is thermal conductivity, A is the area of the surface, and $\frac{\partial T}{\partial x}$ is the temperature gradient in the direction of heat flow. The general three-dimensional heat conduction equation is [218]

$$\boldsymbol{\rho C\frac{\partial T}{\partial t} = k\left(\frac{\partial^2 T}{\partial x^2} + \frac{\partial^2 T}{\partial y^2} + \frac{\partial^2 T}{\partial z^2}\right) + \alpha I(x, y, z, t)} \qquad \textbf{(3.25)}$$

where ρ is density, C is the specific heat, T is the temperature, α is the fraction of radiant energy absorbed per unit time (t) and unit volumes of metal, and $I(x, y, z, t)$ is the intensity of laser radiation [W/cm²]. Rosenthal [219], [220] determined the first analytical solution for three-dimensional distribution of heat due to a moving point heat source in a semi-infinite substrate.

$$\boldsymbol{T(\xi, y, z) - T_0 = \frac{\alpha P}{4\pi\lambda R} exp\left(-\frac{V\xi}{(2\delta)} - \frac{VR}{(2\delta)}\right),} \qquad \textbf{(3-26)}$$

Hooper [195] and Yuan and Gu [210] found that the last part of the melt pool to cool and solidify would be the top surface due to the fact that conduction is the predominant cooling method experienced by the melt pool. However, it should be noted that Yuan and Gu [210] also reported that

the Marangoni convection had great effects on the mass and heat transfer within the molten pool, as well as the pool geometry. Losses due to convection can be described by Newton's law of cooling [218]:

$$\boldsymbol{q = hA(T_{\omega} - T_{\infty})} \quad \textbf{(3.27)}$$

where q is the heat transfer rate, h is the convection heat transfer coefficient, T_{ω} is the temperature of the surface, and T_{∞} is the temperature of the fluid. Radiation heat transfer can be derived by using the Stefan-Boltzmann law of thermal radiation, which is described by the following equation [218]

$$\boldsymbol{q_{emitted} = \sigma A T^4} \quad \textbf{(3.28)}$$

where σ is the proportionality constant called the Stefan-Boltzmann constant and has the value $5.669 \times 10^{-8}\ \mathrm{W/m^2 \cdot K^4}$. Ma and Bin [211] stated that thermal exchange with the surroundings is mainly due to convection heat transfer within the L-PBF system. This, however, is conflicting with other publications [195], [210]. Understanding the different heat transfer mechanisms in L-PBF is crucial to comprehend the different effects on the powder bed during the process. This may be even more important for WC based MMCs, since the bulk materials are made up of metal binders with relatively low melting points and WC with an extremely high melting point.

3.4.3. Binding mechanisms and fluid behaviour

Knowledge of the different binding mechanisms used in laser processing of materials is important to understand the limitations of the process. There are a few binding mechanisms present in L-PBF, namely, solid state sintering (SSS), liquid phase sintering (LPS), partial melting, and full melting. These binding mechanisms as well as different fluid behaviours are discussed in the following sections. It is very important to understand the fluid behaviour of a molten pool during L-PBF, as it determines the morphology of the surfaces and consequently the density of the final part. Ideally, the molten pool or laser track should spread well, be continuous, and evenly spread over the underlying layers. However, this is not always the case with various materials and process parameters, and thus the various phenomenon responsible for this behaviour should be well understood [221]. Materials well suited for L-PBF have good laser absorptivity, and balanced properties of thermal conductivity, surface tension, and viscosity [164].

3.4.3.1. Solid state sintering

At temperatures in excess of roughly half of the absolute melting temperature, metal powder particles bond due to solid state diffusion during sintering. This involves the formation of 'necks' or solid bended mass transport mechanisms between adjacent powder particles. Various chemical and physical reactions occur, with the most important mechanism being diffusion. The main driver for

sintering is the reduction of free energy as a result of particles fusing together. The mass flow is initiated through stresses from decreased surface curvatures and an elimination of the surface area [222]. Possible solid state sintering mechanisms are evaporation and condensation, viscous or plastic flow, grain boundary diffusion, surface diffusion, and volume diffusion [221]. The rate of solid state sintering is influenced by a number of factors such as the material, pressed density, particle size, heating rate, temperature, atmosphere, and time [221]. A number of materials can be processed using SSS, as long as the temperature is high enough to deliver the required kinetic energy for transport of vacancies across the grain boundaries. However, SSS is a slow process, which for L-PBF requires reheating of the powder particles in order to increase the diffusion rate of atoms for an acceptable laser scanning velocity [223].

In an attempt to consolidate titanium powder through SSS using L-PBF, researchers [224] used low intensity laser light (100 – 300 W/cm^2) for a long period of 5 seconds. Gusarov et al. [224] found that the temperature stayed below the α/β-transition temperature of 890 °C. With respect to L-PBF, it can be questioned as to whether sintering kinetics laws are applicable, as the laser interaction time is in the milliseconds. With short interaction times only limited diffusion can occur if the powder bed is not preheated to high temperatures [221].

3.4.3.2. Liquid phase sintering

Liquid phase sintering is a consolidation technique that is applicable to a mixture of two metal powders, a powder with various alloys, or a metal and a ceramic powder. This mixture consists of a structural material which has a high melting point, and a binder metal which has a low melting point [225]. With laser processing, the laser energy should be high enough to raise the powder temperature between the melting points of the two metals. However, due to the short interaction time with the laser, only a limited degree of rearrangement of solid particles can take place. LPS involves a number of different stages. The LPS process undergoes melting, wetting or liquid flow, rearrangement, and densification, followed by pore removal and solute precipitation. The first stage involves the rearrangement of solid particles due to capillary forces caused by melt formation. This is followed by dissolution reprecipitation and then solid-state sintering [222]. For improved densification with a reduction in pores, the grain size of the binding particles should be smaller than that of the structural material. The bigger particles should be well wetted due to their larger mass and higher enthalpy. Low laser energy will result in the formation of large pores owing to the bigger particles not being completely wetted by the liquid or partial liquid phase binder. However, high laser energy could lead to the formation of excess liquid resulting in compact distortion. Therefore, optimal laser energy and the correct ratio of binder to structural material is crucial for a good sintered structure [222]. Different types of powders and powder mixtures can be used. Common types are a mixture of particles of high

and low melting point materials, composite grains, or coated grains [223]. Composite grains result in higher SLS green density and a better surface roughness than a mixture of separate WC and Co powders [226]. When the melting points between the structural and binder materials are close together, melting of some of the structural particles can occur. In such an instance the process is referred to as partial melting rather than liquid phase sintering, due to the substantially higher amount of melt present [221].

Applying the L-PBF process to WC-Co is often classed as LPS depending on the energy density experienced by the material. It could be detrimental to the WC material properties should it be heated to its melting point, which is roughly 2870 °C. Since the cobalt's melting point is 1493 °C and the binder element starts to evaporate at 2900 °C [50], [53], the final WC-Co component would materialise with a different chemical composition than the starting powder material. Also, it is important to note that with the laser processing of WC-Co, due to the short sintering time through limited interaction with the laser beam, only the rearrangement sintering stage is reached. The densification phase is not reached due to the rapid heat loss and steep thermal gradients experienced by the material. Thus some authors opt to employ a post processing densification operation such as infiltration or HIPing [12], [29]. The laser processing of cemented tungsten carbide is discussed in more detail in Chapter 4.

3.4.3.3. Full melting

High heat inputs result in the complete melting of the powder particles during laser interaction. This process can be referred to as selective laser melting rather than selective laser sintering. This is where all of the terminology can become quite confusing. For instance, a SLM process requires exactly the same components as an SLS process. The main difference is the temperature experienced by the powder from the laser and whether full melting occurs. Nearly fully dense parts can be produced with SLM, however, since the material is completely melted to a liquid phase, the process is more difficult to control than the SLS process. The main causes of this are the thermocapillary and capillary effects, the large shrinkage and residual stresses, and the high levels of oxidation [221], [223]. For each new material, a suitable process window needs to be determined through experimentation. Thus, only a few materials are commercially available for the L-PBF process [223].

3.4.3.4. Surface tension

The liquid-vapour surface tension (γ_{LV}) of metals varies from 300 mN/m for alkali and semi metals to about 1800 mN/m for d-transition metals. For tungsten the surface tension force is 2361 mN/m and the surface tension temperature coefficient or gradient ($d\gamma_{LV}/dT$) is -0.31, which means the surface tension decreases with increasing temperature [146]. Surface tensions vary widely depending on the

materials involved [221]. Sidambe et al. [184] mentions how the high melting point of tungsten contributes to a high cohesive energy and high surface tension which, in turn, leads to poor process stability. The desired melt pools should have good wetting and spreading behaviour to ensure low porosity of the final parts.

3.4.3.5. Viscosity

The dynamic viscosity of liquid metals ranges from 0.2 mPa·s for alkali metals to 5 mPa·s for d-transition metals. The viscosity of tungsten is stated to be as high as 8 mPa·s [146]. Viscosity decreases with increasing temperature and therefore can be defined as:

$$\boldsymbol{\eta = \eta_0 exp\left(\frac{Q}{RT}\right)} \qquad \textbf{(3-29)}$$

where η is the viscosity of liquid metals, η_0 is a constant, Q is the activation energy for flow, R is the universal gas constant, and T is the absolute temperature. According to Agarwala et al. [227] and Tolochko et al. [228], the viscosity of a solid-liquid mixture during the L-PBF process can be defined as:

$$\boldsymbol{\mu = \mu_0 \left(1 - \frac{1-\varphi_L}{\varphi_M}\right)^{-2}} \qquad \textbf{(3-30)}$$

where μ_0 is the base viscosity that includes temperature terms, φ_L is the volume fraction of liquid phase, and φ_M is the volume fraction of the solids. During L-PBF the particle bonding is controlled by the base viscosity, which is strongly dependent and inversely proportional to the temperature. For WC-Co, the base viscosity should be low enough to allow for complete wetting of the reinforcing (WC) particulates so as to ensure sufficient densification. However, at the same time the solid-liquid viscosity should be high enough to prevent the balling effect [227].

3.4.3.6. Wetting properties

The wetting behaviour of a liquid on a solid substrate is fundamental to the L-PBF process since it determines the spreading of the melt pool in its liquid phase and thus determines the infiltration characteristics, actual layer thickness, and scan track width. The wetting of a liquid on a solid substrate is described by the equation of Young [229], where the contact angle is derived with:

$$\boldsymbol{cos\,\theta = \frac{\gamma_{SV} - \gamma_{LS}}{\gamma_{LV}}} \qquad \textbf{(3-31)}$$

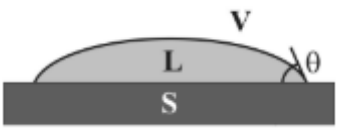

Figure 3.25: Wetting angle schematic for equation 3-31 adapted from [221]

where γ_{SV} is the surface tension of the solid – vapour interface, γ_{LS} is the surface tension of the liquid – solid interface, and γ_{LV} is the surface tension of the liquid – vapour interface [221]. Oxide films

present on a substrate results in higher contact angles for the liquid material due to the surface tensions being lower than the majority of metals. The wetting is also very important for pore reduction, as the proceeding layers need to be able to fill any melt gaps in the previously sintered layers.

The fluid motion that occurs in melt pools with non-uniform temperature can be described by the Marangoni equation. In melt pools, the surface tension of the material is dependent on the temperature experienced. This induces Marangoni flow in regions with low to high surface tension. The strength of thermocapillary flow is estimated from the dimensionless Marangoni number:

$$\boldsymbol{M_a = \frac{d\gamma_{LV}}{dT}\frac{dT}{ds}\frac{L}{2\eta\delta}} \qquad \textbf{(3-32)}$$

where M_a is the Marangoni number, $\frac{d\gamma_{LV}}{dT}$ is the surface tension gradient, $\frac{dT}{ds}$ is the thermal gradient, L is the characteristic length of the melt pool, η is the viscosity, and δ is the thermal diffusivity [230].

During laser sintering of WC, Gu and Shen [231] found that the presence of WC particles in the melt pool influence the Marangoni effect, and thus the material flow is restricted, thereby limiting the neighbouring WC grains from aggregating. Significant grain refinement or use of submicron grains could improve the wettability between the binder and the matrix, to obtain a strong interfacial bonding. Gu and Shen [232] discussed that melting of a metal matrix Co and Cu formed a molten pool containing both liquid and solid phases. By using a Gaussian laser beam in sintering, a large temperature gradient forms between the centre and edge of the molten pool, hence giving rise to the surface tension gradient and the resultant Marangoni convection The formation of Marangoni convection induces capillary forces for liquid flow, facilitating an efficient densification of the structural particles with the wetting liquid [232].

With respect to cemented tungsten carbides, the mechanism that is not yet fully understood, is the migration of liquid cobalt-based binders when sintering carbide articles comprising of layers with different carbon contents. The migration occurs from a layer with a high carbon content into a layer with a low carbon content [233]. According to Liu et al. [234] the flow of liquid cobalt can be driven by the difference in capillary forces, which may be caused by the difference in the binder composition and WC grain size. The wettability of tungsten carbide by liquid cobalt-based binders is complete at low carbon contents and becomes inadequate with increased carbon content. Konyashin et al. [233] found the wetting angle of WC by a cobalt binder saturated with carbon was relatively poor at 15°. The capillary forces and the carbon content play a large role in the wettability of WC by the liquid cobalt binder. The regions with the low carbon content tend to attract the liquid cobalt binder from areas with higher carbon content. This migration of cobalt could also be caused by other well-known phenomena such as reaching of thermodynamic equilibrium of chemical potentials of the binder components in the liquid phase and various capillary forces at different WC grain sizes. Zhou et al.

[146] studied the molten characteristics of tungsten processed with L-PBF and found that the time required to solidify the tungsten molten pool is substantially shorter (46 µs) than the time to completely spread a molten droplet (86.3 µs). This indicates tungstens intrinsic tendency towards balling and thus the conventional melting of WC-Co should be avoided or performed strategically different from predictable L-PBF.

3.4.3.7. Evaporation

High heat inputs into different materials can cause evaporation during the L-PBF process. When a material of a certain chemical composition is exposed to high temperatures, the separate elements can be brought to their respective boiling points and evaporate from the material structure. This then causes a deviation in the material's chemical composition from the original starting material. The evaporation process also induces a recoil pressure on the surface of the melt pool. This can lead to trapped gas below the melt, which results in increased porosity. Vapour formation above the melt surface can also lead to a decrease in laser energy that is absorbed by the material [221]. According to He et al. [235], the peak temperature of the molten pool during laser welding, often exceeds the boiling temperature of the elements. Khan and Debroy [236] showed that the rates of vaporisation of different elements at low pressure, during laser welding can be calculated from the Langmuir relation:

$$\boldsymbol{J_i = A_c P_i / \sqrt{2\pi M_i RT}} \qquad \textbf{(3-33)}$$

where J_i is the vaporisation rate [kg-mole/m²s], A_c is a dimensionless parameter, P_i is the partial pressure of element i [N/m²], M_i is the molecular weight of element i [kg/kg-mole], R is the gas constant [kg m²/(s² kg-mole K)] and T is the temperature [K]. Since A_c is not known, the following dimensionless form of the equation can be used:

$$\boldsymbol{J_i / J_j = (P_i / P_j)\,(M_j / M_i)^{\frac{1}{2}}} \qquad \textbf{(3-34)}$$

The equilibrium partial pressure P_i of an element i over the molten pool depends upon the composition of the molten pool and the temperature. The equilibrium vapor pressure P_i can be approximated for temperatures T between the evaporation temperature T_{LV} at a pressure P_o and the critical temperature T_{cr} as:

$$\boldsymbol{P_i = P_o \exp\left(\frac{-\Delta G_{LV}}{RT}\right) = P_o \exp\left(\frac{-L_{evap}(T - T_{LV})}{RTT_{LV}}\right)} \qquad \textbf{(3-35)}$$

where ΔG_{LV} is the free energy of formation, and L_{evap} is the latent heat of evaporation. This equation is only valid for temperature ranges where the ratio of latent heat to the difference in compressibility between the liquid and vapor is constant.

Keyhole formation is one of the issues in L-PBF which causes porosity in a part. When the melt pool is heated to a high enough temperature, a recoil momentum produced by the vaporised material exerts

a force on the molten material and a cavity forms under the solidified track [200]. The recoil momentum pressure produced by the vaporisation can be calculated within kinetic theory as [237]:

$$P_r \sim 0.56 P_s \tag{3-36}$$

where P_r is the recoil momentum pressure, and P_s is the saturated vapor pressure over the surface of temperature T_s. The saturated vapor pressure is given by:

$$P_s = P^* \exp\left[\lambda\left(\frac{1}{T_b} - \frac{1}{T_s}\right)\right] \tag{3-37}$$

where P^* is the atmospheric pressure in the process chamber, λ is the evaporation energy per atom [eV], and T_b is the boiling point temperature [K]. To create a keyhole pore and force the molten material out of the cavity, the recoil pressure must exceed the pressure produced by the surface tension where [237]:

$$P_r > \frac{\gamma}{\sigma} \tag{3-38}$$

where γ is the surface tension at boiling temperature [N/m] and σ is the half-width of the Gaussian beam. For a moving Gaussian beam moving with a scan velocity, v, the temperature at the centre of the beam is [200]:

$$T = \frac{\sqrt{2} n I \sigma}{k\sqrt{\pi}} \tan^{-1}\sqrt{\frac{2D}{v\sigma}} \tag{3-39}$$

where n is the absorptivity of the powder, I is the laser intensity, k is the thermal conductivity, and D is the thermal diffusivity. So, rearranging the equation and assuming *tan* is small, the keyhole threshold scan velocity v is:

$$v_t = \frac{4D}{\sigma}\left[\frac{\sqrt{\pi} k T_b}{n I \sigma}\right]^{-2} \tag{3-40}$$

It is crucial to stay above the keyhole threshold scan velocity to avoid uncontrolled porosity build up inside the parts. The laser parameters selected has a strong influence on the evaporation of the material. Leitz et al [238] expressed the amount of vaporized material by using the Cahn-Hillard equation [238]:

$$Q'_v = \dot{m} \cdot \Gamma \cdot \left(\frac{1-\phi}{\rho_{vapour}} + \frac{\phi}{\rho_{metal}}\right) \tag{3-41}$$

where $\dot{m}$ is the evaporation rate [kg/(m^2.s)], ρ_{vapour} is the vapor density [kg/m^3], ρ_{metal} is the metal density [kg/m^3], Γ is the evaporation on the metal surface [1/m], ϕ is the phase function, and Q'_v is the evaporation [1/s]. When it comes to cemented tungsten carbides, Li et al. [9] found that out of the three major binder elements (Co, Fe, Ni), the Ni had the highest evaporation rate with Co having the lowest. Thus, for the L-PBF process, a cobalt binder is the preferred choice for this study. Bricín [239] mentions that the amount of vaporised binder is greater, the higher the power of laser used or the lower the speed of the motion of the laser spot, thus it is crucial to identify the parameter range

where high evaporation occurs. For WC-Co some of the properties relevant to evaporation can be observed in Table 3.4.

Table 3.4: Properties, vapor pressure and partial pressure of present elements [9]

	W	C	Co
Atomic Weight	183.84	12.00	58.933
Boiling Point	5828 K	-	3200 K
Nominal Molar Fraction (X_i)	0.537	-	0.088
Nominal/Measured ratio of weight fraction	1.09	-	0.82
P_i^0 (at 3200 K)	< 1 Pa	-	1.013 x 10^5 Pa
$P_i = X_i P_i^0$	-	-	0.891 x 10^4 Pa
J_i/J_{Ni}	-	-	0.433

From Table 3.4, given that cobalt has a lower boiling point than tungsten and tungsten carbide, the selected laser parameters should be such that the evaporation of cobalt due to high heat input is limited during laser processing.

3.4.3.8. Oxidation

Oxidation is often common with L-PBF due to several possible causes such as the presence of oxygen in the process chamber, the trapped oxygen in the powder bed, the pores of the powder particles, moisture on the powder particles and the high temperatures involved. Oxidised powder has been linked to defects induced during L-PBF such as porosity and cracks, decrease in powder flowability, reduced wettability of the molten scan track, and increased surface roughness of the part [156]. Laser absorptance of oxides is substantially different to that of metals. Oxidation of the subsequent layers or substrate can lead to a deterioration in the wetting by the liquid melt pool during the melting process. The oxidation reaction of a metal M in an environment containing oxygen is:

$$\boldsymbol{xM + O_2 \leftrightarrow M_x O_2} \qquad \textbf{(3-42)}$$

$$\text{With } \boldsymbol{\Delta G = RT \ln p_{O_2}}$$

where ΔG is the free energy of the reaction, T is the absolute temperature, and p_{O_2} is the partial pressure of oxygen. Metals are more susceptible to oxidation when the free energy of the reaction is high. The metals also do not oxidise when p_{O_2} is lower than its equilibrium value [221]. One issue with the processing of tungsten carbide with L-PBF is the fact that both tungsten and carbon have a high oxidation affinity and sensitivity. So any oxygen present in the build chamber could pose an issue for the final part quality [146].

3.5. Summary of Chapter 3

Chapter 3 begins with an overview of additive manufacturing and the different processes that have been used by researchers to produce tungsten carbide parts. The chapter then shifts focus to the laser

powder bed fusion technology due to the scope of the research. The laser powder bed fusion process chain was then summarised and discussed. The complexity of the process is highlighted through the vast number of parameters that are displayed with many of the important parameters being studied and discussed in further detail. The chapter then moves from a macroscopic level where the process is reviewed down to a finer level where the physics, thermodynamics, and fluid dynamics of the process are reviewed and discussed.

Chapter 4

Laser Powder Bed Fusion of Tungsten Carbide

A preliminary study of literature showed several publications on the manufacture of tungsten carbide parts using L-PBF [4], [50]–[52], [240]. In the following sections, the history of laser powder bed fusion of tungsten carbide cobalt is discussed as well as the challenges and integrity issues from the process. The literature was then critically analysed to identify the main scientific gaps, which this study could fill. It should be noted that the processes selective laser melting, LaserCUSING, and direct metal laser sintering (DMLS from the 90's when only sintering was possible with the laser power available) all now refer to the laser melting process, as the material is conventionally completely melted. A method for complex material systems such as WC-Co consisting of two or more components having different melting points are, on the other hand, referred to as laser sintering, due to only the partial melting of only one of the materials. This is of course, only applicable if the melting temperature of the tungsten carbide is not reached during the process, which in a number of publications, it is [30], [50]. However Iveković et al. [241] observed three different bonding mechanisms when processing tungsten heavy alloys with L-PBF. These mechanisms were liquid phase sintering, partial melting, and complete melting. So, the terminology that was used in this study, regardless of the phase or bonding mechanism was laser powder bed fusion. However, in the interest of accurately reporting the works of other authors, the term they used to describe the technology was used.

4.1. History of L-PBF of Tungsten Carbides

4.1.1. 1992-2016

Zong et al. [26] from the University of Texas at Austin appeared to be the first to publish works on the laser sintering of tungsten carbide based powders in 1992. They successfully produced a WC-Co-Ni part, which was reported to be strong with rough surfaces. The University of Leuven in Belgium published their first laser sintering research on tungsten carbide powder around 1997 [242]. The researchers used mixed and mechanically alloyed WC-Co powder and processed this powder with low sintering energy densities [50], [243]. The relative density that was achieved through this was roughly 40% and had to be redensified through additional post processing operations [12], [214], [223], [225]. In 1999 the University of Texas at Austin derived similar results in density through their

approach [244]. The German Fraunhofer IWS and Fraunhofer ILT research institutes also succeeded in the sintering of hardmetals in 1999 but were unable to obtain a high enough density through parameter optimisation alone [225]. Laoui et al. [226] conducted experiments by laser sintering single two-dimensional hardmetal powders. It was reported that the use of mechanical alloyed powders improved the density and surface finish of the sintered layers relative to the properties obtained by conventionally mixed powders. During the 90's the highest achievable density without post processing was roughly 40%.

In 2002, Wang et al. [12] published a paper, which was devoted to the experimental study and simulation of DMLS of WC-Co hard metal powders. In this paper, the effect of laser power and scan speed on mixed WC-9wt%Co powder was studied. A sample was produced through this work, with a laser power of 8 W and scan speed of 10 mm/s. Wang et al. [12] found that the results were better with a lower laser power (8 or 18 W) and slow scan speeds (10 – 15 mm/s). A green part density of 37% to 40% was achieved before infiltration.

In 2004 Maeda and Childs [8] presented preliminary results on the influence of powder size, shape, and cobalt composition on the ability to create cohort layers with SLS of various WC-Co powders. The work however, relied on post infiltration processes to densify the SLS parts. The highest theoretical density that was achieved was 47% before infiltration. This was derived from a laser power of 200 W and energy density of 100 J/mm². The study reported that the increase of cobalt content did not result in higher density parts and the use of granulated powder did not show good results. The granulated powder had pores inside the granules, which were present even after infiltration.

In order to combine the superior mechanical and thermal properties of WC-Co and copper, in 2006 Gu and Shen [231], [232] attempted to develop a WC-Co reinforcing Cu matrix composite. They were able to achieve a relative density of roughly 90.7% through parameter optimisation of the laser power and scan speed. Their study revealed that for a given scan speed, an adequate increase in the laser power can lead to a high densification with a homogeneous distribution of the reinforcing particulates.

In 2008, Gu and Shen [245] continued their work on WC-Co reinforcing copper matrix composites but moved towards the nanoscale. In this study they were able to decrease the porosity giving a theoretical density of 94.3%. The original nanometric nature of the WC reinforcing was retained even after exposure to the highly non-equilibrium laser irradiation.

In 2009, Kumar [240] from the University of Utah pursued an approach where pores were generated in the microstructure in order to densify the component through infiltration. Various compositions of

WC-Co powders were processed on a SLS machine. A relative density of 63% was achieved through parameter optimisation on a WC-9wt%Co powder and final density after infiltration was reported to be 96%. During parameter optimisation only the layer thickness and laser power were varied.

From 2010 to 2013, there was a significant breakthrough in the single stage compression of agglomerated and sintered WC-Co powder using laser melting. The Fraunhofer IPK and Fraunhofer IPT research institutes were able to achieve a relative density of 98% through parameter optimisation [50]. These results were also achieved by the Bremen Institut für angewandte Strahltechnik (BIAS) and TU Clausthal in Germany [52]. Gu and Meiners [246] were able to achieve a densification level of 96.3% with high laser energy input (2.55 kW/mm², 800 mm/s) of WC cemented carbide based hardmetals.

In 2015, Uhlmann et al. [50] gave an overview of the latest research results, published by Fraunhofer IPK in Berlin, Fraunhofer IPT in Aachen, BIAS in Bremen and IWB in Munich. Parametric studies were conducted and the impact of the laser scan speed as well as the laser power on the relative density of the sintered sample was determined. It was concluded that a high volumetric energy density of 1667 J/mm³ results in a high relative density but also evaporation of the cobalt binder. In May 2015 a patent was filed by Stoyanov [247] which covered a method of producing a cutting tool having an internal cavity from a starting powder using a selective laser sintering, selective laser melting, or binder jetting process. The assignee was cutting tool manufacturing company Kennametal Inc. Gu [248] utilised two different types of lasers to prepare WC-cemented carbide parts. The highest densification level achieved was 96.3% with a maximum hardness of 1870.9 $HV_{0.1}$.

In 2016, Reuber and Schwanekamp [30] developed a process chain for the resource efficient production of special solid tools using SLM. Reuber and Schwanekamp also stated that sufficient quality of WC-Co tools produced with SLM was not yet achievable for industrial production. Schwanekamp and Reuber [49] reported the effects of several different strategies in order to reduce internal stresses through an optimised temperature input approach. From review of the literature, it appears that they were the first to publish successful cutting with a L-PBF produced WC-Co tool. The tools were effectively used to machine AlCuMgPb and 42CrMo4 steel in a turning process. Khmyrov et al. [249] were able to produce crack free components by increasing the cobalt content and avoiding the formation of the brittle W_3Co_3C phase. Van Staden [98] did experiments with tool grade WC-6.6wt%Co powder and produced several layers on a tool steel substrate. The layer samples were analysed with microscopic imaging, SEM, EDS, and surface roughness profile measurement. The samples with high power, low scan speed and high hatch spacing were reported to be the most desirable.

4.1.2. 2017 -2020

In January 2017, Schwanekamp et al. [36] published the geometrical and topological potentialities and restrictions in SLS of carbide precision tools. In June 2017 Yamada et al. [250] concluded that both the powder and laser conditions need to be optimised so as to reduce cracks and improve porosity. Kumar and Czekanski [24] published a method for the optimisation of parameters for SLS of WC-Co in October 2017. Khmyrov et al. [251] revealed that, in general, the microstructure of WC-Co samples corresponds to the observed phase composition. Khmyrov et al. [252] were also able to obtain single track and monolayer samples of nano-structured WC-Co hardmetal through the SLM process. These samples consisted of a 25 wt.% WC and 75 wt.% Co and were found to be crack free, continuous, uniform, and well attached to the sintered WC-Co substrate. Domashenkov et al. [253] used conventional and nanocomposite WC-12wt%Co powders to produce samples with SLM. The samples were found to have significant changes in the microstructure and crystalline phases from the SLM process. The microhardness of the nanophase powder sample was slightly increased when compared to the microhardness of the conventional powder samples. Schubert et al. [254] also contributed to the body of knowledge with SLM of commercially available WC-17wt%Co.

Kumar [255] went on to publish a paper on process chain development for AM of cemented carbide in 2018. Brookes [256] stated that SLS of WC-Co has the advantage of direct forming and densification in one step, however, near-100% dense samples were not possible. Due to the localised high energy input, chemical imbalances like W_2C, carbon or eta-phase formation and locally different cobalt contents occur, leading to cracks and inner residual stresses. Brookes also suggested adding additional carbon to the WC-Co powder in an attempt to cancel out the experimental losses and deleterious eta-phase.

Li et al. [257] presented detailed microstructure characterisation on nickel-coated tungsten carbide parts fabricated with SLM. The laser parameters were kept in the range of 200 W to 280 W for power and 800 mm/s to 1600 mm/s for the scan speed, with laser spot diameter and layer thickness being 60 µm and 50 µm respectively. With these parameters, Li et al. [257] reported a porosity value of only 2.49% in their samples. Gu et al. [258] performed SLM experiments with WC reinforced Fe-based composites. It was reported that an increase in density can be achieved through an increase in laser power and a decrease in scanning speed, which is in line with the findings of other authors [50]. However, the micro-hardness was reported to be enhanced to a maximum of 511.6 $HV_{0.2}$, which is relatively low due to the high ratio of Fe to WC (3:1).

Uhlmann et al. [25] published their works on a concept and process chain for producing WC-Co based electrical discharge machine (EDM) electrodes with flushing channels using SLM. They found that

the best EDM results were achieved with electrodes that were produced using low energy density and subject to post HIP treatment due to better cobalt arrangement. Tomas et al. [37] conducted a study on the laser sintering of WC cutter shafts with integrated cooling channels. Cutter shafts were manufactured from WC-17wt%Co in a SLM machine with preheating at 650 °C. To reduce the η-phase in the parts, different heat treatment experiments were conducted. The paper concluded that the mechanical properties of the SLM produced cutter shafts were similar to those of conventionally produced hard metals.

In 2019 Li et al. [9] presented results where WC 80 wt% and gas-atomized NiAlCoCrCuFe 20 wt% were used in the SLM process to produce test samples. The samples were found to not possess the same mechanical properties over the entire area. The Vickers hardness and fracture hardness values were compared to conventionally sintered WC-Co and in some cases were found to be more favourable. Sidambe et al. [184] showed the effects of SLM processing parameters on the densification, microstructure and crystallographic texture of pure tungsten. They were able to obtain bulk densities ranging from 94 to 98%. However, micro-cracks and defects were also found due to the residual stresses induced in the part during the melting process.

Ku et al. [259] created a powder mixture of 90 wt% WC and 10 wt% Fe-Ni-Zr with an average particle size distribution of 1.11 µm. The powder had a poor flowability in comparison to a conventional Ti6Al4V powder for L-PBF. Out of 14 parameter sets, only 6 were successful in producing mechanically stable samples. Of which the highest theoretical density that was achieved was 95%. The sample with the highest density did, however, have cracks and large pores. Ku et al. [259] also found that the specific energy density of 16 J/mm² (laser power of 60 W and scan speed of 75 mm/s) was sufficient to completely wet the WC grains with the binder. Iveković et al [241] showed some success with the SLM of a tungsten heavy alloy (WHA) in the volumetric energy density range of 250-350 J/mm³. It was reported that with a suitable post processing heat treatment, the microstructure, and the properties of the SLM WHA parts were comparable to those produced with conventional powder metallurgy.

In July 2019, Fortunato et al. [29] published on their success of manufacturing a WC-Co cutting tool for gear production using SLM. A WC-17wt%Co powder supplied by LPW was used and exposed with a triple pass scanning strategy. The maximum achieved density was 98.7% and the part was reported to be virtually crack free. The triple pass strategy divided the effective total energy density into three scans of varying energy input (100 J/mm³, 210 J/mm³, and 310 J/mm³). This allowed for a less severe thermal load on the sample during the laser melting process.

In 2020, Al-Thamir et al. [260] studied the L-PBF processability of atypical WC-Co composite feedstock. This was achieved by performing single track experiments on WC_M-Co (12 wt% Co) composite using a 304 stainless steel substrate preheated to 200 °C. Only a small process window was capable to produce continuous tracks. Fries et al. [3] manufactured crack-free WC-17wt%Co inserts with L-PBF using powder bed heating of 900 °C and VED >463 J/mm³. The machining tests were conducted on the brass alloy Cu39Zn3Pb, the titanium alloy Ti6Al4V, and Inconel 718. The machining of steels was abandoned due to the high wear tendency.

4.2. L-PBF Integrity Issues

In order to avoid certain undesired properties or defects in L-PBF, the powder and exposure parameters should be optimised, taking into account their mutual interactions. Defects that are inherently associated with L-PBF are pores, cracks, delamination of layers, warping or curling, and changes in local material properties [34]. Properties or defects that need to be controlled during the L-PBF of WC-Co are porosity, microcracking, toughness, delamination, surface quality, and dimensional accuracy [50], [240], [249]. Some of the factors affecting these properties are defined in literature and are presented in the following sections.

4.2.1. Porosity

Gu and Shen [245] explain how porosity is inherent of the L-PBF process and the fact that the powder is not compressed after each layer. Thus, the powder layer contains a large amount of gas in between the particles. This gas is likely to get trapped as bubbles in the laser melt pool, during the localised melting and solidification of single tracks in extremely short time intervals (typically less than 4 ms) resulting in a certain amount of closed porosity. However, porosity in the final part could be caused by several factors. Maeda and Childs [8] found laser energy density to be the most dominant factor affecting the porosity of a L-PBF WC-Co part.

The AIF research report on Generieren und Fügen von SLM-Bauteilen aus Hartmetall [52] showed how the porosity is dependent on the laser parameters as well as the cobalt content of the powder. This phenomena was uncontested amongst various researchers [50], [240]. Reuber and Schwanekamp [30] found chemical composition, particle size distribution, and porosity of the powder, to be influencing factors on the bulk density of the final product. However, the powder particle distribution was not taken into consideration by Uhlmann et al. when determining the factor interaction [50]. The porosity of WC-Co samples produced using L-PBF and two different Praxair powders can be observed in Figure 4.1. The effects of varying the track offset and cobalt content on the porosity can clearly be seen in these images. The higher cobalt content had a higher theoretical density but the

sample in the image looks somewhat deformed when compared to the others. This could indicate that the parameters used to produce the sample were still not optimal to achieve a strong working part.

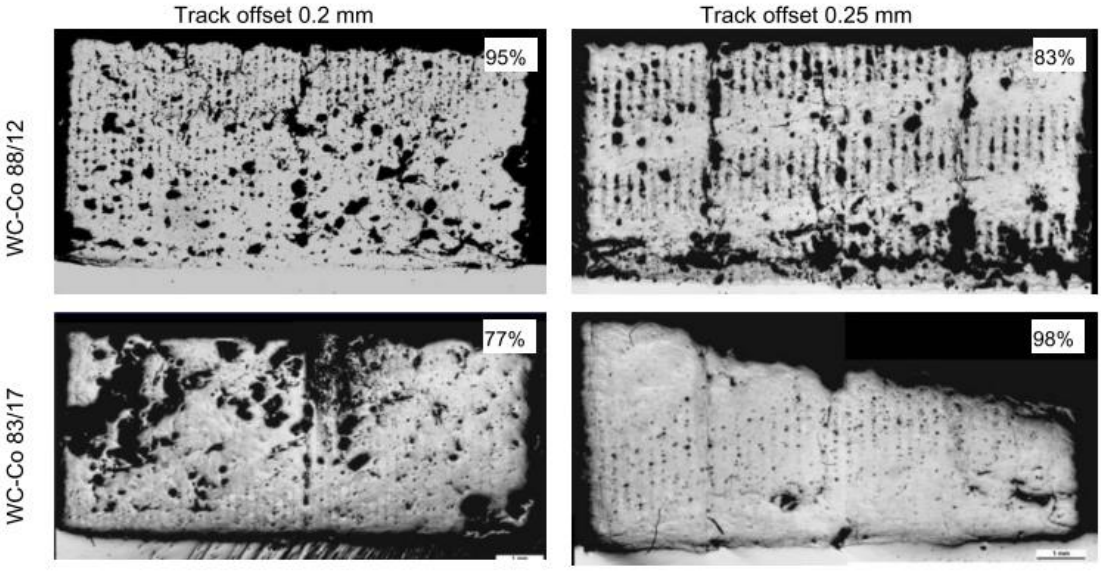

Figure 4.1: Qualitative comparison of treatment results with WC-Co 83/17 and WC-Co 88/12 with a laser power of 140 W, scan speed of 25 mm/s, spot size of 0.2 mm with their corresponding densities reproduced from [52]

Brookes [261] suggested that instead of reaching the melting point of tungsten carbide during L-PBF, that the focus be put on melting the cobalt and allowing it to partially wet the tungsten carbide. The L-PBF process would then need to be followed by a heat treatment post process in a carburising atmosphere to form stoichiometric WC-Co and rid the part of the W_2C phase. This should then be followed by a HIP or sinter-HIP process to consolidate the part and remove the remaining porosity. Fortunato et al. [29] found that a higher cobalt content in the starting powder increased the quality of the metallic matrix, reducing the number of cracks and pores after solidification. An excessively high energy density was also found to cause the vaporisation temperature of the cobalt to be reached. This is detrimental to the final part quality and the density of the part as the lack of cobalt does not allow for the filling of pores, especially if the starting percentage of cobalt is already low. It was also determined that HIP treatment increases the density of parts with lower or higher cobalt contents. However, parts with lower cobalt content had larger pores, which were not removed through the HIP process.

4.2.2. Microcracking

Uhlmann, Bergmann, and Grindin [50] found that all of the samples that were produced using L-PBF showed a pronounced tendency to crack regardless of the varying process parameters. However, Khmyrov et al. [249] was able to produce crack free layers by having a high percentage of cobalt content (25 wt.%). The cracks and porosity of WC-Co samples produced with different parameter sets can be observed in Figure 4.2.

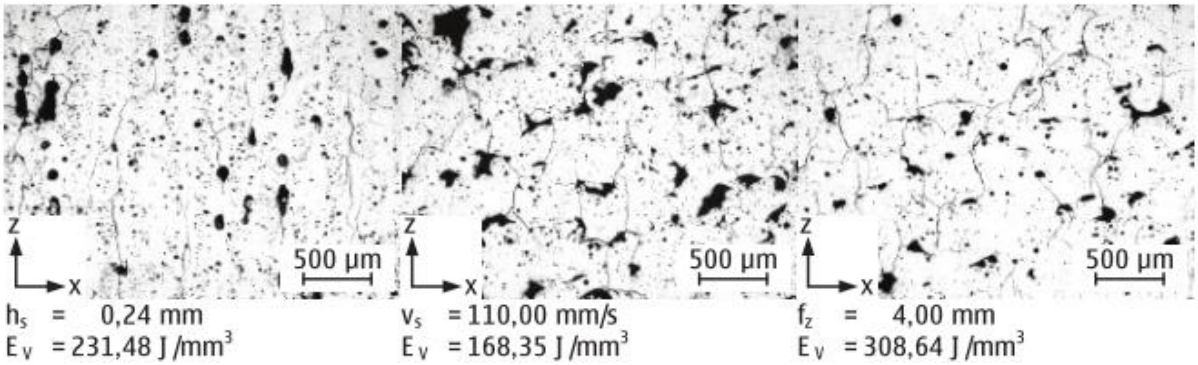

Figure 4.2: Porosity and cracks of the test samples characterised by their different factor levels reproduced from [50]

Fortunato et al. [29] showed that an increase in the total energy density that the part is exposed to, led to a reduction in the cracks. It was speculated that this could be due to the minimisation of temperature differences during production and subsequently the rate at which thermal expansion and contraction took place. However, it is important to note that the total energy density was divided and exposed on the material through a triple pass scanning strategy. Fortunato et al. [29] also found that cracking or overheating of the parts was strongly dependent on the surface area of the total exposure slice. They found that the total exposure area should be greater than 3.2 cm², however, no upper limit was tested but it is assumed it would be limited by the machine build plate area (78.54 cm²) and the cooling times experienced between layers.

Residual stress can be closely linked to deformation and toughness. Sharp voids due to porosity as depicted in Figure 4.2 can result in high stress concentrations, which combined with high residual stresses may pose a serious problem for crack initiation and propagation [262]. Krawitz and Drake [263] studied the residual stresses in cemented carbides and reported that thermal residual stress varies with binder content and carbide particle size for a series of WC–Co composites as depicted in Figure 4.3. It can be observed that as the amount of a phase increases, its average residual stress decreases. Also, as the WC particle size for a given composition decreases, the stress magnitude in both phases increases. Thus, for the L-PBF process, a larger grain size in the starting WC-Co powder may be preferred.

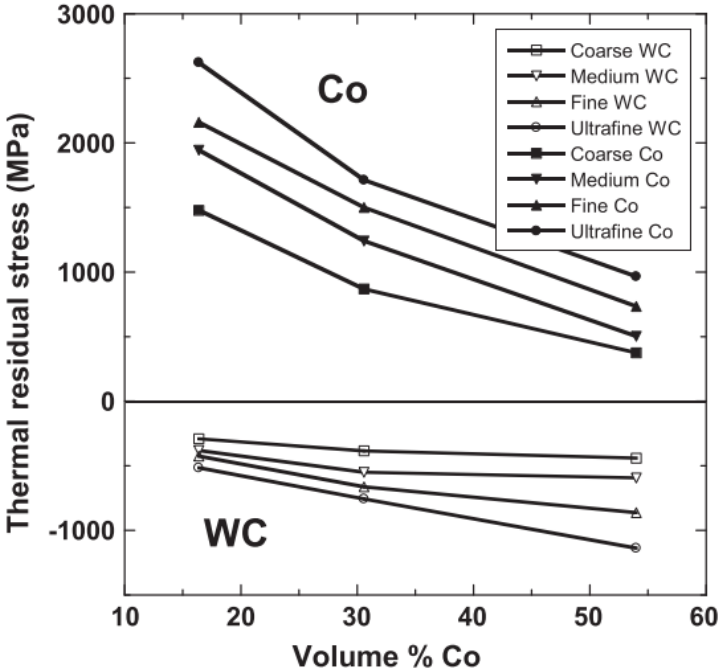

Figure 4.3: The strong effect of carbide particle size on thermal residual stress for a matrix of WC-Co samples reproduced from [263]

4.2.3. Microstructure

The grain size of the WC and metal binder content of the tools are controlled to balance the hardness, wear resistance, and toughness of the final tool, which is tailored to the type of application of the tool. For instance, if the application requires abrasive wear and little impact, the hardness and wear resistance is favoured over toughness. Though, if the application calls for a lot of impact and minimal grinding, then the toughness will be favoured over the wear resistance/hardness [264]. Brittle material rapidly forms micro-cracks when exposed to an impact, which leads to a short product life span. Thus, the microstructures must be manipulated in order to accommodate the different application requirements [1].

Murakami reagent is a common etchant used to reveal the microstructure of WC-Co parts. With respects to the microstructure of WC-Co parts produced with L-PBF, the microstructures are reported to be significantly different to the conventionally produced parts. Enneti et al. [185] observed large, uncontrolled columnar grain growth in their samples. Chen et al. [83] showed that SLM can introduce anisotropic micro-structures in cemented carbides. The L-PBF process led to a significant, rapid, and non-uniform WC grain growth in both vertical and horizontal cross-sections of the L-PBF processed carbides and both cross-sections show similar grain size distributions. Chen et al. [83] also found that a prominent microstructural feature for L-PBF processed carbides is the lamellar structure with alternating coarse and fine WC grains in the vertical cross-section (parallel to the laser beam), and there was no lamellar structure in the horizontal cross-section (perpendicular to the laser beam).

Li et al. [257] identified major microstructure features in their works with nickel-based cemented carbide. Characterisation of the M_2C dendrite band, the un-melted WC-W_2C powder and the Ni-based metal matrix was performed. Prismatic MC carbide formed in the molten pools, M_2C formed large scale layered structures, and η-phase were transformed from M_2C within the repeated heating regions. Domashenkov et al. [253] highlighted how thermal decomposition of WC leads to the formation of W_2C dicarbides and the appearance of the complex Co-W-C ternary phase. This decomposition leads to a decreased microhardness of the final parts. Gu and Shen [231] suggest that during the L-PBF melting of a WC metal matrix, the smaller WC particles are completely dissolved in the liquid binder. However, due to the rapid cooling induced through conduction and convection, the molten WC might precipitate again in the form of refined and dispersed particles.

4.2.4. Toughness, delamination, and curling

The toughness of a cutting tool is reliant on the binder and alloy content. When WC-Co is exposed with a high energy input, the alloying elements and binder evaporate, thus leaving only the tungsten carbide behind. This results in a brittle cutting tool with a low toughness and low porosity. However, if the WC-Co is exposed with a low energy input, only the LPS process takes place. This results in a high toughness and subsequently a high porosity [50]. A high porosity also inhibits the tool to cyclic loading applications, as crack initiation and formation from inherent pores is a problem.

Delamination occurs due to weak local bonds between layers and/or the base plate. Delamination generally occurs when suboptimal melting parameters are used and the heat distribution is not high enough to sufficiently bond the layers together [240]. High energy input and crack tendency were found by Ott [51] to result in part delamination of WC components. There appears to be a link between the porosity, crack tendency, toughness, and delamination with the energy input. A high energy input was reported to reduce porosity and cracks but also reduce the toughness through evaporation of the binder and subsequently lead to delamination between layers. Thus, balancing of the mandatory part properties and the energy input is important to realise parts suitable for the application at hand. As with conventional tungsten carbide cutting tools, there is always a trade-off between hardness and toughness. Hence the vast number of grades created for various applications and hardness/toughness requirements.

4.2.5. Surface quality and dimensional accuracy

The dimensional accuracy of the part is mainly affected by the laser offset. Since the offset depends on the size of the melt pool, it must be adapted if process parameters are changed [36]. Any sintered powder on the outside surfaces of the part will also affect the dimensional accuracy and surface quality. Iveković et al. [241] found a clear correlation between the thickness of the sintered powder

on the outer surface and the applied energy density. The study revealed that the powder particles attached to the outer surface of the part occurred through liquid phase sintering. This causes a high surface roughness on the outer edges, which in turn also affects the dimensional accuracy of the final part. Schwanekamp et al. [36] studied the geometric and topologic design aspects in L-PBF of WC-Co with regards to the characteristic design features of application optimised cutting tools. They mention that to partially improve the process-specific surface roughness and dimensional accuracy and to avoid curling and warping, different scan strategies with distinct parameter sets should be applied for critical regions. Van Staden et al. [265] found that by varying the process parameters there is a significant effect on the top surface finish of WC-Co single layer samples [98]. The results from this study can be observed in Figure 4.4.

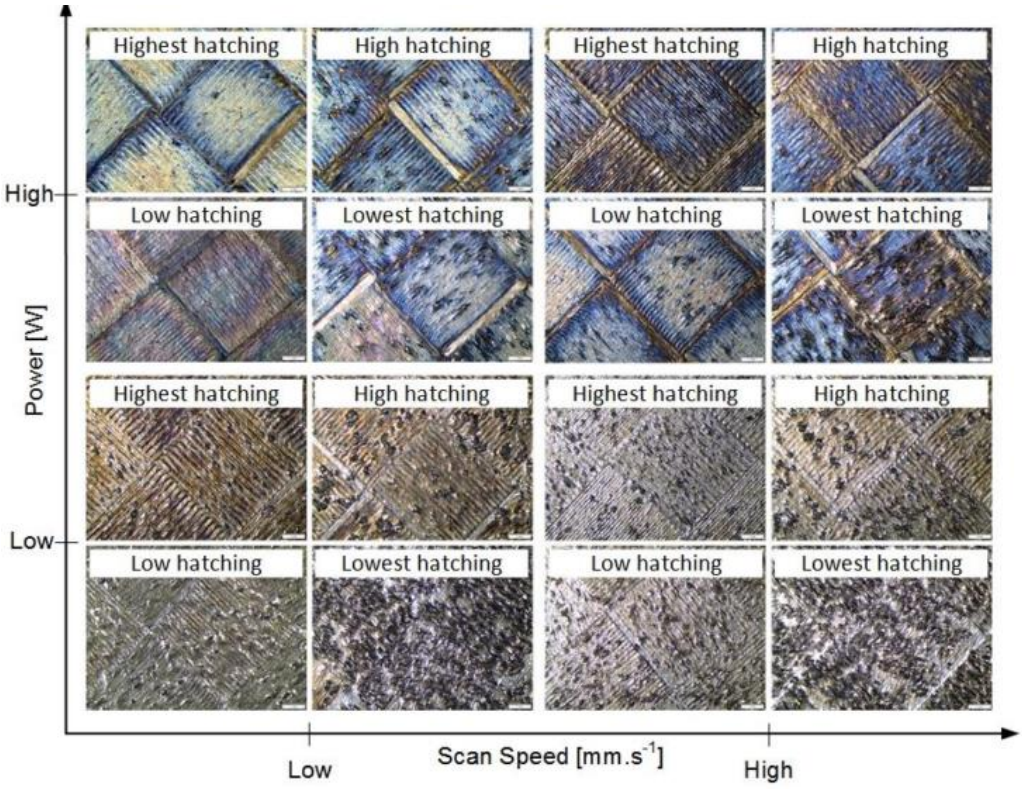

Figure 4.4: Microscope images of a single layer WC-Co sample combined with process parameters reproduced from [265]

From Figure 4.4, the surface finish of the top surfaces was best for high energy density values (high power, low scan speed). But by increasing the energy density, the powder build-up on the sides of the part increases, which in turn decreases the surface quality. In line with the suggestions from Schwanekamp et al. [36], different scanning strategies and parameter sets may need to be used for the part edges and top surfaces in order to improve the overall surface quality of L-PBF WC-Co produced components.

There appears to be a number of relationships between different part properties and the laser parameters/scanning strategies. It is clear from literature that the factors influencing the integrity and

quality of WC-Co L-PBF parts and their relative interactions are not yet fully understood. This further inhibits the use of the L-PBF process for manufacturing of dimensionally accurate tungsten carbide components with mechanical and material properties suitable for cutting.

4.3. Scientific Gaps Identified in Literature

The processing of tungsten carbide with L-PBF is extremely challenging due to the high melting point, high thermal conductivity, high melt viscosity, the material's affinity for oxygen at high temperatures, and brittle nature at room temperatures. This results in cracked, porous microstructures [28]. From the 59 publications on L-PBF of tungsten carbide-based materials reviewed, the use of high volumetric energy densities (>200 J/mm³) and power was the prominent solution to achieving a relatively high density. Use of a high VED consequently results in high evaporation rates of the cobalt binder, thus many of the researchers opted to mitigate this issue through using a powder with a higher cobalt content (WC-17wt%Co) for their final parameter optimisation and optimised cutting tools [3], [29], [49]. The use of the lower cobalt content powder (WC-12wt%Co) throughout this study could be beneficial to highlight any major issues that may not be prominent in higher cobalt content builds. A scientific gap in this sense is the final parameter optimisation and use of a WC-12wt%Co powder to produce the final cutting tools for testing.

Very few of the researchers even mention the scanning strategies or laser patterns used in their experimentation. Even though some researchers [29], [36], [49] indicate that the strategies used are critical to avoiding defects and improving the properties of the final L-PBF WC-Co components. It is apparent that there is a disconnection between the scanning strategies used and their effects on the final part quality. Schwanekamp et al. [36], suggested that different scanning strategies be used for different geometries of the tools in order to achieve better dimensional accuracy. However, there are many different strategies that are used by different machine manufacturers to expose the layers. Thus, the effects of the different scanning strategies on the final part properties, as well as the final cutting ability, do not seem to be well researched.

The development of WC based powders for the L-PBF process has progressed significantly over the years. The bulk of the progress on cutting tool development and testing of L-PBF produced cutting tools was only observed in the last six years (2016 - 2021). From the research, several materials have been cut with L-PBF produced tools. These materials include AlCuMgPb, 42CrMo4 steel, brass alloy Cu39Zn39Pb, titanium alloy Ti6Al4V, and nickel alloy Inconel 718. However, the researchers [3], [49] mentioned high wear rates for cutting of steels but do not accurately report the modes of failure experienced. Thus, there is limited data on the cutting of steels with L-PBF cutting tools. This further

limits the understanding of the different material grades and their cutting capabilities for different materials.

Preheating or thermal post processes were performed by all of the researchers who completed successful cutting tests with L-PBF WC tools [3], [29], [49]. Thermal postprocessing is a common practice for L-PBF parts to relieve the high stress concentration derived from the localised micro-melting and solidification of laser scanned tracks. Residual stresses are very high when the parts are still connected to the base plates [126] and this stress is significantly reduced upon separation. This leads to cracking and deformation of the part and hence thermal stress relieving should be applied before the part is removed from the base plate. To reduce the amount of post processing on the final tools and to understand the effects of just the L-PBF process on the final cutting performance, it was decided to not pursue any thermal post processing operations for this study.

4.4. Potential Modifications to Conventional L-PBF to Process WC-Co

This section discusses potential modifications to the conventional L-PBF process in order to improve the processability and decrease the issues during the laser sintering/melting of WC-Co parts. Some strategies or modifications that can be employed are:

- Coating and heating the base plate
- Varying the laser focal point/spot diameter
- Multi-pass laser melting strategy
- Multi-pass and multi-coat strategy
- Differential layer thickness strategy
- Controlling the powder particle distribution

Many of these strategies are unconventional and may pose more problems or changes than solutions. Some, however, are discussed and deliberated in more detail in the following sections.

4.4.1. Coating and heating of the base plates

Material compatibility is of high importance for base plates in the L-PBF process. The material to be processed must be compatible with the base plate material in order to ensure adequate adhesion of the L-PBF part to the plate. The DIN 1.2343 tool steel (in this case) base plates can be coated through a HVOF thermal spraying process with the same WC-Co powder that is to be used in the L-PBF process. This ensures decent bonding between the initial layers and the substrate of the base plate without altering the building parameters, and subsequently the material properties, to increase

adhesion. This also limits the contamination through diffusion of the base plate elements in the L-PBF part which was reported by Li et al. [9].

The base plate can also be heated to ensure it does not act as a heat sink during the processing of the initial layers. Since the bulk material has a higher conductivity compared to the powder bed, heat is removed from the initial layers a lot faster. Heating the base plate at a specific constant temperature for the period of the build, may assist with keeping the heat in the part to reduce the thermal gradients, and thus the residual stresses during the L-PBF process [266], [267].

4.4.2. Differential laser focal point

Varying the laser spot diameter by adjusting the focal point, can affect a number of properties in the final part [169]. Studies showed that the widening of the beam diameter for the processing of the refractory hard metal alloys is beneficial [52]. The beam diameter influences the laser intensity profile, in a similar manner to the power. This allows the user to optimise the scan speed, and hatch spacing in the most economical way, by maximising the power available. Through shifting the focal point, the material will be exposed to a lower intensity at the highest power. This is however, at a detriment to accuracy due to the increased spot diameter.

4.4.3. Multi-pass strategy

Various researchers have been successful in producing WC-Co components through fundamental changes to the conventional L-PBF process. Reuber and Schwanekamp [30] and Fortunato et al. [29] successfully produced WC-Co cutting tools with L-PBF by applying multiple pass scanning strategies. Although their methodologies differed slightly, the principle of applying a high energy density divided into stages is identical. This would make sense for the processing of WC-Co with L-PBF, since for conventional cemented tungsten carbide processing, the sintering process is performed in four main steps as described in Section 2.3.2 [78].

For a chrome molybdenum steel alloy, a significant reduction of residual stresses has been achieved through multiple exposure of each layer by Shiomi et al. [268]. At the same time, the porosity is also reduced. This approach is also followed for WC-Co in the PraeziGen project [49].The effects of the multi-pass strategy on pores, cracks, and the brittle phases can be observed in Table 4.1.

Table 4.1: Impact by trend of the different measures on the formation of pores, cracks, and brittle phases adapted from [49]

Measure	Pores	Cracks	Brittle Phases
Decrease of Δt	↓	↓	↑
Post-exposure	↓	↓	-
Increase of E_V	↓	↑	↑

For the multiple laser pass strategy applied to WC-Co powder, the laser parameters and time between melts could play crucial roles. The initial step where shrinkage takes place due to the reduction of oxides is where a first, low intensity, low energy, laser pass could be employed. The second step of solid-state sintering could be performed with a low laser intensity and medium energy density. In the third step of the sintering process the melting temperature of the cobalt binder is reached (roughly 1300 °C – 1600 °C [79]) and should be performed with corresponding laser speeds and power where the temperature experienced by the powder is between the melting temperature of the binder and the tungsten carbide [222]. The fourth step or the cooling down period could be performed at an even lower energy density than the first step in order to assist with a slow cooling process and reduce the thermal gradient experienced by the material. Due to the nature of the laser processing being rapid, the time in which the laser interacts with the material is crucial to assist with the rearrangement of solid carbide particles. It is unknown as to how many laser passes are required and at what intensity. However, the increase in laser passes also results in a longer build time and consequently a longer time for the residual heat in the part to dissipate.

Another reason why the multiple pass strategy could improve the porosity and quality aspects of a part is because of laser radiation pressure. As radiation pressure with Gaussian laser beams is present, care should be taken to not force the powder particles away from the working cross-sectional area during the laser scan pass, thus creating denudation zones. According to Mahrle and Beyer [70], the magnitude of the laser radiation pressure is dependent on the laser power and the beam radius. The relationship is directly proportional to laser power and inversely proportional to laser beam radius as depicted in Figure 3.23.

When melting commercially available powders developed for the L-PBF process, such as Ti-6Al-4V, maraging steel, or stainless steels, the main metals (by weight) that make up these alloys, all have similar melting temperatures. For example, with Maraging Steel (DIN 1.2709) the main metals that make up the alloy are iron (±64 wt%), nickel (±19 wt%), cobalt (±10 wt%), molybdenum (±5.2 wt%), and titanium (±1.2 wt%). All of which, except molybdenum, have a melting temperature which falls in the range of 1450 °C – 1700 °C. The apparent density for the commercially available maraging steel powders (3.90 g/cm^3) is similar to that of the Kennametal JK117 WC-17wt%Co powder (3.3 – 4.0 g/cm^3) that was obtained for this study. Assuming both powders were exposed to a laser power of 180 W, scanning speed of 600 mm/s, with a spot diameter of 50 µm, the maraging steel particles should instantly melt and bond with the underlying layers due to the main constituents all being in the same melting band. However, with the WC-17wt%Co powder, only the 17 wt% of cobalt should melt when being exposed to the beam, thus only 26 vol% of a homogeneous particle should be in the

liquid phase when passed by the laser. So, if the laser's radiation pressure is high enough but the laser energy is not high enough to melt the tungsten, an excess of particles could be forced away from the melt track leaving the track bare, with a large denudation zone and with no powder fused to the substrate or underlying layers. Consequently, when applying a high energy scan to the powder and subsequently reaching the melting temperature of the tungsten, the powder is more likely to bond to the substrate or underlying layers before being forced away by the radiation and evaporation pressure. In literature, Achee et al. [269] investigated laser pre-sintering for denudation reduction in L-PBF of Ti-6Al-4V. This work could be replicated and applied to WC-Co.

4.4.4. Differential layer thickness strategy

Uhlmann et al. [50] tested two different layer thicknesses (30 µm and 50 µm) when processing WC-Co and achieved conflicting effects on the two most important properties (porosity and cobalt content). The results of this validation test are presented in Figure 4.5. Thus, to determine whether the density effects of the 30 µm layer and the cobalt content effects of the 50 µm could be exploited. A strategy whereby the layer thickness is alternated after each layer, is suggested.

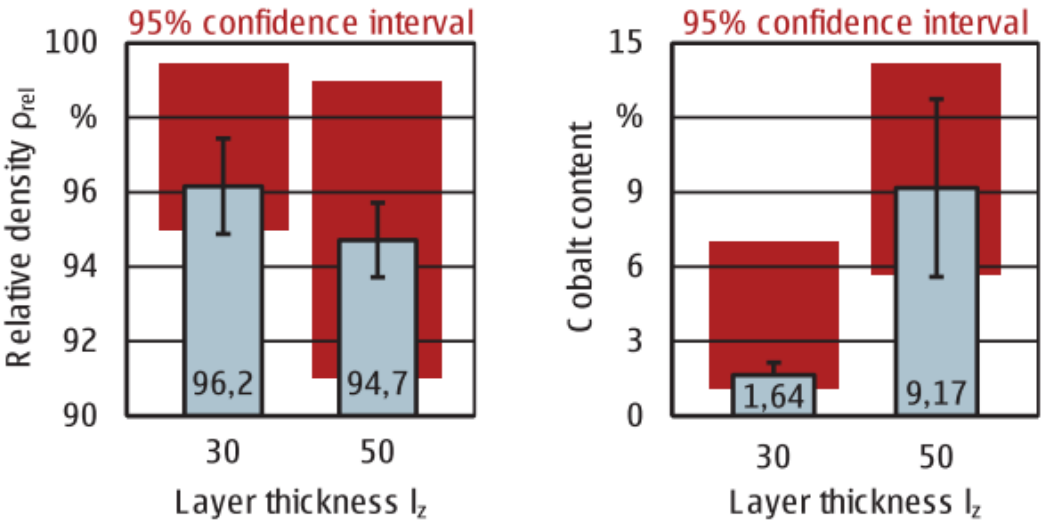

Figure 4.5: Comparison of achieved values with 95% confidence interval reproduced from [50]

With this strategy, the part would be sliced into two different layer thicknesses such as 25 µm and 50 µm layers. The process parameters could be kept constant for each layer thickness, or they could vary. However, the alternating of the layer thickness during the build would affect the interlayer bonds, the heat distribution, and also the melt pool.

4.4.5. Powder particle distribution

According to Sutton et al. [138] the reflectivity of the powder bed increases with decreasing particle size, which causes less absorption of laser power. With WC-Co already having a low absorption, it would be best to increase the average powder particle size in order to decrease the reflectivity.

However, this may also pose a negative effect on the final part density due to the fact that the packing density will also decrease with increasing the powder particle sizes on average.

The most suitable powder particle distribution could be determined through experimentation by varying the D_{10}, D_{50}, and D_{90} content. This approach was recommended by Reuber and Schwanekamp [30] to maximise relative density. Powder with a wider range of particle size, provides higher powder bed density / packing factor, generates higher density parts under low laser energy intensity, and generates smoother side surfaces. Powder with a narrower range of particle size provides better flowability, generates parts with higher UTS and higher hardness [141].

4.5. Summary of Chapter 4

This chapter started by reviewing the history (from 1992 to 2020) of processing WC based powders with L-PBF technologies. Then some of the issues that were highlighted by various authors when processing WC with L-PBF were listed and discussed in detail. The scientific gaps in the publications that were reviewed were then identified and highlighted. The main gaps highlighted were the use of scanning strategies to improve the part quality and the use of the WC-12wt%Co L-PBF produced tools in cutting tests. Finally, some potential modifications to the conventional L-PBF process to possibly improve the quality of WC-Co parts were discussed.

Chapter 5

Experimental Methodology

The experimental methodology and design of experiments is fundamental to achieving the aims of any research project. Depending on the methodologies chosen, different results and outcomes could arise, which could contribute to the success or failure of the project. Conventional approaches could result in conventional results with very little innovation in the process, especially when the project involves an aspect of product development [270], [271]. This chapter highlights the problem solving and experimental methodologies followed. The experiments performed are also mapped and briefly described for the reader to fully understand the approach taken.

5.1. Problem Solving Methodology

Design Thinking is a human-centred, iterative process that can be used to find solutions to specific problems. A Design Thinking approach was taken for this study to ensure a holistic view of the problem and possible solutions. Design Thinking was used as a tool to foster creativity by crossing experiences with multiple perspectives, which aids in stimulating inductive and deductive reasoning [272]. The six main characteristics of Design Thinking are listed below with a brief note on where they were applied in this study:

- Human and user centred: Mitsubishi Materials Corporation has been an important stakeholder from the beginning of the study. Many of the decisions made in this study orientate around the requirements from Mitsubishi as well as their strict quality standards. Other stakeholders included cutting tool resellers as well as the artisans who use the tools daily. In order to create a viable solution, the problem and stakeholder requirements needed to be understood from the different human perspectives.
- Holistic: the problems, as well as the solutions, have been viewed in a holistic manner, whereby many factors and possible solutions were considered both on a microscopic and macroscopic level. A comprehensive analysis and general understanding of many of the L-PBF phenomena were obtained.
- Co-creative: a co-creative approach was undertaken to aid with different views and solutions to the problem. Many experts were consulted, and stakeholders were approached for collaboration and input on certain areas.
- Problem solving: the main aim of this study was to solve a specific problem or at least to contribute to a viable solution. Problem solving is at the core of Design Thinking methodology.

- Multidisciplinary: an understanding of many disciplines was required to explore and understand the problems from different perspectives. This included, but was not limited to, particle physics, melt pool dynamics, fluid behaviour, laser physics, material characterisation, design of cutting tools, and thermodynamics.
- Abductive reasoning: through abductive reasoning, incomplete data could be taken and manipulated in various ways to become useful for the study. However, to some degree, this also resulted in time delays to the study and various minor experiments that were performed.

5.2. Design of Experiments Methodology

Correctly designed and conducted experiments allow for accurate data generation and sufficient statistical power to draw precise and reasonable conclusions from experimentation. Experimental design is an important tool to determine the relationships between factors and responses in a methodical and resource efficient manner [273]. A Design of Experiments (DoE) is a "structured way of planning, designing, conducting, and analysing of experiments" [274]. Since all parameters cannot have the same effect on a process, the DoE is used to investigate, understand, and establish the importance and influence of parameters that govern a process on the outcomes of the process [274]. As shown in the previous sections, L-PBF has up to 207 parameters that effect the process [137], [178]. It is not to say that each of these parameters would have the same effect on the process. Thus, in order to successfully develop certain materials for L-PBF, the key parameters need to be established along with their relative interactions with each other and the relative importance to the success of the process. It should be noted that a lot of the parameters and their effects are also machine dependent and often cannot be copied and applied to another machine, while expecting the same outcome. Various designs and their limitations were studied and discussed in greater detail in the following sections.

5.2.1. One-factor-at-a-time

One of the most common experimental investigation methods is the One-Factor-at-a-Time (OFAT) method. In this approach, one factor is varied across its levels whilst the other factors are kept at their entry level. This method can often lead to misleading or unsatisfactory results, as each factor is not tested at a variety of levels against other factors and thus important interactions between the factors may not be identified or present during the experimentation [273], [274]. The OFAT design was utilised by Uhlmann et al. [50] for preliminary investigation into the effect of focus position, laser power, scan speed, and scan line spacing on the relative density, hardness, and surface roughness of WC-Co cuboidal samples.

5.2.2. Full factorial design

One of the most intuitive design methods is the full factorial experimental design. Factors are varied together and all possible combinations of factors, at their various levels, are investigated. This design was used by Uhlmann et al. [25] and Casalino et al. [109] for optimisation of L-PBF parameters for WC-Co and 18 Ni Marage 300 respectively. Where the number of levels is kept the same across all the factors, the number of runs is equal to l^k, where l is the number of levels and k is the number of factors. The two-level full factorial design consists of k factors and $l = 2$ levels due to the complexity, time, and cost constraints on having a large number of experiments associated with a higher number of factors and levels. The number of required experimental runs is the product of the number of levels for each factor [274]. An important assumption regarding the two-level factors, is that the response is approximately linear over the chosen factor range. Mixed level factorials are when the factors have a different number of levels in a design. So, for instance, one could have a design with three factors where two of those factors have three levels and the other has only two levels. A full factorial design is not recommended for five and above factors [273].

5.2.3. Fractional factorial

With the full factorial design, the resource efficiency of the design decreases with an increase in the number of factors. When the number of factors increases to five and above, a fractional factorial design can be considered. In a fractional factorial design, only a subset of the full factorial runs is considered for experimentation. This gives valuable information on the main effects with some information on the interactions between the various factors. Cavazzuti [275] states that the sample size of a fractional factorial design can be one-half, one-quarter, etc. of the full factorial design. It is important to note that fractional factorials should only be conducted after screening experiments have been performed in order to establish which combination of factors has negligible or the least effect on the results. Fractional factorial designs are notable by their chosen design resolution (R). The resolution specifies the degree to which the experimental design is confounded. Where confounding is the ascription of the combined influence of two or more experimental effects on the response factor, as opposed to each effect's unique influence [274]. A fractional factorial design can be utilised to describe which factors have the highest significant impact on the response factors. Though this is highly dependent on the amount of time and resources available, the number of main factors present, and the acceptable level of confounding. A fractional factorial design was employed by Averyanova et al. [276] for L-PBF of single tracks and first layers of 17-4 PH powder.

5.2.4. Taguchi method

The Taguchi method, also referred to as orthogonal arrays, consists of a set of fractional factorial designs which ignore interaction and concentration on main effect estimation [277]. This method eliminates the need to run a large number of costly and time consuming experiments by making use of orthogonal arrays [278]. Another unique feature of the Taguchi method is the use of Signal to Noise (S/N) ratios. The important controllable factors (Signal) should be maximised while the uncontrollable factors (Noise) should be minimised during this process so as to derive the best results from the least number of experimental runs. The Taguchi method creates a robust process by being insensitive to noise or uncontrollable factors [273]. When the accuracy of the results and the interaction between factors is not critical, orthogonal arrays are predominantly useful. Due to the fact that the L-PBF process has a number of crucial factors that are interactive, the Taguchi method was not suitable for deriving accurate experimental runs in this study.

5.2.5. Central composite design

A central composite design or CCD (also referred to as a Box and Wilson design) constitutes of a two-level full factorial or fractional factorial design. However, the points at the centre of the experimental domain and the “star” points outside the domain, make it possible to estimate the curvature of the response surface without using a complete full factorial design [279]. The star points represent the extreme values (low and high) for each factor in the design. A CCD always contains twice as many star points as there are factors in the design. One important feature of a CCD is the iso-variance per rotation (rotatability). Which means the prediction error is identical for all points located in the same distance from the centre of the domain [280]. Chatterjee et al. [281] utilised a central composite rotatable design to see the effects of layer thickness and hatch spacing on the porosity and hardness of low carbon steel with SLS. Schwanekamp and Reuber [4] also utilised a CCD for a L-PBF parameter study on WC-Co powders with preheating. 15 different parameter settings were used with 8 cube points, 6 axial points, and 1 centre point. However, several points were repeated to determine the process variability. Due to its properties and limitations CCD was considered as a strong candidate for the designs for specific experiments in this study.

5.2.6. Optimal designs

Optimal designs are computer generated designs which aid the experimenter in creating efficient response surface methodology designs. A D-Optimal design is used for multi-factor experiments with both quantitative and qualitative factors. The design can be used with factors that have a mixed number of levels. Hence this procedure could be used to design an experiment with two qualitative factors having two levels each and a quantitative factor having five levels. D-Optimal designs

minimise the generalised variance of the estimated regression coefficients. This design can be used when you cannot run a completely replicated factorial design [277].

The D-Optimal design algorithm requires that an approximate mathematical model, which defines the functional form of the relationship between the factors (independent variables) and the response. Applying the pre-specified model as an optimality criterion results in minimizing the generalised variance of the parameter estimates. The algorithm selects points that minimize the volume of the confidence ellipsoid for the coefficients. The reasons for utilising a D-Optimal design instead of standard classical designs can be that the standard factorial or fractional factorial designs require too many runs for the amount of resources or time allowed for the experiment or the design space is constrained i.e. the process space contains factor settings that are not feasible [282]. D-Optimality produces a design that best estimates the effects of the factors, which is predominantly appropriate for screening studies. An I-Optimal design (also called IV or Integrated Variance) provides a lower average prediction variance across the region of experimentation. I-Optimality is desirable for response surface methods where prediction is important. The computer algorithm picks points that minimise the integral of the prediction variance across the design space.

Letenneur et al. [283] utilised the D-Optimal design to optimise the L-PBF process for various materials such as Inconel 625, Ti6Al4V, and iron powders. Mele et al. [284] also used a D-Optimal design in order to investigate the effect of supports and overhangs on the accuracy and roughness in L-PBF. They used the optimal design to reduce the number of runs of a full-factorial design from 135 runs to just 20. The optimal designs were chosen for further investigation to be used in this study due to the benefits and flexibility of the designs.

5.2.7. Selection of design methodology

Response surface methodology (RSM) is a collection of statistical and mathematical techniques useful for developing, improving, and optimising processes [285]. RSM designs are utilised for prediction and experimental mapping of the effects with respect to the input parameters. RSM is a graphical perspective of the problem environment. A central composite design and optimal designs can be utilised to effectively plot response surfaces for a design space. Depending on the type of experiment, a D-Optimal design is favoured over the CCD, due to the limitations of constraint on full factorial and central composite designs. The L-PBF process is complex, and a number of parameter combinations result in the introduction of different physical phenomenon. As an example, laser parameters corresponding to a low energy density result in a lack of fusion, poor melt pool morphology, and poor interlayer bonding. On the other hand, laser parameters that correspond to a high energy density result in evaporation of elements, larger denudation zones, high residual stress,

and collapsed melt pool geometry [269], [286], [287]. However, with a CCD, depending on the parameter range, the experimenter is required to utilise parameters that may result in experimental runs that introduce these different physical phenomena, thus resulting in failed or different and often misunderstood results when compared to others in the design space. Conversely, with the D-Optimal design, the design space can be constrained to avoid the areas where one suspects a change in the melting process. The two different designs have been run and can be observed in Figure 5.1 for the same ranges of 50 – 200 W power, 200 – 1200 mm/s scan speed, and 80 – 130 µm hatch spacing. The D-Optimal design was constrained by the VED with VED > 30 J/mm³.

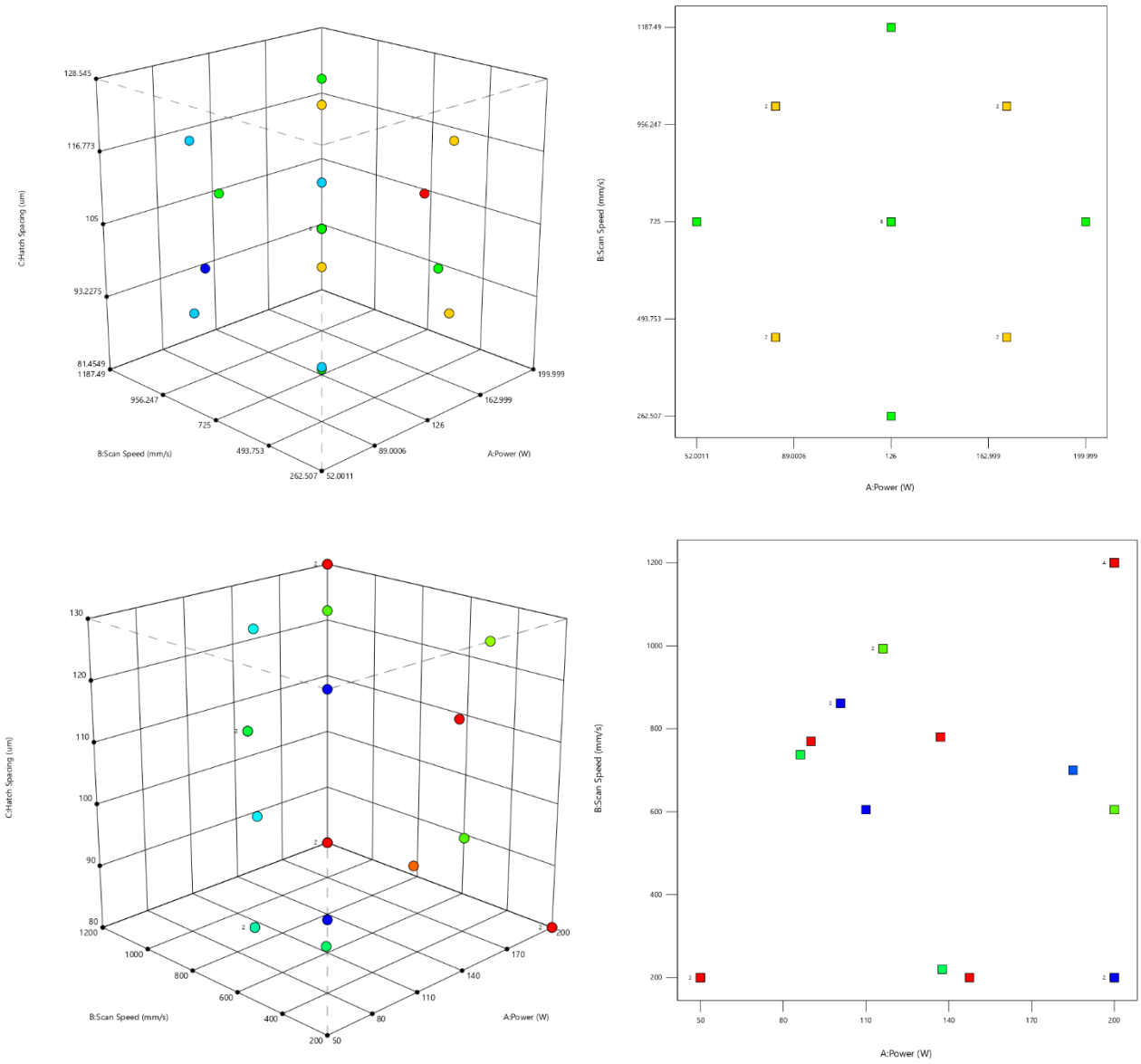

Figure 5.1: (Top) Central Composite Design and (Bottom) D-Optimal design for identical parameter ranges

The D-Optimal design covers the experimental runs for the highest and lowest values of the different parameter ranges as well as a number of other points spread out over the design space. Although orthogonality is not possible with the D-Optimal design, the resultant response surface derived from

the results should be more than adequate to determine the effects of the various factors and their interactions, especially if some of the runs fail due to poor parameter combinations.

5.2.8. Basic principles of statistical methods

According to Antony and Cavazzuti [274], [275] there are three basic principles of experimental design, namely randomisation, replication, and blocking. The principles should be applied to avoid or completely remove mental bias of the experimenter. Experimental bias could have a detrimental effect on the statistical significance of certain factors [274]. These principles should be used to improve the efficiency and effectiveness of experimentation.

Randomisation refers to the random order in which experimental runs are performed [274], [275]. Randomisation is done to reduce the effects that experimental bias can have on the outcome. This certifies that the conditions of an experimental run do not affect the conditions of another run. If noise factors are present, the effects will be averaged out when randomising the runs.

Replication is the process of repeating experimental trials in an arbitrary manner to obtain statistically precise results and experimental error estimation [274], [275]. Replication can be performed on the entire experiment or just a portion of it. Experimental error, factor, or interaction effects can be quite significant, and replication would have to be performed in order to make these effects less significant. It should be noted that repetition and replication are not the same thing.

Blocking is the method of refining experimental design efficiency by removing the effects of peripheral variation caused by noise factors [274]. Cavazzuti [275] states that blocking is used to isolate known systematic bias effects in order to prevent them from concealing the main effects. To perform blocking, experiments are arranged in blocks (or groups) that are similar in nature. The variability is therefore condensed, and the precision of the experiment is improved.

5.2.9. Statistical analysis of results

Design-Expert by Stat-Ease Inc. (Minneapolis, USA) software was utilised for design of experiments and statistical analysis of data. The threshold for statistical significance of correlation was set to $p = 0.05$ (5%) for the entire study. The statistical power of each experimental setup was balanced between the available resources and the realistic number of runs possible. The analysis time and costs were also considered as an influence on the number of experimental runs that were performed. Assistance with a DoE was received from the Centre for Statistical Consultation (CSC) at Stellenbosch University.

5.3. Experimental Investigation Mapping

The experimental process followed in this study is graphically depicted in Figure 5.2. The experimental investigations are divided into three main sections or chapters namely, background and feasibility studies (green), process and parameter optimisation (purple) and cutting tests and verification (blue). These sections are further subdivided to ensure the experiments are well understood and absorbed by the reader. Each experiment builds on the next while they follow the problem-solving process described by Polya [288]. This was achieved by defining the problem, generating possible solutions, evaluating selected solutions, and then implementing the solutions and evaluating their success over the next experimental set, so as to build on the previous knowledge obtained. Each aspect is then discussed further in the sections that follow.

5.3.1. Powder, benchmark, and feasibility studies

The first experiments conducted for this study were the powder, benchmark, and feasibility studies. These studies were separated into three different experiments that were performed and are discussed further in the following sections.

5.3.1.1. Powder study

In order to determine whether the three powders obtained were suitable for the L-PBF process, a powder characterisation was completed. The powders were analysed and inspected against their respective certificates of conformity from the suppliers where applicable. The powder was characterised for the L-PBF process through image analysis, Hall flow, scanning electron microscopy, energy dispersive X-ray spectrometry, and powder x-ray diffraction (PXRD).

5.3.1.2. Benchmarking of an Insert

To understand the specifications/requirements of a conventional cutting tool with respect to composition and properties, an uncoated Mitsubishi Materials Corporation insert was analysed. The uncoated APMT insert was chosen, as minimal additional processing steps were performed on the insert after sintering. With the analysis of the insert, a holistic view was obtained as to what materials and properties a conventional uncoated cemented tungsten carbide insert possesses. The insert was also compared to the raw UTi20T powder, to understand the changes that are brought on from the sintering process. These properties could then be used as a standard for the L-PBF process and tools that were to be manufactured.

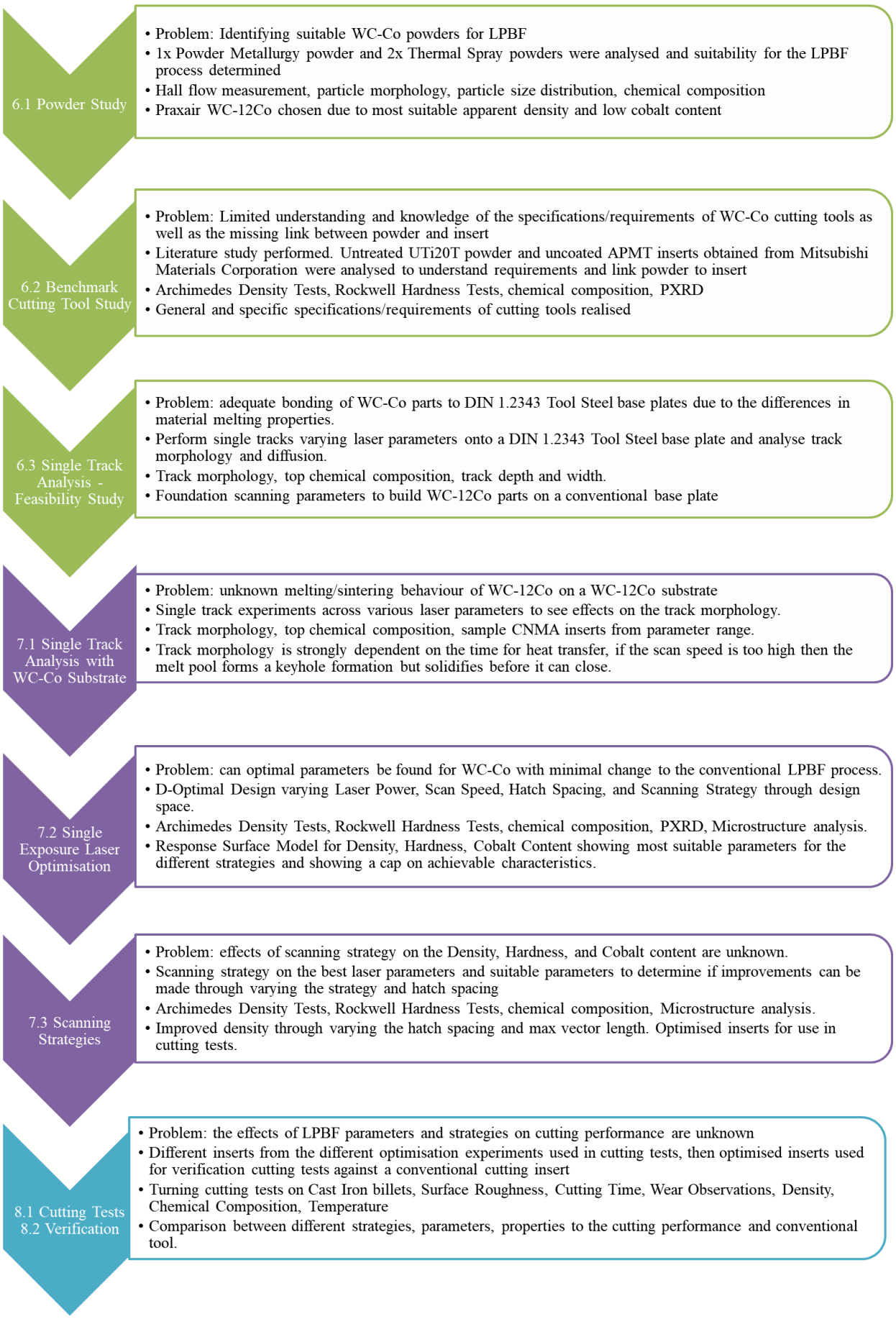

Figure 5.2: Experimental process followed in this study

5.3.1.3. Single track analysis – feasibility study

Single track optimisation is a common practice amongst some researchers [33], [178], [182] to determine the suitable L-PBF process parameters for a specific material. Conventionally, base plates of a similar material to the L-PBF powder are used to promote adhesion and prevent delamination during the L-PBF process. However, WC-Co base plates or coated plates can become very costly to process and post process. So, to reduce costs, use of the conventional DIN 1.2343 base plates were investigated. A single-track feasibility study was performed to determine the processability and adhesion of WC-Co on DIN 1.2343 tool steel (H11) base plates. For this part of the study, a machine with a higher laser power (400 W) capability was chosen, as to not limit the maximum laser energy density that could be applied to the material. Single tracks of WC-12wt%Co were exposed onto the DIN 1.2343 base plate and the tracks were then critically analysed to determine a suitable way forward for build plate adhesion.

5.3.2. Process and parameter optimisation

The next set of experiments focused on the process and parameter optimisation. Conventional optimisation methods through single track scans and cuboid manufacturing were performed. The laser and process parameter optimisation experiments concentrated on varying specific laser parameters to determine their effects on specific responses. The scanning strategies experiments observed the effects of different hatch spacings, vector, segment, and layer strategies on the same specific responses.

5.3.2.1. Single track analysis with WC-Co substrate

Unlike the previous single-track analysis, the aim of this experiment was to determine the interaction of the WC-12wt%Co with the underlying base plate of the same material, when exposed with varying laser powers, scan speeds, and focal offsets. The reason for this was to identify the sintering and evaporation threshold for the cobalt binder, as well as the laser melting mode that corresponds to specific parameters. This assisted with identifying the correct parameters to limit evaporation of the binder and to sinter the WC to not degrade it through high temperature input. Once the single-track experiments were studied, a suitable parameter range was chosen to produce sample CNMA 120404 inserts. The inserts were analysed to determine the feasibility of utilising them for cutting.

5.3.2.2. Laser and process parameter optimisation

One of the conventional and reported methods [50], [265] for L-PBF process optimisation of tungsten carbide materials, is laser parameter optimisation. This is performed by designing an experiment, which varies the scanning strategy, laser power, scan speed, hatch spacing, and/or layer thickness at certain levels, according to the design. There are numerous designs that have been used in various

research publications previously discussed in Section 5.2. A D-Optimal design was chosen as motivated in the previous section, and cuboid samples were produced according to the suggested design runs. The hardness, density, cobalt composition, and crystal structure of the various experimental samples were analysed using numerous analytical apparatus and methods. Once a suitable scanning strategy and laser parameter range were realised through the results, sample CNMA turning inserts were produced and analysed to determine the feasibility of utilising them for cutting.

5.3.2.3. Scanning strategies

Initially various strategies and multiple laser pass methods were reviewed and are discussed in Section 4.4. Although other authors were successful with applying multiple laser passes to improve the quality of WC-Co parts [29], [30], attempts made in this study were met with failure, as most of the parts delaminated off the base plate during the initial 30 layers. Since the single laser pass parameter optimisation results indicated a hard limit for the maximum achievable density, scanning strategies were chosen as the next area of focus. Several CNMA samples were produced for analysis and determination of the effects of the scanning strategy and hatch spacing on the density, hardness, and cobalt content.

5.3.3. Cutting tests and verification

Since the main aim of this study was to improve the understanding of various influencing factors and their effects on cemented tungsten carbide cutting tools, it was essential to perform cutting tests. Even by observing the bulk properties and microstructures of L-PBF produced cutting tools, it is difficult to conclude that one tool produced with certain strategies and parameters is better than another with respect to cutting ability. Thus, the next set of experiments was divided into two sections, preliminary cutting tests and verification.

5.3.3.1. Preliminary cutting tests

To determine the cutting ability of the different inserts produced with different parameters and scanning strategies, the inserts with intact cutting edges from the various stages of experimentation were selected and run through cutting tests. The effects of laser parameters and scanning strategies could be linked to the density, hardness, and cobalt content of the inserts, as well as their respective cutting times given these characteristics. The scanning strategy and parameters of the best performing inserts were used to produce inserts for the final verification stage.

5.3.3.2. Verification

The metal cutting tests were conducted to verify whether the L-PBF produced tools were comparable to conventionally produced tools in terms of cutting performance. Conventionally produced CNMA

120404 Grade K10 inserts were obtained from Mitsubishi Materials Corporation. The inserts were tested against the L-PBF produced ones in terms of certain tool life criteria and cutting performance over a set distance. The ISO3685:1993 standard was used as a guideline for the testing.

5.4. Summary of Chapter 5

Chapter 5 highlighted the research methodology and the different experiments performed throughout the study. A Design Thinking approach was taken and the reasoning behind this approach was discussed. Different experimental designs were reviewed and discussed with respect to their use in L-PBF parameter studies. The selection of certain designs was discussed and motivated. The main structure of the experiments was summarised, and each experiment was briefly explained.

Chapter 6

Powder, Benchmark, and Feasibility Studies

The feasibility studies were performed in order to determine whether L-PBF can be used on WC-Co with few changes to the conventional processes and methods. Since there are no known readily available tungsten carbide powders developed specifically for the L-PBF process, the powder study was performed to study three commercial powders and their suitability for the L-PBF process. This was followed by the analysis of commercially available, uncoated cutting inserts to establish a quality benchmark. Thereafter, single-track scans were performed on a DIN 1.2343 base plate to determine the adhesion of the track to the plate and to qualitatively analyse the tracks.

6.1. Powder Study

From Figure 2.2 in Section 2.2.1, it can be noted that for metal cutting, the common range for tungsten carbide grain size and cobalt content is 0.4 – 2.5 µm and 6 – 17 %, respectively. This range aligns with the upper limit of the ultrafine grain sizes to the lower limit of coarse grain sizes. Thus, for this study, the chosen powder was kept within these specifications. With regards to the cobalt content, it was noted by Uhlmann et al. [50] and Schwanekamp et al. [49] that some cobalt evaporates during the L-PBF process and thus the upper limits from 12% to 17% cobalt content were chosen in order to avoid embrittlement of the final parts due to the lack of binder. According to Laoui et al. [226], composite powder grains result in higher SLS green density and a better surface roughness than a mixture of separate WC and Co powders. Thus, in this study, WC-Co powders that were either agglomerated and sintered or spray dried and sintered (excluding the PM Mitsubishi powder), such that each powder particle contains the correct homogeneous chemical composition were used. Three powders were chosen to analyse with respect to their usability in the L-PBF process. The first powder was from Mitsubishi Materials Corporation (Tokyo, Japan) and is the UTi20T grade, which is conventionally used in PM to produce various insert types, including the APMT insert analysed in Section 6.2. The second powder was from Praxair Technology Inc. (Connecticut, USA) and is a common thermal spray powder WC-727-1 with 12 wt% cobalt content. The third and final powder is also commonly used in thermal spraying processes and is the JK117 powder from Kennametal (Pennsylvania, USA). The Kennametal JK117 powder has a 17 wt% cobalt content. More information on the various powder properties from the manufacturers can be found in Table 6.1.

Table 6.1: Supplier specifications of the three different tungsten carbide powders obtained for this study

Manufacturer Designation		Mitsubishi UTi20T	Praxair (WC-727-1/1342VM)	Kennametal (JK 117)
ISO		M20		
WC [wt%]	W [wt%]		82.5%	77.80%
	C [wt%]		5.5%	5.20%
Co [wt%]		9%	12%	17%
TiC [wt%]			0%	0%
TaC [wt%]			0%	0%
NiC [wt%]			0%	0%
Rockwell Hardness A [HRA]		90.5		88.8
Grain Size		Coarse < 3 µm	Fine	Medium Course
Thermal Conductivity [W/m·K]		38		
Thermal Expansion [x10-6/K]		5.5		
TRS [GPa]		2		
Fracture Toughness [MPa/m²]		8.3		
Process		Spray Dried	Agglomerated and Sintered	Spray Dried and Sintered
Source		[56]	[289]	[290]

6.1.1. Powder properties and characteristics

Some of the powder properties are given on the supplier's websites or data sheets. Other properties are measured by the supplier for each specific batch and supplied with a certificate of conformity if applicable. Certification of conformity and further analysis of the powders is often required to validate the conformity to the supplier specifications and identify any defects in the particles such as porosity, or skewed powder particle distribution. The readily available information for the three different powders is discussed in the next section, followed by the experimental setups used to analyse the various powders further. The requirements for L-PBF powders according to Vock et al. [291] and Sutton et al. [138] can be summarised to be smooth, spherical, chemically homogeneous particles, with no internal porosity, a PSD that promotes adequate flow (< 30 s/50 g Hall Flow), a good packing factor, high apparent or bulk density, low to no moisture content and finally, minimal cohesive forces. However, there is a lot of trade-offs and balancing needed, as some of these requirements are proportionally contradictory to each other. It should be noted that not all tungsten carbide powder can be used in L-PBF processes, as the van der Waals forces act on the powder particles keeping the powder in a cohesive state, consequently having a poor flowability [292]. Other powders simply do not possess spherical particles that fall within the precise range or shape requirements. The powder particle size range for L-PBF was considered when selecting the correct powder for the correct process parameters. The PSD is often +10 µm to -55 µm with an average particle size (D_{50}) of 32 µm.

6.1.1.1. Mitsubishi powder

The Mitsubishi Materials Corporation powder is a UTi20T grade, which is used for production of uncoated C5/C6 carbide grade tools with high edge strength. These tools are designed for general

purpose turning and milling of steel. The tools are ideal for cutting stainless steel, and for difficult machining conditions, such as interrupted cutting. The powder is not commercially available outside of the Mitsubishi Materials Corporation and the author was fortunate to procure some samples of the powder from the Tsukuba manufacturing plant in Japan, courtesy of Mitsubishi Materials Corporation. The UTi20T grade was never designed or intended for use in the L-PBF process but rather for PM processes such as press and sinter.

6.1.1.2. Praxair powder

The Praxair powder chosen for this study was agglomerated and sintered WC-727-1 / 1342 VM with specified particle size distribution range of 16-45 µm and chemical composition of 12 wt% cobalt, 5.5 wt% carbon, and tungsten balance. The carbide grain sizes are fine, meaning they range from 1.0 – 1.3 µm in size. The powder particles are required to be spherical in shape for use in various thermal spraying processes.

6.1.1.3. Kennametal powder

The Kennametal powder used in this study was the spray dried and sintered JetKote JK117 (STELCAR 9528) with specified particle size distribution range of 15-53 µm and chemical composition of 16.9 wt% cobalt, 5.1 wt% carbon, and tungsten balance. The carbide grain sizes are intermediate, meaning they range from 2.1 – 3.4 µm in size. Further analysis of the powders was required to determine their suitability for the L-PBF process. Additional analysis is almost always required to ensure the powder possesses the required properties and so that any inexplicable effects on the final parts could be correctly traced or linked to the original powder properties/defects.

6.1.2. Experimental setup

To determine and validate the flowability and apparent density of the powders, Hall flow measurements were conducted according to ASTM B212 - 13 and ASTM B213 – 13. To inspect the particle morphology and granulometry, the powder was adhered to carbon tape and analysed on the Zeiss MERLIN field emission scanning electron microscope (FE-SEM). Several particle sites, as well as individual particles were inspected. ImageJ open-source software (NIH, Washington D.C., USA) was used to determine the powder particle size distribution and average particle size of at least three sites on three samples containing a minimum of 200 powder particles. For completeness, compositional scans were performed through energy dispersive x-ray spectroscopy and analysed with AZtecTEM software from Oxford Instruments. It is recognised however, that EDS is a semi-quantitative method best suited for the analysis of flat surfaces, and is associated with a significant margin of error on uneven surfaces like powder particles. In this case, EDS was used to assess whether there were substantial deviations in composition from the specifications and the certificates of

conformity (Appendix B.2) obtained from the suppliers. The starting powder phases were identified by Powder X-ray diffraction with a Bruker D2 Phaser benchtop powder diffractometer according to the methodology and settings highlighted in Appendix A under X-ray diffraction.

6.1.3. Results and discussion

The results for each powder are derived and initially discussed separately in this section. The results are then compared against each other at the end of this section.

6.1.3.1. Mitsubishi powder

The Mitsubishi UTi20T powder was not subjected to any post mixing, milling, or spray drying treatment and was in a submicron, distributed state. Some particles appeared to form spherical agglomerates as depicted in Figure 6.1. Even through multiple sieving trials, the spherical particles could not be separated from the submicron powders. The Mitsubishi powder had no flow through the Hall flow funnel opening, which preliminarily indicated a poor flowability. Carney funnels are appropriately used for testing flowability of more cohesive particles. However, this test was not necessary to conduct, since the powder was ruled to be not suitable for L-PBF on the basis of the lack of flow through the Hall funnel and high satellite particle content. From the ImageJ analysis, the Mitsubishi powder had a particle size distribution of 16 µm to 60 µm excluding the satellite nano powders. The average particle size D_{50} was 29 µm. If these particles went through a post sintering process whereby the satellite particles were removed and the spherical particles remained in a solidified state, it is most likely that they would be adequate for use in the L-PBF process.

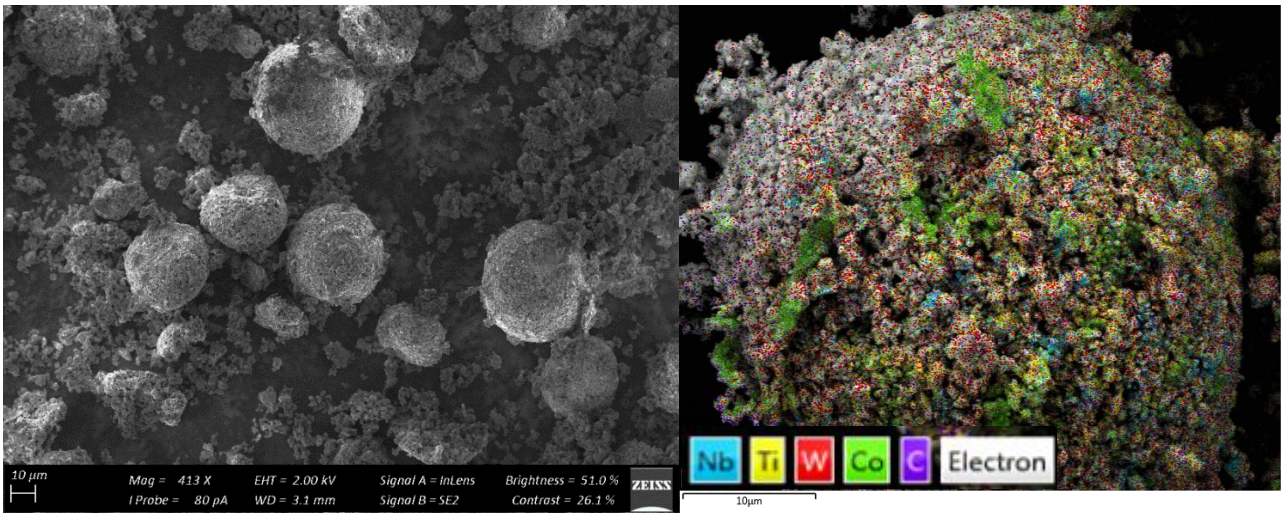

Figure 6.1: Mitsubishi UTi20T powder observed with SEM (Left) is the spherical agglomerates and (Right) is the EDS map of the elemental composition of a powder particle

The powder particle (Figure 6.1 Right) appears to have very little porosity present when inspected on the surface. A summary of the chemical composition results obtained through EDS for the Mitsubishi UTi20T powder can be observed in Table 6.2. However, the limitations of EDS for determining

chemical composition on spherical particles should be noted and a large margin of error could be expected.

Table 6.2: Chemical composition of Mitsubishi UTi20T powder

Result Type	W [wt%]	C [wt%]	Co [wt%]	Ti [wt%]	Nb [wt%]
Max	76.33	8.52	11.98	11.27	7.94
Min	63.68	2.97	6.06	4.43	6.33
Average	68.43	6.74	9.2	8.19	7.44
Standard Deviation	4.33	2.02	2.35	2.78	0.62

Nevertheless, the measured cobalt composition of the Mitsubishi powder was in line with the manufacturer specification as listed in Table 6.1. The powder does not seem to be suitable for the L-PBF process, as the average cobalt content is too low. With possible evaporation of the cobalt during laser sintering/melting, the cemented tungsten parts could be too brittle to be used in any commercial applications. Also, it is apparent that the Mitsubishi powder contains TiC, and NbC particles. In this early stage of development of WC-Co for L-PBF, the effects of these carbides may cause some confusion and add additional factors or effects that would need to be considered during experimentation. Additives such as niobium carbide improve the thermal properties of the binder element. Thermal deformation, adhesion, and wear are resisted by lowering the binder content. NbC also increases the softening temperature of the binder material [293] which, in the case of L-PBF, may cause other issues and increase the sintering temperature such that it is closer to the evaporation temperature of the cobalt.

6.1.3.2. Praxair powder

The Praxair powder had a Hall Flow reading of 12.0 s/50 g and an apparent density of 4.8 g/cm³. The measured flow was relatively high and more than adequate for the L-PBF process where Hall Flow should generally be less than 30.0 s/50 g. The ImageJ analysis derived a particle size distribution in the range of 3 µm to 56 µm with an average PSD of 25 µm. The powder was observed to have some granules with internal porosity shown in Figure 6.2. As reported by Maeda and Childs [8] this could lead to porosity in the final SLS part, as the trapped gas cannot escape the particle during the laser process.

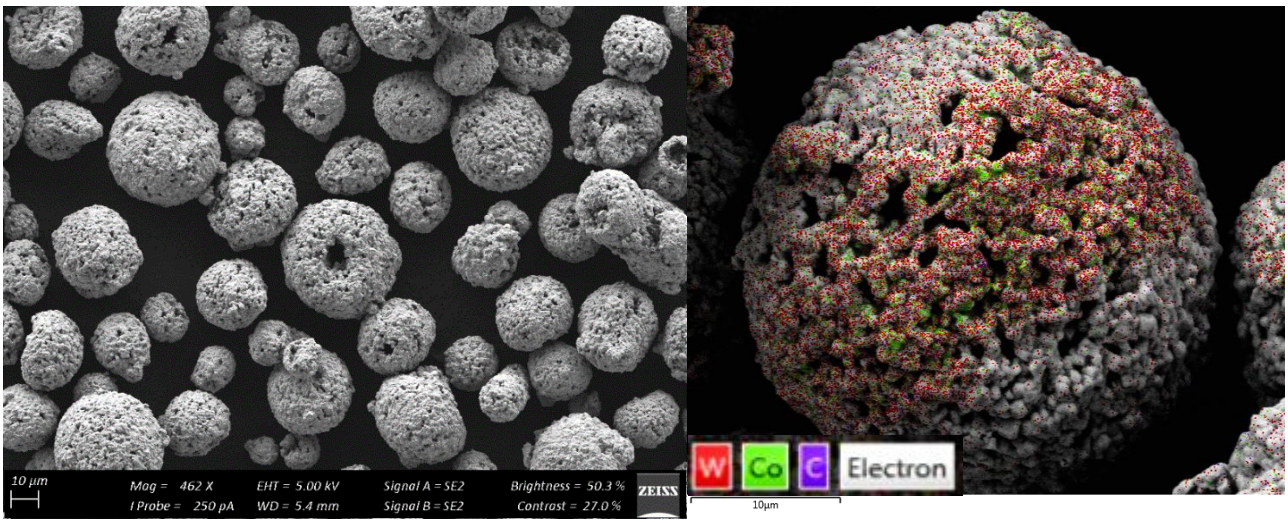

Figure 6.2: Praxair powder observed with SEM (Left) porosity inside powder particles and (Right) EDS map of elemental composition of a single particle

The particles were mostly spherical in morphology with some particles fused together, most likely during the sintering process. Satellite particles were also present on the larger particles. The surface roughness of the particles appears to be rough in comparison to those of an alloy like Ti6Al4V because it is an agglomerated and sintered particle and not a solid particle. From the images presented above and the nature of the sintering process it can be noted that the tungsten carbide and cobalt are dispersed around each particle in order to remain in a spherical state. This should assist with adhesion and sintering of the particle during the L-PBF process. The summary of the chemical composition for the Praxair WC-727-1 powder is displayed in Table 6.3.

Table 6.3: Chemical composition of Praxair WC-727-1 powder

Result Type	W [wt%]	C [wt%]	Co [wt%]	Ti [wt%]	Nb [wt%]
Max	86.89	7.46	23.13	0	0
Min	70.92	4.3	8.39	0	0
Average	81.26	5.65	13.09	0	0
Standard Deviation	6.78	1.17	6.76	0	0

The EDS readings were broadly in line with the XRF readings reported on the certificate of conformity received from the supplier as well as the original specifications listed in Table 6.1. The Praxair powder had no additional elements other than WC-Co. The average tungsten content was substantially higher than that of the UTi20T powder, which may result in a harder cutting tool. However, conversely the cobalt content is roughly 4% higher which is quite significant for cutting tools and may substantially decrease the final hardness. Other than the porosity present in a number of particles, the Praxair powder appears to be well suited for the L-PBF process as it meets many of the requirements for a L-PBF powder in terms of flowability, morphology, and PSD.

6.1.3.3. Kennametal powder

The Kennametal powder had a Hall Flow reading of 15.0 s/50 g and an apparent density of 3.8 g/cm³. The apparent density and flowability of the Kennametal powder is lower than that of the Praxair powder. A lower apparent density was found to contribute to a significantly lower final part density by Chen et al. [83]. The PSD was measured to be in the range of 15 µm to 63 µm with a D_{50} of 38 µm. The powder granules and EDS map images can be found in Figure 6.3.

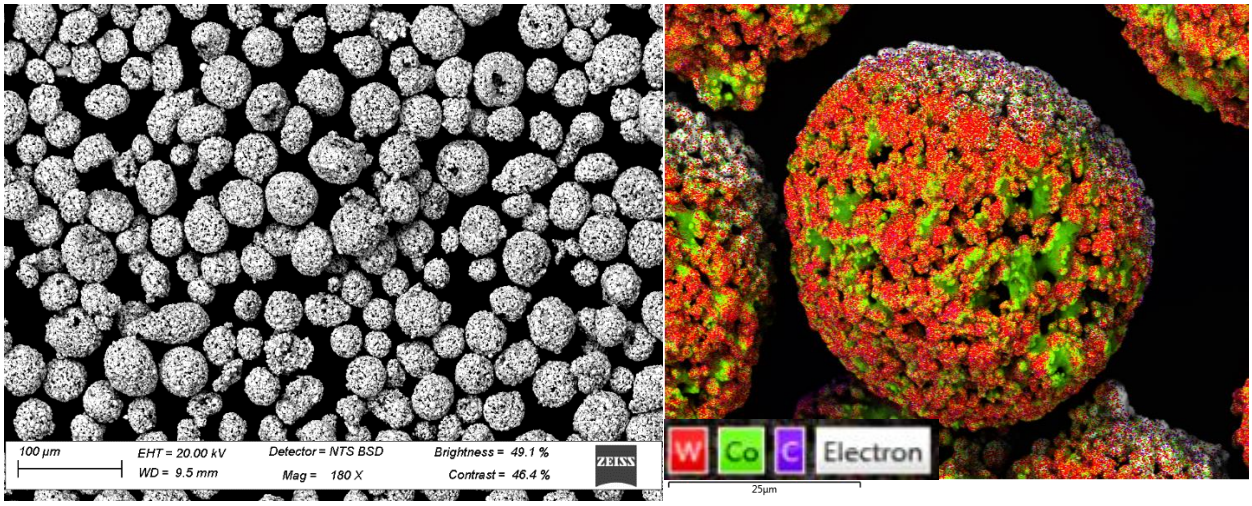

Figure 6.3: Kennametal powder observed with SEM (Left) porosity inside individual powder particles and (Right) EDS map of elemental composition of a single particle

The Kennametal powder particles were irregular in shape and were not completely spherical. This could have been a factor affecting the flow rate from the Hall Flow test results when compared to the Praxair powder. The internal porosity and lower density of cobalt could also contribute to the lower flowability obtained. The particle size distribution was wider than that of the Praxair powder and the average particle size was also larger. The surface chemistry analysis results from the EDS for the Kennametal JK117 powder can be observed in Table 6.4.

Table 6.4: Chemical composition of Kennametal JK117 powder

Result Type	W [wt%]	C [wt%]	Co [wt%]	Ti [wt%]	Nb [wt%]
Max	78.45	7.17	25.42	0	0
Min	68.1	5.88	15.3	0	0
Average	73.07	6.39	20.54	0	0
Standard Deviation	4.15	0.44	4.04	0	0

The Kennametal powder also only contained the WC-Co elements and had the highest cobalt content out of all three powders. The measured cobalt content was observed to be higher (20.54%) than that presented in the specifications in Table 6.1 and the certificate of conformity (16.9% cobalt measured by ICP-OE). This could well be due to the inaccuracy associated with the EDS method on powder particles, as noted earlier. Baring the lower apparent density and flowability, the Kennametal powder could still be suitable for the L-PBF process.

6.1.3.4. Comparison of all three powders

All three of the powders analysed had different benefits and shortcomings with respect to their morphology, granulometry, and chemistry. A visual comparison of the chemistry for the three powders is derived in Figure 6.4 and should be compared to the specifications listed in Table 6.1. The Certificate of Conformity measurements were used for the Praxair and Kennametal powders since the measurement instruments were more reliable than EDS. However, since the Mitsubishi powder was not supplied with a certificate because it is not commercially available, the EDS results were used.

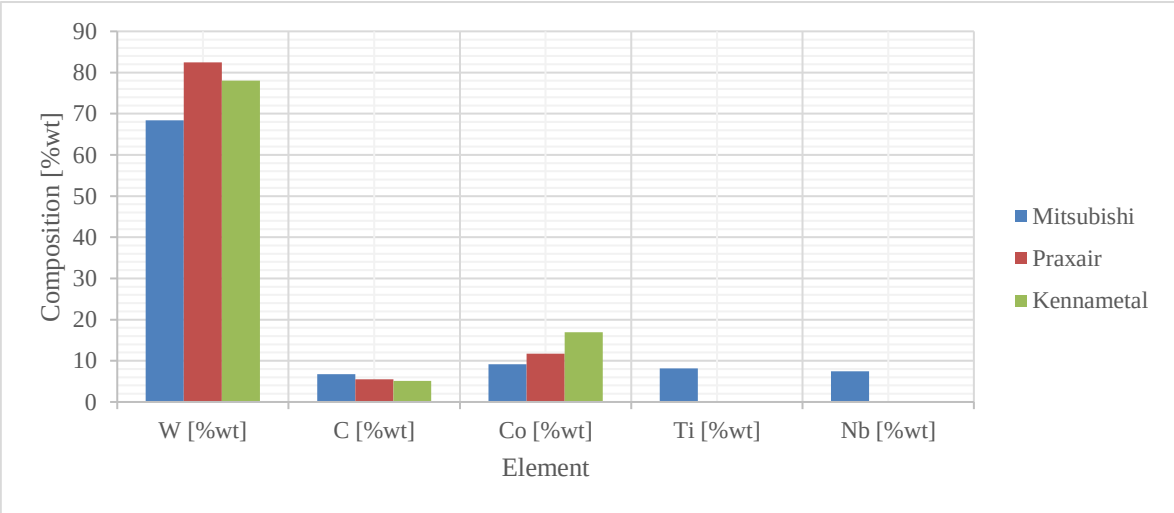

Figure 6.4: Chemical composition comparison of the three different powders

The crystal structures of the powders were also important to determine whether there were any undesirable phases present in the starting powder material. These unwanted structures could result in parts with the same phases, rendering any process optimisation attempts with L-PBF, unsuccessful. The PXRD results obtained are presented in Figure 6.5.

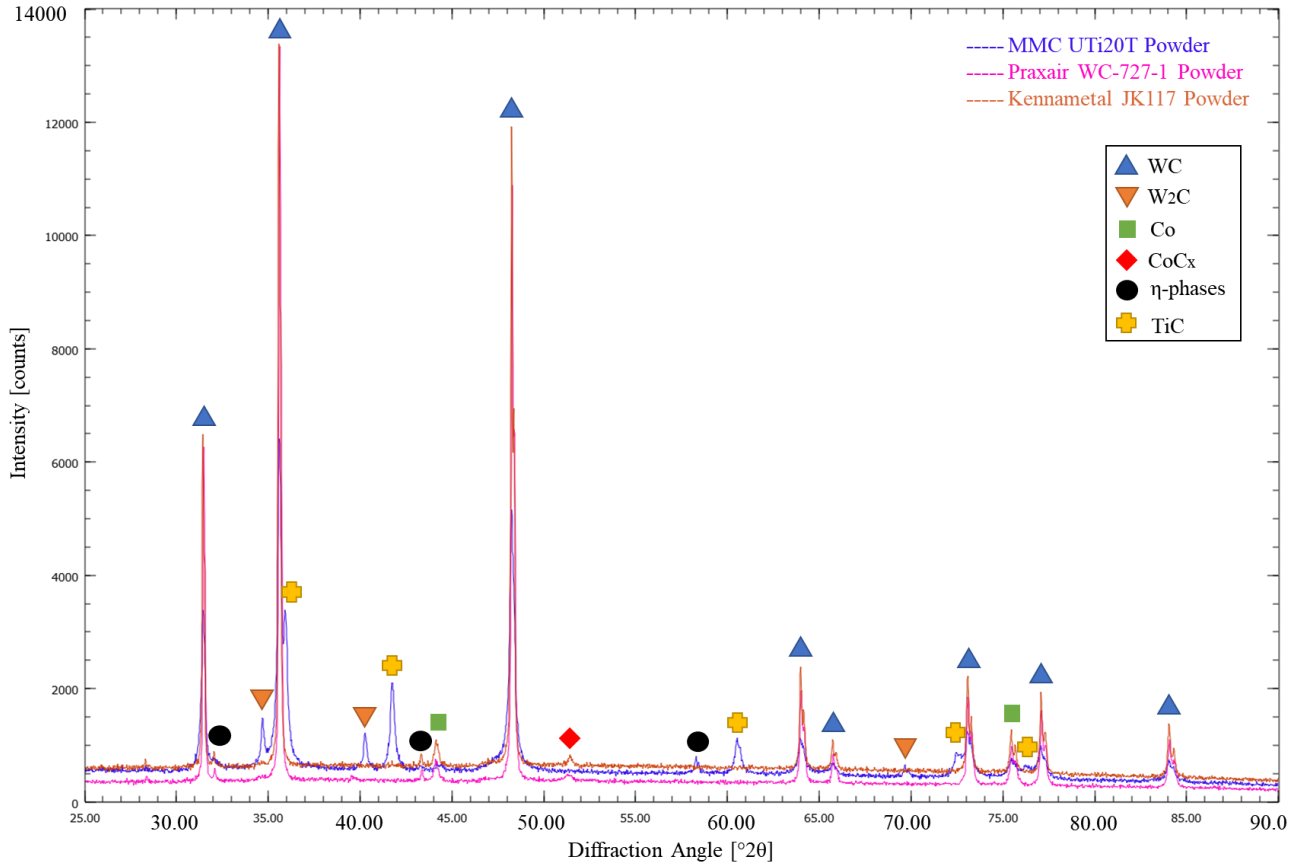

Figure 6.5: PXRD comparison of the Mitsubishi, Praxair, and Kennametal powders

The intensity peaks are higher for certain powders due to the fact that there may be more periodicity present in a section of the sample. So, more particles per unit area would have been exposed to and diffracted the X-rays, which would thus increase the intensity measured. From the XRD results, a number of phases can be recognized and matched with the standard data. For all of the powders, the WC and Co phases can be clearly identified. The Praxair and Kennametal powders appear to have the same phases present, as their peaks all correlate with each other. The Mitsubishi powder appears to have W_2C peaks present at $2\theta = 35°$, 40°, and 69°. There are also the undesired η-phase peaks present at $2\theta = 32°$, 43° and 58°, which exists in all of the powders. The W_2C crystal structure is brittle in nature and has detrimental effect on final part properties, especially cutting tools. The metastable CoC_x peaks were present for both the Praxair and Kennametal powders.

6.1.4. Summary and conclusion

The apparent density of the 17% cobalt Kennametal powder was less than that of the 12% cobalt Praxair powder. With respect to L-PBF this could be an issue, which negatively effects the final part properties. The internal porosity of the powder particles could cause gas to be trapped in the melt pool during the L-PBF process. This results in inherent porosity throughout the final part.

A number of researchers [29], [30], [52] have performed L-PBF experiments with both WC-12wt%Co and WC-17wt%Co powders. The type of carbide alloy had a great influence on the final component quality. With WC-12wt%Co, overall a high cracking tendency was found and a low presence of the cobalt binder. This was due to the comparatively low proportion of the ductile metal matrix and evaporation during laser exposure. With the WC-17wt%Co powders, localised higher densities were achieved by the researchers. Thus, many of the researchers tended to focus their efforts on the WC-17wt%Co for further study. As with WC-12wt%Co, albeit in a weakened form, a conflict between the desired final properties was also present in that a high density led to a high risk of cracking [52].

However, since WC-12wt%Co is the more difficult material to utilise in L-PBF, effects and errors would be magnified with this powder versus the WC-17wt%Co. The higher presence of cobalt could mitigate or mask many of the issues that could arise. Thus, in this study the Praxair WC-12wt%Co powder was chosen for further L-PBF experimentation to determine and understand the main influencing factors and their effects.

6.2. Benchmark Cutting Tool

To understand what the characteristics of a conventional cutting tool are, a conventional uncoated cutting tool had to be studied. Mitsubishi Materials Corporation UTi20T untreated powder was obtained, along with APMT1135PDER uncoated inserts (Figure 6.6) made from the same powder. The aim was to analyse the powder and the inserts to realise the benchmark characteristics for this study and to further understand what the requirements of a cutting insert are.

Figure 6.6: (Left) Mitsubishi Materials Corporation APMT1135 inserts with cutter body and (Right) digital model of APMT1135 insert

6.2.1. Experimental setup

In order to characterise the APMT inserts, the density, hardness, chemical composition, and phases were analysed for inserts from two different production batches. The densities of 10 APMT inserts were measured according to the Archimedes principle as per the methodology highlighted in Appendix A. The hardness of the 10 inserts was determined through indentation with a diamond

penetrator on a Zwick Roell ZHR Indotec Rockwell Hardness tester. Compositional scans of three ground flat and polished inserts were conducted with Energy Dispersive X-Ray Spectroscopy on the Zeiss MERLIN FE-SEM. Powder X-ray Diffraction phases of an insert was collected using a Bruker D2 Phaser diffractometer. All of the equipment used for these analyses and the methodology applied can be observed in Appendix A: Measurement and Experimental Equipment under each relevant heading.

6.2.2. Results and discussion

The results from the density, hardness, chemical composition, and XRD experiments are discussed in this section. The measured densities can be observed as they are tabulated in Table B.2 in Appendix B. The measured (Archimedes test) average density for the 10 inserts was 11.834 g/cm³ with a standard deviation of 0.083. However, by using the readings from the EDS scans and the law of mixtures, the theoretical density was calculated to be 13.813 g/cm³. This clearly highlights the limitations of utilising the Archimedes principle with relative density for calculating the porosity of a PM part. As it is very difficult to obtain and confidently apply the theoretical density to an MMC without checking the microstructure and WC grain sizes. From these results, one can still observe the consistency of each insert in terms of the bulk density. As highlighted above, there was a very small, measured deviation between the different insert densities and the resulting densities are quite consistent. This indicates that the press and sinter process is very well controlled. Thus, for the L-PBF inserts, a requirement would be consistency in terms of density between a number of manufactured components produced with the same process parameters.

The results from the hardness tests conducted on the 10 APMT inserts can be studied in Table B.3 in Appendix B. Six measurements were taken per insert. The average hardness for all 60 readings was 90.0 HRA and the standard deviation was 0.16 HRA for all 60 readings. This also substantiates how consistent the inserts from Mitsubishi are over the different batches and how consistent the L-PBF inserts should be so as to be accepted commercially.

In Table 6.1 it shows that Mitsubishi Materials Corporation reported the hardness of the UTi20T grade inserts to be 90.5 HRA. This means the hardness readings taken were within 1 % of that reported by Mitsubishi. This also confirms how consistent the quality of the commercial inserts is. This makes the use of L-PBF for insert production even more challenging, as the L-PBF process manufactures components in a layer wise fashion. This gives rise to the chance of more inconsistency between parts. Thus, another requirement for inserts produced with L-PBF would be consistent hardness across the insert and across different components.

The chemical composition of the three inserts and the powder can be observed in Figure 6.7.

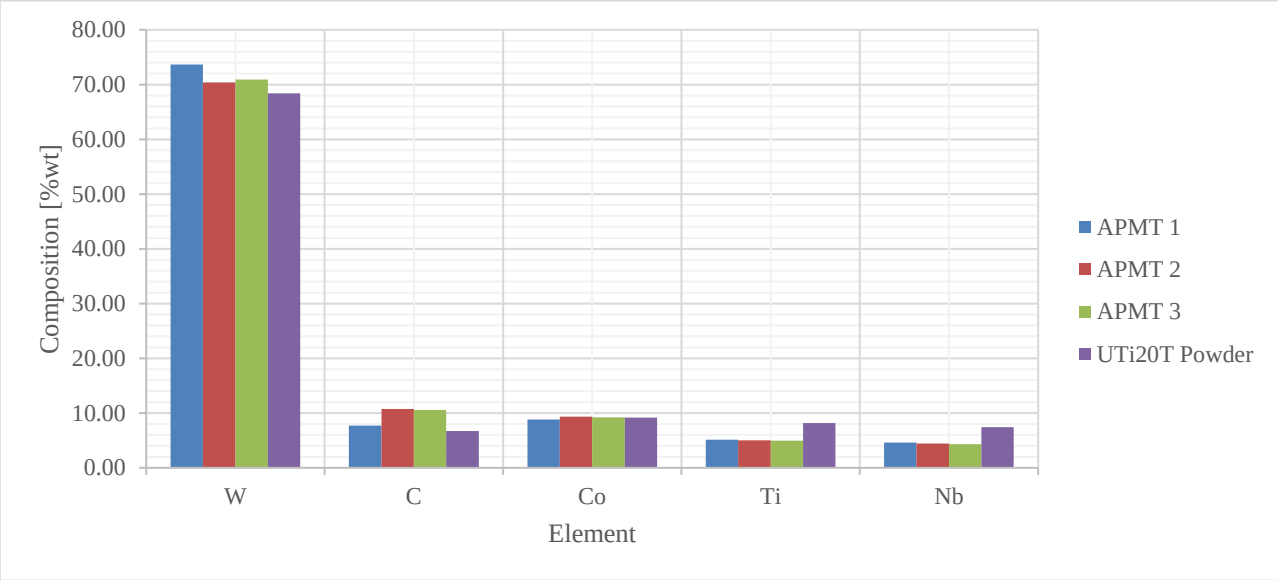

Figure 6.7: Chemical composition of the 3 APMT inserts and the UTi20T powder from the EDS analysis

One can observe that the chemical composition for the three APMT inserts is relatively consistent across all of the inserts. However, some discrepancies in the powder's elemental composition against the insert's composition could be noted. The cobalt content is consistent, but the titanium, niobium, and carbon content differ slightly. However, the limitations of SEM EDS with respect to accuracy with samples than are not flat and polished should be noted. Other possible reasons listed are highlighted by Konyashin and Lengauer [294].

The summary of the chemical composition of the three APMT inserts is tabulated in Table 6.5.

Table 6.5: Chemical composition of the three Mitsubishi APMT inserts

Result Type	W [wt%]	C [wt%]	Co [wt%]	Ti [wt%]	Nb [wt%]
Max	74.98	12.80	10.29	5.44	4.98
Min	69.89	7.08	7.45	4.56	3.83
Average	71.44	9.81	9.25	5.06	4.44
Standard Deviation	1.52	1.77	0.76	0.29	0.31

The chemical composition results for cobalt specifically, correspond to the properties of the UTi20T powder listed in Table 6.1 and were comparable to the surface chemical composition of the inserts as reported by Mitsubishi Materials Corporation. The cobalt content measurements obtained for the APMT inserts were comparable to those listed in Table B.4 in Appendix B. Noting this, the next requirement derived from the chemical composition results would be that the cobalt quantity should remain unchanged by the consolidation process. Thus, care should be exercised to not evaporate the cobalt during the L-PBF process. This may prove to be difficult, as many authors who have made attempts to produce crack free and high density WC-Co parts with L-PBF, also report the evaporation of the cobalt [29], [30], [50]. The results from the PXRD of the UTi20T powder and an APMT insert

can be observed in Figure 6.8. It is vitally important to compare the powder and insert structures to derive the effects of the manufacturing processes on the final part.

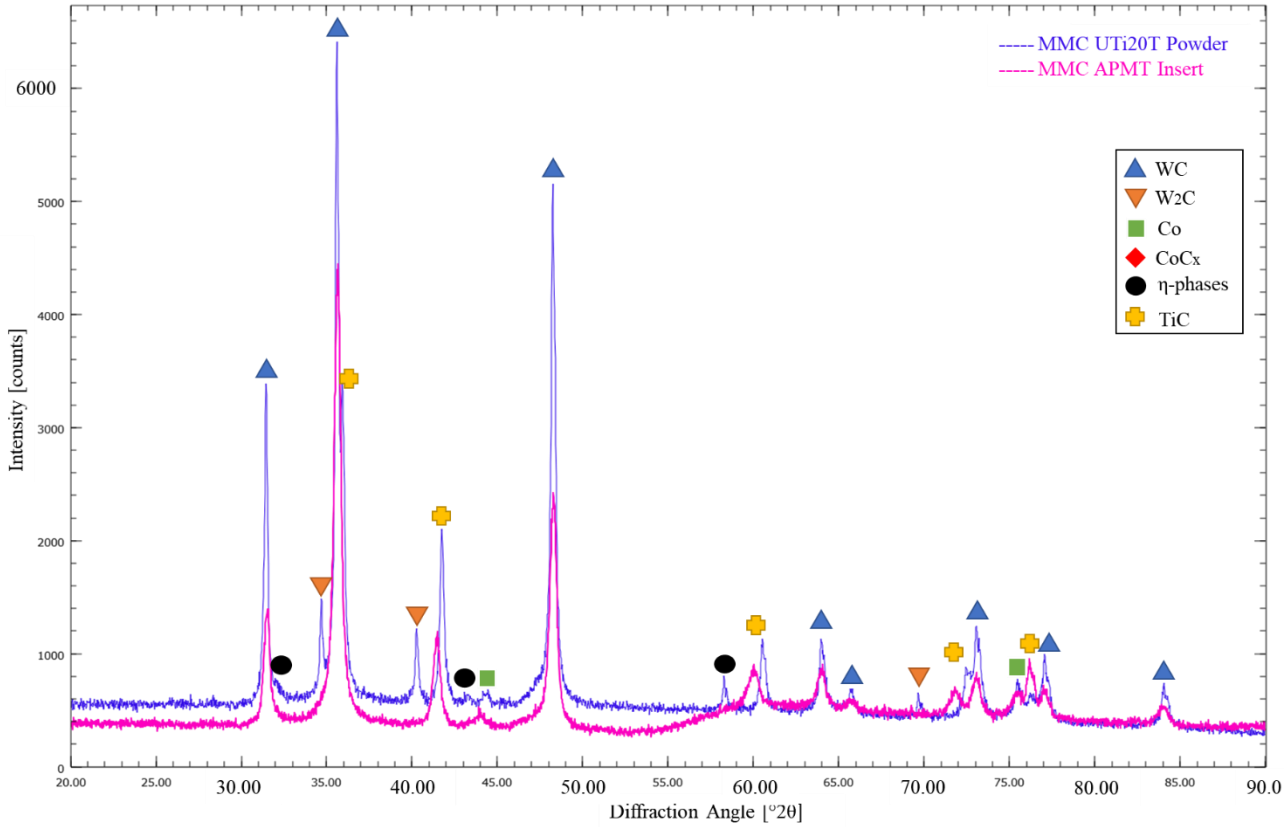

Figure 6.8: PXRD analysis of UTi20T powder vs an uncoated APMT insert manufactured from the same powder

When comparing the phases present in the UTi20T powder vs the uncoated inserts made from the same material, one can note a definite change in the presence of certain structures. The powder has a clear presence of W_2C and η-phases, yet the final insert does not possess any W_2C or η-phases in the crystal structure. The W_2C structure is undesirable for a cutting tool due to its brittle nature. The change in structure could be attributed to the sintering process where the carbon from either the TiC or NbC, chemically reacts with the W_2C and diffusion takes place forming the preferred WC structure [295]. Thus, the next requirement for a L-PBF produced cutting tool would be that the final crystal structure of the tool should be free of the W_2C phase and η-phase after post processing.

6.2.3. Summary and conclusion

The density, hardness, chemical composition, and phases of a conventional cutting insert were analysed. The powder grade used to manufacture the APMT type insert was also analysed and compared in terms of chemical composition and structure. A number of requirements for L-PBF inserts were realised through the analyses of the conventional cutting inserts. These general requirements are:

- Consistency in density across different inserts (±0.1 g/cm³ deviation)
- Consistency in hardness across individual and different inserts (±0.2 HRA deviation)

- Cobalt or binder quantity should remain unchanged from powder to final part
- Final crystal structure of the L-PBF part should be free of the W_2C phase and other undesirable phases.

For the Praxair powder composition and grade, additional specific requirements dependent on the cobalt content could be derived through analysis of Sandvik Coromant's conventional WC-Co grade properties in Table B.1 in Appendix B under Section B.1. The density and hardness versus cobalt content for various grain sizes are graphically represented in Figure B.2 and Figure B.3 respectively. For a cobalt content range from 6 to 15 wt%, a corresponding calculated density range of 13.9 to 14.9 g/cm³ and hardness range of 85.6 to 92.4 HRA can be expected depending on the final WC grain size.

6.3. Single Track Analysis – Feasibility Study

As mentioned previously, single track process optimisation is a common practice amongst various authors. In the SLM-Bauteilen aus Hartmetall report by TU Clausthal Institut für Schweißtechnik (ISAF) and Trennende Fertigungsverfahren Bremer Institut für Angewandte Strahltechnik (BIAS), single track melts were performed using various Praxair hardmetal powders. The individual tracks shown in Figure 6.9 consisted of three different tungsten carbide alloys namely, WC-12wt%Co, WC-17wt%Co and WC-36CR-20Co. The tracks were exposed on 50 x 50 x 10 mm plates made from DIN 1.2343 steel. These specific tracks were generated with a layer thickness of 50 µm and linear energy densities of 4400 J/m (88 J/mm²) and 5600 J/m (112 J/mm²) and have homogeneous structure in terms of width and morphology. It can be noted that the quality of the track for all the various materials was best at a energy input of 5600 J/m. However, it was stated in the report, that parameter combinations with lower energy inputs led to insufficient melting and poor track morphology [52].

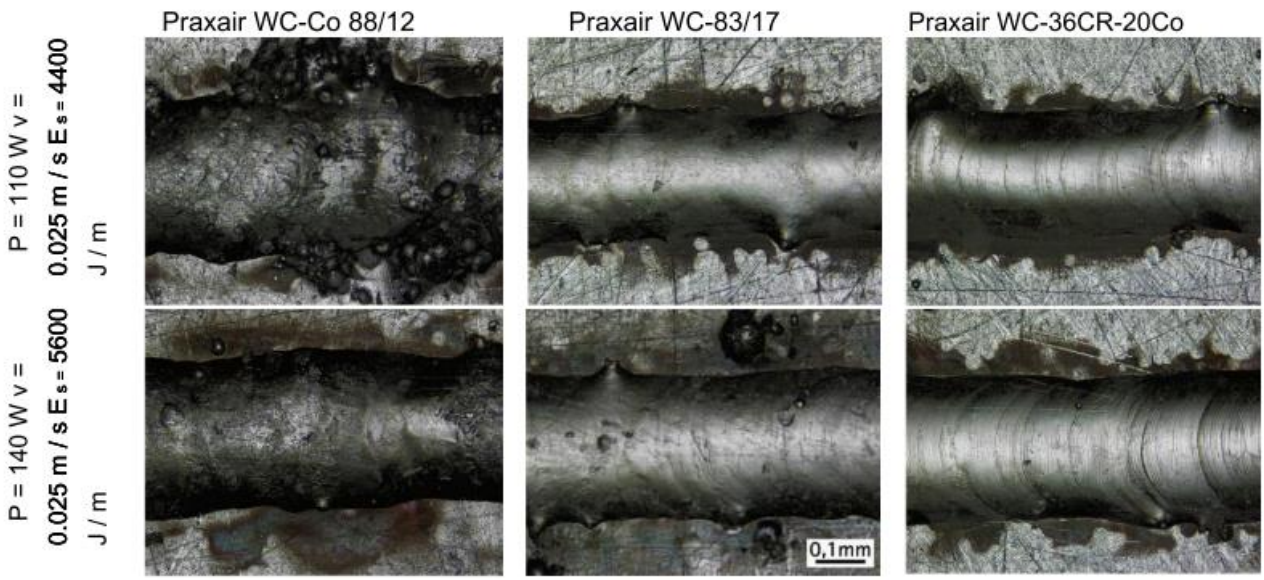

Figure 6.9: Individual tracks resulting from a 0.2 mm laser spot diameter and the subsequent energy input reproduced from [52]

From the investigations in [52] carried out with the WC-17wt%Co material, the study was unable to obtain 3D cuboid component densities above 50% with a laser energy input lower than 600 J/m. In the range between 700 J/m to 4400 J/m individual tracks were tested to determine whether sufficient connection to the base plate and optimal track morphology were achievable. It was reported that by utilising the parameter sets used for the stable single tracks, a mean density for 3D cuboid samples of more than 80% was only achievable at laser energies of 5600 J/m (112 J/mm²) [52].

A similar approach was chosen for this study with some variation to the parameter sets as well as the methodology and reasoning behind performing the single-track optimisation. For this experiment, the laser spot diameter was not increased from the conventional machine focal diameter and the laser energy was kept significantly lower in comparison. The main purpose of conducting this single-track analysis was to determine the adhesion of the WC-12wt%Co material to a DIN 1.2343 tool steel base plate as a feasibility study. The DIN 1.2343 base plate is the conventionally used material for normal L-PBF manufacturing with DIN 1.2709 maraging steel due to material compatibility. Thermal spray coatings of base plates with a compatible WC-Co powder can be costly and require expensive and time consuming post processing operations to reuse. The availability and manufacturability of the uncoated DIN 1.2343 base plates is far greater than that of a WC-Co base plate and thus making it more commercially viable to use this type of base plate. However, material compatibility may bar the use of these plates for manufacturing large WC-Co parts. Thus, the adhesion of single tracks to the DIN 1.2343 base plates was investigated.

6.3.1. Experimental setup

Single melt tracks (48) were exposed on machined, sandblasted and cleaned wrought DIN 1.2343 base plates using an EOSINT M280 DMLS machine (EOS GmbH, Krailling, Germany). The tracks were exposed using three varied laser power settings (50 W, 150 W, 300 W) with varying scan speeds. The layer thickness was constant and set to 50 µm with a laser beam diameter of ~80 µm. The tracks were 20 mm in length and were scanned 1 mm apart from each other. The samples were processed at the Centre for Rapid Prototyping and Manufacturing (CRPM) at the Central University of Technology (CUT) in the Free State, South Africa. The summary of equipment used for this experimentation can be observed in Table 6.6 and Appendix A.

Table 6.6: Experimental equipment used for single track optimisation

L-PBF Machine	EOSINT M 280 DMLS Machine
Laser	400 W Yb-fibre laser
SEM Microscope	Zeiss MERLIN SEM with BSD and EDS
Optical Microscopes	Olympus SZX 7 stereomicroscope and GX 51 inverted microscope

The powder used was Praxair agglomerated and sintered WC-727-1 / 1342 VM with specified particle size distribution range of 16-45 µm and chemical composition of 12 wt% cobalt, 5.5 wt% carbon, and tungsten balance. A schematic of the base plate is shown in Figure 6.10 with the 24 runs and the replicates with the positioning of the tracks on the plate.

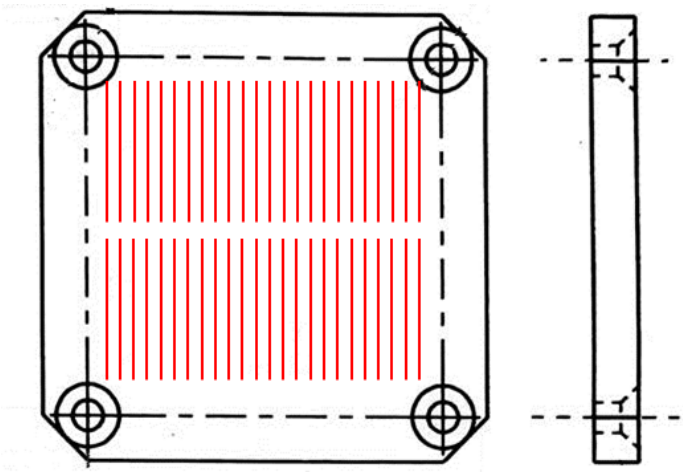

Figure 6.10: Baseplate schematic with the 24 runs replicated twice

The 24 runs covered a range of specific energy densities. The laser power was set, and the subsequent scanning speeds were selected such that the specific energy density was lower than 20 J/mm^2, especially for the higher laser powers. Since the base plate is a tool steel, the energy input range was selected to be lower than those found in Figure 6.9 [52]. The complete set of process parameters is shown in Table 6.7.

Table 6.7: Experimental runs for single scan tracks.

Track Number	Laser Power [W]	Scanning Speed [mm/s]	Specific Energy Density [J/mm^2]
1	50	60	16.67
2	50	80	12.50
3	50	100	10.00
4	50	120	8.33
5	50	140	7.14
6	50	160	6.25
7	50	180	5.56
8	50	200	5.00
9	150	400	7.50
10	150	600	5.00
11	150	800	3.75
12	150	1000	3.00
13	150	1200	2.50
14	150	1400	2.14
15	150	1600	1.88
16	150	1800	1.67
17	300	1000	6.00
18	300	1200	5.00
19	300	1400	4.29
20	300	1600	3.75
21	300	1800	3.33
22	300	2000	3.00
23	300	2200	2.73
24	300	2400	2.50

Once the single tracks were exposed onto the base plates the track morphology and penetration depth had to be analysed. The track morphology was observed by creating a montage scan of the tracks on the Zeiss MERLIN FE-SEM. An EDS line scan was also performed on the top of the tracks to determine the elemental composition of the track and how much diffusion took place between the base plate and the WC-12wt%Co. The elemental composition of the base plate elements was of high importance, the alloying elements of particular interest being Fe, C, Si, Mn, Cr, Mo, and V [296]. The tops of the tracks were also analysed qualitatively. The base plate was sectioned and polished to view and measure the track width and penetration depth. The sectioning was performed using an AgieCharmilles CA20 Wire EDM machine. The track sections were ground, polished and then analysed using an Olympus GX51 inverted microscope and Olympus Stream Essentials software. To validate the adhesion to the base plate in all three dimensions, six APMT inserts were manufactured using the top L-PBF parameter set.

6.3.2. Results and discussion

The montage scan of the plate with the SEM showed all the scan tracks and their top view morphology. Figure 6.11 shows the results of the qualitative analysis of the single scan tracks. The track morphology and defects were analysed, and the tracks were categorised into one of the three

types namely, irregular broken 'splattered' tracks, regular 'splattered' tracks, and straight continuous tracks.

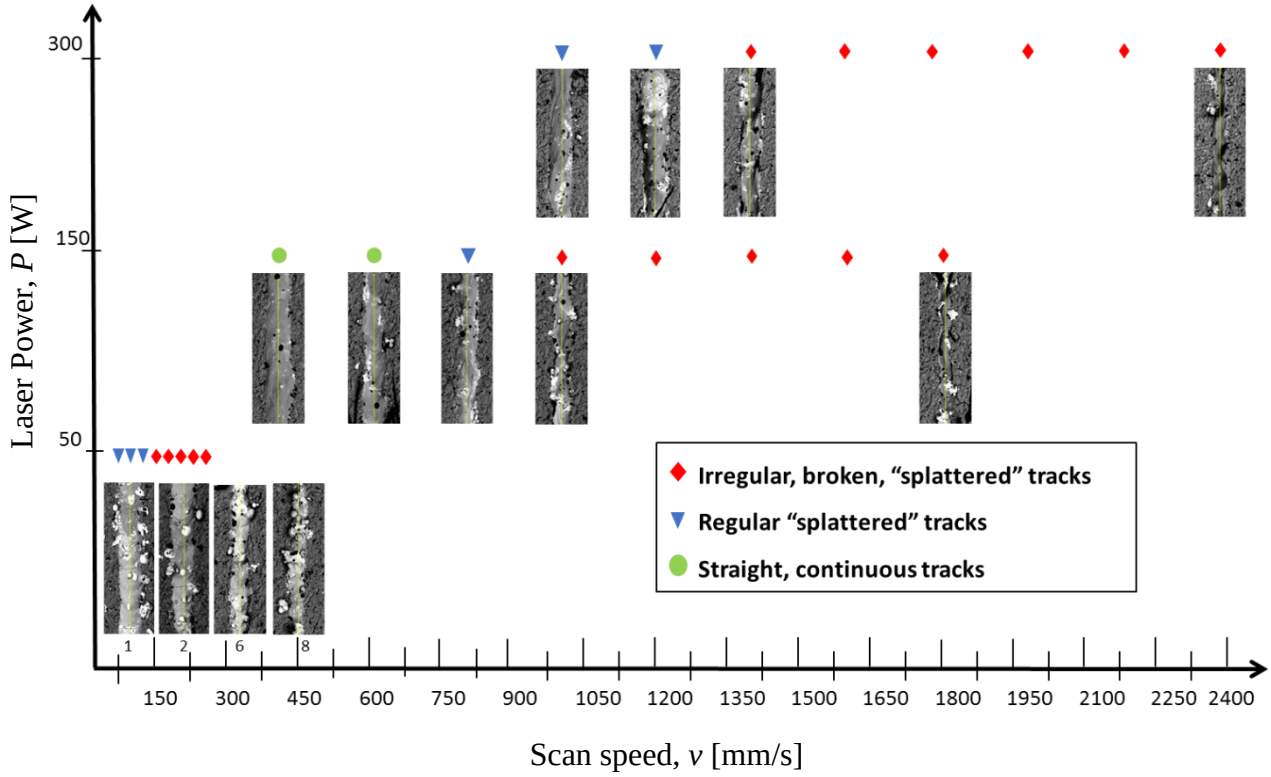

Figure 6.11: Qualitative analysis of the WC-Co single track scans

The only two tracks that were found to be continuous and straight were at 150 W laser power with the corresponding scan speeds of 400 mm/s and 600 mm/s (tracks 9 and 10). These powers and energy densities resemble those found to be successful in [52]. The continuity or discontinuity (balling or irregular) of a scan track is determined by several factors including the hydrodynamic movement of the molten liquid before solidification, which was discussed in Section 3.4.3 [297]. Since the cemented tungsten carbide is an MMC, further analysis of the top surface of the single tracks was necessary. A metal matrix composite like WC-Co does not act like a normal alloy in terms of sintering/melting behaviour and thus further inspection was required. Also, the base plate consists of several elements that could positively or negatively affect the track morphology. Thus, EDS line scans of the top track morphology were performed at three sections of the track (Start, middle, end). The results from these analyses can be observed in Figure 6.12 and in Appendix B under Section B.3.

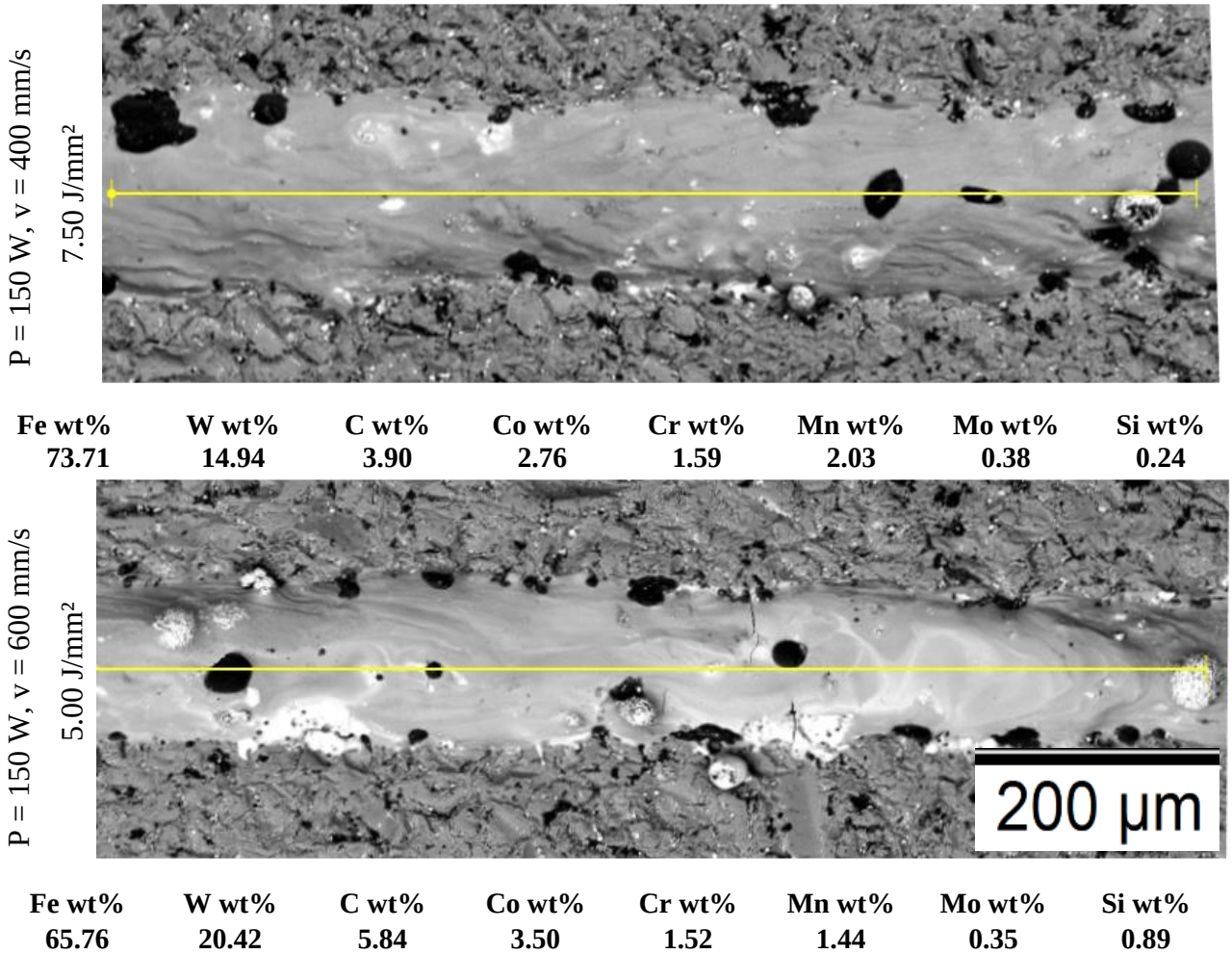

Figure 6.12: SEM images with EDS line scan of the top track morphology of parameter sets 9 (150 W, 400 mm/s) and 10 (150 W, 600 mm/s)

Through inspecting the single tracks qualitatively, un-melted WC-Co powder particles could be observed in all the 50 W tracks. A higher number of powder particles were observed in the tracks with a lower specific energy density (< 5.00 J/mm^2). One should note that the single tracks showed dilution due to the elemental diffusion from the base plate. Depending on the process parameters used, it is suspected that the elemental diffusion from the base plate can occur at least into the first 10 layers of the build. However, this was not necessary to test in this study, since the first 17 layers fell into the cutting zone for base plate removal and no traces of the base plate elements were present in the bulk samples produced after polishing and EDS. The EDS results from each track were analysed and graphed, such that the dilution of the main elements with a starting composition of greater than 10 wt% (W, Co, Fe) could be compared to the laser scanning parameters. A graphical representation of the top surface track dilution for different laser powers and scan speeds can be observed in Figure 6.13.

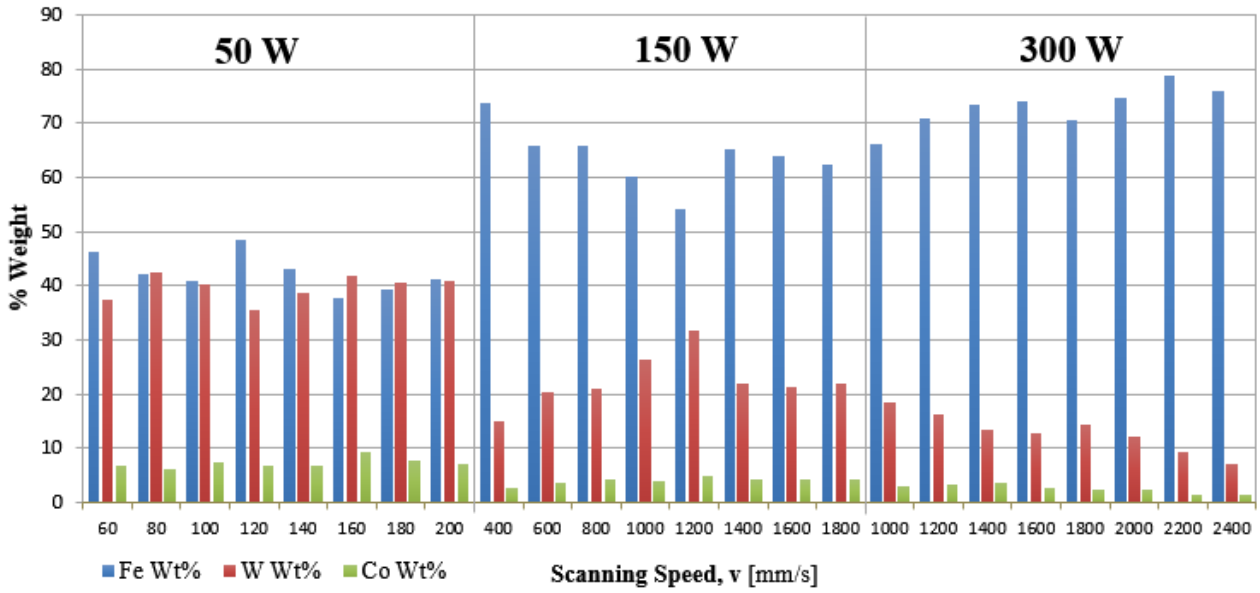

Figure 6.13: Graph of wt% composition of Fe, W, Co for all tracks to compare dilution to scanning parameters

One should take note of the decrease of tungsten on the surface of the tracks with the increasing laser power. This could be due to the radiation pressure of the beam as well as the Marangoni effect. These two phenomena would act on the single track during the laser scan and the denser or top materials would be forced to the bottom of the melt pool while in a liquid state. The cobalt content also decreases with an increase in laser power. However, at low laser power, the small increase in scanning speed has very little effect on the final chemical composition of the track. There appears to be a trend linked to the laser power/intensity and not necessarily laser energy which, would require further analysis or experimentation to identify. Since the laser focal diameter was not varied, the laser intensity changes were only due to laser power changes.

Once the top morphology was completely analysed, the base plate was sectioned, and further analyses of the cross sections were performed. The track width and penetration depth were measured and are graphically depicted against the scanning speed for the different laser powers in Figure 6.14.

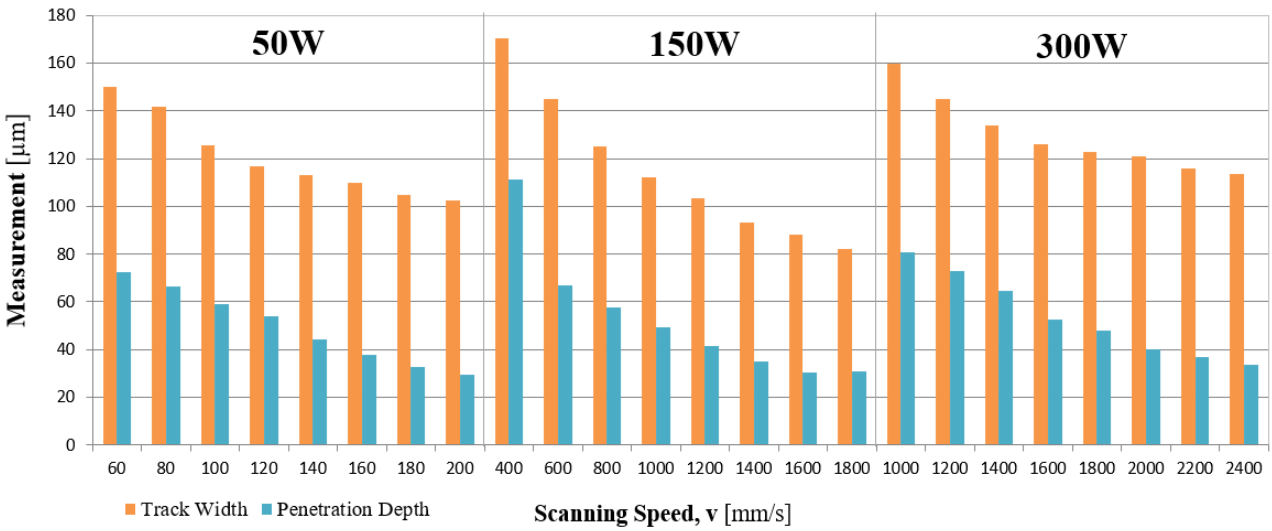

Figure 6.14: Track Width and Penetration Depth vs Scanning Speed analysed by [298]

The trend of decreasing depth and width with increasing scanning speed can be observed and linked to the laser energy density used. The track depth and width for the 150 W, 400 mm/s parameter set was the highest compared to all of the other runs. This indicated that the adhesion of the first few layers would be best with this parameter set. However, it was also unclear as to what extent the binding and wetting effects of the iron in the melt pool were and whether the adhesion would still be adequate after several layers using these parameters. Thus, six APMT inserts were built on the DIN 1.2343 base plate using the 150 W, 400 mm/s, and 100 µm (hatch spacing) parameter set to determine whether the adhesion was acceptable in more than one dimension. The six APMT inserts can be observed adequately adhered to the base plate in Figure 6.15.

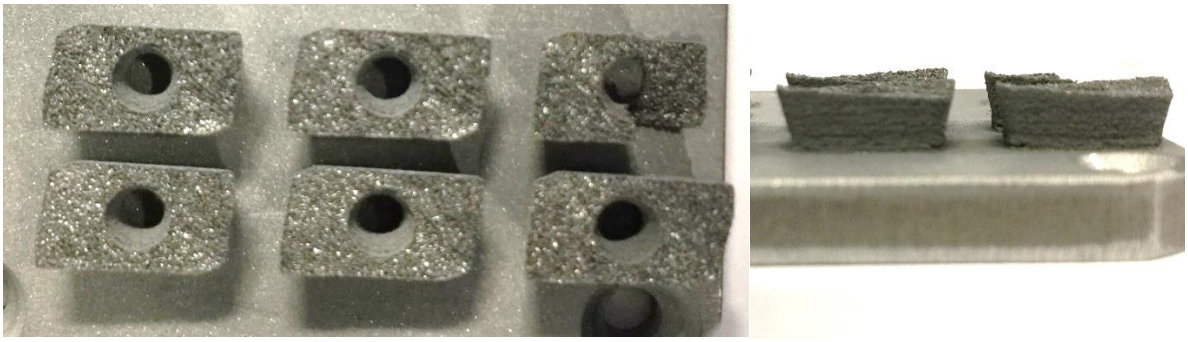

Figure 6.15: Six APMT inserts manufactured with L-PBF on a DIN 1.2343 base plate (Left) top view (Right) side view with cracking

All six APMT inserts printed correctly, however all inserts showed signs of cracks and layer separation near the bottom of the inserts. One of the inserts broke in half during handling of the sample.

6.3.3. Summary and conclusion

Single scan tracks were exposed at different energy densities and were qualitatively and quantitatively analysed. The straight, continuous tracks are the most desirable for the L-PBF process. The most

promising process parameters were found to be 150 W laser power with a 400 mm/s or 600 mm/s scan speed. The 150 W, 400 mm/s scan speed also had the thickest scan track width and deepest penetration into the substrate material. This parameter set was chosen for printing APMT inserts to determine its suitability for further use in this study. These parameters could be utilised for the initial layers (not more than 10) of a WC-Co build to coat the base plate for better adhesion between WC-Co parts and the DIN 1.2343 steel.

6.4. Chapter 6 Summary

In this chapter, the powder, benchmarking, and feasibility studies were conducted in order to obtain a sound knowledge base and to manage certain limitations of L-PBF on WC-Co materials. The different powders were analysed and the Praxair WC-12wt%Co powder was chosen for further study. A conventionally produced insert was analysed and the criteria for a cutting tool were derived. These criteria were as follows: density range of 14.1 g/cm³ to 14.5 g/cm³ (depending on cobalt content), hardness range of 89 – 92.5 HRA, a cobalt or binder content between 9% - 13%, and a crystal structure free of the W_2C phase and η-phases. In order to improve adhesion between the base plate and the WC-Co parts, a starting strategy was derived from single track analysis. The strategy was tested whereby WC-12wt%Co APMT inserts were produced using laser parameters of 150 W, 400 mm/s with a 100 µm hatch spacing on a DIN 1.2343 base plate.

Chapter 7
Process and Parameter Optimisation

In this chapter, the process and parameter optimisation experiments are reported. Initially, another single-track experiment was conducted to determine the melt pool morphology and cobalt evaporation threshold, this time on a WC-12wt%Co substrate. Then, a laser parameter optimisation was performed through varying the laser power, scan speed, hatch spacing, and the scanning strategy. The scanning strategies were chosen as the next area of potential improvement and several CNMA inserts were produced and analysed in the scanning strategy experiment.

7.1. Single Track Analysis with WC-Co Substrate

In order to elucidate the melting/sintering behaviour of the WC-Co during L-PBF, selected single track experiments were performed on a WC-12wt%Co coated substrate. This was performed to minimise the contamination of other alloys from the DIN 1.2343 base plate in the single tracks, as experienced in the previous single-track experiment. The main aim of this experiment was to determine the sintering and evaporation threshold for the cobalt binder and to observe the melting behaviour and the single-track formation for various parameters. The investigations and the prior studies [52] showed that widening of the beam surface for the processing of the refractory hard metal alloys is beneficial. Thus, the spot diameter was varied in this experiment to test this hypothesis.

7.1.1. Experimental setup

Single tracks were exposed on a wrought DIN 1.2343 base plate, which was coated with a 500 µm – 600 µm layer of Praxair WC-12wt%Co powder with a High Velocity Oxygen Fuel (HVOF) coating process. The coating on the base plate was then ground flat (100 µm – 200 µm off) to ensure an even surface for the L-PBF process. The exposure scans were performed using a Concept Laser M2 Cusing machine with a 200 W Rofin StarFiber laser. The same Praxair WC-727-1 / 1342 VM powder was used. The powder was dried in a lab grade oven at 120 °C for 5 hours before being loaded into the machine. The experimental equipment used for this phase of the study can be observed in Table 7.1 and in Appendix A.

Table 7.1: Experimental Equipment used for Single Track Optimisation

L-PBF Machine	Concept Laser M2 Cusing machine
Laser	200 *W* Yb-fibre Rofin StarFiber Laser
Inert Gas	Afrox High Purity 99.998% Argon
SEM Microscope	Zeiss MERLIN SEM with BSD and EDS
Wire EDM e	GF AgieCharmilles CA20
Optical Microscopes	Olympus SZX 7 stereomicroscope and GX 51 inverted microscope

The experimental setup in the Concept Laser M2 Cusing machine handling unit, as well as the schematic of the base plate, can be observed in Figure 7.1. A total of 48 single tracks were exposed on the plate using the parameters shown in Table 7.2. The spacing between each scan track was 1.5 mm, and the tracks were scanned one at a time with about 2 minutes between scans. This was performed to allow any residual heat to dissipate after the scans.

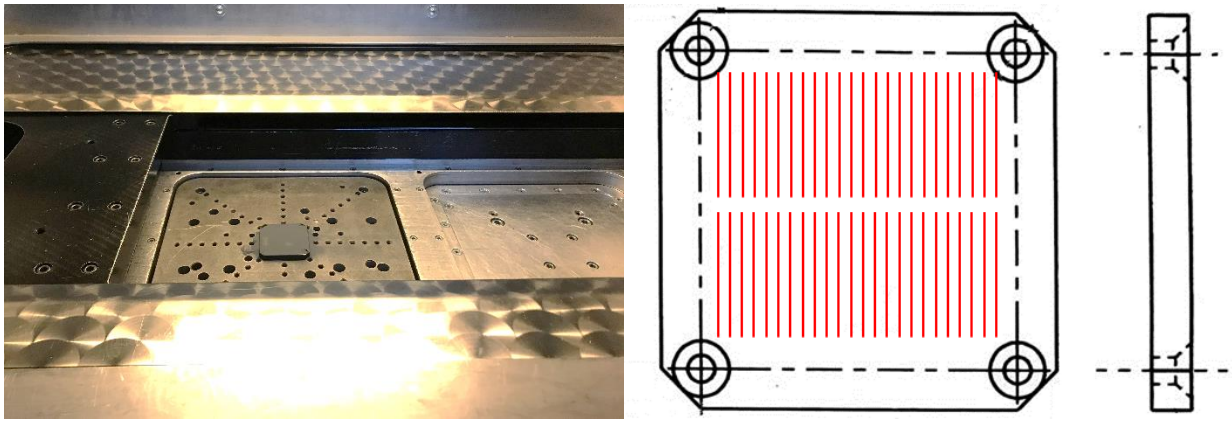

Figure 7.1: Single track experimental setup with (Left) the WC coated base plate installed on the Concept Laser M2 Cusing machine and (Right) schematic of the base plate and single-track experimental runs

The purpose of this experiment was to determine the influence of laser power, scan speed, and spot diameter on the single-track morphology and cobalt content. The layer thickness was set to 30 µm. The laser focal offset was tested at two different levels. The one level was Z = 0 mm and the other was Z = - 2 mm. Theoretically, this correlates to spot diameters of 50 µm and 80 µm respectively. The machine process chamber was flooded with high purity Argon and kept at a residual oxygen content of less than 1000 ppm. An illustration of how the focal offset was varied to change the laser spot diameter for this experiment can be observed in Figure 7.2.

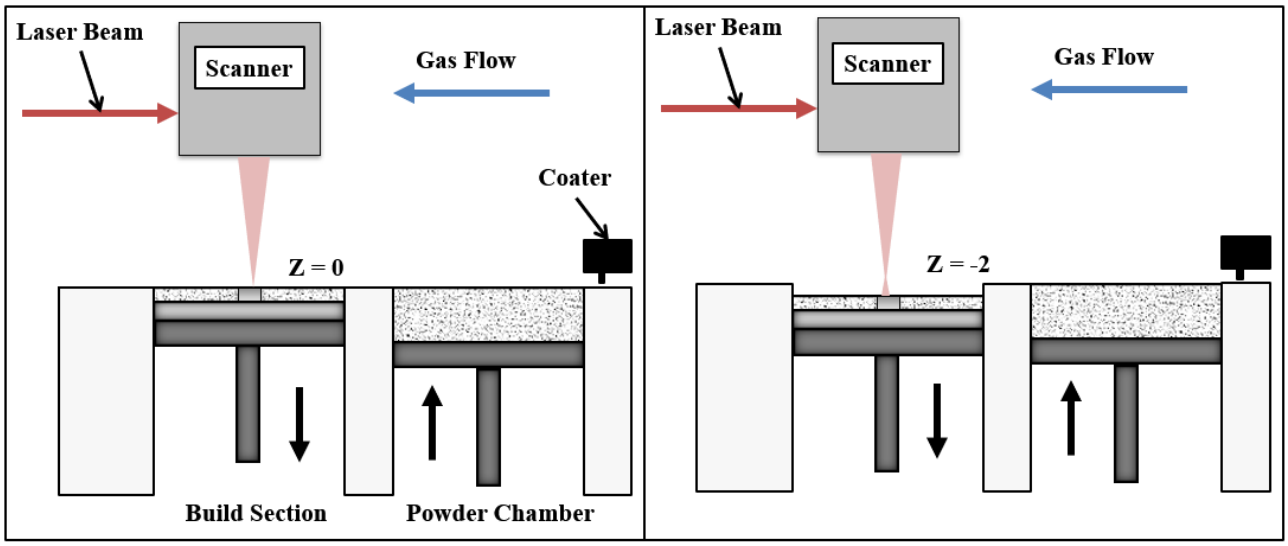

Figure 7.2: Single Track experimental setup with focal offset illustration

For the experimental parameters, the aim was to keep constant specific energy density sets while varying the laser power at four levels in 50 W increments from 50 W to 200 W. The specific energy density was varied at six different levels from 11.11 J/mm^2 down to 4.17 J/mm^2. The corresponding scan speed was then calculated for each run using these criteria.

Table 7.2: Experimental runs for second single scan tracks on WC-Co substrate.

Track Number	Laser Power [W]	Scanning Speed [mm/s]	Specific Energy Density [J/mm^2]	Focal Offset [mm]
1	50	150	11.11	Z = 0 | Z = -2
2	50	200	8.33	Z = 0 | Z = -2
3	50	250	6.67	Z = 0 | Z = -2
4	50	300	5.56	Z = 0 | Z = -2
5	50	350	4.76	Z = 0 | Z = -2
6	50	400	4.17	Z = 0 | Z = -2
7	100	300	11.11	Z = 0 | Z = -2
8	100	400	8.33	Z = 0 | Z = -2
9	100	500	6.67	Z = 0 | Z = -2
10	100	600	5.56	Z = 0 | Z = -2
11	100	700	4.76	Z = 0 | Z = -2
12	100	800	4.17	Z = 0 | Z = -2
13	150	450	11.11	Z = 0 | Z = -2
14	150	600	8.33	Z = 0 | Z = -2
15	150	750	6.67	Z = 0 | Z = -2
16	150	900	5.56	Z = 0 | Z = -2
17	150	1050	4.76	Z = 0 | Z = -2
18	150	1200	4.17	Z = 0 | Z = -2
19	200	600	11.11	Z = 0 | Z = -2
20	200	800	8.33	Z = 0 | Z = -2
21	200	1000	6.67	Z = 0 | Z = -2
22	200	1200	5.56	Z = 0 | Z = -2
23	200	1400	4.76	Z = 0 | Z = -2
24	200	1600	4.17	Z = 0 | Z = -2

Once the single tracks were exposed, the plate was carefully taken for further analysis. The single tracks were analysed using the same methodology and Zeiss MERLIN FE-SEM as the previous experiments. The chemical compositions of the tracks were analysed using an EDS line scan on top of the single tracks. 30 readings were taken per track and normalised. Images of the top of the tracks were also taken using different magnifications. These were initially qualitatively analysed and then measured and quantitatively analysed using ImageJ software.

After suitable tracks were identified given certain criteria, the corresponding parameter sets were utilised to design an optimisation experiment of 20 runs. The CNMA insert geometry was the selected geometry for this study and can be observed in Appendix B under Section B.1. CNMA samples were manufactured, and the density, hardness, and cobalt content were measured. The density was measured using the Archimedes principle as described in Appendix A under Archimedes Density Testing. The Rockwell Hardness tests were performed on a Zwick Roell ZHR Indotec Rockwell Hardness Tester according to the procedure highlighted in Appendix A under Hardness Testing. The cobalt content was measured through compositional scans of the samples bottom surface with EDS.

The orientation of the insert when printing is fundamentally important. Due to the nature of the L-PBF process being a layer wise manufacturing process, the final parts do not display isotropic mechanical properties. When the orientation is such that the rake face is parallel with the layer build direction the flank face could shear off during a cutting operation due to it only being held together by interlayer bonds. Thus, for printing of all inserts, it was decided to only print inserts such that the rake face was perpendicular to the build direction.

7.1.2. Results and discussion

The single tracks were successfully scanned on the WC-Co coated substrate. The final single tracks on the coated base plate can be observed in Figure 7.3. The SEM images of the top surfaces of the scans were qualitatively analysed. The track morphology, melting mode, and defects were analysed, and the tracks were categorised into one of the three types namely, keyhole mode tracks, conduction mode tracks, and lack of fusion / broken tracks. All of the track images can be observed in Appendix B under Section B.4.

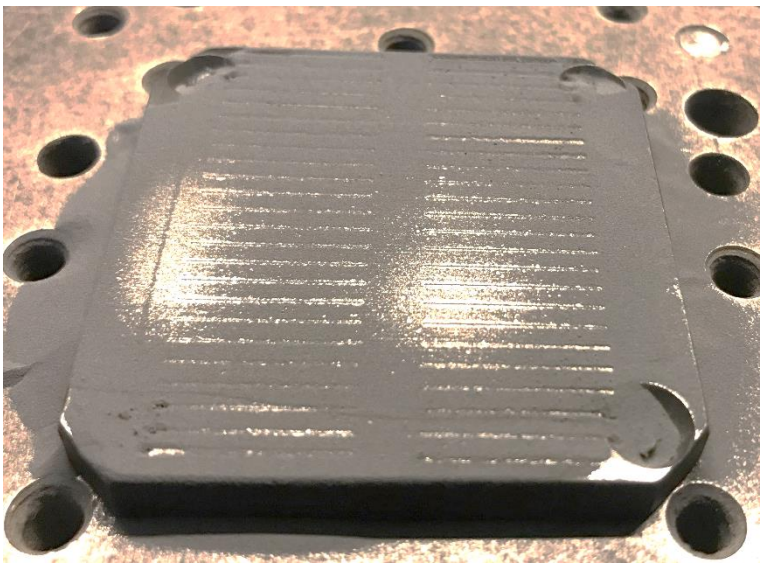

Figure 7.3: WC-12wt%Co Single Tracks on coated substrate

The Z = 0 mm focal offset (spot diameter of 50 µm) tracks can be observed in Figure 7.4. Most of the tracks exposed with a laser power higher than 50 W exhibited keyhole mode melt pools that did not close. The best track with a continuous morphology and closed convex melt pool was the 50 W, 150 mm/s. However, this track also had a number of unmolten particles adhered to it. Several cracks were also noted along the sides of the track.

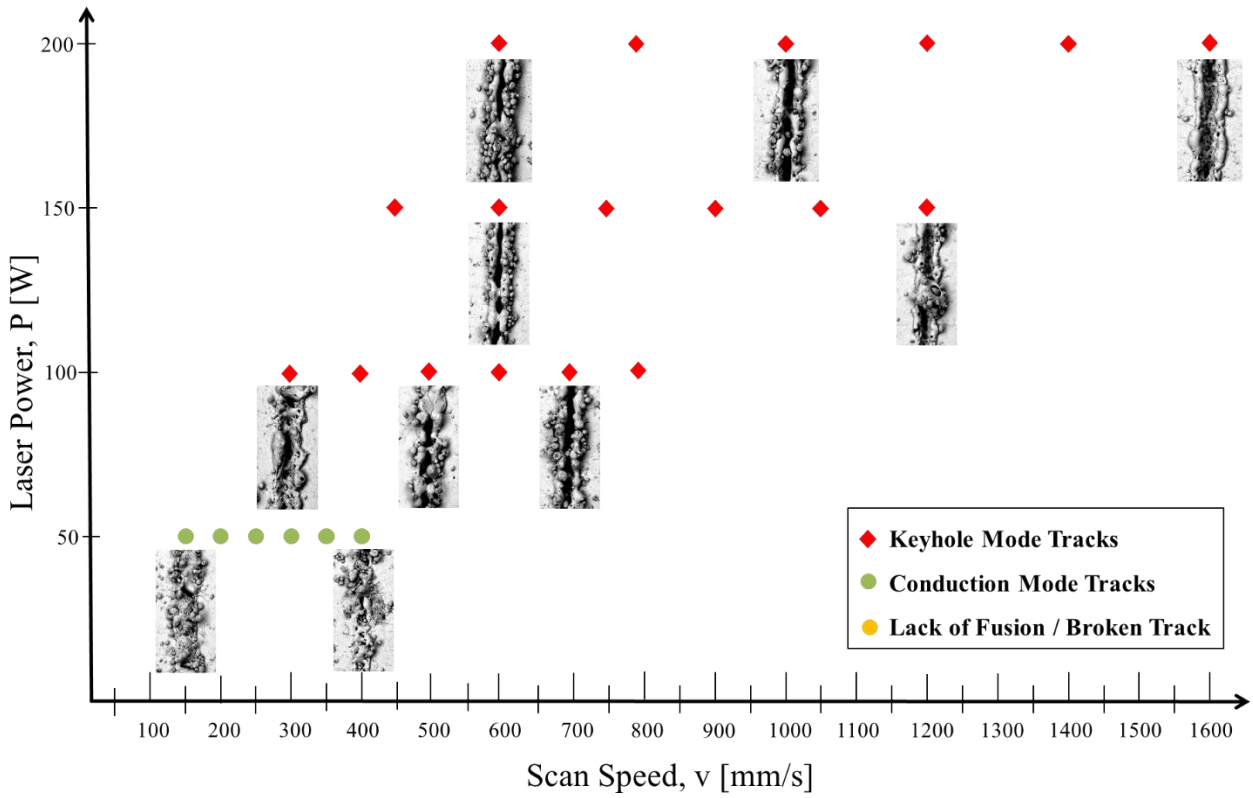

Figure 7.4: Qualitative analysis of the WC-Co single track scans on WC-Co coated substrate for spot diameter of 50 µm

The Z = -2 mm focal offset (spot diameter of 80 µm) tracks can be observed in Figure 7.5. Although a few of the tracks displayed conduction melting mode morphology, the tracks were mainly concave

in shape and appeared to dip below the reference substrate height. The keyhole melting mode was also observed for most of the tracks with laser power greater than 50 W. However, lack of fusion or broken tracks were observed for the higher speeds and powers of 150 W and 1200 mm/s as well as 200 W and 1600 mm/s. This indicates a limit for the intensity and scan speed for the higher laser power of 200 W. These results also show the difference between using the WC-Co coated substrate versus a DIN 1.2343 base plate (Section 6.3) and how the additional elements (Fe) in the substrate can influence the melt pool formation and mitigate any issues due to a low binder usage.

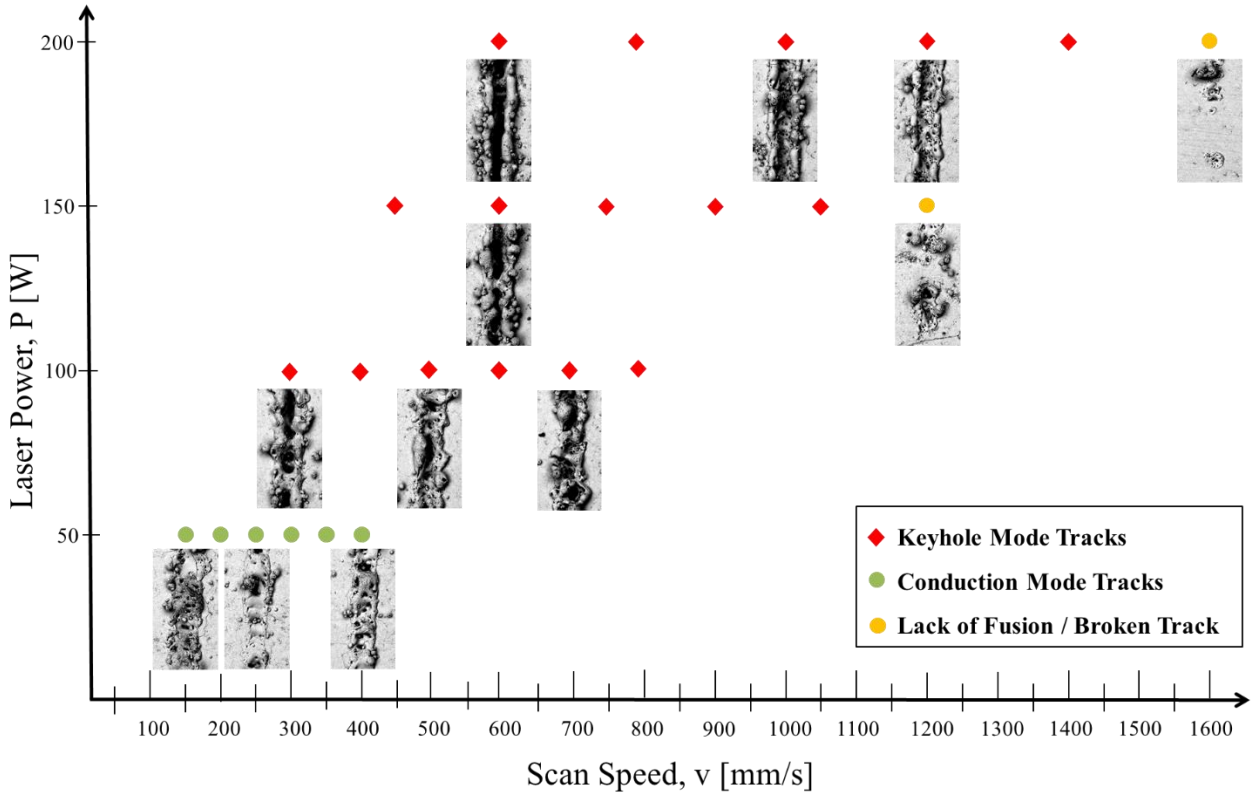

Figure 7.5: Qualitative analysis of the WC-Co single track scans on WC-Co coated substrate for spot diameter of 80 µm

Accounting for all of the important physical phenomena, is crucial to identifying the effects of the laser interaction with this complex material. The morphology of the melt pools observed for each single track was generally unstable, with poor spreading of the melt. Apart from the keyholing that occurred on several tracks, a large number of molten particles were observed on both sides of the single tracks. Numerous tracks where the laser was focused (Z = 0 mm), also appeared to have keyholing issues, whereby the keyhole valley did not close up as the material appeared to solidify before it could flow over the valley. A graphical example of this phenomenon adapted from Khairallah et al. [299] can be observed in Figure 7.6. The physics of this phenomenon was also explained by Tang et al. [287]. However, with a conventional material such as maraging steel, the melt pool remains in a liquid state long enough until the sides of the melt collapse into and fill the cavity created by the laser. With WC-Co, it appears that, depending on the laser scan speed, the melt

pool solidifies too rapidly before it can close the keyhole valley. Thus, alluding to the fact that the scan speed and subsequently the heat transfer from the laser for a given time interval, are highly significant to alleviate keyhole pores and produce adequate melt tracks.

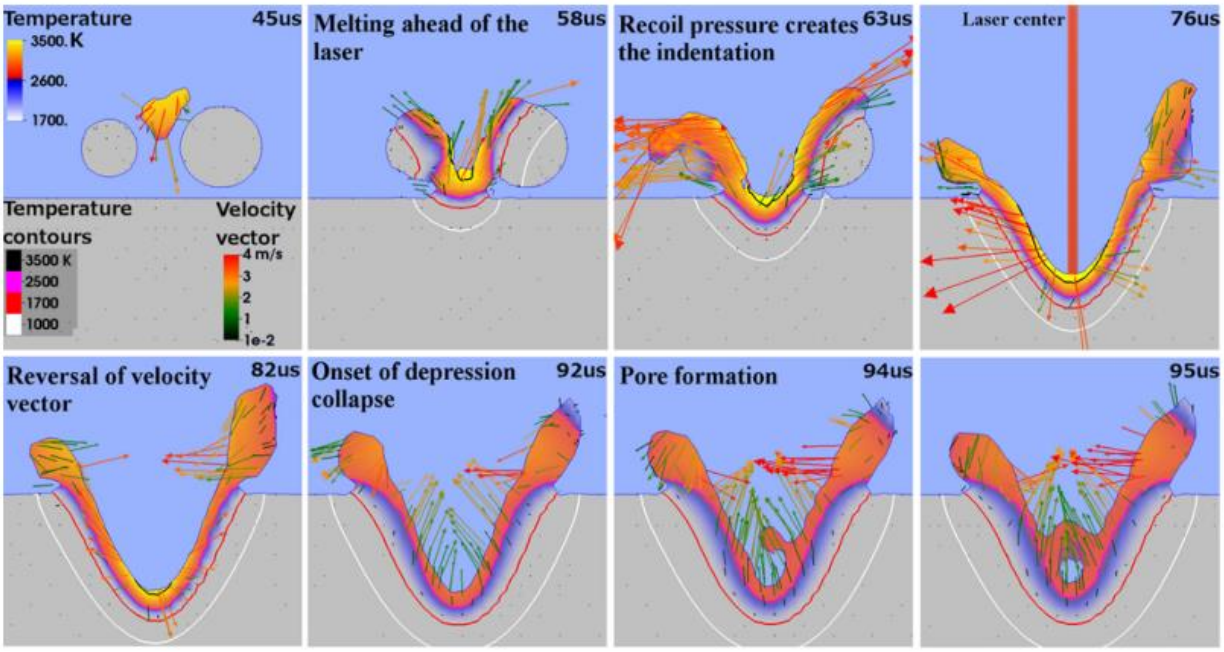

Figure 7.6: Lateral 2D slices of a single track showing the temperature and velocity field of the melt as the laser scans (direction out of page) by a fixed location adapted from [299]

Two scan tracks with the same specific energy density can be observed in Figure 7.7 for the 50 µm laser spot diameter experimental runs.

P = 50 W, v = 150 mm/s

11.11 J/mm²

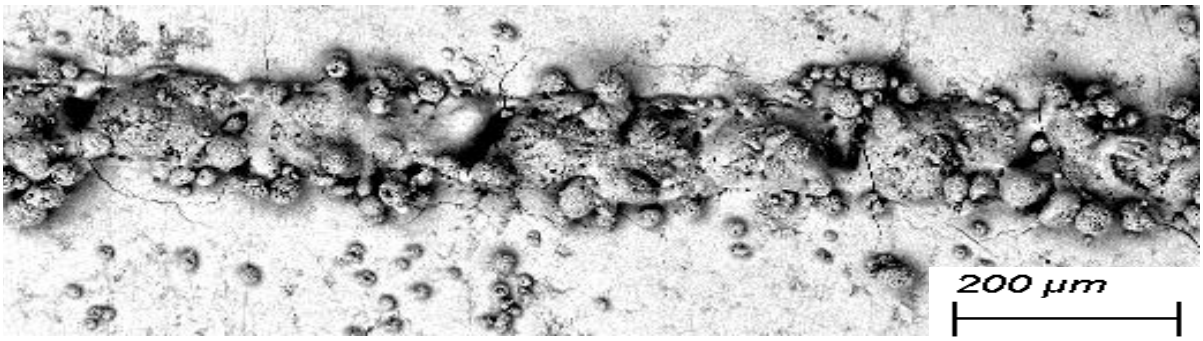

W wt%	C wt%	Co wt%
57.58	32.43	9.99

P = 200 W, v = 600 mm/s

11.11 J/mm²

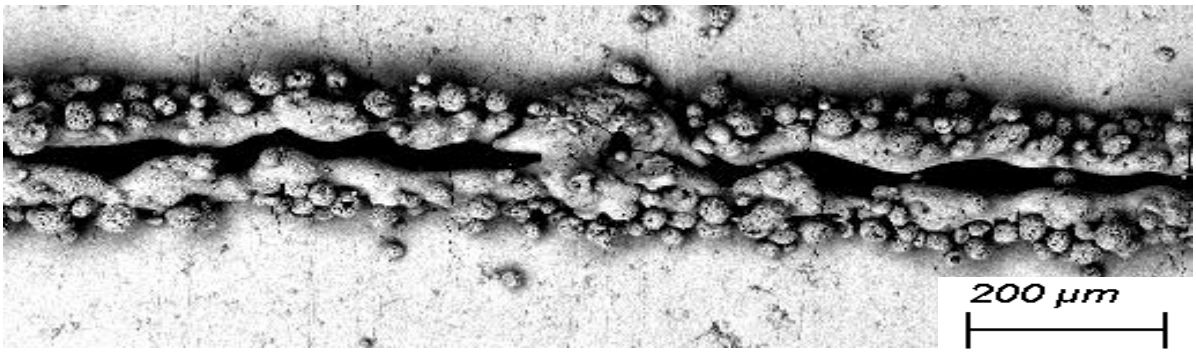

W wt%	C wt%	Co wt%
74.52	13.36	12.13

Figure 7.7: SEM images with EDS line scan of the top track morphology of parameter sets 1 (50 W, 150 mm/s) and 19 (200 W, 600 mm/s)

The comparison of the two scan tracks clearly demonstrates the necessity of considering material flow and heat transfer when working with L-PBF and WC-Co. Evaporation is also important to consider since the melt pool dimensions can also be altered during this process. Moreover, the surface morphologies with and without evaporation are completely different since the recoil pressure triggered by the keyhole formation, which in turn affects the heat and flow behaviour as evaporation occurs [300]. The melt pool morphology and melting mode is strongly influenced by the recoil pressure which suppresses the effect of the Marangoni convection [301]. Consequently, the deep cavity develops and small vortices to the sides of the melt pool are established.

It is well known that a high-energy laser beam tends to apply a significant action of the plasma backpressure on the melt pool, due to the piston effect occurring in the laser irradiation zone. Furthermore, the short-duration, high-energy density laser waves give rise to superfast heating and melting, which is inevitably followed by a rapid solidification process [245]. Based on Boccalini and Goldenstein's [302] results, the laser-induced cooling rate can reach a high value of 10^6 K/s. By utilising laser parameters that only promote the melting of the cobalt binder, the flow of the melt is further affected. Since only roughly 20% by volume of the particulate should undergo a phase change to liquid while the remaining particles become wetted in a slurry of molten cobalt and solid WC particulate. Gu and Shen [231] found that the presence of WC particulate in the melt pool influenced the Marangoni effect, and the material flow was restricted. This limited the neighbouring WC grains from aggregating. They recommended that significant grain refinement or use of submicron grains could improve the wettability between the binder and the matrix, to obtain a strong interfacial bonding.

It must also be noted that the base plate was at ambient temperature of around 21 °C for this experiment. Thus, it could have acted as a heat sink during the single-track experimental runs, which would have prematurely cooled the tracks causing them to solidify rapidly and result in the unique shapes. Given that there were no additional tracks melted next to the single tracks, the heat input effects of an adjacent track after a set time are not well understood. Another issue is that after a set number of layers, the previous layers should also insulate the successive layers from the heat sink effect. Heating of the base plate could result in fundamentally different results for the same process parameters.

Microscope images of the cross sections of the single tracks can be observed in Figure 7.8. The track in the left image is the first track scanned at Z = 0 mm with 50 W power and 150 mm/s scan speed.

This track was continuous and exhibited conduction melting. The track on the right shows a keyhole melt track, which was exposed with a 200 W power and 600 mm/s scan speed. One should take note of the pores around the track. The keyhole track closely resembles the track in Figure 7.6 at 95 µs.

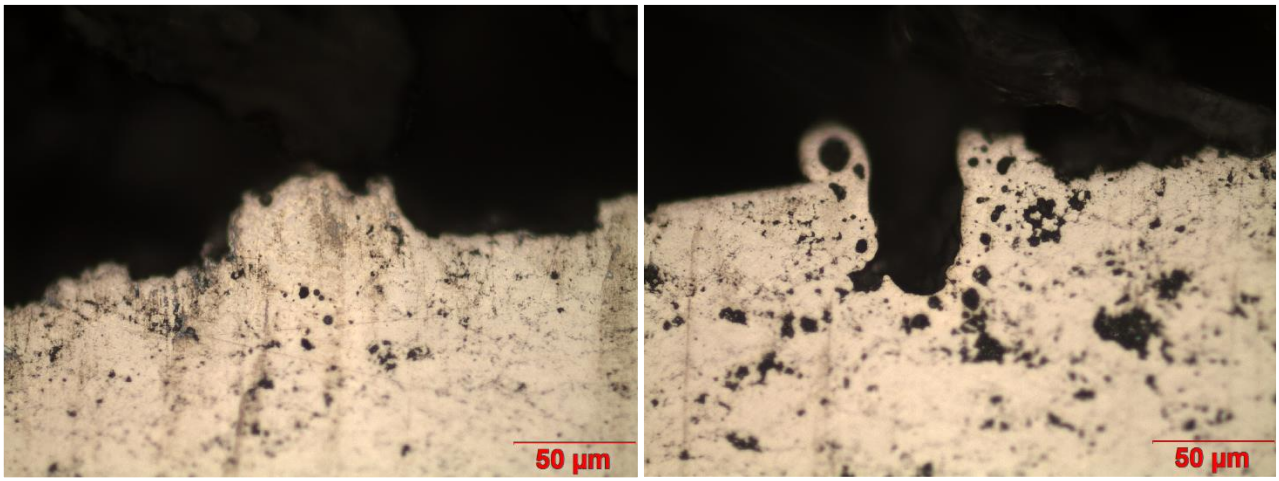

Figure 7.8: Cross-sectional view of the two single tracks with (Left) run 1 (50 W, 150 mm/s) and (Right) is run 19 (200 W, 600 mm/s)

The top SEM images of the scans were analysed and the measured cobalt content readings from the results were graphed in Figure 7.9.

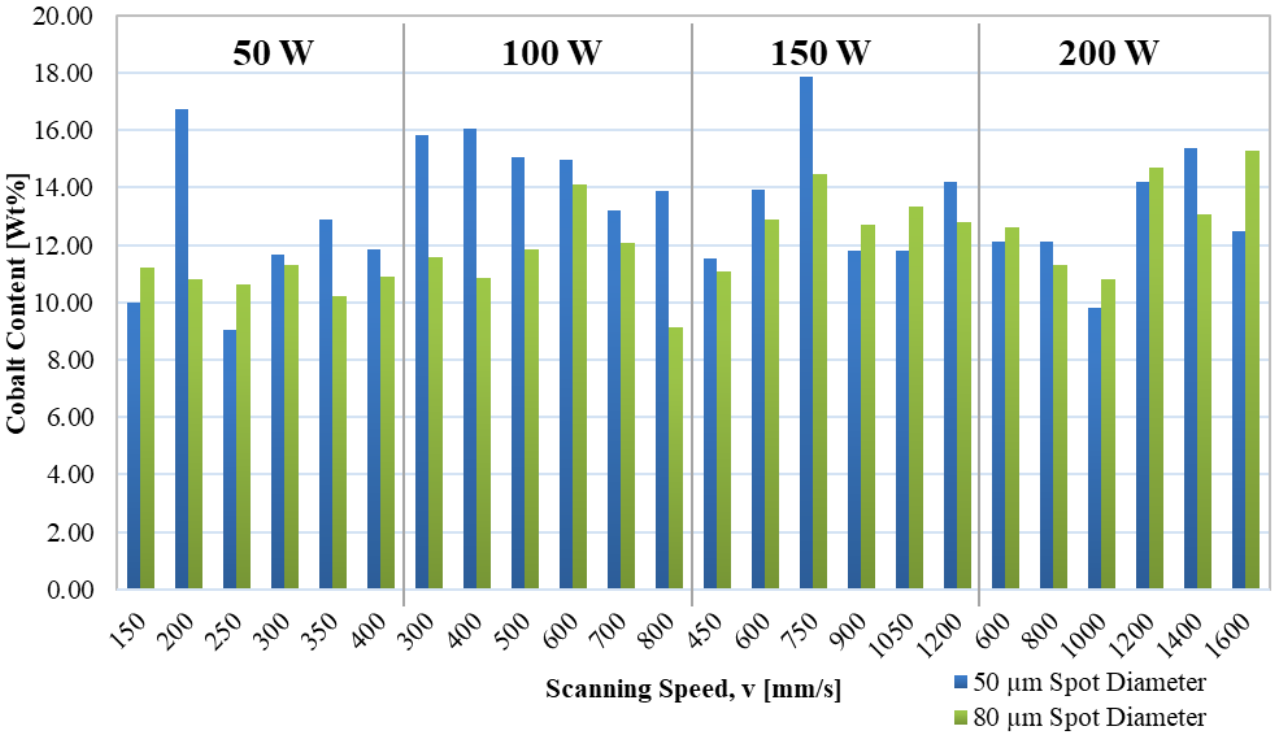

Figure 7.9: Summarised results of cobalt content vs scanning speed for the different single tracks

There does not appear to be a distinct linear trend between the various laser parameters and the cobalt content. An ANOVA was performed to test for significance but none of the parameters had a p value less than 0.1. So, the track morphology was the main factor that influenced the experimental range for the next design. A 20-run experiment was designed with the ranges 40 – 60 W power, 100 – 200

mm/s scan speed, and 40 – 60 µm hatch spacing. An optimal design was used to ensure efficient coverage of the design space. Only 14 CNMA inserts were manufactured with minor visible surface issues. The samples can be observed in Figure B.4 in Appendix B. There was no indication of delamination on the samples or curling from the build plate on the successful 14 samples. The six samples that failed were stopped early in the build due to signs of delamination from the plate. This was performed to ensure they did not interfere with the other samples during the build. The results and the corresponding parameters can be observed in Table 7.3. Note that the inserts that failed had a low power and high scan speed in the design space. This indicates a limit for the 50 W power was 199 mm/s. Two of the successful samples could not undergo hardness testing due to their high brittleness observed.

Table 7.3: Summary of results for the 20 runs, optimised single track range

Input Laser Variables				80-Degree Alternating Raster Strategy		
Power [W]	**Scan Speed [mm/s]**	**spacing [µm]**	**VED [J/mm³]**	**Density (g/cm³)**	**Hardness Average [HRA]**	**Cobalt Content [wt%]**
51	100	46	369	11.93	36.1±3.6	15.06
60	147	51	269	11.81	32.9±6.1	13.96
49	145	52	219	12.29	29.1±1.0	15.36
60	200	60	167	11.85		14.96
60	200	40	250	12.15	29.4±1.1	14.99
40	183	60	122	Failed		
50	199	51	164	Failed		
40	100	44	305	12.12	39.8±3.5	14.88
56	100	60	311	13.31	39.8±3.0	10.46
40	159	47	178	Failed		
50	148	40	278	11.50	32.7±4.8	15.52
43	114	57	217	12.21		14.54
50	199	51	164	Failed		
50	148	40	278	11.45	35.2±4.3	16.92
49	145	52	219	11.20	30.0±1.0	17.71
43	114	57	217	11.69	35.9±3.8	15.70
40	200	40	167	Failed		
56	153	60	204	11.22	30.6±2.2	16.69
60	100	40	500	12.87	50.4±3.9	10.96
60	147	51	269	Failed		

Due to the failed samples, the design space was not adequate to derive a suitable and significant response surface. The highest achievable density was 13.31 g/cm³, which was subsequent to utilising a high VED of 311 J/m³. Though, consequent to this, the cobalt binder was measured to be lower than the starting powder, indicating that some evaporation took place. The highest measured density was comparatively high for L-PBF, considering the low power used. However, the density was still

relatively low in contrast to PM produced cutting tools. The low hardness values across the board could be attributed to the high cobalt content measured. The higher cobalt content present in the samples does not support the evaporation theory for some of these parameters. The cobalt content was measured to be higher than the content of the starting Praxair powder for most of the VED values less than 311 J/m³. Due to the low hardness values for the various parameter sets, it could be stated that these inserts might not be suitable for cutting operations of certain metals without further post processing operations. Given the criteria of a suitable cutting tool, none of the parameters were able to produce a dense, hard, and 12 wt% cobalt cutting tool.

7.1.3. Summary and conclusion

Single tracks were exposed onto a WC-12wt%Co coated substrate with varying specific energy densities and laser power. The track morphology was qualitatively analysed and certain phenomena that occurred during the laser melting process were revealed. The cobalt content for the various tracks was measured and no significant effect could be attributed to the changes. An experiment was designed using the parameter range derived from the best track morphology and CNMA inserts were produced. Six parameter sets failed to produce successfully built inserts, which indicated a lower limit for the melting process. The other 14 L-PBF inserts had relatively low density and hardness in comparison to conventional cutting tools.

7.2. Laser Parameter Optimisation

Owing to the various parameter optimisation studies found on WC-Co, an optimisation experiment was developed to determine whether minimal change to the conventional L-PBF process could result in an optimised WC-Co insert. It was previously discussed in Chapter 4, how many authors [50], [246], [265] varied the laser parameters such as laser power, scan speed, and hatch spacing in order to develop a suitable process window for WC parts depending on a certain requirement. However, most of the publications reviewed made use of high power and a high volumetric energy density (>200 J/mm³), and did not mention the scanning pattern or strategy used. Many of them also noted evaporation of the cobalt binder at these high VED values. Thus, in this laser parameter optimisation experiment, a large VED range (30 – 1000 J/mm³) was used while varying the scanning pattern and strategy. This was performed to identify the effects of process parameters on the density, hardness, and evaporation of the cobalt binder, so as to optimise the process for manufacturing of tungsten carbide cutting tools.

7.2.1. Experimental setup

Cuboidal (10 x 10 x 10 mm³) experimental samples were produced on a Concept Laser M2 Cusing machine with a 200 W Rofin StarFiber Laser. A single cube was designed and sliced in Materialise

Magics Software version 22.1. The laser spot diameter was kept constant at ~50 µm and the layer thickness was 30 µm. The base plate was DIN 1.2343 steel, and the build chamber was flooded with nitrogen gas and maintained at a 0.1% residual oxygen content. The equipment and methodology used for the experiments and analyses can be observed in Table 7.4 as well as Appendix A: Measurement and Experimental Equipment.

Table 7.4: Experimental equipment used for laser parameter optimisation

L-PBF Machine	Concept Laser M2 Cusing machine
Laser	200 W Yb-fibre Rofin StarFiber Laser
Slicer	Materialise Magics V22.1 with CL Slicer
Wire EDM	AgieCharmilles CA20
Analytical Balance	Kern Analytical Balance
Hardness Tester	Zwick Roell ZHR Indotec
SEM Microscope	Zeiss MERLIN SEM with BSD and EDS
Optical Microscopes	Olympus SZX 7 stereomicroscope and GX 51 inverted microscope
PXRD	Bruker D2 Phaser benchtop powder diffractometer

The powder used was the same Praxair agglomerated and sintered WC-727-1 / 1342 VM. The measured PSD was 3 – 56 µm with D_{50} of 25 µm. The measured average chemical composition was 13.09 wt% cobalt and 5.65 wt% carbon, with tungsten balance.

A metal recoater blade was utilised rather than a rubber one, as it is less forgiving to suboptimal parameters and warping of parts from the powder bed. Metal recoater blades also have less deflection, which allows for more force being applied to the powder bed during a coating pass. This results in denser packing of the powder bed [49].

Due to the nature of the L-PBF process, the number of influencing factors, and their interactions, the D-Optimal design was chosen to only output experimental runs that were constrained by a certain mathematical model. The model chosen to constrain the experimental runs was the volumetric energy density. The equation (equation 3.13) for volumetric energy density can be found in Section 3.4.1. The VED with the hatch spacing and not the laser focal diameter was chosen, since the hatch spacing was one of the factors to be varied. The VED also incorporates the laser power, scan speed, and layer thickness, which are the most important parameters for laser melting/sintering [180]. The runs were designed to include blocking, randomisation, and replication.

For the first experimental design the ranges were set to 50 – 200 W laser power, 200 – 1200 mm/s scanning speed, and 80 – 130 µm hatch spacing with a VED value greater than 30 J/mm³. A 20-sample experimental run was derived through the D-Optimal design. However, 11 of the samples from this run failed due to the low power (<100 W) and VED (<60 J/mm³) values. Thus, no statistical

significance was apparent due to the lack of data. So, for the second iteration of experiments, the parameter ranges were refined for laser power, scan speed, hatch spacing, and VED to 100 – 200 W, 100 – 1100 mm/s, 70 – 130 µm, and >60 J/mm³ respectively. The scanning strategy was also varied to determine whether this had an influence on the final outcomes. The raster scan was used for one experimental set without varying direction throughout the build. A diagonal raster scan with a 90-degree alternating rotation (diagonal alternating strategy) was used for the other experimental set. These scanning strategies can be observed in Figure 7.10. It should be noted that with the specific Concept Laser M2 Cusing machine used and the SCANLAB scanner, the laser tracks are continuous, and the laser does not turn off between vectors as depicted in the images below.

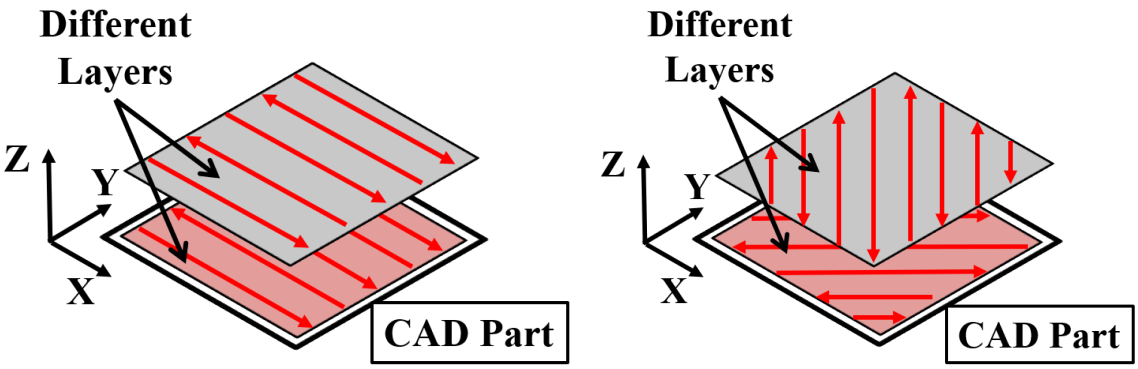

Figure 7.10: Scanning strategies used where (Left) is the raster scan without varying direction throughout the build and (Right) is a diagonal raster scan with alternating 90-degree rotation

A total of 40 experimental runs were performed for each scanning strategy. After completion of the experimental runs, the samples were removed from the base plate with an AgieCharmilles CA20 wire EDM. The cubes were ground on the top and bottom surfaces before being analysed. The bottom surfaces were polished according to the Struers guide for metallographic preparation of sintered carbide powder metallurgy parts [303]. The density was measured using the Archimedes principle as described in Appendix A under Archimedes Density Testing. With the Archimedes immersion method for the measurement of density, the density values represent a skeletal density, which excludes the open porosity inside the sample volume. Therefore, the measured densities are not representative of the bulk sample but rather the material at a micro scale. The Archimedes method also allows for the measurement of trapped, unfused powder, which could also contribute to the density measurement. It is also noteworthy to understand that the theoretical density of the bulk material is generally calculated with the assumption that the bulk density of the starting powder material is the same as the final L-PBF material. This however, is often not the case due to the changes in the chemical composition that occur during the L-PBF process, such as, evaporation of the binder, and oxidation of the tungsten [259]. The Rockwell Hardness tests were performed on a Zwick Roell ZHR Indotec Rockwell Hardness Tester according to the procedure highlighted in Appendix A under Hardness Testing. The results from the density and hardness tests were statistically analysed in Design

Expert 13. Compositional scans of the samples bottom surface were conducted with EDS on the Zeiss MERLIN FE-SEM using a beam voltage of 20 kV and back scatter detection mode. Selected samples phases were identified by powder X-ray diffraction using a Bruker D2 Phaser diffractometer according to the process highlighted in Appendix A under X-ray diffraction.

Upon completion of the analyses, response surfaces were generated for density, hardness, and cobalt content. Further improvement through selecting the optimal parameter range for the two different scanning strategies was performed. Two sets of 20 CNMA inserts were manufactured in an attempt to improve the results and verify the response surfaces. A 20-run experiment with high VED (232 < VED < 763 J/mm³) was designed for the diagonal alternating strategy. The power was set at 200 W, scan speed was 100 – 300 mm/s, and hatch spacing was 70 – 130 µm. For improving and verifying the raster strategy, a 20-run experiment was designed where the VED was decreased (94 < VED < 274 J/mm³). The laser parameters that were chosen were 180 – 200 W laser power, 450 – 700 mm/s scan speed, 50 – 90 µm hatch spacing and performed with the raster strategy with an 80-degree orientation to ensure constant vector length on the insert while varying the rotation through each layer. These parameters were run through an optimal design to derive an optimised design space and limit the runs. The inserts were subject to the same experimental analyses as described for the cuboid experiments.

7.2.2. Results and discussion

The first attempt at a parameter optimisation run using the D-Optimal design can be observed in Figure B.5 in Appendix B. With the first run of 20 parameter sets, only nine of the samples materialised. Eleven of the samples delaminated and warped off the base plate during the first few layers. The nine successful samples were analysed with respect to hardness and density. However, due to the high failure rate of the samples, no statistical significance was found. The lack of successful samples was attributed to the low volumetric energy density used in the DoE. Thus, for the second iteration of design, a minimum volumetric energy density of 60 J/mm³ was used as the lower threshold value. The 40 (x2) experimental runs with the density and hardness results are tabulated in Table 7.5. Even during the second iteration experimental run, parts of the printed cubes separated from the substrate during the process. The construction of those particular parameters had to be stopped either due to delamination or severe deformation. A number of the cubes adhering to the substrate had a high brittleness. These could be removed from the substrate and broken without the aid of tools and with very little effort. An image of the samples and these highlighted issues can be observed in Figure 7.11.

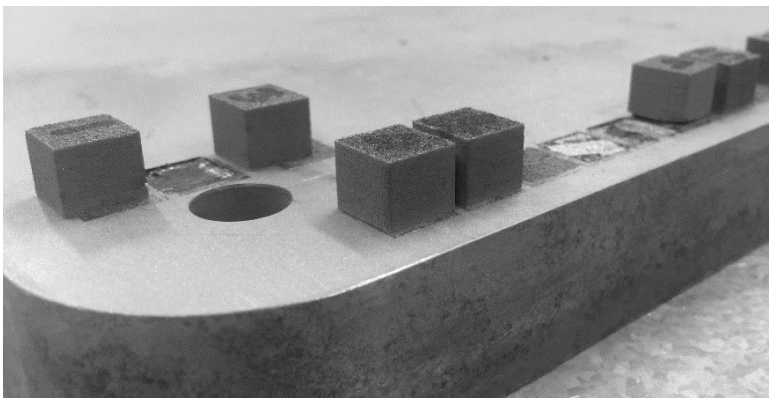

Figure 7.11: Experimental samples with some still attached to the plate, some stopped due to premature failure and some delaminating off the plate

Table 7.5: Summary of results for the 40 run single scan parameter optimisation

Input Laser Variables				Raster Strategy			Diagonal Alternating		
Power [W]	Scan Speed	spacing [µm]	VED [J/mm³]	Density (g/cm³)	Hardness Average [HRA]	Cobalt Content [wt%]	Density (g/cm³)	Hardness Average [HRA]	Cobalt Content [wt%]
140	1100	70	60.61	Failed			12.94		8.44
190	100	94	673.76	Failed			15.18		2.93
200	1100	70	86.58	12.92	46.8±6.5	10.92	12.65	34.6±3.6	17.31
200	100	130	512.82	Failed			Failed		
150	600	130	64.10	12.75	39.7±7.2	10.92	12.37		10.29
200	100	70	952.38	Failed			15.35		9.53
200	1100	70	86.58	13.00	38.0±7.1	10.89	12.51	35.0±9.7	
200	1100	100	60.61	12.69	33.5±5.6	15.76	12.42		14.15
200	100	130	512.82	Failed			14.70	77.9±3.3	6.31
200	100	130	512.82	Failed			14.94	82.3±3.5	7.21
200	800	130	64.10	12.79	43.0±5.1	11.52	Failed		
200	500	100	133.33	13.12	65.9±4.6	8.81	Failed		
100	700	70	68.03	12.91		9.04	Failed		
140	100	76	614.04	Failed			Failed		
150	100	100	500.00	Failed			Failed		
100	700	76	62.66	Failed			Failed		
140	1100	70	60.61	12.71		11.54	Failed		
150	100	100	500.00	Failed			13.81	77.7±4.0	7.00
200	800	130	64.10	12.82	52.8±3.9	8.47	12.55		14.82
200	100	70	952.38	Failed			15.01	82.4±0.8	3.80
200	1100	100	60.61	12.97	36.9±8.3	8.02	Failed		
160	500	70	152.38	13.28	60.0±6.8	11.95	13.26	65.5±5.7	
140	1100	70	60.61	12.96		11.29	Failed		
150	800	100	62.50	12.65	30.8±1.4	10.15	Failed		
100	500	106	62.89	12.99		25.01	Failed		
200	700	70	136.05	13.30	61.7±8.7	12.78	13.11	56.5±8.3	19.9
100	100	100	333.33	14.14		5.98	13.67	69.2±9.1	6.32
100	400	130	64.10	12.85	33.0±7.0	14.31	Failed		
200	700	70	136.05	13.22	60.5±8.7	7.80	12.86	61.2±3.4	8.8
100	100	130	256.41	Failed			13.48	62.8±8.9	5.58
100	100	70	476.19	Failed			13.75	66.9±3.9	7.58
100	700	70	68.03	12.72		8.39	Failed		
200	100	70	952.38	Failed			Failed		
100	100	70	476.19	Failed			13.83	65.0±13.9	7.61
100	100	70	476.19	Failed			13.45	72.7±5.3	6.31
150	100	130	384.62	Failed			14.47	77.0±6.4	6.49
200	1100	100	60.61	12.89	30.9±9.0	18.85	12.85		8.18
100	100	130	256.41	Failed			13.86	58.7±4.2	8.22
100	400	130	64.10	12.99		10.63	13.46		17
150	600	130	64.10	12.73	45.5±6.2	12.86	Failed		

From the experimental runs, 18 out of 40 runs failed using the raster strategy while 16 out of 40 runs failed using the diagonal alternating scan strategy. These failures could be caused by a number of issues such as high residual stress, poor interlayer bonds, evaporation of the binder, poor melt tracks, and insufficient energy input, to list a few. From the results in Table 7.5, it can be noted that the maximum achievable density was 15.35 g/cm³ using the diagonal alternating scan, however, this sample was too brittle to undergo Rockwell hardness testing. The highest achievable density for the raster scanning strategy was 14.14 g/cm³, however, this sample did not materialise as a cube and was also too brittle to undergo hardness testing. The microstructure and surface image of sample 20 (15.01 g/cm³) from the diagonal alternating scan strategy can be observed in Figure 7.12.

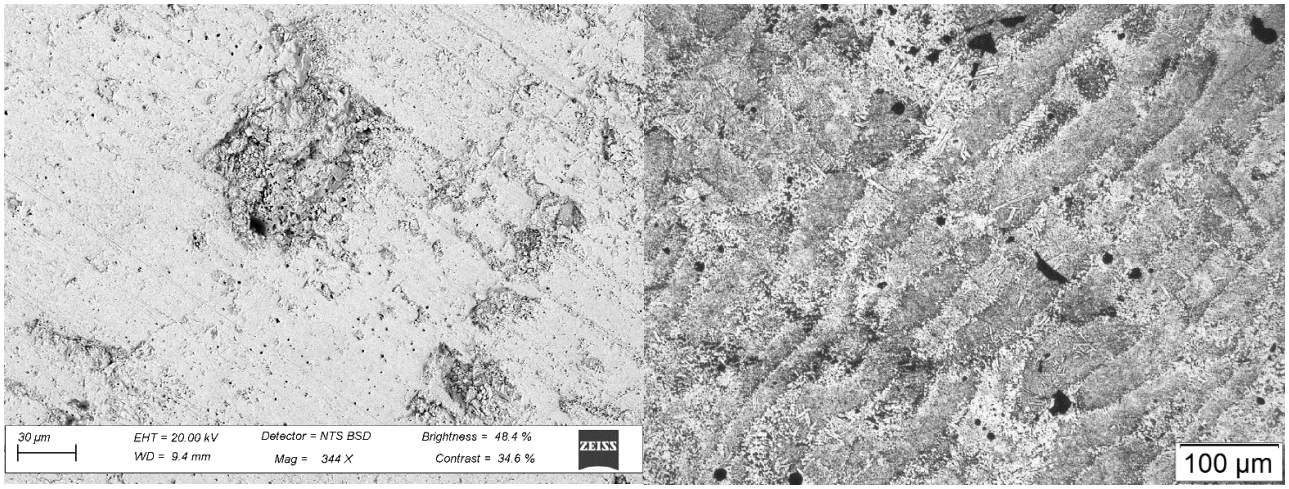

Figure 7.12: Microscopy images of sample 20 (200 W, 100 mm/s, 70 µm) surface with (Left) SEM image and (Right) Optical microscope image after etching

One can observe limited porosity and cracks on the sample and the directions of the scan tracks can be clearly noted moving corner to corner on the image. Elongated WC-Co islands across the diagonals of the sample were detected which correspond to the diagonal scanning strategy laser scan directions. The microstructure comprised of sections with relatively fine WC grains and coarse or abnormally large WC grains. The abnormally coarse-grained sections form due to highly localized heating of the WC-Co granules leading to the very intensive WC grain growth in those sections. The density measurements graphed against the volumetric energy density can be observed in Figure 7.13.

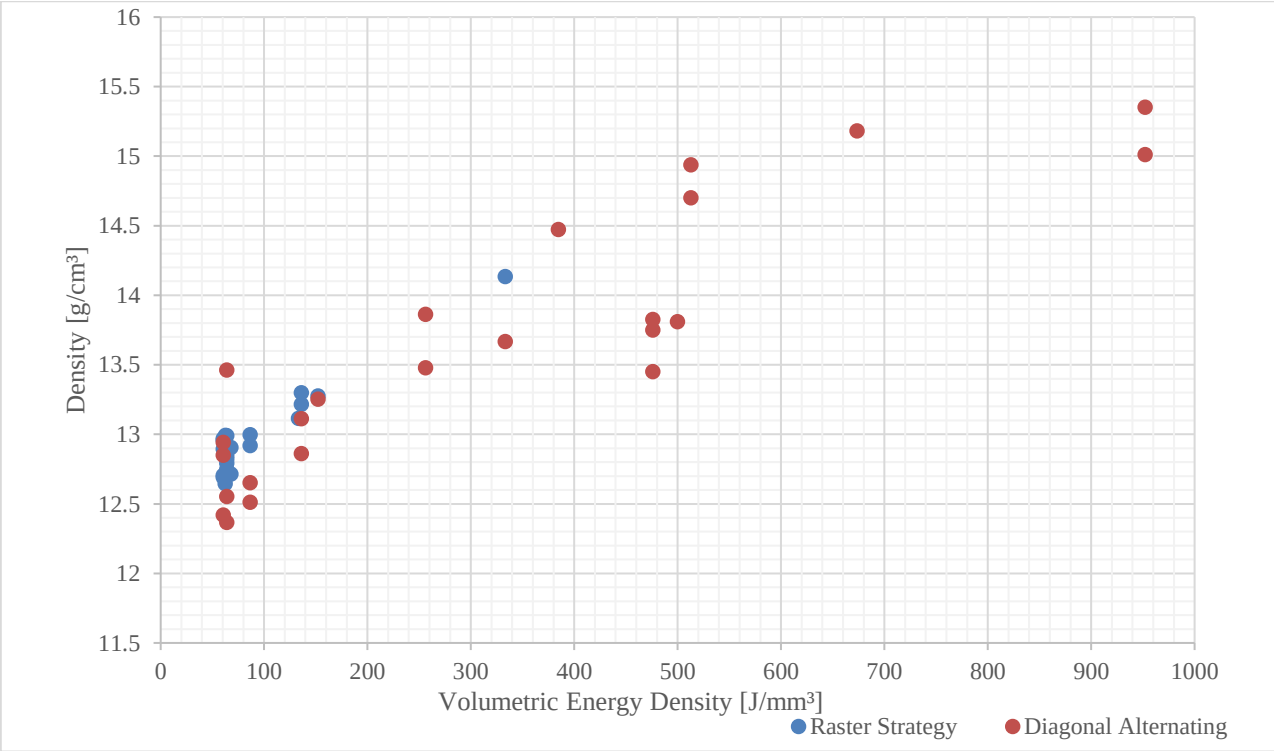

Figure 7.13: Density as a function of volumetric energy density for the two different scanning strategies

The maximum achievable density of the L-PBF samples was dependent on the scanning strategy as well as the VED applied. The density was directly proportional to the VED for both scanning strategies. However, a clear limit on the maximum achievable density can be observed for the different strategies. The raster strategy graph plateaus around the 14.3 g/cm³ and 334 J/mm³ mark, while the diagonal alternating strategy appears to have two different trends. One where the density and VED plateau around 13.9 g/cm³ and 477 J/mm³ correspondingly and the other where the horizontal asymptote of approximately 15.5 g/cm³ was almost reached with the high VED range tested in this experiment. The diagonal alternating samples that were in the range of 470 – 513 J/mm³ drastically varied in their density measurements from 13.45 – 14.94 g/cm³. This could indicate that there are other factors (such as open porosity, compositional and grain size variations) that may affect the density at this high energy input. The suspected cause of the higher density would be the change of phase of the WC (to liquid W + solid C) through excessive energy input and increased temperatures experienced in the melt pool. This would result in better formed tracks, as more of the material would enter the liquid phase (in comparison to just the 20 vol% of the cobalt binder). However, by doing this the cobalt binder would also change into the gas phase and evaporate from the structure [304]. The WC phase changes for higher temperatures can be observed in the phase diagrams reviewed by Fernandes and Senos [153].

The results from Fortunato et al. [29] for the single laser pass closely resemble the density results and curve of the raster scan strategy. They also reported that there was a maximum volumetric energy

density reachable with a single laser pass, which limits the maximum achievable density. Fortunato et al. [29] highlighted that after a VED value of 375 J/mm^3, intact cylinders could not be produced. However, in this study, this was only true for the raster strategy. This suggests that the laser pattern, scan strategy, and geometry of the samples could have a large effect on the maximum achievable density of a WC-Co part. One also needs to be cautious since the density can also be increased through the evaporation of the cobalt binder. Thus, the density should be reported alongside the cobalt content.

A response surface regression was performed on the results from both the raster scan strategy and the diagonal alternating scan strategy. An ANOVA was performed to test for significance. The assumptions for the ANOVA were met and confirmed with residual analysis. The statistical results from the ANOVA can be found in Table 7.6.

Table 7.6: ANOVA for Reduced Quadratic Model for Density Response

Source	Sum of Squares	Mean Square	F-value	p-value	
Model	24.55	3.07	65.69	< 0.0001	significant
A-Power	0.9308	0.9308	19.92	< 0.0001	significant
B-Scan Speed	6.28	6.28	134.42	< 0.0001	significant
C-Hatch Spacing	0.1306	0.1306	2.80	0.1030	
D-Scan Strategy	0.1879	0.1879	4.02	0.0523	
AB	1.95	1.95	41.64	< 0.0001	significant
AC	0.1580	0.1580	3.38	0.0740	
A^2	0.2294	0.2294	4.91	0.0329	significant
B^2	3.92	3.92	83.92	< 0.0001	significant

For the density results, a reduced quadratic model resembled the best fit with respect to the model and factor significance as well as the Adjusted and Predicted R^2. Most of the factors were significant with $p < 0.01$. The other parameters such as scanning strategy and the interaction between power and hatch spacing could be significant with $p< 0.075$. Also, for hatch spacing, a p value of $p< 0.11$, could still indicate some significance. The three-dimensional plots of the raster scan response surfaces can be observed in Figure 7.14.

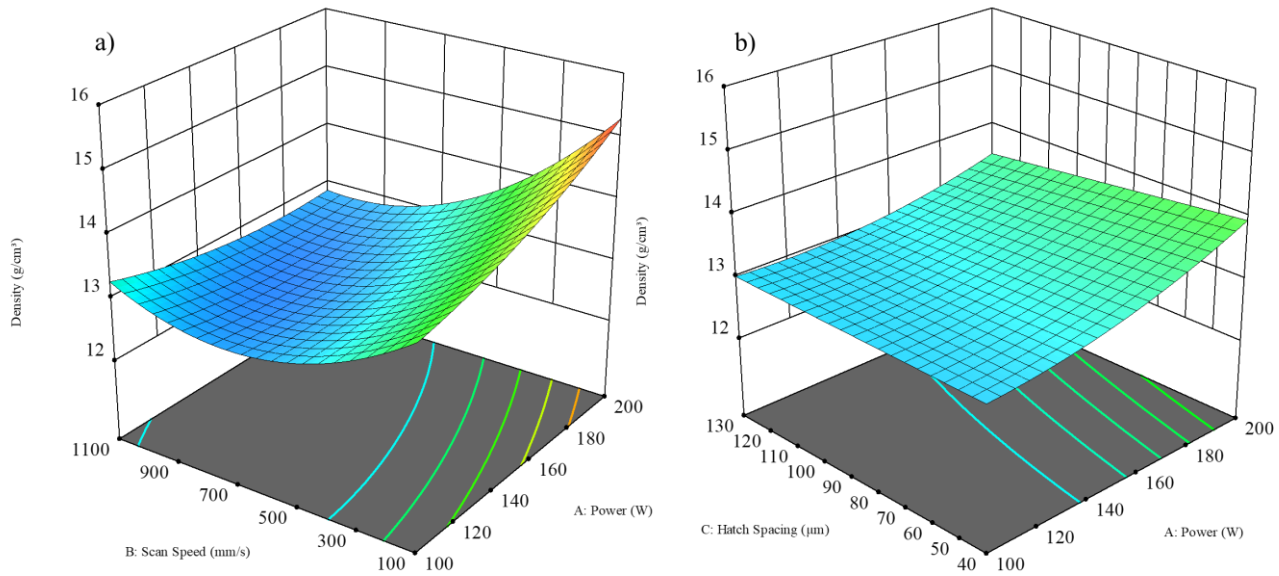

Figure 7.14: Raster Scan Strategy, Density result response surface plots for a) Power vs Scan Speed and b) Power vs Hatch Spacing

The response surfaces in Figure 7.14 indicate that a high laser power, low scan speed and low hatch spacing is preferred. Thus, supporting the theory that a high energy density is required for a high density. This theory does not consider the evaporation of the lighter alloying elements, like cobalt, which results in a higher density for some parts that would have a higher tungsten content due to this phenomenon. The response surfaces for the diagonal alternating scan strategy can be studied in Figure 7.17.

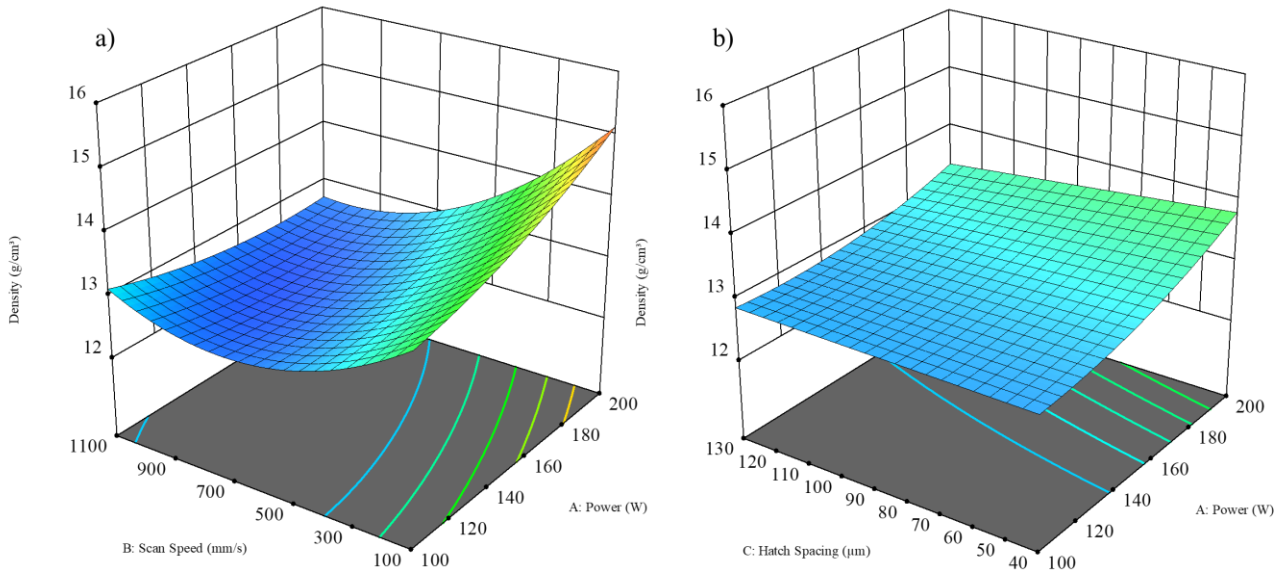

Figure 7.15: Diagonal alternating Scan Strategy, Density result response surface plots for a) Power vs Scan Speed and b) Power vs Hatch Spacing

The response surfaces for the two different scanning strategies appear very similar in shape. The surfaces and relationships for both strategies are clearly defined. However, the model shows that a higher density is achievable with the raster scan when this was not possible due to the VED plateau. Uhlmann et al. [25] found that the HIP process leads to a moderate density increase in WC-Co parts

of 1 %. If the samples are built horizontally, their density dropped by 0.6 %. They pinpointed the reason for this in the applied meander (raster) exposure strategy. With longer scan lengths, the temperature declines in the interaction zone of the laser beam and the material due to heat conduction effects. The molten pools temperature gradient fluctuates more rapidly, and therefore the formation of pores can be prompted. The underlying differences between the two strategies used in this study could also reveal remnants of these effects and are discussed further at the end of this section.

The hardness measurements graphed against the volumetric energy density can be observed in Figure 7.16. The hardness values follow a very similar trend to the density curves in Figure 7.13, however, a number of samples failed during measurement due to their brittle structure. This caused some issues with the statistical power and significance of the results.

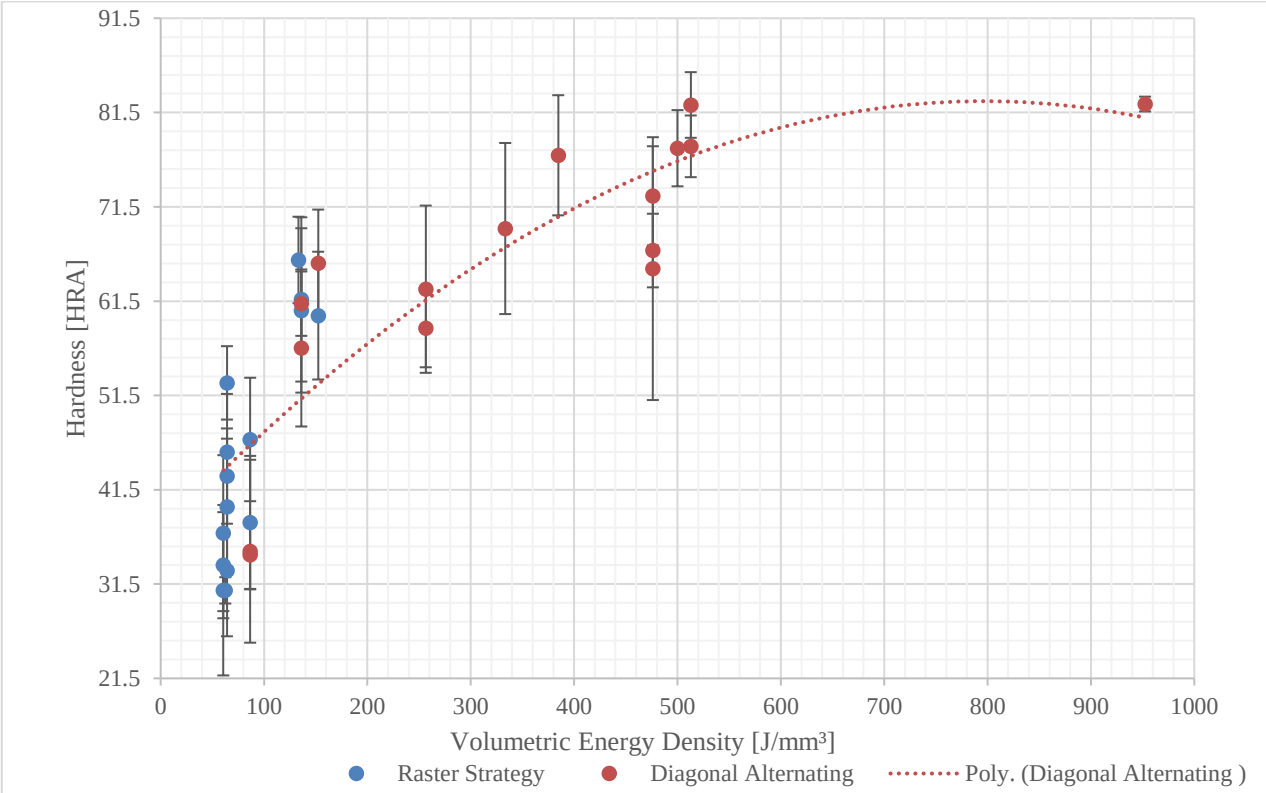

Figure 7.16: Hardness as a function of volumetric energy density for the two different scanning strategies

The VED appears to have very little influence on the hardness repeatability, as the hardness measurements for a given VED vary considerably. This is more apparent with the raster strategy. A positive and decreasing polynomial trend of increasing hardness with increasing VED can be identified for the Diagonal Alternating strategy. However, the response surfaces of the interactions between the factors used to calculate the VED reveal more information. The ANOVA for the hardness response can be observed in Table 7.7. The model that fit best was a two-factor interaction where the interaction between power and scan strategy, as well as all the other factors were significant with $p < 0.043$.

Table 7.7: ANOVA for Reduced 2FI Model for Hardness Response

Source	Sum of Squares	Mean Square	F-value	p-value	
Model	7950.49	1135.78	75.94	< 0.0001	significant
A-Power	1794.62	1794.62	119.53	< 0.0001	significant
B-Scan Speed	4446.44	4446.44	296.16	< 0.0001	significant
C-Hatch Spacing	260.62	260.62	17.36	0.0003	significant
D-Scan Strategy	68.73	68.73	4.58	0.0423	significant
AD	242.08	242.08	16.12	0.0005	significant

The three-dimensional plots of the response surfaces for average hardness and the different laser parameters (Laser power, hatch spacing) can be observed in Figure 7.17 for the raster scan strategy and diagonal alternating strategy respectively. For the raster scan strategy, the laser power had a higher influence on the hardness in comparison to the diagonal alternating strategy. This could be due to the constant vector length in the raster strategy (10 mm) whereby the change in power would be more pronounced over the entire part since the individual scan tracks wholistically are longer than the diagonal alternating strategy (~0 mm – 14.14 mm).

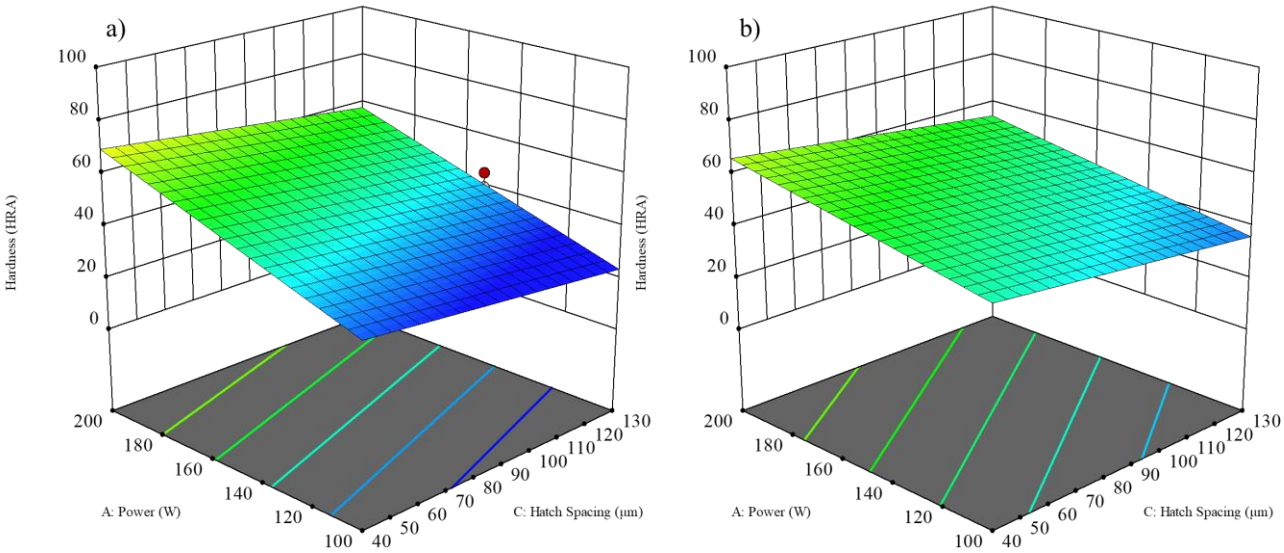

Figure 7.17: Average hardness response surface plots for a) power vs hatch spacing for raster strategy, b) power vs hatch spacing for diagonal alternating strategy

The one factor plots for laser power, scanning strategy, scan speed, and hatch spacing and their effects on the average hardness can be observed in Figure B.8 in Appendix B. Most of the parameter sets indicate that a higher energy density will result in a relatively high hardness (<50 HRA). The hatch spacing appeared to have minimal effect on the average hardness of the samples within the range that was tested. On average, the diagonal scanning strategy had a higher hardness for the various laser powers. However, the scan speed appears to have the largest effect on the hardness with an inversely proportional relationship. The chemical composition results from the EDS for the cobalt content by weight of the various successful samples can be observed in Figure 7.18.

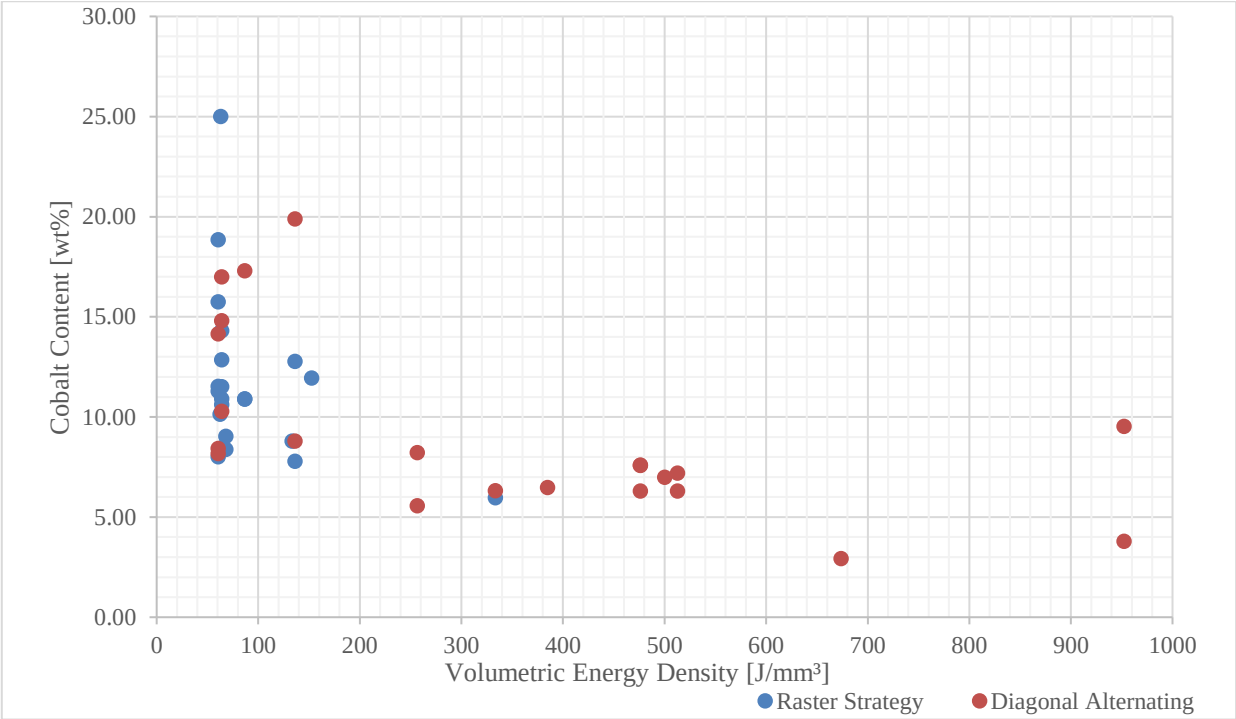

Figure 7.18: Cobalt content by weight as a function of volumetric energy density for the two different scanning strategies

A negative, decreasing quadratic trend can be observed for the cobalt content against the VED. The VED appears to have a large effect on the cobalt content. An ANOVA was performed, and the most suited model (linear) was derived for the cobalt content response. Only the model and scanning speed was found to be significant with $p < 0.02$ and $p < 0.01$ respectively. The scanning speed vs cobalt content responses are graphed in Figure B.9 in Appendix B for the two different scanning strategies. The linear responses for scan speed indicate that a higher scan speed is desired for a greater cobalt content. This supports the trend with the VED that was identified in Figure 7.18.

Table 7.8: ANOVA for Linear Model for Cobalt Content Response

Source	Sum of Squares	Mean Square	F-value	p-value	
Model	229.29	57.32	3.61	0.0135	significant
A-Power	14.79	14.79	0.9313	0.3405	
B-Scan Speed	159.27	159.27	10.03	0.0030	significant
C-Hatch Spacing	21.81	21.81	1.37	0.2484	
D-Scan Strategy	0.3809	0.3809	0.0240	0.8777	

In Figure 7.19, the power and scan speed have a fairly limited interaction. The cobalt content does not appear to vary much with respect to changes in the power.

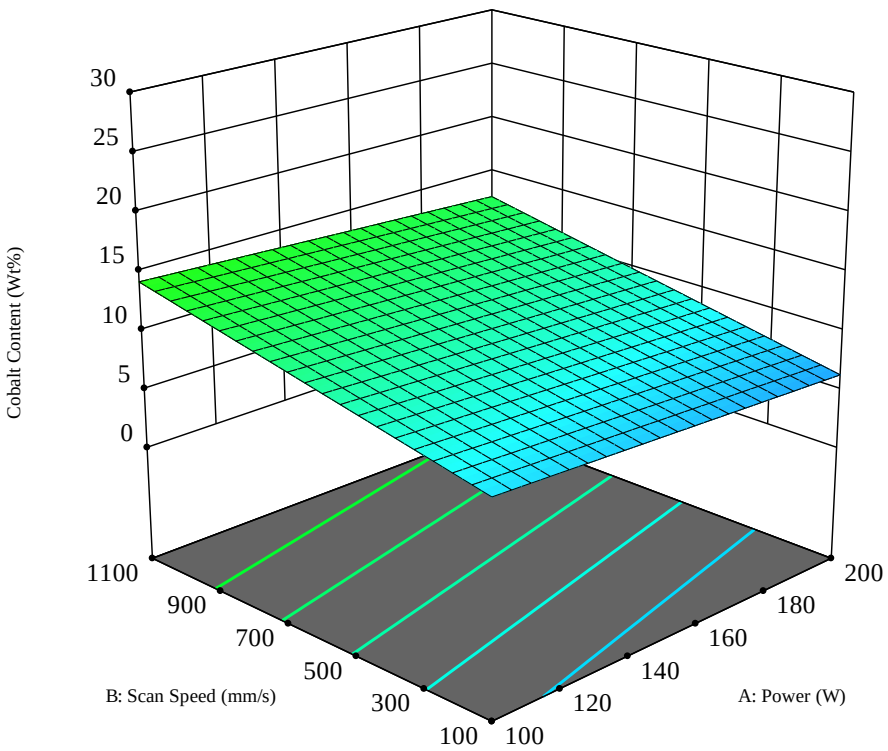

Figure 7.19: Cobalt content result response surface plots for Power vs Scan Speed for the average over the two different scanning strategies

By varying the vector length, the time between scans is altered, which means that smaller vectors could have a higher heat concentration due to the time constrained cooling rates. The smaller vectors effectively become a heat concentration point due to the close consecutive neighbouring scans. However, the opposite is true for when the vector length is increased in sections of the scans. This may cause some inconsistency of cobalt content and hardness across the part. This phenomenon may also be the cause as to why some samples using one scanning strategy (Raster) materialised while others using a different scanning strategy (Diagonal) did not. This was especially apparent for runs with a high VED, where different limits were applicable for the different strategies. The cobalt content results were also compared to the density and hardness of the samples and graphed in Figure 7.20.

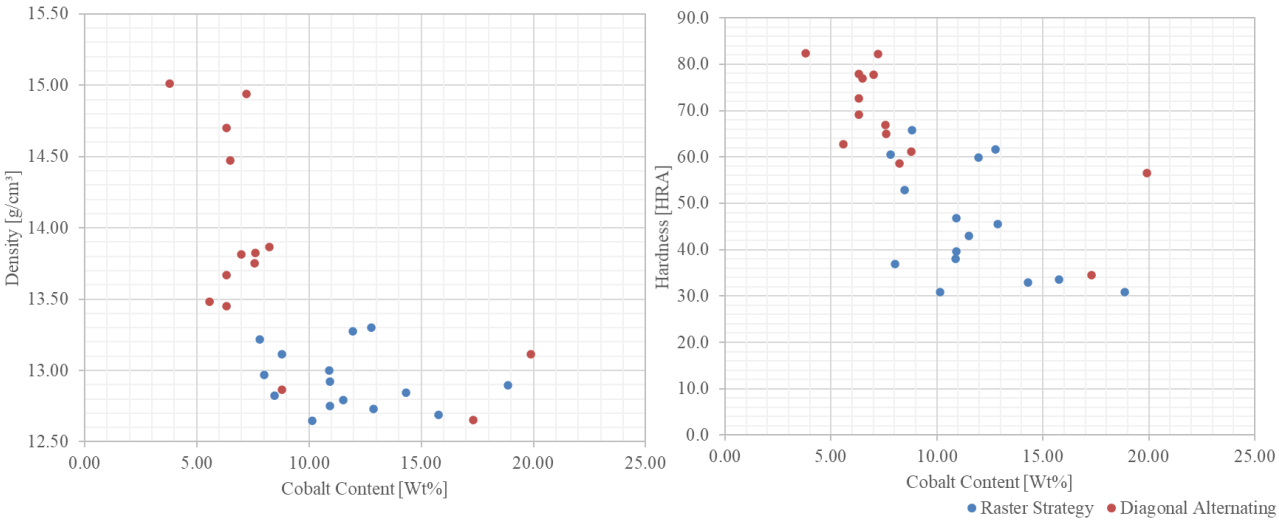

Figure 7.20: (Left) Density vs cobalt content and (Right) Hardness vs cobalt content for the different scanning strategies

The density and cobalt content are inversely proportional to each other and as expected, the hardness and cobalt content are also inversely proportional to each other. Both graphs have a negative decreasing quadratic relationship. The density vs cobalt content graph is cause for concern as it indicates that to obtain a high density and pore free component, the laser energy has to be high enough to evaporate the cobalt and perhaps even melt the WC structure. The phase change from melting WC can be derived from the X-ray diffraction results.

X-ray diffraction was very important to determine if the brittle W_2C phase was introduced into the samples through the L-PBF process. There were two distinct carbide phases present in the samples, namely the equilibrium WC phase and the di-tungsten carbide W_2C phase. Other η-phases were also present in the crystal structure. The starting Praxair powder had no measured W_2C present and thus this could only be introduced through the L-PBF process. The XRD results for the original powder and run 20 (with the density of 15.01 g/cm³) are graphed in Figure 7.21. The other XRD comparisons can be observed in Appendix B in Section B.5. A phase change for all of the various samples analysed, was recorded regardless of the scanning strategy or laser parameters applied.

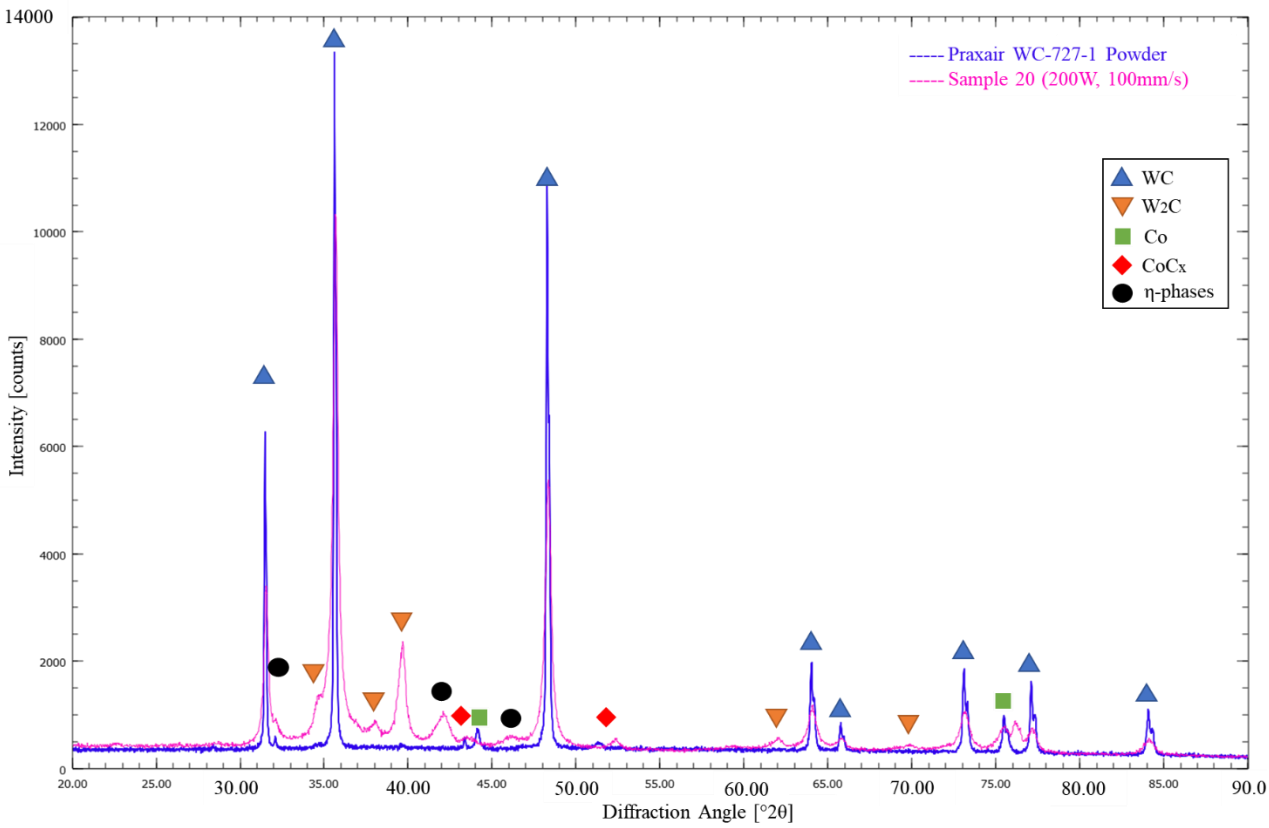

Figure 7.21: XRD of Praxair powder and sample 20 produced using the diagonal alternating strategy with 200 W, 100 mm/s and 70 µm

It was concluded by Pötschke et al. [305] that the gettering of oxygen by the inhibitors such as titanium, vanadium, and niobium, prevents the decarburisation of WC and the formation of pure tungsten. Since the inhibitors are added as carbides they may act as a source of carbon. Thus, with the carbide grade received from Praxair, there are no grain growth inhibitors added, which could also explain the W_2C phases present in the samples after the L-PBF process. Considering that the oxygen content in the process chamber was relatively high at ~1000 ppm, the oxygen could have bonded to the carbon in the metal matrix while the laser energy was exposed to the material. In the UTi20T grade powder and inserts, niobium and titanium carbide were added and thus the presence of the W_2C phase in the powder was not present in the final insert. Thus, further substantiating this notion. The reaction of the oxygen with the WC is generally dependent on the flow rate of gas (containing O_2) over the melt as well as the temperature of the melt with respect to time.

The scanning strategy differences appear to influence the density, hardness, cobalt content, and VED that can be achieved. The fundamental differences of the two strategies are:

- The raster scan strategy has consistent vector lengths and direction over the entire build
- The diagonal alternating scan strategy has varying vector lengths in each layer and the vector directions rotate in an alternating fashion by 90 degrees after each layer.

Noting these differences in the scanning strategies, for the purpose of consistency and control, the raster scan strategy would be ideal since it comprises of consistent vector length over the entire build for the given sample geometry.

For the optimisation runs, the high VED experimental range (232 < VED < 763 J/mm³) was processed using the Diagonal Alternating strategy, and all of the samples and replicates failed from layers 10 – 30. The failed samples can be observed in Figure B.6 in Appendix B.5. This indicated that the high VED parameters from the cuboid experiments were instable, and the parameters were not scalable for different geometries and sizes, given the part geometry, base plate material, and powder used. After the failure of the high VED experiments to try and validate the response surfaces, the low VED experiment (94 < VED < 274 J/mm³) was conducted. All 20 CNMA inserts were realised with no visible surface or integrity issues. The images of these samples can be observed in Figure B.7 in Appendix B. There was no indication of delamination on the samples or curling from the build plate. The fact that all the parameters printed with no issues, indicates a higher process stability at this parameter range for the specific insert geometry. The experimental parameters and the results are tabulated in Table 7.9.

Table 7.9: Summary of results for the 20 run, optimised range, single scan parameter

Input Laser Variables				80-Degree Alternating Raster Strategy		
Power [W]	**Scan Speed [mm/s]**	**Hatch spacing [µm]**	**VED [J/mm³]**	**Density (g/cm³)**	**Hardness Average [HRA]**	**Cobalt Content [wt%]**
191	695	69	133	12.40	44.6±7.1	11.67
200	450	82	180	13.42		9.96
191	569	90	124	12.62	47.0±3.7	11.41
191	695	69	133	12.49		11.29
189	591	51	210	13.05	53.7±6.1	10.94
197	485	55	246	13.47	56.4±3.1	10.04
200	700	90	106	11.92	46.8±5.5	12.69
200	655	50	204	13.02	55.9±5.4	9.73
197	485	55	246	13.54	58.6±6.9	9.1
180	568	69	154	12.91	63.9±1.3	10.72
180	568	69	154	13.00	47.8±0.7	10.36
189	460	73	187	13.36	52.9±5.8	10.31
181	575	89	118	12.24	43.0±5.7	11.37
180	450	90	148	13.05	51.8±5.1	11.09
184	450	50	273	13.70	47.3±5.7	10.57
180	700	50	171	12.55	55.0±5.6	11.27
199	591	73	155	12.66	45.6±3.8	12.65
180	700	90	95	11.70	45.5±4.6	15.23
191	695	69	133	12.43	43.3±5.5	10.64
191	569	90	124	12.47	49.8±8.5	8.5

A maximum achievable density was only 13.70 g/cm³ for the optimised parameter set. The corresponding hardness for this sample was 47.3 HRA. By utilising the response surfaces derived from the parameter optimisation experiments, the various laser parameters for the runs in Table 7.9 could be plotted and their responses (density, hardness, cobalt content) predicted. The predicted vs actual plots were derived for the different responses and can be observed in Figure 7.22.

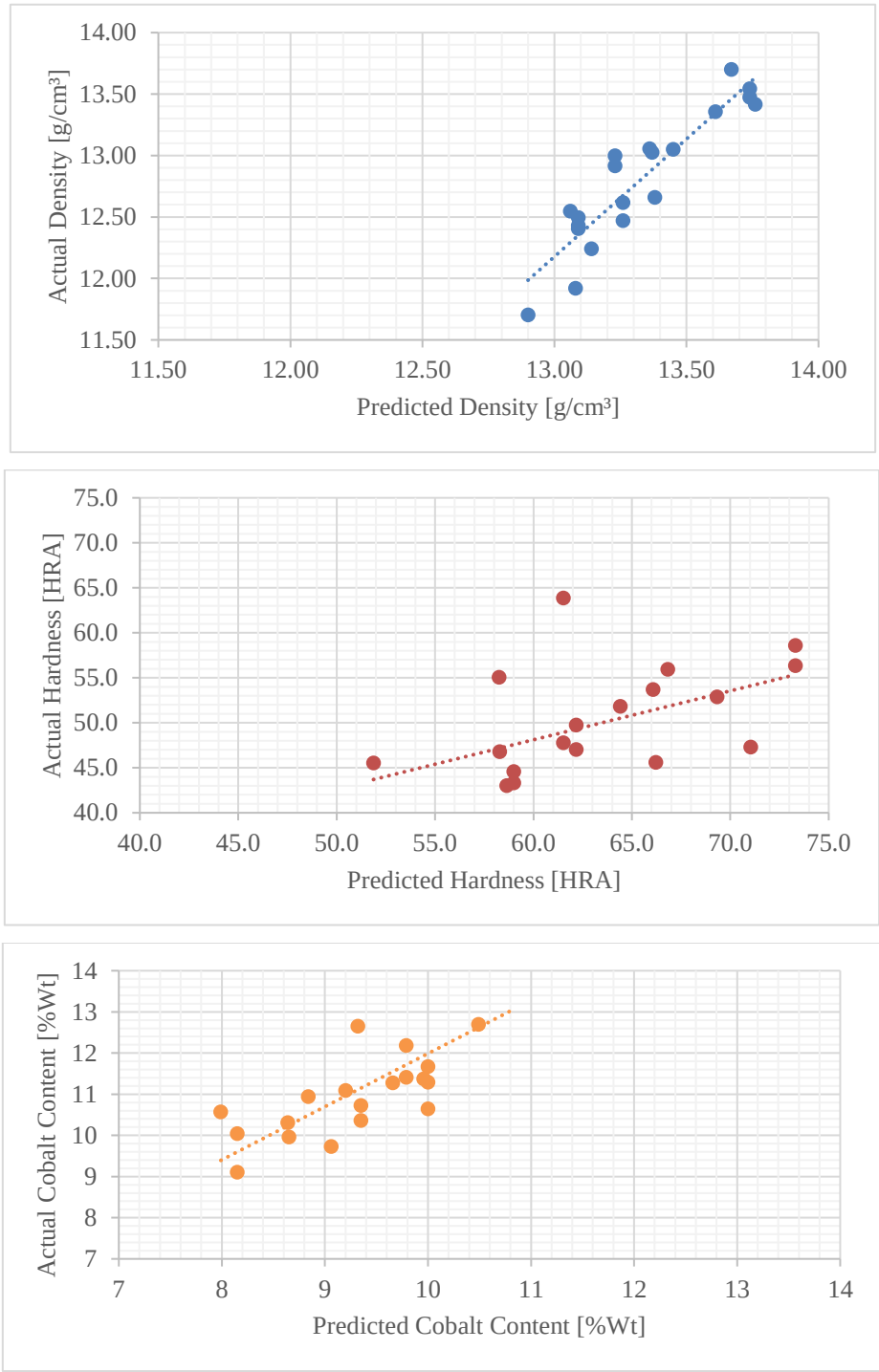

Figure 7.22: Predicted vs Actual Plots for Density, Hardness, and Cobalt Content

For the predicted vs actual density, the lower predicted densities were higher than what was achieved, however, as the predicted density increased the model accuracy also increased. For the predicted vs

actual hardness, the model predicted higher hardness values than what was realised. With the cobalt content plot, the predicted was observed to be lower than the actual measured content. The average deviation from the predicted values for density were the lowest, followed by cobalt content and then hardness. This indicated that the hardness could be the most unstable response due to inhomogeneity across the samples. This was also apparent through the high average standard deviation of 5 HRA across the measurement points of each sample.

Figure 7.23 highlights one of the limiting issues that occurs when processing WC-Co with a laser. The scan tracks can be clearly identified (moving left to right and vice versa) however, there are large areas with missing material and cracks that move perpendicular to the direction of the scan tracks. The missing material could be caused by lack of fusion, lack of wetting by the cobalt, clumping of WC particles, etc. and would require further investigation and analysis into the melting process. However, it also leads to question whether these defects/pores are caused by the post processing operations such as EDM wire-cutting and polishing and whether these defects could be eradicated through applying various heat treatment post processing operations.

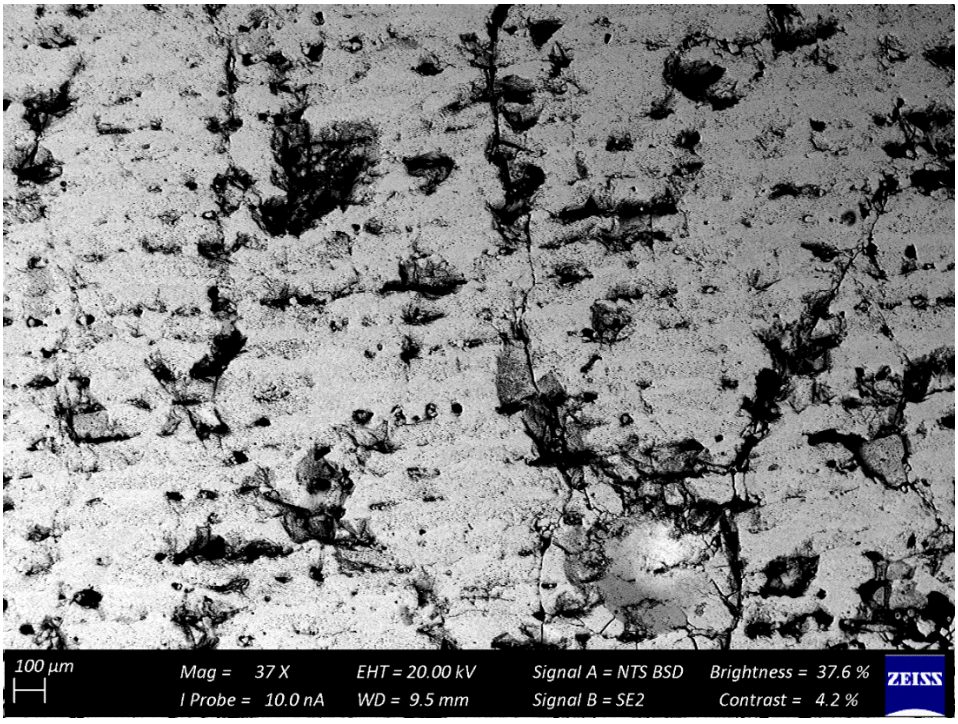

Figure 7.23: SEM image of the polished surface of a raster scanned sample 12 produced with 200 W, 500 mm/s and 100 µm

Numerous interactions were statistically verified between the investigated process parameters. In order to achieve an effective optimization of the critical quality characteristics, the intensity and direction of the respective interactions must be considered. A summary of the expanded findings can be obtained from Table 7.10.

Table 7.10: Summary of statistically analysed factors and interactions with their effects on density, hardness, and cobalt content.

Model	Factor	Effects		
		Density	Hardness	Cobalt Content
Linear	↑ A – Power	+	+	-*
	↑ B – Scan Speed	-	-	+
	↑ C – Hatch Spacing	-*	-	+*
	D Scan Strategy (Raster)	+	-	0*
2-factor interaction	↑A. ↓B	+	NA	NA
	↑A. ↓C	+	NA	NA
	A. D	NA	+	NA
Quadratic	↑A^2	+	NA	NA
	↑B^2	-	NA	NA

* - Not significant, 0 – no apparent effect, NA – Not Modelled

The results from the response summary correspond to those presented by Uhlmann et al. [50]. However, the derived response surface models are slightly different with respect to the model complexity for the various responses. Also, hardness measurements did not feature in the response surface design of Uhlmann et al. [50]. These two optimisation experiments applied to the CNMA geometry inserts, indicates a ceiling of what is achievable by just varying the laser parameters. A balance needs to be achieved through other methodology, rather than just increasing the VED.

7.2.3. Summary and conclusion

A single exposure laser optimisation experiment was designed by varying the main laser parameters (laser power, scan speed, and hatch spacing) within a specified range and constrained by the volumetric energy density. The laser scanning strategy was also varied to determine the effects of two different laser patterns and layer strategies on the final part characteristics. Significant response surfaces were derived for the density, hardness, and cobalt content responses. An optimised parameter set was chosen using the response surfaces and the criteria range for a cutting tool derived in Section 6.2. Another experimental design was performed and run on the Concept Laser M2 Cusing machine. The CNMA samples were analysed and a hard limit for the achievable density without increasing the VED through increasing the power or decreasing the scan speed was noted.

Literature was consulted, further studies were performed, and a deeper understanding of the particle physics, laser physics, and melting mechanisms was critical. This required a change in thinking and reasoning. As the study initially progressed using reasoning by analogy, whereby the former assumptions and prior knowledge obtained through the literature study, steered this work in a certain

direction. A first principles thinking approach was adopted, and thus the building blocks of a L-PBF part, were revisited (i.e., scanning strategies).

7.3. Scanning Strategies

Scanning strategies can be utilised to improve various physical and mechanical properties in a L-PBF manufactured part [306]. In the previous experiments, the scanning strategy was found to have a significant effect on the density and hardness. The scanning strategy could also be linked to whether a certain laser parameter set would realise WC-12wt%Co components successfully or not. The aim of this section was to investigate the effects of the scanning strategy on some of the quality aspects of a L-PBF produced cutting insert. This was performed through the investigation of the effects of layer rotation, hatch spacing and maximum vector length on the density, hardness, and cobalt content of CNMA inserts. This type of investigation resembles that of the one performed by Jhabvala et al. [198] whereby the effects of different scanning strategies on the temperature profiles and thermal stresses were studied. Maeda and Childs [8] suggested that when trying to improve the density of WC-Co parts during SLS, the laser power be set to maximum and the scan speed be reduced. They found that the decreasing of hatch spacing does not work, as the melt tracks cooled between laser scans. However, Jhabvala et al. [198] indicated that by using different scanning strategies the temperature gradient can be maintained in the scan tracks. Hooper [195] also found that there is a significant temperature difference in the tracks by the turns of the laser. The importance of the maximum vector length and hatch spacing for WC-Co parts is not well understood and thus far, there is a lack of publications readily available on the subject. From the single tracks on a WC-Co substrate experiment, it was noted that the 200 W, 600 mm/s tracks formed a valley and not a well-formed track. However, when these same parameters were used to produce CNMA inserts, complete parts with no delamination or curling were realised. This indicated that the interaction between tracks may be fundamentally important for improving the properties of L-PBF WC-Co parts. Hence the need for this type of investigation.

7.3.1. Experimental setup

In this experiment the layer rotation, hatch spacing, and maximum vector length were varied though applying different scanning strategies. Figure 7.24 illustrates what is meant by the maximum vector length and the hatch spacing. Theoretically, the hatch spacing, and length of the scanning vectors could have a significant effect on the thermal gradients and morphology of the tracks. As an example, for two adjacent tracks in the figure, there are different thermal gradients experienced by the material along those tracks. In the red dot section, the laser would have just melted the one track before turning around and returning to melt the next track. Thus, the cooling time for the first melted track, at that

section, is very short and the thermal gradient experienced is not that steep. However, this would be the opposite for the green and yellow sections of the tracks. As the distance and time for laser travel between points increases, the thermal gradient and subsequent thermal shock observed by the scan track is increased when the laser exposes the next track.

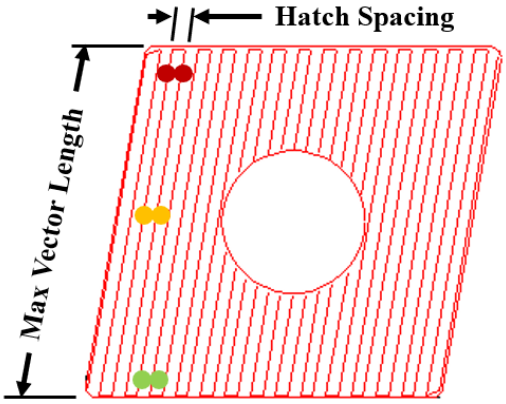

Figure 7.24: Illustration of maximum vector length and hatch spacing

The experimental equipment and powder were kept the same as the optimisation experiment in Section 7.2.1. The only difference was the scanning strategies and the laser parameters used. The laser parameters were kept constant and were carefully selected from the parameter optimisation. The criterion for selection was based on the fact that evaporation of the cobalt binder should be kept to a minimum to not reach the melting point of WC. Thus, the parameter set best corresponding to a cobalt content, close to the original powder specification measured, was chosen. The selected laser parameters were 190 W laser power, 550 mm/s scan speed, and the hatch spacing was varied at three different levels (60, 80, and 100 µm). The focal diameter and layer thickness were unchanged at ~50 µm and 30 µm respectively. The argon gas flow rate was kept constant over the build and was kept at 1000 ppm or less. The chosen insert for manufacture was the ISO insert CNMA 120404 geometry which can be observed in Appendix B under Section B.1. All file preparation, positioning, and slicing was performed with Magics software version 23.1 with the Concept Laser Slicer plugin. To alleviate the heat sink effect and contamination from the tool steel base plate, the plate exposure strategy using the parameters found in Section 6.3 was used to first expose 5-10 WC-Co layers on the plate before using the chosen build parameters. No post heat treatment was performed on any of the builds.

The selected scanning strategies can be observed in Table 7.11, Table 7.12, and Table 7.13. The strategies used can be classed into three different sets, namely, the full vector length strategies, the stripe scan strategies, and the island scan strategies. If one breaks the various strategies down into their constituents, one can note the differences are scan rotation, vector length, and hatch spacing. The first set of strategies consists of three different scanning methods that effectively are the control of the experiment i.e., the max vector length was not reduced through segmenting the part geometry.

The first being the parallel raster strategy whereby the scan tracks were kept parallel to the part edges and did not vary in length (12.7 mm) over the build. The second strategy was the diagonal raster strategy whereby the scan tracks are exposed from corner to corner of the part geometry and the vector length (max 16.33 mm) varies over the entire part geometry. The third strategy of the first set is the 67-degree continuous rotation raster strategy whereby the scan pattern rotates by 67 degrees after each layer and the vector length varies with the geometry with a max vector length of 16.33 mm.

Table 7.11: Control Scan Strategies varied to determine the effects on the part quality

Scan Strategy	Layer n	Layer n + 1	Layer n + 2
Parallel raster, 80 degree alternating rotation	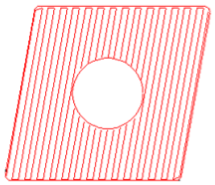	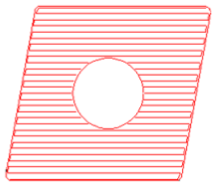	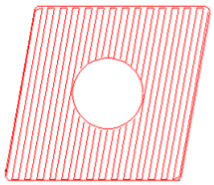
Diagonal raster, 80 degree alternating rotation	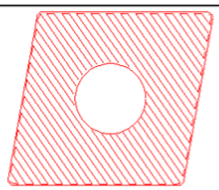	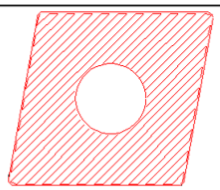	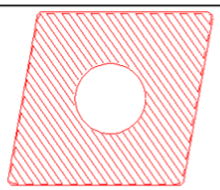
Raster strategy, 67 degree continuous rotation	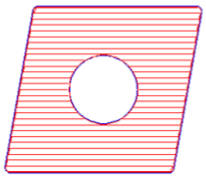	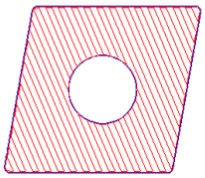	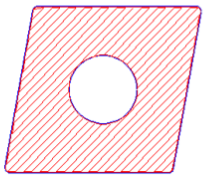

The next three strategies were derived from the EOS 67-degree stripe strategy, whereby the part layer was divided into stripes of a certain width and exposed in a raster fashion. The stripes are rotated by 67 degrees after every layer throughout the build, so as to never melt tracks in the same orientation over the length of the build. The stripe widths were varied at three different levels and were chosen by dividing the CNMA length (12.7 mm) by 2 and 6 respectively to be the + (6.4 mm) and – (2.1 mm) levels. The middle level, 0, was then calculated (4.25 mm). The stripes were not shifted in the x and y direction during the build.

Table 7.12: 67 Degree Stripe Scan Strategies adapted from the EOS Strategy

Scan Strategy	Layer n	Layer n + 1	Layer n + 2
Rectangle Stripes, raster, 2,1 mm width, 67 degree rotation, 0 mm shift	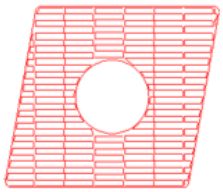	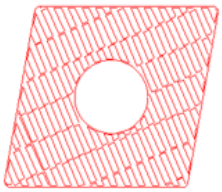	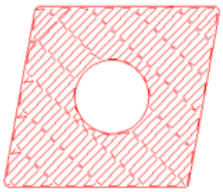
Rectangle Stripes, raster, 4,25 mm width, 67 degree rotation, 0 mm shift	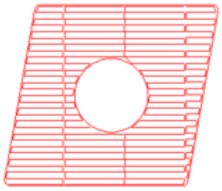	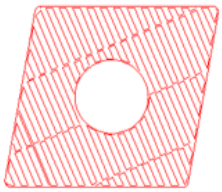	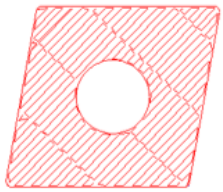
Rectangle Stripes, raster, 6,4 mm width, 67 degree rotation, 0 mm shift	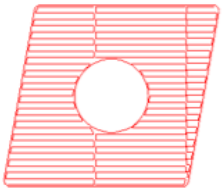	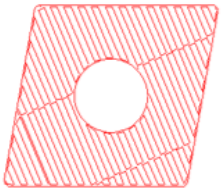	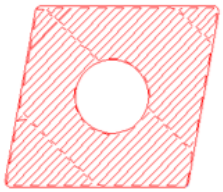

The final set of strategies were derived from Concept Laser's default patented island scanning strategy, whereby the entire geometry was divided into square islands of a certain size. In this case the island sizes corresponded to the three different sizes used in the stripe strategy. Conventionally the island strategy does not rotate between layers, however, it was decided to rotate the islands such that the vectors remain parallel to the edges of the inserts. The patented island strategy also shifts by a defined dimension in the x and y directions. Thus, this was also employed and there was an x and y shift of the islands between layers corresponding to a fifth of the island size.

Table 7.13: 80 Degree Island Scan Strategies adapted from the Concept Laser default strategy

Scan Strategy	Layer n	Layer n + 1	Layer n + 2
Parallel square islands, raster, 2,1 mm, 80 degree alternating rotation, 0,42 mm shift	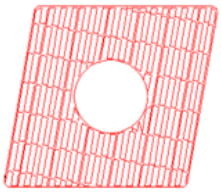	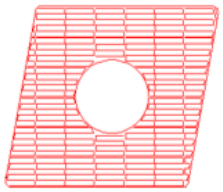	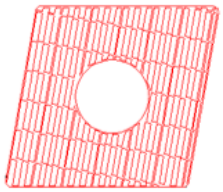
Parallel square islands, raster, 4,25 mm, 80 degree alternating rotation, 0,85 mm shift	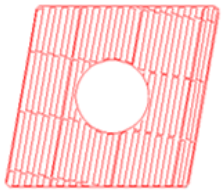	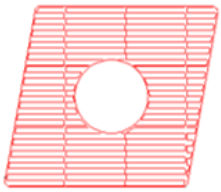	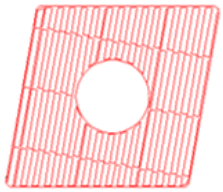
Parallel square islands, raster, 6,4 mm, 80 degree alternating rotation, 1,28 mm shift	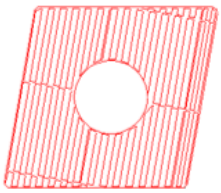	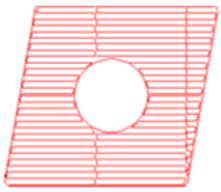	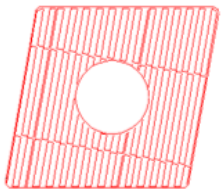

The design space was created using Design Expert version 13. The experimental runs were generated and the design space for the three sets of scanning strategies can be observed in Figure B.15 in Appendix B.6. After the samples were removed from the base plate, they were subjected to density analysis using the Archimedes method, Rockwell Hardness testing, and SEM EDS following the same methodology on the same equipment, used in the previous experiments, highlighted in Appendix A. The bottom surfaces were ground and polished according to the Struers guide for metallographic preparation of sintered carbide powder metallurgy parts [303]. The results were also analysed using Design Expert version 13 and different significant models resulted for the various responses. The effects of the scan rotation, maximum vector length and hatch spacing on the density, hardness, and cobalt content were discussed and reported in the next section.

7.3.2. Results and discussion

The 57 experimental runs were performed but were met with a number of failed components during the building process. Only 31 of the 57 runs resulted in successfully built parts. The others failed through delamination during the build at various stages and were stopped so as to not influence the other parts on the bed. The summary of the results can be observed in Table B.8 in Appendix B.6. Given that the laser parameter set used (190 W. 550 mm/s) was stable for the optimisation experiments in Section 7.2 (Table 7.9), one could speculate that the hatch spacing, vector length, and scanning strategy used may have a significant effect on whether a sample is realised successfully or not. The successful runs and failures were graphed for the two different scan rotations (80 degree

alternating and 67 degree) in Figure 7.25. One should note that some parameter sets failed, but the replicates were successful.

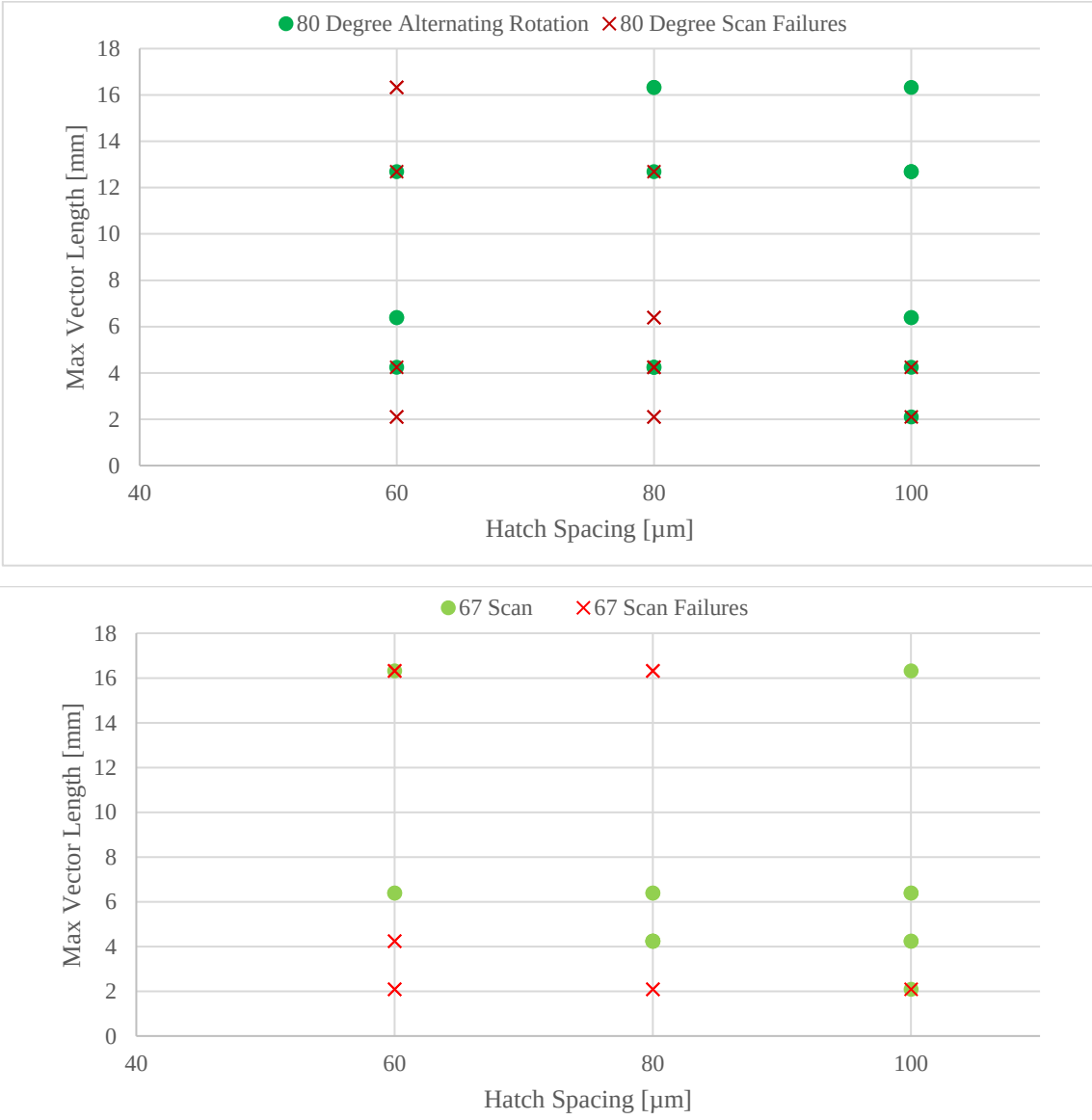

Figure 7.25: Graphs of max vector length vs hatch spacing for the (Top) 80-degree alternating rotation and (Bottom) 67-degree rotation runs indicating the success and failure parameters

A relationship between the hatch spacing and vector length and the failure susceptibility of the L-PBF parts can be observed. With all of the strategies, the runs with a higher hatch spacing (100 µm) and higher maximum vector length (≥ 6.4 mm) were less susceptible to failure during the manufacturing process. This could be expected given that with shorter and closer scan tracks, the heat input per unit area drastically increases as there is very little time between exposure of tracks. Thus, the previous track is not cooled down enough before the next one is scanned next to it with a certain overlap (Hatch spacing). So, the previous track's temperature is increased drastically, which results in evaporation of material, and an increase in the thermal gradient for the entire scanned segment. This results in a higher residual stress concentration in that area, which leads to delamination and warping of the part from the base plate. Similar findings were reported by Jhabvala et al. [198]. They

found that the overheating phenomena was not due to excessive energy deposition but by the way in which the energy was deposited in time. Jhabvala et al. [198] also found that the thermal stresses caused by the different scanning strategies can produce residual bending stresses and cracks in certain directions of the scan vectors.

The high heat input per unit area was especially apparent in the runs with lower maximum vector lengths and smaller hatch spacings. One can note the failure occurrence highlighted in Figure 7.26. The image on the left was taken just after the laser exposed the 2.1 mm, 67-degree stripe part. The red glow in the left image was caused by the part delaminating off the base plate. The section was retaining the heat for a longer period in comparison to the rest of the part due to lack of conduction through the base plate. The suspected cause of this was the high heat input per unit area per unit time for a corner of the part. Through observing the scan vectors highlighted in the centre image of Figure 7.26, one can note a small area of scan tracks in the corner of the insert. Since the part was segmented into 2.1 mm stripes and the slice area cannot be divided equally by the 2.1 mm, the remainder would be smaller than 2.1 mm. This inopportunely gives rise to the required conditions for the overheating phenomena highlighted by Jhabvala et al. [198] to take place. These phenomena occurred on the majority of the segmented parts due to the localised heating from small vector segments around the edges.

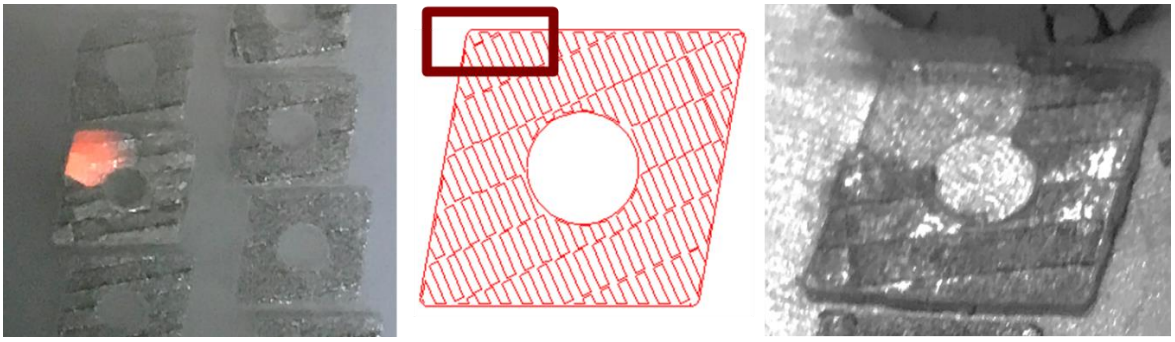

Figure 7.26: 67 Stripe part, max vector length of 2.1 *mm* and 60 *µm* hatch spacing with (Left) part slice just after being exposed by the laser, (Centre) scanning patterns for that slice, (Right) delamination from base plate

The density, hardness, and cobalt content for each of the scanning strategies used were graphed and can be observed in Figure 7.27, Figure 7.28, and Figure 7.29 respectively. From the density graph, a clear trend can be observed with density decreasing proportionally with increasing hatch spacing. However, there may be more effects due to interactions of the other factors and would require further investigation.

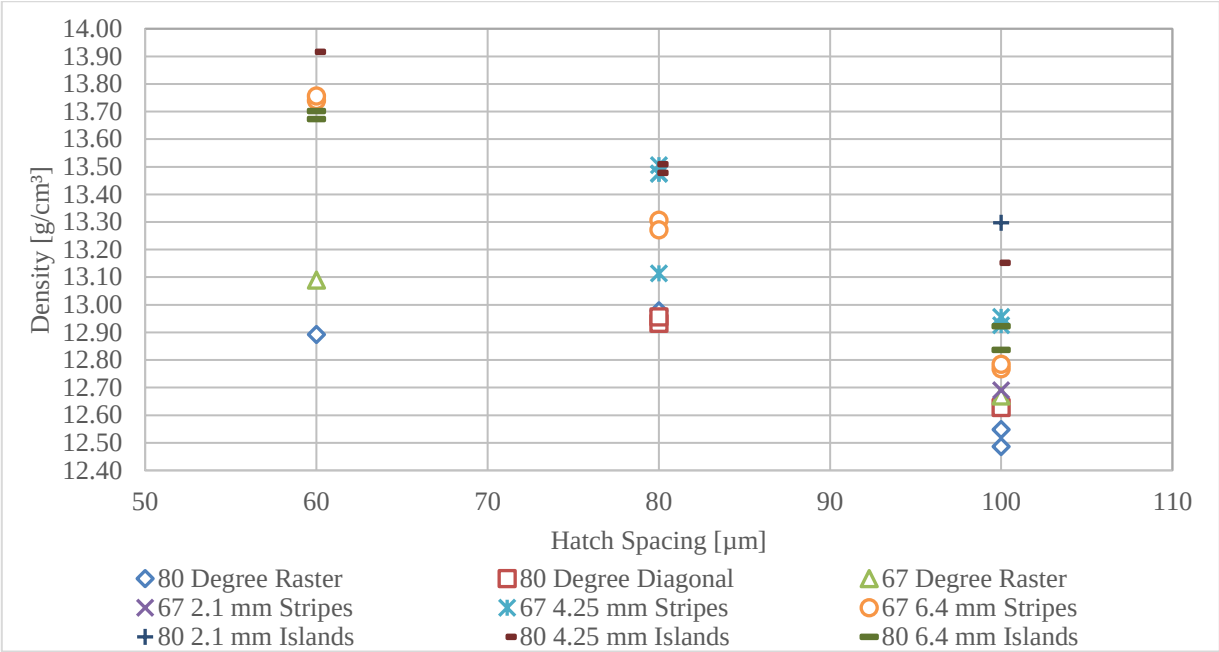

Figure 7.27: Graph of density vs hatch spacing for the different strategies and vector lengths

The hardness values in Figure 7.28 remains constant for the 60 µm and 80 µm hatch spacing for the various scanning strategies that were able to materialise parts. The overall hardness values tend to decrease for the 100 µm hatch spacing samples. This indicates that the hardness of samples has a linear decreasing relationship with the hatch spacing. However, the interactions between factors would also need to be determined to derive a suitable conclusion.

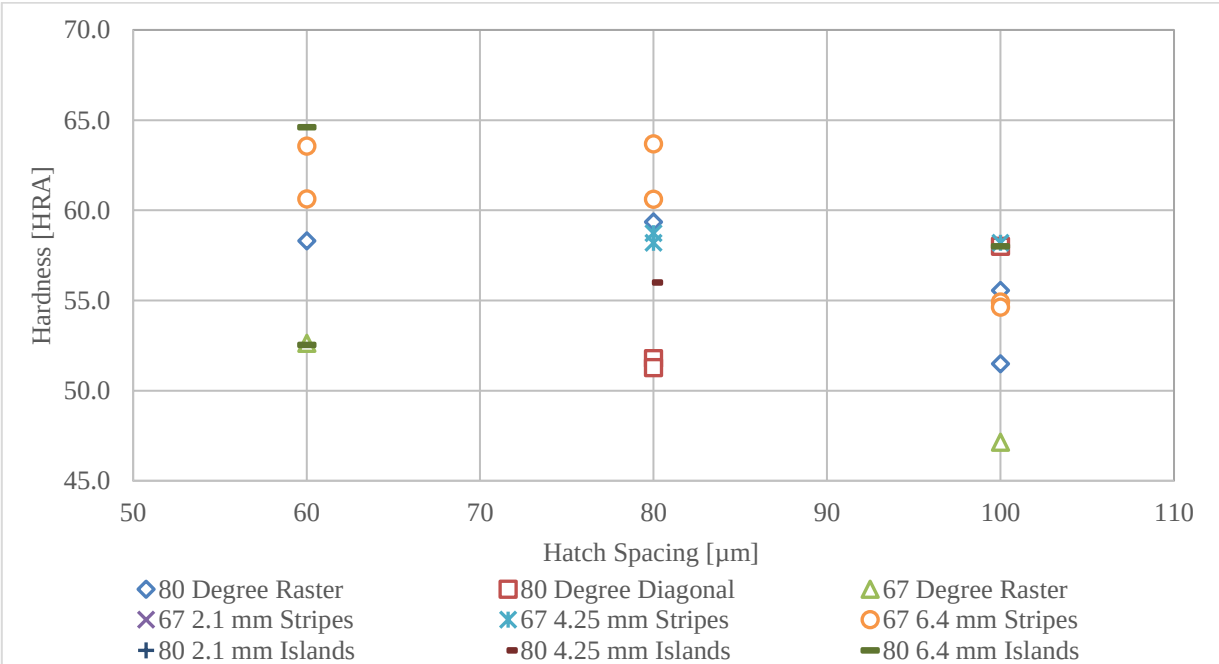

Figure 7.28: Graph of hardness vs hatch spacing for the different strategies and vector lengths

With the binder content, one could note that the cobalt content readings vary drastically depending on the hatch spacing and scanning strategy used. For the smaller hatch spacing, the range was from 5.49 % to 10.12 % with the majority of the samples being in the 9 % to 10.12% range. However,

when the hatch spacing increases, so does the distribution of the readings of the cobalt content for the various scanning strategies. For the 80-degree raster strategy there was a linear increasing trend with increasing hatch spacing, which is contradictory to the marginal linear decreasing relationship observed for the 67-degree, 6.4 mm stripe strategy. This indicates that there could be other interactions between factors that need to be noted.

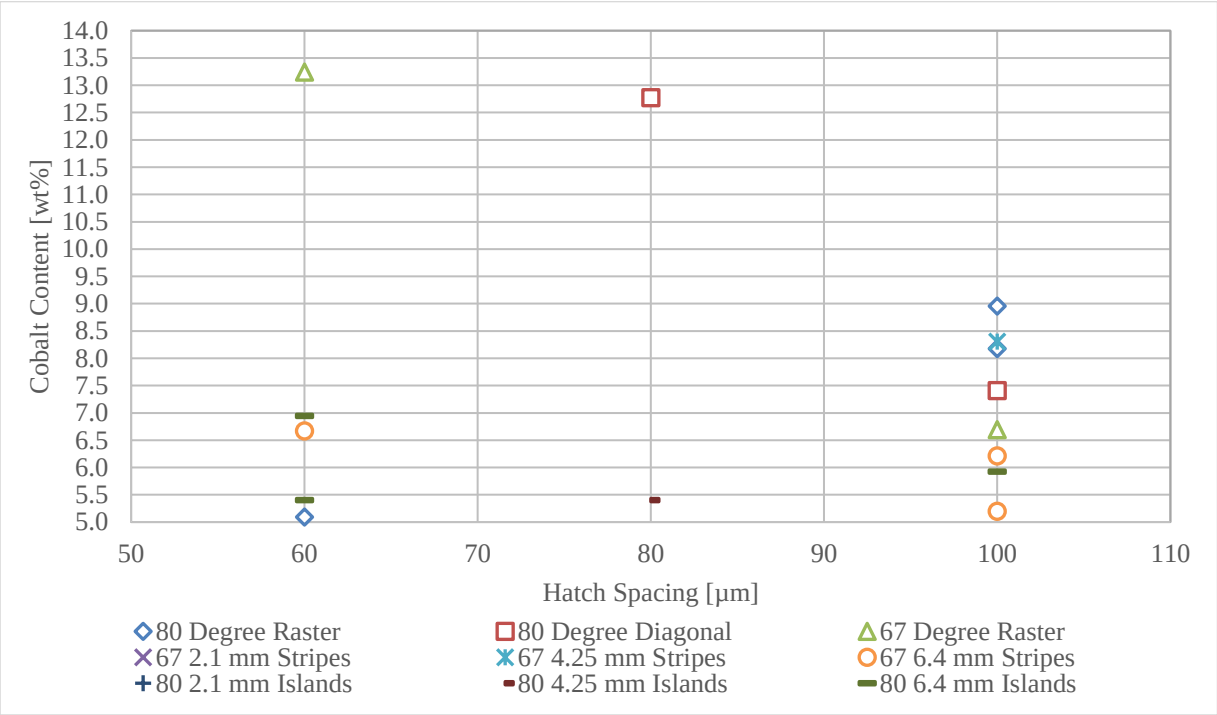

Figure 7.29: Graph of cobalt content vs hatch spacing for the different strategies and vector lengths

When viewed holistically, for the density, hardness, and cobalt content readings, the 67-degree 6.4 mm stripe strategy appeared to be the most consistent and have the best values for each response with a low failure rate. The island scanning strategy appeared to be the most inconsistent strategy with the highest failure rate. To understand the interactions between the factors and the responses, the results were processed in Design Expert software for the responses. Using RSM an ANOVA was performed to test for significance for each of the three different responses. The assumptions for the multiple ANOVA were met and confirmed with residual analyses. The statistical results from each ANOVA for the density, hardness, and cobalt content responses can be found in Table 7.14, Table 7.15, and Table 7.16 respectively. For density, a two-factor interaction model was found to be the best suited and most significant model. The hatch spacing, maximum vector length and the interaction between those two factors were highly significant with $p < 0.0006$. The interaction between the maximum vector length and the scan rotation was also found to be significant with $p < 0.02$.

Table 7.14: ANOVA for 2FI Model for Density Response

Source	Sum of Squares	Mean Square	F-value	p-value	
Model	4.44	0.4935	35.39	< 0.0001	significant
A-Hatch Spacing	2.67	1.33	95.68	< 0.0001	significant
B-Max Vector Length	1.31	1.31	94.05	< 0.0001	significant
C-Scan Rotation	0.0063	0.0063	0.4530	0.5082	
AB	0.3065	0.1532	10.99	0.0005	significant
AC	0.0727	0.0363	2.61	0.0975	
BC	0.1899	0.1899	13.62	0.0014	significant

The graphs derived through Design Expert for the density response can be observed in Figure 7.30.

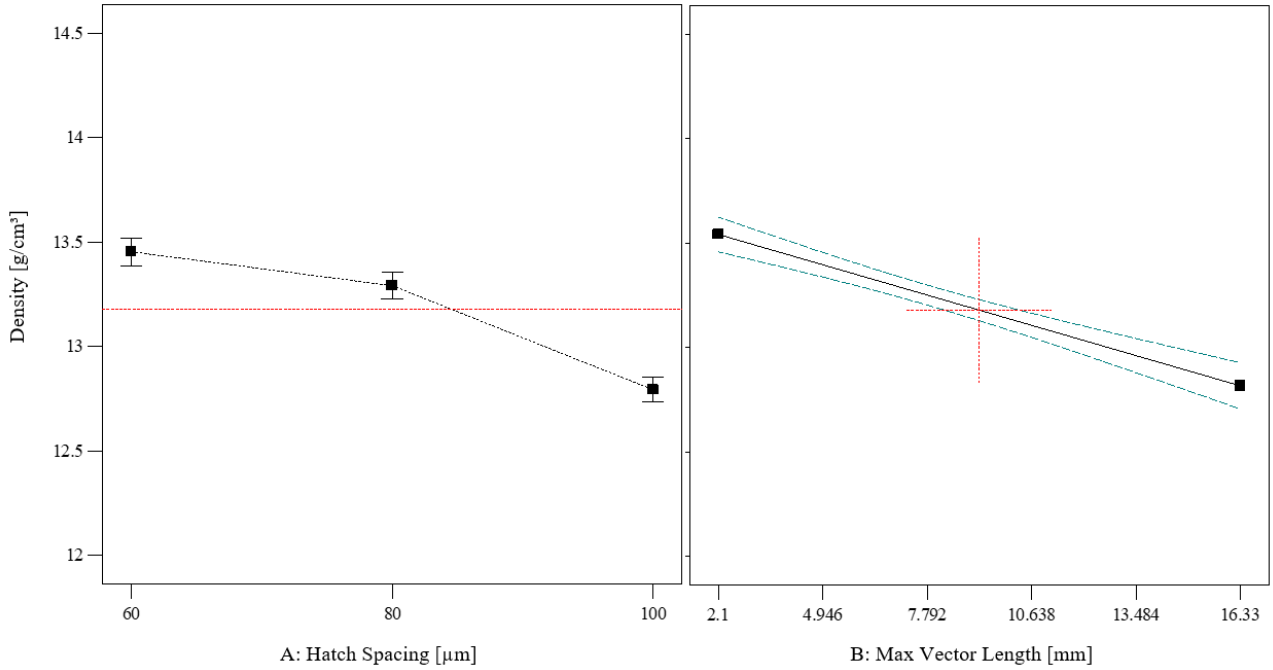

Figure 7.30: Graph of the (Left) density response vs hatch spacing and (Right) density response vs maximum vector length

The hatch spacing has a significant influence on the final part density given the interaction and influence of the maximum vector length. The density is inversely proportional to the hatch spacing and maximum vector length. However, it should still be noted that the process tends to become unstable (with a high part failure rate) when the hatch spacing, and maximum vector length are decreased. These findings are supportive of those from Simchi [194], where it was reported that an increasing delay period between successive irradiation leads to the decrease in energy stored in the track, which consequently results in the density decreasing.

For hardness, a reduced two-factor interaction model was found to be the most significant model with $p < 0.03$. The maximum vector length was the most significant factor with $p < 0.02$. The results from the ANOVA for hardness can be observed in Table 7.15.

Table 7.15: ANOVA for Reduced 2FI Model for Hardness Response

Source	Sum of Squares	Mean Square	F-value	p-value	
Model	219.07	43.81	3.37	0.0287	significant
A-Hatch Spacing	57.09	28.55	2.20	0.1436	
B-Max Vector Length	109.18	109.18	8.40	0.0105	significant
C-Scan Rotation	0.8786	0.8786	0.0676	0.7982	
BC	38.84	38.84	2.99	0.1031	

The significant interaction between the maximum vector length and the scan rotation can be observed in Figure 7.31 for the hardness response. The relationship between hardness and maximum vector length was linear decreasing with the 80-degree rotation being less susceptible to change for the various vector lengths.

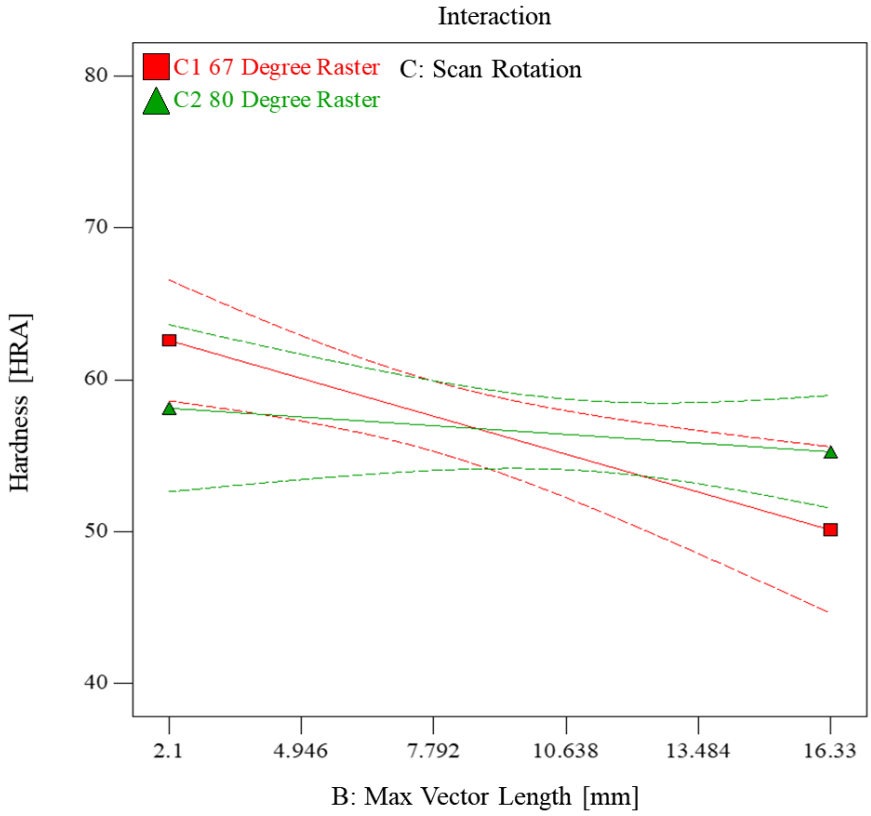

Figure 7.31: Graph of the interaction of the hardness response vs maximum vector length for the two different scan rotations

For the cobalt content, a reduced two-factor interaction model was also found to be the most significant model with $p < 0.002$. The scan rotation was the most significant factor with $p < 0.03$ and the interaction between the maximum vector length and scan rotation was more significant with $p < 0.01$.

Table 7.16: ANOVA for Reduced 2FI Model for Cobalt Content Response

Source	Sum of Squares	Mean Square	F-value	p-value	
Model	27.15	9.10	7.15	0.0011	significant
B-Max Vector Length	0.5780	0.5780	0.4541	0.5061	
C-Scan Rotation	6.88	6.88	5.41	0.0278	significant
BC	10.90	10.90	8.56	0.0069	significant

The significant interaction between the maximum vector length and the scan rotation is graphically represented in Figure 7.32 for the cobalt content. The relationship between cobalt content and maximum vector length for the 80-degree rotation is directly proportional while the relationship is inversely proportional for the 67-degree rotation.

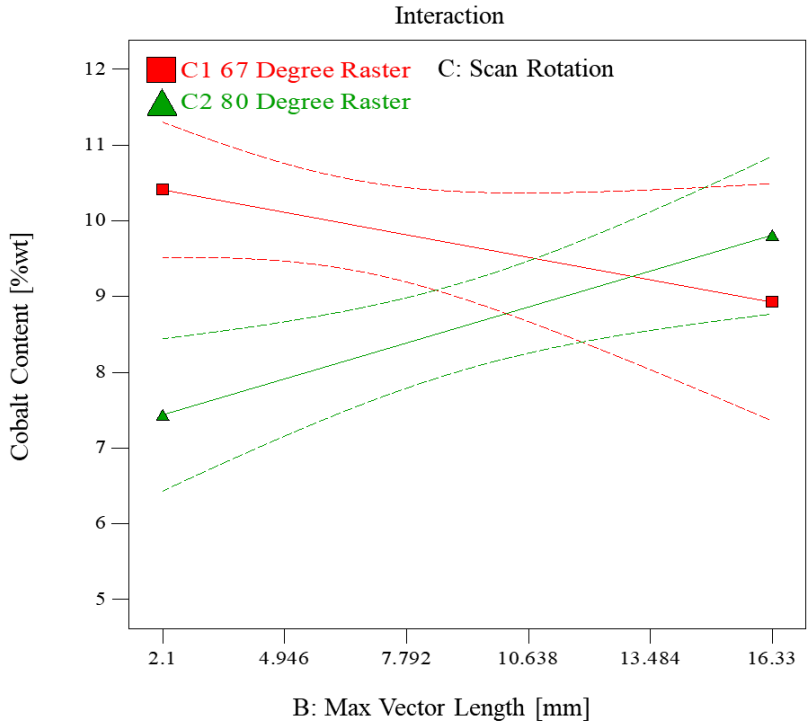

Figure 7.32: Graph of the interaction of the cobalt content response vs maximum vector length for the two different scan rotations

The cross-sectional microstructures of a single layer for two different strategies can be observed in Figure 7.33. The top image is from the 67-degree stripe strategy with a 6.4 mm maximum vector length and a 100 µm hatch spacing while the bottom image is from the 80-degree diagonal strategy with a 100 µm hatch spacing. A non-homogeneous bi-modal WC structure was apparent with extra coarse grains (> 5 µm) and medium coarse (2.1 – 3.4 µm) in both samples. Enlarged WC grains greater than 10 µm could be observed in both images. This indicates rapid grain growth, which could be due to high temperature inputs and the lack of grain growth inhibitors [66]. Both microstructures appear to have circular micro and nano pores (< 2 µm diameter) in specific areas across the scan lines. These pores indicate entrapped gas, which can be attributed to the laser parameters (keyholing) and poor layering [27]. Other irregular shaped pores between the WC grains could be due to the sintering mechanism and high grain boundary mobility [259]. There were longitudinally distinct differences in the microstructure which were most likely due to the scan direction of the laser beam. The microstructures observed closely resemble those reported by Schwanekamp and Reuber [49]. Since the Hall-Petch relation describes the hardness of tungsten cemented carbides increases with decreasing grain size [43], the relatively low hardness readings observed across all of the L-PBF samples could be attributed to the large grains (> 10 µm) present in the microstructure.

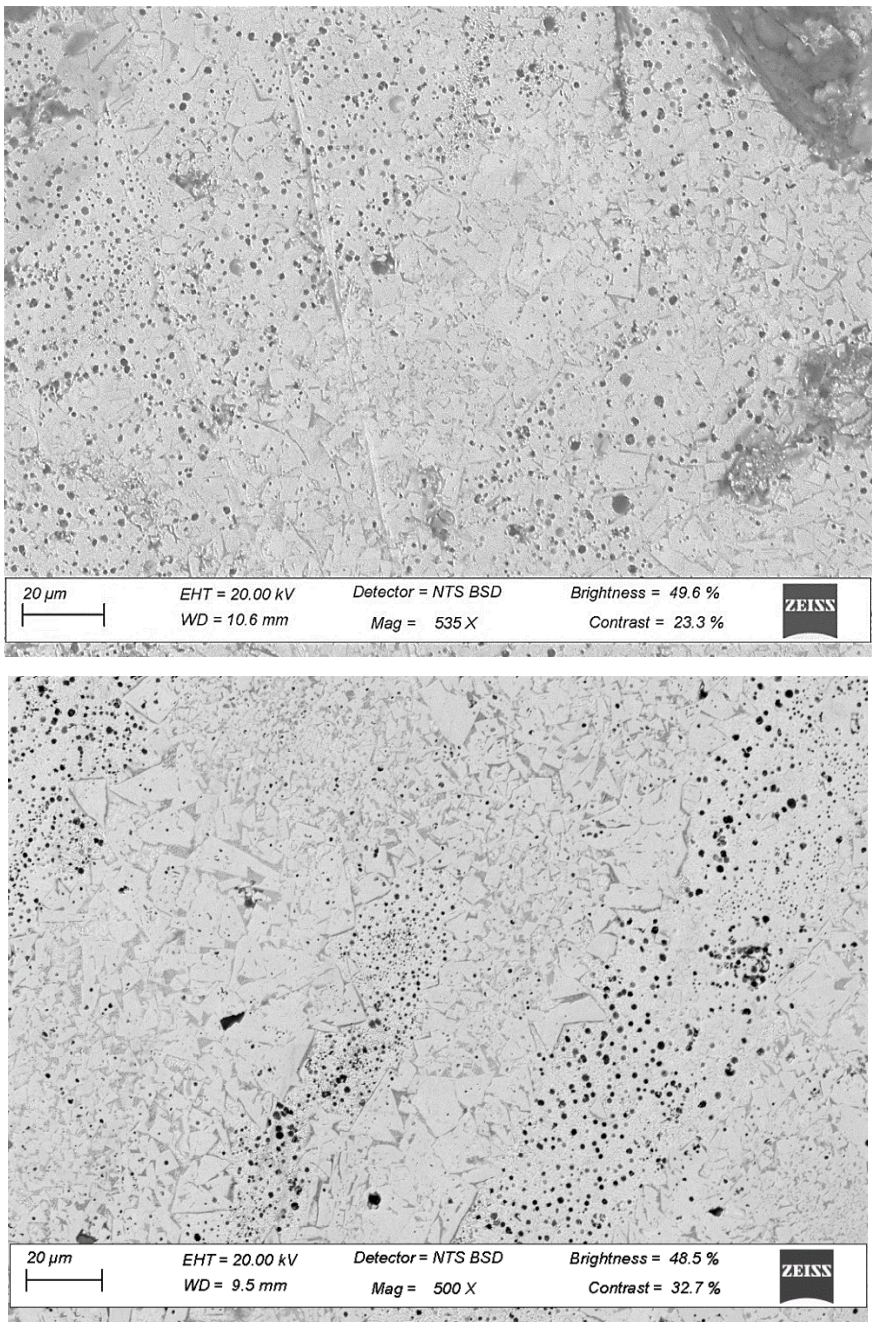

Figure 7.33: Microstructures observed under SEM for (Top) 67 Degree Stripe strategy with 100 µm hatch spacing and 6.4 mm max vector length and (Bottom) 80 Degree diagonal strategy with 100 µm hatch spacing

The effects and interactions were summarised and can be observed in Table 7.17. There were fewer interactions observed in this experiment in comparison to the laser parameter optimisation experiment. Although it should be noted that the density, and hardness were improved through varying the scanning strategies.

Table 7.17: Summary of statistically analysed factors and interactions with their effects on density, hardness, and cobalt content.

Model	Factor	Effects		
		Density	Hardness	Cobalt Content
Linear	↓ A-Hatch Spacing	+	+*	NA
	↓ B-Max Vector Length	+	+	+*
	C-Scan Rotation	0*	0*	+ (67), – (80)
2-factor interaction	↓A. ↓B	+	NA	NA
	↑A.C	-*	NA	NA
	↑B.C	-	-*	+(80), – (67)

* - Not significant, 0 – no apparent effect, NA – Not Modelled

The effects of the hatch spacing on density and hardness are in line with what was obtained in the previous experiments (Table 7.10). The most prominent effect was that of the maximum vector length on all of the measured responses. By decreasing the maximum vector length, the density, hardness, and cobalt content in the parts all improve. This is due to the low thermal conductivity of the WC-Co powder. By keeping the vector lengths relatively small, the cooling time between successive scan tracks is reduced, thus maintaining the temperature of the track, and reducing the thermal gradient experienced. This results in a more stable melt over the layer, which results in a higher density, hardness, and cobalt content. However, one should proceed cautiously when reducing the maximum vector length, as there was also a clear limit at the lower values where the melt becomes unstable again which results in delamination and failure of the parts during the L-PBF process.

7.3.3. Summary and conclusion

The effects of the hatch spacing, maximum vector length, and scan rotation were analysed for the various properties required for cutting tools. It can be noted that the properties of L-PBF produced WC-12wt%Co parts can be improved or varied though employing different scanning strategies and not by solely varying the laser power and scan speed. Since WC-Co has a relatively low thermal conductivity, the methods employed to reduce the thermal gradient experienced by the track are crucial for stable scan track and part formation. The density and hardness were found to improve by decreasing the maximum vector length of the scanning pattern. The hatch spacing was also found to have a significant effect on the density through an inversely proportional relationship. The average cobalt content was measured to be 9.25 wt% for all of the samples, suggesting that the evaporation of cobalt cannot be attributed to laser power and scan speed alone.

7.4. Chapter 7 Summary

In order to better understand the effects of some of the main parameters on specific properties during L-PBF manufacture of WC-12wt%Co components, several experiments were designed and run. Initially, single tracks on a WC-Co substrate revealed the various melt pools corresponding to specific parameters. CNMA inserts were produced but did not meet the criteria with respect to hardness for a cutting tool. Then a single exposure laser optimisation experiment was designed by varying the main laser parameters (laser power, scan speed, and hatch spacing) within a specified range, constrained by the volumetric energy density. The laser scanning strategy was also varied to determine the effects of two different laser patterns and layer strategies on the final part characteristics. A part with a high density of 15.01 g/cm^3 was realised but this result was strongly linked to a high VED and consequently a high evaporation of the cobalt binder. When applying the same strategy and parameter range to parts of a different geometry to the optimisation cuboids, all of the parts delaminated and failed during the initial layers of the L-PBF process. Thus, a different parameter set was chosen whereby the evaporation of the cobalt was limited. Several inserts were produced with L-PBF using the stable parameter set, but this indicated a limit to the highest achievable density through laser parameter optimisation alone. Thus, another study was required to determine whether the properties of L-PBF WC-12wt%Co parts could be improved through varying the scanning strategy and hatch spacing. This was performed through the investigation of the effects of layer rotation, hatch spacing and maximum vector length on the density, hardness, and cobalt content of CNMA inserts. The maximum vector length and hatch spacing had a significant effect on the density and hardness of the inserts. However, the process became unstable with the short vectors (2.1 mm) and low hatch spacing (60 µm) values, which resulted in delamination and failure of the parts during the L-PBF process.

Chapter 8

Preliminary and Verification Cutting Tests

Due to the nature of the L-PBF process being a layer wise production method (where parts are produced layer by layer using various exposure strategies), it is difficult to fully characterise a part without dissecting it a number of times using different processing methods to get a holistic view of the internal properties on various layers. The bulk part properties of the L-PBF CNMA inserts produced were analysed throughout this study but the results are fundamentally different depending on the laser parameters and scanning strategies used during the L-PBF process. Thus, it would be imprudent and premature to state that one cutting tool is better than the other based solely on the microstructure and bulk properties observed. Therefore, performing cutting tests is fundamental to determine superiority between the inserts and subsequently the laser parameters and scanning strategies used. The various cutting tests, as well as the final verification of the experimental results with respect to the end-user application are performed in this section. All cutting tests were performed using the ISO3685:1993 standard for tool-life testing with single-point turning tools as a guide.

8.1. Preliminary Cutting Tests

Given the complexity of the L-PBF process and the fact that the parts are manufactured layer by layer, certain scanning strategies and laser parameters may be beneficial or detrimental to the cutting ability. To understand the effects of the various parameters incurred during this study, inserts that were realised with at least a single intact cutting point were tested against each other in a turning operation. The aim of this section was to determine whether the scanning strategy and laser parameters used to materialise the inserts during this study, influence the cutting ability of the insert. A further aim was to observe the link between cutting time and the bulk properties of the L-PBF inserts.

8.1.1. Experimental setup

To test the effects of different parameters and scanning strategies, experimental samples from the various stages of the experimentation were analysed and chosen for use in the preliminary cutting tests. The criterion for selection was that the insert had to have at least one intact cutting edge after grinding and polishing. 18 inserts in total met this criterion for selection. Three inserts were chosen from the single-track experimentation, four from the laser parameter optimisation experimentation, and the remaining inserts were from the scanning strategy experiment.

The selected sample inserts, along with their laser parameters and properties can be observed in Table 8.3. The experiment where each insert originated from is also labelled where ST was the single-track

optimisation run from Section 7.1, OR was the optimisation run from Section 7.2. The remaining inserts were from Section 7.3.2. The 80R was the 80-degree raster strategy run with the varying hatch spacings, 80D was the 80-degree diagonal strategy with varying hatch spacings, 67R was the 67-degree rotation raster strategy with varying hatch spacing, and 67S was the 67-degree rotation stripe strategy with the 6.4 mm width and varying hatch spacing.

In order to test the cutting inserts, cutting tests were performed on a Trens SN40A (Trenčín, Slovakia) classic manual lathe. The reason the tools are tested in this manner and not on a specific wear testing machine is because with this method the tool is subjected to the various wear types it would incur in a normal machining process [86]. However, the conditions and environment in this case were more controlled. A 130 mm diameter x 1000 mm cast iron round bar was obtained, descaled, and then cut with the L-PBF CNMA inserts. The cast iron specification BS1452 Grade 250 (ISO185 Grade 25 equivalent) is continuous cast grey iron with fine grain structure combined with fine graphite flake size and dense homogeneous structure. A centre hole was drilled for a running centre and 30 mm was used for clamping in the three-jaw chuck. The cutting length was 950 mm with a depth of cut of 0.5 mm in the radius. The feed and spindle speed were kept constant for each of the runs at 0.24 mm/rev at 355 rpm. A Mahr MarSurf PS10 surface roughness tester was used to measure the workpiece surface roughness after each pass. The surface was measured 10 mm from the start of the cut and then in intervals of 100 mm, after which the final measurement was performed 10 mm from the end of the cut. The experimental equipment used can be observed in Table 8.1.

Table 8.1: Experimental equipment used in preliminary cutting tests

Lathe	Trens SN40A Classic manual lathe
Tool Holder	Mitsubishi PCLNR2020K12
Inserts	CNMA 120404
Coolant	None / Dry Cutting
Surface Roughness Measurement	Mahr MarSurf PS10
Optic Microscope	Olympus SZX 7 stereomicroscope
	GX 51 inverted microscope
SEM Microscope	Zeiss MERLIN SEM with BSD and EDS

The experimental setup of the Trens SN40A lathe and the cutting tool holder are depicted in Figure 8.1. The cast iron billet can be observed already set up in the lathe and all of the casting skin was skimmed off through the initial clean-up of the part before experimental machining commenced.

Figure 8.1: Experimental setup of the (Left) lathe and (Right) cutting tool holder and insert

The experimental conditions of the cutting test can be found in Table 8.2. Several test inserts, both conventional and L-PBF produced, were utilised to determine the best suited cutting conditions for the inserts, material, and machine before the final cutting tests began. The contact time of each insert was recorded, as well as the length of the cut on the billet. The inserts were to be run until failure or until the end of the workpiece was reached, which ever came first. Failure was characterised by either rapid deterioration of the workpiece surface finish or complete destruction of the tool's cutting edge.

Table 8.2: Experimental conditions for preliminary cutting tests

Workpiece properties at room Temperature				
Workpiece Material	Cast Iron BS1452 Grade 250			
Chemical Composition	Carbon	Manganese	Silicon	Phosphorous
	2.90 – 3.65 %	0.40 – 0.70 %	1.80 – 2.90 %	0.30 % max
Workpiece Hardness	180 -230 Brinell Hardness (Theoretically)			
Ultimate Tensile Strength	220 – 240 MPa(Theoretically)			

Cutting Conditions for Grey Cast Iron		
Cutting Parameters	**Recommended by Mitsubishi**	**Used for Experiment**
Depth of cut (a_p)	2.5 to 6.0 mm	0.5 mm
Spindle Speed (n)	-	355 RPM
Feed (f)	0.2 to 0.6 mm/rev	0.24 mm/rev
ISO grade	K10, K20	K10 equivalent
Cutting Speed (v_c)	50 - 150 m/min	133.7 – 144.9 m/min
Edge life	20 min	To be determined

The only post processing operations that were performed on the inserts were removal from the base plate with wire EDM and polishing and grinding of the bottom face. Due to the printed inserts being manufactured in a layer wise fashion, the inserts rake and flank surface will have two underlying issues that should be rectified during the cutting process if no post grinding operations are performed.

The first is that the staircase effect from the layer wise manufacturing will be present if no post process grinding has been performed on the insert. This surface defect should disappear during the cutting

operation as the surface of the cutting tool wears down. However, after some time the cutting edge should begin to wear uniformly until failure. Thus, the surface finish on the workpiece should start off with a rough finish until the staircase effect on the insert is worn down. Then the workpiece surface finish should improve once the tool flank surface finish has improved. The workpiece surface finish will then gradually decline as the tool flank gradually wears down. Although post process grinding was performed on their tool, this phenomenon was also experienced by Schwanekamp and Reuber [49].

The second potential issue is that the partially melted or sintered particles that are solidified to the edge of the insert during the L-PBF process should also be removed with a post-processing operation. Ivekovic et al. [241] measured the thickness of the sintered powder layer as a function of energy density and found that the higher the energy density, the thicker the layer of powder built up on the edge. If post processing is not performed this layer should come off during the early stages of the cutting process, however as with the above example this may lead to a rougher surface finish on the workpiece initially.

8.1.2. Results and discussion

The summarised and tabulated results from the preliminary cutting tests can be observed in Table 8.3. The results can be evaluated against their original process parameters and bulk properties displayed in the table. One can note that many of the inserts failed very early on and did not meet the criteria per the ISO3685:1993 standard, which recommends that the tool life (i.e., contact time) should not be less than 5 minutes for normal materials or not less than 2 minutes for expensive materials. Many of the inserts did not make it past 2 minutes for the selected cutting parameters.

However, there were three inserts that showed promising results and were manufactured using the same scanning strategy. The diagonal raster, 80-degree alternating scanning strategy had the best cutting performance over all the other inserts, in terms of contact time with the workpiece before failure. Many of the inserts experienced premature failure on contact with the workpiece. While other inserts experienced catastrophic failure, through rapid deterioration of the cutting edge after a period of successful cutting, catastrophic failure did not occur on the diagonal raster inserts and the cutting was only stopped due to rapid deterioration of the workpiece surface finish.

Table 8.3: Summarised results from the preliminary cutting tests

	Input Laser Variables					Bulk Properties			Cutting Responses		
Sample Set	**Power [W]**	**Scan Speed [mm/s]**	**Hatch Spacing [µm]**	**VED [J/mm³]**	**Scanning Strategy**	**Density (g/cm³)**	**Hardness Average [HRA]**	**Cobalt Content [wt%]**	**Cutting Time [mm:ss]**	**Cutting Length [m]**	**Average roughness *Ra* [µm]**
ST	60	147	51	269	80 Degree Alternating Raster	11.81	32.9±6.1	13.96	00:00	0	NA
ST	49	145	52	219	80 Degree Alternating Raster	11.20	30.0±1.0	17.71	00:00	0	NA
ST	43	114	57	217	80 Degree Alternating Raster	11.69	35.9±3.8	15.70	00:00	0	NA
OR	197	485	55	246	80 Degree Alternating Raster	13.47	56.4±3.1	10.04	00:05	12	NA
OR	189	460	73	187	80 Degree Alternating Raster	13.36	52.9±5.8	10.31	00:26	60	NA
OR	180	450	90	148	80 Degree Alternating Raster	13.05	51.8±5.1	11.09	00:00	0	NA
OR	191	695	69	133	80 Degree Alternating Raster	12.43	43.3±5.5	10.64	00:00	0	NA
80R	190	550	100	115	80 Degree Alternating Raster	12.49	51.5±9.0	8.24	00:56	129	5.487
80R	190	550	80	144	80 Degree Alternating Raster	12.98	59.4±2.8	9.08	00:24	55	5.669
80R	190	550	60	192	80 Degree Alternating Raster	12.89	58.3±5.1	10.12	00:07	16	7.493
80D	190	550	100	115	80 Degree Diagonal Alternating	12.63	58.0±7.4	10.61	09:30	1323	5.209
80D	190	550	80	144	80 Degree Diagonal Alternating	12.93	51.8±3.2	10.68	09:06	1298	4.347
80D	190	550	80	144	80 Degree Diagonal Alternating	12.96	51.3±12.8	8.40	01:11	167	6.126
67R	190	550	100	115	67 Degree Raster Continuous	12.67	47.1±6.7	8.92	00:58	134	5.438
67R	190	550	60	192	67 Degree Raster Continuous	13.09	52.6±13.2	9.01	00:12	28	6.766
67S	190	550	100	115	67 Degree 6.4 mm Stripe	12.79	54.6±5.2	10.04	00:16	37	9.007
67S	190	550	80	144	67 Degree 6.4 mm Stripe	13.27	60.6±3.5	9.80	00:49	113	6.022
67S	190	550	60	192	67 Degree 6.4 mm Stripe	13.76	63.6±6.7	9.49	00:13	30	5.762

To visually compare the cutting time to each insert's bulk properties, the cutting time was graphed against the density, hardness, and cobalt content and can be observed in Figures 8.2, 8.3, and 8.4 respectively.

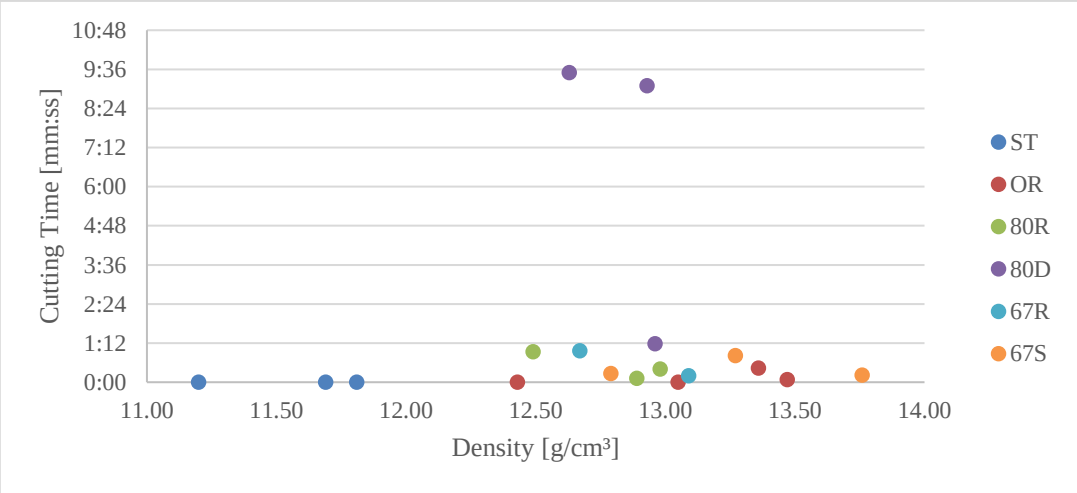

Figure 8.2: Cutting time vs density for the preliminary cutting tests for each set of inserts

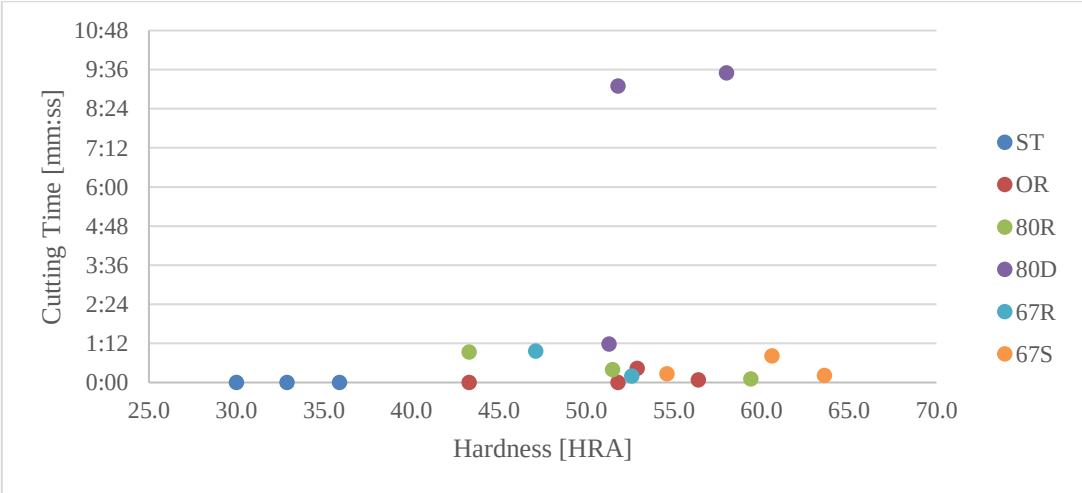

Figure 8.3: Cutting time vs hardness for the preliminary cutting tests for each set of inserts

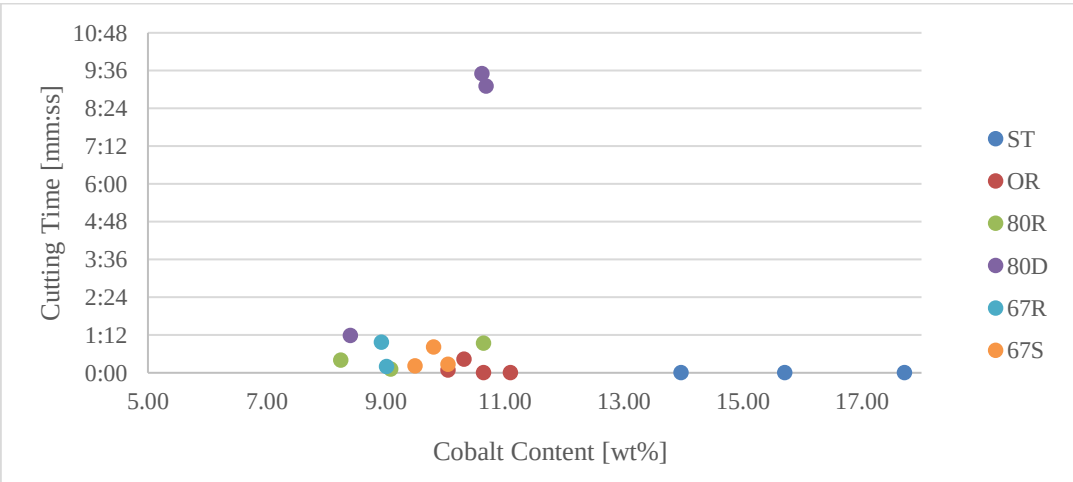

Figure 8.4: Cutting time vs cobalt content for the preliminary cutting tests for each set of inserts

From the density, hardness, and cobalt content graphs there are clearly no correlations that can be observed between the cutting time and the three different bulk properties of the respective inserts. The main conclusion that can be drawn from the data, is that the cutting time of a specific geometry insert is strongly influenced by the scanning strategy and specific parameters used to realise said insert. Two inserts after their cutting tests from two different strategies can be observed in Figure 8.5.

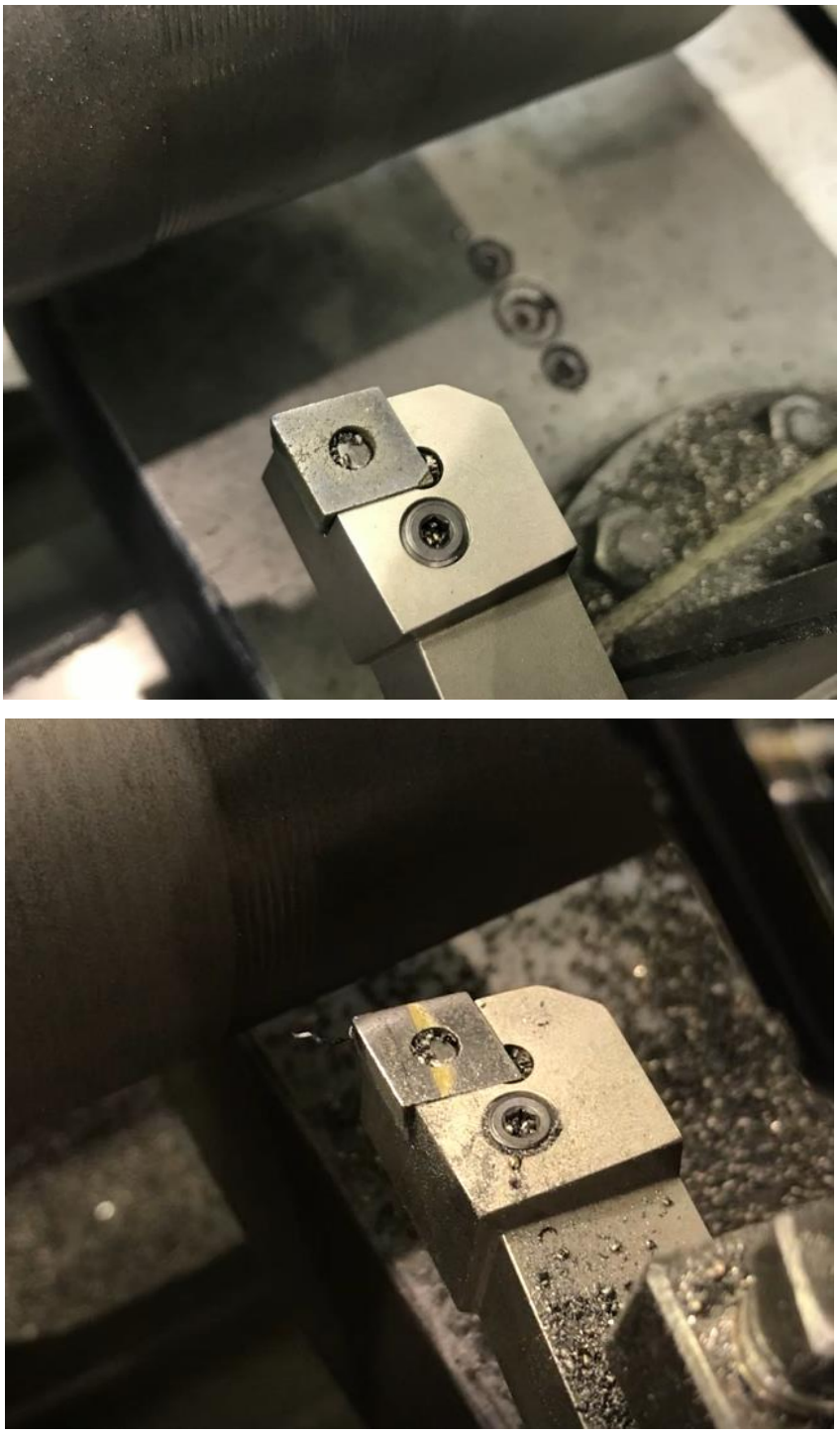

Figure 8.5: (Top) 80-degree diagonal raster CNMA insert with 100 µm hatch spacing after the longest contact time of 9M30S (Bottom) 67-degree 6.4 mm Stripe CNMA with 80 µm hatch spacing after contact time of 49S.

The two inserts in Figure 8.5 possessed similar bulk properties however, there was a clear difference in their cutting time. It is interesting to note that even though the microstructures for a single layer

look similar for the 67-degree stripe and the 80-degree diagonal strategies (as per Figure 7.33), the cutting time was substantially different. This indicates that other factors need to be considered when manufacturing cutting tools with L-PBF. Observation of single layers in a single plane is not adequate to deduce whether an insert is suitable for cutting or not, as the interaction and orientation between layers needs to be considered.

It is suspected that the main cause for the success of the 80-degree diagonal raster strategy was the fact that the scanning tracks start and end at the cutting tips. So, the first vector length is very short ~0 mm at the start of the 0.4 mm radius. Then the second one is a little bit longer and as they proceed; they get increasingly longer until they reach the maximum vector length of 16.33 mm, after which they decrease in size back to ~0 mm at the opposite cutting tip. As shown in the previous section in Table 7.17, by decreasing the maximum vector length, there is a significant improvement of the density and hardness observed. So, this improvement could be localised just to the cutting tip of the 80-degree diagonal raster inserts.

8.1.3. Summary and conclusion

Inserts selected from the previous three optimisation experiments in Chapter 7 were evaluated and utilised in preliminary cutting tests to determine their cutting ability and to deduce which factors had the greatest effects on cutting contact time. The L-PBF scanning strategy was observed to be the most significant factor for successful cutting operations. A diagonal raster strategy with an 80-degree alternating rotation produced the best cutting inserts for the specific CNMA insert geometry with respect to cutting ability.

8.2. Verification Cutting Tests

Verification is performed to evaluate whether the product complies with the requirements or specifications. The main requirement for the L-PBF inserts was to cut metal for a given time under certain cutting conditions. Hence, testing of the L-PBF produced inserts against commercially available press and sinter produced inserts initially proved to present some challenges and had to be carefully planned. The main issue was to ensure consistency of the tests while fairly comparing the different inserts on a like-for-like basis. Thus, fully understanding the L-PBF powders as well as the final chemical composition of the printed inserts was a crucial requirement. By inspecting the powders, the chemical composition and carbide particle size, indicate the grade of the final insert to fall into the ISO K-grade designation. K grade is generally used to machine cast irons and thus was the material of focus for this study. The CNMA insert geometry can be observed in Appendix B under Section B.1.

8.2.1. Experimental setup

Six CNMA inserts (two spare) were manufactured with L-PBF using the same experimental setup and machine parameters as used previously. The powder used was still the original Praxair WC-12wt%Co agglomerated and sintered powder. Two sets of three inserts were manufactured by only varying the hatch spacing for each set. The laser parameters were chosen from the results of the preliminary cutting tests and were 190 W power, 550 mm/s scan speed, as well as a hatch spacing of 100 µm (L-PBF CNMA 1 and 2) and 90 µm (L-PBF CNMA 3 and 4) for each respective set. The scan strategy chosen was the 80-degree alternating diagonal raster scan strategy. The inserts were honed and polished on the bottom face where they were separated from the base plate (with Wire EDM) such that the average surface roughness (*Ra*) was less than 1.5 µm. No stress relieving or heat treatment processes were performed on the inserts post build and prior to cutting. The six L-PBF produced inserts can be observed still on the base plate in Figure 8.6. The three in the front row are the 100 µm hatch spacing inserts and the three in the back are the 90 µm inserts. All of the inserts to be used for cutting were analysed with respect to density, cobalt content at the cutting tip, flank roughness, and face roughness. The density and cobalt content were analysed following the same procedures and equipment used in the previous experiments. The surface roughness measurements were performed using the Mahr MarSurf PS10 handheld tester using the same methodology as in the preliminary cutting tests. The testing methodology and apparatus are discussed in further detail in Appendix A.

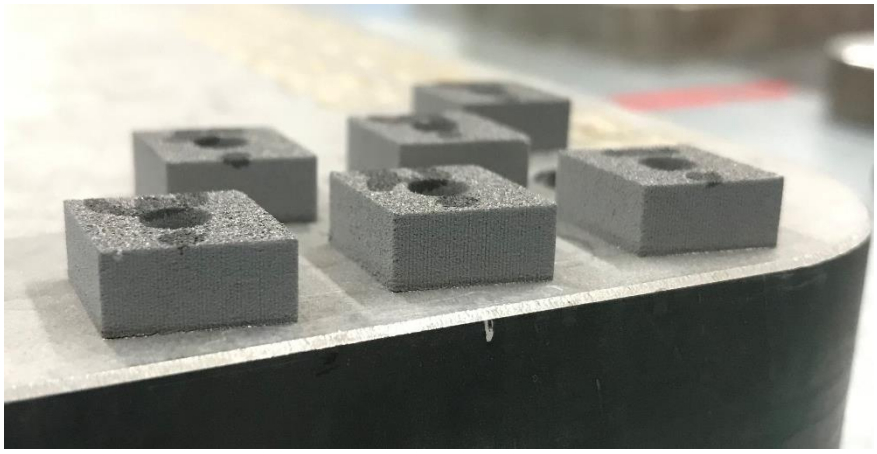

Figure 8.6: Six CNMA Inserts printed from WC-12wt%Co powder for final verification

Four of the six L-PBF cutting inserts were compared to two commercially produced Mitsubishi Materials Corporation CNMA 120404 HTi10 inserts in terms of cutting time, cutting temperature, maximum flank wear, and average workpiece surface roughness. The testing equipment used in the previous cutting tests (Section 8.1.1) were kept the same in this section with the addition of a Raytek MX4 high performance infrared thermometer for temperature measurements of the insert's cutting edge during cutting. The temperature was measured in 30 second intervals and the temperature at the

start and end of the cut were recorded. The experimental conditions of the cutting tests can be found in Table 8.4. The tool life criteria were set to failure of the cutting edge, failure to provide a good surface (Failure to cut), or finishing of the cut on the billet, which ever came first. Two cutting edges of each insert were used at two different cutting speeds. Since the machine tool used was a geared lathe and the spindle drive was not infinitely variable, the cutting tests were performed at two different spindle speeds (250 and 355 RPM). The corresponding cutting speed [m/min] was calculated and reported for each diameter at the surface of the workpiece to be cut.

Table 8.4: Experimental conditions for the verification cutting tests

Workpiece properties at room Temperature				
Workpiece Material	Cast Iron BS1452 Grade 250			
Chemical Composition	Carbon	Manganese	Silicon	Phosphorous
	2.90 – 3.65 %	0.40 – 0.70 %	1.80 – 2.90 %	0.30 % max
Workpiece Hardness	180 -230 Brinell Hardness (Theoretically)			
Ultimate Tensile Strength	220 – 240 MPa (Theoretically)			

Cutting Conditions for Grey Cast Iron		
Cutting Parameters	**Recommended by Mitsubishi**	**Used for Experiment**
Depth of cut (a_p)	2.5 to 6.0 mm	1.0 mm
Spindle Speed (n)	-	250 and 355 RPM
Feed (f)	0.2 to 0.6 mm/rev	0.2 mm/rev
ISO grade	K10, K20	K10 equivalent
Cutting Speed (v_c)	50 – 150 (100) m/min	92 - 138 m/min
Edge life	20 min	TBC

The insert cutting edges and faces were inspected using optical and scanning electron microscopy on the apparatus mentioned in Appendix A. The wear of the inserts was measured from the microscope images using ImageJ software. Images of the cutting chips for specific inserts were also taken using the stereomicroscope.

8.2.2. Results and discussion

The cutting tests were successfully conducted and each L-PBF produced insert had at least one cutting edge that was able to perform a cut. The results for the cutting tests can be observed in Table 8.5 where the insert properties, cutting parameters and cutting responses are displayed. The failure and wear mechanisms were also reported according to the definitions discussed in Section 2.5. There was a clear difference between the inserts manufactured with the different hatch spacings. The cutting times for the inserts with the 100 µm hatch spacing were significantly longer than the cutting times for the inserts with the 90 µm hatch spacing. Out of the L-PBF inserts, the L-PBF CNMA 1-1 insert had the best cut with respect to workpiece surface finish. The average surface roughness measurements of the workpiece after cutting were comparable to the conventional inserts.

Table 8.5: Verification cutting test results

	Insert Conditions and Properties				Cutting Parameters						Cutting Responses							
Insert Number	**Density [g/cm³]**	**Cobalt Content at edge [wt%]**	**Flank Roughness *Ra* [µm]**	**Face Roughness *Ra* [µm]**	**Spindle Speed [RPM]**	**Workpiece Starting Diameter [mm]**	**Workpiece Final Diameter [mm]**	**Actual Depth of Cut [mm]**	**Machined Zone [mm]**	**Cutting Speed v_c [m/min]**	**Cutting Time [mm:ss]**	**Cutting Length [m]**	**Insert Temp 1 min into Cut [°C]**	**Insert Temp End of Cut [°C]**	**Max Insert Temperature [°C]**	**End of Life Criteria**	**Flank Wear V_B Max [mm]**	**Ave. Workpiece roughness *Ra* [µm]**
L-PBF CNMA 1-1	12.26	10.57	5.971	0.152	250	125	123.4	0.8	950	98	16:30	1620	156.0	248.1	248.1	End of Workpiece	0.78	4.347
L-PBF CNMA 1-2		9.66	6.874	0.451	355	123.4	123.4	0	0	138	00:00	0				Premature Failure	NA	
L-PBF CNMA 2-1	12.39	10.14	5.977	0.635	250	123.4	121.65	0.875	950	97	16:29	1598	332.1	270.0	383.4	End of Workpiece	0.63	5.540
L-PBF CNMA 2-2		9.62	5.484	0.226	355	121.65	120.4	0.625	950	136	11:46	1596	231.0	285.6	295.3	End of Workpiece	0.74	6.530
L-PBF CNMA 3-1	12.46	9.46	5.895	1.025	250	120.4	118.9	0.75	235	95	04:07	389	203.5	149.8	209.6	Catastrophic Failure	NA	5.574
L-PBF CNMA 3-2		8.93	6.259	0.824	355	118.9	118.9	0	0	133	00:00	0				Premature Failure	NA	
L-PBF CNMA 4-1	12.50	9.98	5.132	0.354	250	118.9	118.9	0	0	93	00:00	0				Premature Failure	NA	
L-PBF CNMA 4-2		9.44	5.365	1.336	355	118.9	117.4	0.75	224	133	02:50	376	202.5	261.7	261.7	Catastrophic Failure	NA	5.063
PM CNMA 1-1	14.89	4.13	0.27	0.210	250	117.4	115.15	1.125	950	92	16:14	1497	140.6	195.3	195.3	End of Workpiece	0.38	4.318
PM CNMA 1-2		4.62	0.283	0.275	355	115.15	113.25	0.95	950	128	11:38	1494	153.5	183.2	189.0	End of Workpiece	0.37	4.410
PM CNMA 2-1	14.85	4.05	0.294	0.243	250	122	119.95	1.025	950	96	16:28	1586	160.0	204.4	204.4	End of Workpiece	0.43	5.157
PM CNMA 2-2		4.52	0.302	0.265	355	119.95	117.98	0.985	950	134	11:41	1563	153	201.5	201.5	End of Workpiece	0.33	3.911

The cutting edge and workpiece for L-PBF CNMA 1-1 and Mitsubishi PM CNMA 1-1 can be observed in Figure 8.7 after a single pass over the full 950 mm length of the workpiece. Both inserts remained intact throughout the cut and showed no visible signs of failure. The magnified flanks of the inserts are depicted further on in this section.

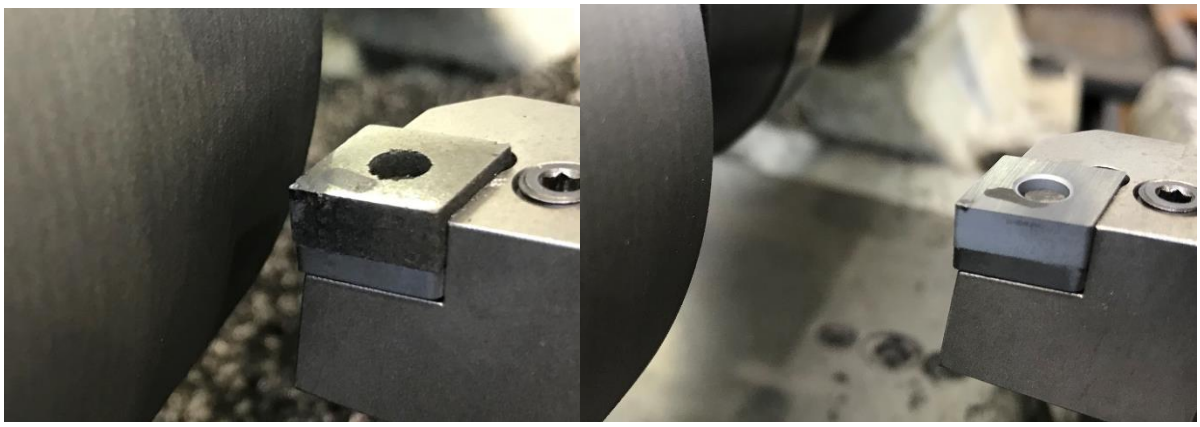

Figure 8.7: (Left) L-PBF CNMA 1 – edge 1 after completing a 16M30S cutting time at a cutting speed of 98 m/min with a depth of cut of 0.8 mm and (Right) Mitsubishi CNMA 1 – edge 1 after completing a 16M14S cutting time at a cutting speed of 92 m/min with a depth of cut of 1.125 mm

It should be observed that the actual cutting depths for the L-PBF inserts were less than the selected 1 mm depth of cut. This can be attributed to the staircase effect and the powder adhered to the flank edge of the L-PBF inserts due to the lack of post grinding operations. Nevertheless, an average difference of -0.24 mm from the 1 mm depth of cut was achieved for the L-PBF inserts during machining. The cutting time versus cutting speed for the different insert edges and inserts are depicted in Figure 8.8. The colour differences correspond to the different cutting edges while the shape differences correspond to the different inserts.

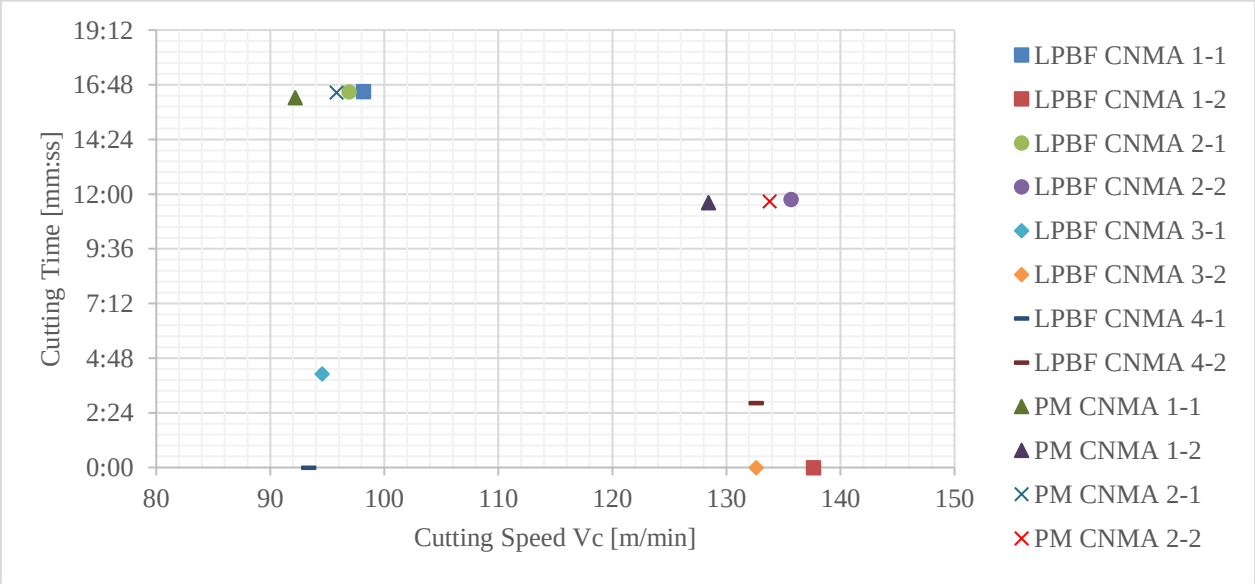

Figure 8.8: Graph of cutting time vs cutting speed for the various cutting edges

Only one of the L-PBF inserts (L-PBF CNMA 2) was able to complete both cuts on both cutting edges. Premature failure of at least one cutting edge of all the other L-PBF inserts occurred as the

inserts made contact with the workpiece material at the start of the cut. The wear could not be measured on the inserts that experienced premature failure. Common wear criteria for sintered tools according to ISO 3685:1993 is the maximum width of the flank wear land (VB_B *max*) is 0.6 mm, the average width of the flank wear land (VB_B) is 0.3 mm, and the depth of the crater (*KT*) is 0.12 mm for 0.2 mm/rev feed. The main wear mechanisms observed on the cutting edges were flank wear and crater wear. The crater wear was difficult to measure since the cast iron material had been fused to the cutting edge where the crater wear occurred. The flank wear land did not appear regularly worn for any of the inserts. The flank wear for Mitsubishi PM CNMA-2-1 and the L-PBF CNMA 1-1 can be observed in Figure 8.9. All microscopic images taken of the wear can be observed in Appendix B under Section B.7.

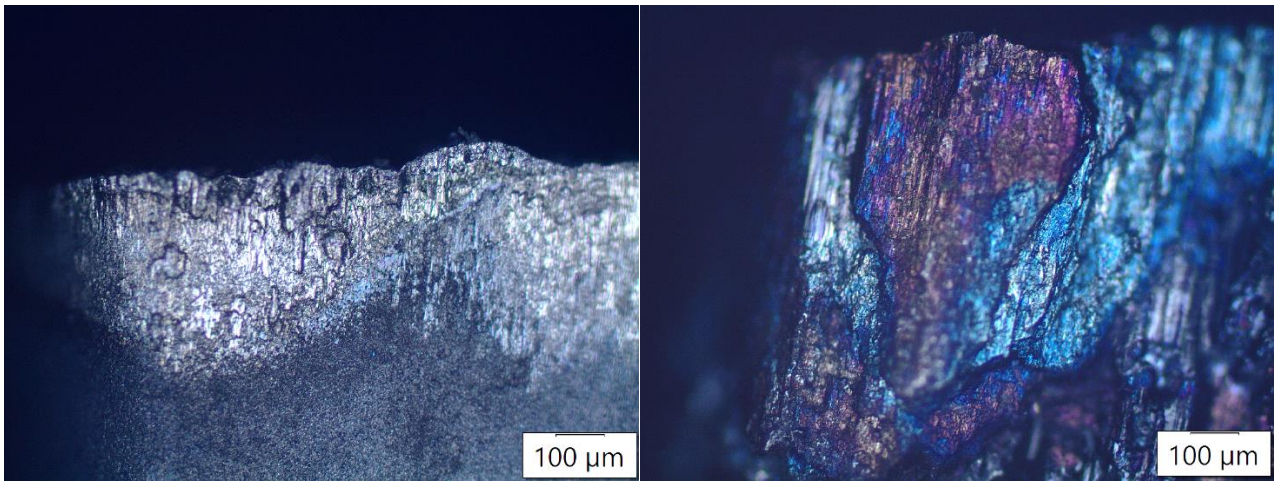

Figure 8.9: Flank wear for (Left) Mitsubishi PM CNMA 2-1 and (Right) L-PBF CNMA 1-1 observed under an optical microscope

The contact face of the L-PBF and conventional inserts were analysed before and after cutting under SEM and can be observed in Appendix B.7. The cutting face of L-PBF CNMA 1 – edge 1 can be observed in Figure 8.10. One can identify the cast iron residue on the edge of the insert through the darker discolouration on the insert tip after cutting. One should also note how the cutting edge became more defined and rounded after cutting. This was expected as the initial cut removed the staircase effect from the L-PBF process, and any residual powder adhered to the cutting surface. The corner radius of the tool after cutting was very close to the original CAD dimension of 0.4 mm.

To improve future quality of the tool and the cutting tolerances, post grinding of the faces and cutting edges should be performed before cutting to ensure the cutting tolerances and initial workpiece surface roughness are consistent. According to the ISO 3685:1993 Standard, the roughness of the face and flank of the tool should not exceed an *Ra* of 0.25 µm. The average flank and face roughness for the L-PBF inserts were 5.870 µm and 0.625 µm respectively. These values are substantially higher than the standards requirement, but due to the scope limiting post processing operations, this issue was accepted.

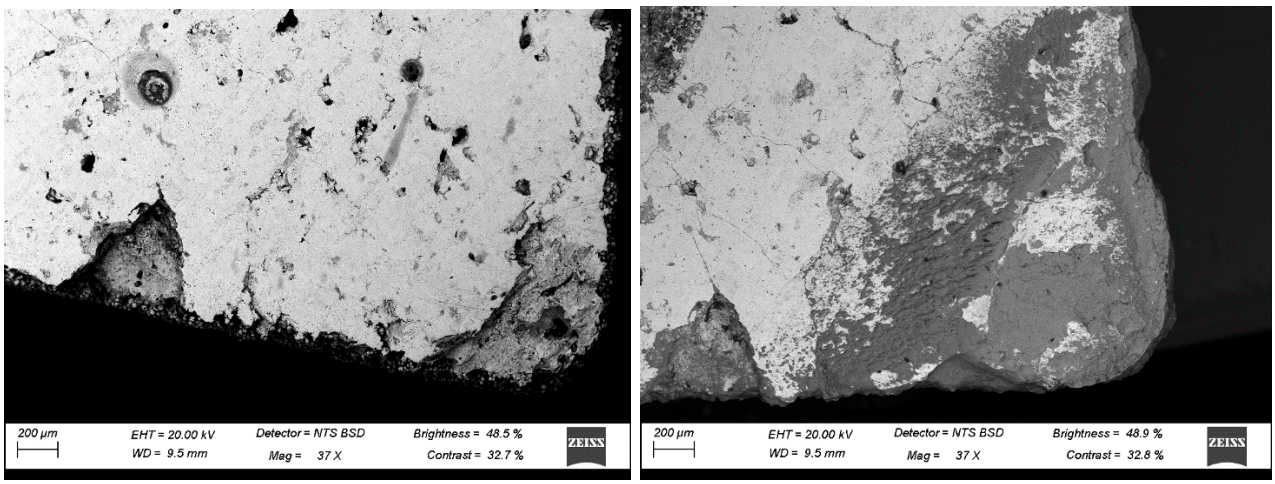

Figure 8.10: Images of the bottom polished face of the CNMA 1- edge 1 inserts with (Left) cutting edge before cut and (Right) cutting edge after the cut

Observation of the cutting chips is crucial during cutting tests to determine if the process parameters and cutting conditions are correct. For grey cast iron, the chip formation can range from powdered chips to long chips and the material often exhibits good chip control under all conditions. The cutting chip formation for the conventional insert and L-PBF insert for the same cutting conditions can be observed in Figure 8.11.

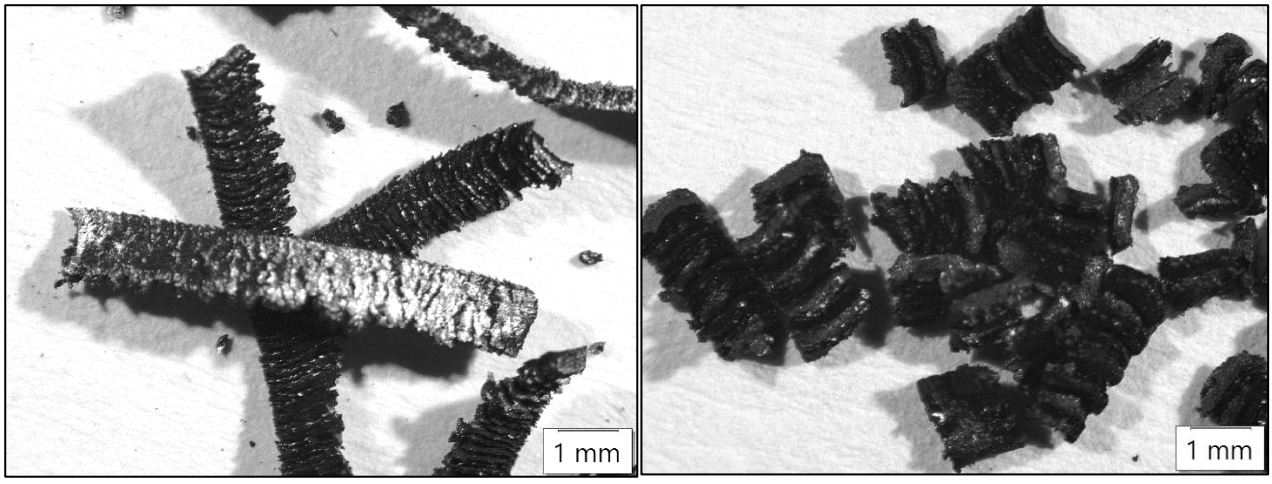

Figure 8.11: Cast iron cutting chips for (Left) PM CNMA 1-1 and (Right) L-PBF CNMA 1-1 observed under an optical microscope

The chips from the conventional Mitsubishi insert were longer than those of the L-PBF tool. This could be due to the depth of cut being slightly greater for the conventional tool since there was minimal edge loss at the start of the cut. Both chips appear discontinuous and segmented, which is expected when machining grey cast irons [307]. The surface roughness differences between the conventional inserts and the L-PBF inserts could have contributed to the results of the wear as well premature failure of the L-PBF inserts. Knowles et al. [262] mentioned that the high levels of surface roughness and micro-defects (such as pores), near the edges may pose a serious problem for crack initiation and propagation. They also mention that these issues may be overcome by various post

processing techniques. Thus, the effects of various post processing operations should be studied in future works.

8.2.3. Summary and conclusion

Four inserts produced with L-PBF were successfully tested against conventionally produced CNMA inserts. From the eight L-PBF cutting edges, five were successful in performing a cut longer than 2 minutes. Two of the L-PBF inserts were able to cut until the end of the workpiece was reached. These were the inserts produced with a 100 µm hatch spacing. Due to the limited number of samples, a high statistical significance could not be derived. However, due to the preliminary cutting tests also using the same parameters and scanning strategies while displaying similar cutting results, the relevance of the results achieved cannot be attributed to chance. The 100 µm inserts were comparable to conventionally produced tungsten carbide inserts with respect to cutting performance such as contact time and workpiece surface roughness. On average, after roughly 16M30S contact time, the L-PBF cutting tools exhibited 0.7 mm maximum flank wear versus 0.4 mm for similar conventional inserts.

8.3. Chapter 8 Summary

Preliminary cutting tests were performed and various suitable inserts from the experiments in Chapter 7 were tested against each other to determine their cutting ability. There was a clear link between the cutting time and the scanning strategy used. Optimised L-PBF inserts were produced with the knowledge gained from the preliminary cutting tests and tested against conventional CNMA inserts from Mitsubishi Materials Corporation. The inserts were comparable with respect to contact time and surface roughness of the workpiece.

Chapter 9

Conclusions and Recommendations

In this chapter, the conclusion, original contributions to the research field, and scope of future work are discussed. To reduce repetition, in-depth conclusions can be found in the summary and conclusion sections that follow each experiment. The following conclusion presents the results of the study and highlights the objectives that were achieved. Then the original scientific contributions to the research field are discussed. This is then followed by the scope of future work that summarises the suggested focus areas of future research activities in the L-PBF of WC-12wt%Co field.

9.1. Conclusion

This research investigated and revealed various influences of certain laser parameters and scanning strategies and their effects on cutting tools produced by L-PBF with WC-12wt%Co powder. The research successfully achieved the main aim and specific objectives that were set out at the beginning of this study.

In line with the first objective, a comprehensive literature study was performed at three different focus areas, namely, conventional cutting tools, AM with a focus on L-PBF, and L-PBF of tungsten carbide-based materials. The different studies aided in understanding the theoretical requirements of conventional cutting tools, the L-PBF process, and the numerous factors and phenomena involved, as well as the successes and failures experienced by other researchers with L-PBF of WC based materials. Several issues were highlighted, and the main scientific gaps were revealed. One of the most prevalent gaps was the utilisation of WC-12wt%Co L-PBF produced cutting tools in final cutting tests on steels. Another gap that was identified was a clear disconnection present between the process parameters and scanning strategies used and their effects on final part cutting ability. Certain limitations were discovered with respect to L-PBF tungsten carbide powder availability, and the adhesion of WC-Co parts to the conventional tool steel base plates.

Powder, benchmarking, and feasibility studies were then conducted so as to obtain a sound knowledge base and to manage the apparent limitations of L-PBF on WC-Co materials. With the knowledge obtained from the literature study, the benchmarked cutting tool, and the adhesion feasibility experiment, the next objective could be addressed. The second objective was addressed by conducting various process and parameter optimisation experiments. Three different approaches to optimisation were taken to derive a holistic solution to the problem: a single-track study, a cuboid laser parameter study, and a scanning strategy study. Through experimentation, the significant factors such as laser

power, scan speed, hatch spacing, and scanning strategy were statistically analysed in the applicable studies, and their corresponding interactions were revealed. The effects of these factors and their interactions on density, hardness, and binder content were obtained and graphically modelled.

From the study of single tracks on a WC-Co substrate, 15 out of 20 CNMA inserts were produced through an optimisation run. Only 1 of the 15 inserts had a density above 13 g/cm³ (13.31 g/cm³) and all of the inserts had hardness values (average < 33 HRA) that were too low when compared to conventional PM cutting tools. From the cuboid optimisation study, 20 out of 20 CNMA inserts were successfully produced. The highest achievable density was 13.70 g/cm³, with 9 of the inserts having a density above 13 g/cm³. The 20 samples had an average hardness of 50.5 HRA excluding two samples that were too brittle to measure. This was a significant improvement from the single-track optimised inserts. Though, it should be noted that there was still minor evaporation of cobalt in the cuboid optimised samples, with an average cobalt content of 10.98 wt%. From the cuboid experiments, the scanning strategy used was found to have a significant effect on density and hardness but was also linked to the process stability to successfully realise CNMA inserts. The scanning strategies thus became the next area of focus and optimisation to further improve the properties of L-PBF CNMA inserts.

In the scanning strategy experiment, 9 variations of scanning strategies were tested to determine the effects of the layer rotation, hatch spacing, and maximum vector length on the density, hardness, and cobalt content of L-PBF CNMA inserts. 31 out of 57 inserts were realised with the laser parameters that were considered to be stable in the previous studies with the common raster scanning strategy. A high density of 13.92 g/cm³ was achieved through use of a modified island scanning strategy with maximum island size of 4.25 x 4.25 mm. However, this specific sample was too brittle to undergo hardness testing. The density measurements for all 31 successful samples ranged from 12.49 to 13.92 g/cm³ (13.14 g/cm³ average) with an improved average hardness of 56.8 HRA. The highest hardness (64.6 HRA) was achieved through use of the modified island scan strategy with a maximum island size of 6.4 x 6.4 mm and 60 µm hatch spacing. The average cobalt content was measured to be 9.25 wt% suggesting that the evaporation of cobalt cannot be attributed to laser power and scan speed alone.

By utilising suitable CNMA cutting inserts from the three different optimisation studies, preliminary cutting tests were performed to link the laser and process parameters, scanning strategies, and part properties to the cutting ability of the L-PBF inserts. Only one scanning strategy stood out and was able to maintain significant contact time with the cast iron workpiece. The 80-degree alternating diagonal raster scan strategy was observed to have the best cutting performance over all of the other

inserts tested from the different optimisation studies. Knowledge gained from all these experiments allowed for improved WC-12wt%Co cutting tools to be manufactured using the L-PBF process. Four verification WC-12wt%Co inserts were produced with L-PBF, utilising the 80-degree alternating diagonal raster scan strategy, for final cutting tests. The four L-PBF inserts were tested on a manual lathe against two conventionally produced cutting tools with respect to cutting contact time, maximum flank wear, maximum cutting temperature, and average workpiece surface finish. Two of the L-PBF inserts were able to cut until the end of the workpiece was reached. These inserts experienced contact times and cutting results comparable to commercially available PM produced cutting inserts of a similar grade. On average, after roughly 16M30S contact time, the L-PBF cutting tools exhibited 0.7 mm maximum flank wear versus 0.4 mm for the similar conventional inserts. This indicated that more work on L-PBF of WC-Co cutting tools is required to obtain improved cutting and wear performance. The average surface roughness difference between the conventional inserts and the L-PBF inserts that completed the cut were 0.2 µm and 2.4 µm for the 250 and 355 RPM speeds respectively. The results derived in this study suggest that L-PBF could, one day, be a viable solution for research, developments, and small batch production of WC-Co cutting tools. The scope of future work section highlights possible areas of focus for forthcoming studies.

9.2. Original Scientific Contributions to Research

The scientific contribution of this study was unique in several ways and was demonstrated through the various experiments conducted. For the L-PBF processing of WC-Co powder to manufacture cutting tools, a number of studies [3], [29], [49] opted to use a powder with a higher cobalt content (WC-17wt%Co) for their final parameter optimisation. This was performed in aid of mitigating some of the defects observed during the L-PBF process. However, the focus of this study was to test various laser parameters and scanning strategies, to gain a better understanding of the various influencing factors and their effects on L-PBF produced WC-12wt%Co cutting tools. The influence of different parameter sets for laser power, scan speed, hatch spacing, vector length, and scanning strategy were modelled for the density, hardness, and cobalt content responses. Unlike the successful research performed by other authors [3], [29], [49] the use of a high volumetric energy density (VED) through varying laser parameters and/or multiple laser pass strategies were not the focus of this study.

From the literature review conducted, a relationship between various L-PBF tool properties, L-PBF process parameters used, and final tool cutting ability was not apparent. A lack of information with respect to the process parameters and scanning strategies used by researchers also limited the reproducibility of their results on a different machine. Thus, in this study, the L-PBF tool properties, process parameters, and scanning strategies used were directly linked to the cutting ability of the WC-

12wt%Co tools. The scanning strategy used was observed to have a significant effect on the cutting ability of the L-PBF tool.

Several materials have been cut over the years (2016 - 2021) with WC-17wt%Co L-PBF produced cutting tools. These materials include AlCuMgPb, 42CrMo4 steel, brass alloy $CuZn_{39}Pb_3$, $TiAl_6V_4$, and Inconel 718. However, the researchers [3], [49] mentioned high wear rates for cutting of steels. Thus, the novelty in this study was that L-PBF inserts were manufactured from WC-12wt%Co powder and tested against conventional inserts for cutting of grey cast iron. The cutting tests were successful for inserts manufactured with the same scanning strategy for the preliminary and verification cutting tests without any preheating or thermal post processing being applied to the L-PBF cutting tools. This was not observed in any of the other studies that reported cutting tests [3], [29], [49].

9.3. Scope for Future Work

To improve on the work from this study, a number of avenues can be explored to advance the knowledge and understanding of applying the L-PBF process to WC-12wt%Co in order to produce cutting tools. These avenues are powder types and grades, L-PBF process parameters, scanning strategies, and thermal and mechanical post processing.

Testing different powder types with additions of various grain growth inhibitors and binders could be performed to improve the microstructures and properties of the L-PBF tools for specific materials to be cut. As discussed in Chapter 2, with conventional tools, there are a number of grades available for different applications and materials to be cut. With L-PBF, there is currently a limited selection of WC-Co based powders available. To the best of the authors knowledge, not one of them is specifically developed for the L-PBF process. Most of the available WC-Co powders were developed for the thermal spraying process. Thus, factors like particle size distribution, and different binder and alloying types could improve WC-Co L-PBF parts significantly and should form part of future work.

In this study, the influence of certain laser parameters, and scan strategies fell into the main scope. However, other influencing factors could also be explored such as recoater type, inert gas type and gas flow. Future study could be done to understand the effects of the different strategies that were listed in Section 4.4. In literature, Achee et al. [269] investigated laser pre-sintering for denudation reduction in L-PBF of Ti6Al4V. Future work could replicate this study and apply it to WC-Co materials to determine if there is any improvement in the final part properties.

Given that thermal post processing operations were not performed in this study, exploration of this avenue could result in better cutting performance. Future works could study different thermal post

processing methods to understand the effects on the properties of the L-PBF cutting tools and whether or not the critical properties can be improved. Since limited mechanical post processing was performed on the inserts to limit the factors, the effects of the insert surface finish on the wear and failure could not be studied. Different mechanical post processing effects on the surface treatment of the L-PBF cutting tools should be studied further to identify if the quality and repeatability can be further improved.

References

[1] H. Wang, T. Webb, and J. W. Bitler, "Study of thermal expansion and thermal conductivity of cemented WC-Co composite," *Int. J. Refract. Met. Hard Mater.*, vol. 49, no. 1, pp. 170–177, 2015.

[2] G. S. Upadhyaya, "Materials science of cemented carbides — an overview," *Mater. Des.*, vol. 22, pp. 483–489, 2001.

[3] S. Fries *et al.*, "Laser-Based Additive Manufacturing of WC–Co with High-Temperature Powder Bed Preheating," *Steel Res. Int.*, vol. 91, no. 3, pp. 1–7, 2020.

[4] T. Schwanekamp and M. Reuber, "Parameter study on laser beam melting of WC- Co at 800 ° C pre-heating temperature," in *Proceedings of the 7th International Conference on Additive Technologies*, 2018, no. January, pp. 78–84.

[5] E. Uhlmann, A. Bergmann, and W. Gridin, "Studie zur Verarbeitung von Wolframkarbid-Kobalt für die additive Fertigung von innenkonturierten Werkzeugen," in *7. Berliner Runde Neue Konzepte für Werkzeugmaschinen*, 2012, pp. 209–227.

[6] R. Bauri and D. Yadav, "Introduction to Metal Matrix Composites," in *Metal Matrix Composites by Friction Stir Processing*, 2018, pp. 1–16.

[7] D. Ovcina, "The Effect of Punch Contraction, Springback and Compaction Tooling Design On The Cutting Edge of Positive WC-Co Compacts," University of the Witwatersrand, 2010.

[8] K. Maeda and T. H. C. Childs, "Laser sintering (SLS) of hard metal powders for abrasion resistant coatings," *J. Mater. Process. Technol.*, vol. 149, no. 1–3, pp. 609–615, 2004.

[9] C. W. Li, K. C. Chang, and A. C. Yeh, "On the microstructure and properties of an advanced cemented carbide system processed by selective laser melting," *J. Alloys Compd.*, vol. 782, pp. 440–450, 2019.

[10] V. K. Balla, S. Bose, and A. Bandyopadhyay, "Microstructure and wear properties of laser deposited WC-12%Co composites," *Mater. Sci. Eng. A*, vol. 527, no. 24–25, pp. 6677–6682, 2010.

[11] Y. Xiong, J. E. Smugeresky, L. Ajdelsztajn, and J. M. Schoenung, "Fabrication of WC – Co cermets by laser engineered net shaping," vol. 493, pp. 261–266, 2008.

[12] X. C. Wang, T. Laoui, J. Bonse, J. P. Kruth, B. Lauwers, and L. Froyen, "Direct Selective Laser Sintering of Hard Metal Powders: Experimental Study and Simulation," *Int. J. Adv. Manuf. Technol.*, vol. 19, no. 5, pp. 351–357, 2002.

[13] ASTM International, "ASTM F2792–12a Standard Terminology for Additive Manufacturing Technologies," ASTM, 2013.

[14] R. K. Enneti and K. C. Prough, "Wear properties of sintered WC-12%Co processed via Binder

Jet 3D Printing (BJ3DP)," *Int. J. Refract. Met. Hard Mater.*, vol. 78, no. October 2018, pp. 228–232, 2019.

[15] X. Ren, H. Shao, T. Lin, and H. Zheng, "3D gel-printing-An additive manufacturing method for producing complex shape parts," *Mater. Des.*, vol. 101, pp. 80–87, 2016.

[16] X. Zhang, Z. Guo, C. Chen, and W. Yang, "Additive manufacturing of WC-20Co components by 3D gel-printing," *Int. J. Refract. Met. Hard Mater.*, vol. 70, no. October 2017, pp. 215–223, 2018.

[17] W. Lengauer *et al.*, "Fabrication and properties of extrusion-based 3D-printed hardmetal and cermet components," *Int. J. Refract. Met. Hard Mater.*, vol. 82, no. February, pp. 141–149, 2019.

[18] U. Scheithauer *et al.*, "Droplet-Based Additive Manufacturing of Hard Metal Components by Thermoplastic 3D Printing (T3DP)," vol. 160, pp. 155–160, 2017.

[19] F. Breu, S. Guggenbichler, and J. Wollmann, "Three Dimensional Printing of Tungsten Carbide-Cobalt using a Cobalt Oxide Precursor," *Solid Free. Fabr. Symp.*, vol. 13, pp. 616–631, 2003.

[20] R. K. Enneti, K. C. Prough, T. A. Wolfe, A. Klein, N. Studley, and J. L. Trasorras, "Sintering of WC-12%Co processed by binder jet 3D printing (BJ3DP) technology," *Int. J. Refract. Met. Hard Mater.*, vol. 71, no. October 2017, pp. 28–35, 2018.

[21] J. A. Picas, Y. Xiong, M. Punset, L. Ajdelsztajn, A. Forn, and J. M. Schoenung, "Microstructure and wear resistance of WC-Co by three consolidation processing techniques," *Int. J. Refract. Met. Hard Mater.*, vol. 27, no. 2, pp. 344–349, 2009.

[22] I. Konyashin *et al.*, "Additive manufacturing of WC-13%Co by selective electron beam melting: Achievements and challenges," *Int. J. Refract. Met. Hard Mater.*, vol. 84, no. July, p. 105028, 2019.

[23] H. Peng, C. Liu, H. Guo, Y. Yuan, and S. Gong, "Fabrication of WCp / NiBSi metal matrix composite by electron beam melting," *Mater. Sci. Eng. A*, vol. 666, pp. 320–323, 2016.

[24] S. Kumar and A. Czekanski, "Optimization of parameters for SLS of WC-Co," *Rapid Prototyp. J.*, vol. 23, no. 6, pp. 1202–1211, 2017.

[25] E. Uhlmann, A. Bergmann, and R. Bolz, "Manufacturing of carbide tools by Selective Laser Melting," *Procedia Manuf.*, vol. 21, pp. 765–773, 2018.

[26] G. Zong *et al.*, "Direct Selective Laser Sintering of High Temperature Materials," in *International Solid Freeform Fabrication Symposium*, 1992.

[27] M. Padmakumar, "Additive Manufacturing of Tungsten Carbide Hardmetal Parts by Selective Laser Melting (SLM), Selective Laser Sintering (SLS) and Binder Jet 3D Printing (BJ3DP) Techniques," *Lasers Manuf. Mater. Process.*, vol. 7, no. 3, pp. 338–371, 2020.

[28] A. Iveković *et al.*, "Selective laser melting of tungsten and tungsten alloys," *Int. J. Refract. Met. Hard Mater.*, vol. 72, no. December 2017, pp. 27–32, 2018.

[29] A. Fortunato, G. Valli, E. Liverani, and A. Ascari, "Additive Manufacturing of WC-Co Cutting Tools for Gear Production," *Lasers Manuf. Mater. Process.*, vol. 6, no. 3, pp. 247–262, 2019.

[30] M. Reuber and T. Schwanekamp, "Additive Herstellung von Zerspan- werkzeugen aus WC-Co-Hartmetall," *Industry 4.0 Management*, vol. 32, pp. 12–16, 2016.

[31] J. P. Kruth and M. Badrossamay, "Part and Material Properties in Selective Laser Melting of Metals," in *Proceedings of the 16th International Symposium on Electromachining*, 2010.

[32] E. Yasa and J. P. Kruth, "Application of Laser Re-Melting on Selective Laser Melting Parts," *Adv. Prod. Eng. Manag.*, vol. 6, no. 4, pp. 259–270, 2011.

[33] H. Krauss and M. F. Zaeh, "Investigations on manufacturability and process reliability of selective laser melting," *Phys. Procedia*, vol. 41, pp. 815–822, 2013.

[34] E. Wycisk, A. Solbach, S. Siddique, D. Herzog, F. Walther, and C. Emmelmann, "Effects of defects in laser additive manufactured Ti-6Al-4V on fatigue properties," *Phys. Procedia*, vol. 56, pp. 371–378, 2014.

[35] X. C. Wang, T. Laoui, J. Bonse, J. P. Kruth, B. Lauwers, and L. Froyen, "Direct selective laser sintering of hard metal powders: Experimental study and simulation," *Int. J. Adv. Manuf. Technol.*, vol. 19, no. 5, pp. 351–357, 2002.

[36] T. Schwanekamp, M. Bräuer, and M. Reuber, "Geometrical and topological potentialities and restrictions in selective laser sintering of customized carbide precision tools," in *Lasers in Manufacturing Conference*, 2017, pp. 1–11.

[37] J. Tomas, T. Schubert, T. Bernthaler, M. Merkel, G. Schneider, and D. Sellmer, "Laser sintering of tungsten carbide cutter shafts with integrated cooling channels," in *International Conference on Progress in Additive Manufacturing*, 2018, pp. 297–302.

[38] J. Agyapong, "Additive Manufacturing of Novel Cemented Carbides with Self Lubricating Properties," no. December, 2019.

[39] A. Hosseini and H. A. Kishawy, "Cutting Tool Materials and Tool Wear," in *Machining of Titanium Alloys*, J. P. Davim, Ed. Berlin: Springer, 2014, pp. 31–56.

[40] B. Stoughton, *The metallurgy of iron and steel*. New York: McGraw-Hill publishing company, 1908.

[41] *Mitsubishi Tooling Technology*, 1st ed. Tokyo: Mitsubishi Material Corporation, 2005.

[42] G. S. Upadhyaya, *Cemented Tungsten Carbides: Production, Properties and Testing*. New Jersey: Noyes Publications, 1998.

[43] General Carbide, "The designer's guide to tungsten carbide," p. 59, 2015.

[44] K. Tsuda, "History of development of cemented carbides and cermet," *SEI Tech. Rev.*, no. 82,

pp. 16–20, 2016.

[45] H. Hassanin, F. Modica, M. A. El-Sayed, J. Liu, and K. Essa, "Manufacturing of Ti–6Al–4V Micro-Implantable Parts Using Hybrid Selective Laser Melting and Micro-Electrical Discharge Machining," vol. 18, no. 9, pp. 1544–1549, 2016.

[46] Sandvik, "Sandvik Annual Report 2016," Sandviken, 2016.

[47] B. Bartheidel, M. Körner, and Siemens AG, "Manufacturing Intelligence," 2015.

[48] Kennametal, "Kennametal Annual Report," 2016.

[49] T. Schwanekamp and M. Reuber, "Additive manufacturing of application optimized tungsten carbide precision tools," in *6 th International Conference on Additive Technologies*, 2016, no. January 2016, pp. 100–114.

[50] E. Uhlmann, A. Bergmann, and W. Gridin, "Investigation on Additive Manufacturing of Tungsten Carbide-cobalt by Selective Laser Melting," *Procedia CIRP*, vol. 35, pp. 8–15, 2015.

[51] M. Ott, "Multimaterialverarbeitung bei der additiven strahl- und pulverbettbasierten Fertigung," Universität München, 2012.

[52] N. N., "Generieren und Fügen von SLM-Bauteilen aus Hartmetall," 2013.

[53] L. N. L. de Lacalle, A. Lamikiz, J. F. de Larrinoa, and I. Azkona, "Chapter 2: Advanced Cutting Tools," in *Machining of Hard Materials*, J. P. Davim, Ed. New York: Springer, 2011, pp. 33–86.

[54] J. García, V. Collado Ciprés, A. Blomqvist, and B. Kaplan, "Cemented carbide microstructures: a review," *Int. J. Refract. Met. Hard Mater.*, vol. 80, no. August 2018, pp. 40–68, 2019.

[55] International Organization for Standardization, "ISO 513:2012 - Classification and application of hard cutting materials for metal removal with defined cutting edges — Designation of the main groups and groups of application Classification," 2012.

[56] Mitsubishi Materials Corporation, "Mitsubishi Materials Cemented Carbide Grades," 2020. [Online]. Available: http://www.mitsubishicarbide.com/en/technical_information/tec_turning_tools/tec_turning_insert/tec_turning_grades/tec_turning_cemented_carbide. [Accessed: 14-Apr-2020].

[57] AZoM, "Tungsten (W) - The Different Properties and Applications," 2013. [Online]. Available: https://www.azom.com/article.aspx?ArticleID=9119. [Accessed: 16-Apr-2019].

[58] AZoM, "Carbon - Graphite Materials," 2001. [Online]. Available: https://www.azom.com/properties.aspx?ArticleID=516. [Accessed: 16-Apr-2019].

[59] AZoM, "Tungsten Carbide - An Overview," 2002. [Online]. Available: https://www.azom.com/properties.aspx?ArticleID=1203. [Accessed: 16-Apr-2019].

[60] AZoM, "Cobalt (Co) – Properties, Applications," 2013. [Online]. Available:

https://www.azom.com/article.aspx?ArticleID=9077. [Accessed: 16-Apr-2019].

[61] Kennametal, "Cutting Tool Blanks: Grade Specifications and Application Chart," 2017.

[62] Dymet Alloys, "Dymet Alloys Grade Chart," 2012. [Online]. Available: https://www.dymetalloys.co.uk/tungsten-carbide-grade-chart/. [Accessed: 17-Apr-2020].

[63] Z. Z. Fang, "Correlation of transverse rupture strength of WC-Co with hardness," *Int. J. Refract. Met. Hard Mater.*, vol. 23, no. 2, pp. 119–127, 2005.

[64] Z. Z. Fang, X. Wang, T. Ryu, K. S. Hwang, and H. Y. Sohn, "Synthesis, sintering, and mechanical properties of nanocrystalline cemented tungsten carbide - A review," *Int. J. Refract. Met. Hard Mater.*, vol. 27, no. 2, pp. 288–299, 2009.

[65] L. E. Mccandllsh, B. H. Kear, and B. K. Kim, "New Method of Making WC-Co Powder Liquid phase sinter at 1425 ° C," *Nanostructured Mater.*, pp. 119–124, 1992.

[66] X. Wang, Z. Z. Fang, and H. Y. Sohn, "Grain growth during the early stage of sintering of nanosized WC-Co powder," *Int. J. Refract. Met. Hard Mater.*, vol. 26, no. 3, pp. 232–241, 2008.

[67] R. Porat, S. Berger, and A. Rosen, "Dilatometric Study of the Sintering Mechanism of Nanocrystalline Cemented Carbides," *Nanostructured Mater.*, vol. 7, no. 4, pp. 429–436, 1996.

[68] M. Groppe, "Cemented Carbides," in *CIRP Encyclopedia of Production Engineering*, L. Laperrière and G. Reinhart, Eds. Berlin, Heidelberg: Springer Berlin Heidelberg, 2014, pp. 127–135.

[69] S. I. Cha, S. H. Hong, and B. K. Kim, "Spark plasma sintering behavior of nanocrystalline WC-10Co cemented carbide powders," *Mater. Sci. Eng. A*, vol. 351, no. 1–2, pp. 31–38, 2003.

[70] A. Mahrle and E. Beyer, "Theoretical evaluation of radiation pressure magnitudes and effects in laser material processing," *Phys. Scr.*, vol. 94, no. 7, 2019.

[71] A. V. Shatov, S. A. Firstov, and I. V. Shatova, "The shape of WC crystals in cemented carbides," *Mater. Sci. Eng. A*, vol. 242, no. 1–2, pp. 7–14, 1998.

[72] L. Thijs, F. Verhaeghe, T. Craeghs, J. Van Humbeeck, and J.-P. Kruth, "A study of the microstructural evolution during selective laser melting of Ti-6Al-4V," *Acta Mater.*, vol. 58, no. 9, pp. 3303–3312, 2010.

[73] B. Vandenbroucke and J.-P. Kruth, "Selective laser melting of biocompatible metals for rapid manufacturing of medical parts," *Rapid Prototyp. J.*, vol. 13, no. 4, pp. 196–203, 2007.

[74] Iscar Ltd, "The Development Stages," 2017. [Online]. Available: http://www.iscar.com/newarticles.aspx/countryid/1/newarticleid/171. [Accessed: 20-Jul-2005].

[75] D. B. Arnold, "Trends that Drive Cutting Tool Development," *Modern Machine Shop*, 2000. [Online]. Available: http://www.mmsonline.com/articles/trends-that-drive-cutting-tool-

development. [Accessed: 01-May-2017].

[76] P. J. Pappafava, "The Manufacturing Process for Cemented Tungsten Carbides," Pennsylvania.

[77] V. Martins, W. C. Rodrigues, P. L. Ferrandini, D. J. Villarinho, G. H. Knörnschild, and L. Schaeffer, "Comparative studies of WC-Co and WC-Co-Ni composites obtained by conventional powder metallurgy," *Mater. Res.*, vol. 14, no. 2, pp. 274–279, 2011.

[78] R. M. German, *Sintering Theory and Practice*. John Wiley & Sons, Inc., 1996.

[79] Mitsubishi Materials Corporation, *Tooling Technology Level 2*, 1st ed. Tokyo: Mitsubishi Material Corporation, 2006.

[80] C. J. R. González-Oliver, E. A. Álvarez, and J. L. García, "Kinetics of densification and grain growth in ultrafine WC-Co composites," *Int. J. Refract. Met. Hard Mater.*, vol. 59, pp. 121–131, 2016.

[81] W. D. Schubert, H. Neumeister, G. Kinger, and B. Lux, "Hardness to toughness relationship of fine-grained WC-Co hardmetals," *Int. J. Refract. Metals Hard Mater.*, vol. 16, pp. 133–142, 1998.

[82] Sandvik Coromant, "Understanding cemented carbides," 2008.

[83] J. Chen *et al.*, "Microstructure analysis of high density WC-Co composite prepared by one step selective laser melting," *Int. J. Refract. Metals Hard Mater.*, vol. 84, no. May, p. 104980, 2019.

[84] H. Xie, X. Song, F. Yin, and Y. Zhang, "Effect of WC/Co coherency phase boundaries on Fracture toughness of the nanocrystalline cemented carbides," *Sci. Rep.*, vol. 6, no. July, pp. 1–8, 2016.

[85] H. A. Abdel-Aal, M. Nouari, and M. El Mansori, "The effect of thermal property degradation on wear of WC-CO inserts in dry cutting," *Wear*, vol. 265, no. 11–12, pp. 1670–1679, 2008.

[86] D. M. Kennedy and M. S. J. Hashmi, "Methods of wear testing for advanced surface coatings and bulk materials," *J. Mater. Process. Technol.*, vol. 300, no. 3–4, pp. 246–253, 1998.

[87] International Organization for Standardization, "ISO 3685: Tool-life testing with single-point turning tools," 1993.

[88] J. Mitchell, "Canadian Metalworking," *Failure modes – how they can improve your machining processes*, 2013. [Online]. Available: https://www.canadianmetalworking.com/canadianmetalworking/news/metalworking/failure-modes-how-they-can-improve-your-machining-processes. [Accessed: 30-Mar-2020].

[89] M. P. Groover, *Principles of Modern Manufacturing*, Fifth Edit. Wiley, 2013.

[90] J. C. Keefe, "Manufacturing Technology Laboratory, Lehigh University."

[91] Sandvik Coromant, "Sandvik Coromant," 2020. [Online]. Available: https://www.sandvik.coromant.com/en-gb/knowledge/materials/pages/wear-on-cutting-

edges.aspx. [Accessed: 30-Mar-2020].

[92] G. A. Oosthuizen, "Wear characterisation in milling of Ti6Al4V – A wear map approach," Stellenbosch University, 2010.

[93] P. de Vos, "Mechanical loads and cutting geometries in turning operations," 2016. [Online]. Available: https://mfgtechupdate.com/2016/03/mechanical-loads-and-cutting-geometries-in-turning-operations/. [Accessed: 01-Jun-2017].

[94] I. Gibson, D. W. Rosen, and B. Stucker, *Additive Manufacturing Technologies: Rapid Prototyping to Direct Digital Manufacturing*. New York: Springer, 2010.

[95] M. Królikowski and K. Filipowicz, "Verification of Geometrical Accuracy of Selective Laser Melting (SLM) Built Model," *VERSITA Adv. Manuf. Sci. Technol.*, vol. 37, no. 3, pp. 85–91, 2013.

[96] D. T. Pham and R. S. Gault, "A comparison of rapid prototyping technologies," *Int. J. Mach. Tools Manuf.*, vol. 38, no. 10–11, pp. 1257–1287, 1998.

[97] N. Guo and M. C. Leu, "Additive manufacturing: Technology, applications and research needs," *Front. Mech. Eng.*, vol. 8, no. 3, pp. 215–243, 2013.

[98] A. C. van Staden, "A Fundamental Analysis on Additive Manufacturing of a Cemented Tungsten Carbide," Stellenbosch University, 2016.

[99] J.-P. P. Kruth, "Material incress manufacturing by Rapid Prototyping Techniques," in *Annals of the CIRP 40(2)*, 1991, vol. 40, no. 2, pp. 603–614.

[100] J.-P. Kruth, M. C. Leu, and T. Nakagawa, "Progress in Additive Manufacturing and Rapid Prototyping," *CIRP Ann. - Manuf. Technol.*, vol. 47, no. 2, pp. 525–540, 1998.

[101] Y. Yang, C. Zhang, D. Wang, L. Nie, D. Wellmann, and Y. Tian, "Additive manufacturing of WC-Co hardmetals : a review," *Int. J. Adv. Manuf. Technol.*, vol. 108, pp. 1653–1673, 2020.

[102] G. N. Levy, R. Schindel, and J. P. Kruth, "Rapid Manufacturing and Rapid Tooling With Layer Manufacturing (Lm) Technologies, State of the Art and Future Perspectives," *CIRP Ann. - Manuf. Technol.*, vol. 52, no. 2, pp. 589–609, 2003.

[103] H. K. Rafi, N. V Karthik, H. Gong, T. L. Starr, and B. E. Stucker, "Microstructures and Mechanical Properties of Ti6Al4V Parts Fabricated by Selective Laser Melting and Electron Beam Melting," vol. 22, no. December, pp. 3872–3883, 2013.

[104] M. F. Zaeh and G. Branner, "Investigations on residual stresses and deformations in selective laser melting," *Prod. Eng. Res. Dev.*, vol. 4, no. 1, pp. 35–45, 2010.

[105] J. P. Kruth, L. Froyen, J. Van Vaerenbergh, P. Mercelis, M. Rombouts, and B. Lauwers, "Selective laser melting of iron-based powder," *J. Mater. Process. Technol.*, vol. 149, no. 1–3, pp. 616–622, 2004.

[106] N. Read, W. Wang, K. Essa, and M. M. Attallah, "Selective laser melting of AlSi10Mg alloy:

Process optimisation and mechanical properties development," *Mater. Des.*, vol. 65, pp. 417–424, 2015.

[107] I. Yadroitsev, I. Yadroitsava, P. Bertrand, and I. Smurov, "Factor analysis of selective laser melting process parameters and geometrical characteristics of synthesized single tracks," *Rapid Prototyp. J.*, vol. 18, no. 3, pp. 201–208, 2012.

[108] P. Hanzl, M. Zetek, T. Baksa, and T. Kroupa, "The influence of processing parameters on the mechanical properties of SLM parts," *Procedia Eng.*, vol. 100, no. January, pp. 1405–1413, 2015.

[109] G. Casalino, S. L. Campanelli, N. Contuzzi, and A. D. Ludovico, "Experimental investigation and statistical optimisation of the selective laser melting process of a maraging steel," *Opt. Laser Technol.*, vol. 65, pp. 151–158, 2015.

[110] Y. Bar-Cohen, *Advances in Manufacturing and Processing of Materials and Structures*. CRC Press, 2018.

[111] G. Kasperovich and J. Hausmann, "Improvement of fatigue resistance and ductility of TiAl6V4 processed by selective laser melting," *J. Mater. Process. Technol.*, vol. 220, pp. 202–214, 2015.

[112] J. Bültmann, S. Merkt, C. Hammer, C. Hinke, and U. Prahl, "Scalability of the mechanical properties of selective laser melting produced micro-struts," *J. Laser Appl.*, vol. 27, 2015.

[113] P. J. T. Conradie, D. M. M. Dimitrov, G. A. Oosthuizen, and P. A. Hugo, "Resource efficiency assessment of combining selective laser melting and five axis milling for titanium components," in *Proceedings of Rapid Product Development Association of South Africa Conference*, 2014, pp. 1–8.

[114] E. Brinksmeier, G. Levy, D. Meyer, and A. B. Spierings, "Surface integrity of selective-laser-melted components," *CIRP Ann. - Manuf. Technol.*, vol. 59, no. 1, pp. 601–606, 2010.

[115] M. B. Bauza *et al.*, "Study of accuracy of parts produced using additive manufacturing," in *2014 ASPE Spring Topical Meeting: Dimensional Accuracy and Surface Finish in Additive Manufacturing*, 2014, pp. 1–8.

[116] S. O. Onuh and Y. Y. Yusuf, "Rapid prototyping technology : applications and benefits for rapid product development," *J. Intell. Manuf.*, vol. 10, pp. 301–311, 1999.

[117] E. Santos, F. Abe, Y. Kitamura, K. Osakada, and M. Shiomi, "Mechanical properties of pure titanium models processed by selective laser melting," in *Proceedings of the Solid Freeform Fabrication Symposium*, 2002, pp. 180–186.

[118] G. Ziolkowski, E. Chlebus, P. Szymczyk, and J. Kurzac, "Application of X-ray CT method for discontinuity and porosity detection in 316L stainless steel parts produced with SLM technology," *Arch. Civ. Mech. Eng.*, vol. 14, no. 4, pp. 608–614, 2014.

[119] C. Qiu, N. J. E. Adkins, and M. M. Attallah, "Microstructure and tensile properties of selectively laser-melted and of HIPed laser-melted Ti-6Al-4V," *Mater. Sci. Eng. A*, vol. 578, pp. 230–239, 2013.

[120] F. Abe, E. Costa Santos, Y. Kitamura, K. Osakada, and M. Shiomi, "Influence of forming conditions on the titanium model in rapid prototyping with the selective laser melting process," *Proc. Inst. Mech. Eng. Part C J. Mech. Eng. Sci.*, vol. 217, no. 1, pp. 119–126, 2003.

[121] L. E. Murr *et al.*, "Microstructure and mechanical behavior of Ti-6Al-4V produced by rapid-layer manufacturing, for biomedical applications," *J. Mech. Behav. Biomed. Mater.*, vol. 2, no. 1, pp. 20–32, 2009.

[122] K. A. Ghany and S. F. Moustafa, "Comparison between the products of four RPM systems for metals," *Rapid Prototyp. J.*, vol. 12, no. 2, pp. 86–94, 2006.

[123] D. Hagedorn-Hansen, R. Cichon, M. B. Bezuidenhout, P. A. Hugo, and G. A. Oosthuizen, "Geometric Deviation of Hybrid Parts Produced by Selective Laser Melting," in *Rapid Product Development Association of South Africa*, 2015, pp. 1–9.

[124] M. Matsumoto, M. Shiomi, K. Osakada, and F. Abe, "Finite element analysis of single layer forming on metallic powder bed in rapid prototyping by selective laser processing," *Int. J. Mach. Tools Manuf.*, vol. 42, no. 1, pp. 61–67, 2002.

[125] H. Pohl, A. Simchi, M. Issa, and H. C. Dias, "Thermal Stresses in Direct Metal Laser Sintering," in *Proc. of the Solid Freeform Fabrication Symp*, 2001, pp. 366–372.

[126] P. Mercelis and J.-P. Kruth, "Residual stresses in selective laser sintering and selective laser melting," *Rapid Prototyp. J.*, vol. 12, no. 5, pp. 254–265, 2006.

[127] B. Qian, Y. S. Shi, Q. S. Wei, and H. B. Wang, "The helix scan strategy applied to the selective laser melting," *Int. J. Adv. Manuf. Technol.*, vol. 63, no. 5–8, pp. 631–640, 2012.

[128] C. R. Knowles, T. H. Becker, and R. B. Tait, "Residual Stress Measurements and Structural Integrity Implications for Selective Laser Melted Ti-6AL-4V," *South African J. Ind. Eng.*, vol. 23, no. 2, pp. 119–129, 2012.

[129] E. Yasa, J. P. Kruth, and J. Deckers, "Manufacturing by combining Selective Laser Melting and Selective Laser Erosion/laser re-melting," *CIRP Ann. - Manuf. Technol.*, vol. 60, no. 1, pp. 263–266, 2011.

[130] S. Dadbakhsh, L. Hao, and N. Sewell, "Effect of selective laser melting layout on the quality of stainless steel parts," *Rapid Prototyp. J.*, vol. 18, no. 3, pp. 241–249, 2012.

[131] K. Kempen, L. Thijs, B. Vrancken, J. Van Humbeeck, and J.-P. Kruth, "Producing Crack-Free, High Density M2 Hss Parts By Selective Laser Melting: Pre-Heating the Baseplate," *Proc. 24th Int. Solid Free. Fabr. Symp.*, pp. 131–139, 2013.

[132] J. P. Kruth, B. Vandenbroucke, J. Van Vaerenbergh, and I. Naert, "Digital manufacturing of

biocompatible metal frameworks for complex dental prostheses by means of SLS/SLM," *Virtual Model. Rapid Manuf. Adv. Res. VIRTUAL RAPID Prototyp.*, pp. 139–145, 2005.

[133] S. Dadbakhsh, L. Hao, P. G. E. Jerrard, and D. Z. Zhang, "Experimental investigation on selective laser melting behaviour and processing windows of in situ reacted Al/Fe 2O 3 powder mixture," *Powder Technol.*, vol. 231, pp. 112–121, 2012.

[134] A. E. Patterson, S. L. Messimer, and P. A. Farrington, "Overhanging Features and the SLM/DMLS Residual Stresses Problem: Review and Future Research Need," *Technologies*, vol. 5, no. 2, p. 15, 2017.

[135] B. Vrancken, L. Thijs, J.-P. Kruth, and J. Van Humbeeck, "Heat treatment of Ti6Al4V produced by Selective Laser Melting: Microstructure and mechanical properties," *J. Alloys Compd.*, vol. 541, pp. 177–185, 2012.

[136] M. Amini and S. Chang, "Process monitoring of 3D metal printing in industrial scale," *ASME 2018 13th Int. Manuf. Sci. Eng. Conf. MSEC 2018*, vol. 1, no. June, 2018.

[137] O. Rehme, C. Verlag, and I. A. Jentzsch-cuvillier, *Cellular Design for Laser Freeform Fabrication*, vol. 49, no. 0. Cuvillier, 2010.

[138] A. T. Sutton, C. S. Kriewall, M. C. Leu, and J. W. Newkirk, "Powder characterisation techniques and effects of powder characteristics on part properties in powder-bed fusion processes," *Virtual Phys. Prototyp.*, vol. 12, no. 1, pp. 3–29, 2017.

[139] J. H. Tan, W. L. E. Wong, and K. W. Dalgarno, "An overview of powder granulometry on feedstock and part performance in the selective laser melting process," *Addit. Manuf.*, vol. 18, pp. 228–255, 2017.

[140] Entegris, "What is the Effect of Sample Size on Particle Size Distribution Measurements?," 2016.

[141] B. Liu, R. Wildman, C. Tuck, I. Ashcroft, and R. Hague, "Investigaztion the effect of particle size distribution on processing parameters optimisation in selective laser melting process," *22nd Annu. Int. Solid Free. Fabr. Symp. - An Addit. Manuf. Conf. SFF 2011*, no. mm, pp. 227–238, 2011.

[142] A. C. Hoffmann and H. J. Finkers, "A relation for the void fraction of randomly packed particle beds," *Powder Technol.*, vol. 82, no. 2, pp. 197–203, 1995.

[143] N. P. Karapatis, G. Egger, P. Gygax, and R. Glardon, "Optimization of Powder Layer Density in Selective Laser Sintering," pp. 255–264.

[144] A. T. Sutton, C. S. Kriewall, M. C. Leu, and J. W. Newkirk, "Powders for Additive Manufacturing Processes: Characterization Techniques and Effects on Part Properties," *Solid Free. Fabr. Proc.*, pp. 1004–1030, 2016.

[145] C. Meier, R. Weissbach, J. Weinberg, W. A. Wall, and A. J. Hart, "Critical influences of

particle size and adhesion on the powder layer uniformity in metal additive manufacturing," *J. Mater. Process. Tech.*, vol. 266, no. November 2018, pp. 484–501, 2019.

[146] X. Zhou, X. Liu, D. Zhang, Z. Shen, and W. Liu, "Balling phenomena in selective laser melted tungsten," *J. Mater. Process. Technol.*, vol. 222, no. September, pp. 33–42, 2015.

[147] P. K. Samal and J. W. Newkirk, *ASM Handbook: Powder Metallurgy*, vol. 7. Ohio: ASM International, 2015.

[148] R. Baitimerov, P. Lykov, D. Zherebtsov, L. Radionova, A. Shultc, and K. G. Prashanth, "Influence of powder characteristics on processability of AlSi12 alloy fabricated by selective laser melting," *Materials (Basel).*, vol. 11, no. 5, pp. 0–14, 2018.

[149] R. Engeli, T. Etter, S. Hövel, and K. Wegener, "Processability of different IN738LC powder batches by selective laser melting," *J. Mater. Process. Technol.*, vol. 229, pp. 484–491, 2016.

[150] D. Tomus *et al.*, "Controlling the microstructure of Hastelloy-X components manufactured by Selective Laser Melting," *Phys. Procedia*, vol. 41, no. 0, pp. 823–827, 2013.

[151] K. Kempen, L. Thijs, E. Yasa, M. Badrossamay, W. Verheecke, and J. P. Kruth, "Process optimization and microstructural analysis for selective laser melting of AlSi10Mg," *22nd Annu. Int. Solid Free. Fabr. Symp. - An Addit. Manuf. Conf. SFF 2011*, no. May 2014, pp. 484–495, 2011.

[152] M. Averyanova, P. Bertrand, and B. Verquin, "Studying the influence of initial powder characteristics on the properties of final parts manufactured by the selective laser melting technology," *Virtual Phys. Prototyp.*, vol. 6, no. 4, pp. 215–223, 2011.

[153] C. M. Fernandes and A. M. R. R. Senos, "Cemented carbide phase diagrams: A review," *Int. J. Refract. Met. Hard Mater.*, vol. 29, no. 4, pp. 405–418, 2011.

[154] A. Gåård, P. Krakhmalev, and J. Bergstrom, "Microstructural characterization and wear behavior of (Fe , Ni) – TiC MMC prepared by DMLS," *J. Alloys Compd.*, vol. 421, pp. 166–171, 2006.

[155] D. Gu and Y. Shen, "Influence of reinforcement weight fraction on microstructure and properties of submicron WC-Cop/Cu bulk MMCs prepared by direct laser sintering," *J. Alloys Compd.*, vol. 431, no. 1–2, pp. 112–120, 2007.

[156] C. L. A. Leung, S. Marussi, M. Towrie, R. C. Atwood, P. J. Withers, and P. D. Lee, "The effect of powder oxidation on defect formation in laser additive manufacturing," *Acta Mater.*, vol. 166, pp. 294–305, 2019.

[157] J. A. Slotwinski and E. J. Garboczi, "Metrology Needs for Metal Additive Manufacturing Powders," *Jom*, vol. 67, no. 3, pp. 538–543, 2015.

[158] A. S. Kurlov and A. I. Gusev, *Springer Series in Materials Science 11*, vol. 184, no. 3–4. 2010.

[159] R. L. Brown and J. C. Richards, "Kinematics of the flow of dry powders and bulk solids,"

Rheol Acta, vol. 4, pp. 153–165, 1965.

[160] R. K. Kesava, P. R. Nott, and S. Sundaresan, *An introduction to granular flow*. New York: Cambridge University Press, 2008.

[161] J. Weinberg, "A Precision Blade Mechanism for Powder Recoating in Selective Laser Melting," Massachusetts Institute of Technology, 2018.

[162] S. Wen *et al.*, "High-density tungsten fabricated by selective laser melting: Densification, microstructure, mechanical and thermal performance," *Opt. Laser Technol.*, vol. 116, no. March, pp. 128–138, 2019.

[163] O. R. Walton, "Review of Adhesion Fundamentals for Micron-Scale Particles," vol. 26, no. 26, pp. 129–141, 2008.

[164] C. Tan, K. Zhou, W. Ma, B. Attard, P. Zhang, and T. Kuang, "Selective laser melting of high-performance pure tungsten: parameter design, densification behavior and mechanical properties," *Sci. Technol. Adv. Mater.*, vol. 19, no. 1, pp. 370–380, 2018.

[165] E. M. Lifshitz, "The Theory of Molecular Attractive Forces between Solids," *Sov. Phys.*, vol. 2, no. 1, pp. 73–83, 1956.

[166] A. Manakov and H. S. Ivo, "A Mathematical Model and Calibration Procedure for Galvanometric Laser Scanning Systems," *Vision, Model. Vis.*, pp. 207–214, 2011.

[167] X. Luo, J. Li, M. Lucas, C. Technology, and M. Turnpike, "Galvanometer scanning technology for laser additive manufacturing," *Laser 3D Manuf. IV*, vol. 10095, p. 1009512, 2017.

[168] D. Hagedorn-Hansen, "The Effects of Developed Selective Laser Melting Strategies on Titanium Hybrid Parts," Stellenbosch University, 2017.

[169] G. E. Bean, D. B. Witkin, T. D. McLouth, D. N. Patel, and R. J. Zaldivar, "Effect of laser focus shift on surface quality and density of Inconel 718 parts produced via selective laser melting," *Addit. Manuf.*, vol. 22, no. July 2017, pp. 207–215, 2018.

[170] F. Bordin, "Terrestrial Laser Scanner in the characterization of forest targets," Universidade Federal Do Rio Grande Do Sul, 2015.

[171] S. C. Popescu, "Lidar Remote Sensing," in *Advances in Environmental Remote Sensing: Sensors, Algorithms, and Applications*, 2011, pp. 57–84.

[172] E. Y. A. A. Wornyoh, V. K. Jasti, and C. F. Higgs, "A review of dry particulate lubrication: Powder and granular materials," *J. Tribol.*, vol. 129, no. 2, pp. 438–449, 2007.

[173] M. Eosint, "Technical Description EOSINT M 280 Technical description Technical Description EOSINT M 280," *Eos (Washington. DC).*, no. December, pp. 1–33, 2010.

[174] B. Ferrar, L. Mullen, E. Jones, R. Stamp, and C. J. Sutcliffe, "Gas flow effects on selective laser melting (SLM) manufacturing performance," *J. Mater. Process. Tech.*, vol. 212, no. 2, pp. 355–364, 2012.

[175] W. J. Sames, F. A. List, S. Pannala, R. R. Dehoff, and S. S. Babu, "The metallurgy and processing science of metal additive manufacturing," *Int. Mater. Rev.*, vol. 6608, no. March, 2016.

[176] L. E. Murr *et al.*, "Microstructures and properties of 17-4 PH stainless steel fabricated by selective laser melting," *J. Mater. Res. Technol.*, vol. 1, no. 3, pp. 167–177, 2012.

[177] A. Ladewig, G. Schlick, M. Fisser, V. Schulze, and U. Glatzel, "Influence of the shielding gas flow on the removal of process by-products in the selective laser melting process," *Addit. Manuf.*, vol. 10, pp. 1–9, 2016.

[178] I. Yadroitsev and I. Smurov, "Selective laser melting technology: From the single laser melted track stability to 3D parts of complex shape," *Phys. Procedia*, vol. 5, no. PART 2, pp. 551–560, 2010.

[179] O. Rehme and C. Emmelmann, "Reproducibility for properties of Selective Laser Melting products," in *Proceedings of the Third International WLT-Conference on Lasers in Manufacturing 2005*, 2005.

[180] I. Yadroitsev, P. Krakhmalev, and I. Yadroitsava, "Hierarchical design principles of selective laser melting for high quality metallic objects," *Addit. Manuf.*, vol. 7, pp. 45–56, 2015.

[181] I. Yadroitsev, P. Krakhmalev, I. Yadroitsava, S. Johansson, and I. Smurov, "Energy input effect on morphology and microstructure of selective laser melting single track from metallic powder," *J. Mater. Process. Technol.*, vol. 213, no. 4, pp. 606–613, 2013.

[182] R. Li, Y. Shi, J. Liu, Z. Xie, and Z. Wang, "Selective laser melting W-10 wt.% Cu composite powders," *Int. J. Adv. Manuf. Technol.*, vol. 48, no. 5–8, pp. 597–605, 2010.

[183] B. Nie, L. Yang, H. Huang, S. Bai, P. Wan, and J. Liu, "Femtosecond laser additive manufacturing of iron and tungsten parts," *Appl. Phys. A Mater. Sci. Process.*, vol. 119, no. 3, pp. 1075–1080, 2015.

[184] A. T. Sidambe, Y. Tian, P. B. Prangnell, and P. Fox, "Effect of processing parameters on the densification, microstructure and crystallographic texture during the laser powder bed fusion of pure tungsten," *Int. J. Refract. Metals Hard Mater.*, vol. 78, no. July 2018, pp. 254–263, 2019.

[185] R. K. Enneti, R. Morgan, and S. V. Atre, "Effect of process parameters on the Selective Laser Melting (SLM) of tungsten," *Int. J. Refract. Met. Hard Mater.*, vol. 71, pp. 315–319, 2018.

[186] D. Hagedorn-Hansen, M. Bezuidenhout, D. Dimitrov, and G. Oosthuizen, "The Effects of Selective Laser Melting Scan Strategies on Deviation of Hybrid Parts," *South African J. Ind. Eng.*, vol. 28, no. 3, pp. 200–212, 2017.

[187] H. Jia, H. Sun, H. Wang, Y. Wu, and H. Wang, "Scanning strategy in selective laser melting (SLM): a review," *Int. J. Adv. Manuf. Technol.*, vol. 113, no. 9–10, pp. 2413–2435, 2021.

[188] R. Stamp, P. Fox, W. O'Neill, E. Jones, and C. Sutcliffe, "The development of a scanning strategy for the manufacture of porous biomaterials by selective laser melting," *J. Mater. Sci. Mater. Med.*, vol. 20, no. 9, pp. 1839–1848, 2009.

[189] E. Yasa and J. Deckers, "Investigation on occurrence of elevated edges in selective laser melting," in *International Solid Freeform Fabrication Symposium*, 2009, pp. 180–192.

[190] A. H. Nickel, D. M. Barnett, and F. B. Prinz, "Thermal stresses and deposition patterns in layered manufacturing," *Mater. Sci. Eng. A*, vol. 317, no. 1–2, pp. 59–64, 2001.

[191] W. Di, Y. Yongqiang, S. Xubin, and C. Yonghua, "Study on energy input and its influences on single-track,multi-track, and multi-layer in SLM," *Int. J. Adv. Manuf. Technol.*, vol. 58, no. 9–12, pp. 1189–1199, 2012.

[192] R. H. Morgan, A. J. Papworth, C. Sutcliffe, P. Fox, and W. O'Neill, "High density net shape components by direct laser re-melting of single-phase powders," *J. Mater. Sci.*, vol. 37, no. 15, pp. 3093–3100, 2002.

[193] L. Thijs, M. L. Montero Sistiaga, R. Wauthle, Q. Xie, J. P. Kruth, and J. Van Humbeeck, "Strong morphological and crystallographic texture and resulting yield strength anisotropy in selective laser melted tantalum," *Acta Mater.*, vol. 61, no. 12, pp. 4657–4668, 2013.

[194] A. Simchi, "Direct laser sintering of metal powders: Mechanism, kinetics and microstructural features," *Mater. Sci. Eng. A*, vol. 428, no. 1–2, pp. 148–158, 2006.

[195] P. A. Hooper, "Melt pool temperature and cooling rates in laser powder bed fusion," *Addit. Manuf.*, vol. 22, no. May, pp. 548–559, 2018.

[196] J. Robinson, I. Ashton, P. Fox, E. Jones, and C. Sutcliffe, "Determination of the effect of scan strategy on residual stress in laser powder bed fusion additive manufacturing," *Addit. Manuf.*, vol. 23, no. February, pp. 13–24, 2018.

[197] D. Wang, C. Yu, J. Ma, W. Liu, and Z. Shen, "Densification and crack suppression in selective laser melting of pure molybdenum," *Mater. Des.*, vol. 129, no. April, pp. 44–52, 2017.

[198] J. Jhabvala, E. Boillat, T. Antignac, and R. Glardon, "Study and simulation of different scanning strategies in SLM," *Innov. Dev. Des. Manuf. - Adv. Res. Virtual Rapid Prototyp.*, no. August 2016, pp. 369–375, 2010.

[199] U. Scipioni Bertoli, A. J. Wolfer, M. J. Matthews, J. P. R. Delplanque, and J. M. Schoenung, "On the limitations of Volumetric Energy Density as a design parameter for Selective Laser Melting," *Mater. Des.*, vol. 113, pp. 331–340, 2017.

[200] W. E. King, H. G. Barth, V. M. Castillo, D. Hahn, and C. Kamath, "Observation of keyhole-mode laser melting in laser powder-bed fusion additive manufacturing," *J. Mater. Process. Technol.*, 2013.

[201] A. Großmann *et al.*, "Dimensionless process development for lattice structure design in laser

powder bed fusion," *Mater. Des.*, p. 108952, 2020.

[202] D. Gu and Y. Shen, "Balling phenomena in direct laser sintering of stainless steel powder: Metallurgical mechanisms and control methods," *Mater. Des.*, vol. 30, no. 8, pp. 2903–2910, 2009.

[203] D. D. Gu, W. Meiners, K. Wissenbach, and R. Poprawe, "Laser additive manufacturing of metallic components: materials, processes and mechanisms," *Int. Mater. Rev.*, vol. 57, no. 3, pp. 133–164, 2012.

[204] M. Guo *et al.*, "Selective laser melting additive manufacturing of pure tungsten: Role of volumetric energy density on densification, microstructure and mechanical properties," *Int. J. Refract. Met. Hard Mater.*, vol. 84, no. July, p. 105025, 2019.

[205] J. P. Oliveira, T. G. Santos, and R. M. Miranda, "Revisiting fundamental welding concepts to improve additive manufacturing : From theory to practice," *Prog. Mater. Sci.*, vol. 107, no. 100590, pp. 1–43, 2020.

[206] I. Koutiri, E. Pessard, P. Peyre, O. Amlou, and T. De Terris, "Influence of SLM process parameters on the surface finish, porosity rate and fatigue behavior of as-built Inconel 625 parts," *J. Mater. Process. Technol.*, vol. 255, pp. 536–546, 2018.

[207] P. Bajaj, J. Wright, I. Todd, and E. A. Jägle, "Predictive process parameter selection for Selective Laser Melting Manufacturing : Applications to high thermal conductivity alloys," *Addit. Manuf.*, vol. 27, no. September 2018, pp. 246–258, 2019.

[208] M. A. Bramson, *Infrared Radiation*. Boston: Springer, 1968.

[209] J. Zhang *et al.*, "Influence of Particle Size on Laser Absorption and Scanning Track Formation Mechanisms of Pure Tungsten Powder During Selective Laser Melting," *Engineering*, vol. 5, no. 4, pp. 736–745, 2019.

[210] P. Yuan and D. Gu, "Molten pool behaviour and its physical mechanism during selective laser melting of TiC/AlSi10Mg nanocomposites: simulation and experiments," *J. Phys. D. Appl. Phys.*, vol. 48, no. 3, 2015.

[211] L. Ma and H. Bin, "Temperature and stress analysis and simulation in fractal scanning-based laser sintering," *Int. J. Adv. Manuf. Technol.*, vol. 34, no. 9–10, pp. 898–903, 2006.

[212] D. Q. Zhang, Q. Z. Cai, J. H. Liu, L. Zhang, and R. D. Li, "Select laser melting of W-Ni-Fe powders: Simulation and experimental study," *Int. J. Adv. Manuf. Technol.*, vol. 51, no. 5–8, pp. 649–658, 2010.

[213] T. Childs, C. Hauser, and M. Badrossamay, "Selective laser sintering (melting) of stainless and tool steel powders: experiments and modelling," *Proc. Inst. Mech. Eng.*, vol. 219, no. 4, pp. 339–357, 2005.

[214] J. P. Kruth, G. Levy, F. Klocke, and T. H. C. Childs, "Consolidation phenomena in laser and

powder-bed based layered manufacturing," *CIRP Ann. - Manuf. Technol.*, vol. 56, no. 2, pp. 730–759, 2007.

[215] I. A. Roberts, C. J. Wang, R. Esterlein, M. Stanford, and D. J. Mynors, "A three-dimensional finite element analysis of the temperature field during laser melting of metal powders in additive layer manufacturing," *Int. J. Mach. Tools Manuf.*, vol. 49, no. 12–13, pp. 916–923, 2009.

[216] K. Zeng, D. Pal, and B. E. Stucker, "A Review of Thermal Analysis Methods in Laser Sintering and Selective Laser Melting," in *Proceedings of the Solid Freeform Fabrication Symposium*, 2012, pp. 796–814.

[217] K. Dai and L. Shaw, "Finite element analysis of the effect of volume shrinkage during laser densification," *Acta Mater.*, vol. 53, no. 18, pp. 4743–4754, 2005.

[218] J. P. Holman, *Heat Transfer*, Tenth Edit. New York: McGraw-Hill, 2010.

[219] D. Rosenthal, "Mathematical theory of heat distribution during welding and cutting," *Weld. Journal*, vol. 20, no. 5, pp. 220–234, 1941.

[220] D. Rosenthal, "The theory of moving sources of heat and its application to metal treatments," *Trans. ASME*, 1946.

[221] M. Rombouts, "Selective laser sintering/melting of iron-based powders," KU Leuven, 2006.

[222] Y. P. Kathuria, "Microstructuring by selective laser sintering of metallic powder," *Surf. Coatings Technol.*, vol. 116–119, pp. 643–647, 1999.

[223] J.-P. P. Kruth *et al.*, "Binding mechanisms in selective laser sintering and selective laser melting," *Rapid Prototyp. J.*, vol. 11, no. 1, pp. 26–36, 2005.

[224] A. Gusarov, T. Laoui, L. Froyen, V. Titov, and N. Tolochko, "Numerical Simulation of Laser Solid State Sintering of Loose Titanium Powder," in *EURO RP 2001*, 2001, pp. 1–5.

[225] J. P. Kruth, X. Wang, T. Laoui, and L. Froyen, "Lasers and materials in selective laser sintering," *Assem. Autom.*, vol. 23, no. 4, pp. 357–371, 2003.

[226] T. Laoui, L. Froyen, and J.-P. Kruth, "Effect of mechanical alloying on Selective Laser Sintering of WC-9Co powder," *Powder Metall.*, vol. 42, no. 3, pp. 203–205, 1999.

[227] M. Agarwala, D. Bourell, J. Beaman, H. Marcus, and J. Barlow, "Direct selective laser sintering of metals," *Rapid Prototyp. J.*, vol. 1, no. 1, pp. 26–36, 1995.

[228] N. Tolochko, S. Mozzharov, T. Laoui, and L. Froyen, "Selective laser sintering of single- and two-component metal powders," *Rapid Prototyp. J.*, vol. 9, no. 2, pp. 68–78, 2003.

[229] N. Eustathopoulos, M. G. Nicholas, and B. Drevet, *Wettability at High Temperatures*. Oxford: Elsevier Science, 1999.

[230] S. Lu, H. Fujii, and K. Nogi, "Marangoni convection and weld shape variations in Ar–O2 and Ar–CO2 shielded GTA welding," *Mater. Sci. Eng.*, no. 380, pp. 290–297, 2004.

[231] D. Gu and Y. Shen, "WC-Co particulate reinforcing Cu matrix composites produced by direct laser sintering," *Mater. Lett.*, vol. 60, no. 29–30, pp. 3664–3668, 2006.

[232] D. Gu and Y. Shen, "Processing and microstructure of submicron WC-Co particulate reinforced Cu matrix composites prepared by direct laser sintering," *Mater. Sci. Eng. A*, vol. 435–436, pp. 54–61, 2006.

[233] I. Konyashin *et al.*, "Wettability of tungsten carbide by liquid binders in WC–Co cemented carbides: Is it complete for all carbon contents?," *Int. J. Refract. Met. Hard Mater.*, vol. 62, pp. 134–148, 2017.

[234] Y. Liu, H. Wang, Z. Long, and P. K. Liaw, "Microstructural evolution and mechanical behaviors of graded cemented carbides," vol. 426, pp. 346–354, 2006.

[235] X. He, T. Debroy, and P. W. Fuerschbach, "Alloying element vaporization during laser spot welding of stainless steel," *J. Phys. D. Appl. Phys.*, vol. 36, no. 23, pp. 3079–3088, 2003.

[236] P. A. A. Khan and T. Debroy, "Alloying Element Vaporization and Weld Pool Temperature during Laser Welding of AlSl 202 Stainless Steel," *Metall. Trans. B*, vol. 15, no. 4, pp. 641–644, 1984.

[237] D. Bäuerle, *Laser processing and chemistry*, vol. 186, no. 1–4. New York: Springer Berlin Heidelberg, 2011.

[238] K. Leitz, P. Singer, A. Plankensteiner, B. Tabernig, H. Kestler, and L. S. Sigl, "Thermo-Fluiddynamical Modelling of Laser Beam-Matter Interaction in Selective Laser Melting," *COMSOL Conf. 2016*, 2016.

[239] D. Bricín, "Is it Possible to Process Sintered Carbides by Selective Laser Melting Technology?," pp. 121–126.

[240] S. Kumar, "Manufacturing of WC-Co moulds using SLS machine," *J. Mater. Process. Technol.*, vol. 209, no. 8, pp. 3840–3848, 2009.

[241] A. Iveković, M. L. Montero-Sistiaga, K. Vanmeensel, J. P. Kruth, and J. Vleugels, "Effect of processing parameters on microstructure and properties of tungsten heavy alloys fabricated by SLM," *Int. J. Refract. Met. Hard Mater.*, vol. 82, no. March, pp. 23–30, 2019.

[242] J.-P. Kruth, L. Froyen, B. Morren, and J. E. Bonse, "Selective laser sintering of WC-Co 'hard metal' parts," in *8th International Conference on Production Engineering (ICPE-8)*, 1997, pp. 149–156.

[243] T. Laoui, L. Froyen, and J.-P. Kruth, "Selective laser sintering of hard metal powders," in *Rapid Prototyping and Manufacturing Conference*, 1998, pp. 435–467.

[244] L. Jepson, J. Perez, J. J. Beaman, D. Bourell, and K. Wood, "Development of a Multi-Material Selective Laser Sintering Process," in *Proceedings of the 1999 NSF Design and Manufacturing Grantees Conference*, 1999.

[245] D. Gu and Y. Shen, "Direct laser sintered WC-10Co/Cu nanocomposites," *Appl. Surf. Sci.*, vol. 254, no. 13, pp. 3971–3978, 2008.

[246] D. Gu and W. Meiners, "Microstructure characteristics and formation mechanisms of in situ WC cemented carbide based hardmetals prepared by Selective Laser Melting," *Mater. Sci. Eng. A*, vol. 527, no. 29–30, pp. 7585–7592, 2010.

[247] P. Stoyanov, "Cutting Tool Made by Additive Manufacturing," US 20160332236A1, 2016.

[248] D. Gu, "In Situ WC-Cemented Carbide-Based Hardmetals by Selective Laser Melting (SLM) Additive Manufacturing (AM): Microstructure Characteristics and Formation Mechanisms," in *Laser Additive Manufacturing of High-Performance Materials*, Berlin, Heidelberg: Springer, 2015.

[249] R. S. Khmyrov, V. A. Safronov, and A. V. Gusarov, "Obtaining crack-free WC-Co alloys by selective laser melting," *Phys. Procedia*, vol. 83, pp. 874–881, 2016.

[250] J. Yamada, H. Ibe, K. Sato, and N. Kato, "Functional WC Cemented Carbide by the Direct Selective Laser Forming," Gifu, 2017.

[251] R. S. Khmyrov, A. P. Shevchukov, A. V. Gusarov, and T. V. Tarasova, "Phase composition and microstructure of WC–Co alloys obtained by selective laser melting," *Mech. Ind.*, vol. 18, no. 7, p. 714, 2017.

[252] R. S. Khmyrov, V. A. Safronov, and A. V. Gusarov, "Synthesis of Nanostructured WC-Co Hardmetal by Selective Laser Melting," *Procedia IUTAM*, vol. 23, pp. 114–119, 2017.

[253] A. Domashenkov, A. Borbély, and I. Smurov, "Structural modifications of WC/Co nanophased and conventional powders processed by selective laser melting," *Mater. Manuf. Process.*, vol. 32, no. 1, pp. 93–100, 2017.

[254] T. Schubert, A. Breninek, T. Bernthaler, D. Sellmer, M. Schneider, and G. Schneider, "Investigations on Additive Manufacturing of WC-Co Hard Metals by Laser Beam Melting," *Pract. Metallogr.*, vol. 54, no. 9, pp. 577–595, 2017.

[255] S. Kumar, "Process chain development for additive manufacturing of cemented carbide," *J. Manuf. Process.*, vol. 34, no. June, pp. 121–130, 2018.

[256] K. J. A. Brookes, "Additive hardmetals: Johannes Pötschke of Fraunhofer IKTS surveys the field," *Met. Powder Rep.*, vol. 73, no. 3, pp. 128–132, 2018.

[257] C. W. Li, K. C. Chang, A. C. Yeh, J. W. Yeh, and S. J. Lin, "Microstructure characterization of cemented carbide fabricated by selective laser melting process," *Int. J. Refract. Met. Hard Mater.*, vol. 75, no. April, pp. 225–233, 2018.

[258] D. Gu, J. Ma, H. Chen, K. Lin, and L. Xi, "Laser additive manufactured WC reinforced Fe-based composites with gradient reinforcement/matrix interface and enhanced performance," *Compos. Struct.*, vol. 192, no. July 2017, pp. 387–396, 2018.

[259] N. Ku, J. J. Pittari, S. Kilczewski, and A. Kudzal, "Additive Manufacturing of Cemented Tungsten Carbide with a Cobalt-Free Alloy Binder by Selective Laser Melting for High-Hardness Applications," *Jom*, vol. 71, no. 4, pp. 1535–1542, 2019.

[260] M. Al-Thamir, D. G. McCartney, M. Simonelli, R. Hague, and A. Clare, "Processability of atypical WC-Co composite feedstock by laser powder-bed fusion," *Materials (Basel).*, vol. 13, no. 1, pp. 1–12, 2020.

[261] K. J. A. Brookes, "3D-printing style additive manufacturing for commercial hardmetals," *Met. Powder Rep.*, vol. 70, no. 3, pp. 137–140, 2015.

[262] C. R. Knowles, T. H. Becker, and R. B. Tait, "Residual Stress Measurement and Structural Integrity Implications for Selective Laser Melted Ti-6Al-4V," *South African J. Ind. Eng.*, vol. 23, no. 3, pp. 119–129, 2012.

[263] A. Krawitz and E. Drake, "Residual stresses in cemented carbides - An overview," *Int. J. Refract. Met. Hard Mater.*, vol. 49, no. 1, pp. 27–35, 2015.

[264] H. O. Andrén, "Microstructures of cemented carbides," *Mater. Des.*, vol. 22, no. 6, pp. 491–498, 2001.

[265] A. C. Van Staden, D. Hagedorn-Hansen, G. A. Oosthuizen, and N. Sacks, "Characteristics of single layer Selective Laser Melted tool grade cemented tungsten carbide," in *International Conference on Competitive Manufacturing, COMA '16*, 2016, pp. 141–146.

[266] B. Vrancken, "Study of Residual Stresses in Selective Laser Melting," KU Leuven, 2016.

[267] A. Hussein, L. Hao, C. Yan, and R. Everson, "Finite element simulation of the temperature and stress fields in single layers built without-support in selective laser melting," *Mater. Des.*, vol. 52, no. November 2016, pp. 638–647, 2013.

[268] M. Shiomi, K. Osakada, K. Nakamura, T. Yamashita, and F. Abe, "Residual Stress within Metallic Model Made by Selective Laser Melting Process," *Ann. CIRP*, vol. 53, no. 1, pp. 195–198, 2004.

[269] T. Achee, G. Guss, A. Elwany, and M. Matthews, "Laser Pre-sintering for Denudation Reduction in the Laser Powder Bed Fusion Additive Manufacturing of Ti-6Al-4V Alloy," *Addit. Manuf.*, p. 101985, 2021.

[270] Prithvi, "5 Reasons Conventional Product Development does not lead to Innovation," *The 2GEMBA Blog*, 2020. [Online]. Available: https://2gemba.com/5-reasons-conventional-product-development-does-not-lead-to-innovation/. [Accessed: 11-Jan-2021].

[271] J. M. Morgan and J. K. Liker, *Designing the Future*. New York: McGraw-Hill Education, 2019.

[272] J. Cerejo and A. Barbosa, "The Application of Design Thinking Methodology on Research Practices: a Mind-Map of Tools and Methods | Álvaro Barbosa and Joana Cerejo -

Academia.edu," *Educ. Media Des. Think. Educ.*, no. September, pp. 1–10, 2012.

[273] D. C. Montgomery, *Design and Analysis of Experiments, 10th Edition*. Wiley, 2019.

[274] J. Antony, "Fundamentals of Designing Experiments.," in *Design of Experiments for Engineers and Scientists*, London: Elsevier Ltd., 2003, pp. 6–16.

[275] M. Cavazzuti, "Design of Experiments," in *Optimization Methods: From Theory to Design*, Heidelberg: Springer-Verlag, 2013, pp. 13–42.

[276] M. Averyanova, D. Lyon, E. Nationale, E. Cicala, P. Bertrand, and D. Grevey, "Experimental design approach to optimize selective laser melting of martensitic 17-4 PH powder : part I – single laser tracks and first layer," vol. 1, pp. 28–37, 2012.

[277] NCSS, "NCSS Statistical Software," 2018. [Online]. Available: https://www.ncss.com/software/ncss/ncss-documentation/#DesignofExperiments.

[278] S. D. Bolboacă and L. Jäntschi, "Design of Experiments: Useful Orthogonal Arrays for Number of Experiments from 4 to 16," *Entropy*, vol. 9, pp. 198–232, 2007.

[279] P. Sahoo and T. K. Barman, "ANN modelling of fractal dimension in machining," in *Mechatronics and Manufacturing Engineering*, Woodhead publishing ltd., 2012, pp. 159–226.

[280] B. Ait-Amir, P. Pougnet, and A. El Hami, "Meta-Model Development," in *Embedded Mechatronic Systems 2*, Elsevier, 2015, pp. 151–179.

[281] A. N. Chatterjee, S. Kumar, P. Saha, P. K. Mishra, and A. Roy Choudhury, "An experimental design approach to selective laser sintering of low carbon steel," *J. Mater. Process. Technol.*, vol. 136, no. 1–3, pp. 151–157, 2003.

[282] "Engineering Statistics Handbook." [Online]. Available: https://www.itl.nist.gov/div898/handbook/pri/section5/pri521.htm. [Accessed: 12-Jun-2018].

[283] M. Letenneur, A. Kreitcberg, and V. Brailovski, "Optimization of laser powder bed fusion processing using a combination of melt pool modeling and design of experiment approaches: Density control," *J. Manuf. Mater. Process.*, vol. 3, no. 1, 2019.

[284] M. Mele, A. Bergmann, G. Campana, and T. Pilz, "Experimental investigation into the effect of supports and overhangs on accuracy and roughness in laser powder bed fusion," *Opt. Laser Technol.*, vol. 140, no. February, p. 107024, 2021.

[285] R. H. Myers and D. C. Montgomery, *Response Surface Methodology: Process and Product Optimisation Using Designed Experiments*. New York: Wiley, 1994.

[286] M. J. Matthews, G. Guss, S. A. Khairallah, A. M. Rubenchik, P. J. Depond, and W. E. King, "Denudation of metal powder layers in laser powder bed fusion processes," *Acta Mater.*, vol. 114, pp. 33–42, 2016.

[287] C. Tang, K. Q. Le, and C. H. Wong, "Physics of humping formation in laser powder bed fusion," *Int. J. Heat Mass Transf.*, vol. 149, 2020.

[288] G. Polya, *How to Solve It*. Princeton University, 1945.

[289] Praxair, "Powder Solutions Catalogue," 2014. [Online]. Available: https://www.praxairsurfacetechnologies.com/-/media/corporate/praxairsurface/us/documents/brochures/powders-solutions-catalog.pdf.

[290] Kennametal, "Stellite Alloys [Brochure]," Pennsylvania, 2018.

[291] S. Vock, B. Klöden, A. Kirchner, T. Weißgärber, and B. Kieback, "Powders for powder bed fusion: a review," *Prog. Addit. Manuf.*, vol. 4, no. 4, pp. 383–397, 2019.

[292] K. M. Andersson, "Aqueous Processing of WC-Co Powders," Royal Institute of Technology, 2004.

[293] P. K. Katiyar, P. K. Singh, R. Singh, and A. L. Kumar, "Modes of failure of cemented tungsten carbide tool bits (WC/Co): A study of wear parts," *Int. J. Refract. Met. Hard Mater.*, vol. 54, pp. 27–38, 2016.

[294] I. Konyashin and W. Lengauer, "Sintering mechanisms of functionally graded cemented carbides," *Mater. Sci. Forum*, vol. 835, no. April, pp. 116–198, 2016.

[295] L. V. McCarty, R. Donelson, and R. f. Hehemann, "A diffusion model for tungsten powder carburization," *Metall. Trans. A*, vol. 18, no. 13, pp. 969–974, 1987.

[296] Böhler, "Hot work tool steels," *Tool Steels Prop. Perform.*, pp. 101–144, 2016.

[297] A. Zenani, T. C. Dzogbewu, W. B. Du Preez, and I. Yadroitsev, "Optimum Process Parameters for Direct Metal Laser Sintering of Ti6Al Powder Blend," *Univers. J. Mech. Eng.*, vol. 8, no. 4, pp. 170–182, 2020.

[298] C. M. Olivier, "Evaluating the Effects of Selective Laser Sintering Processing Parameters on the Melt Pool Dimensions of Tungsten Carbide through Numerical Thermal Modeling," Stellenbosch University, 2019.

[299] S. A. Khairallah, A. T. Anderson, A. Rubenchik, and W. E. King, "Laser powder-bed fusion additive manufacturing: Physics of complex melt flow and formation mechanisms of pores, spatter, and denudation zones," *Acta Mater.*, vol. 108, pp. 36–45, 2016.

[300] Y. C. Wu *et al.*, "Numerical modeling of melt-pool behavior in selective laser melting with random powder distribution and experimental validation," *J. Mater. Process. Technol.*, vol. 254, no. July 2017, pp. 72–78, 2018.

[301] T. Heeling, M. Cloots, and K. Wegener, "Melt pool simulation for the evaluation of process parameters in selective laser melting," *Addit. Manuf.*, vol. 14, pp. 116–125, 2017.

[302] M. Boccalini and H. Goldenstein, "Solidification of high speed steels," *Int. Mater. Rev.*, vol. 46, no. 2, pp. 92–115, 2001.

[303] Struers, "Metallographic preparation of powder metallurgy parts," 2019.

[304] T. Schwanekamp, J. Gussone, and M. Reuber, "Impact of laser irradiation on microstructure

and phase development of tungsten carbide - cobalt," *Procedia CIRP*, vol. 94, pp. 239–242, 2020.

[305] J. Pötschke, T. Gestrich, and V. Richter, "Grain growth inhibition of hardmetals during initial heat-up," *Int. J. Refract. Met. Hard Mater.*, vol. 72, no. October 2017, pp. 117–125, 2018.

[306] E. Malekipour and H. El-Mounayri, "Scanning strategies in the PBF Process - A Critical Review," in *ASME International Mechanical Engineering Congress and Exposition*, 2021, no. February.

[307] A. Checchi, G. Bissacco, and H. N. Hansen, "A mechanistic model for the prediction of cutting forces in the face-milling of ductile spheroidal cast iron components for wind industry application," *Procedia CIRP*, vol. 77, no. Hpc, pp. 231–234, 2018.

[308] Hofmann, "Material Data CL 41TI ELI Titanium Alloy," Lichtenfels, 2014.

[309] Concept Laser GmbH, "M2 Cusing Operation Manual," Germany, 2010.

[310] Rofin, "Rofin Starfiber." [Online]. Available: https://www.rofin.com/fileadmin/user_upload/content/5_produkte/3_faserlaser/Dat_StarFiber_100-600_V1_2015_E.pdf. [Accessed: 14-Oct-2016].

[311] ASTM International, "ASTM B962-13: Standard Test Methods for Density of Compacted or Sintered Powder Metallurgy (PM) Products Using Archimedes' Principle," 2013.

[312] ASTM International, "ASTM B-311: Standard Test Method for Density of Powder Metallurgy (PM) Materials Containing Less Than Two Percent Porosity 1," *ASTM Int. West Conshohocken*, pp. 1–5, 2008.

[313] Subcommittee B09.06, "ASTM B294-17: Standard Test Method for Hardness Testing of Cemented Carbides." [Online]. Available: https://www.astm.org/Standards/B294.htm. [Accessed: 01-May-2019].

[314] Zwick Roell, "Zwick Roell," 2020. [Online]. Available: https://www.zwickroell.com/products/hardness-testing-machines/rockwell-hardness-testers/zhr/.

[315] General Carbide, "Rockwell A to Vickers HV30 Hardness conversion chart."

[316] O. Corporation, "Olympus Stereomicroscope System SZX7." [Online]. Available: http://www.olympusamerica.com/files/seg_bio/szx7_brochure.pdf. [Accessed: 01-Nov-2016].

[317] O. Corporation, "GX 51 Inverted Microscope." [Online]. Available: http://www.olympus-ims.com/en/microscope/gx51/#!cms[tab]=%2Fmicroscope%2Fgx51%2Fspecifications. [Accessed: 01-Nov-2016].

[318] Landolt-Börnstein, *Properties of hardmetals and cermets*, Group VIII. Springer Materials, 2002.

Appendices

Appendix A: Measurement and Experimental Equipment

An understanding of the instruments that were used in a study is very important. The research outputs are limited by the capabilities of the research instruments and the ability of the researcher to correctly use them. In order to complete the research, several machines and analytical equipment were used. These machines and their setup processes are discussed in the following sections and a basic description is given for each machine. The parameters and methodologies used for analysis for some of the equipment are also discussed in this section, since the same equipment was used in multiple experimentation throughout this study.

A.1. Concept Laser M2 Cusing L-PBF Machine

To produce the experimental samples a L-PBF machine was used. The STC-LAM at the University of Stellenbosch has a Concept Laser M2 Laser Cusing machine (Lichtenfells, Germany) shown in Figure A.1. The technical data of the machine can be observed below in Table A.1.

Figure A.1: Concept Laser M2 Cusing Machine at Stellenbosch University

Table A.1: M2 Laser Cusing machine specifications adapted from [308]

Specification Description	Values
Build Envelope LaserCUSING	250 mm x 250 mm x 280 mm (x, y, z)
Layer Thickness LaserCUSING	20 µm – 50 µm
Production Speed	2 – 20 cm³/hour (material dependant)
Laser System	Fibre Laser 200 Watt
Maximum Scanning Speed	7 m/s
Connected Loads	Power Consumption 7.0 kW
	Power Supply 3/N/PE AC 400V, 32A
	5 bar Compressed Air
Inert Gas Consumption	Approximately 2.5 m³/hour
Operating Conditions	15 - 35°C

The machine setup and experimentation process were followed according to the process chain in Figure A.2. However, the post processing step was not followed as per the figure. Initial powder acceptance and preparation was not included in the process chain figure.

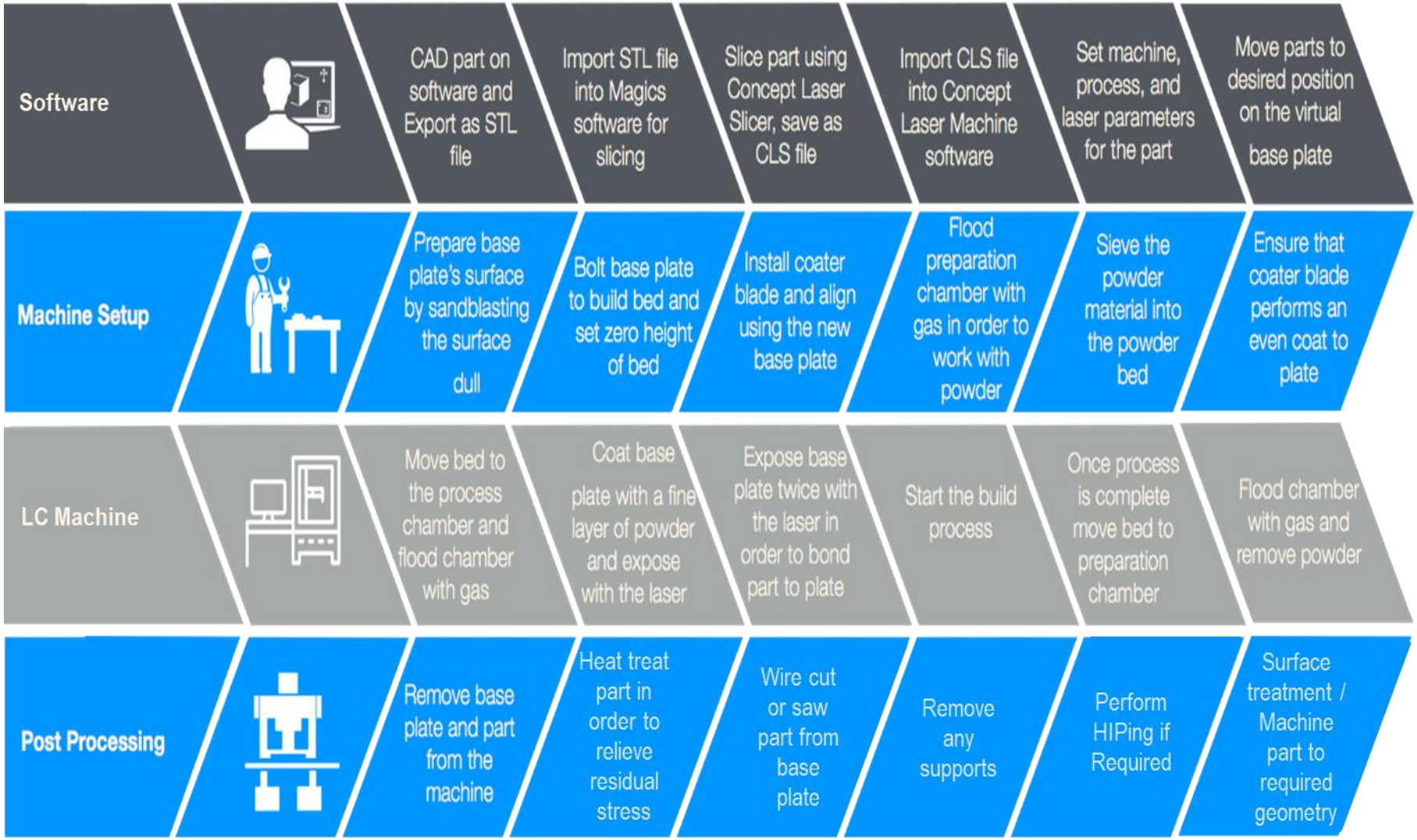

Figure A.2: Summarised L-PBF process chain to create a part on the M2 Cusing machine from Concept Laser GmbH.

The M2 Cusing machine has several parameters that the user can change and others that cannot be changed. These parameters are classed into three groups, namely, Machine Parameters, Cusing Process Parameters, and Laser Parameters. Each of these parameter sets, and the variable parameters are displayed in the following sections.

A.1.1. Machine Parameters

The variable machine parameters on the Concept Laser machine's software can be observed in Table A.2.

Table A.2: M2 Cusing Machine parameters that can be varied by the user [309]

Parameter	Variable Values
Coater blade type	Flexible rubber blade or Steel blade
Layer thickness	20 – 50 µm
Speed	
Coater in process	1-1000 mm/s
Coater manual	1-1000 mm/s
Extra coating	1-1000 mm/s
Fan	
Revolution Process	0-100%
Filter Clean blow	
Time interval for blow	0 - 300 min
Number of cleans	0 - 10
Break between	5000 ms
Pressure in Glovebox	
Overpressure	0.01 – 0.1 Bar

A.1.2. Cusing Process Parameters

The variable Cusing process parameters on the Concept Laser machine software can be observed in Table A.3.

Table A.3: M2 Cusing process parameters that can be varied by the user [309]

Parameter	Variable Values
Exposure sequence	Vectors then Contours or Contours then Vectors
Powder Delivering Height	
Correction Factor	100 – 1000%
Start Slices	1-10 [Slices]
Factor	100 – 1000%
Additional Slices	
Number of additional slices	0 – 100 [Slices]
Scanning System	
Waiting time for beam off	0.0 - 100.0 ms
Waiting time for beam on	0.0 - 100.0 ms
Waiting time at edges	0.0 - 100.0 ms
Waiting time after laser jump max	0.0 - 100.0 ms

Waiting time after laser jump min	0.0 - 100.0 ms
Saturation after in mm	0.0 - 100.0 mm

A.1.3. Laser Parameters

The variable laser parameters on the Concept Laser machine software can be observed in Table A.4.

Table A.4: M2 Cusing laser parameters that can be varied by the user [309]

Parameter	Units	Core	Skin	Contours	Support
Power	Watts	20-200	20-200	20-200	20-200
Scan Speed	mm/s	1-7000	1-7000	1-7000	1-7000
Focus/Spot Diameter (d)	µm	70 - 200	70 - 200	70 - 200	70 - 200
Operation Mode	-	CW/Pulse	CW/Pulse	CW/Pulse	CW/Pulse
Hatching	-	5 Hatch Patterns	6 Hatch Patterns	Contour Scan	-
Hatch Spacing (a1)	-	0 - 10	0 - 10	-	-
Beam Compensation (a2)	-	0 - 10	0 - 10	-	-
Exposure	-	Expose every n slice	Expose every n slice	Expose every n slice	Expose every n slice

A.1.4. Rofin StarFiber Laser

The L-PBF process requires a special laser in order perform the fast, accurate, scans which the AM process demands. The laser that came with the Concept Laser M2 Machine is the Rofin StarFiber 200W laser (Michigan, United States). The specifications of the laser are displayed in Table A.5.

Table A.5: Rofin Starfiber 200 laser specifications [310]

Specification Description	Units	Value
Wavelength	nm	1070
Max. average power	W	200
Pulse frequency	kHz	Single shot up to 170
Pulse width	µs	1 - cw
Beam diameter	mm	0.05
Beam divergence (86% level)	mrad	collimated
Aperture	mm	0.15

A.2. EOSINT M 280 DMLS Machine

The EOSINT M280 at the CRPM at the Central University of Technology was utilised for some of the testing due to the machine at the STC being non-operational. The EOSINT machine used as well as the machine specifications can be observed in Figure A.3 and Table A.6 respectively.

Figure A.3: EOSINT M280 at CUT CRPM

Table A.6: Specifications of the EOSINT M280 at CUT

Specification Description	Values
Build Envelope	250 mm x 250 mm x 325 mm (x, y, z)
Layer Thickness	20 µm – 50 µm
Production Speed	2 – 20 cm³/hour (material dependant)
Laser System	Yb-Fibre Laser 400 Watt
Maximum Scanning Speed	7 m/s
Connected Loads	Power Consumption 8.5 kW
	Power Supply 3/N/PE AC 400V, 32A
	7 bar Compressed Air at 20 m³/h
Inert Gas Consumption	Approximately 100 l/min at 4 bar

A.3. AgieCharmilles CA20U EDM Wire-cutting Machine

All sample removal from the base plate and cutting of samples was performed with EDM wire-cutting on the GF AgieCharmilles CA20U from GF Machining Solutions (Geneva, Switzerland), which is depicted in Figure A.4.

Figure A.4: GF AgieCharmilles CA20 Wire-EDM

The cutting parameters used can be found in Table A.7. A brass wire thickness of 0.25 mm was used.

Table A.7: Cutting parameters used for Wirecutting the Tungsten Carbide samples off the base plate

Parameter Name	Value	Parameter Name	Value
Module	0	WTy	Entry
I	15	Reg	0
UHP	0	p [bar]	13
ISH	-2	k [uS]	5
P	50	SMode	0
Ton	28	Ppos	0
SSoll	30	Pneg	1
SPL	0	Str	8
TSET	Entry cut	Tmis	Default
FW [N]	17	Teros	Default
AW [mm/s]	165	VS	0.01
MS	0	Taper	0
B	1	Q	Q13

A.5. Archimedes Density Testing

The density testing was conducted under laboratory conditions based on the Archimedes method with reference to the applicable ASTM standards [311], [312]. All test samples were immerged in ethanol in an ultrasonic cleaner for 10 minutes to clean the surfaces. The samples were then dried entirely using a sample dryer and were left in the testing environment for several days. The weighing of the samples was performed on a Kern ABT 120 5DM analytical balance (Figure A.5) with a readability of 0.1 mg and a repeatability of 0.1 mg for the density testing weight range (+42 g). Lab grade 99% Ethanol was used for liquid-impregnation and the liquid for buoyancy. No vacuum pump was used for the impregnation process and the samples were submerged for impregnation for 30 minutes.

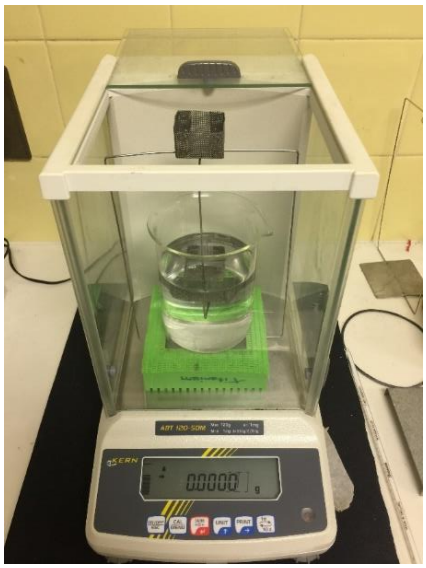

Figure A.5: Kern ABT 120-5DM analytical balance set up for Archimedes density analysis

A.6. Hardness Testing

The Rockwell Hardness Tests were performed on a Zwick Roell ZHR Indotec Rockwell Hardness Tester (Figure A.6) with reference to the applicable ASTM standard [313]. The samples were tested on the HRA scale with an applied weight of 60 kgf and a hold time of 3 seconds. A diamond indenter was used for all tests.

Figure A.6: Zwick Roell ZHR Indotec Rockwell Hardness tester reproduced from [314]

The hardness testing points for the cuboid and CNMA samples can be observed in Figure A.7. Six points were measured on all the cuboid samples and four points were measured on all of the CNMA samples. The average hardness was reported for each.

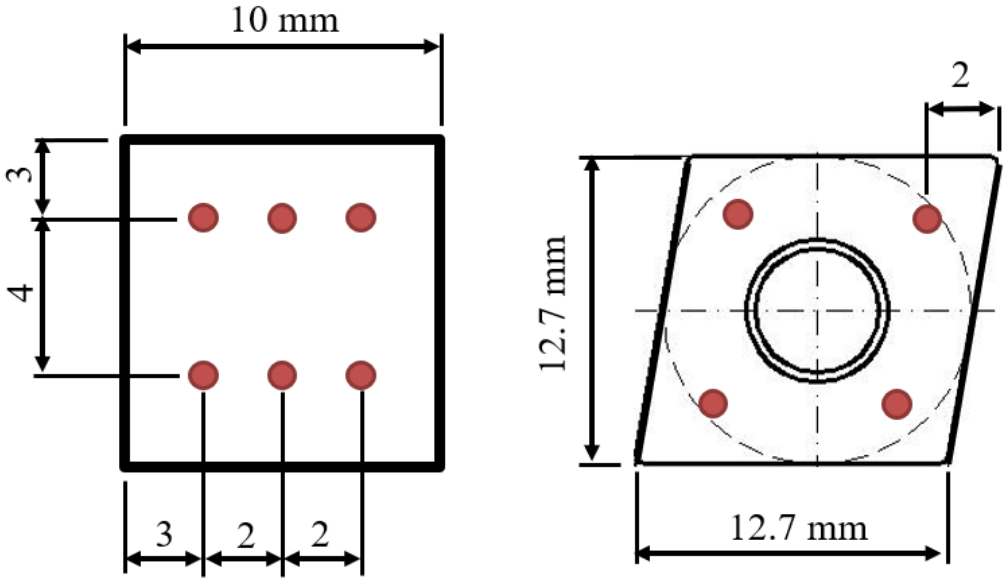

Figure A.7: Hardness testing points for the (Left) Cuboid samples and (Right) CNMA samples

The hardness conversion charts for Rockwell HRA to HRC as well as Hardness Vickers HV10/30 to HRA can be observed in Table A.8 and Table A.9 respectively.

Table A.8: Rockwell Hardness Conversion (HRA – HRC) adapted from [43]

Rockwell "A"	Rockwell "C"
91.8 – 92.8	79.5 – 81.5
91.5 – 92.5	79.0 – 81.0
90.5 – 91.5	77.0 – 79.0
90.2 – 91.2	76.5 – 78.5
89.8 – 90.8	75.6 – 77.6
89.0 – 90.0	74.0 – 76.0
88.5 – 89.5	73.0 – 75.0
88.0 – 89.0	72.0 – 74.0
87.5 – 88.5	71.0 – 73.0
87.0 – 88.0	71.0 – 72.0
86.0 – 87.0	69.0 – 71.0
83.0 – 84.5	63.0 – 66.0
81.5 – 83.0	61.0 – 63.0

Table A.9: Vickers to Rockwell Hardness Conversion (HV10/30 – HRA) adapted from [315]

HV10	HV30	HRA
800	790	83.4
900	890	84.7
1000	990	86.0
1100	1090	87.3
1200	1190	88.2
1300	1290	89.4
1400	1380	90.3
1500	1480	91.1
1600	1580	91.8
1700	1680	92.4
1800	1770	92.9
1900	1870	93.4
2000	1960	93.8

A.7. Microscopy Systems

A.7.1. Electron Microscopy

All scanning electron microscopy and was performed on the Zeiss MERLIN field emission scanning electron microscope (FE-SEM) (Oberkochen, Germany), at the Stellenbosch University Central Analytical Facilities, which can be observed in Figure A.8. The system is fitted with the following detectors:

- Secondary Electron Detector (SED)
- Variable Pressure Secondary Electron Detector (VPSED)
- Backscattered Electron Detector (BSD)
- Scanning Transmission Electron Detector (STEM)
- Energy Dispersive X-ray Spectrometer (EDS or EDX)

Figure A.8: Zeiss MERLIN SEM at the Central Analytical Facility at Stellenbosch University

Compositional scans were conducted with Energy Dispersive X-Ray Spectroscopy using a beam voltage of 20 kV and working distance of 9.5 mm. The back scatter detector was inserted for the measurements. Large areas of the physical ground and polished samples were selected, and rectangular emission zones were drawn for EDS measurement. The readings were normalised over the area. The EDS measurements were analysed with AZtecTEM software from Oxford Instruments (Abingdon, United Kingdom).

A.7.2. Optical Microscopy

The Olympus SZX 7 stereomicroscope and GX 51 inverted microscope were used to inspect samples and hatch melt pools. The two microscopes located at Stellenbosch University's Material Science Research Group laboratory at the Mechanical and Mechatronic Engineering department can be observed in Figure A.9.

Figure A.9: (Left) Olympus SZX 7 Stereomicroscope and (Right) Olympus GX 51 Inverted Microscope

The specifications of the SZX7 and the GX 51 can be observed in Table A.10. The SC30 camera is used on both of the microscopes, to duplicate the image onto a computer. The Stream Essentials software was used for the camera control and to view the camera images in real time. Stream Essentials can also be utilised to measure the distance between pixels of microscope images. The magnification options of the microscopes as well as the important camera information is displayed in Table A.10.

Table A.10: Olympus SZX 7 Stereomicroscope, GX 51 Microscope and SC30 Camera Specifications [316], [317]

Specification Description	Value
Olympus SZX 7	
Zoom Ratio Values	7:1 (0.8x, 1x, 1.6x, 2x, 3.2x, 4.8x, 5.6x)
Light Source	White LED transmitted illumination stand
Olympus GX 51	
Zoom Ratio Values	5x, 10x, 20x, 50x, 100x
Light Source	100 W Halogen
SC30 Camera	
Total pixels	3.3 megapixel CMOS Sensor
Image Sensor	CMOS Sensor
Resolution	1024 x 768 pixels at 28 fps
Exposure Range	57 µs – 75 s
Software	Stream Essentials

A.8. X-ray Diffraction

All x-ray diffraction was performed on the Bruker D2 PHASER (Karlsruhe, Germany) benchtop powder diffractometer at the Stellenbosch University Barbour Laboratory, managed by Leigh Loots. The Bruker D2 Phaser diffractometer with Bragg−Brentano geometry uses Cu Kα radiation (λ = 1.5418 Å) at 30 kV and 10 mA. Intensity data were captured with a Lynxeye detector with 2θ scans performed in the range 20−90° with a 0.020° step size while the samples were spun at 30 rpm. The system used can be observed in Figure A.10.

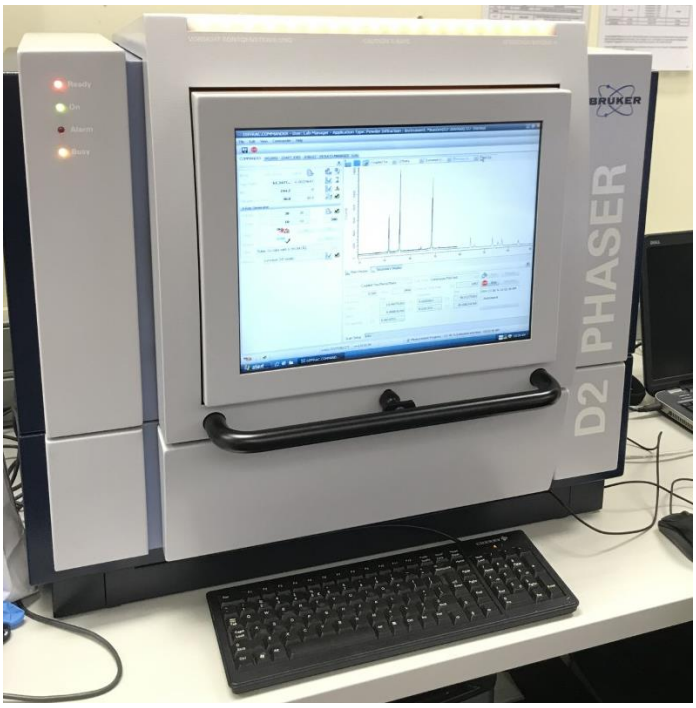

Figure A.10: Bruker D2 Phaser XRD

The readings from the XRD were analysed using Profex 4.2.1 open-source software.

A.9. Surface Roughness Testing

The MarSurf PS10 handheld surface roughness tester (Figure A.11) was utilised for all surface roughness testing. The unit was calibrated before each use using the calibration tab that accompanied the device. A traversing length (*Lt*) of 4.8 mm was used for all readings where possible. On parts smaller than 4.8 mm the traversing length was set to 1.5 mm. The cut-off wavelength (*Lc*) was set to 0.8 mm. The measuring speed was set to 1.0 mm/s with a 350 µm probe. The unit was placed on the sample, levelled, and run. The *Ra*, *Rz*, and *Rmax* were read off the unit.

Figure A.11: MarSurf PS10 Surface Roughness Tester

Appendix B: Experimental Data and Images

B.1. Insert Selection for Use in Study

The insert geometry was selected very early on in this study based on the simplistic and standardised shape, as well as the lack of complex chip breakers. The CNMA 120404 turning insert, which is an ISO standard geometry, fit these criteria and was the insert of choice. The dimensions of the CNMA insert and tool holder are depicted in Figure B.1. The insert is an 80-degree rhomboid shape with a negative rake and neutral cutting direction. The insert has four cutting edges (two per side) depending on the tool holder used. The corner radius for this insert is small and therefore not very strong in comparison to a 0.8 mm radius, which is used in heavier cutting operations. The CNMA 120404 HTi10 insert from Mitsubishi is conventionally not coated and is made from a WC-Co grade without any additional carbide additives. The insert grade falls under the K ISO group which is used for cast irons and alloyed steels (Figure 2.3). The tool holder is the PCLNR2020K12 type which is an ISO Standard lever lock type suitable for light to heavy cutting.

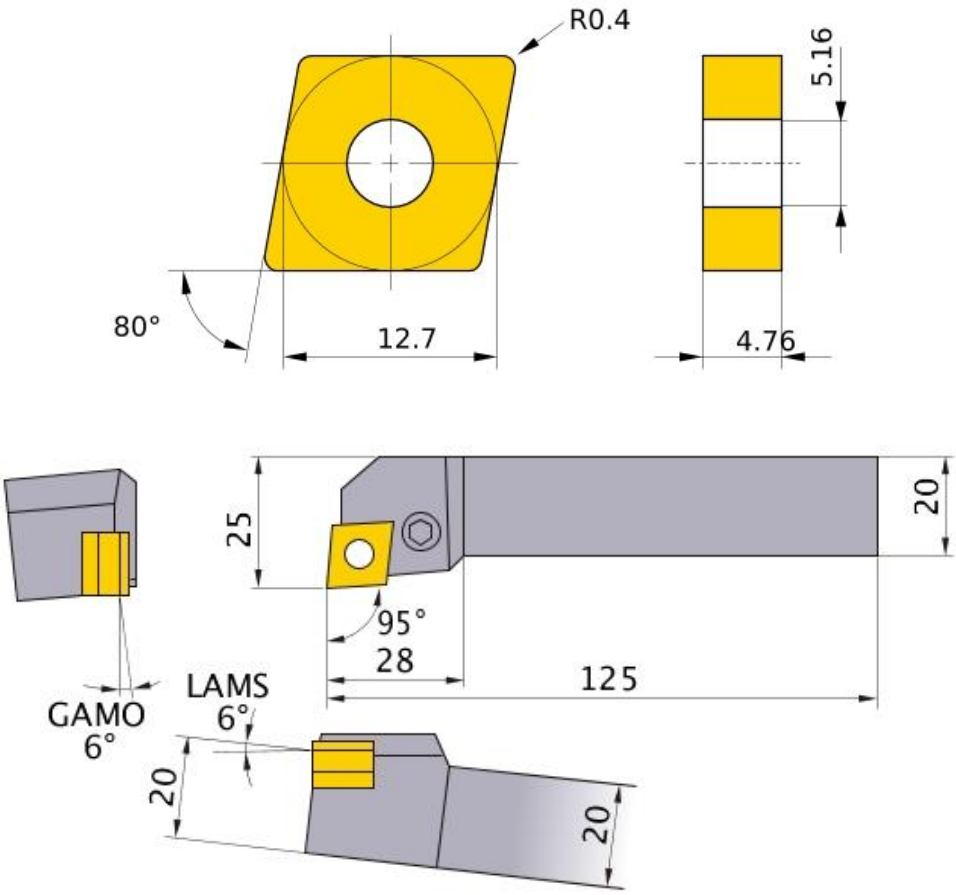

Figure B.1: (Top) ISO Insert CNMA 120404 geometry and dimensions and (Bottom) PCLNR 2020 K12 Tool Holder from [56]

The properties of different grades from Sandvik Coromant can be observed in Table B.1.

Table B.1: Properties for various grades of WC-Co products from Sandvik Coromant adapted from [318]

ISO Code	Sandvik Code	Cobalt Content [wt%]	WC Grain Size	Density [g/cm³]	Hardness [HRA]
	H3F	3.0	Extra Fine	15.30	93.9
K30	H10F	10.0	Extra Fine	14.50	92.1
K40	H15F	15.0	Extra Fine	13.95	90.4
K05	H3M	3.5	Fine	15.20	93.0
	H7M	6.5	Fine	14.85	92.4
K10, K20	H7N	6.0	Medium	14.90	91.4
	H10N	9.5	Medium	14.50	90.4
	H12N	12.0	Medium	14.30	89.3
	H13N	13.0	Medium	14.25	88.6
	H15N	15.0	Medium	13.90	87.5
	H10P	9.5	Medium-coarse	14.50	88.3
	H15P	15.0	Medium-coarse	13.90	86.0
	H10C	9.5	Coarse	14.50	88.3
	H13C	13.0	Coarse	14.20	86.5
	H10T	10.0	Extra-coarse	14.55	85.6

From Table B.1 the graphs for cobalt content vs density and cobalt content vs hardness were plotted and can be observed in Figure B.2 and Figure B.3 respectively.

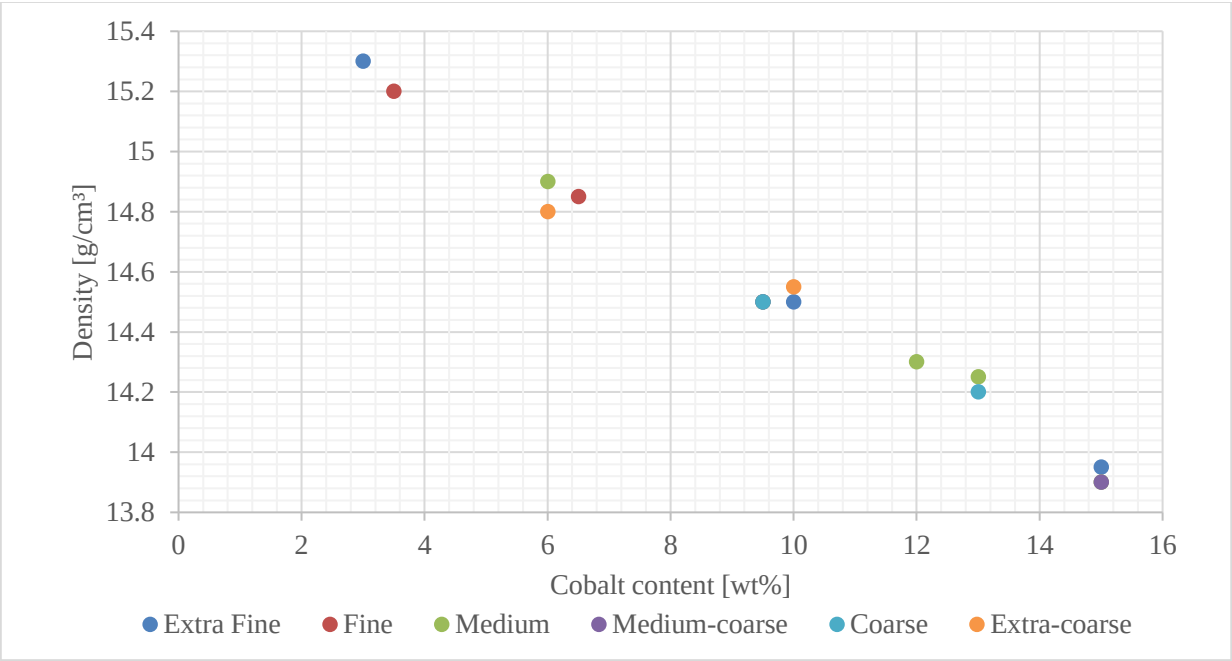

Figure B.2: Graph of cobalt content vs density for the different Sandvik WC-Co grades

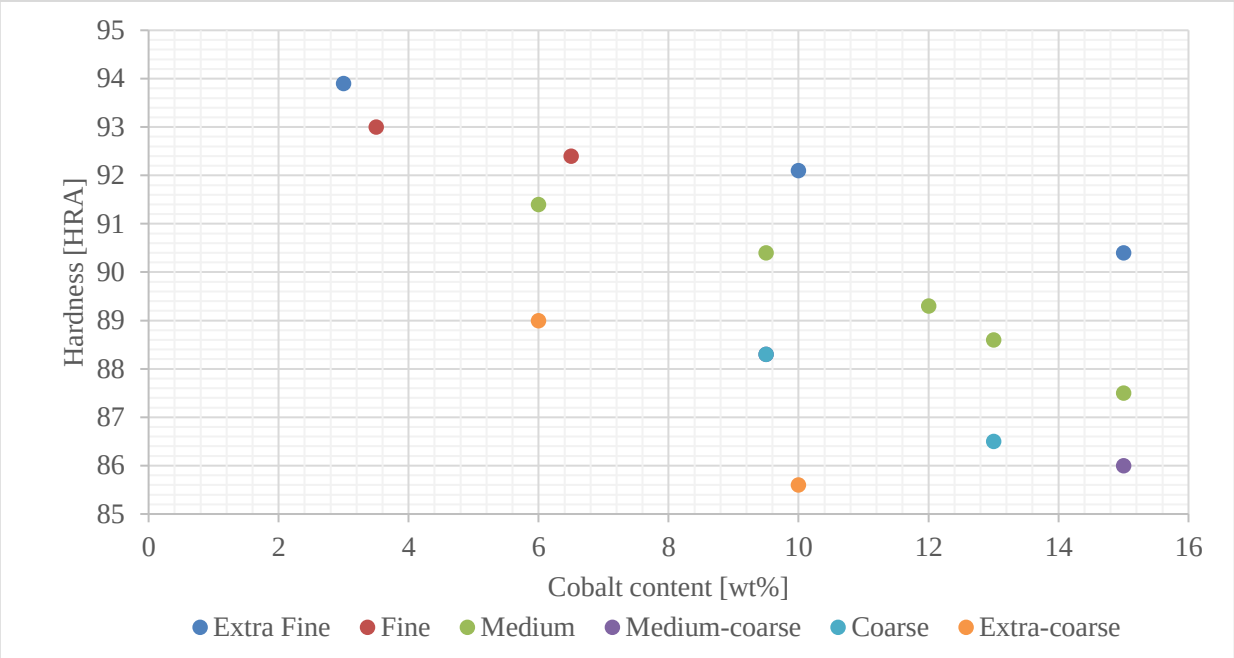

Figure B.3: Graph of cobalt content vs hardness for the different Sandvik WC-Co grades

B.2. Powder Certificates and Benchmark Tool Experimental Results for Sections 6.1 and 6.2

The Certificates of Conformity for the Praxair and Kennametal powders can be observed below:

Certificate of Analysis & Certificate of Conformity

PRAXAIR SURFACE TECHNOLOGIES
1555 Main Street, Indianapolis, IN 46224

Product Name:	1342VM / PST	Customer:	WEARTECH		Ship Date: 31.08.18
Praxair Spec:	011113-BK	Shipping Order #:	70029758		Printed Date:
Item Number	011113-10	Customer PO #:	POA50978		
Lot Number:	343	Quantity:	20	UM: LBS	

All elements measured in weight percent unless otherwise specified. Sampling Method per ASTM B215.

Apparent Density	Test Method	Test Lab	Min	Max	Result	OK
Density (g/cc)	ASTM B212	Praxair	4.6	5.6	4.8	Yes
Chemistry	**Test Method**	**Test Lab**	**Min**	**Max**	**Result**	**OK**
Carbon (total)	Leco	Praxair	5.15	5.75	5.47	Yes
Cobalt	XRF	Praxair	11.00	13.00	11.72	Yes
Iron	XRF	Praxair		0.25	0.06	Yes
Total All Other	Calculation	Praxair		1.00	0.24	Yes
Tungsten	By Difference	Praxair	81.00		82.50	Yes
Hall Flow per ASTM B213	**Test Method**	**Test Lab**	**Min**	**Max**	**Result**	**OK**
Hall Flow (sec)		Praxair	8	14	12	Yes
Microtrac per ASTM B822	**Test Method**	**Test Lab**	**Min**	**Max**	**Result**	**OK**
-15	Microtrac	Praxair		15.0	3.4	Yes
-16	Microtrac	Praxair	3.5	5	3.9	Yes
-22	Microtrac	Praxair		Report	15.2	Yes
-31	Microtrac	Praxair		Report	47.5	Yes
SEM (Scanning Electron Microscope) - Particle Shape Analysis	**Test Method**	**Test Lab**	**Min**	**Max**	**Result**	**OK**
500x (20 Microns)		Praxair			PASS	Yes
Sieve per ASTM B214	**Test Method**	**Test Lab**	**Min**	**Max**	**Result**	**OK**
+230	ASTM B214	Praxair		0.5	0.0	Yes
+325	ASTM B214	Praxair		1.5	0.9	Yes
-230/+325	ASTM B214	Praxair		5.0	0.9	Yes
-270	ASTM B214	Praxair	99.0		100.0	Yes
-325	ASTM B214	Praxair	94.5		99.1	Yes

PST: 176244 C-100864

Spec ranges shown above in italics are target or nominal specifications only.

* indicates test is not required for routine acceptance.

KENNAMETAL

QUALITY CERTIFICATE

Date: 27.05.2020
Purchase order item/date
POA51424 / 13.05.2020
Delivery item/date
8070067076 000010
Order item/date
29720251 000010 / 13.05.2020
Customer number / Customer Material Number
70769617 /

SHIPPED FROM
Kennametal Stellite-Goshen
Goshen, IN 46526
574-534-2585

SOLD TO:
WEARTECH,
187 GALJOEN ROAD
2305 0000
0000 WADEVILLE South Africa

Matnr/Descr : 5438458 495282S005-GOS
STELCAR 9528 - JK117

Characteristic	Unit	Value	Lower	Upper
Batch: 409631-2 QUANTITY: 5.000KG				
Inspection lot : 890000160254				
CHEMICAL ANALYSIS - External Laboratory				
Chemical Analysis by ICP-OE				
Carbon/Sulfur Analysis by Combustion				
Nitrogen/Oxygen Analysis by IGF				
Carbon (C)	%	5.1	SPEC: 4.5	- 5.6
Cobalt (Co)	%	16.9	SPEC: 15.0	- 18.0
Iron (Fe)	%	0.0	MAX: 1.0	
Tungsten		Balance		
Total All Other Elements	%	< 1.0	MAX: 1.0	
PHYSICAL PROPERTIES				
ASTM B212-17 & ASTM B213-17				
Apparent Density	g/cm3	3.8	SPEC: 3.3	- 4.0
Hall Flow	s	15	SPEC: 14	- 21
SIEVE ANALYSIS				
ASTM B214-16, ISO 4497, NF EN 24497				
230 Mesh / 63 Micron	%	0.0	MAX: 0.0	
270 Mesh / 53 Micron	%	0.0	MAX: 2.0	
325 Mesh / 45 Micron	%	2	SPEC: 1	- 7
Pan	%	98	SPEC: 91	- 99

The results from the Archimedes density test of the 10 APMT inserts can be observed in Table B.2.

Table B.2: Density measurements of the 10 APMT inserts using Archimedes Principle

Sample	Density [g/cm³]
1	11.772
2	11.851
3	11.744
4	11.791
5	11.972
6	11.833
7	11.822
8	11.795
9	11.836
10	11.961
SD	0.083
Average	11.834

The 60 hardness testing results from the 10 different APMT inserts can be observed in Table B.3.

Table B.3: MMC APMT inserts Rockwell Hardness results

Sample	1 HRA	2 HRA	3 HRA	4 HRA	5 HRA	6 HRA	Ave HRA	SD
1	89.6	89.8	90.0	89.9	90.0	90.0	89.9	0.2
2	89.6	90.0	89.9	89.6	90.1	90.0	89.9	0.2
3	89.9	90.0	90.0	89.9	90.1	90.2	90.0	0.1
4	89.9	90.0	90.1	90.0	90.2	89.9	90.0	0.1
5	90.0	90.1	90.0	89.9	90.1	90.1	90.0	0.1
6	89.9	90.1	90.1	90.0	90.1	90.1	90.1	0.1
7	89.7	90.2	90.0	89.6	90.1	90.2	90.0	0.3
8	90.0	90.2	90.2	90.1	90.2	90.2	90.2	0.1
9	89.9	90.2	90.1	90.1	90.2	90.2	90.1	0.1
10	89.9	90.2	90.2	89.9	90.2	90.1	90.1	0.1

The properties of the UTi20T grade from Mitsubishi Materials Corporation can be found in Table B.4.

Table B.4: Properties and information on different Mitsubishi tool grades [56]

ISO	Grade	Hardness (HRA)	Thermal Conductivity (W/m•K)*	Thermal Expansion (x10-6/K)	Young's Modulus (GPa)*	T.R.S(GPa)*
P M	UTi20T	90.5	38	5.5	520	2.0
K N	HTi05T	92.5	79	4.5	600	1.5
	HTi10	92.0	79	4.6	630	2.0
S	MT9005/RT9005	92.2	79	4.5	600	2.0
	MT9015/RT9010	92.0	79	4.6	630	2.2
	TF15	91.5	71	5.3	580	2.5

	Grade	ISO Code	Grain Size (μm)	Co (mass%)	TRS (GPa) *1	Hardness		Thermal Conductivity (W/m·K)	Fracture Toughness (MPa·m½)
						HRA *2	HV *3		
Coarse Grain	ZU525H	P30	<3.0	12.5	2.1	90.5	1450	41	9.5
	ZN520	P40	<3.0	12.0	2.2	89.3	1300	40	12.0
	UTi20T	M20	<3.0	9.0	2.0	90.5	1450	38	8.3
	GTi20	V30	<2.5	11.0	2.7	89.0	1270	67	14.1

*1 ISO03327 *2 HRA= Typical Value ISO03738 *3 ISO03878

B.3 Single Track – Feasibility Study Results for Section 6.3

The SEM and EDS images and results for the single track on a tool steel base plate feasibility study can be observed in the following tables.

Table B.5: Single track line scan images and EDS data for all tracks

50 W, 60 mm/s							
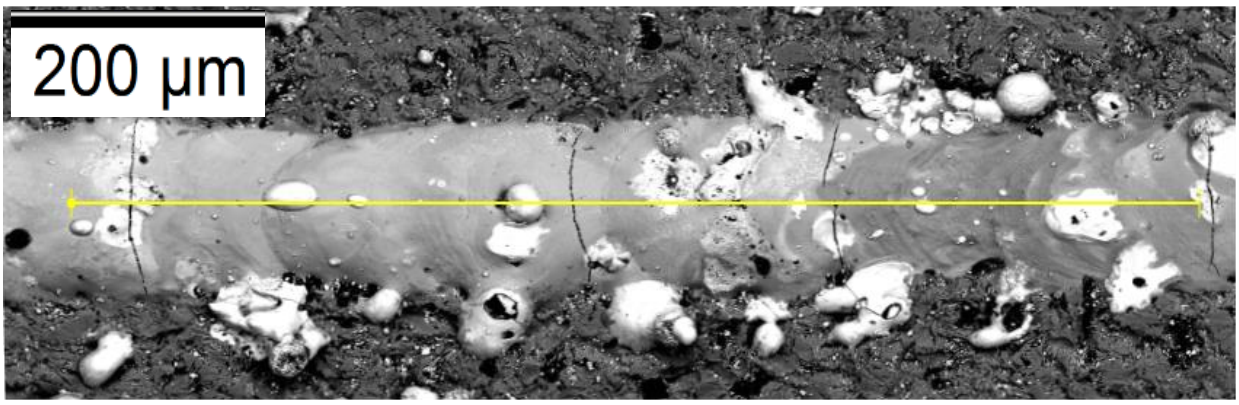							
Fe [wt%]	W [wt%]	C [wt%]	Co [wt%]	Cr [wt%]	Mn [wt%]	Mo [wt]	Si [wt%]
46.26	37.33	8.09	6.65	0.95	0.53	0.14	0.01
50 W, 80 mm/s							
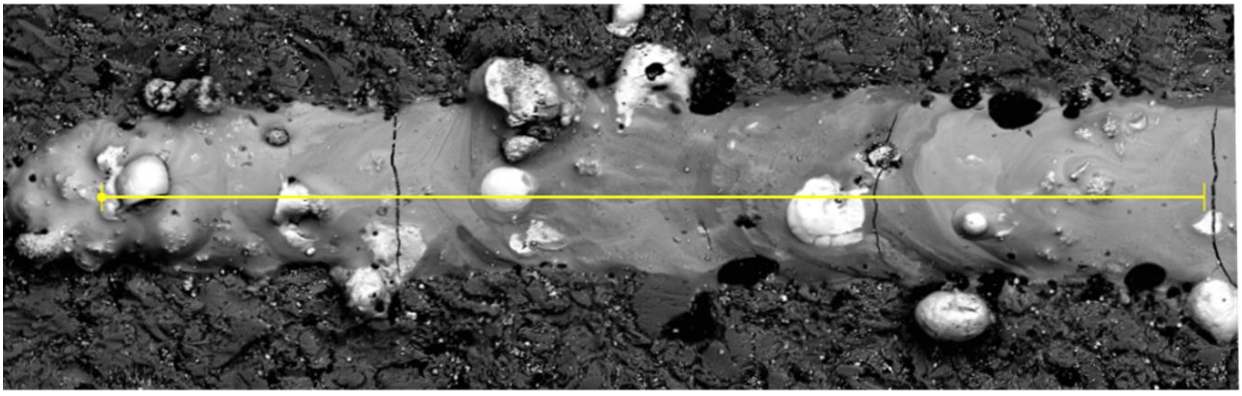							
Fe [wt%]	W [wt%]	C [wt%]	Co [wt%]	Cr [wt%]	Mn [wt%]	Mo [wt]	Si [wt%]
42.06	42.38	6.99	6.20	1.70	0.51	0.13	0.01
50 W, 100 mm/s							
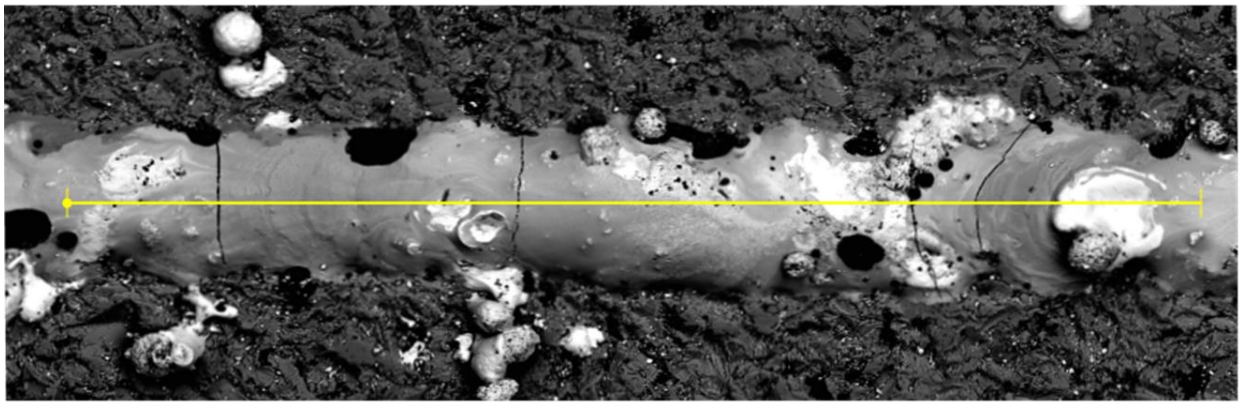							
Fe [wt%]	W [wt%]	C [wt%]	Co [wt%]	Cr [wt%]	Mn [wt%]	Mo [wt]	Si [wt%]
40.90	40.32	9.84	7.31	0.83	0.55	0.14	0.05

50 W, 120 mm/s

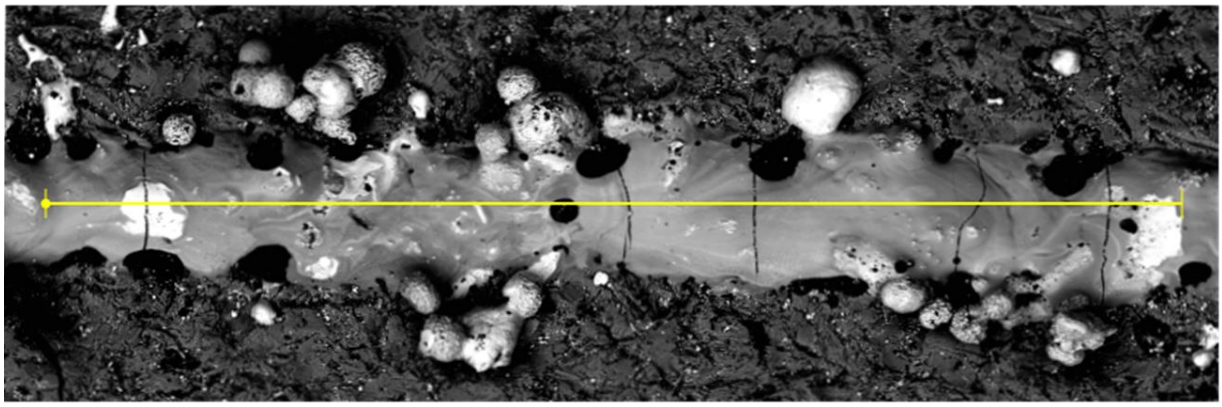

Fe [wt%]	W [wt%]	C [wt%]	Co [wt%]	Cr [wt%]	Mn [wt%]	Mo [wt]	Al [wt%]	Si [wt%]
48.44	35.67	7.20	6.84	0.99	0.57	0.23	0.00	

50 W, 140 mm/s

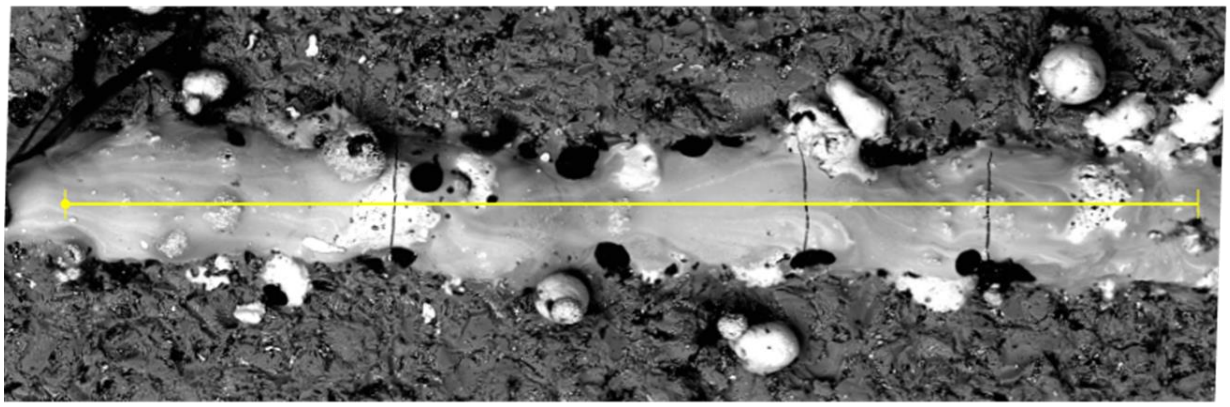

Fe [wt%]	W [wt%]	C [wt%]	Co [wt%]	Cr [wt%]	Mn [wt%]	Mo [wt]	Al [wt%]	Si [wt%]
43.16	38.55	9.59	6.95	1.01	0.55	0.12	0.03	

50 W, 160 mm/s

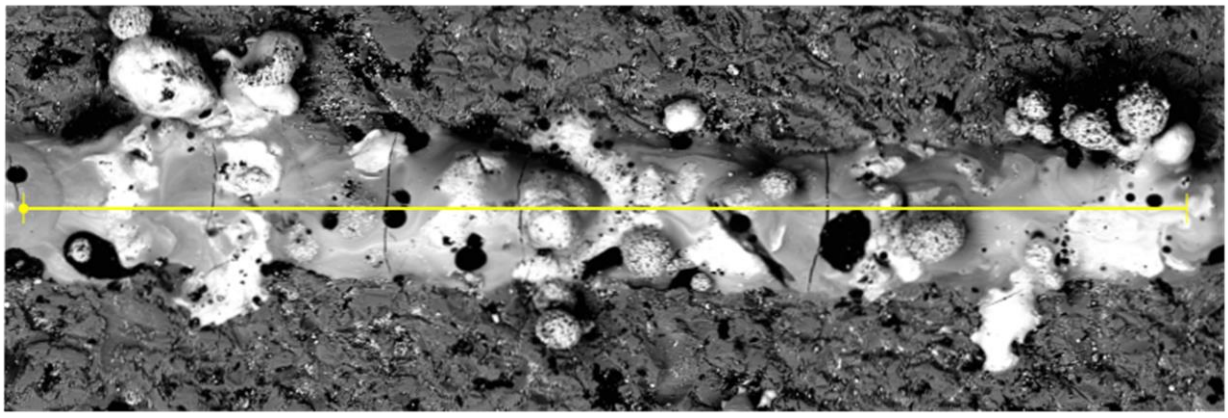

Fe [wt%]	W [wt%]	C [wt%]	Co [wt%]	Cr [wt%]	Mn [wt%]	Mo [wt]	Al [wt%]	Si [wt%]
37.82	41.93	8.84	9.48	0.82	0.56	0.11	0.35	

50 W, 180 mm/s

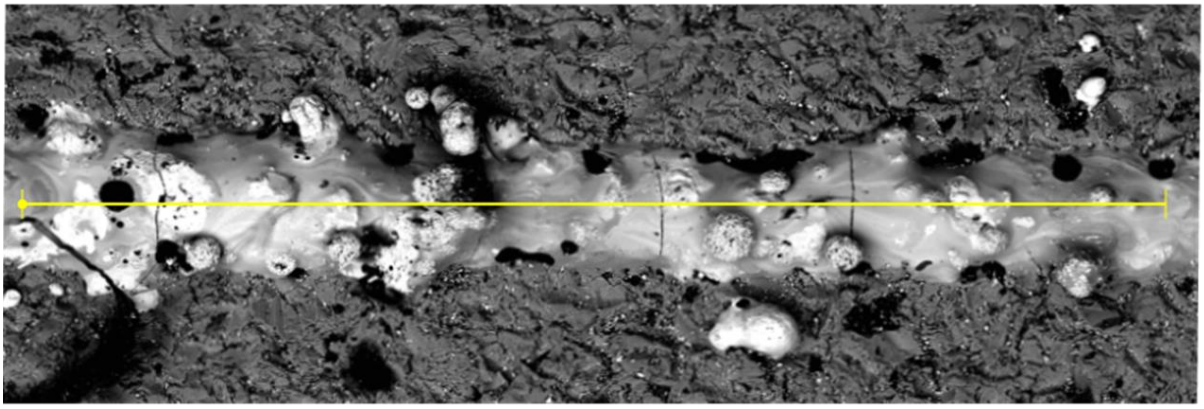

Fe [wt%]	W [wt%]	C [wt%]	Co [wt%]	Cr [wt%]	Mn [wt%]	Mo [wt]	Al [wt%]	Si [wt%]
39.35	40.50	9.98	7.67	0.90	0.73	0.13		0.17

50 W, 200 mm/s

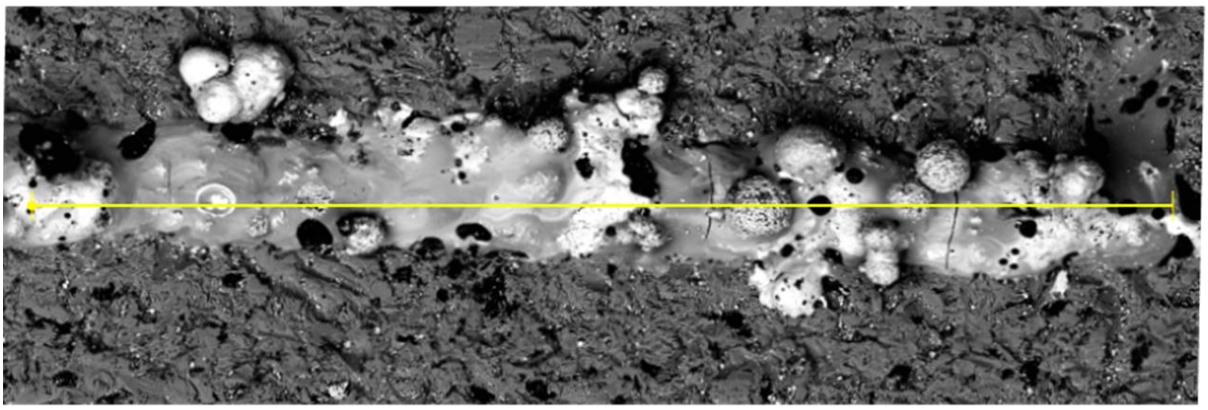

Fe [wt%]	W [wt%]	C [wt%]	Co [wt%]	Cr [wt%]	Mn [wt%]	Mo [wt]	Al [wt%]	Si [wt%]
41.09	41.01	8.38	7.12	0.93	0.88	0.12		0.24

150 W, 400 mm/s

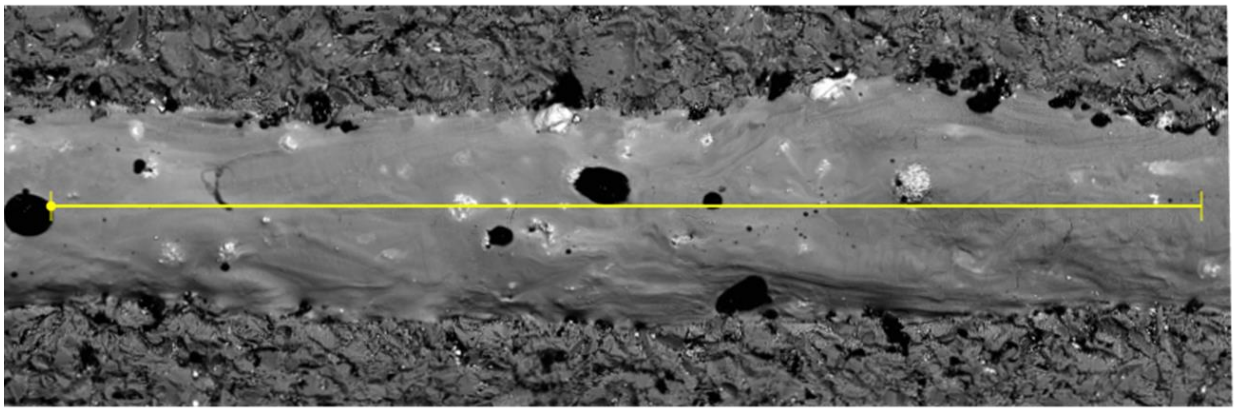

Fe [wt%]	W [wt%]	C [wt%]	Co [wt%]	Cr [wt%]	Mn [wt%]	Mo [wt]	Al [wt%]	Si [wt%]
73.71	14.94	3.90	2.76	1.59	2.03	0.38		0.24

150 W, 600 mm/s

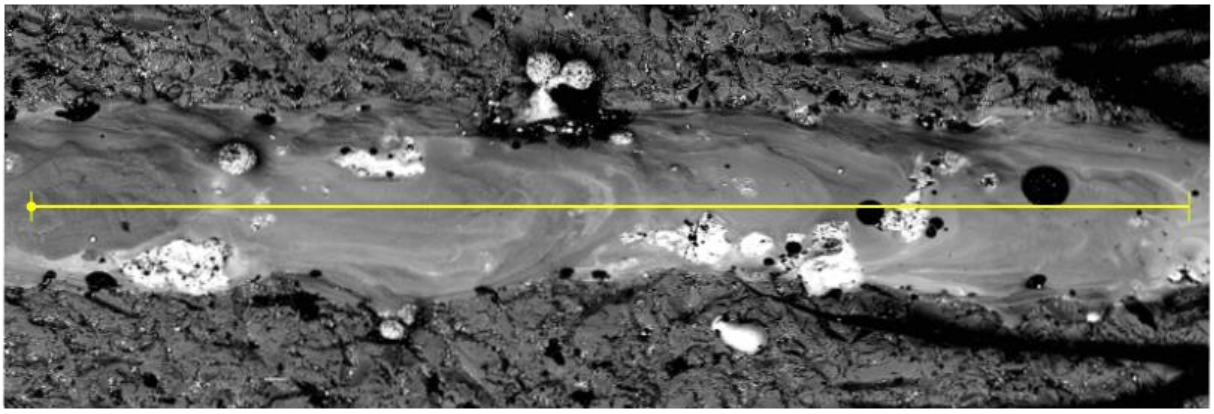

Fe [wt%]	W [wt%]	C [wt%]	Co [wt%]	Cr [wt%]	Mn [wt%]	Mo [wt]	Al [wt%]	Si [wt%]
65.76	20.42	5.84	3.50	1.52	1.44	0.35		0.89

150 W, 800 mm/s

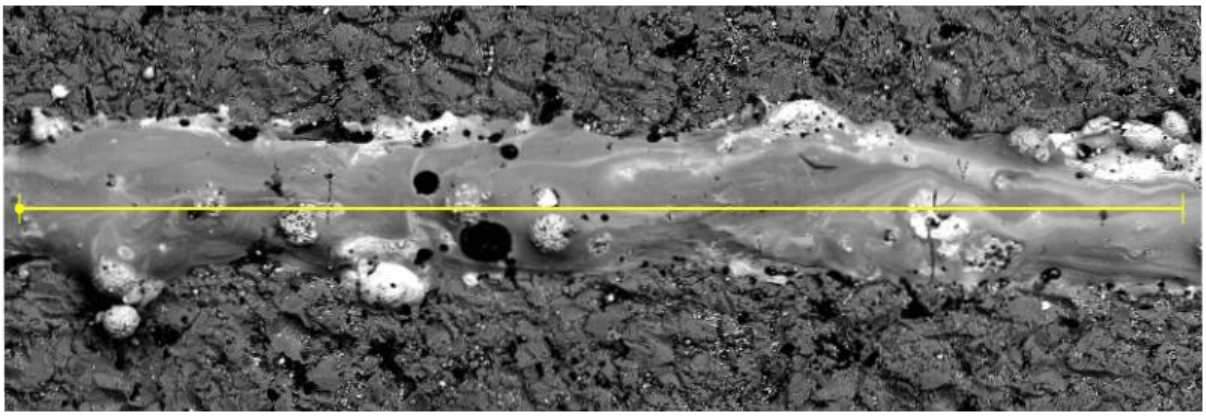

Fe [wt%]	W [wt%]	C [wt%]	Co [wt%]	Cr [wt%]	Mn [wt%]	Mo [wt]	Al [wt%]	Si [wt%]
65.97	20.89	5.24	4.34	1.45	1.34	0.39		0.22

150 W, 1000 mm/s

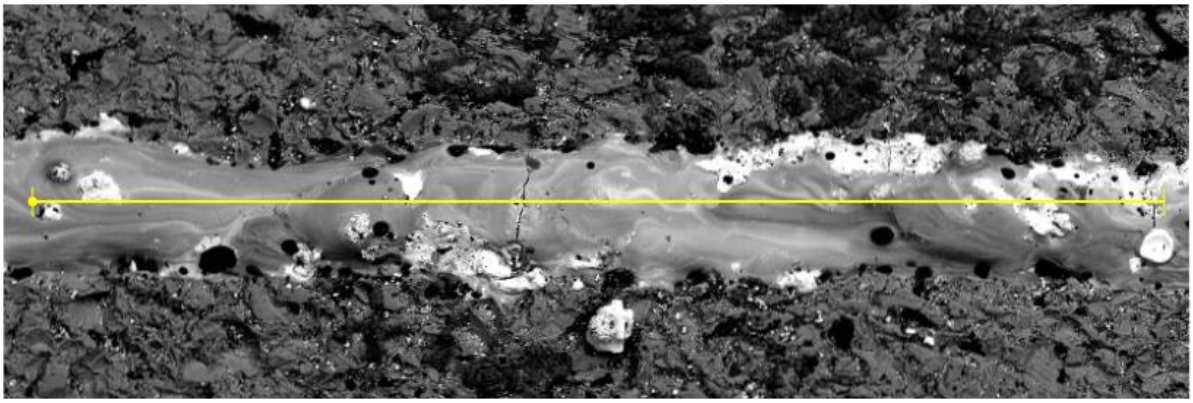

Fe [wt%]	W [wt%]	C [wt%]	Co [wt%]	Cr [wt%]	Mn [wt%]	Mo [wt]	Al [wt%]	Si [wt%]
60.14	26.23	6.94	4.09	1.31	0.92	0.31		0.01

150 W, 1200 mm/s

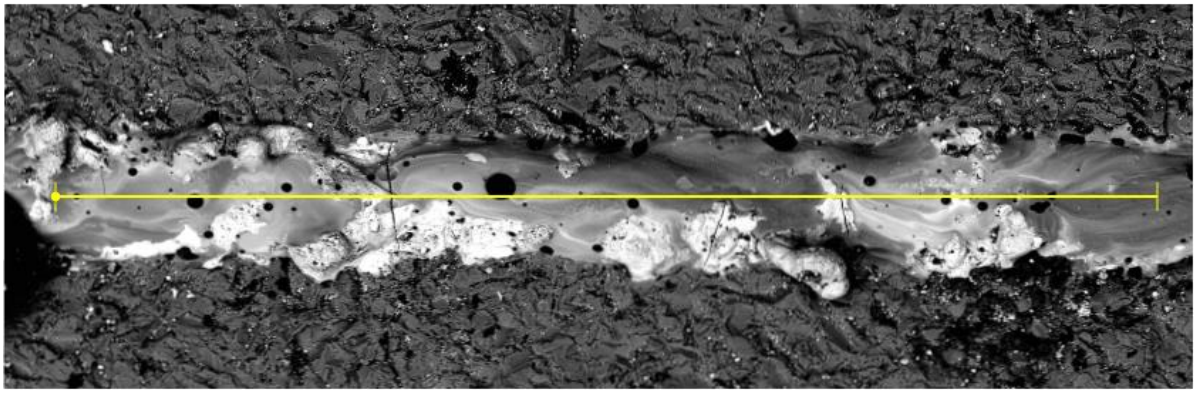

Fe [wt%]	W [wt%]	C [wt%]	Co [wt%]	Cr [wt%]	Mn [wt%]	Mo [wt]	Al [wt%]	Si [wt%]
54.21	31.75	6.55	4.87	1.21	1.01	0.23		0.10

150 W, 1400 mm/s

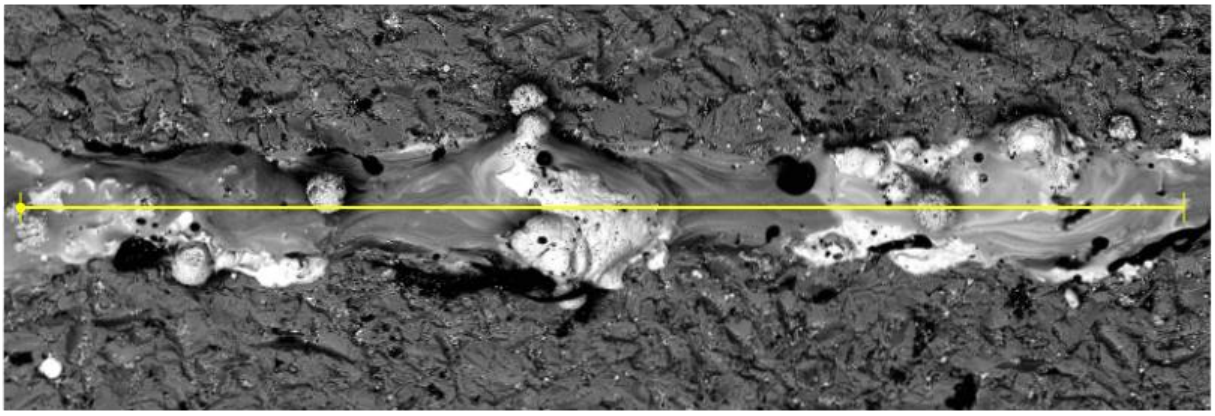

Fe [wt%]	W [wt%]	C [wt%]	Co [wt%]	Cr [wt%]	Mn [wt%]	Mo [wt]	Al [wt%]	Si [wt%]
65.24	21.86	5.58	4.40	1.44	1.00	0.38		0.06

150 W, 1600 mm/s

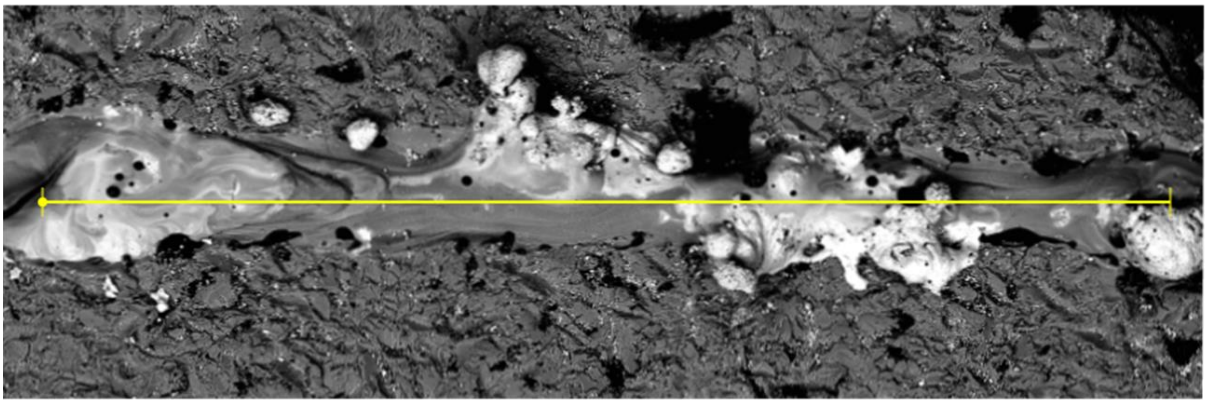

Fe [wt%]	W [wt%]	C [wt%]	Co [wt%]	Cr [wt%]	Mn [wt%]	Mo [wt]	Al [wt%]	Si [wt%]
63.88	21.20	7.49	4.14	1.39	1.19	0.55		0.11

150 W, 1800 mm/s

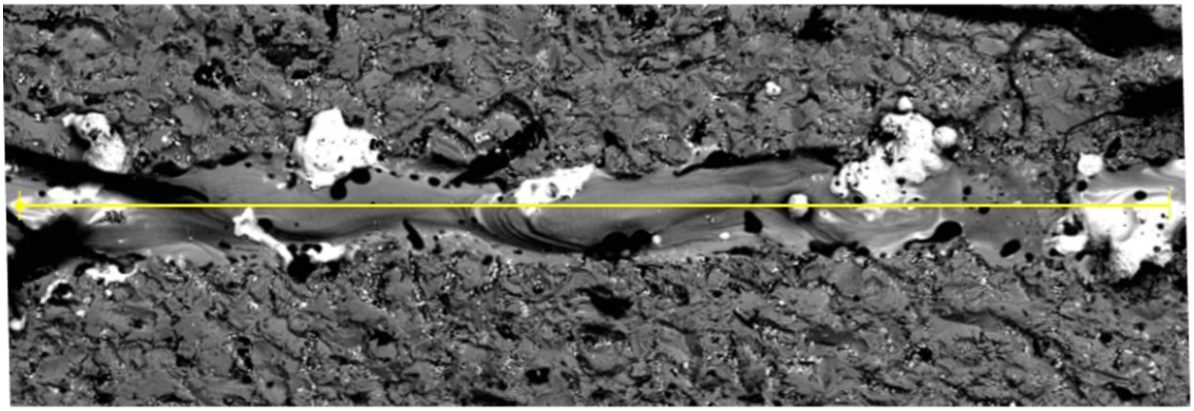

Fe [wt%]	W [wt%]	C [wt%]	Co [wt%]	Cr [wt%]	Mn [wt%]	Mo [wt]	Al [wt%]	Si [wt%]
62.31	21.93	7.20	4.26	1.53	1.65	0.35		0.62

300 W, 1000 mm/s

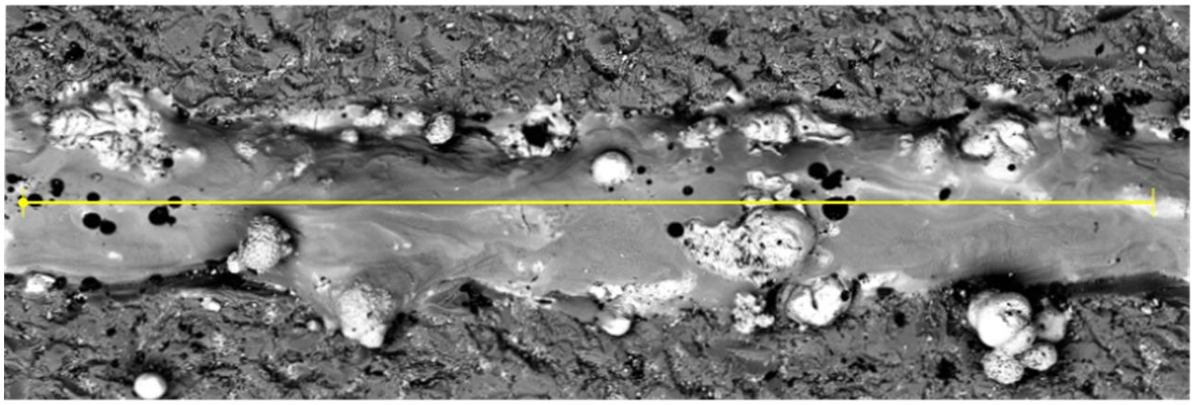

Fe [wt%]	W [wt%]	C [wt%]	Co [wt%]	Cr [wt%]	Mn [wt%]	Mo [wt]	Al [wt%]	Si [wt%]
66.29	18.62	6.62	3.11	1.57	2.46	0.52		0.54

300 W, 1200 mm/s

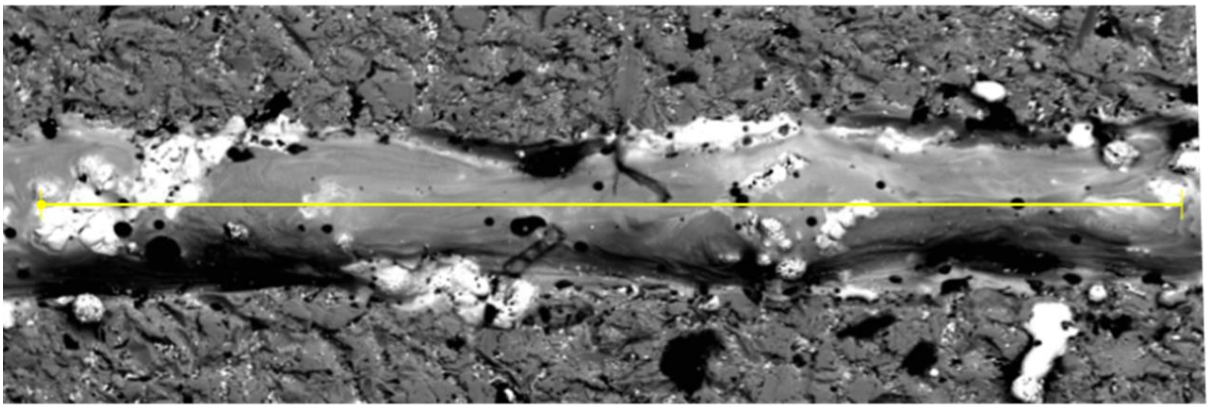

Fe [wt%]	W [wt%]	C [wt%]	Co [wt%]	Cr [wt%]	Mn [wt%]	Mo [wt]	Al [wt%]	Si [wt%]
71.01	16.12	5.97	3.23	1.59	1.34	0.59		0.11

300 W, 1400 mm/s

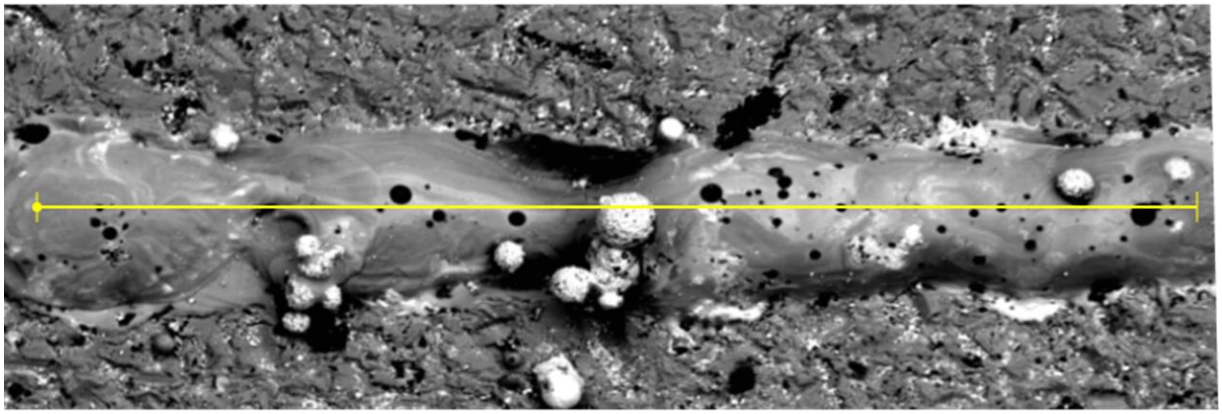

Fe [wt%]	W [wt%]	C [wt%]	Co [wt%]	Cr [wt%]	Mn [wt%]	Mo [wt]	Si [wt%]
73.32	13.48	4.41	3.58	1.75	2.15	0.44	0.56

300 W, 1600 mm/s

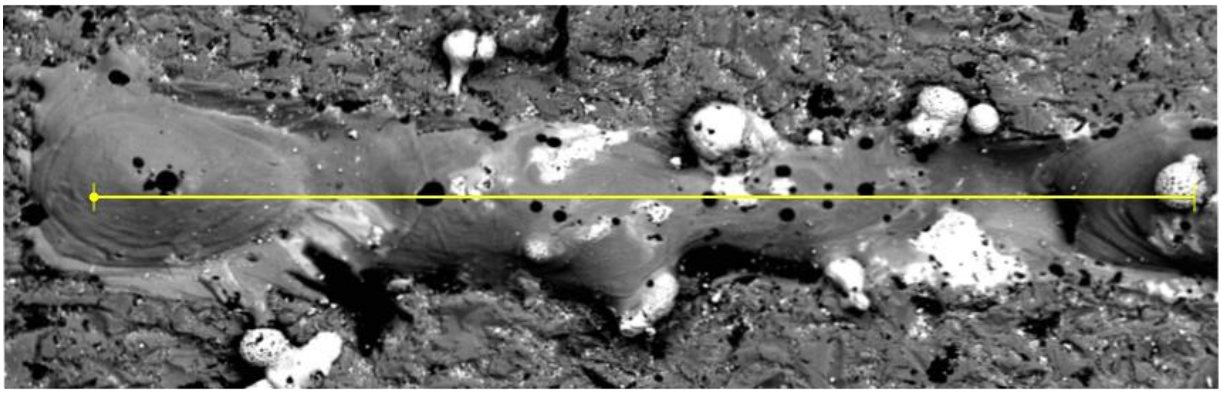

Fe [wt%]	W [wt%]	C [wt%]	Co [wt%]	Cr [wt%]	Mn [wt%]	Mo [wt]	Si [wt%]
74.02	12.86	6.97	2.75	1.62	1.25	0.40	0.07

300 W, 1800 mm/s

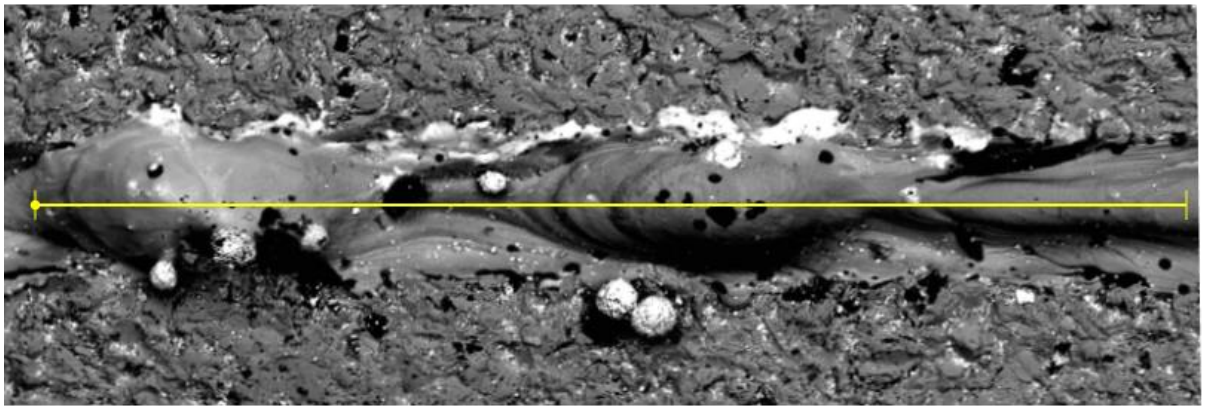

Fe [wt%]	W [wt%]	C [wt%]	Co [wt%]	Cr [wt%]	Mn [wt%]	Mo [wt]	Si [wt%]
70.76	14.37	7.58	2.53	1.66	1.92	0.45	0.32

300 W, 2000 mm/s

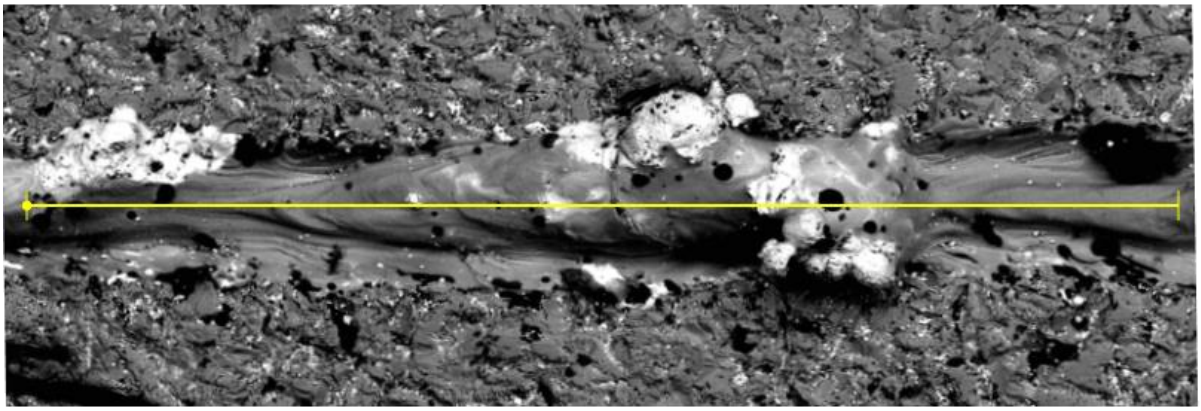

Fe [wt%]	W [wt%]	C [wt%]	Co [wt%]	Cr [wt%]	Mn [wt%]	Mo [wt]	Al [wt%]	Si [wt%]
74.64	12.04	6.84	2.27	1.77	1.67	0.39		0.20

300 W, 2200 mm/s

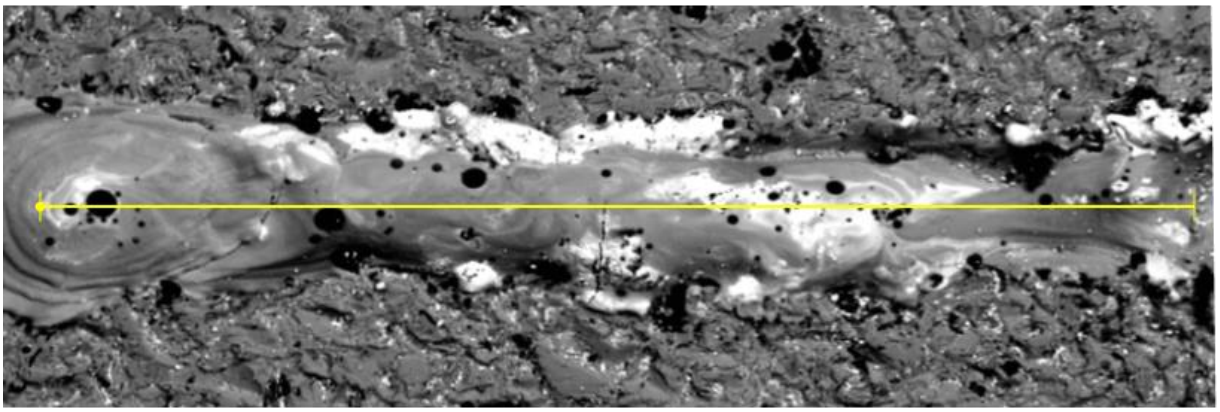

Fe [wt%]	W [wt%]	C [wt%]	Co [wt%]	Cr [wt%]	Mn [wt%]	Mo [wt]	Al [wt%]	Si [wt%]
78.82	9.29	5.31	1.57	1.81	2.00	0.50		0.45

300 W, 2400 mm/s

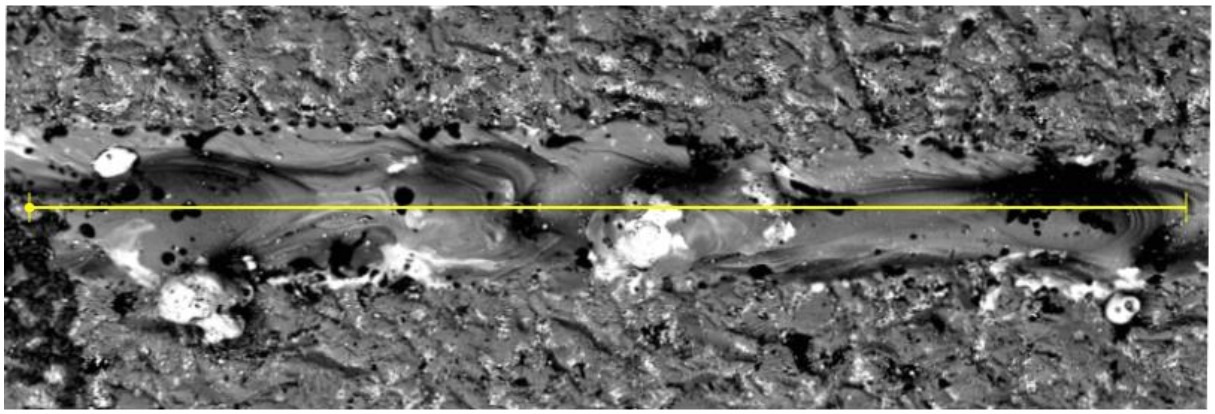

Fe [wt%]	W [wt%]	C [wt%]	Co [wt%]	Cr [wt%]	Mn [wt%]	Mo [wt]	Al [wt%]	Si [wt%]
75.91	7.21	10.97	1.47	1.92	1.54	0.49		0.28

B.4. Single Tracks on WC Substrate Results for Section 7.1

The SEM and EDS images and results for the single track on a WC-Co coated base plate study can be observed in the following tables.

Table B. 6: Single track images of all tracks for WC-Co substrate experiment

Z = 0 mm, Spot size = 50 µm	**Z = -2 mm, Spot size = 80 µm**
50 W, 150 mm/s	
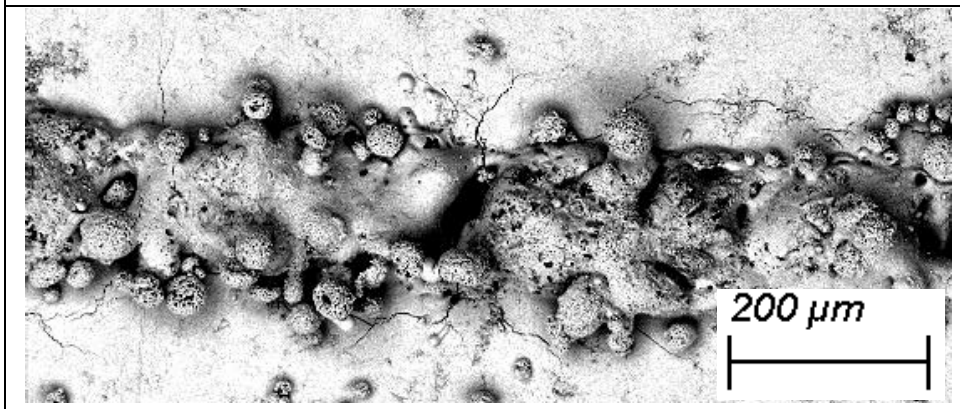	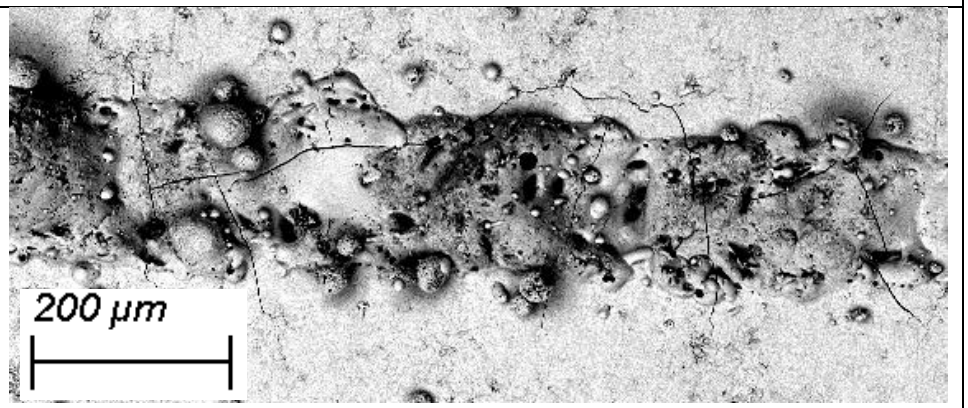
Cobalt content = 9.99 wt%	**Cobalt content = 11.21 wt%**
50 W, 200 mm/s	
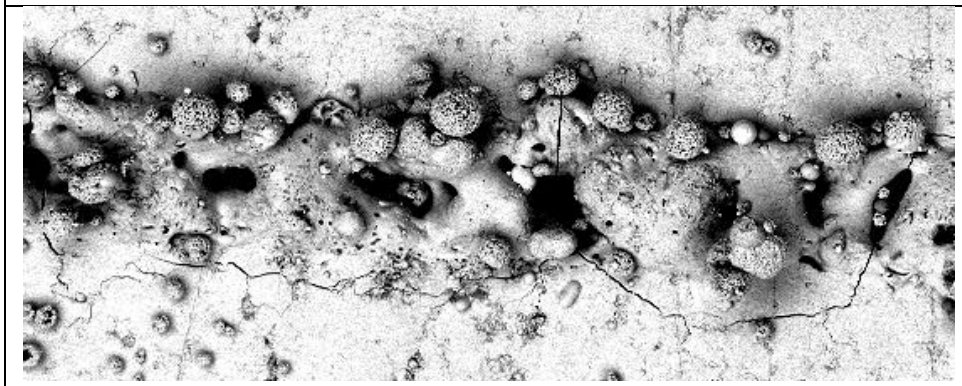	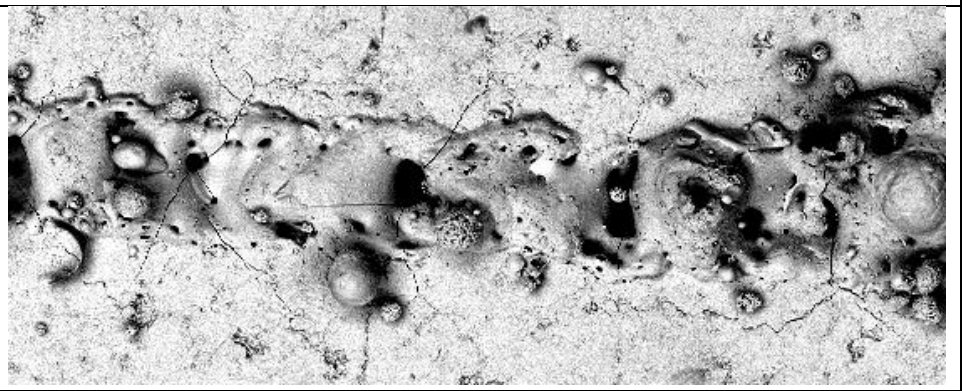
Cobalt content = 16.74 wt%	**Cobalt content = 10.82 wt%**

50 W, 250 mm/s	
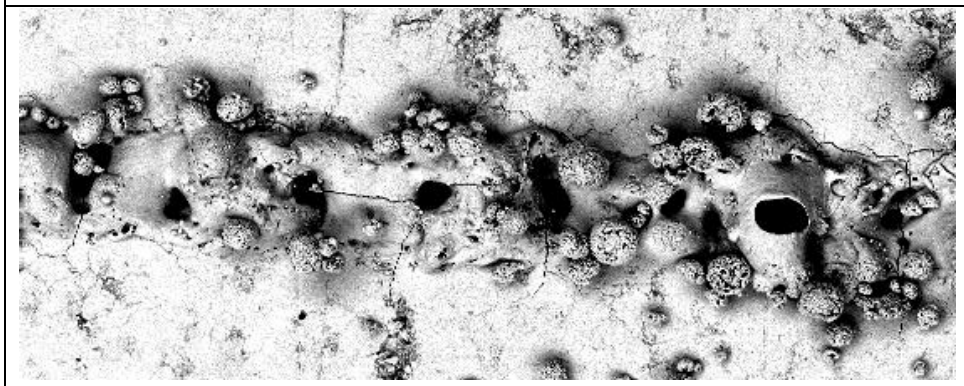	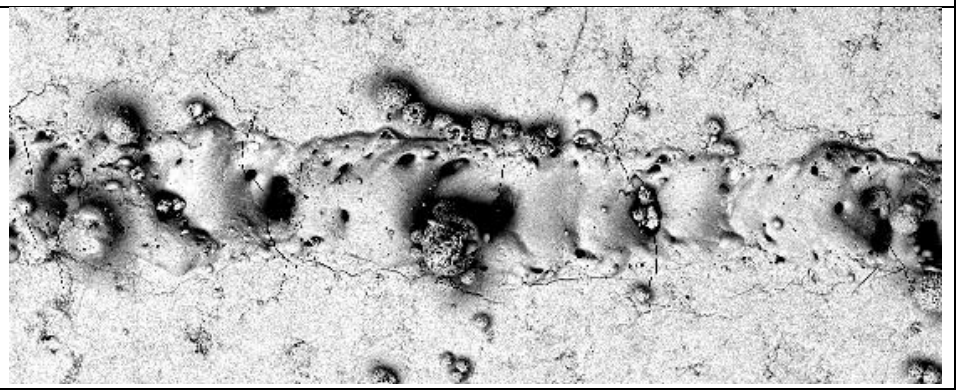
Cobalt content = 9.03 wt%	**Cobalt content = 10.60 wt%**
50 W, 300 mm/s	
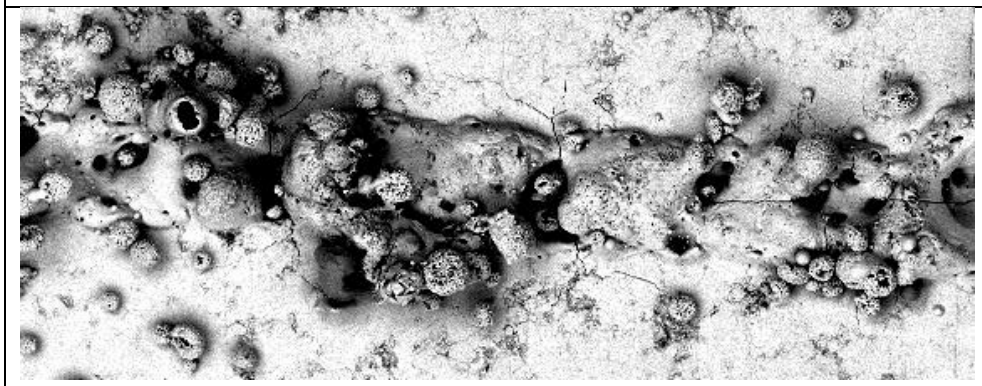	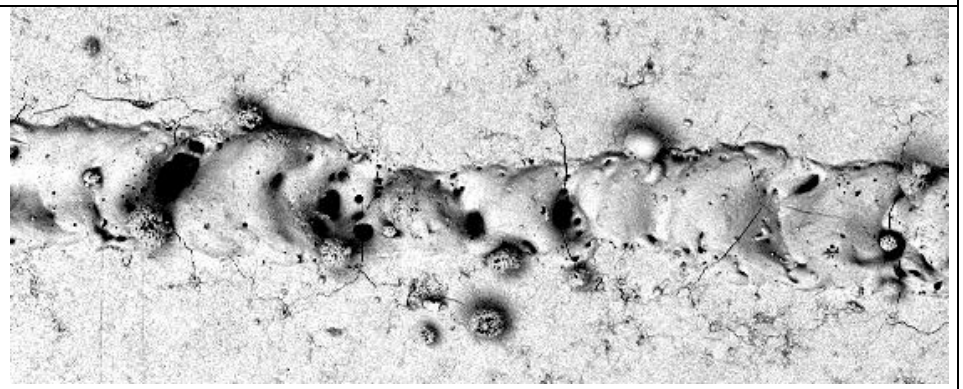
Cobalt content = 11.68 wt%	**Cobalt content = 11.32 wt%**

50 W, 350 mm/s	
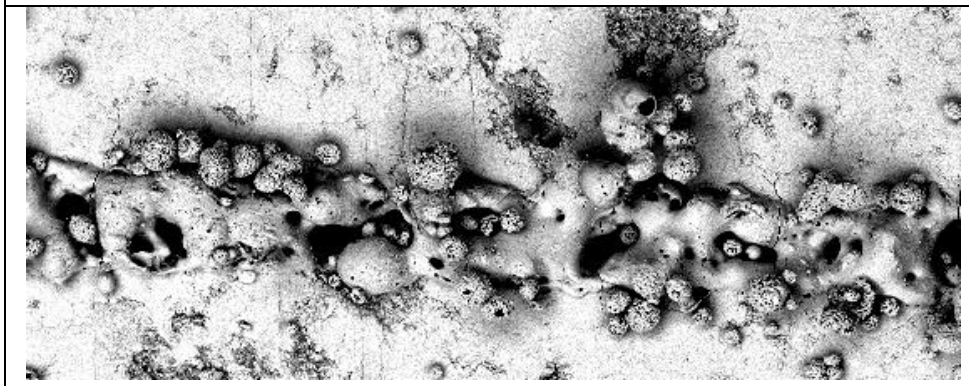	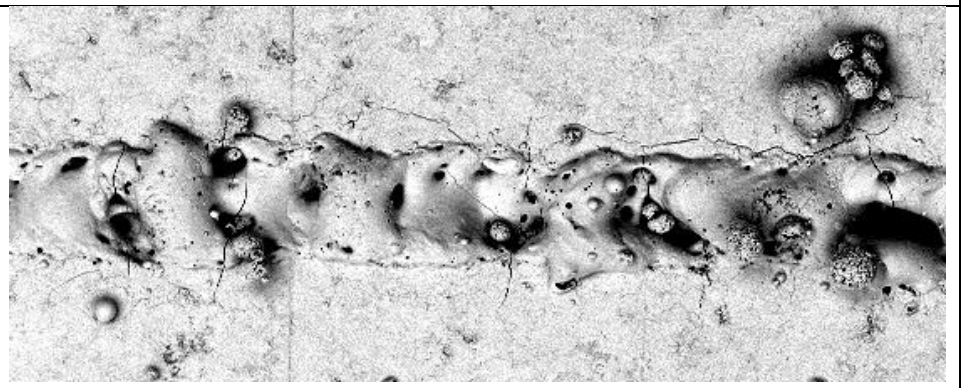
Cobalt content = 12.87 wt%	**Cobalt content = 10.23 wt%**
50 W, 400 mm/s	
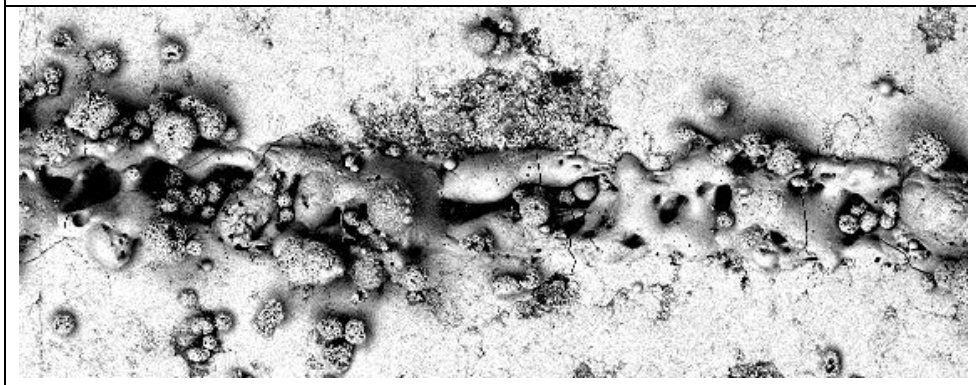	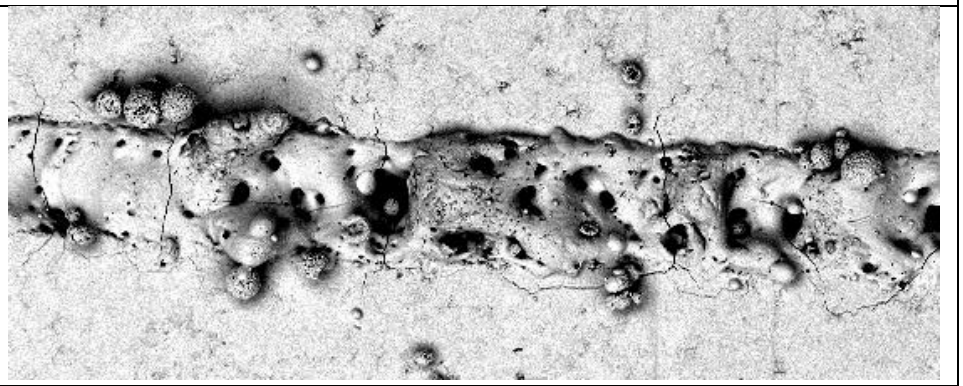
Cobalt content = 11.83 wt%	**Cobalt content = 10.88 wt%**

100 W, 300 mm/s	
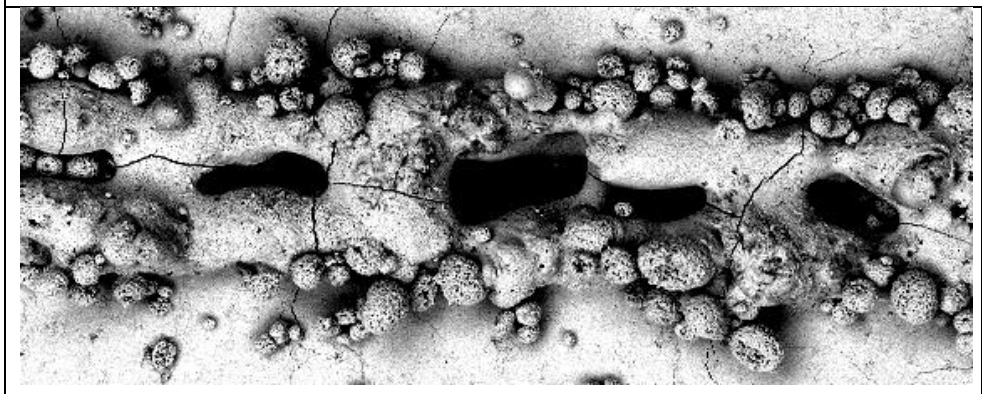	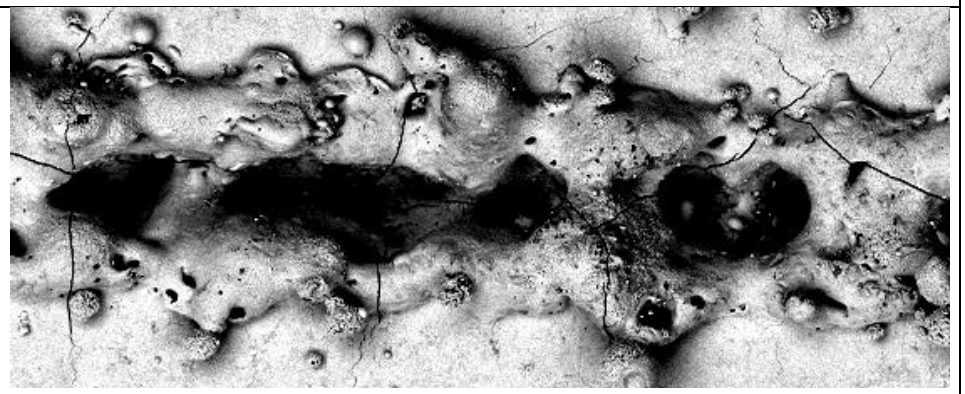
Cobalt content = 15.82 wt%	**Cobalt content = 11.60 wt%**
100 W, 400 mm/s	
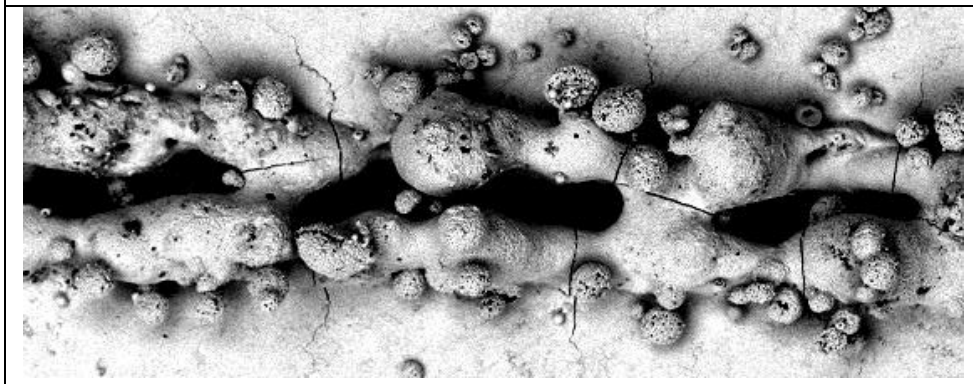	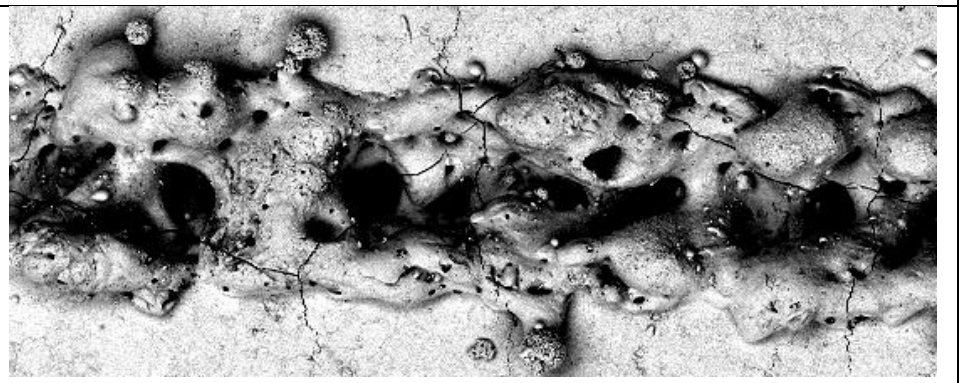
Cobalt content = 16.04 wt%	**Cobalt content = 10.87 wt%**

100 W, 500 mm/s	
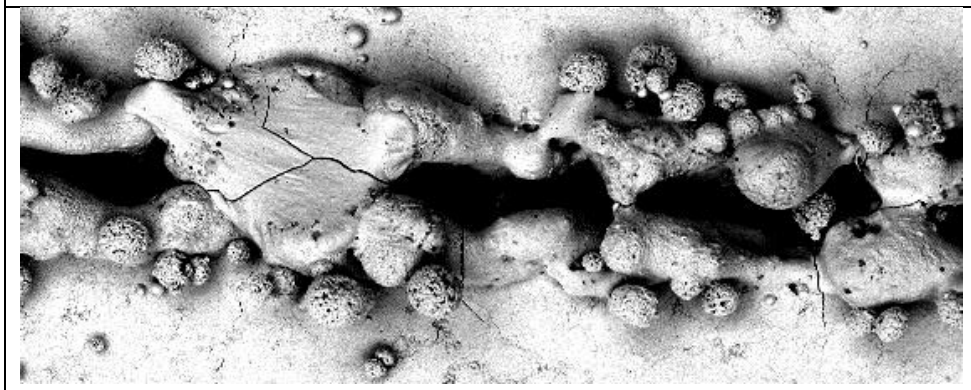	
Cobalt content = 15.05 wt%	**Cobalt content = 11.86 wt%**
100 W, 600 mm/s	
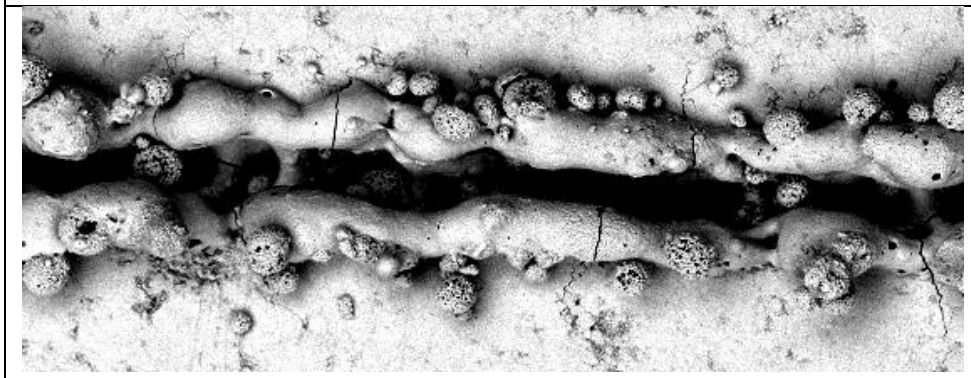	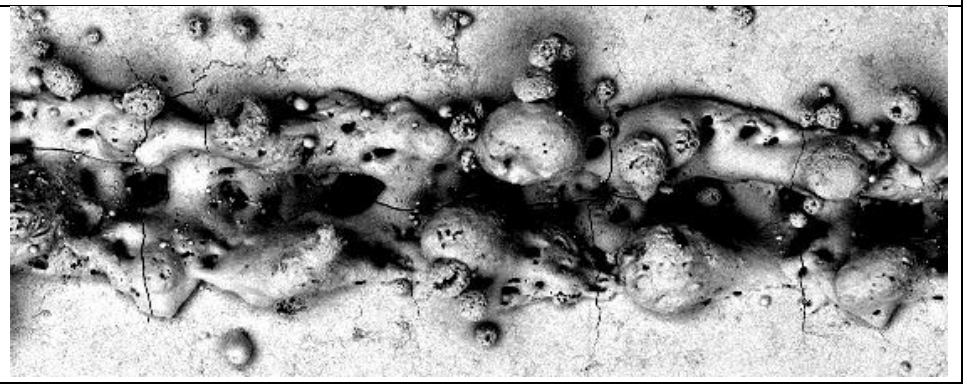
Cobalt content = 14.99 wt%	**Cobalt content = 14.11 wt%**

100 W, 700 mm/s	
	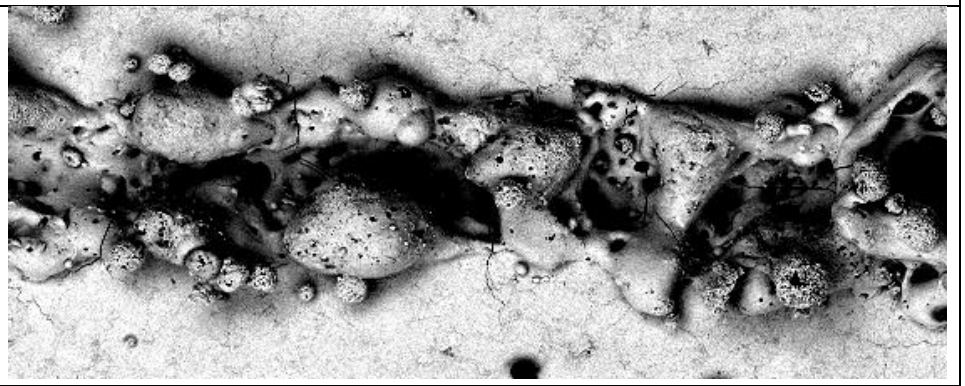
Cobalt content = 13.22 wt%	**Cobalt content = 12.07 wt%**
100 W, 800 mm/s	
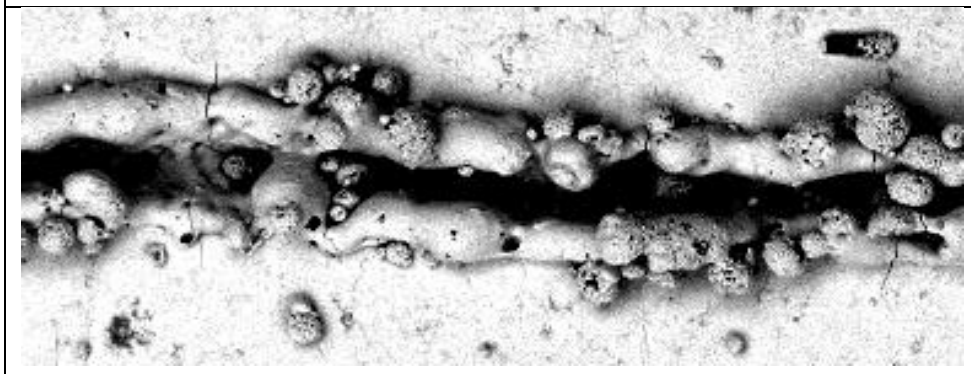	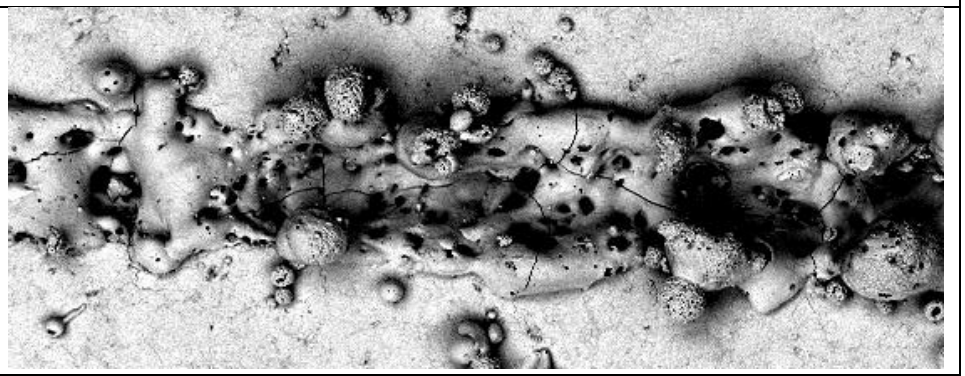
Cobalt content = 13.91 wt%	**Cobalt content = 9.12 wt%**

150 W, 450 mm/s	
	
Cobalt content = 11.52 wt%	**Cobalt content = 11.06 wt%**
150 W, 600 mm/s	
	
Cobalt content = 13.91 wt%	**Cobalt content = 12.90 wt%**

150 W, 750 mm/s	
	
Cobalt content = 17.87 wt%	**Cobalt content = 14.47wt%**
150 W, 900 mm/s	
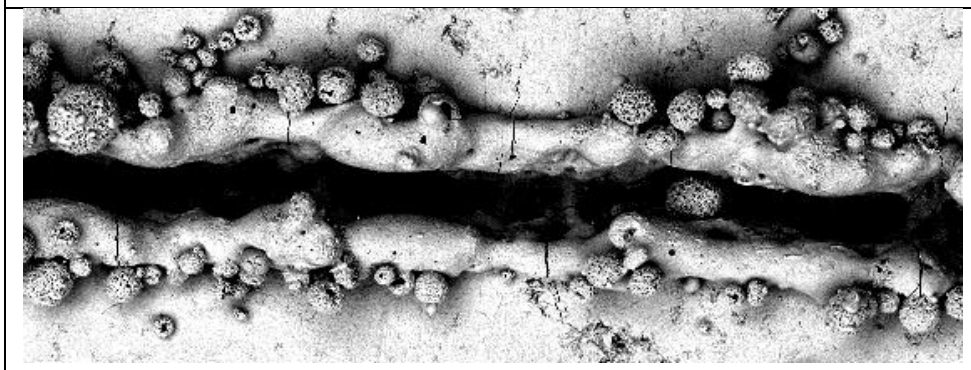	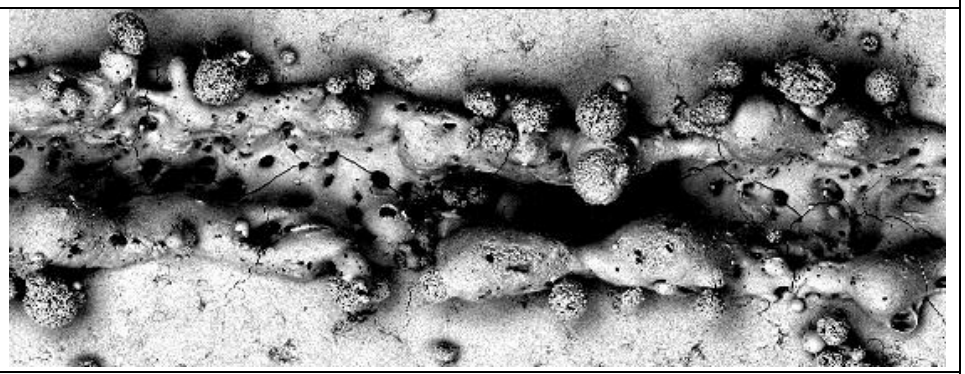
Cobalt content = 11.79 wt%	**Cobalt content = 12.69 wt%**

150 W, 1050 mm/s	
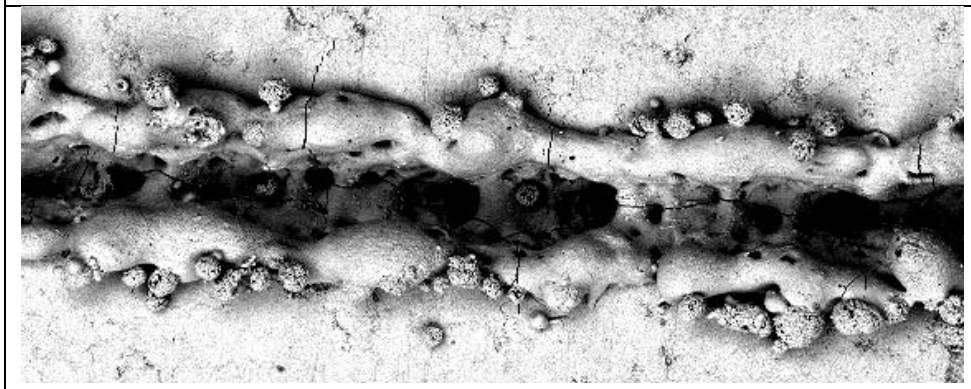	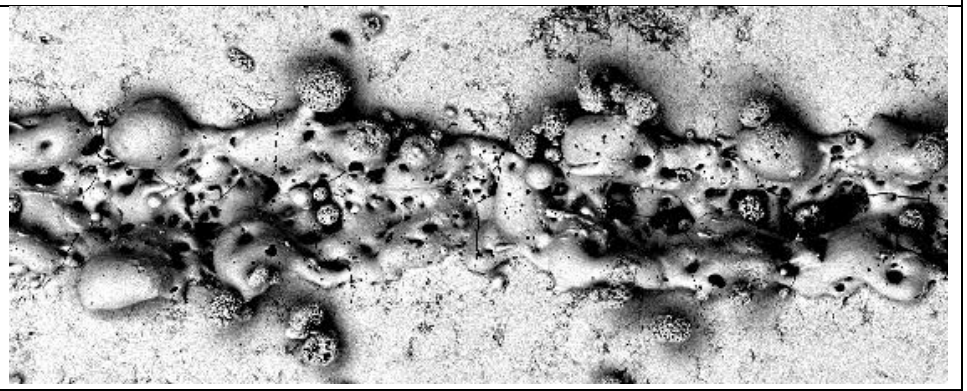
Cobalt content = 11.78 wt%	**Cobalt content = 13.34 wt%**
150 W, 1200 mm/s	
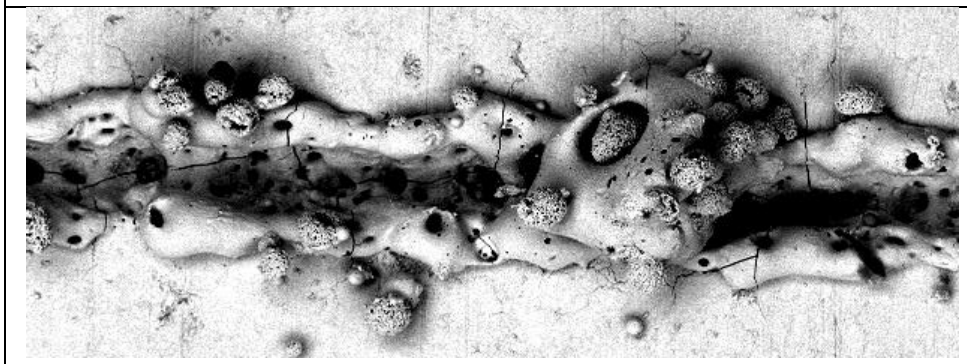	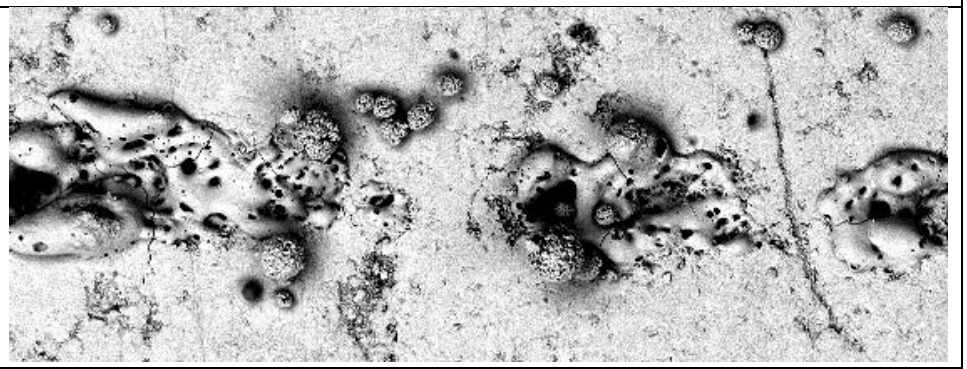
Cobalt content = 14.19 wt%	**Cobalt content = 12.79 wt%**

200 W, 600 mm/s	
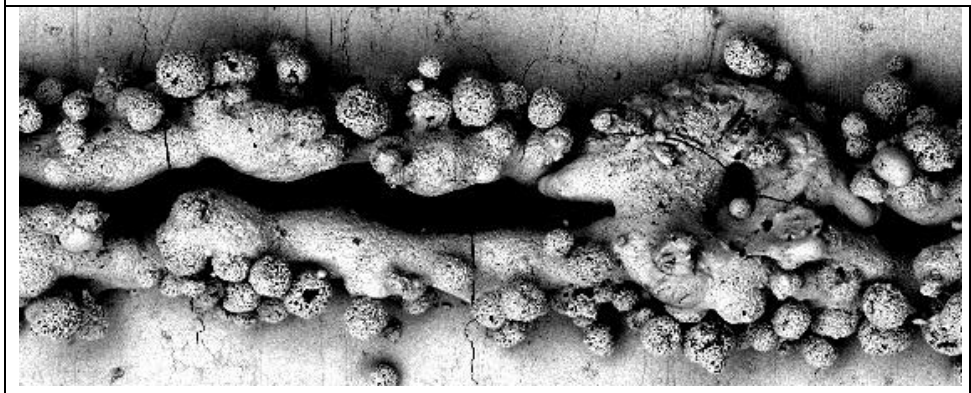	
Cobalt content = 12.13 wt%	**Cobalt content = 12.64 wt%**
200 W, 800 mm/s	
	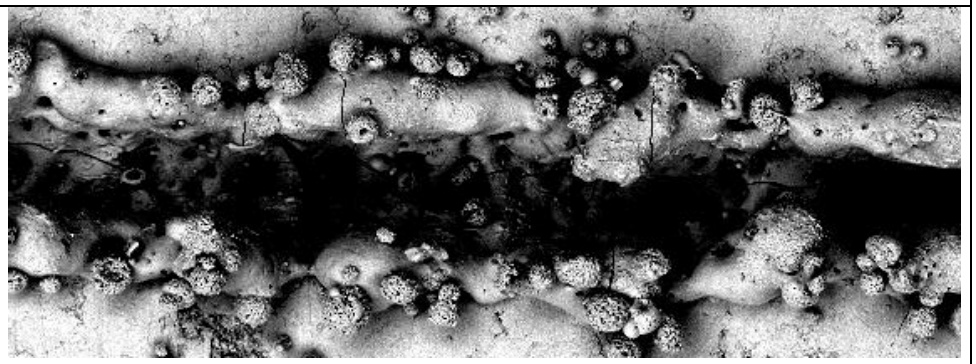
Cobalt content = 12.11 wt%	**Cobalt content = 11.32 wt%**

200 W, 1000 mm/s	
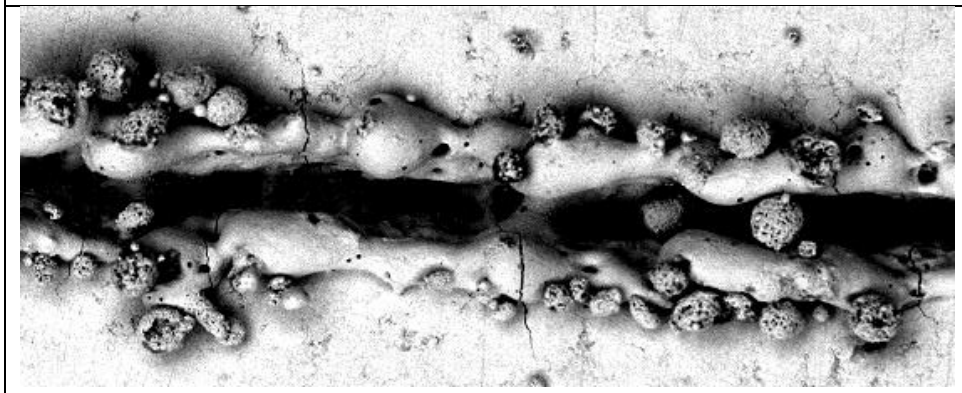	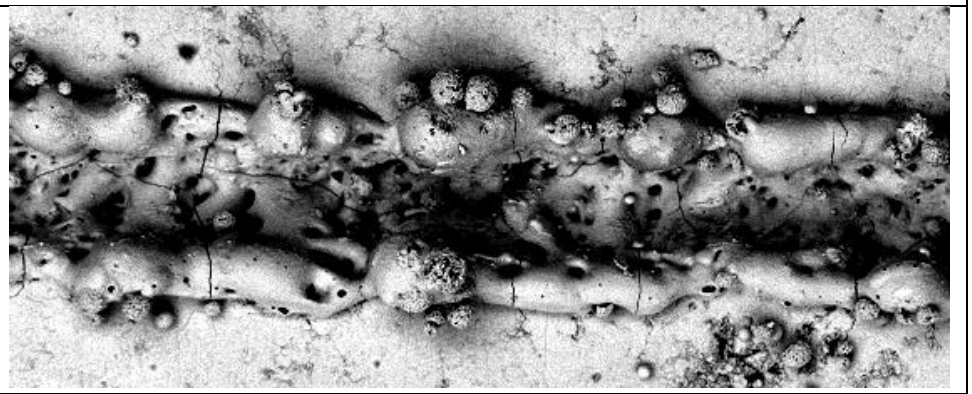
Cobalt content = 9.84 wt%	**Cobalt content = 10.82 wt%**
200 W, 1200 mm/s	
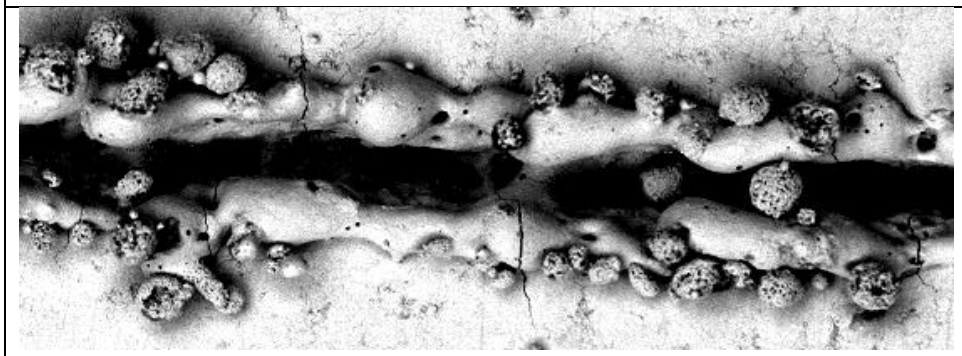	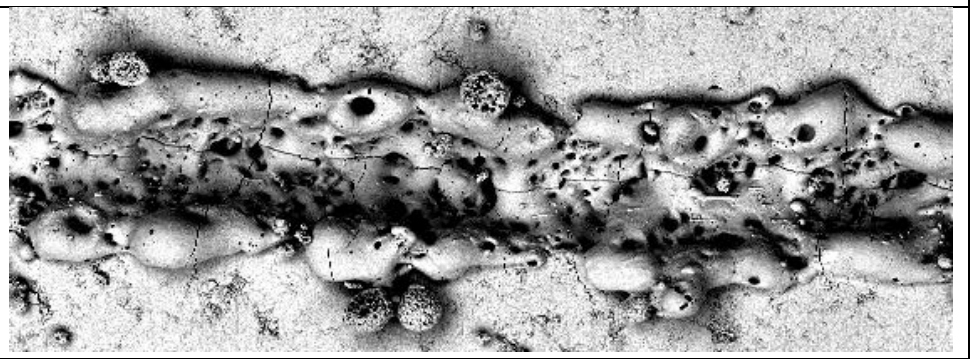
Cobalt content = 14.19 wt%	**Cobalt content = 14.68 wt%**

200 W, 1400 mm/s	
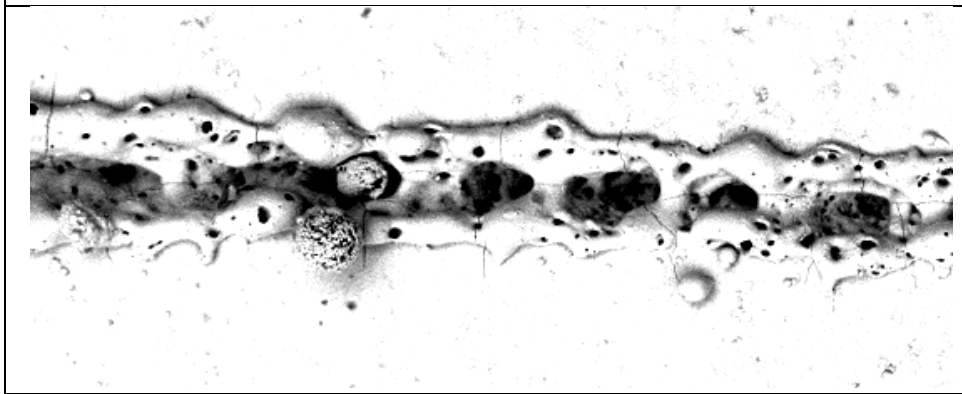	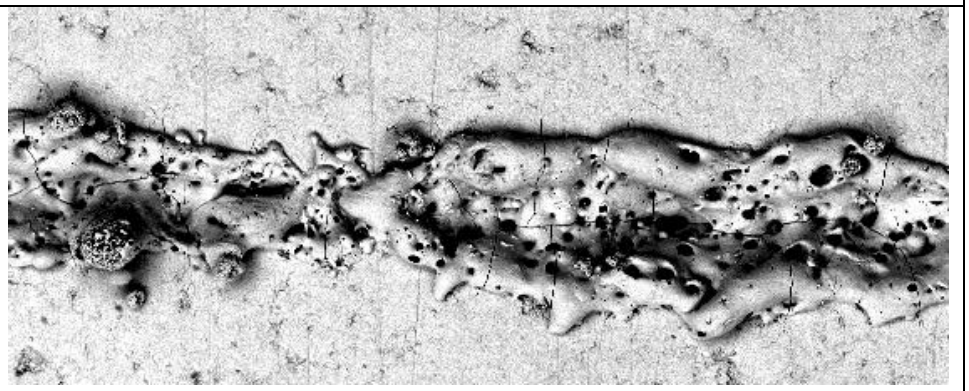
Cobalt content = 15.38 wt%	**Cobalt content = 13.06 wt%**
200 W, 1600 mm/s	
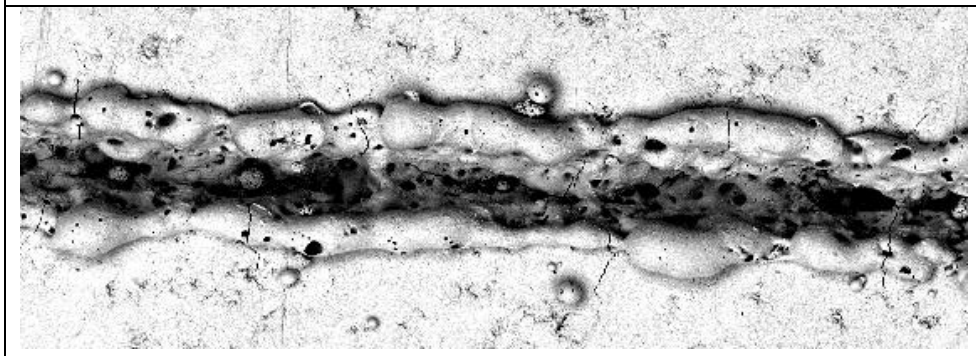	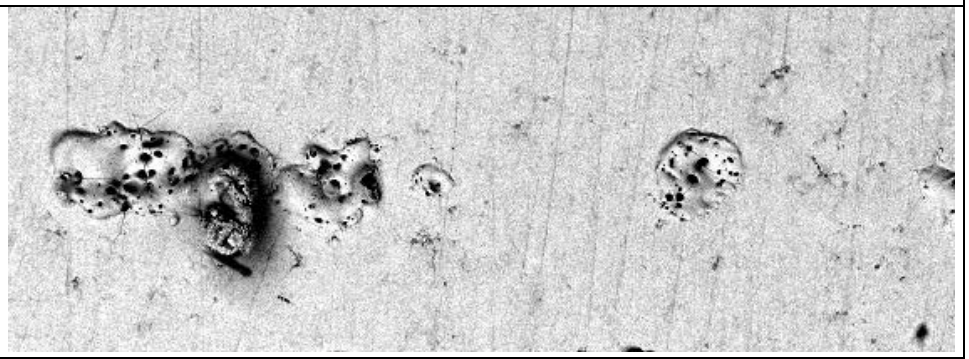
Cobalt content = 12.48 wt%	**Cobalt content = 15.30 wt%**

The CNMA inserts manufactured with L-PBF using the parameter range from the single track experiment can be observed in Figure B.4.

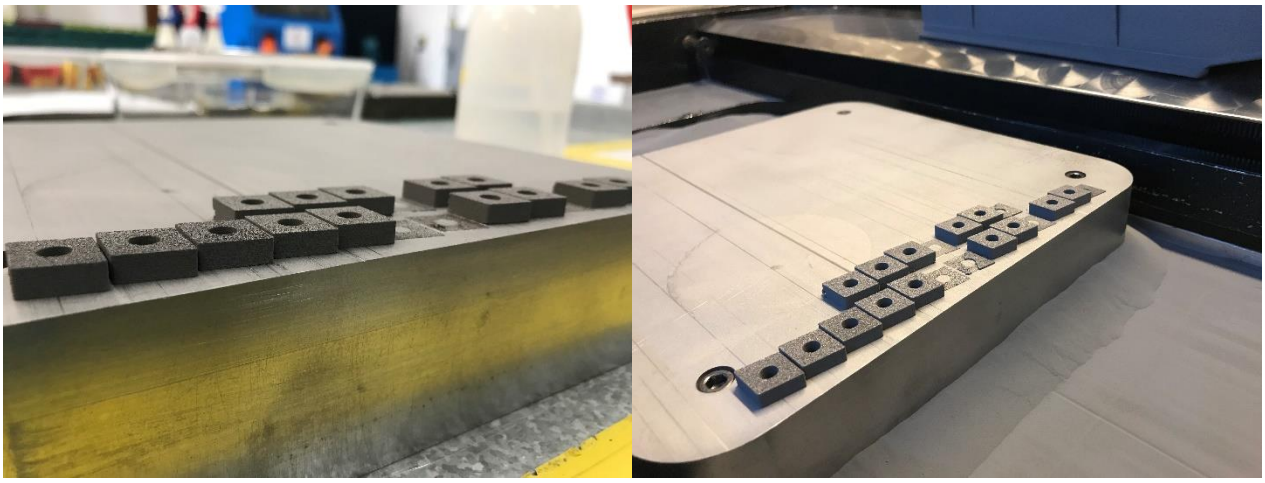

Figure B.4: 14 CNMA inserts manufactured using the single track optimised range and 80-degree alternating raster strategy

B.5. Laser Parameter Optimisation Results for Section 7.2

The failed and successful samples from the first iteration of the D-Optimal parameter optimisation experiment can be seen in Figure B.5.

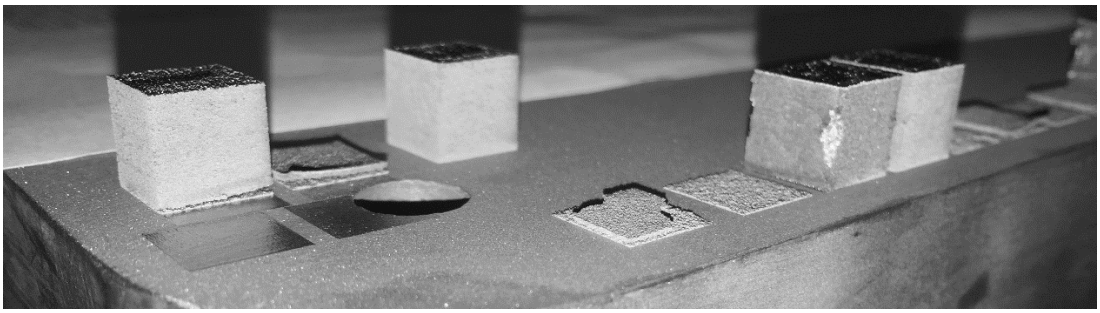

Figure B.5: First iteration of D-optimal parameter optimisation with failed experimental runs

The failed High VED Diagonal Alternating strategy runs can be found in Figure B.6.

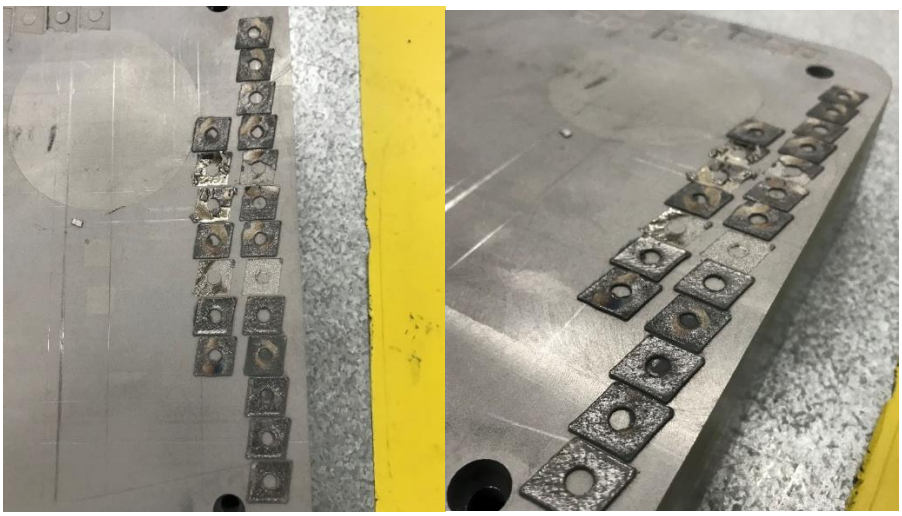

Figure B.6: Failed high VED experimental runs on CNMA inserts

The successful optimised run with the Raster strategy can be observed in Figure B.7.

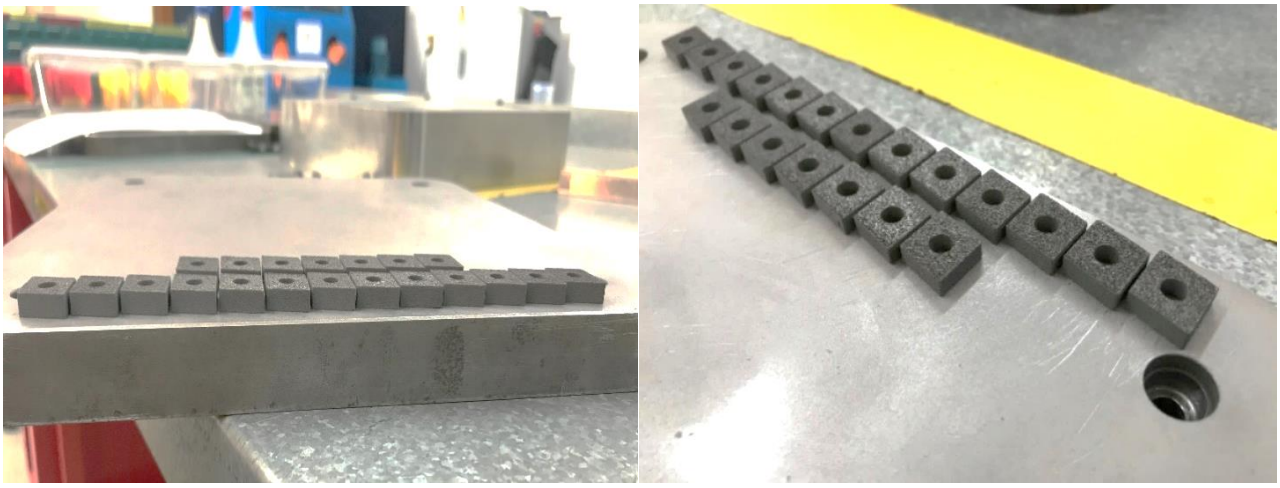

Figure B.7: 20 CNMA inserts manufactured using the optimised range and 80-degree alternating raster strategy

The one factor plots for the hardness response averaged over the different scanning strategies can be observed in Figure B.8.

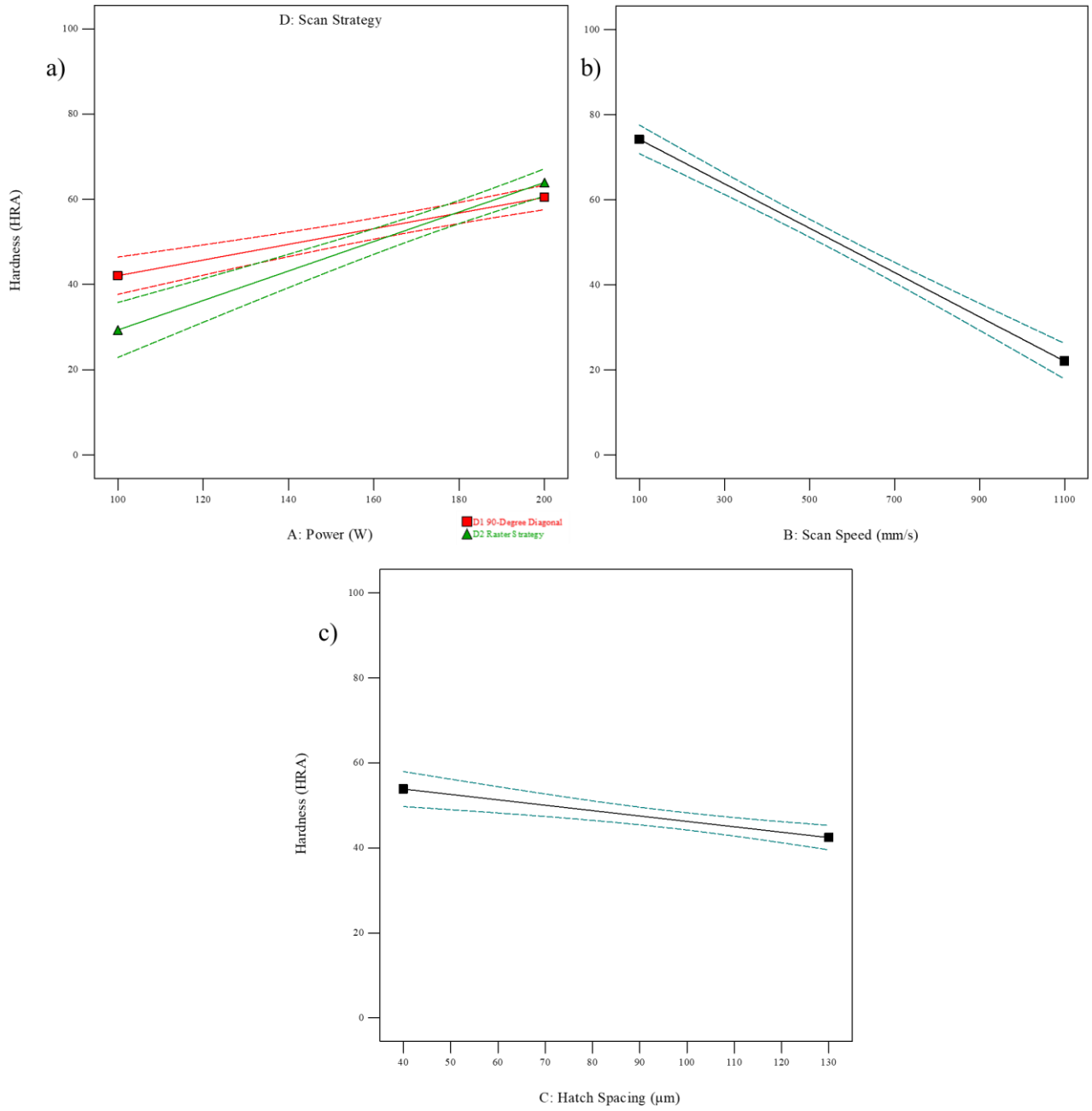

Figure B.8: Hardness one factor plots averaged over the different scanning strategies a) Power vs Hardness with Scanning Strategy interaction, b) Scan Speed vs Hardness and, c) Hatch Spacing vs Hardness

The one factor plots for the cobalt content response for the different scanning strategies can be noted in Figure B.9.

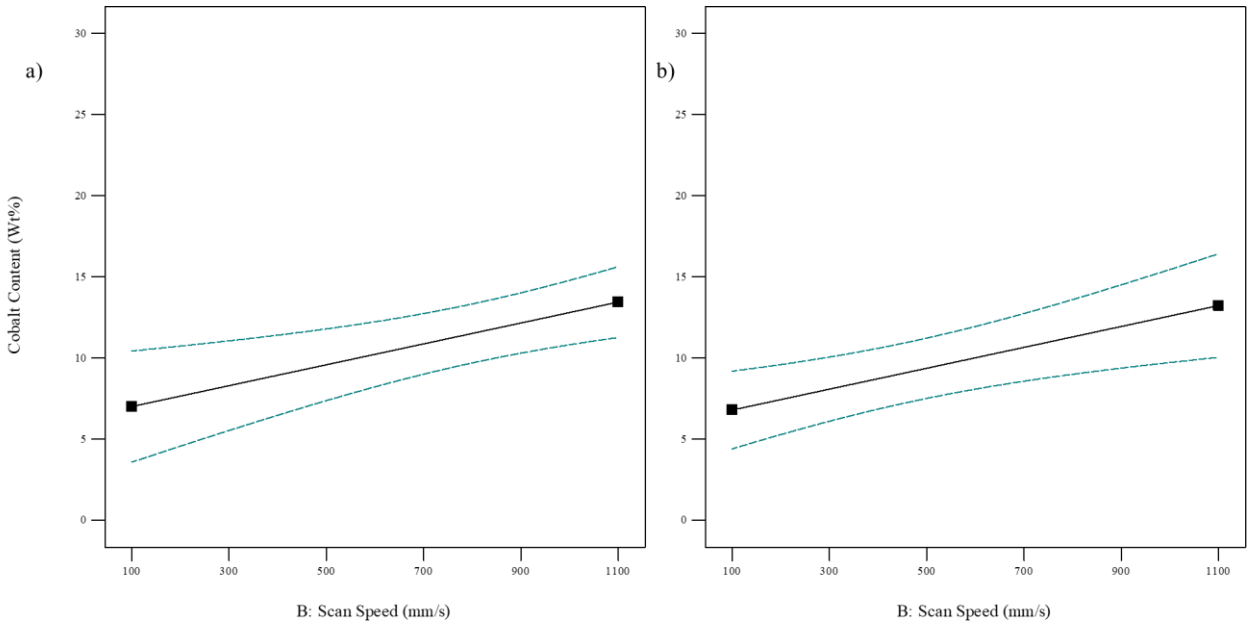

Figure B.9: One factor plots for a) cobalt content vs scan speed for raster scan strategy, and b) cobalt content vs scan speed for diagonal alternating strategy

The XRD graphs for the various samples can be observed in Figure B.10, Figure B.11, Figure B.12, Figure B.13, and Figure B.14.

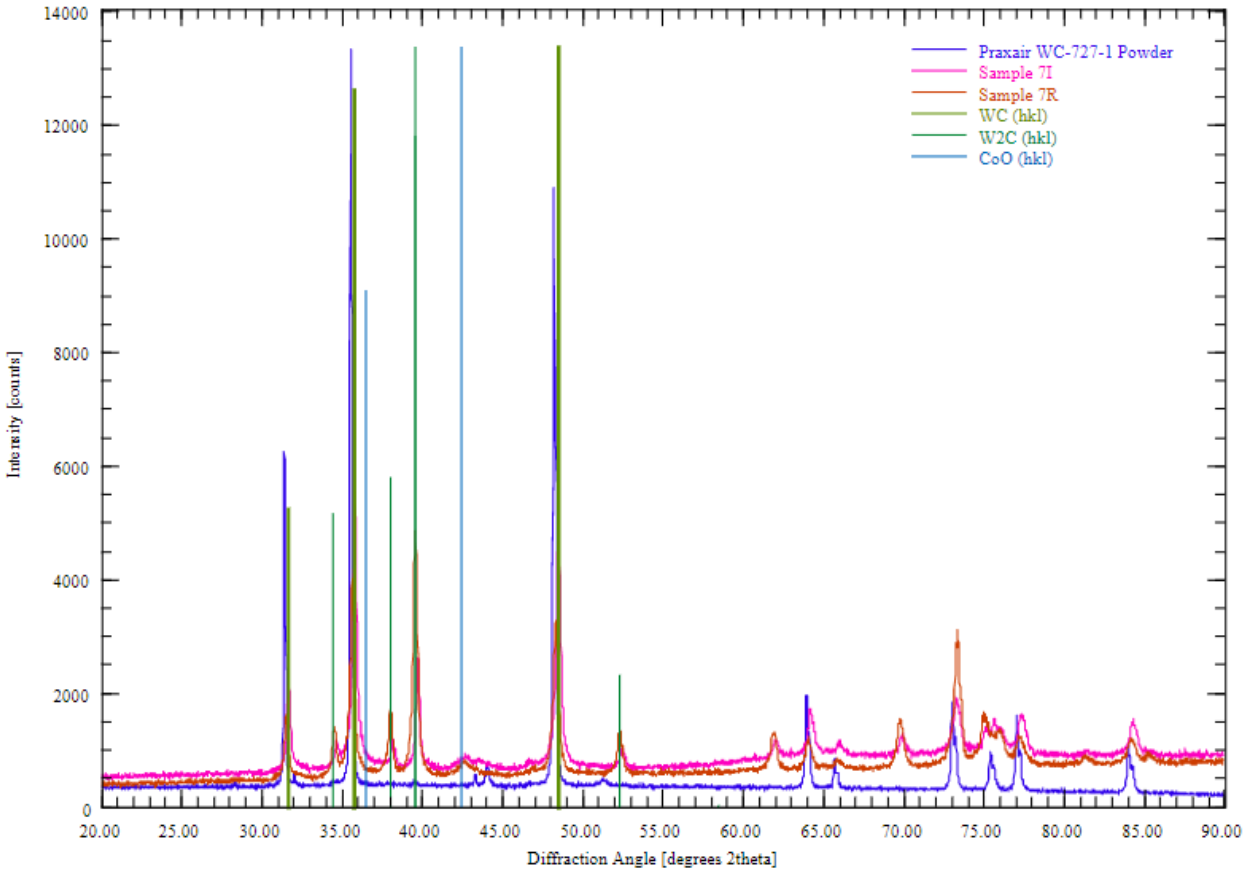

Figure B.10: XRD of Praxair powder and Sample 7I vs 7R

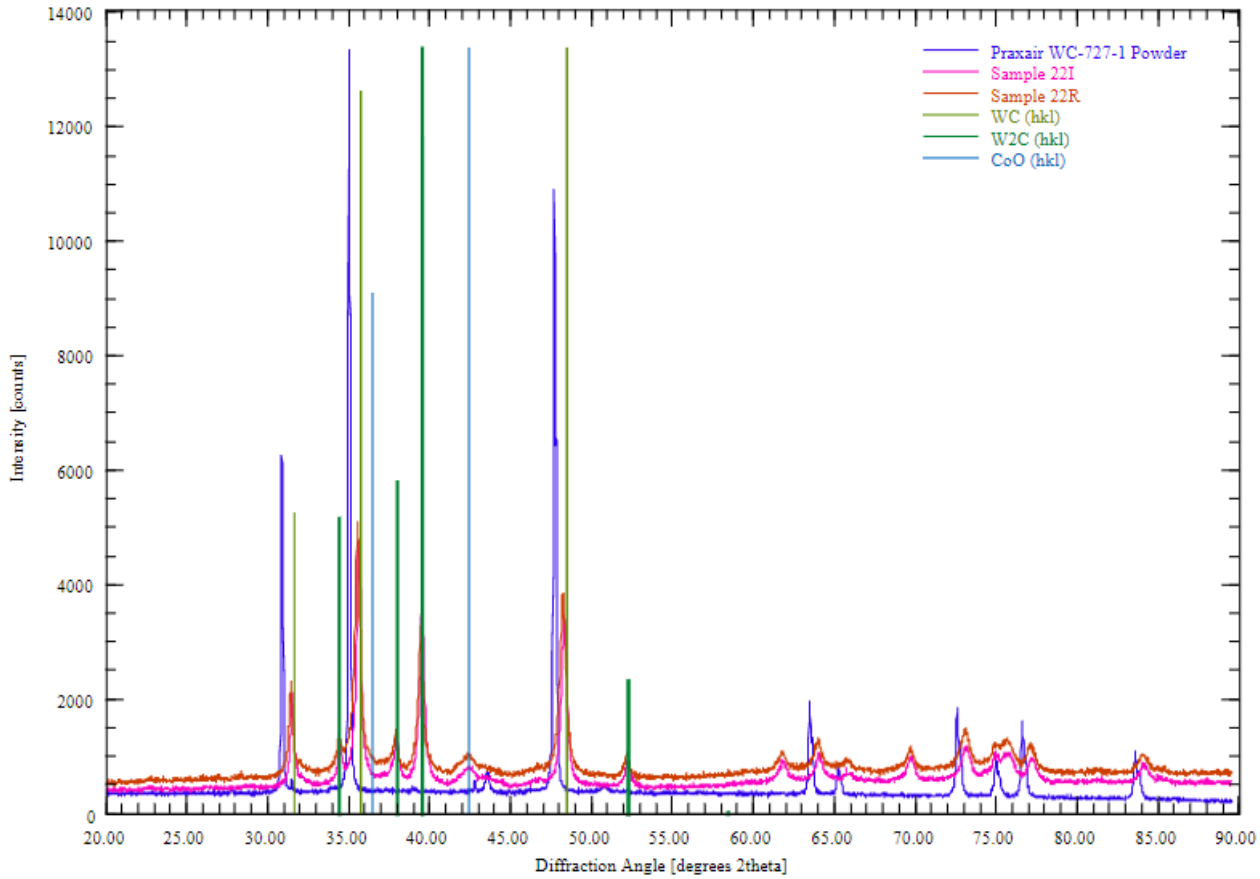

Figure B.11: XRD of Praxair powder and Sample 22I vs 22R

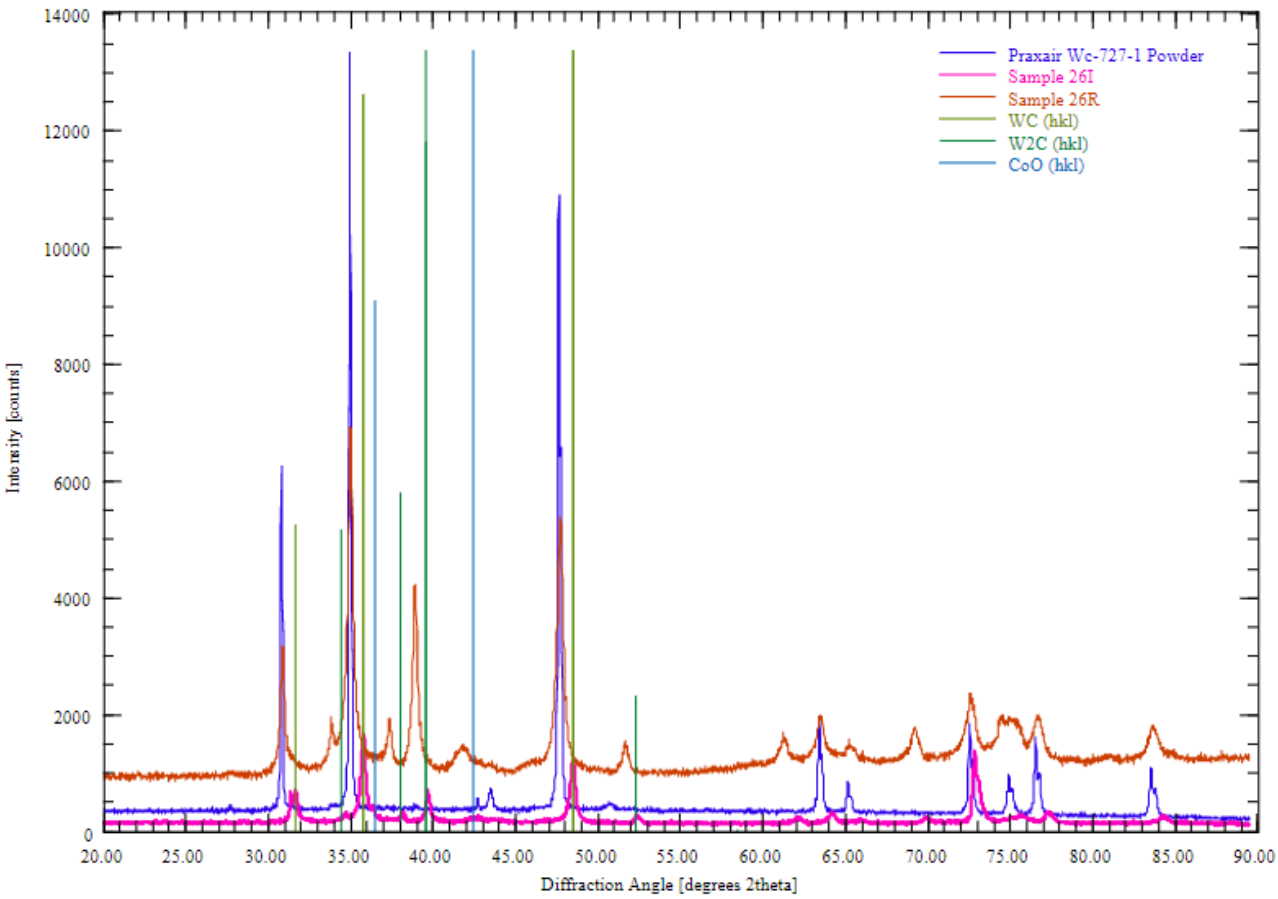

Figure B.12: XRD of Praxair powder and Sample 26I vs 26R

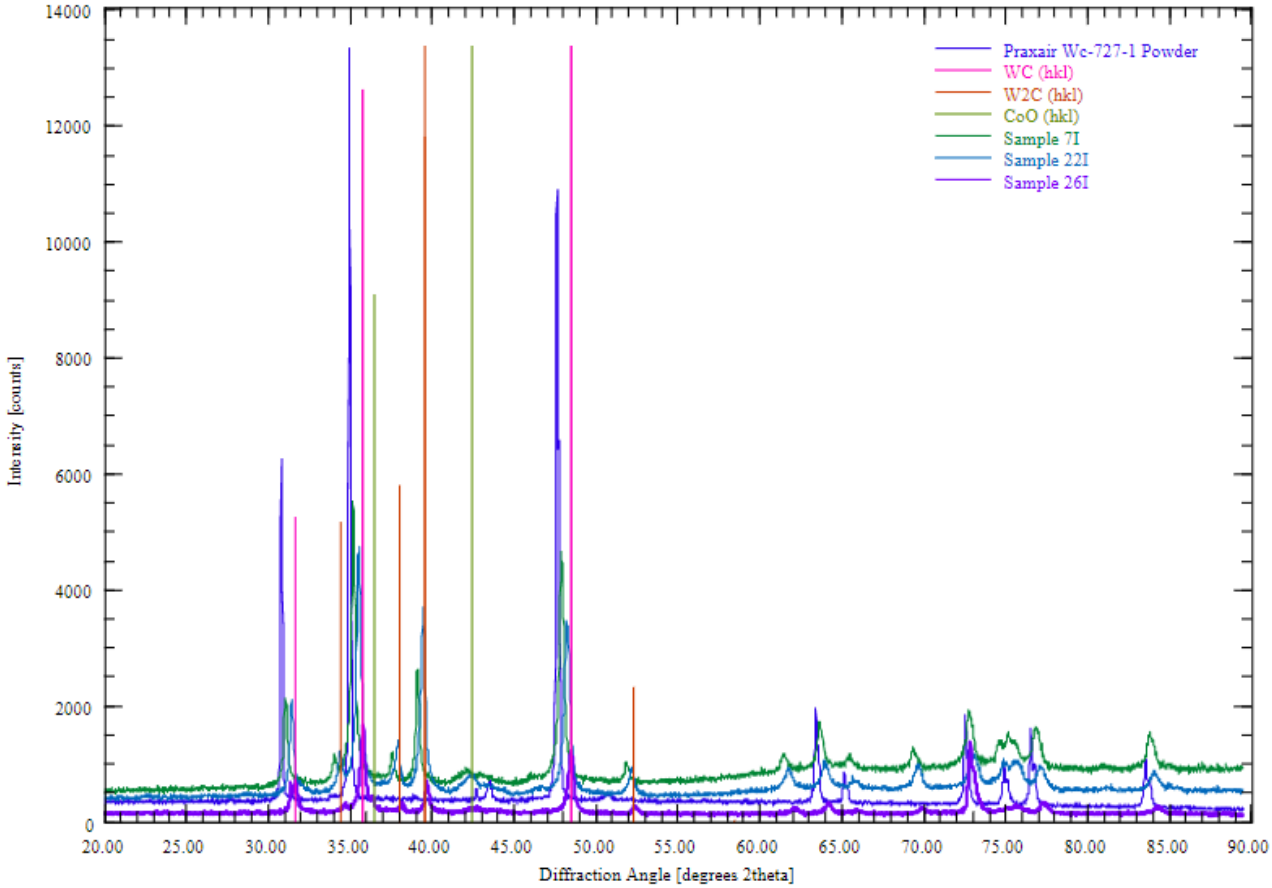

Figure B.13: XRD comparison of Praxair powder to Island Strategy

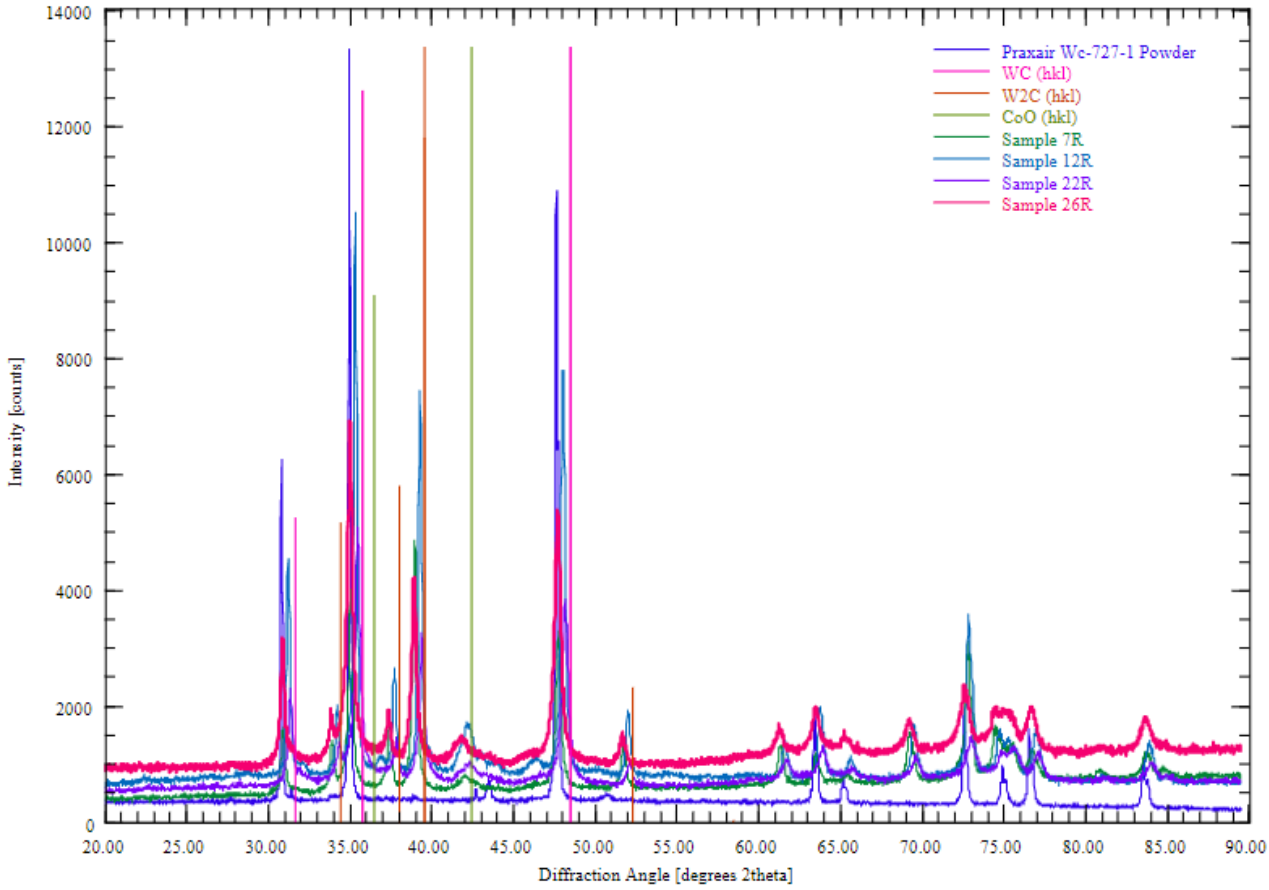

Figure B.14: XRD comparison of Praxair powder to Raster Strategy

The response predicted vs actual table for the cuboid parameter optimisation can be observed in Table B.7.

Table B.7: 20 Run Predicted vs Actual using the Response Surfaces derived from the cuboid parameter optimisation

				Density [g/cm³]					Hardness [HRA]					Cobalt Content [Wt%]				
Power	**Scan Speed**	**Hatch Spacing**	**VED**	**Predicted**	**95% CI Low**	**95% CI High**	**Actual**	**Difference**	**Predicted**	**95% CI Low**	**95% CI High**	**Actual**	**Difference**	**Predicted**	**95% CI Low**	**95% CI High**	**Actual**	**Difference**
191	695	69	133	13.09	12.92	13.26	12.40	5%	58.99	55.46	62.53	44.6	24%	10.00	7.49	12.52	11.67	-17%
200	450	82	180	13.76	13.59	13.94	13.42	3%	72.55	68.53	76.58		100%	8.65	5.7	11.62	9.96	-15%
191	569	90	124	13.26	13.11	13.41	12.62	5%	62.17	59.21	65.14	47.0	24%	9.79	7.44	12.15	11.41	-17%
191	695	69	133	13.09	12.92	13.26	12.49	5%	58.99	55.46	62.53	39.1	34%	10.00	7.49	12.52	11.29	-13%
189	591	51	210	13.36	13.14	13.58	13.05	2%	66.07	61.38	70.77	53.7	19%	8.84	5.58	12.12	10.94	-24%
197	485	55	246	13.74	13.51	13.96	13.47	2%	73.30	68.47	78.14	56.4	23%	8.15	4.67	11.65	10.04	-23%
200	700	90	106	13.08	12.93	13.22	11.92	9%	58.28	55.47	61.11	46.8	20%	10.49	8.22	12.77	12.69	-21%
200	655	50	204	13.37	13.14	13.60	13.02	3%	66.82	61.94	71.71	55.9	16%	9.06	5.73	12.4	9.73	-7%
197	485	55	246	13.74	13.51	13.96	13.54	1%	73.30	68.47	78.14	58.6	20%	8.15	4.67	11.65	9.10	-12%
180	568	69	154	13.23	13.04	13.41	12.91	2%	61.52	57.84	65.19	63.9	-4%	9.35	6.75	11.96	10.72	-15%
180	568	69	154	13.23	13.04	13.41	13.00	2%	61.52	57.84	65.19	47.8	22%	9.35	6.75	11.96	10.36	-11%
189	460	73	187	13.61	13.43	13.79	13.36	2%	69.32	65.35	73.29	52.9	24%	8.64	5.73	11.54	10.31	-19%
181	575	89	118	13.14	12.99	13.30	12.24	7%	58.63	55.84	61.42	43.0	27%	9.96	7.78	12.13	11.37	-14%
180	450	90	148	13.45	13.29	13.62	13.05	3%	64.41	61.13	67.70	51.8	20%	9.2	6.74	11.65	11.09	-21%
184	450	50	273	13.67	13.44	13.90	13.70	0%	71.03	66.03	76.03	47.3	33%	7.99	4.43	11.55	10.57	-32%
180	700	50	171	13.06	12.85	13.27	12.55	4%	58.25	53.33	63.17	55.0	6%	9.66	6.65	12.67	11.27	-17%
199	591	73	155	13.38	13.21	13.56	12.66	5%	66.21	62.47	69.95	45.6	31%	9.32	6.57	12.08	12.65	-36%
180	700	90	95	12.90	12.75	13.04	11.70	9%	51.87	49.29	54.46	45.5	12%	10.8	8.87	12.74	15.23	-41%
191	695	69	133	13.09	12.92	13.26	12.43	5%	58.99	55.46	62.53	43.3	27%	10.00	7.49	12.52	10.64	-6%
191	569	90	124	13.26	13.11	13.41	12.47	6%	62.17	59.21	65.14	49.8	20%	9.79	7.44	12.15	12.18	-24%

B.6. Scanning Strategy Optimisation Results for Section 7.2

The design space for the Scanning Strategy experiments can be found in Figure B.15.

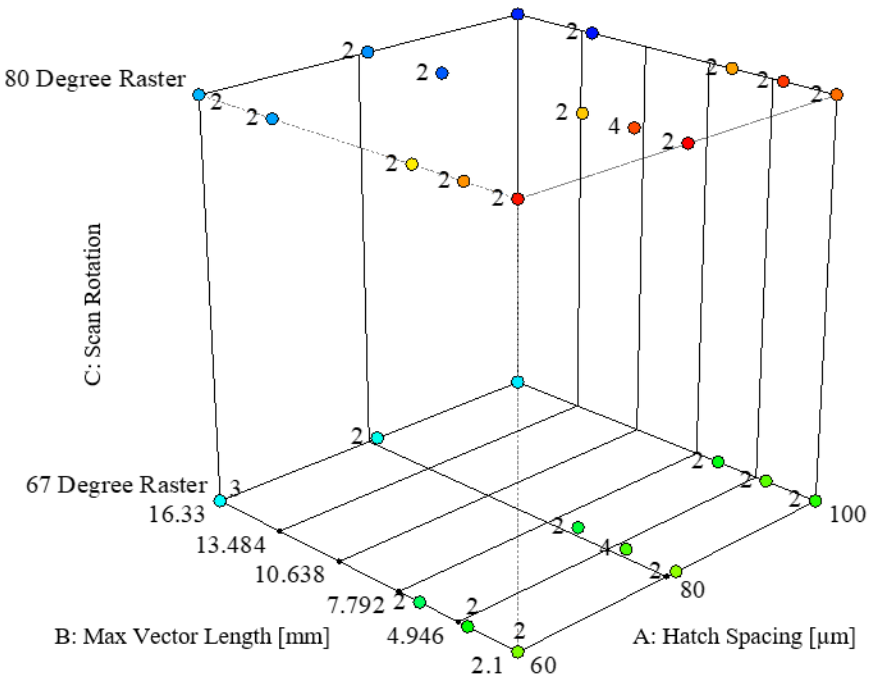

Figure B.15: Design space for the various scanning strategies to determine the effects of scan rotation, vector length, and hatch spacing on density, hardness, and cobalt content.

The summary of the results from Experiment 7.3 can be found in Table B.8. The scanning strategies have been slightly abbreviated to shorten the description from the ones in Table 7.11, Table 7.12, and Table 7.13. 80 Degree Raster corresponds to the parallel raster 80 degree alternating rotation strategy, 80 Degree Diagonal corresponds to the diagonal raster 80 degree alternating rotation strategy, 67 Degree corresponds to the Raster strategy, 67 degree continuous rotation strategy, and the 67 Stripes and 80 Island strategies correspond to those in Table 7.12, and Table 7.13 respectively.

Table B.8: Summary of results for the 57 run scanning strategy experiment

Input Variables			Responses		
Hatch Spacing [µm]	**Max scan vector length [mm]**	**Scan Strategy**	**Density [g/cm³]**	**Average Hardness [HRA]**	**Cobalt Content [wt%]**
80	12.7	80 Degree Raster	Failed		
100	12.7	80 Degree Raster	12.49	51.5±9.0	8.24
100	16.33	80 Degree Diagonal	12.63	58.0±7.4	10.61
60	16.33	80 Degree Diagonal	Failed		
60	16.33	67 Degree	Failed		
80	12.7	80 Degree Raster	12.98	59.4±2.8	9.08
100	12.7	80 Degree Raster	12.55	55.6±8.2	9.45
80	16.33	80 Degree Diagonal	12.93	51.8±3.2	10.68
80	16.33	80 Degree Diagonal	12.96	51.3±12.8	8.4
60	12.7	80 Degree Raster	Failed		
60	16.33	80 Degree Diagonal	Failed		

80	16.33	67 Degree	Failed		
60	16.33	67 Degree	Failed		
100	16.33	67 Degree	12.67	47.1±6.7	8.92
60	16.33	67 Degree	13.09	52.6±13.2	9.01
80	16.33	67 Degree	Failed		
60	12.7	80 Degree Raster	12.89	58.3±5.1	10.12
100	2.1	67 Stripes	12.69		10.77
80	4.25	67 Stripes	13.48	58.2±1.6	9.86
100	6.4	67 Stripes	12.77	54.9±6.2	10.64
80	4.25	67 Stripes	13.51		11.11
60	4.25	67 Stripes	Failed		
60	6.4	67 Stripes	13.74	60.6±3.5	9.49
60	6.4	67 Stripes	13.76	63.6±6.7	9.49
80	6.4	67 Stripes	13.31	63.7±3.3	10.21
80	6.4	67 Stripes	13.27	60.6±3.5	9.8
100	4.25	67 Stripes	12.96	58.2±8.3	10.15
100	6.4	67 Stripes	12.79	54.6±5.2	10.04
60	4.25	67 Stripes	Failed		
80	4.25	67 Stripes	13.11	58.7±4.6	10.31
100	2.1	67 Stripes	Failed		
60	2.1	67 Stripes	Failed		
80	4.25	67 Stripes	13.47		8.03
100	4.25	67 Stripes	12.93		11.3
80	2.1	67 Stripes	Failed		
60	2.1	67 Stripes	Failed		
80	2.1	67 Stripes	Failed		
100	2.1	80 Island	13.30		7.58
80	4.25	80 Island	13.51		6.18
100	6.4	80 Island	12.84	58.0±5.9	9.07
80	4.25	80 Island	13.48	56.0±5.4	9.04
60	4.25	80 Island	13.92		9.88
60	6.4	80 Island	13.70	64.6±5.4	9.71
60	6.4	80 Island	13.67	52.5±6.9	5.49
80	6.4	80 Island	Failed		
80	6.4	80 Island	Failed		
100	4.25	80 Island	13.15		7.19
100	6.4	80 Island	12.92		6.78
60	4.25	80 Island	Failed		
80	4.25	80 Island	Failed		
100	2.1	80 Island	Failed		
60	2.1	80 Island	Failed		
80	4.25	80 Island	Failed		
100	4.25	80 Island	Failed		
80	2.1	80 Island	Failed		
60	2.1	80 Island	Failed		
80	2.1	80 Island	Failed		

B.7. Verification Cutting Test Results for Section 8.2

The before and after SEM images of the CNMA cutting edges can be observed in Table B.9. The flank wear images of the inserts after cutting can be observed in Table B.10.

Table B.9: SEM Images of the CNMA cutting edges before and after cutting tests

Printed CNMA 1 – Edge 1 before cutting at 250 RPM	Printed CNMA 1 – Edge 1 after cutting at 250 RPM
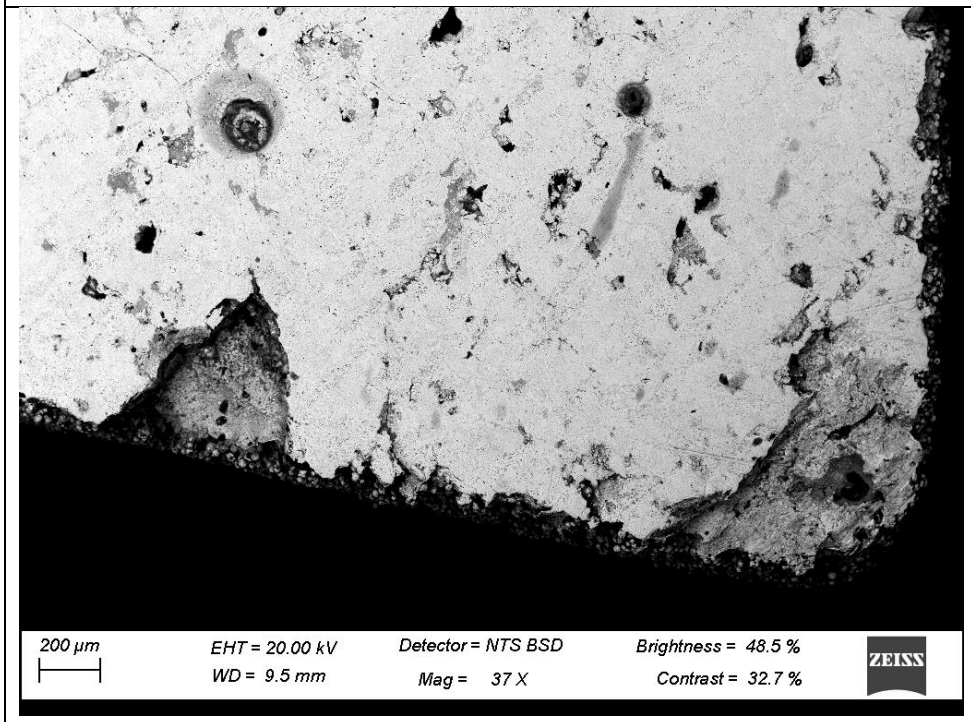	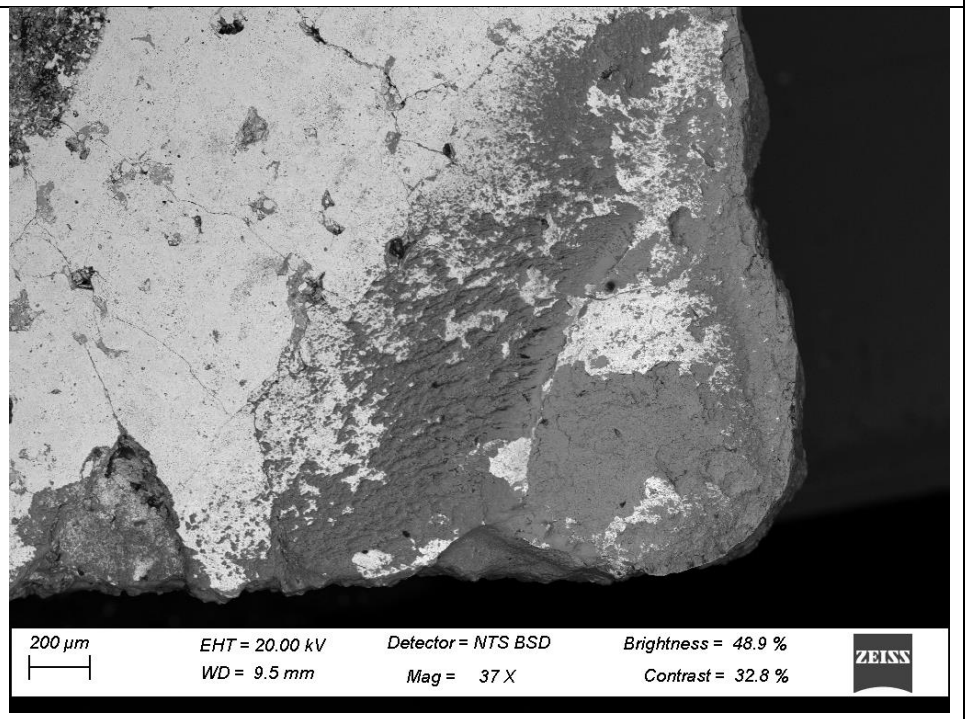

Printed CNMA 1 – Edge 2 before cutting at 355 RPM	Printed CNMA 1 – Edge 2 after cutting at 355 RPM
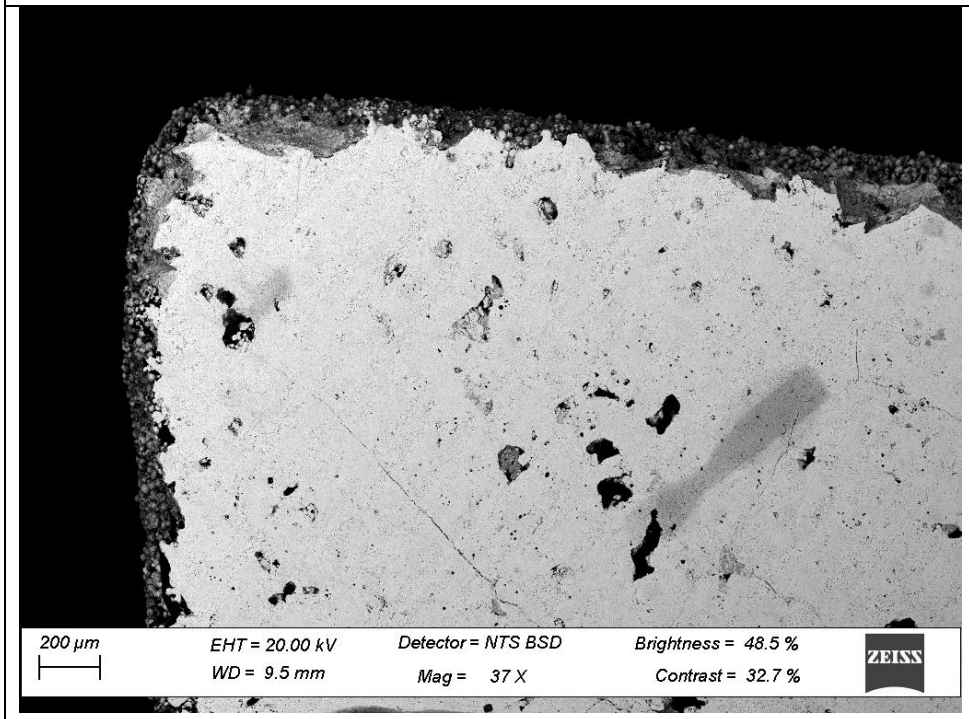	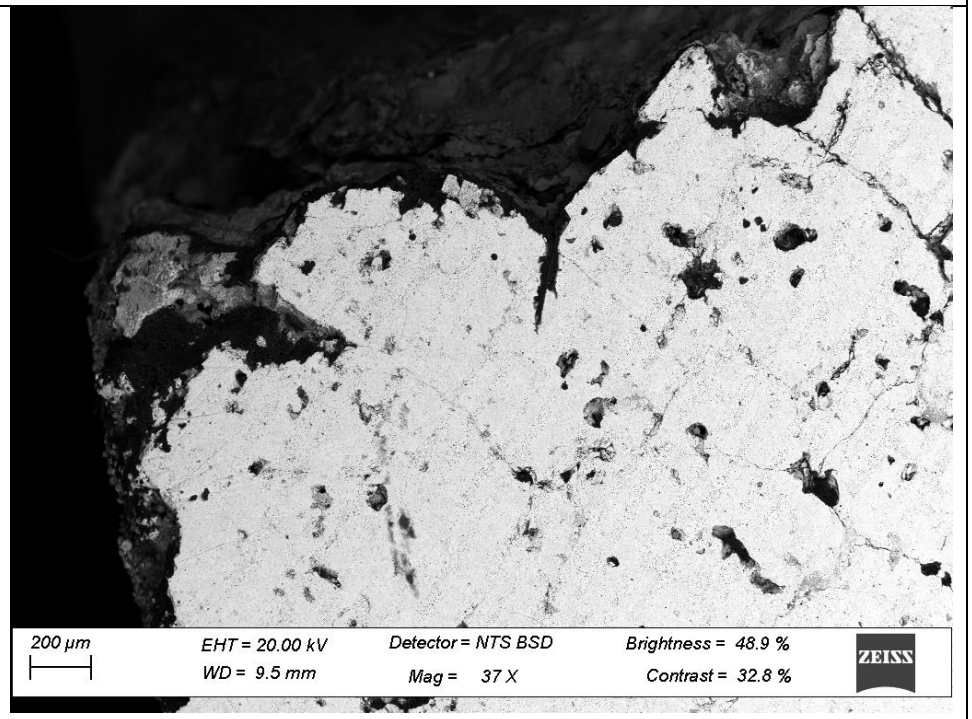

Printed CNMA 2 – Edge 1 before cutting at 250 RPM	Printed CNMA 2 – Edge 1 after cutting at 250 RPM
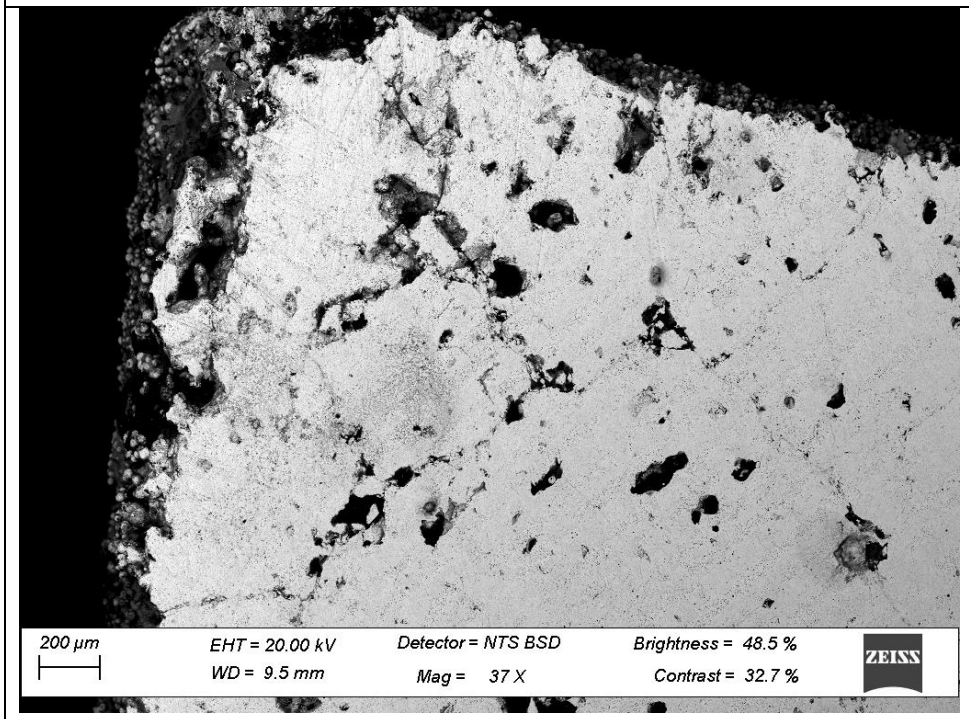	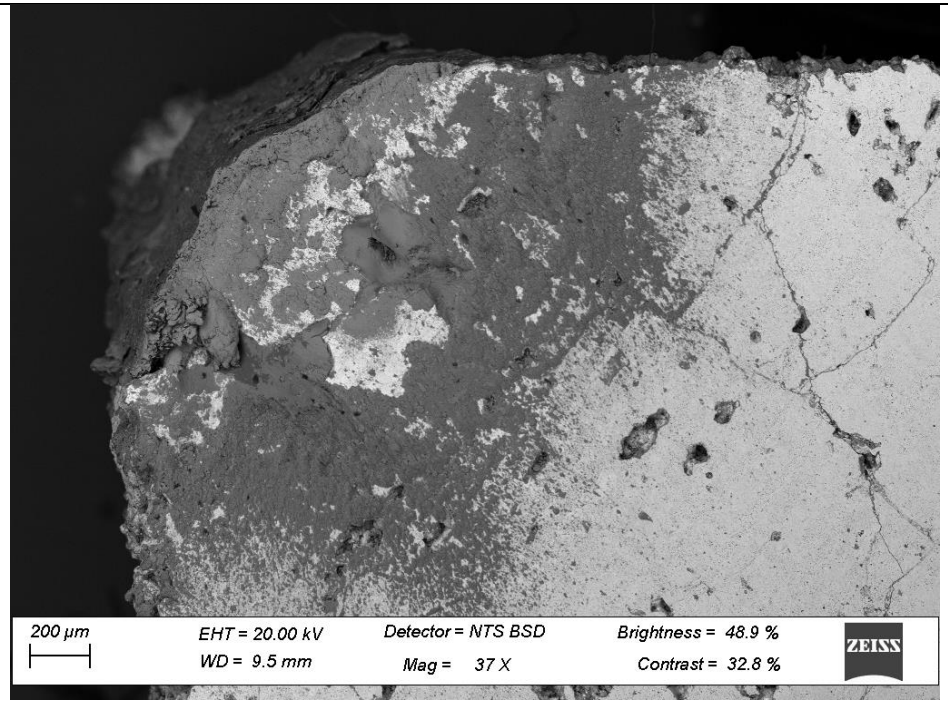

Printed CNMA 2 – Edge 2 before cutting at 355 RPM	Printed CNMA 2 – Edge 2 after cutting at 355 RPM
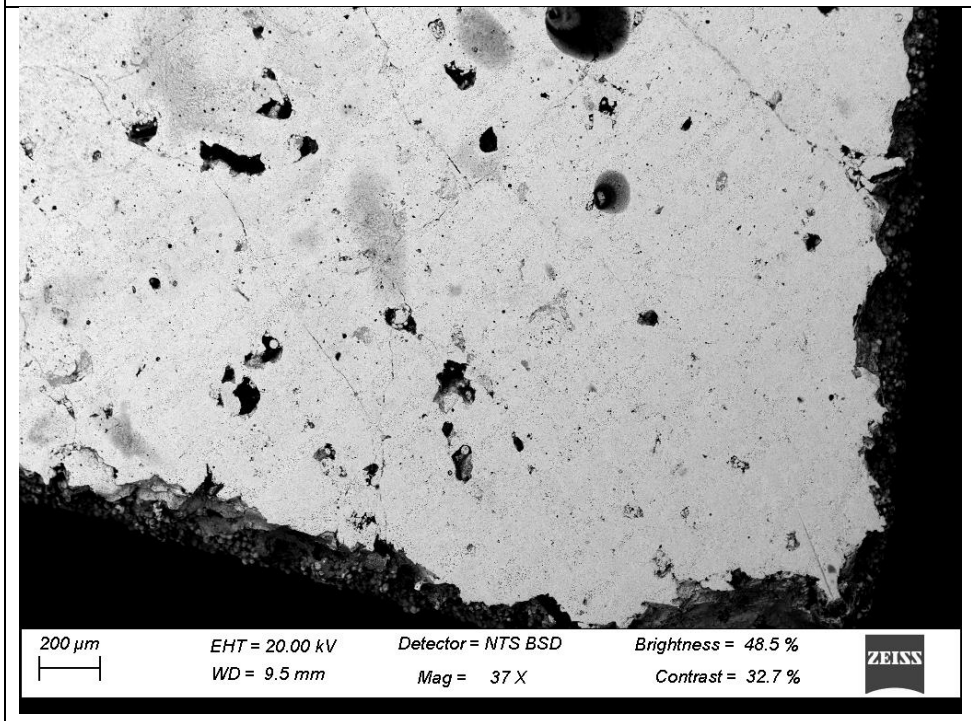	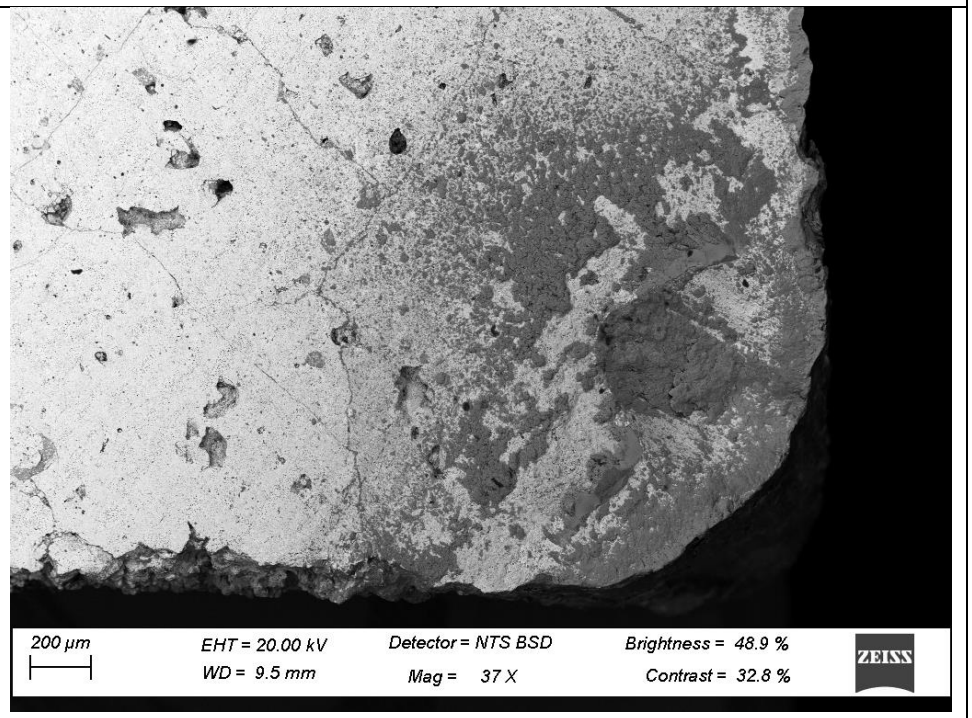

Printed CNMA 3 – Edge 1 before cutting at 250 RPM	Printed CNMA 3 – Edge 1 after cutting at 250 RPM
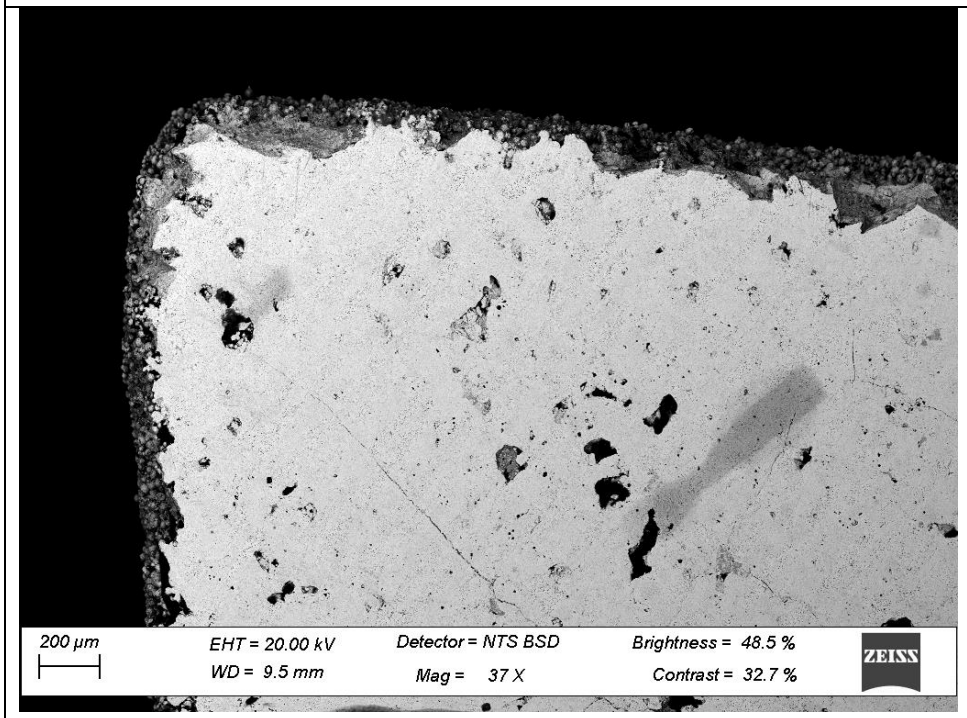	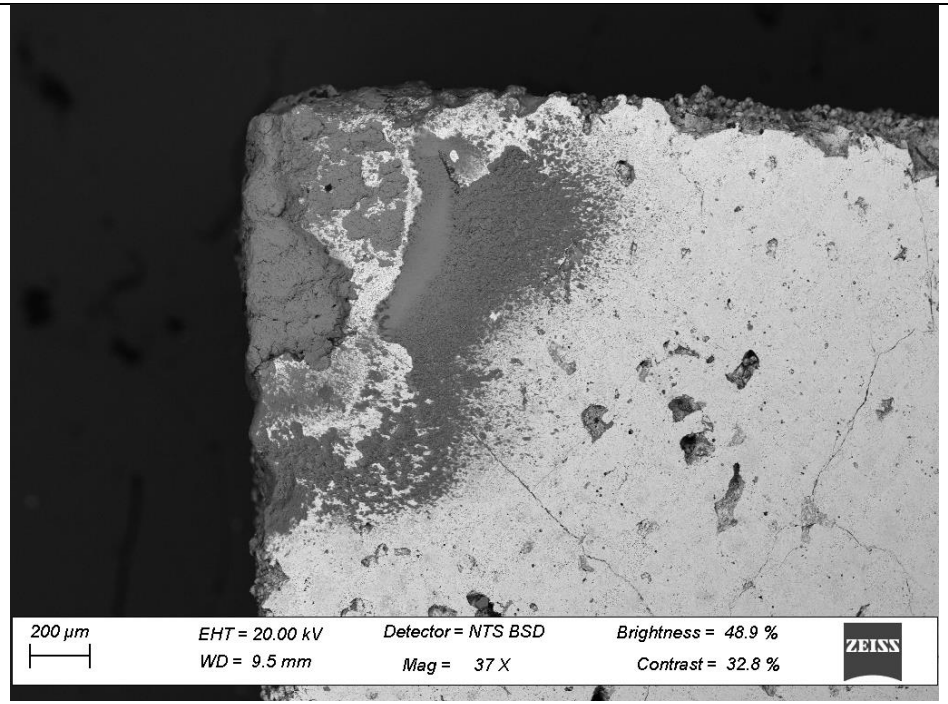

Printed CNMA 3 – Edge 2 before cutting at 355 RPM	Printed CNMA 3 – Edge 2 after cutting at 355 RPM
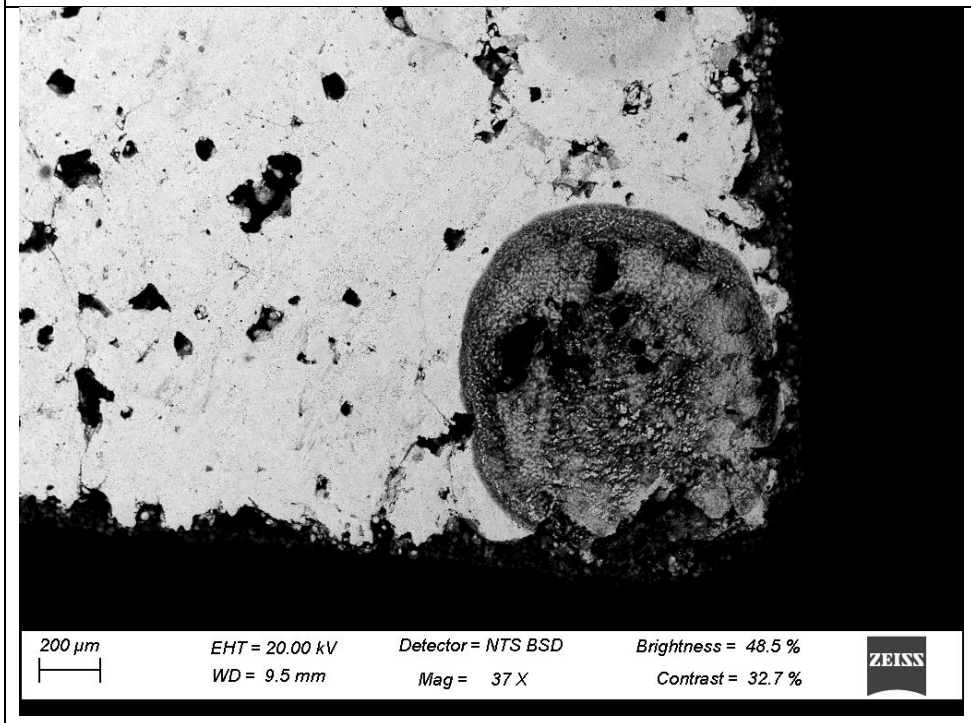	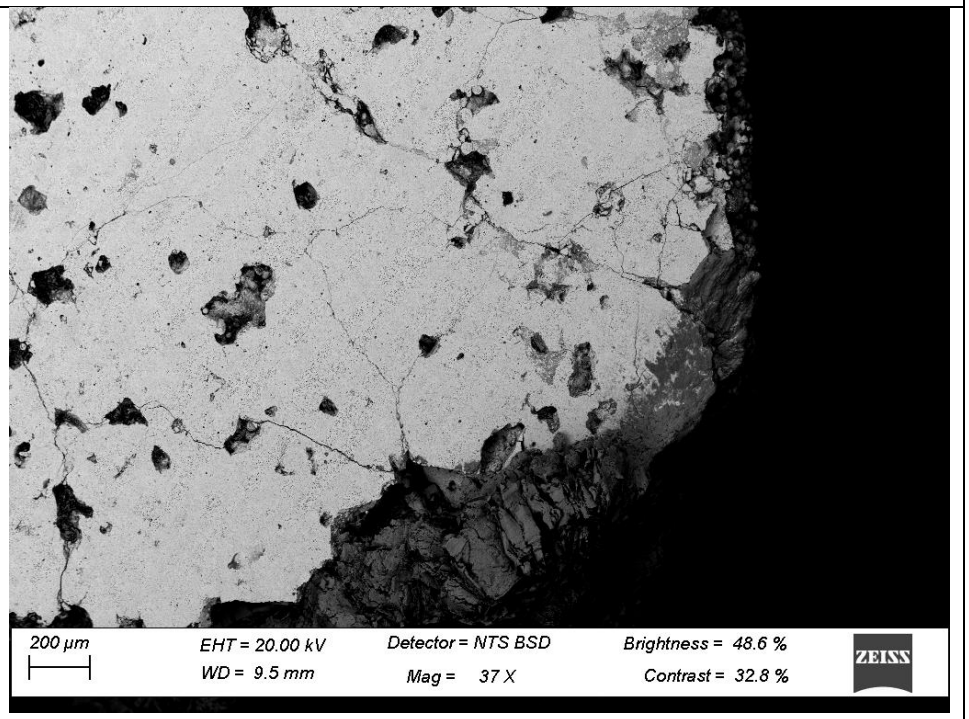

Printed CNMA 4 – Edge 1 before cutting at 250 RPM	Printed CNMA 4 – Edge 1 after cutting at 250 RPM
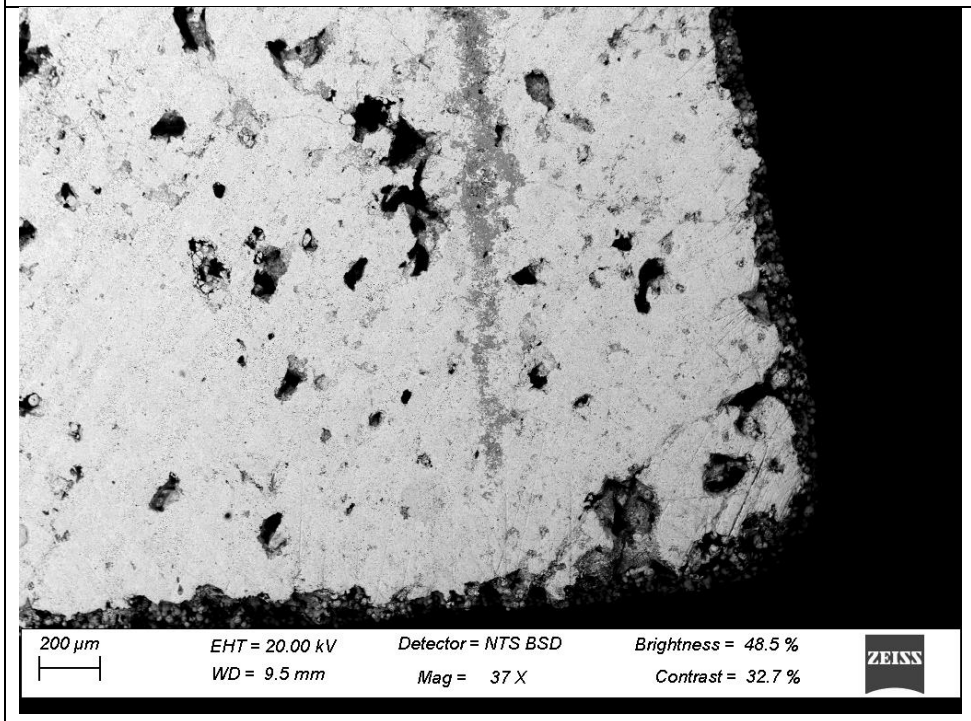	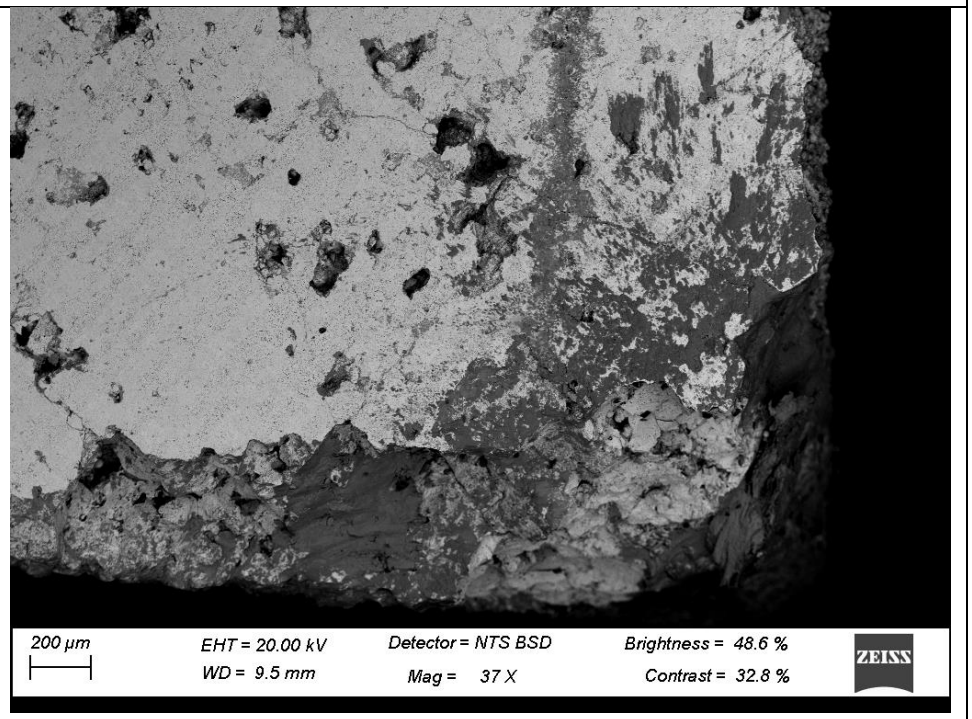

Printed CNMA 4 – Edge 2 before cutting at 355 RPM	Printed CNMA 4 – Edge 2 after cutting at 355 RPM
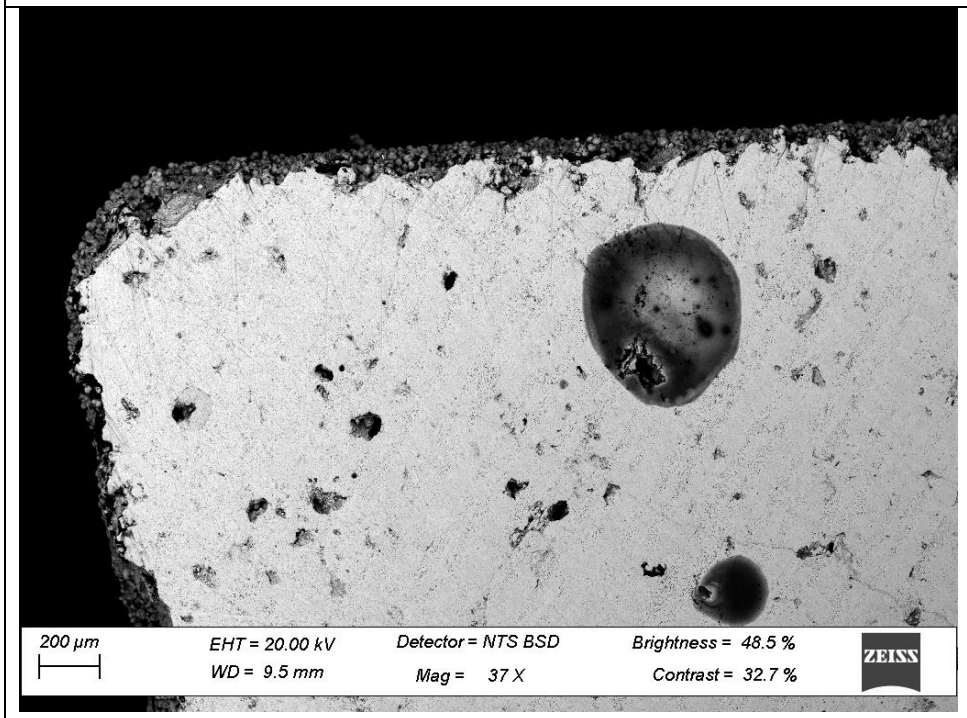	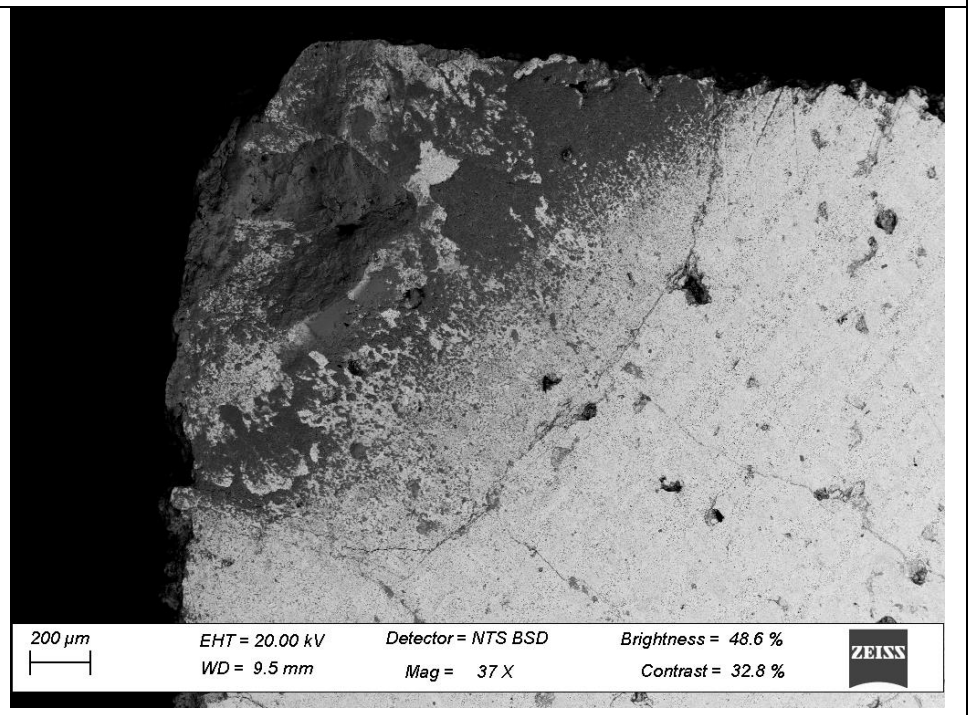

Mitsubishi CNMA 1 – Edge 1 after cutting at 255 RPM	Mitsubishi CNMA 1 – Edge 2 after cutting at 355 RPM
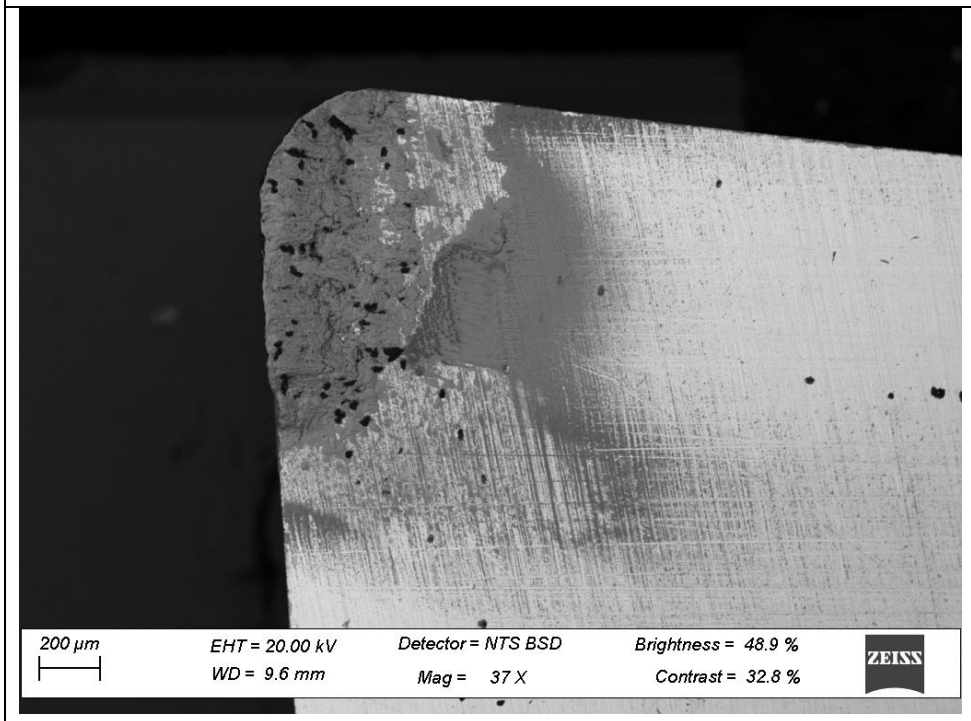	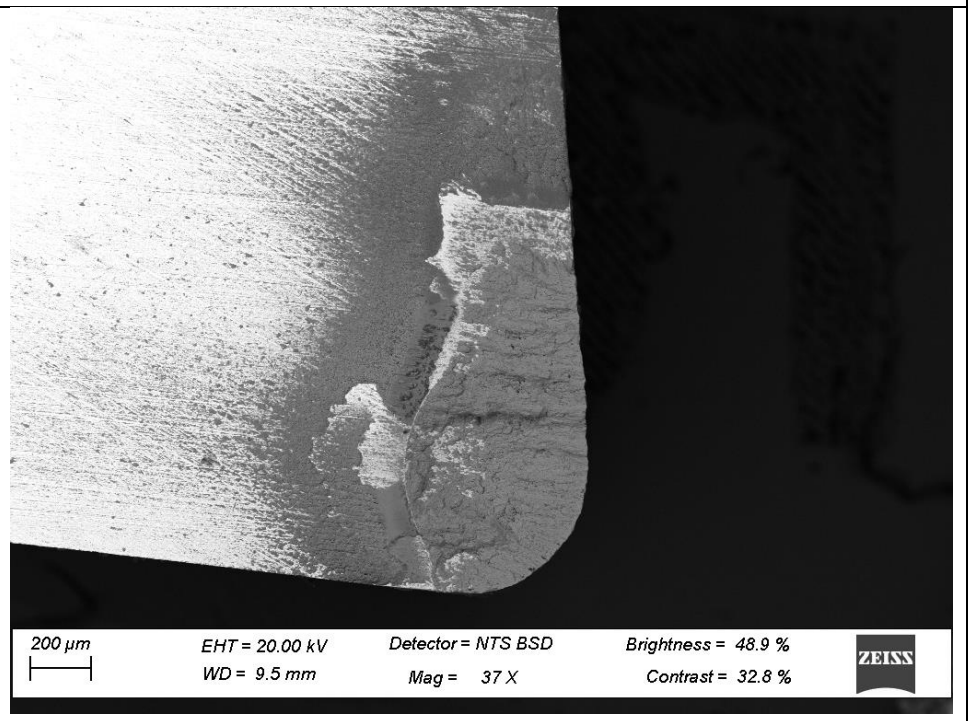

Mitsubishi CNMA 2 – Edge 1 after cutting at 255 RPM	Mitsubishi CNMA 2 – Edge 2 after cutting at 355 RPM
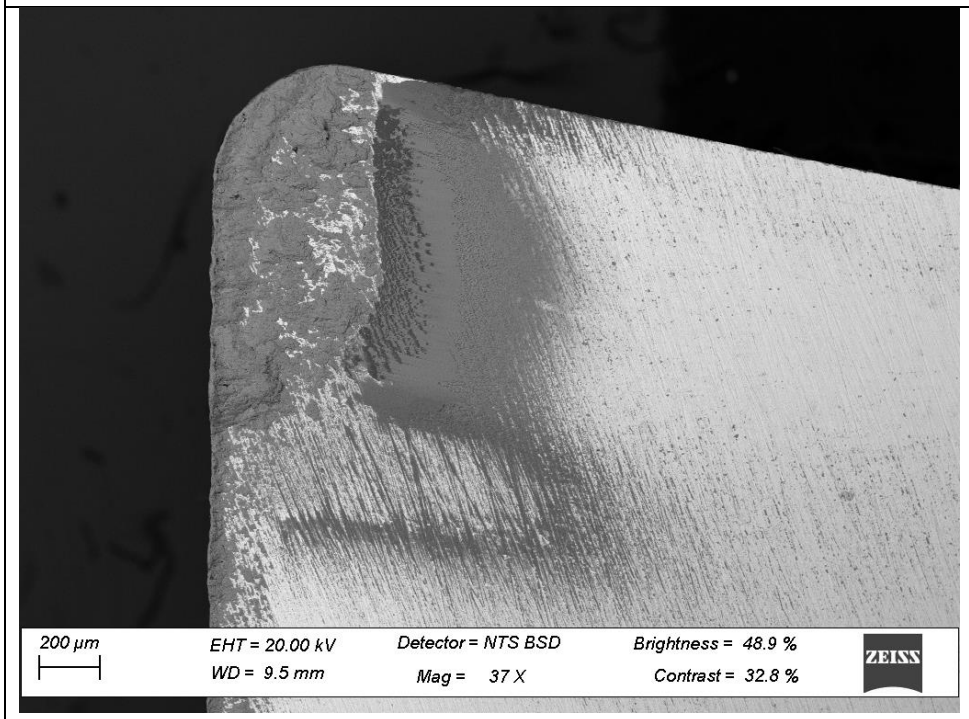	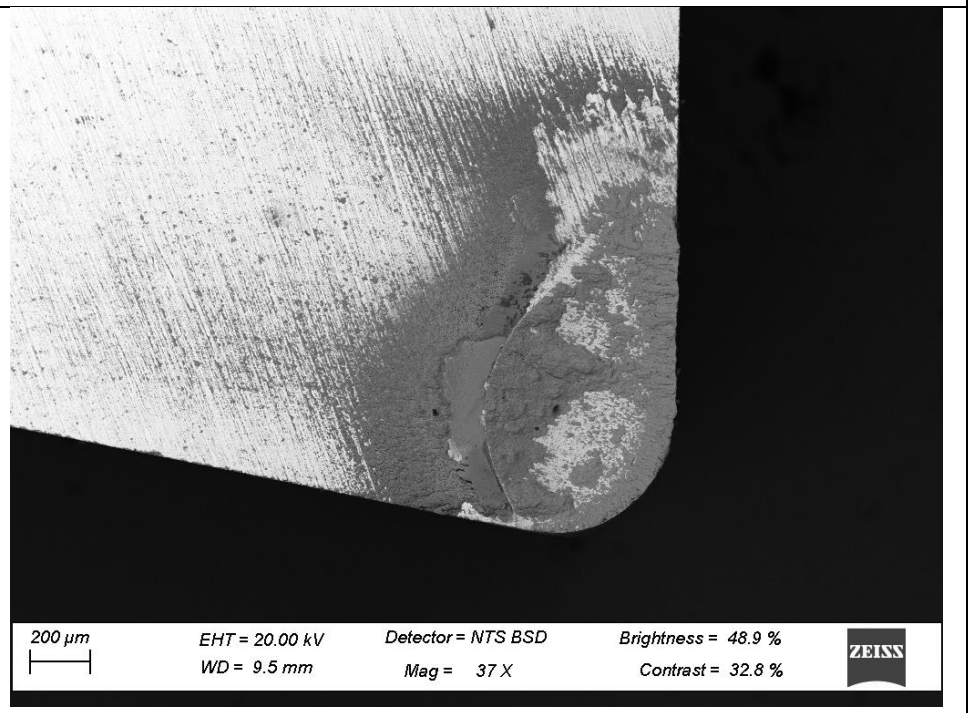

Table B.10: Optical microscope images of the CNMA cutting flanks after cutting tests

Printed CNMA 1 – Flank 1 after cutting at 250 RPM
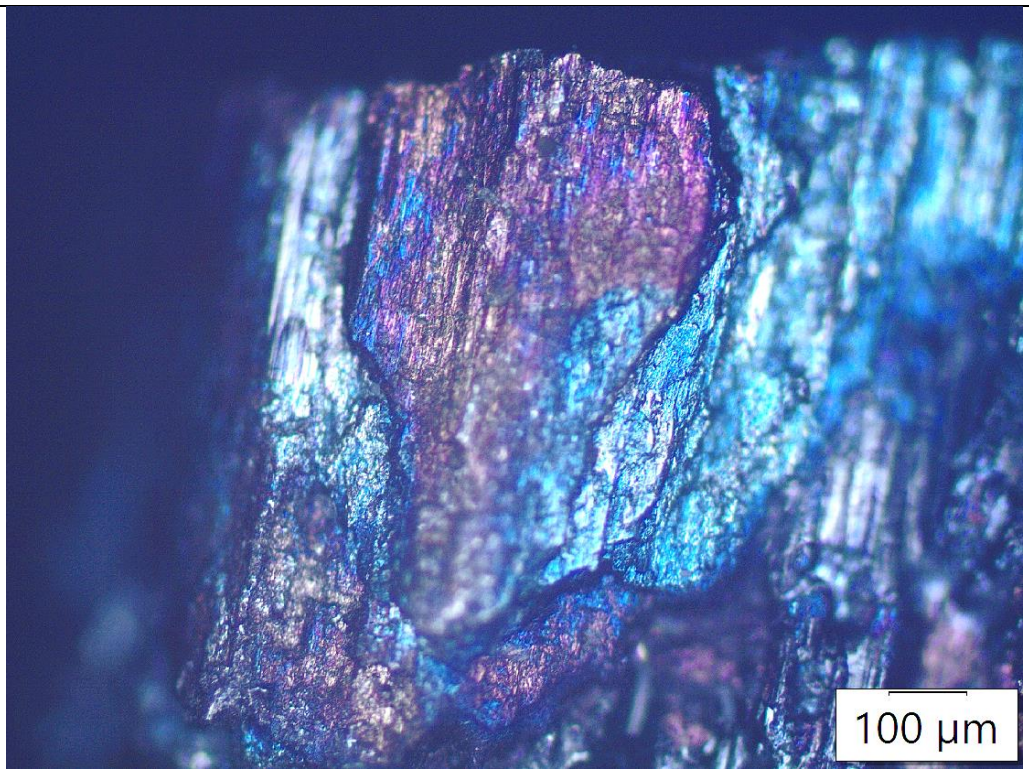
Printed CNMA 1 – Flank 2 after cutting at 355 RPM
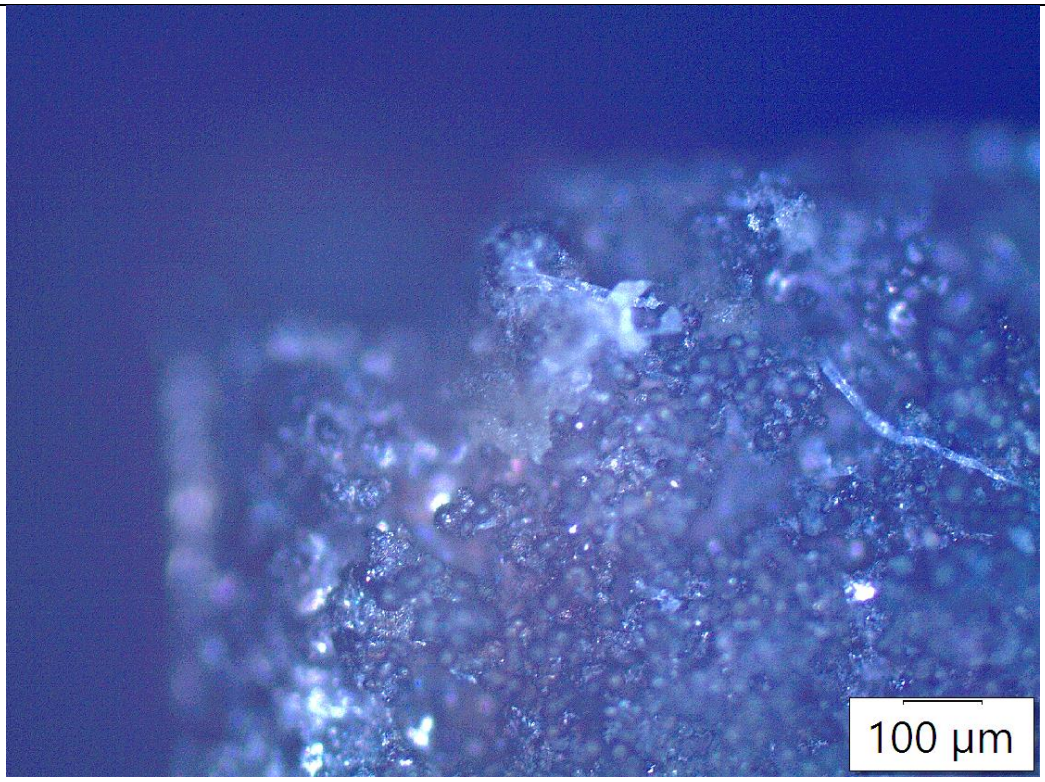

Printed CNMA 2 – Flank 1 after cutting at 250 RPM
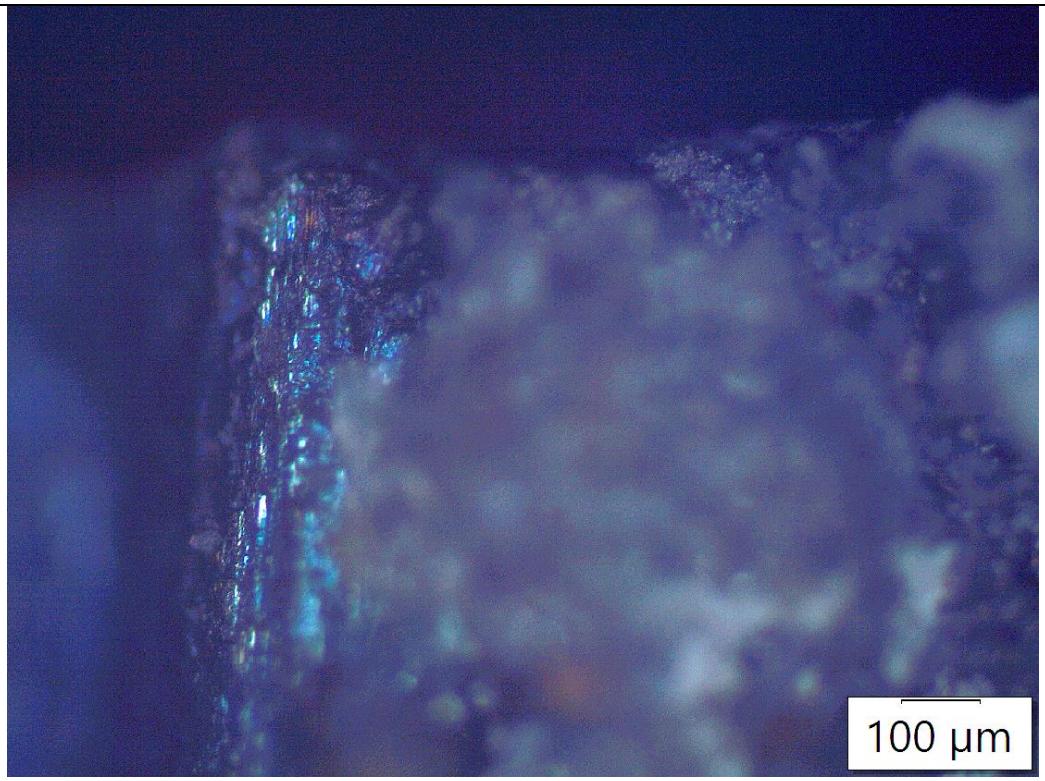
Printed CNMA 2 – Flank 2 after cutting at 355 RPM
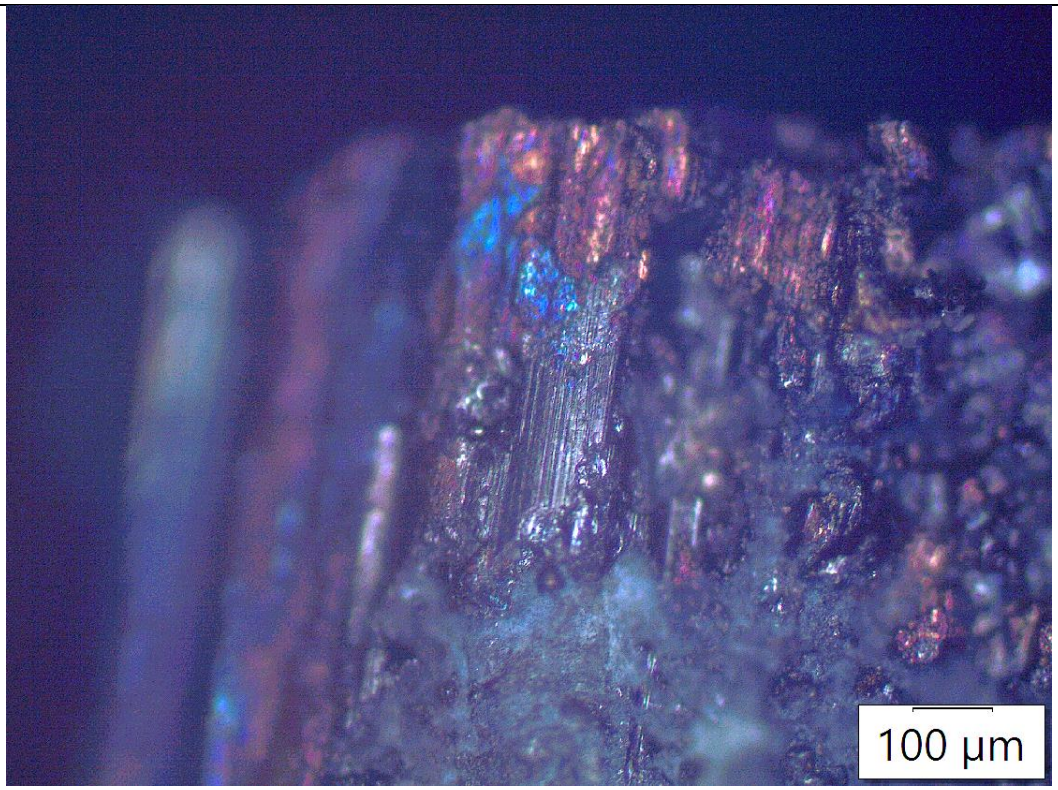

Printed CNMA 3 – Flank 1 after cutting at 250 RPM
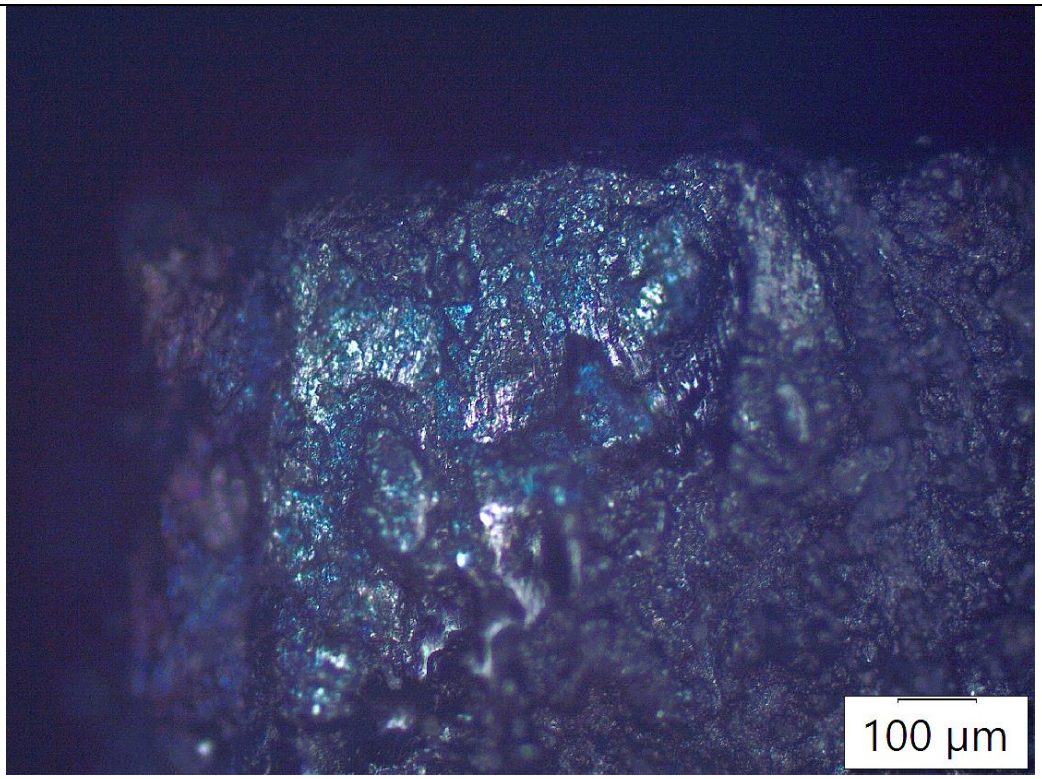
Printed CNMA 3 – Flank 2 after cutting at 355 RPM
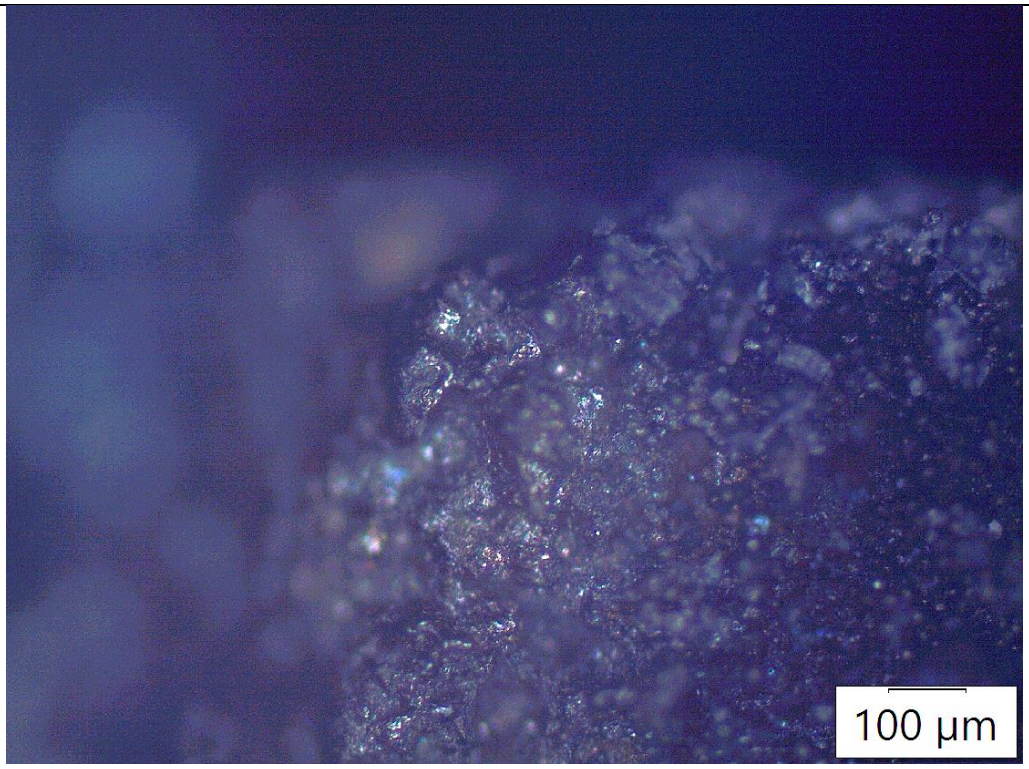

Printed CNMA 4 – Flank 1 after cutting at 250 RPM

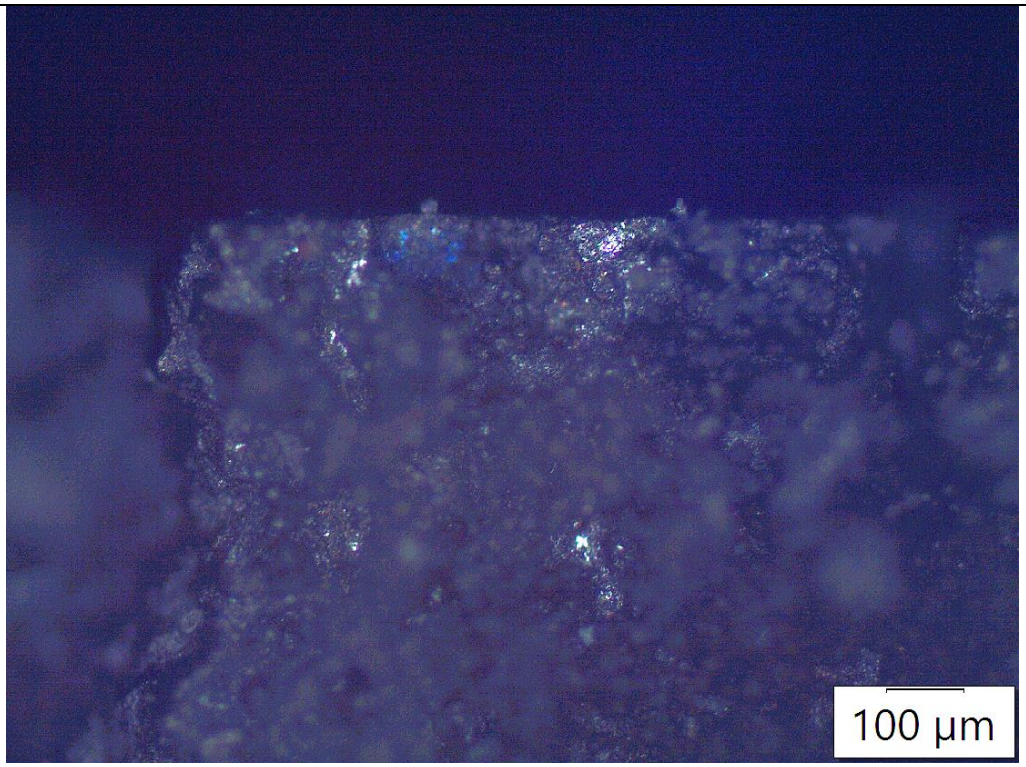

Printed CNMA 4 – Flank 2 after cutting at 355 RPM

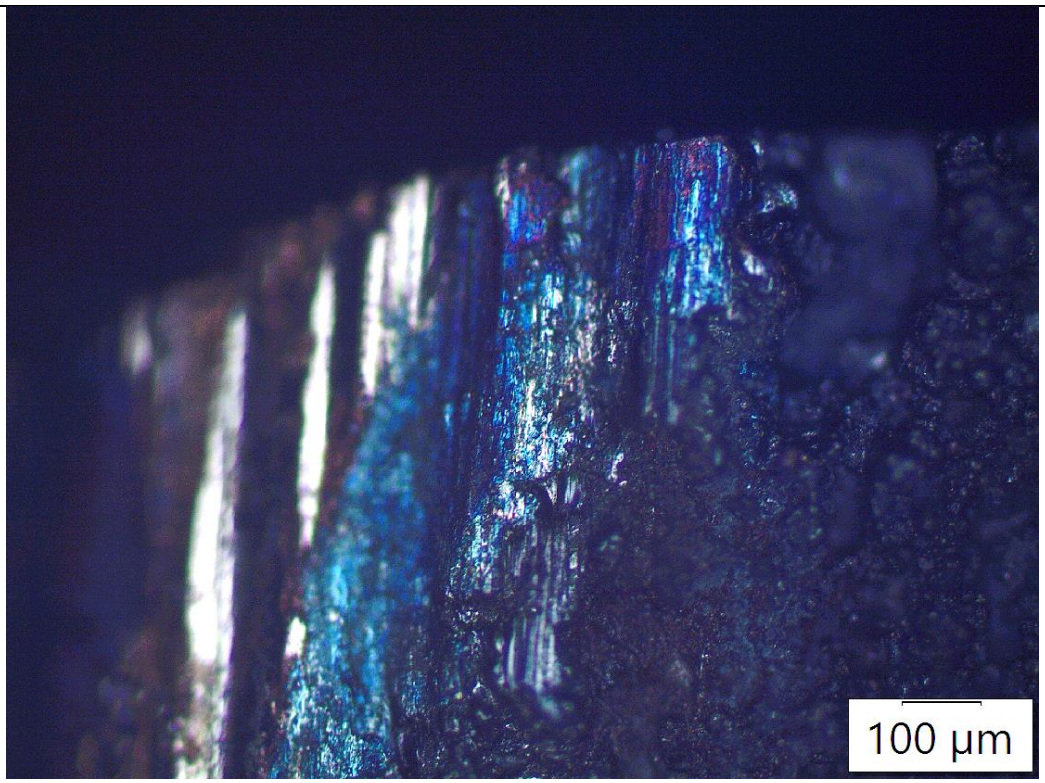

Mitsubishi CNMA 1 – Flank 1 after cutting at 250 RPM

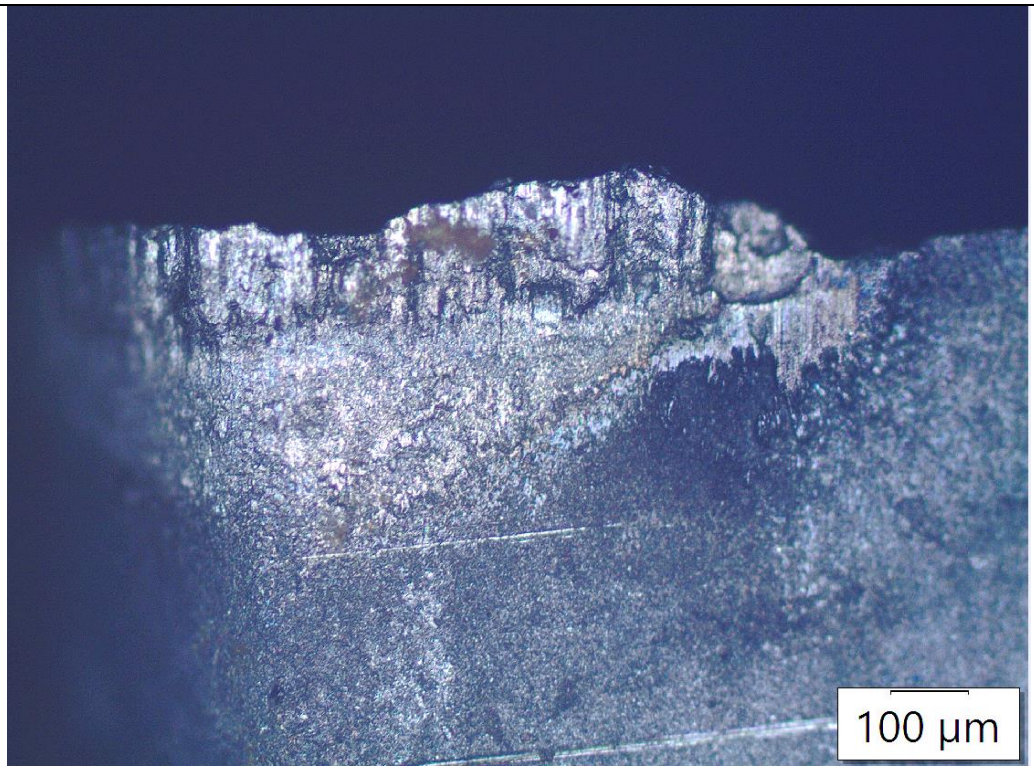

Mitsubishi CNMA 1 – Flank 2 after cutting at 355 RPM

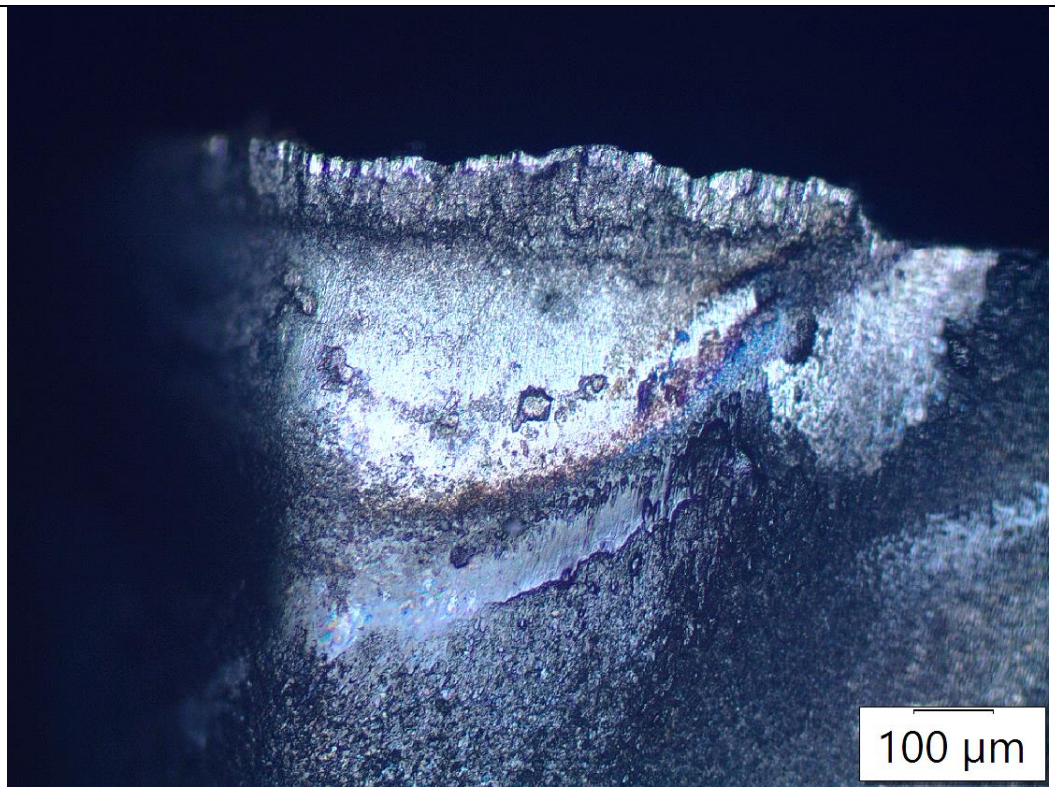

Mitsubishi CNMA 2 – Flank 1 after cutting at 250 RPM

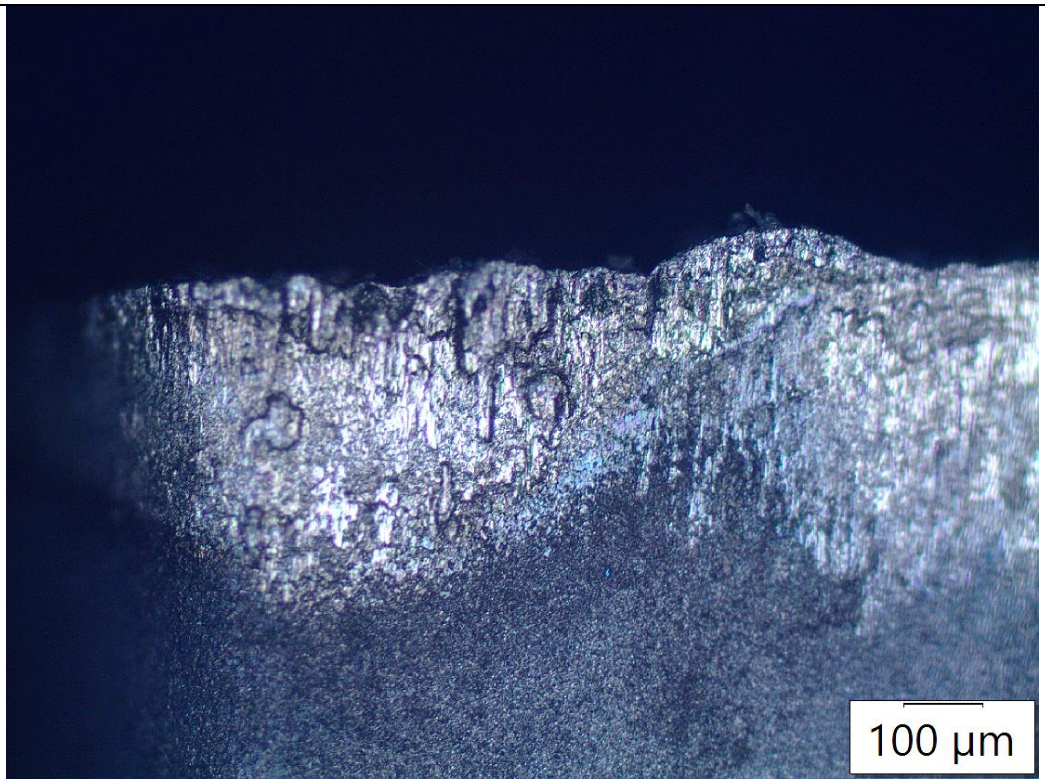

Mitsubishi CNMA 2 – Flank 2 after cutting at 355 RPM